Bio-inspired artificial synapse with chemically mediated intercompartment communication for single molecule cell-synthetic cell interaction studies

A thesis submitted for the degree of Doctor of Philosophy

at the University of Cardiff

by

Aspasia Zoupa

January 2024

Cardiff University
School of Pharmacy and Pharmaceutical Sciences

Declaration

I declare that this thesis, entitled "Bio-inspired artificial synapse with chemically mediated intercompartment communication for single molecule cell-synthetic cell interaction studies", is the result of my own research except where otherwise stated.

Aspasia Zoupa

January 2024

Abstract

Direct transient or stable cell-cell interactions drive numerous physiological processes critical to the maintenance and function of multicellular organisms. Yet, studying cell-cell associations is challenging given the teeming activity of biological membranes. Existing biomimetic models entail structural constraints incapable of encapsulating the dynamic nature of intermembrane interactions.

Inspired by direct transient intermembrane communication, where information is relayed through ligand-receptor engagement, we constructed a double membrane system with a synapse-like architecture. This bio-inspired model is comprised of two artificial lipid membranes, a droplet interface bilayer (DIB), and an encapsulated giant unilamellar vesicle (GUV), interlinked by cholesterol-tethered hybridized DNA complementary strands. The complementary single DNA strands are end-cholesterol modified for membrane integration and internally labelled for single molecule tracking.

The trans-synaptic DNA-mediated coupling is characterized by single molecule Förster Resonant Energy Transfer (smFRET) measurements and diffusion coefficient (D) estimation. Chemical signal communication across interconnected bilayers is instigated by concentration gradient-dependent content (ion and ATP) flow mediated via protein channels (aHL nanopores) in both DIB and GUV membranes. Elicited vesicular biochemical responses, including initiation of actin filament growth and Ca^{2+}-dependent change in fluorescence intensity, are measured by TIRF microscopy.

This solid artificial system is expanded to a biohybrid version by tethering individual living cells to the droplet membrane via DIB- anchored integrin-targeting ligands. Artificial membrane-plasma membrane coupling is characterized by morphodynamics analysis, including Kymography and ADAPT analysis. This dual membrane system with synaptic-like intermembrane space

constitutes a novel platform for studying self-organisation of mobile, paired cleft components, inter-membrane signalling, and trans-synaptic adhesion dynamics with single molecule sensitivity.

Both artificial and biohybrid systems are amenable to biomolecular constituent and multicomponent ligand integration, demonstrating this model's potentiality to interrogate fundamental membrane processes and multifaceted cellular responses. This will increase understanding of basic membrane dynamics and guide tool development for synthetic biology, biotechnology applications and next-generation cell-based therapeutic approaches.

List of Symbols and Abbreviations

AC	Alternate current
ADAPT	Automated detection and analysis of protrusions
ADP	Adenosine di-phosphate
APCs	Antigen-presenting cells
ATP	Adenosine triphosphate
Ca^{2+}	Calcium
CCD	Charge-coupled-device camera
D	Diffusion coefficient
dH_2O	Distilled water
DHB	Droplet on hydrogel bilayer
DIB	Droplet interface bilayer
DMEM	Dulbecco's Modified Eagle Medium
DMSO	Dimethyl Sulfoxide
DOPC	1,2-dioleoyl-sn-glycero-3-phosphocholine
DOPG	1,2-dioleoyl-sn-glycero-3-phospho-(1'-rac-glycerol)
DOTAP	1,2-dioleoyl-sn-glycero-3-[phospho-rac-(1-glycerol)]
DPhPC	1,2-diphytanoyl-sn-glycero-3-phosphocholine
dsDNA	Double-stranded deoxyribonucleic acid
ECM	Extracellular matrix
EPT	Emulsion Phase Transfer
ER	Endoplasmic reticulum
ESI	Electron spray ionization
F-actin	Filamentous-actin
FBS	Fetal Bovine Serum
FRAP	Fluorescence recovery after photobleaching
G-actin	Globular-actin

Gal	Galactose
GalNAc	N-acetylgalactosamine
GUV	Giant unilamellar vesicle
Glc	Glucose
HBSS	Hank's balanced salt solution
HEPES	4-(2-hydroxyethyl)-1-piperazineethanesulfonic acid
HPLC	High-performance liquid chromatography
IR	Infrared
IS	Immunological synapse
ITO	Indium-tin oxide
LOI	Line of interest
LUV	Large unilamellar vesicle
Ld	Liquid disordered
Lo	Liquid ordered
MALDI	Matrix assisted laser desorption ionization
Mg^{2+}	Magnesium
MHCs	Major histocompatibility complexes
MLV	Multilamellar lipid vesicle
MS	Mass spectroscopy
MSD	Mean square displacement
N_2	Nitrogen
NA	Numerical aperture
PBS	Phosphate-buffered saline
PDMS	Polydimethylsiloxane
PE	Phosphatidylethanolamine
PEG	Polyethylene glycol
PEO	Polyethylene oxide
pH	Hydrogen ion concentration: pH = -log [H+]
pKa	pKa = -log [Ka]
PM	Plasma membrane
PMMA	Poly(methyl methacrylate)

PS	Phosphatidylserine
RGD	Arginine-Glycine-Aspartic
ROI	Region of interest
RP	Reversed phase
r.p.m	Revolutions per minute
s	Seconds
SLB	Supported lipid bilayer
smFRET	Single-molecule Förster Resonant Energy Transfer
SUV	Small unilamellar vesicle
So	Solid-ordered
ssDNA	Single-stranded deoxyribonucleic acid
SiOH	Silanol group
3D	Three-dimensional
TOF	Time-of-flight
2D	Two-dimensional
TIFF	Tagged Image File Format
TIRF	Total internal reflection fluorescence
Tm	Melting temperature
UV	Ultraviolet

Acknowledgements

Completion of a successful PhD without great leadership and guidance is a misconception. I would like to express my sincere gratitude to Dr Oliver Castell, who contributed immensely to the enriching PhD experience. First and foremost, he gave me the opportunity to conduct this innovative research in his lab and reinforced the significance of professional development and collaboration. He afforded me the freedom and independence to pursue my own ideas and implement them, for which I have been appreciative.

I am also very much indebted to him not only for the in-depth discussions and the insightful comments, but especially for his immeasurable support and understanding during a very challenging period in my life that could have thwarted the continuation of my PhD studies.

I am extremely grateful to Dr David Jamieson for the hours spent aligning lasers and performing all fluorescence/TIRF imaging, as the unusual conditions of conducting my PhD work forestalled my hands-on training on TIRFM. I also thank him for always being willing to help with any practical issues that came up and offering suggestions and directions for possible courses of action.

My other special thanks must go to Prof. Arwyn Jones for offering his knowledge, time, and connections to discuss and solve problems on the spot. He cheerfully contributed to this project with the A549 cell line, enabling us to construct the biohybrid model, and requested his postdoc, Dr Jared Whitehead, to culture the cells, who in turn willingly and readily did it under very time-pressing circumstances. I owe many thanks to him as well for offering his expertise.

In terms of the work done in Chapter 2 of this thesis, I want to extend my sincerest thanks to Dr. Zili Sideratou and Dr. Dimitris Tsiourvas at Demokritos Research Institute in Athens, Greece, for

hosting me in their lab and granting me access to their equipment, enabling me to perform GUV preparation experiments using the emulsion phase transfer method during the period of imposed lockdowns and travel restrictions. I really appreciate your unrelenting support, warm hospitality, and your desire to help me in any way possible.

I have to give enormous thanks to Dr Alex Landen, Chemistry Department, Cardiff University, who voluntarily provided his skills and proficiency in the HPLC equipment and persistently instructed me on how to operate it, a valuable tool for purification of peptide synthesis presented in Chapter 6.

I would also like to express my appreciation to Thomas McCloy, who voluntarily applied his knowledge in Physics to make the instruments for the electroformation procedure in the lab fully operational. I will never forget your kindness and generosity to assist in any way possible.

I must also express thanks to the senior technician Mr Peter Iafrate for exclusively conducting the matrix-assisted laser desorption ionization time of flight (MALDI-TOF) mass spectrometer procedure and providing me with the data analysis in a flash.

Most importantly, I want to express my unconditional thanks to my husband Vagelis Foskolos, who has been continuously supportive through every step of this journey, even when times were the darkest. He listened to me, endured me, and encouraged me in hopeless times.

Above all, I express my thanks and gratitude to Jesus Christ, who opened and kept this door open so that I could complete this work, despite all circumstances being against.

Publications

The work detailed in Chapters 3–7 of this thesis has contributed to the Biophysical Society Conference Poster and Abstract publication, presented in the Appendix and an unpublished manuscript at the point of submission:

Zoupa, A., Jamieson, W.D., Whitehead, J., Jones, A.T., Castell, O.K. (2024, February 10-14*). Bio-inspired artificial synapse with chemically mediated intercompartment communication for single molecule cell-synthetic cell interaction studies* [Conference presentation abstract]. Sixty-eighth annual convention of the Biophysical Society meeting, Philadelphia, Pennsylvania, United States. Biophysical Journal, Volume 123, Issue 3, 188a

Zoupa, A., Jamieson, W.D., Whitehead, J., Jones, A.T., Castell, O.K. (2025). *Artificial synapses for membrane-membrane and artificial cell communication and single molecule study of live-artificial cell interactions.* Paper is being finalized at point of submission.

Table of Contents

Chapter 1: General Introduction

1.1 Introduction

1.1.1 Lipid Bilayer

The lipid bilayer as a universal component of all cell membranes delineates the boundaries of the cell and its compartments needed to perform well-defined functions [1]. Although all cells are comprised of an outer plasma membrane, unlike prokaryotes, eukaryotic cells also possess internal membranes encasing a number of macromolecular structures ranging from the endoplasmic reticulum (ER), the nuclear membrane, the Golgi apparatus, and lysosomes [2].

The functions performed by internal and plasma membranes are implemented through the concerted action of the lipid bilayer and transmembrane and anchored proteins via sophisticated mechanisms [3-6].

The lipid bilayer as a protective barrier around the cell and its organelles, impedes the influx of foreign materials and the leakage of cellular contents [7]. However, over the years it has become clear that the lipid bilayer apart from being identified as a barrier, also serves as an interface through which the signal transduction machinery operates [8]. Bilayer's structural components affect its shape and contribute to diverse cellular functions, such as ion and metabolite transport and communication and regulation processes, allowing cells to selectively interact with their environment [9].

Membrane structure is generally described by the “fluid-mosaic” model proposed by Singer and Nicolson in 1972. The term “fluid” refers to the lipid bilayer conformation of the membrane whereas “mosaic” to the proteins ingrained into the lipids’ framework. Proteins can either reside on the surface of leaflets or be embedded in the bilayer. The former, known as peripheral proteins, when located loosely on the surface layer, or dubbed lipid-anchored/integral proteins, when covalently bind to membrane lipids (Fig. 1) [10].

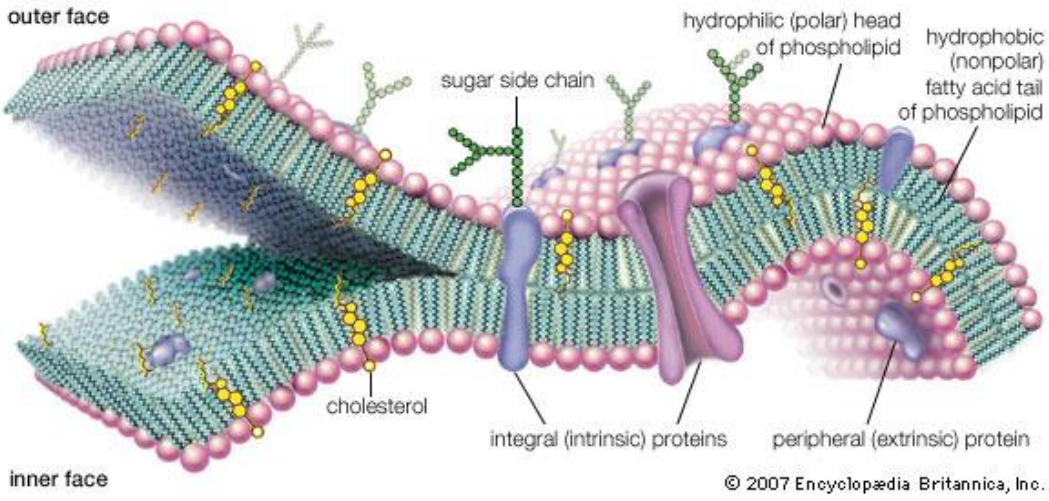

Figure 1.1- Key features of the cell membrane include the lipid bilayer interspersed with ingrained and loosely surface-attached proteins*. Image taken from [11].*

Since the elucidation of this basic membrane structure, it has come to the researchers’ realization that this dynamic platform along with scaffolding molecules and molecular complexes separates and links both physically and functionally different milieus by performing and orchestrating multiple rudimentary tasks [12, 13] which only recently have become better understood.

1.1.2 Functional Role of Membrane Lipids

The primary building blocks of membranes are lipids whose special properties set the basis for the spontaneous aggregation of the bilayer structure, which even arises under artificial conditions. These properties originate from the shape and the amphipathic nature of the membrane lipids, which possess both hydrophilic and hydrophobic groups. The hydrophilic polar head of the lipid, (made of a phosphate and a nitrogen group), has high affinity for water whereas the hydrophobic non-polar tail, (composed of two long fatty acid chains), is repelled by it. Consequently, the hydrophobic cores of the amphipathic molecules cluster together and the hydrophilic portion orients to the aqueous solution giving rise to the bilayer arrangement in membranes [7, 14].

Molecular geometry of lipids plays a significant role in modulating cellular membrane morphology. The core phospholipid in cell membranes, phosphatidylcholine (PC), displays a cylindrical shape, since both headgroup and fatty acid moieties are of equal diameter; a feature that enables a stable lipid bilayer assembly. Nevertheless, other lipids such as phosphatidylethanolamine (PE) and phosphatidylinositol (PI) with small and large headgroup respectively, in relation to the tail, exhibit conical and inverse-conical shapes hindering formation of bilayer phases at physiological conditions (Fig. 1.2). Such lipid polymorphism enhances morphological plasticity of the lipid bilayer [15].

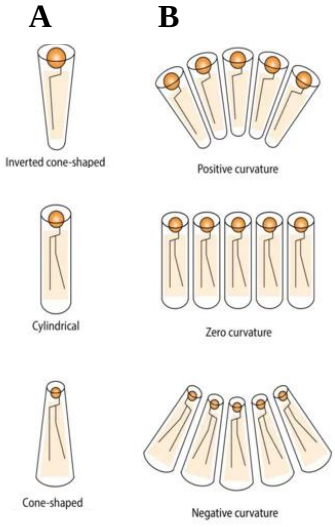

Figure 1.2- Membrane curvature dependency on the constituent lipid species shape. *(A) Schematic illustration of inverse-cone-, cylinder- and cone-shaped lipids; phospholipid classifications based on the relative volumes of lipids' polar head groups and fatty acyl chains[16].*

The aforedescribed lipid properties are also responsible for the sealed lipid bilayer structures since it is energetically favourable to avoid exposure of the hydrophobic hydrocarbon tails to the aqueous environment. The closed lipid bilayer formation of the plasma membrane and the subcellular compartments renders stability and also encourages membrane repair of small tears which create a free edge with water [17]. This is accomplished through lipids' spontaneous rearrangement eliminating the free edge and prohibiting material exuding from the cell or organelles [9].

There are different head group classes, with each one having unique chemical properties. For instance, some head groups are negatively charged and due to the charge-charge repulsions they display, they occupy larger effective cross-sectional areas. However, changes in the pH of the solution can modify lipid charges based on the specific pKa values of the headgroup and consequently modulate their effective cross-sectional area. In contrast, the hydrophobic acyl chains remain unaltered by the environment, but their state depends on their chemical structure [18].

These hydrocarbon chains differ in size length ranging between 14 and 24 carbon atoms [7] and can be fully saturated (acyl chains contain only single bonds between carbon atoms), mono-unsaturated (acyl chains which contain a double bond between two of the carbon atoms in the chain), or polyunsaturated (acyl chains containing more than one double bond) [18].

This variation in length and degree of saturation affects lipid arrangement and membrane behaviour as the tight packing configuration of the fully saturated lipids and the loose packing structure of the unsaturated acyl chains, modify the fluidity, transition temperature, and the lateral membrane pressure state accordingly. Even the weak van der Waals forces establish stronger interactions in extended saturated chains, leading to

membrane stabilization, whereas, the increased cross-sectional area of unsaturated lipids reinforces membrane fluidity [18].

1.1.3 Lipid Composition of Membranes

Membrane lipids cover 50% of the mass of cell membrane in most animals with the remaining being protein [7, 19]. In eukaryotic cells, the three major lipid classes are phospholipids, glycolipids and sterols with phospholipids representing the most abundant lipid class [2, 7, 20].

A phospholipid, as an amphipathic molecule, consists of two hydrophobic non-polar tails and a hydrophilic polar head [19]. The phospholipid tails typically consist of 14 to 22 carbons [7]. One tail is usually unsaturated having one or more cis-double bonds. This configuration induces a bend in one chain structure, while the other being saturated remains straight (Fig. 1.3). This variation in tail length and saturation contributes to the less packed aggregation of the molecules, which thereby enhances membrane fluidity [7, 9, 21].

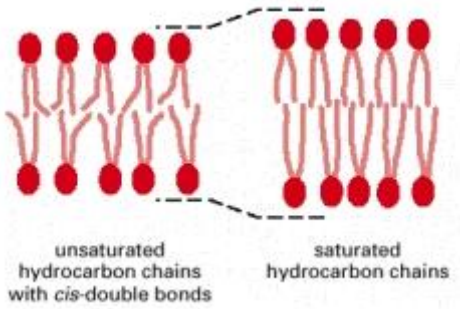

Figure 1.3- Influence of cis-double bonds in acyl chains. *The unsaturated tail (on the left) containing cis-double bonds induces a kink in the tail producing loose packing. The saturated tail (on the right) lacking any cis-double bonds remains straight forming a thicker and more compact lipid bilayer. Image taken from [7].*

The head is constructed from a backbone, a phosphate and an alcohol attached to the phosphate (Fig. 1.4) [22]. The backbone made up of either glycerol or sphingosine links the polar head group to the fatty acid tail and it is what differentiates between the two classes of phospholipids, the phosphoglycerides and sphingolipids, respectively [9, 22].

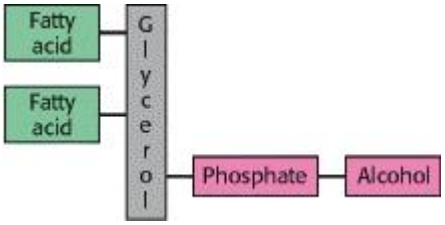

Figure 1.4- Schematic structure of a phospholipid. *Image taken from [22].*

The phosphate group can be linked to the hydroxyl group of one of several alcohols. Phosphoglycerides' common alcohol functional groups are the amino acids, serine, ethanolamine, choline, glycerol and inositol. Hence, the structural formulas created bear the respective names, phosphatidyl serine, phosphatidyl ethanolamine, phosphatidyl choline, diphosphatidyl glycerol and phosphatidyl inositol (Fig. 1.5) [9, 22].

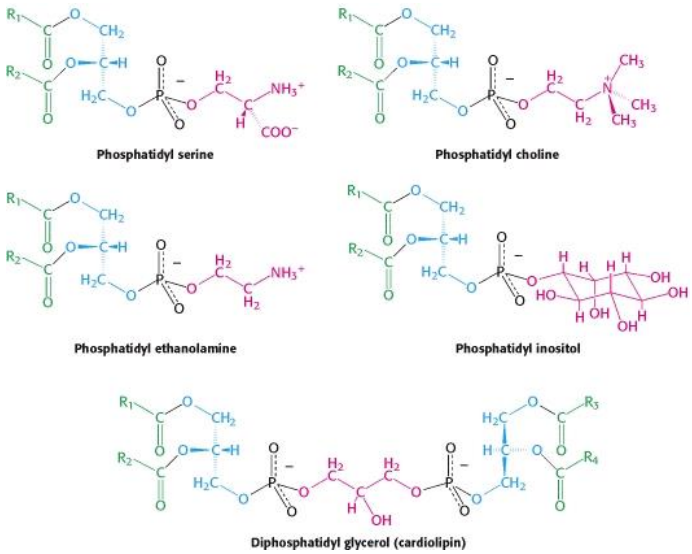

Figure 1.5- Common phosphoglycerides found in membranes. *Image taken from [22].*

Sphingolipids, which is a less abundant class of membrane lipids, contain a sphingosine backbone, along with an amino alcohol and a long unsaturated hydrocarbon chain [22]. A simple sphingolipid is ceramide whose hydrophobic fatty acid tail is linked to the amino group of the sphingosine. Other types of sphingolipids arise from the esterification of additional groups to the terminal hydroxyl group of the sphingosine platform [9]. For instance, in sphingomyelin, the primary hydroxyl group of sphingosine is esterified to phosphoryl choline and an amide bond links the sphingosine backbone to the fatty acid (Fig. 1.6) [22].

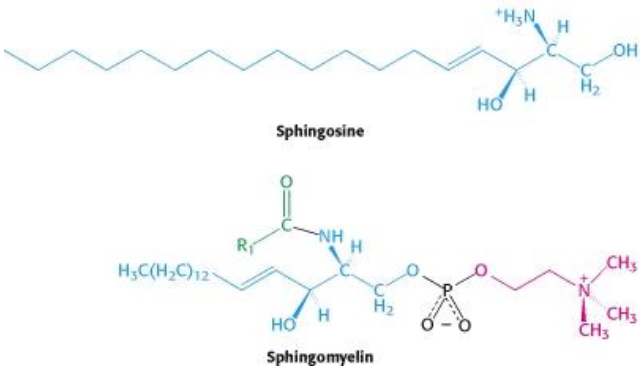

***Figure 1.6- Sphingosine and sphingomyelin structures**. Image taken from [22].*

The basic structure of a glycolipid consists of a mono- or oligosaccharide group attached to the primary hydroxyl group of the sphingosine backbone, giving rise to cerebroside and ganglioside, respectively (Fig. 1.7)[9]. Glycolipids are exclusively distributed throughout the outer leaflet of cellular membranes contributing to plasma membrane asymmetry[22].

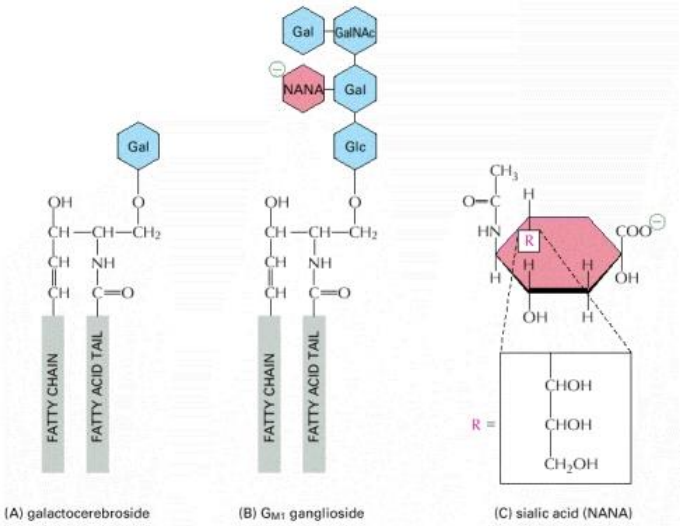

***Figure 1.7- Glycolipid molecules.** (A) Galactocerebroside is a neutral glycolipid due to the uncharged sugar forming its head group. (B) Ganglioside's structure containing one (or more) negatively charged sialic acid residues (also called N-acetylneuraminic acid, or NANA). (C) Sialic acid's structure. Gal = galactose; Glc = glucose, GalNAc = N-acetylgalactosamine; three uncharged sugars. Image taken from [7].*

Sterols constitute another important membrane lipid class. It is an abundant component of animal cell membranes [2] and different sterols are detected in various eukaryotic cell membranes. Specifically, animals contain cholesterol, yeast and fungi use ergosterol, while plant plasma membrane consists of sitosterol and stigmasterol [23]. However, sterols are essentially absent from prokaryotic cell membranes [9].

Cholesterol is composed of four linked hydrocarbon rings. A hydrocarbon tail and a hydroxyl group are attached on the two opposing sides of the steroid (Fig. 1.8) [22]. In the bilayer, this molecule aligns itself parallel to the phospholipid hydrocarbon chain and it positions its hydroxyl group adjacent to the phospholipid head group (Fig. 1.9) [7].

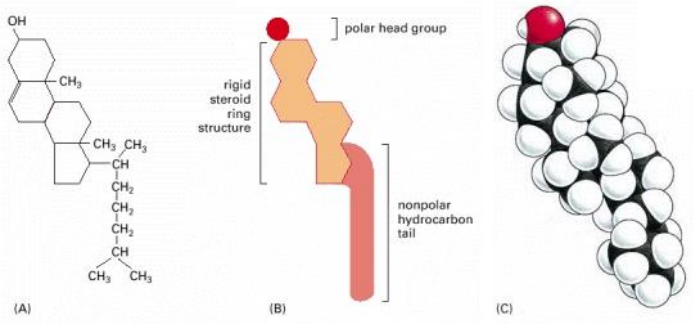

Figure 1.8- Cholesterol structure. *Representation of cholesterol (A) by a formula, (B) by a schematic drawing, and (C) as a space-filling model. Image taken from [7]*.

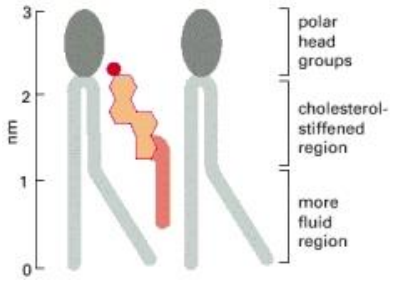

Figure 1.9- Schematic drawing of a cholesterol molecule placed between two phospholipid molecules in a monolayer. *Image taken from [7].*

This orientation partly immobilizes the regions it dwells, decreasing phospholipid fluidity [7]. It also induces a stiffening effect rendering the lipid bilayer less deformable reducing water-soluble permeability [9]. Interestingly, cholesterol's position within the bilayer hinders dense packing of hydrocarbon chains that could potentially lead to crystallization and hence it inhibits phase transitions [7].

1.1.4 Membrane Lipid Asymmetry

A remarkable feature in all eukaryotic cells is the asymmetrical lipid distribution across the bilayer, a phenomenon known as membrane phospholipid asymmetry [24].

Phospholipids with choline in their polar head group, such as phosphatidylcholine and sphingomyelin, reside predominantly in the outer leaflet and constitute 65-75% and more than 85% of the total lipid mass, respectively. Conversely, the majority of the aminophospholipids (with a terminal primary amino group), namely, phosphatidylethanolamine (PE) and phosphatidylserine (PS), enrich the inner leaflet, and compose 80-85% of the lipid molecules for PE and more than 96% for PS, whereas cholesterol is dispersed evenly throughout the two monolayers, and it is uncharged altogether [9, 17, 24-26].

At physiologic pH, PS is negatively charged, with the remaining phospholipids being neutral. This difference in charge generates a functionally relevant asymmetry between the two leaflets of the bilayer as the bulk of PS are present mainly in the inner leaflet [9]. Asymmetric distribution of phospholipids is a consequence of both energy-independent and energy-dependent transport activities. The spontaneous diffusion of phospholipids, where polar head groups can move through the membrane interior is possible, but not sufficient to maintain the asymmetry equilibrium [24]. This transversal diffusion is an energetically unfavourable process as the polar head group is forced through the hydrophobic milieu of the lipid bilayer. However, cholesterol sustains the capability of

undergoing a fast flip-flop between the two bilayer leaflets due to the small effective area of its polar head group which is restricted to one hydroxyl group [17].

At least three distinct energy-dependent activities that can catalyse phospholipid movement between the bilayers efficiently have been proposed: (1) a “flippase”, the Mg-ATP-dependent amino phospholipid translocase, responsible for the inward transport of lipids; (2) a “floppase”, the less specific Mg-ATP-requiring phospholipid translocase, which promotes outward migration of lipids; and (3) a “scramblase”, the Mg-ATP-independent, but Ca^{2+}-dependent transporter which stimulates bi-directional transbilayer movement of all phospholipids [24, 25]. While the first two energy-requiring activities promote and preserve lipid asymmetry, the exchange of phospholipids between the two leaflets mediated through the “scramblases” results in a collapse of phospholipid asymmetry [9, 24].

The discovery that cells invest a considerable amount of adenosine triphosphate (ATP) energy to maintain this bilayer lipid asymmetry signifies its physiologic importance [24]. For instance, several regulatory and structural proteins in the cytosol including protein kinase C, annexin, and membrane skeletal proteins, such as spectrin, bind to the plasma membrane only through interaction with charged phospholipids such as PS [25].

On the other hand, exposure of PS on the outer surface denotes loss of membrane integrity. PS extracellular expression targets the cell for engulfment by macrophages, a signal widely used as a diagnostic marker for apoptosis [9, 24]. Furthermore, dynamic phospholipid translocation is implicated in cellular processes such as membrane budding and endocytosis [25]. Thus, maintenance of membrane lipid asymmetry is of functional significance for cell homeostasis and its disruption is implicated in disease [9].

1.1.5 Molecular Dynamics of Membranes

Our current understanding of the biological membrane architecture is framed within the “fluid mosaic” model suggested by Singer and Nicolson in 1972 [27]. One of the tenets of this membrane model features the two-dimensional fluidic nature of lipid bilayers that occurs due to lateral and rotational movement of both lipids and proteins [9]. Furthermore, this model showcases the dynamic nature of the integral membrane proteins but belittles the functional role of membrane lipids advancing their random distribution in the plane of the membrane [12, 27].

However, myriads of experimental data in the last forty years assign significance to the functional properties of the lipids’ lateral heterogeneity and the deformability of the lipid membrane [1]. The gradual emerging scenario emphasizes how the intrinsic characteristics of membrane lipids determine membrane order and organize the fine structure of cellular membranes [12].

The “lipid raft” hypothesis had the merit to draw researcher's attention on lipids’ importance [12], whose different biophysical tendencies to associate with one another give rise to membrane domains. These domains in turn, are actively involved in various physiological processes such as cell adhesion and motility, signal transduction, viral and bacterial influx and intracellular trafficking [27].

This dynamic membrane behaviour is associated with heterogeneous lateral organization based on lipid-lipid interactions which lead to liquid ordered (Lo) and liquid disordered (Ld) states [27]. These two phases, Lo and Ld, characterized by tightly-packed lipids with reduced lateral mobility and loosely-packed lipids with a high degree of lateral movement, respectively [28], are dynamic structures of transient nature [7].

Their occurrence can be imputed to lipids’ physicochemical properties. Overall, the van der Waals attractive forces are not selective enough to hold adjacent fatty acid tails together; yet, long, saturated fatty hydrocarbon chain structures, as those found in

sphingolipids, allow these attractive forces to operate in contiguous molecules resulting in Lo phase [29].

Interestingly, solid-ordered (So) phase has also been observed in 2-lipid component mixtures of different melting points [30], but not in mammalian cell membranes [31]. The So phase is comprised of all-trans saturated hydrocarbon chains elongated at the maximum and arranged into an ordered and compact fashion [30], with extremely reduced lateral lipid diffusion [17]. This conformation is perturbed by the emergence of C-C bond rotations due to temperatures above phase transition temperature, Tm, inducing the lipid melting from a So to a Ld state where lipids experience fast lateral diffusion [30]. This lateral heterogeneity in lipid distribution, and in particular, the Lo state, is analogous to lipid rafts in biological membranes whose existence has been disputed for many years. However, experimental evidence has revealed that membrane rafts are heterogeneous, sterol- and sphingolipid-enriched nanodomains with various biological functions [30].

This preferential aggregation of sterols with saturated lipids such as sphingolipids in membrane rafts has also been characterized in simple artificial membrane systems [23]. Sphingolipid's long saturated alkyl chain configuration which allows van der Waals interactions to be in force along with cholesterol's higher affinity for negatively charged phospholipids justifies this preferential partitioning [17].

It has been suggested that cholesterol plays a major role in the assembly and maintenance of lipid rafts. Its addition is required for the Lo phase, which despite its tightly packed conformation, acquires a relatively high degree of lateral mobility. Cholesterol depletion, on the other hand, has been reported to induce microdomain dissolution leading to Ld phase [28]. Nevertheless, cholesterol is also present in a Ld lamellar phase with its rigid hydrophobic moiety being intercalated between the lipid chains particularly favouring a trans chain configuration [17].

The Lo domain formations are thicker compared to other parts of the bilayer due to the sphingolipid configuration exhibiting longer and straighter fatty acid chains than other

membrane lipids (Fig.1.3) [7]. This thickness confers better protein accommodation affecting protein localization, organization, diffusion, and function [7, 23].

Taking into account the nanodomain's small size (5–20 nm in diameter) and short lifespan (millisecond or less) [27], a new model of raft formation suggests that small Lo domains suddenly appear and disappear, but their stabilization is dependent on the clusters of membrane proteins that drive lipid domain formation [30]. This nanodomain size and its fleeting existence maximize its functional interactions through inter-protein collisions acting as a medium of signalling. Raft size and its components likely depend on the cell activation state which potentially instigates larger and more stable domain formation efficient to initiate signal transduction. Receptor aggregation upon signal generation can merge highly dynamic nanostructures into a unified group facilitating specific protein localization with different propensities for interaction with other proteins. Thus, rafts serve as nanochambers that favour particular compositional organization in order to enhance signalling efficiency [27]. Conversely, confinement of signalling molecules in remote rafts could hamper cell activation [30].

1.1.6 Types of Cell Signalling

It is firmly established that cell-cell communication is essential for the coordinated performance of cellular events [32] and its execution mandates the orchestrated engagement of both the bilayer framework and its ingrained constituents, the proteins[11].

The mode of communication among cells is mediated through four basic mechanisms [33]. The contact-dependent signalling requires cells to be in direct contact where activation is achieved through ligand-receptor coupling, particularly important in immune response [7], or this contact-dependent interaction allows cells to send signals across gap junctions [33] through which passive diffusion leads the molecular movement [34].

In most cases though, signals are released. In paracrine signalling, molecules secreted by cells can have an effect on cells in the immediate vicinity and the endocrine signalling uses the circulatory system to carry hormones to far afield target cells [34]. The chemical synaptic signalling involves signal molecule transmission over specialized cell junctions, called chemical synapses, from a neuron to a postsynaptic target cell [33].

Although the term “synapse” was initially coined to describe neuronal functional connection, it was later adopted by immunologists to characterize the contacts between T cells and antigen-presenting cells (APCs) as the structural plasticity of the latter was found to be similar to that of the neuronal synapse [32].

In all signalling pathways, regardless of the nature of the signal, the common element is a receptor dwelling on the target cell binding the signal molecule [33]. This knowledge is of great importance as it sets the base for understanding of what is required for a cell response to be triggered and what the scientific steps should be in order to address the mechanism of intercellular communication. Towards this goal, many efforts have been made from a wide range of disciplines. In this report, we will refer to minimal models that have been developed and which among other things have tried to shed light on cell-cell interactions.

1.1.7 Biomimetic Model Membranes and their Applications

As already mentioned, the main function of the biological membrane is to define the boundary among cells and within organelles, a feature that also enables communication and regulated transport within and across the membranes. This cell-cell communication is mediated through membrane’s dynamic organization which modulates conformational changes leading to signaling, trafficking and recognition [35].

The major challenge of studying these interactions in living cells lies both in the myriads of components involved and their synergistic interaction making it impossible to determine their distinct defining input in a variety of biological processes [21].

This complexity of biological membranes has motivated the construction of simplified model systems so that the roles of individual components and their organization and dynamics can be assessed [35]. These models retain the essential constituents of a lipid bilayer structure although their size, geometry and composition can be customized to study the subcomponents of cellular membranes and gain insights that otherwise would remain obscure [17].

It is worth noting that some models can be better representatives of the natural membranes than others, but the selection of the system depends on the specific research area that needs to be probed allowing for relevant interpretation of the results. Factors to be considered include - but are not limited to - lipid composition, membrane curvature and ionic strength of the solution, which all impart certain properties to the membrane model, influencing the results. Thus, while a single component lipid model can be informative, it is important to consider its applications and limitations.

1.1.7.1 Langmuir Monolayers

One of the earliest employed biomimetic systems is lipid monolayers, also termed Langmuir monolayers, which are formed at the aqueous solution-air interface by spreading an aliquot of an amphiphile molecule at the surface of water [17]. The monomolecular layer of an amphiphile, which covers the whole free water surface, can be compressed to occupy the desired surface area by means of sliding barriers (placed in the Langmuir trough) (Fig. 1.10). The Langmuir method allows for control over surface quality, molecular packing, physical state, lateral pressure and composition [10].

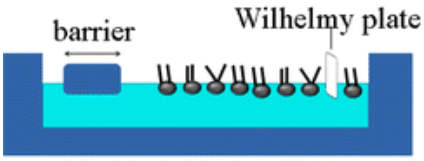

***Figure 1.10- Schematic drawing of the** Langmuir trough with a sliding barrier and a Wilhelmy plate used as a surface pressure sensor. Image taken from [36].*

A Langmuir film, as comprised of only one lipid monolayer, representing one leaflet of cellular membrane, can be applied to studying biomembrane properties, processes unfolding on membrane level and intermembrane component interactions. Another biomedical application of the Langmuir monolayer technique is in the investigation of drug mechanisms active on membrane level [10].

1.1.7.2 Lipid Vesicles

The most widely used membrane models are lipid vesicles or liposomes. Their distinction is based on the type of amphiphiles employed for their preparation. Liposomes are prepared from natural phospholipids, while the name lipid vesicles is reserved for the membrane systems formed by synthetic amphiphiles [10].

Liposomes are very useful tools to characterize the dynamic and semi-permeable natural bilayer. Therefore, vesicles are widely used to study various cellular processes, such as endo- and exocytosis, cell lysis, transport phenomena, or protein-lipid and drug-membrane component interactions [10].

These model membranes are generated from the aqueous dispersion of single lipid or mixture of different types of lipids that arrange in a bilayer conformation and enclose a small aqueous compartment [10].

The preparation method determines the kinds of bilayer structures that can be obtained. Multilamellar lipid vesicles (MLV) are formed by intense hydration of a dried lipid film at temperatures above the lipid phase transition. These vesicles with a size range of 0.5-10 µm are composed of several lipid bilayers separated by water molecules. The size spectrum can be modulated by either extruding MLVs through a porous membrane giving rise to large unilamellar vesicles (LUV) or sonicating MLVs which leads to small unilamellar vesicle (SUV) formation. LUVs size varies from 100 to 500 nm and the mean diameter interior of SUVs is 50 nm [17].

Giant unilamellar vesicles (GUV), displaying a size range of 5-100 µm, can be developed by a variety of methods such as a gentle hydration method, electroformation, an emulsion transfer method, and a micro-fluidic method [37]. Among them, the most widely known approach is either by the gentle hydration technique, involving hydrating a dried lipid film at temperatures above the lipid phase transition for a long period of time (up to 36 h), or by applying an external electrical field, known as the electroformation process [17].

The big advantage of GUV formation by natural swelling is that it doesn't promote lipid oxidation. However, natural swelling is time consuming on the order of days and large amounts of vesicles produced are multilamellar. The small fraction of the obtained GUVs is of poor membrane quality as they display lipid structures attached to the inner or outer leaflet or enclosed in the inner aqueous compartment [10, 17, 38].

The electroformation method, or else known electroswelling, has been mostly used as it generates high GUV yields with less variation in size distribution, increased unilamellarity and fewer membrane defects [37]. It was first introduced by Angelova & Dimitrov [39, 40], and later on, indium tin oxide (ITO) coated glass slides were employed as electrodes to generate GUVs [37].

Electroformation enhances the swelling process due to the periodic distribution of charges achieved by an alternate current (AC) field [38]. This approach allows production of large

amounts of cell-sized vesicles within a period of a few hours [38] and affords flexibility in lipid composition [39]. Here, vesicle formation occurs as an AC field is applied to a hydrated preformed lipid stack facilitating the flow of aqueous solution in between the bilayer stacks and orchestrating an interplay between electrostatic interaction, redistribution of bilayer counter ions as well as electro-osmotic effects. This results in a decrease of both line and surface tensions of the swollen vesicles increasing bilayer separation [38].

GUVs' size makes their visualization through optical or confocal microscopy and individual vesicle micro manipulation feasible [17, 26]. Their existence has been instrumental in studying the phase behaviour of binary and ternary lipid mixtures in bilayers without the intervening participation of other native membrane components such as proteins [35].

Although these lipid assemblies are easy to prepare, they suffer from several constraints. The prime disadvantage of using these lipid vesicles as model membranes is the lack of lipid asymmetry encountered in native membranes [17]. Also, their surface curvature and physical state depends on the lipid concentration and composition. It has been demonstrated by phase diagrams that small composition differences in lipid mixtures strongly affect lipid system phase behaviour [10, 17]. Lastly, a homogeneous vesicle size and layer number is not easy to attain [10].

Due to the aforementioned preparation methods requiring mechanical (e.g., sonication or extrusion), chemical (e.g., change of solubility conditions, incorporation of external compounds) or electrochemical (e.g., change of pH, ionic strength) energy, lipid vesicles are deprived of long-term stability. However, modulation of lipid vesicle composition, size and environmental parameters (temperature, pH, ionic strength, presence of external molecules and ions) allows for generation of more stable systems, viable for prolonged periods of time (up to several months) [17].

1.1.7.3 Supported Lipid Bilayers

Another biomimetic model membrane is the supported lipid bilayers (SLBs). In such model systems, a flat lipid bilayer interacts transiently with a solid surface such as mica, glass or silicon oxide wafers. Currently, the most frequently used method for preparing SLBs involves the rupture of lipid vesicles when exposed to SLBs. In brief, a SUV suspension is heated upon contact with the support at temperatures above the lipid phase transition. Although the process is not completely understood, the lipid vesicles are adsorbed on the surface, and this is followed by their deformation, flattening and rupture. The polar head groups of the first monolayer orient towards the support while the hydrocarbon chains face the lipid chains of the second monolayer. The edges of the bilayer join through hydrophobic interactions giving rise to an uninterrupted supported lipid bilayer [17].

These model systems are characterized by stability and controlled overall composition compared to lipid vesicles. They are ideal for studying reorganization dynamics of proteins between two bilayers. Specifically, as vesicle ruptures over evenly distributed fluorescently labelled proteins attached to a SLB, there is protein reordering on the surface; the new pattern formed is possibly associated with lipid vesicle dynamics and protein mobility [17]. These membrane assemblies can address questions related to direct cell-cell communication mediated through ligand-receptor coupling at the intermembrane level resulting in rearrangement of proteins and initiation of cell activation [35].

An additional advantage is their flat glass support suitable for total internal reflection fluorescence (TIRF) microscopy, enabling high-resolution observation of transient events (such as single vesicle fusion). However, the same support imposes significant restrictions on lipid and protein diffusion kinetics due to their interaction with the underlying glass slide [39].

1.1.7.4 Droplet Interface Bilayers

Among these membrane platforms, increasing emphasis has been placed in recent years on droplet interface bilayer (DIB) [41] and droplet on hydrogel bilayer (DHB)[42, 43]. In the DIB approach, aqueous volumes are submerged in a lipid in oil (such as hexadecane or squalene) solution and spontaneous monolayer lipid self-assembly occurs on the aqueous surface. If two such droplets are brought into contact, droplet interface bilayer forms by displacing the oil between the monolayers (Fig. 1.11) [42, 44, 45].

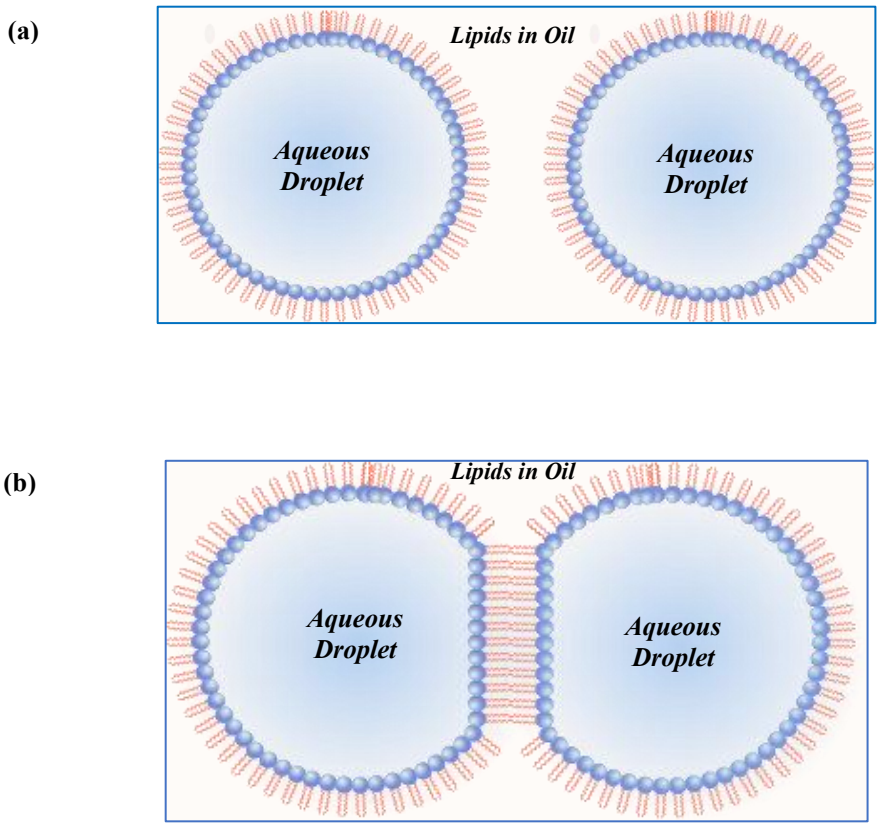

Figure 1.11- Schematic diagram of DIB formation. *(a) First, lipid self-assembly occurs at the oil/water interface around two aqueous droplets. (b) Then the droplets are brought together, and the lipid tails attach as the oil is forced out leading to bilayer formation.*

Two distinct methods of DIB formation have been demonstrated: lipid-out and the lipid-in techniques. In the lipid-out DIB formation, aqueous droplets are immersed by means of agarose-coated Ag/AgCl electrodes in an oil-lipid solution, where droplets are encased by the same monolayer after a stabilization period (< 30 min). Then, two such droplets are brought into close proximity leading to their adherence and subsequently to interface bilayer formation (Fig. 1.12)[42].

The lipid-in method is much shorter in duration (< 5 min) and employs specified lipid composition vesicles contained in the internal aqueous phase [42]. Each of the two droplets can enclose different vesicles enabling the formation of asymmetric bilayers upon contact (Fig. 1.12) [42, 46]. Such asymmetry in a bilayer membrane model confers robustness and durability in the system rendering it suitable for membrane protein behaviour studies with respect to leaflet composition[42].

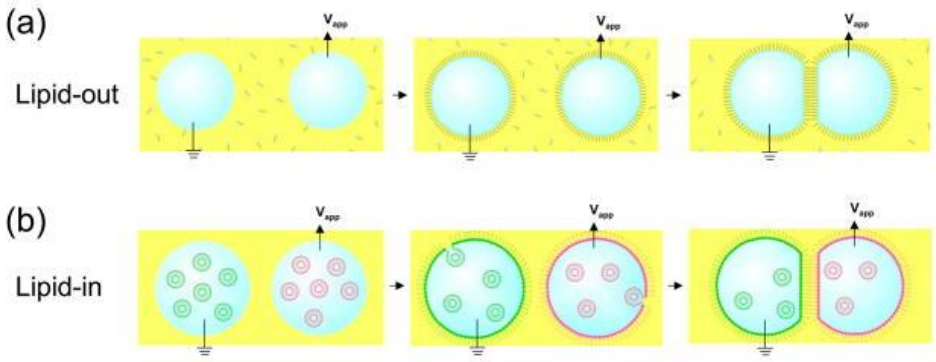

Figure 1.12- Lipid-out and lipid-in DIB formation. *(a) In the lipid-out method, the interfaces of two aqueous droplets are coated with a lipid monolayer after being submerged in an oil-lipid solution. Droplet interface bilayer is formed upon bringing the two droplets into contact. (b) In the lipid-in technique, vesicles of different lipid compositions are incorporated into two droplets. As vesicles coalesce with the oil-water interface of each droplet, monolayer formation occurs. The two droplets are brought into contact with one another forming an asymmetric droplet interface bilayer. Image taken from [42].*

DIBs display extended lifetimes from days to weeks and can withstand voltage potentials of more than 150 mV [42]. Furthermore, they retain 1 giga-ohm seal preventing leakage of vesicle contents thus, rendering them suitable for electrophysiology experiments[41]. This high resistance giga-ohm seal formation preserves the integrity of the bilayer, (i.e. the membrane seal is not ruptured), as well as restricts electrical access to its internal space and enables acquisition of high-quality recordings[47]. Physical contact between individual droplets is subject to micro manipulation permitting precise modulation of their contact area, a feature greatly needed in single-channel studies [42].

1.1.7.5 Droplets at Planar Interfaces

Greater advancement to the DIB approach has been brought by droplet bilayer formation at planar interfaces, known as droplet on hydrogel bilayers (DHBs). The pivotal innovation in DHB lies in its horizontal orientation on a planar substrate [48] which is required to be hydrophilic and able to support lipid monolayer self-aggregation in the presence of a hydrophobic medium (Fig. 1.13) [42]. This is possible by depositing a molten agarose layer on the flat support, which after drying leaves an ultrathin hydrogel coating [49]. The droplets of the DHB are formed in a similar way to the ones in DIBs either by being coated by lipids in an oil solution or by dispersed lipids inside the droplet [42]. The lipid bilayer forms when the aqueous droplet is placed on top of the hydrogel substrate immersed in an oil-lipid solution [49].

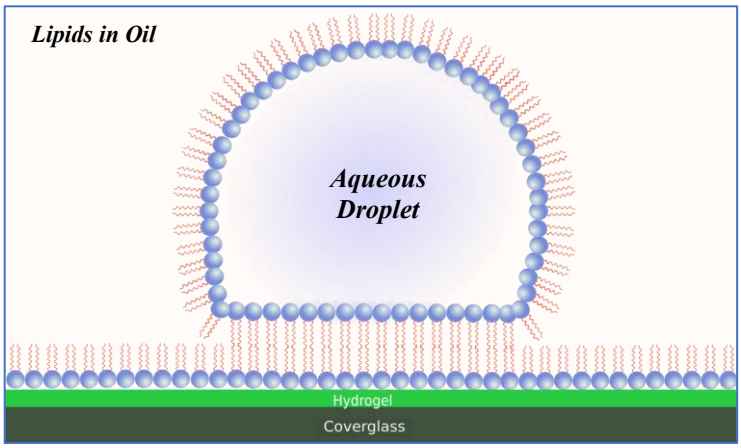

Figure 1.13- A supporting substrate, comprised of a thin agarose layer, is covered with a lipid-in-oil solution forming a lipid monolayer. *An aqueous droplet encased in a lipid monolayer is placed on top of the lipid coated hydrogel, forming a lipid bilayer at the interface between the two aqueous phases.*

The flat substrate of DHB apart from providing enhanced mechanical stability compared to other artificial bilayer methods, can also accommodate straightforward optical imaging of diffusing single fluorescent molecules by employing TIRF microscopy [49] due to the sufficiently thin agarose substrate [42]. These DHB-based systems, exhibit the potential to be used as robust platforms where concurrent visual and electrical measurements at single-molecule level can be conducted [41, 46].

The versatile DHB geometry allows further applications including rapid screening of blockers arrayed in hydrogels whose efficiency can be estimated (by measuring their activity) as a channel/pore incorporated DHB slides across the gel surface. Bilayers also formed at hydrogel interfaces enable quantitative analysis of membrane properties such as capacitance. The enhanced bilayer fluidity in DHBs facilitate investigation of lipid diffusion dynamics (e.g., micro domain formation) and lateral diffusion of membrane-bound proteins since this artificial membrane system is unhindered by the mobility restrictions encountered in SLBs. Along with all these advantages, DHBs extended life span permits the realization of many experiments that otherwise would be impossible to perform by conventional methods [42].

1.1.7.6 Hybrid Membrane Systems

The utility of the aforementioned biomimetic models to bridge the gap between biology and biochemistry, complementing in this way traditional biology, is beyond dispute. Still, these approaches are devoid of capturing a holistic picture of cell-cell interaction which governs various biological mechanisms [50] and whose aberrant function, especially that of the immunological synapse (IS), plays a crucial role to the initiation and progression of diseases [51, 52].

As the synapse regulation between T cell and APC plays a central role in the body's immune response against bacterial, viral infections, autoimmune disorders and tumor growth [51, 53], it has been the target research area of various scientific disciplines; nevertheless, much about it still remains unknown [54].

Our understanding of this cell-cell communication is limited basically due to the scarcity of tools needed to study this interaction. The emergence of SLBs over the last decades constitutes a technique that was adopted and further evolved to accommodate the study of the IS [50].

More specifically, it has been attempted to recapitulate the multilayer molecular assembly and spatial reorganization upon T cell activation in a hybrid synapse between a natural T cell and an artificial planar platform, functionalized with T cell cognate ligands. However, rigid structures fabricated on the substrate acted as barrier configurations conferring a constraint of motion to lateral lipid and protein diffusion [8].

Despite the versatility of this biological technique in characterizing T cell signaling activity, only partial success in mimicking the T cell-APC has been achieved as it entails mobility restrictions effecting the dynamic processes which unfold at the interface [53, 55].

Another hybrid model developed involves synthetic entities, such as 5-6 μm polystyrene beads, designed and decorated with activating antibodies or peptide-major

histocompatibility complexes (MHCs) [56, 57]. These were heralded as attractive tools since their spherical geometry was considered suitable to more closely imitate T cell and APC interaction relative to planar systems. However, the limitation of these bead-based artificial models lies in the absence of dynamic protein remodelling found at the IS [53]. More recent advances have exploited the advantages of three-dimensional (3D) scaffolds to represent and study the conformational changes during the IS arrangement. This system has been synthesized by biofunctionalizing drops of water-in-oil emulsions with gold nanoparticles which can serve as a 3D APC analogue able to host T cells. It has been proposed as a tool to study T cell-APC interaction in an environment that more closely resembles the situation *in vivo* [53].

A salient characteristic of this membrane model is its compatibility to merge membrane mechanical properties, such as elasticity and curvature of both APCs and the encapsulated T cells, with force-dependent arrangements operating during the IS formation [53].

Undoubtedly, this innovative model system has contributed with a significant improvement to the current state of the art regarding the incorporation of essential functional elements involved in the IS. Yet, this free-standing structure limits the potential techniques with which it can be investigated.

1.2 Motivation and Thesis Aim

All this emerging literature reveals an outburst of interest in the biophysical aspects of the T cell-APC pair [42]. At the same time, this background showcases the pressing need for engineering more refined strategies which can improve understanding of basic cell-cell interactions. Such models should combine adjustable mechanical, structural, and functional properties able to capture the spatiotemporal dynamic membrane rearrangements underpinning intermembrane signalling and cell activation and hence, better mimic the natural world.

A relatively new discipline that calls itself bottom-up synthetic biology and intertwines biological insights with quantitative sciences and engineering skills, aims to reconstitute basic cellular phenomena under well-defined conditions and characterize biomolecule interactions [58].

Integration of synthetic constructs with biological systems can expedite investigation of biological processes [59], such as the one that involves local information transit between cells mediated through ligand-receptor coupling [53], a typical example of which is the IS [35].

The highly dynamic nature exhibited in this type of interaction [54] calls for design and manufacturing of platforms able to overcome restrictions already encountered in existing model systems and yield insights regarding the interplay between membrane physical properties and generation of a response.

Along this line, one prevailing aspiration of this PhD thesis is the engineering of a bio-inspired membrane model which can recapitulate rudimentary processes of membrane-membrane interaction and consequently, be used as a proof-of-concept. This proof-of-concept can represent a new platform for synthetic biology to study artificial membrane/live-cell interplay in a controlled environment precluding the challenges of complex network interrelations that arise in natural cell-cell interactions.

Prior to the construction of this biohybrid model, a solid artificial, double membrane assembly is designed, reminiscent of a synapse architecture, with intermembrane adhesion dynamics and intercompartment communication capabilities.

The synapse-like geometry is formed from two synthetic membrane constructs, a droplet interface bilayer (DIB) and an encapsulated giant unilamellar vesicle (GUV), bridged by artificial trans-synaptic DNA linkers.

A DIB is formed by deposition of a lipid monolayer-coated aqueous droplet on a lipid-monolayer coated hydrogel support within an oil environment. GUVs are generated via electroformation or the emulsion phase transfer (EPT) method and bridged by artificial trans-synaptic DNA linkers.

Intercompartmental chemical signal communication is triggered by gradient-dependent content flow mediated through alpha-hemolysin (aHL) nanopores embedded in DIB and GUV membranes. The intermembrane signaling is manifested by elicited vesicular biochemical responses, including initiation of actin polymerization and ionic transfer, which are measured by TIRF microscopy.

As the overall aim of this thesis is the development of a hybrid interface system, the double synthetic membrane assembly is converted to a biohybrid version by GUV substitution with individual living cells. Here, the artificial membrane/live-cell bridging is mediated via DIB membrane integrated integrin-recognizing ligands.

For the end goal materialization, the following short-term objectives need to be realized first:

1. Generate a DIB as shown in Figure 1.13.
2. Generate a GUV (Fig. 1.14).

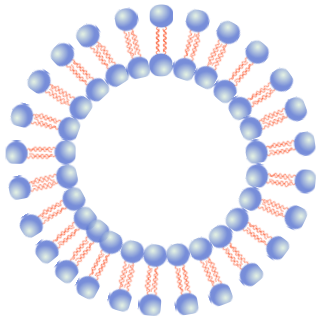

Figure 1.14- Schematic diagram of a GUV.

3. Encapsulate and anchor the GUV to DIB via membrane integrated complementary DNA linkers to represent a preliminary coupling system and monitor membrane dynamics (Fig. 1.15).

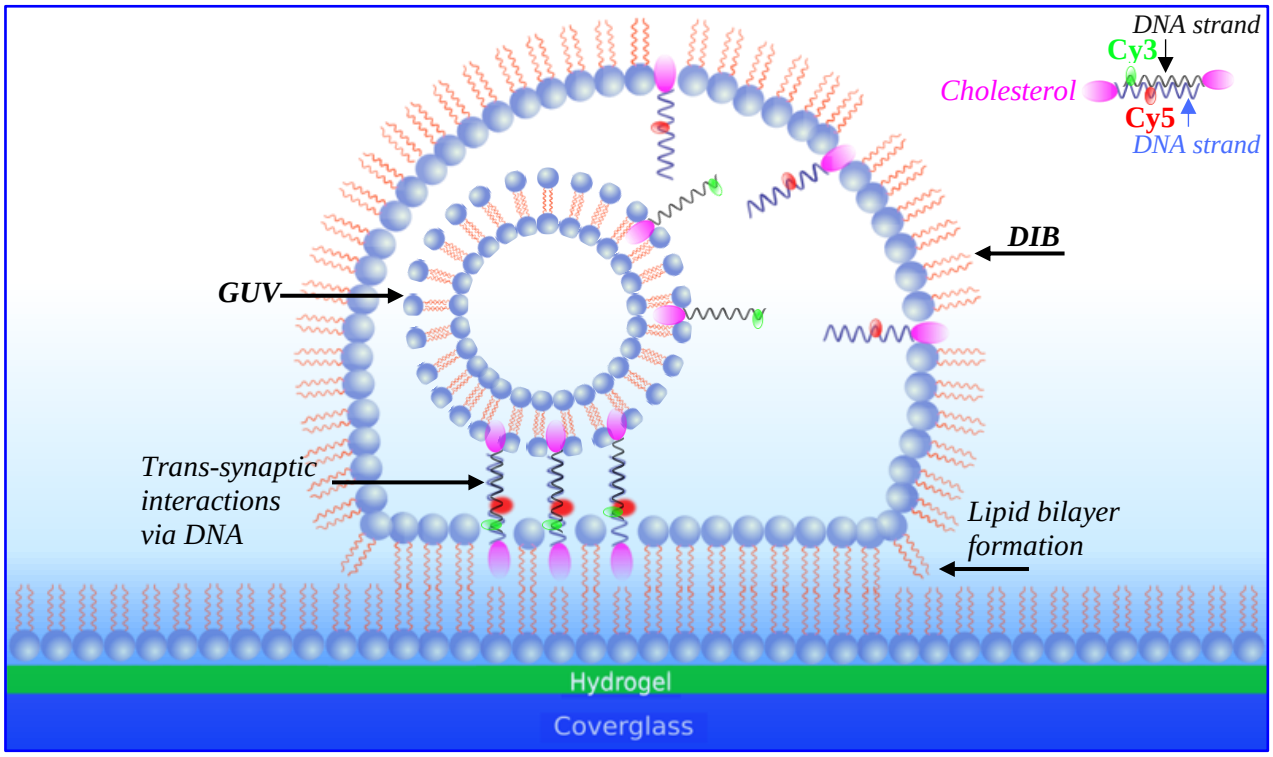

Figure 1.15- Schematics of GUV anchorage to a DIB via DNA-mediated trans-synaptic adhesions. *Hybridized labelled (Cy3-green and Cy5-red fluorophores) complementary DNA strands (double helix) tethered to DIB and GUV bilayers via cholesterol moieties (magenta ellipse). Not to scale.*

4. Reproduce intercompartmental chemical signal communication via permeable ion channel integration into DIB and GUV bilayers with ion-triggered elicited vesicular biochemical responses, e.g., actin assembly (Fig. 1.16).

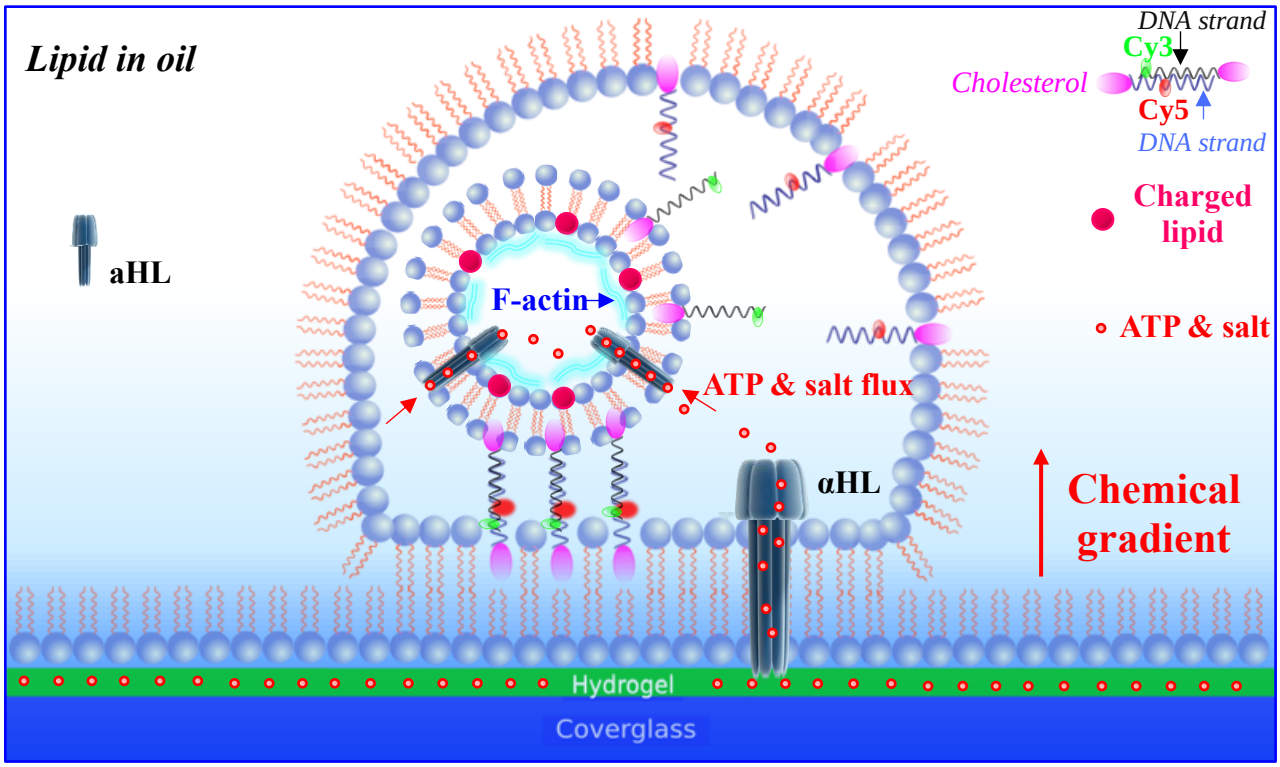

Figure 1.16- Schematic depiction of chemically mediated communication across interconnected compartments through membrane integrated protein channels that enable gradient-dependent ion permeation with resulting biochemical manifestations.

5. Substitute the encapsulated GUV with a living cell and tether it to DIB bilayer via integrin-targeting ligands/peptides and trace actin dynamics (Fig. 1.17).

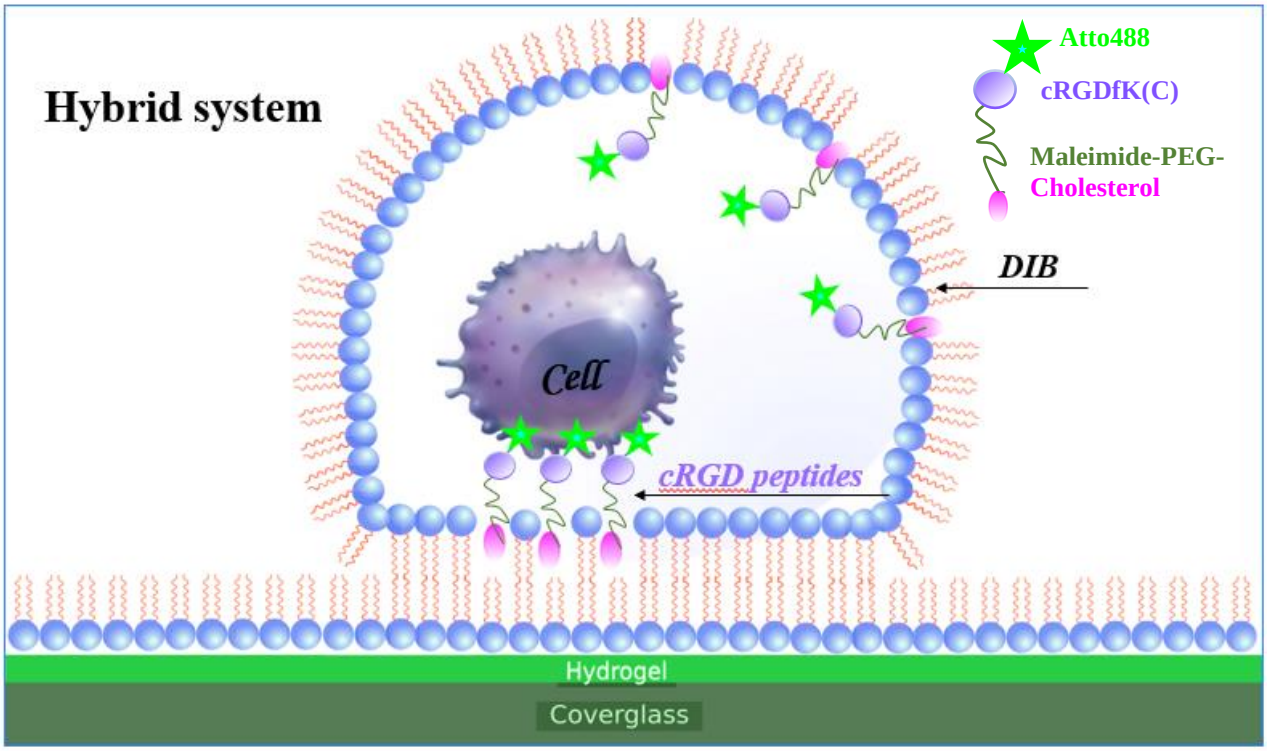

Figure 1.17- Schematics of a living cell anchored to an integrin-recognizing peptide-functionalized DIB. *Integrin-recognizing peptide consists of a cyclic RGD peptide (purple circle) attached to a fluorophore, Atto488 (light green star) at one terminus, and coupled to a cholesterol functionalized PEG polymer linker (PEG-green and cholesterol-magenta) at the other terminus for membrane self-insertion. Not to scale.*

1.3 References

1. Goñi, F., M. *The basic structure and dynamics of cell membranes: An update of the Singer–Nicolson model. Biochimica et Biophysica Acta (BBA)- Biomembranes*, 2014. **1838**(6): p. 1467–1476.
2. Lodish, H., et al. *Molecular Cell Biology. 4th edition*. 2000: W. H. Freeman.
3. O'Shea, P. *Physical landscapes in biological membranes: physico-chemical terrains for spatio-temporal control of biomolecular interactions and behaviour. Philos Trans A Math Phys Eng Sci.*, 2005. **363**(1827): p. 575-88.
4. Isao Ishii, et al. *Lysophospholipid Receptors: Signalling and Biology. Annual Review of Biochemistry*, 2004. **73**: p. 321-354.
5. Taylor, G.J. *Improving Droplet Interface Bilayers as Models for Cell Membranes*. 2016, University of Tennessee- Knoxville.
6. Nishizuka, Y. *Intracellular signaling by hydrolysis of phospholipids and activation of protein kinase C. Science*, 1992. **258**(5082): p. 607-614.
7. Alberts, B., et al. *Molecular biology of the cell. 4th edition.* 2002: Garland Science.
8. Yu, C. and Groves, J.T. *Engineering supported membranes for cell biology | SpringerLink. Medical & Biological Engineering & Computing*, 2010. **48**(10): p. 955-963.
9. Singer, S.J. and Nicolson, G.L. *The fluid mosaic model of the structure of cell membranes. Science,* 1972. **175**(4023): p. 720-31.
10. Hąc-Wydro, K. and Dynarowicz-Łątka, P. *Biomedical applications of the Langmuir monolayer technique. Annales UMCS, Chemistry*, 2008. **63**: p. 47-60.
11. Bernfield, M.R. and Stein, W.D. *Cell*. 2017; Available from: https://www.britannica.com/science/cell-biology/Intercellular-communication.
12. Sonnino, S. and Prinetti, A. *Lipids and membrane lateral organization. Front Physiol*., 2010. **1**: p. 153.
13. Fenz, S.F. and Sengupta, K. *Giant vesicles as cell models. Integr Biol. (Camb),* 2012. **4**(9): p. 982-95.

14. Chiantia, S. and London, E. *Lipid Bilayer Asymmetry*. 2013: Springer Berlin Heidelberg. 1250-1253.
15. Frolov, V.A., Shnyrova, A.V., and Zimmerberg, J. *Lipid polymorphisms and membrane shape. Cold Spring Harb Perspect Biol.*, 2011. **3**(11): p. a004747.
16. Peeters, B.W.A., Piët, A.C.A., and Fornerod, M. *Generating Membrane Curvature at the Nuclear Pore: A Lipid Point of View. Cells*, 2022. **11**.
17. Eeman, M. and Deleu, M. *From biological membranes to biomimetic model membranes (PDF Download Available). Biotechnol. Agron. Soc. Environ.*, 2010. **14**(4): p. 719-736.
18. Le, M.T., Litzenberger, J.K. and Prenner, E.J. *Advances in Biomimetics*. 2011: InTech.
19. Cooper, G.M. *The Cell: A Molecular Approach. 2nd edition*. 2000: Sinauer Associates.
20. Maric, S. *Development of a stealth carrier system for structural studies of membrane proteins in solution*. 2014, University of Copenhagen.
21. Sezgin, E. and Schwille, P. *Model membrane platforms to study protein-membrane interactions. Molecular Membrane Biology*, 2012. **29**(5): p. 144-154.
22. Berg, J.M., Tymoczko, J.L. and Stryer, L. *Biochemistry. 5th edition.* 2002: WH Freeman.
23. Guan, X.L., et al. *Functional interactions between sphingolipids and sterols in biological membranes regulating cell physiology. Mol Biol Cell*, 2009. **20**(7): p. 2083-95.
24. Fadeel, B. and Xue, D.*The ins and outs of phospholipid asymmetry in the plasma membrane: roles in health and disease. Crit Rev Biochem Mol Biol.*, 2009. **44**(5): p. 264-77.
25. Manno, S., Takakuwa, Y., and Mohandas, N. *Identification of a functional role for lipid asymmetry in biological membranes: Phosphatidylserine-skeletal protein interactions modulate membrane stability. Proc Natl Acad Sci USA*, 2002. **99**(4): p. 1943-8.

26. Schubert, T., and Römer, W. *How synthetic membrane systems contribute to the understanding of lipid-driven endocytosis. Biochim Biophys Acta*, 2015. **1853**(11 Pt B): p. 2992-3005.
27. Sengupta, P., Baird, B., and Holowka, D. *Lipid rafts, fluid/fluid phase separation, and their relevance to plasma membrane structure and function. Semin Cell Dev Biol.*, 2007. **18**(5): p. 583-90.
28. Lawrence, J.C., et al. *Real-Time Analysis of the Effects of Cholesterol on Lipid Raft Behavior Using Atomic Force Microscopy - ScienceDirect. Biophysical Journal*, 2003. **84**(3): p. 1827-1832.
29. Quinn, P.J. and Wolf, C.*The liquid-ordered phase in membranes. Biochim Biophys Acta*, 2009. **1788**(1): p. 33-46.
30. Elson, E.L., et al. *Phase separation in biological membranes: integration of theory and experiment. Annu Rev Biophys.*, 2010. **39**: p. 207-26.
31. Maxfield, F.R. and Tabas, I. *Role of cholesterol and lipid organization in disease. Nature*, 2005. **438**.
32. Ahmed, K.A. and Xiang, J. *Mechanisms of cellular communication through intercellular protein transfer. Journal of Cellular and Molecular Medicine*, 2011. **15**(7): p. 1458-1473.
33. Johnson, G.B. and Raven, P.H. *Biology*. 2017.
34. Kumar, N.M. and Gilula, N.B. *The Gap Junction Communication Channel - ScienceDirect. Cell*, 1996. **84**(3): p. 381-388.
35. Chan, Y.M. and Boxer, S.G. *Model membrane systems and their applications - ScienceDirect. Current Opinion in Chemical Biology*, 2007. **11**(6): p. 581-587.
36. Moehwald, H. and Brezesinski, G. *From Langmuir Monolayers to Multilayer Films. Langmuir*, 2016. **32**(41): p. 10445-10458.
37. Bi, H., et al. *Electroformation of giant unilamellar vesicles using interdigitated ITO electrodes. Journal of Materials Chemistry A*, 2013. **1**(24): p. 7125-7130.
38. Stein, H., et al. *Production of Isolated Giant Unilamellar Vesicles under High Salt Concentrations. Front Physiol.,* 2017. **8**: p. 63.
39. Schmid, E.M., Richmond, D.L. and Fletcher, D.A. *Reconstitution of proteins on electroformed giant unilamellar vesicles. Methods Cell Biol*., 2015. **128**: p. 319-38.

40. Angelova, M.I. and Dimitrov, D.S. *Liposome Electro formation. Faraday Discussions of the Chemical Society*., 1986. **81**: p. 303-311.
41. Leptihn, S., et al. *Constructing droplet interface bilayers from the contact of aqueous droplets in oil. Nature Protocols*, 2013. **8**: p. 1048-1057.
42. Bayley, H., et al. *Droplet interface bilayers. Mol Biosyst.*, 2008. **4**(12): p. 1191-208.
43. Dixit, S.S., et al. *Droplet Shape Analysis and Permeability Studies in Droplet Lipid Bilayers. Langmuir*, 2012. **28**(19): p. 7442-51.
44. Barriga, H.M.G., et al. *Droplet interface bilayer reconstitution and activity measurement of the mechanosensitive channel of large conductance from Escherichia coli. J R Soc Interface*, 2014. **11**(98).
45. Barlow, N.E., et al. *Engineering plant membranes using droplet interface bilayers. Biomicrofluidics*, 2017. **11**(2).
46. Gross, L.C.M. *Applications of Droplet Interface Bilayers: Specific Capacitance Measurements and Membrane Protein Corralling*. 2011, University of Oxford. p. 238.
47. Das, D., Wong, A., Friedman, T.N., Kerr, B.J., Kurata, H.T., and Lamothe, S.M. *Reducing agents facilitate membrane patch seal integrity and longevity. Channels (Austin, Tex.)*, 2024. **18**.
48. Rosholm, K.R., et al. *Activation of the mechanosensitive ion channel MscL by mechanical stimulation of supported Droplet-Hydrogel bilayers. Sci Rep.*, 2017. **7**: p. 45180.
49. Thompson, J.R., et al. *Enhanced stability and fluidity in droplet on hydrogel bilayers for measuring membrane protein diffusion. Nano Lett*., 2007. **7**(12): p. 3875-8.
50. Crites, T.J., et al. *Supported Lipid Bilayer Technology for the Study of Cellular Interfaces. Curr Protoc Cell Biol.*, 2015. **68**: p. 24 5 1-24 5 31.
51. Kaiko, G.E., et al. *Immunological decision-making: how does the immune system decide to mount a helper T-cell response? Immunology*, 2008. **123**(3): p. 326-38.
52. Ayuob, N.N. and Ali, S. *Cell Interaction*. 2012: InTech.

53. Platzman, I., Janiesch, J. and Spatz, P. *Synthesis of Nanostructured and Biofunctionalized Water-in-Oil Droplets as Tools for Homing T Cells. American Chemical Society*, 2013. **135**(9): p. 3339-3342.
54. Dustin, M.L., Chakraborty, A.K. and Shaw*, A.S. Understanding the structure and function of the immunological synapse. Cold Spring Harb Perspect Biol.*, 2010. **2**(10): p. a002311.
55. Manz, B.N., et al. *T-cell triggering thresholds are modulated by the number of antigen within individual T-cell receptor clusters. Proc Natl Acad Sci USA*, 2011. **108**(22): p. 9089-94.
56. Turtle, C.J. and Riddell, S.R. *Artificial antigen presenting cells for use in adoptive immunotherapy. Cancer J.*, 2010. **16**(4): p. 374-81.
57. Eggermont, L.J., et al. *Towards efficient cancer immunotherapy: advances in developing artificial antigen-presenting cells - ScienceDirect. Trends in Biotechnology*, 2014. **32**(9): p. 456-465.
58. Czogalla, A.H. Franquelim, G., and Schwille, P. *DNA Nanostructures on Membranes as Tools for Synthetic Biology - ScienceDirect. Biophysical Journal,* 2016. **110**(8): p. 1698-1707.
59. Brea, R.J., Hardy, M.D. and Devaraj, N.K.*Towards Self-Assembled Hybrid Artificial Cells: Novel Bottom-Up Approaches to Functional Synthetic Membranes. Chemistry*, 2015. **21**(36): p. 12564-70.

Chapter 2: *Giant Unilamellar Vesicle Generation via Elecroformation and Emulsion Phase Transfer Methods*

2.1 Introduction

The lipid bilayer, as a universal component of the cell-membrane structure, is involved in a huge range of cellular mechanisms[1]; it provides the compartment boundary in all known living entities[2], and its mechanical properties are implicated in binding and gating mechanisms of proteins[1]. Hence, lipid bilayers assembled *in vitro* should replicate biological membrane key properties such as lamellarity, curvature, shape, asymmetry and the capacity to host transmembrane proteins[1].

Amongst the deluge of the developed membrane models, such as small unilamellar vesicles (SUVs), below 100 nm diameter, large unilamellar vesicles (LUVs), from 100 nm up to 1 μm, the vesicular structures which are the gold standard of cellular mimics, are

the giant unilamellar vesicles (GUVs). They display eukaryotic cell similarity, with diameter between 1 and approximately 100 μm[3] and enable myriad applications as simplified model cellular systems. They are deployed in the reconstitution of cellular machineries and in the analysis of lipid-lipid interactions, where the presence of fluorescent dyes, reveals lipid phase separation events[4-7].

GUVs as cell-sized aqueous spheres can enclose an internal aqueous environment through deposition of a phospholipid bilayer and can display the full scope of biophysical traits associated with plasma membranes[1, 8, 9]. Therefore, they are of great interest not only as cell membrane models, but as drug delivery systems as well[10]. They also open up possibilities for deeper understanding of biological cellular mechanisms and for artificial cell engineering with capabilities of executing specific tasks in mind[3].

Giant unilamellar vesicles, first described about 55 years ago by Reeves and Dowben(1969)[11], are easily observable by optical microscopy due to their cell size. Both natural contrast enhancement techniques (Zernicke phase contrast, differential interference contrast or hoffman modulation contrast) or fluorescence microscopy (confocal/two-photon excitation) are commonly utilized, with the latter method requiring fluorescent probes embedded in the lipid membranes.

The first preparation method was the swelling process[12], which was an adaptation from Reeves and Dowben protocol (1969)[11]. This procedure despite being easy to adapt to physiologically relevant conditions, for GUV generation, a high percentage of negatively charged lipids (~15 mol%) is a necessity[13], limiting available options for lipid content. In addition, the slowness of this strategy (at least a few days for GUV formation) impedes its application to rapid degrading lipid species, such as the unsaturated ones[14].

An alternative process for GUV production was initially proposed in 1986 by Angelova and Dimitrov[15], which accelerates the formation procedure (typically, in 1–3 h) and thereby, promotes work with more fragile lipid mixtures. This method, referred to as electroformation or electroswelling, is based on swelling of lipids (already dissolved in organic solvents) deposited on electrodes, where external electric field is applied[4]. This

leads to GUVs with more complex lipid architectures containing binary or ternary lipid mixtures, as well as natural lipid extract[16-19].

The general belief that GUV electroformation could work only with low salt concentrations, that is ~10 mM NaCl [20, 21], has been overturned, as new protocols have shown successful GUV making under physiological electrolyte concentrations[22]. Such progress constitutes one of the conducive factors towards establishing electroformation as one of the most utilized techniques for GUV generation[4, 15].

Yet, the major disadvantage of this technique, apart from the careful optimization it requires, depending on the lipid charge and buffer condition, lies in the effect the electric field might have on the biomolecules used for *in vitro* reconstitution of cellular machineries [4, 15]. Adding to that, GUV preparation with embedded membrane proteins and acquisition of asymmetric membranes are challenging tasks.

Aside from these two entrenched methods (gentle hydration and electroformation) for GUV production[3, 23-25], elaborate microfluidic systems[23, 26-29] have been developed to date, with the possibility of high precision lossless encapsulation of biological macromolecules[3].The advantage of using microfluidic devices for constructing GUVs lies in control over size, monodispersity and high encapsulation efficiencies, but the basic downsides pertain to complex instrumental and time-consuming setups[30-32].

Conversely, the bulk inverted emulsion-based method, which affords great promise in macromolecule encapsulation, (e.g. DNA[33], enzymes[34], polymers[35], cells[36], micron-sized particles[37]), and permits multicomponent lipid mixture integration, can be implemented using low-cost and no highly specialized equipment such as Eppendorf tubes. Although this is a low-throughput approach, optimization has been demonstrated by microtiter plate utilization that allows multiple, repeatable parallel experiments[31].

Furthermore, GUVs with asymmetric membranes are attainable via inverse emulsion[38] as the two membranes are formed separately, giving the option to the user to specify the desired lipid composition.

2.1.1 GUV Generation Techniques

2.1.1.1 Electroformation Process

The principle idea of the energy driven method of electroformation is that it enhances the swelling process due to the periodic distribution of charges achieved by an alternate current (AC) field[39]. This technique allows production of large amounts of cell-sized vesicles within a period of a few hours[39] and affords flexibility in lipid composition[40], but does not offer control over vesicle size, output and encapsulation efficiency[3].

Lipids, even uncharged zwitterionic ones, after being deposited on an electrode surface, forming bilayer stacks, acquire permanent dipoles. The dipoles “feeling” the applied AC field, synchronize their movements along with it, facilitating the flow of aqueous solution in between the non-hydrated bilayer stacks, forcing lipid molecules to come fully into contact with water. This process subsequently instigates the hydrophobic effect, which transforms the disordered lipid film into a bilayer, where apolar chains are oriented inwards and polar heads are oriented outwards. This results in a decrease of both line and surface tensions of the swollen vesicles increasing bilayer separation (Fig. 2.1)[39].

A

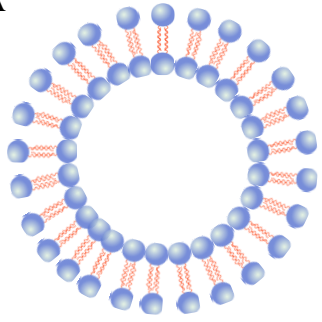

B

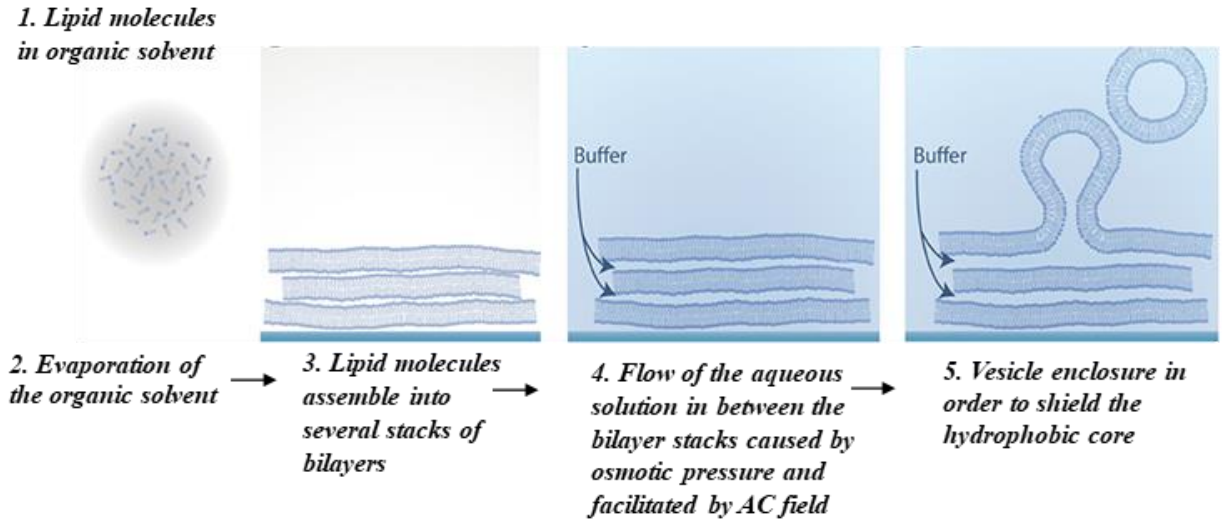

Figure 2.1- (A) Schematic diagram of a GUV. *(B) Schematic illustration of vesicle formation via electroformation. Image adapted from:[41].*

2.1.1.2 Emulsion Phase Transfer (EPT)

The typical procedure of Emulsion Phase Transfer (EPT) starts by dissolving a lipid mixture in oil (e.g. mineral oil[41, 42] dodecane[37] and squalene[43, 44]), which is subsequently layered on top of an aqueous solution to form an oil–water interface owing to lipids' amphipathic nature [Fig. 2.2 (a2), (a3)]. The lower aqueous phase [Fig. 2.2 (a1), (a2)] constitutes the outer environment where GUVs will be deposited. Concomitantly, a small volume of a chosen aqueous solution, which eventually becomes the inner compartment of the vesicle and contains the solutes to be encapsulated, is mixed with the lipid in oil phase in a separate tube [Fig. 2.2 (a4)]. The produced water-in-oil emulsion is stabilized by an assembled lipid monolayer forming the inner membrane leaflet. The emulsion is then added on top of the interface [Fig 2.2 (a4)] and the lipid

coated droplets are driven through the interfacial lipid monolayer by centrifugation acquiring the second, outer lipid leaflet, resulting in the final GUV formation [Fig. 2.2 (a5)][1, 3, 23, 37].

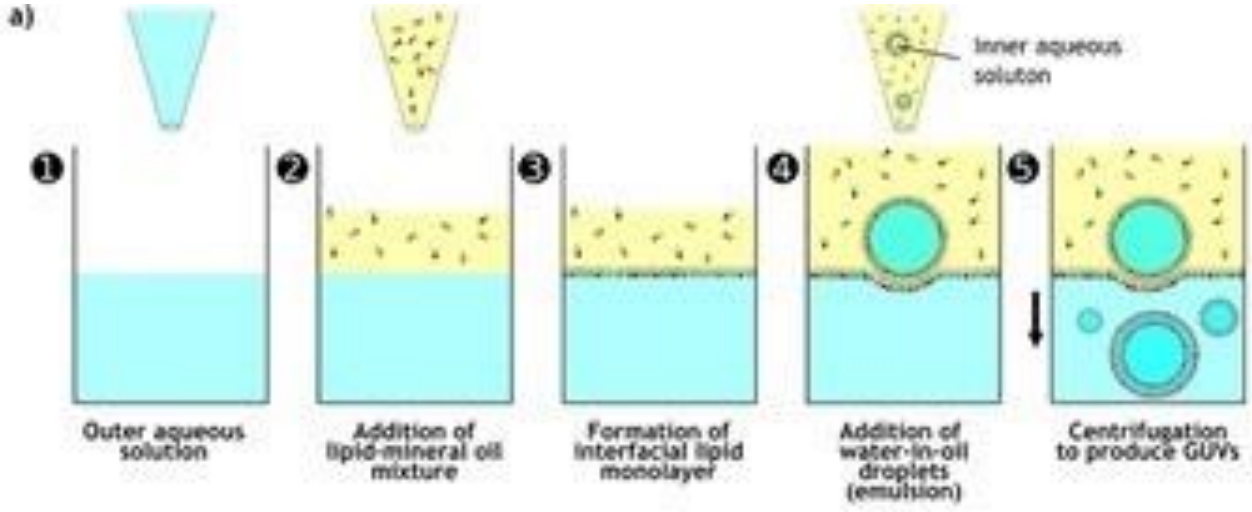

Figure 2.2- Overview of the inverted emulsion method*. Schematic representation of the steps leading to GUV production via the inverted emulsion method. Source:[3]. Briefly, EPT vesicles are produced by driving lipid-monolayer coated water-in-oil droplets through an oil–water interface stabilized by a second lipid-monolayer. As the droplet is driven through the interface under gravity, a second monolayer is deposited, forming the final vesicle[42].*

This technique is not immune to shortcomings, either. The drawbacks are mainly associated with poor yields or relatively small GUVs, driving research groups to adopt the more established methods, e.g. gentle hydration or electroformation[23-25], disregarding the limited range of their experimental possibilities[3].

In addition, a serious consideration in mind regarding the inverted emulsion approach is vesicle membrane functionality, which can be potentially compromised by the presence of oil within the two lipid leaflets. Such possibility hasn't shown significant changes in the vesicle's membrane mechanics, yet, it does pose a hindrance to its widened use when

for instance, channel (e.g. alpha-hemolysin) insertion into the vesicle membrane is a requisite[3].

2.1.2 Chapter's Aims

In the field of bottom-up synthetic biology, lipid vesicles play a significant role in artificial cell construction. Giant unilamellar vesicles (GUVs), presenting similarities to natural bio membranes, have been broadly utilized as versatile tools, expediting studies of membrane properties and cellular processes under controlled conditions.

Aiming to engineer a membrane model, comprised of an enclosed DIB-anchored GUV, we originally employed the electroformation procedure, the most prevalent method for lab-created vesicles. However, downsides pertaining to GUV low encapsulation capacities and loss of transbilayer lipid asymmetry, impeded our artificial construct development.

Building up on the artificial compartmentalized model system, vesicles with high encapsulation efficiencies, control over their internal content and membrane asymmetry were required; traits that could be simultaneously imparted to vesicles by the emulsion phase transfer method. For instance, actin monomer or network incorporation on the inside of vesicles together with biomolecule interaction with the inner leaflet membrane lipids have been pivotal requirements for the bottom-up synthesis of the artificial double membrane system; yet not able to be met by the conventional techniques (electroformation, gentle hydration).

The experimental work of this chapter involves GUV preparation via both the electroformation (***2.2.3 Vesicle Preparation by Electroformation***) and inverted emulsion-based strategies (***2.2.4 Vesicle preparation by Emulsion Phase Transfer***)**.**

In the first part of this study, the electroformation procedure is applied for GUV generation, where buffer of physiological ionic strength is utilized, and data is analyzed with respect

to GUV size, population and morphology characterization (***2.3 Results: Electroformation***).

Subsequently, the EPT method is employed, as it allows encapsulation of large charged chemical species and produces asymmetric GUVs. Specifically, in our preliminary venture to implement the EPT technique, we drew attention to the influence of density gradients of the aqueous solutions, and the presence or absence of the interface lipid monolayer formation, (prior to the addition of the emulsion phase), on vesicle diameter distribution and output. For this set of experiments, DPhPC lipid is exclusively used, and the experimental data are presented in the ***2.5 Results: Phase Transfer Data*** section**.**

In the second part of the EPT approach, a more in-depth investigation is presented, where a wider range of variables is manipulated, such as lipid (DOPC) and lipid mixtures (DOPC+DOPG and DOPC+DOPE-PEG) in symmetric and asymmetric bilayer configurations, aqueous emulsion volume, interfacial lipid concentration, interface incubation time and centrifugal force/speed and duration, and their effects on vesicle concentration and sizes are assessed (***2.7 Results: Phase Transfer Data)***.

This series of experiments provide data and insights into GUV optimization procedures, which apart from helping us determine the variable combinations to be used for producing suitable vesicles for the artificial membrane model fabrication they also raise further scientific questions that would be interesting to be addressed in another study.

2.2 Experimental Section

2.2.1 Materials

1,2-dioleoyl-sn-glycero-3-phosphocholine (18:1 (Δ9-Cis) PC (DOPC)) and mineral oil were purchased from Sigma–Aldrich (Germany). 1,2-dioleoyl-sn-glycero-3-[phospho-rac-(1-glycerol)] (18:1 DOPG), 1,2-diphytanoyl-sn-glycero-3-phosphocholine (16:0 DPhPC) and 1,2-dipalmitoyl-sn-glycero-3-phosphoethanolamine-N-[methoxy(polyethylene glycol)-2000] (16:0 PEG2000 PE) were obtained from Avanti Polar Lipids. CellMask™ Orange plasma membrane stain (C10045) was purchased by Life Technologies. Other chemicals including organic solvents (chloroform and ethanol), sugars (glucose and sucrose), phosphate-buffered saline (PBS) tablets, Calcein, Tris, 4-(2-hydroxyethyl)-1-piperazineethanesulfonic acid (HEPES) were obtained from Sigma–Aldrich (Germany).

2.2.2 Lipids in Oil Preparation

Chloroform-solubilized lipids, DPhPC, DOPC, DOPG, PEG2000 PE (Fig. 2.3), and mineral oil were used to make lipid–oil solutions. All lipids for experimentation were purchased as lyophilized powders and subsequently dissolved in chloroform at 25 mg/ml.

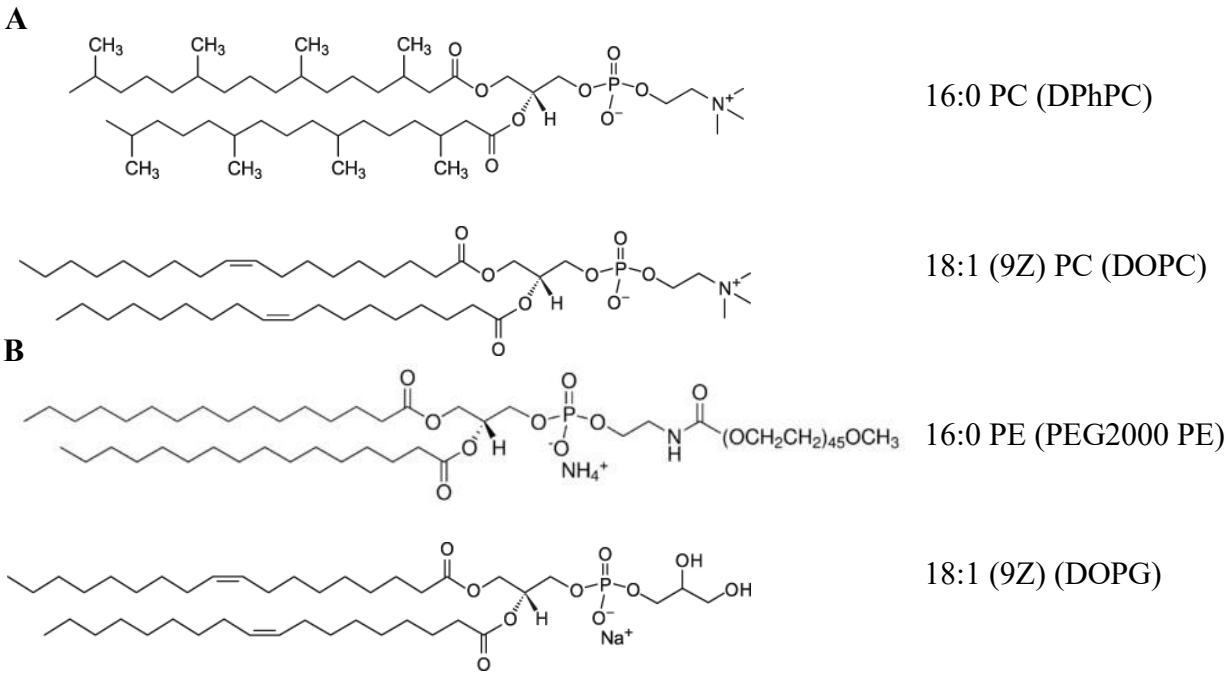

Figure 2.3- Lipids mentioned in this work. *(A) Neutral (zwitterionic) diacylglycerophospholipids: 1,2-diphytanoyl-sn-glycero-3-phosphocholine (DPhPC); 1,2-dioleoyl-sn-glycero-3-phosphocholine (DOPC); (B) Charged diacylglycerophospholipid: 1,2-dipalmitoyl-sn-glycero-3-phosphoethanolamine-N-[methoxy(polyethylene glycol)-2000] (PEG2000 PE); 1,2-dioleoyl-sn-glycero-3-phospho-(1'-rac-glycerol) (DOPG).*

2.2.3 Vesicle Preparation by Electroformation

Giant vesicle suspension from DPhPC was prepared through hydration in the presence of a sinusoidal alternating current (AC) electric field. Indium-tin oxide (ITO)-coated glass slides, square (25 mm × 25 mm × 1.1 mm), 70-100 Ω/sq surface resistivity, purchased from Sigma-Aldrich, were employed. They were cleaned with dH_2O and ethanol and dried by N_2 stream.

15 µl of the DPhPC/chloroform solution at a concentration of 2 mg/ml was applied and spread over the conductive side of one ITO slide which was subsequently submitted to a steady stream of nitrogen for 2 minutes to remove chloroform. Following that, a 2 mm thick rubber gasket was placed approximately in the center of the chamber where 200 µl of a saline solution (TE and 50 mM NaCl, pH 7.83) was added. Then, the two ITO-coated glass slides were positioned to build the growth chamber with the conductive sides facing each other, separated by the 2 mm thick gasket (Fig. 2.4A). The assembled device was connected to a function generator (hewlett packard 33120A 15 MHz/arbitrary waveform generator) via wires mounted around bulldog clips adjusted on the two ITO slides (Fig. 2.4B). Following completion of the electroformation procedure, the upper ITO glass was removed to allow GUV harvest. This experimental setup had been adapted from[45].

Ai

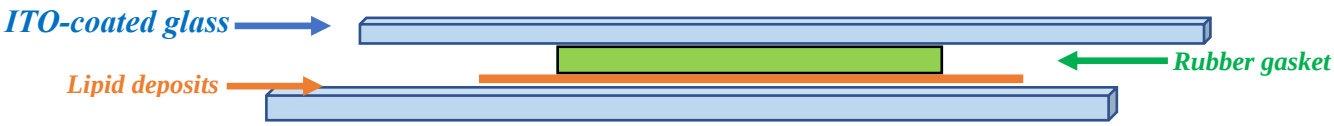

Aii

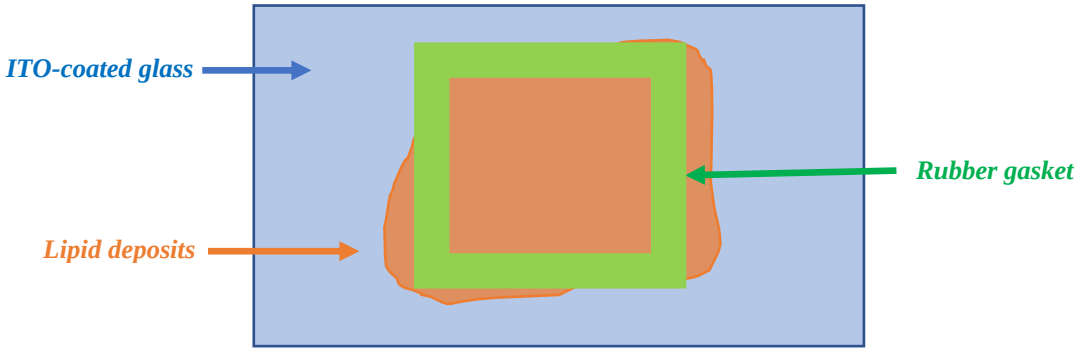

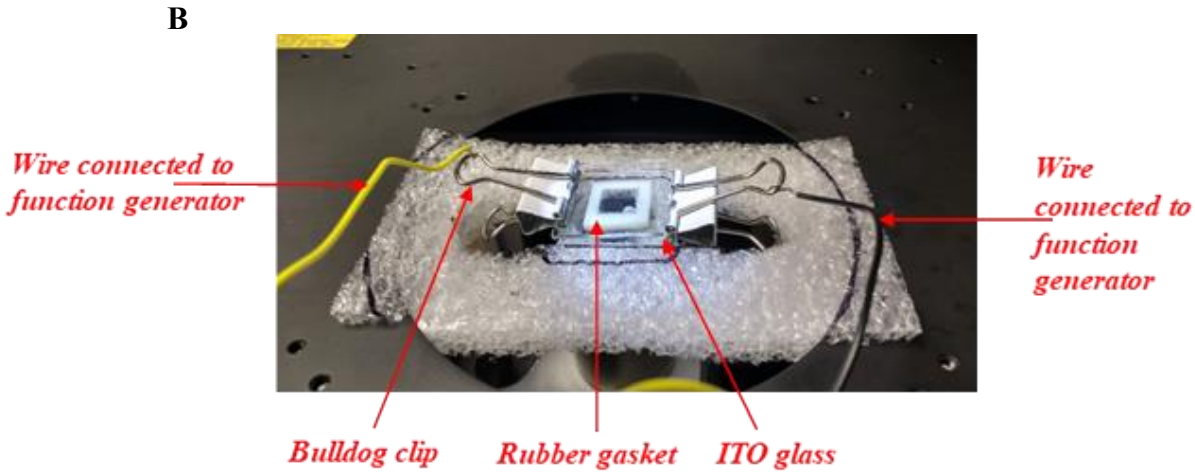

Figure 2.4- (A)Schematic depiction and (B)photographic image of the electroformation experimental setup. *(Ai) Side and (Aii) top view of an electroformation chamber formed with a rubber gasket sandwiched between two ITO-coated glass slides. (B) Wires were attached to bulldog clips through which current was transmitted. Creation of a hole on a foam platform permitted direct vesicle visualization through an inverted microscope connected to a microscope eyepiece camera.*

2.2.3.1 Vesicle Electroformation Protocol

The electroformation process was performed at room temperature where an alternating electrical field at high frequency, 500 Hz, and a sequence of rising amplitude was applied. Specifically, the formation protocol was taken from [45] and involves multiple steps of increasing electric sequence and constant frequency as displayed in the table 2.1 underneath.

Table 2.1 Electric sequence applied for giant unilamellar vesicle electroswelling in ionic solution (TE and 50 mM NaCl, pH 7.83)

Electric field (V m^{-1})	Frequency (Hz)	Duration (min)
260	500	5
670	500	5
1000	500	15
1330	500	30
1670	500	Overnight

2.2.4 Vesicle Preparation by Emulsion Phase Transfer (EPT)

For the encapsulation of internal cargo (0.5 mM fluorescent dye Calcein), the EPT strategy was developed based upon previous methods reported in the literature[3, 26, 46-48].

For the first group of the EPT experiments, (***Results*** presented in ***2.5***), DPhPC lipid film was made by initially dissolving lipids in chloroform; solvent was removed under nitrogen stream and subsequent 30 min vacuum incubation. Mineral oil was employed to dissolve the lipid film (5 mg/ml) through a 30 min sonication period at 40°C.

An emulsion of droplets in oil was made by vortexing 20 µl of 50 mM sucrose, 50 mM NaCl (Tris-EDTA, pH 7.83) in 200 µl of lipid-in-oil for 30 seconds and left it standing for at least 10 min to facilitate a lipid monolayer assembly. For the loaded-vesicle experiments, 0.5 mM Calcein was also contained in the same buffer solution. 100 µl of the stabilized emulsion was then deposited either directly above 250 µl of the aqueous medium (50 mM glucose and 50 mM NaCl or merely 50 mM NaCl) in an Eppendorf forming a water/oil column, or on top of 120 µl of a lipid-oil solution, layered above the aqueous medium,

following a 1 h-incubation to enable interfacial lipid monolayer formation. Then, a centrifugal force (9000 × g, 30 min) was applied to drive the (w/o emulsion)/droplets through the interfacial lipid monolayer. The upper oil phase was extracted, and the aqueous phase was resuspended by pipetting up and down a couple of times.

For the second set of experiments via EPT, (***Results*** presented in ***2.7***), DOPC, and mixtures of DOPC+DOPG (0.5% w/w) and DOPC+PEG2000 PE (10% w/w) thin films of dried lipids were formed in glass vials through chloroform evaporation under nitrogen flow. Solvent leftover traces were removed by placing vials in a desiccator for a period of 30 min.

Finally, mineral oil was added to the glass vials, followed by a sonication step at 40°C for 30 min for better solubilization of lipids in the oil. At this stage, the total lipid concentration in the mineral oil was 5 mg/ml. Lipid concentration of 2.5 mg/ml was deployed only for the interface monolayer assembly used to produce the outer membrane leaflet of the GUV.

The emulsion preparation involved vortexing of 5 µl or 20 µl of 600 mM sucrose, in 200 µl of lipid-in-oil for 20 seconds, which was then left standing for at least 10 min for effective stabilization of a lipid monolayer. The stabilized emulsion was then added above 250 µl of 600 mM glucose, in a 1.5 ml Eppendorf® tube, with an already formed interfacial monolayer composed of 100 µl lipid in oil incubating for 15 min or 1 h.

Immediately after this, the tube was transferred into a centrifuge (Thermo Scienific) and based on the experimental condition, either 50, or 300 g force was applied for periods of 1 min or 5 min driving droplets through the interface and resulting in a pellet at the bottom of the tube. The pellet was resuspended in the 600 mM glucose solution following supernatant extraction.

2.2.5 Inner and Outer Aqueous Solutions

All aqueous solutions were made using MilliQ Millipore® water and the concentrations of inner and outer solutions were such to maintain isosmotic conditions across the membrane.

2.2.6 GUV Staining

For more detailed characterization of GUV structure, the labelling membrane probe, CellMask™ Orange plasma membrane stain (C10045), was diluted in the aqueous GUV suspension. The lipophilic moiety of this amphipathic stain is attached to the vesicle membrane and its negatively charged hydrophilic segment enables probe anchoring in the membrane.

Vesicles were incubated with CellMask Orange for 2 hours prior to imaging and the working solution for its incorporation into the GUV phospholipid membranes was determined at 1:1000. Dye stock was prepared in DMSO at 1 mg/ml and stored in a plastic tube at -20^{o}C.

2.2.7 Plasma Cleaning-Activation

Plasma cleaning involves impurity and contaminant removal from the surface of a material, such as glass surfaces, polydimethylsiloxane (PDMS), plastics, using an energetic plasma from gaseous species. Plasma's activated species include positive ions, negative electrons, free radicals that emerge when a gaseous substance is subjected to strong electromagnetic fields, such as short wave ultraviolet (vacuum UV) range or high temperatures.

The most used gas is oxygen due to its economical and environmentally safe nature. The oxygen species created in the plasma (O_2^+, O_2^-, O_3, O, O^+, O^-, ionized ozone, metastable excited oxygen, and free electrons) react with organic contaminants generating CO_2, CO,

H_2O, and lower molecular weight hydrocarbons, which due to their high vapor pressures are evacuated from the chamber, resulting in ultra clean surfaces[49].

In addition, surface exposure to oxygen plasma introduces polar functional groups[49], mainly the silanol group (SiOH), at the expense of methyl groups (-CH3)[50], changing the surface property from hydrophobic to hydrophilic[51].

2.2.7.1 Plasma Treatment

Oxygen plasma treatment was carried out using a Femto Plasma Cleaner (Diener, Germany), utilizing oxygen as gas. Coverslips were treated at a pressure of 0.35 mbar with oxygen flow rate of 10 sccm (standard cubic centimeters per minute) for 3 min.

2.2.8 Optical Microscopy: Bright field and Phase Contrast Imaging of GUVs

All the work detailed in this chapter was performed using bright-field, phase contrast or fluorescence microscopy.

GUVs formed using DPhPC, DOPC lipids and mixtures of DOPC+DOPG and DOPC+DOPE-PEG were stored in tubes at 4^{o}C overnight. The produced GUVs were extracted from the tube and 30 µl of each sample was placed on plasma treated coverslips for imaging the next day.

For the GUVs generated via electroformation and the first set of EPT experiments, vesicles were viewed with a bright-field and phase-contrast microscope (OLYMPUS IX50), equipped with a 10× objective lens (NA 0.6 Ph2; OLYMPUS LCPlanFI), and images were acquired with a digital camera (OLYMPUS XC10).

For the second set of EPT experiments, acquisitions were conducted with a Nikon Eclipse TS2 inverted microscope (Nikon)**,** equipped with 20× objective and a fast digital camera.

2.2.8.1 Phase-contrast Principle

Phase-contrast imaging is a contrast-enhancing optical technique utilized for transparent specimens, such as living cells, thin tissue slices, vesicles, etc. The principle behind phase contrast imaging is outlined in Fig. 2.5. The illumination from the light source that passes the Condenser Annulus is directed to the sample by the Condenser. Wavefronts that illuminate the specimen either pass through it in an undeviated mode or are diffracted and thus, delayed in phase by structures present in the sample. The undeviated and delayed light, after being collected by the Objective lens, is separated by a Phase Plate enhancing the contrast, which is focused on the Image Plane that we observe in the eyepieces[52].

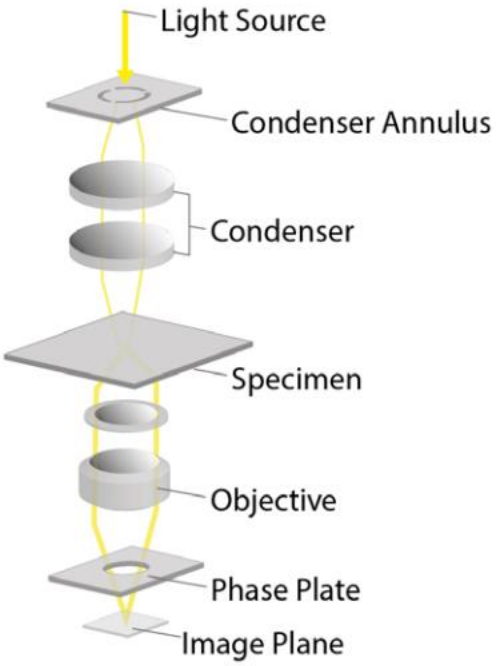

Figure 2.5- Inverted phase contrast microscope configuration. *Source: [52].*

2.2.9 Fluorescence Microscopy

Membrane-stained vesicles and Calcein laden GUVs were imaged by fluorescence

microscopy on a TIRF microscope (Nikon Eclipse Ti- inverted epifluorescence microscope) equipped with a Nikon PLAN APO 60× 1.49 NA Oil objective lens and two laser lines: 473 nm (laser quantum mpc 6000, Ventus), 532 nm laser line (laser quantum smd 600, Ventus).

The excitation wavelengths utilized for CellMask Orange labelled and Calcein loaded GUVs were 532 nm and 478 nm, respectively. Their emissions were detected by filtering out the excitation lights through dichroic filters, (Dichroic: Dio3-R405/488/532/635, BrightLine, USA, and FF640-FDio1 Semrock), and measuring the remaining wavelengths. Images were recorded with a CCD camera (iXon Ultra 897 ANDOR).

2.2.10 Image Analysis

Image analysis was performed with the open source software FIJI, a distribution of the open source software ImageJ [53]. Vesicles were visually detected, and the Multi point Tool was used for counting GUV density by manually marking each vesicle in every image. The (Edit>Selection>Properties) functions were applied to display the counts in a results table, which were pasted onto an Excel sheet for analysis.

Vesicle size distribution was determined by choosing the Line Selection Tool to draw a line from one border of the vesicle to the opposite border (diameter). To measure the length of the line, after the image had been spatially calibrated against known values, the parameter “Length” was set in the “Set Measurements” dialog box, and then Analyze > Measure functions were used to record the vesicle diameter.

To mitigate miscounting issues, each image was opened in FIJI twice; one to measure the vesicle diameter and the other one to mark the corresponding GUV with the Multi point Tool. Equal numbers of recorded diameters and vesicle numbers were verified prior to proceeding to data analysis.

2.2.11 Statistics

Statistical analyses and graphs were performed using GraphPad Prism 9, Excel and Matlab R2020a.

Comparison of yield populations and average GUV diameters (presented in ***2.7 Results***) were carried out using unpaired t test with Welch's correction, when needed, to account for unequal sample sizes and variances between the groups[54]. Each experimental condition was performed in triplicate (n = 3), unless otherwise stated (specifically in ***2.5 Results*** section).

For each condition (in ***2.7 Results***), size and concentration of GUVs were obtained from a total of 3 images randomly taken from a 30 µl droplet of GUV solution placed on a glass coverslip, with the same field of view (538.9 µm × 338.5 µm) for comparable yield assessments. The standard deviations of the GUV yield and reported mean diameter values were calculated for the nine readings in each experimental group. Error bars were taken from the standard deviations throughout (n = 3).

2.3 Results: Electroformation

2.3.1 Electroformation Data: GUV Size and Yield

We initially generated GUVs through the electroformation procedure. GUV populations were produced (by electroformation) using the experimental setup described in ***Methods***: (***2.2.3 Vesicle Preparation by Electroformation***). This technique needed to be developed as it had never been used in our lab before. Micrometer-sized vesicles were formed from DPhPC in 50 mM NaCl and Figure 2.6 depicts some typical GUVs obtained with this protocol as visualised on light inverted microscope.

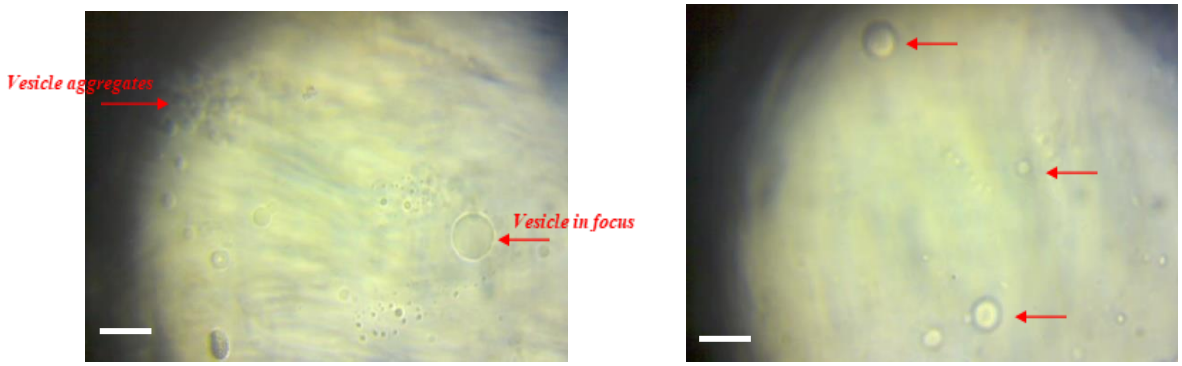

Figure 2.6- Typical GUVs obtained after electroformation in aqueous solution as imaged on an inverted microscope under bright-field with 10× magnification. *Scale bars:100 μm.*

The images in Figure 2.6 confirm that by the end of the electroswelling process, free-floating single vesicles along with aggregates of smaller ones were obtained. GUVs could float since there was no difference in the medium solution between the interior and exterior of the GUVs; consequently, not all GUVs in these pictures were necessarily in the same focal plane. This observation becomes more evident in images obtained from a phase-contrast microscope (Fig. 2.7).

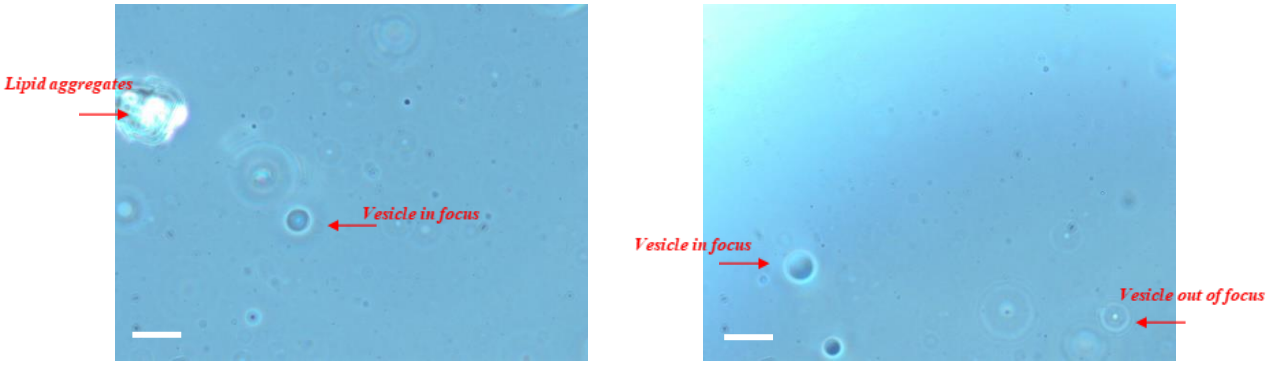

Figure 2.7- Vesicles with non-uniform radii imaged under bright-field on phase-contrast microscopy. *GUVs in focus and out of focus along with lipid aggregates can be observed. Scale bars: 50 μm.*

The electroswelling method gave rise to vesicles of heterogeneous size whose diameter measurements were conducted on phase-contrast microscope images using the FIJI software. Their sizes ranged from 6 up to 79 microns and the histogram shows their size distribution with the most frequently detected ones being from 6 up to 30 microns (Fig. 2.8). Electroformation experiments were conducted 3 times and vesicles displayed similar measurements and morphological features that are described in ***2.3.2 GUV Morphology*** section.

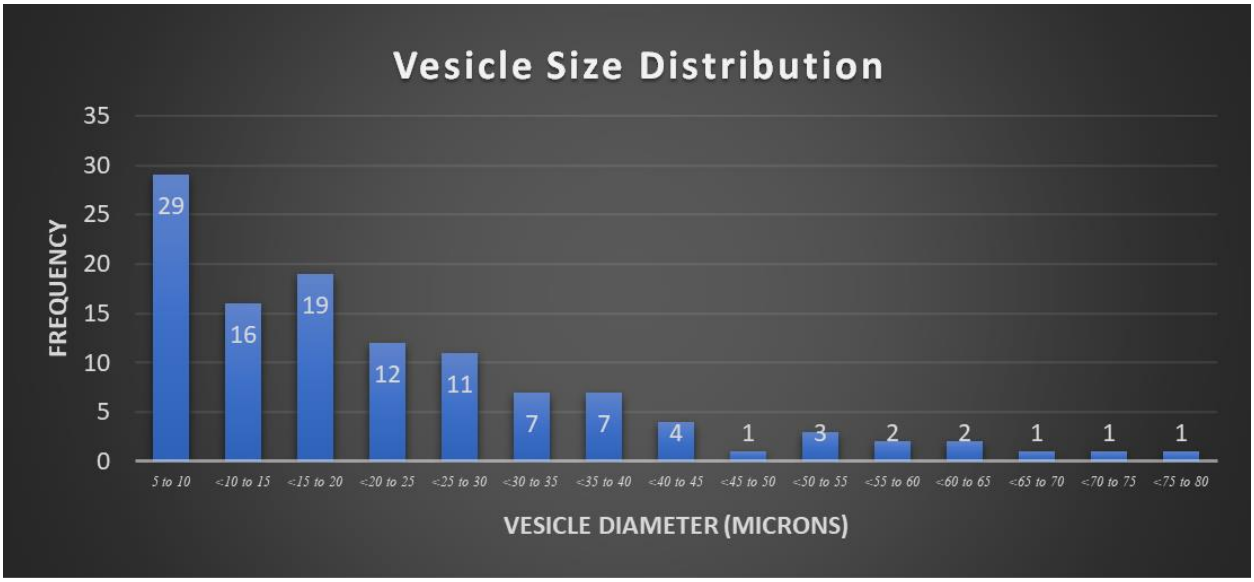

Figure 2.8- Histogram demonstrating GUV size distribution from one dataset. *Vesicle size ranges from 6 up to 30 microns were most frequently produced.*

2.3.2 GUV Morphology

Amphiphilic fluorescent dye (CellMask Orange) incorporation into GUV membranes enabled imaging of vesicle morphology. A sample of the aqueous GUV suspension was transferred on a microscopy slide and visualized on TIRF microscopy in the epifluorescence mode.

A respectable number of pure DPhPC vesicles manifested a well-formed spherical shape (Fig. 2.9), whereas some were significantly smaller with a membrane thread attached to them (Fig. 2.10). This shape deformation has been documented in previous studies in which GUVs were created by electroformation [55, 56].

The appearance of the cylindrical protrusions has been attributed to the excess vesicle area required for the generation of the vesicles' spherical topology [55, 57] and are thought to be formed due to the electroswelling process [57].

These thread-like tubes could also be detected within the vesicle boundaries (Fig. 2.11). Interestingly, tubular structures, either confined within the vesicle territory or protruding outwards were not static and were mostly observed in small-sized GUVs, a feature that has been previously reported [57].

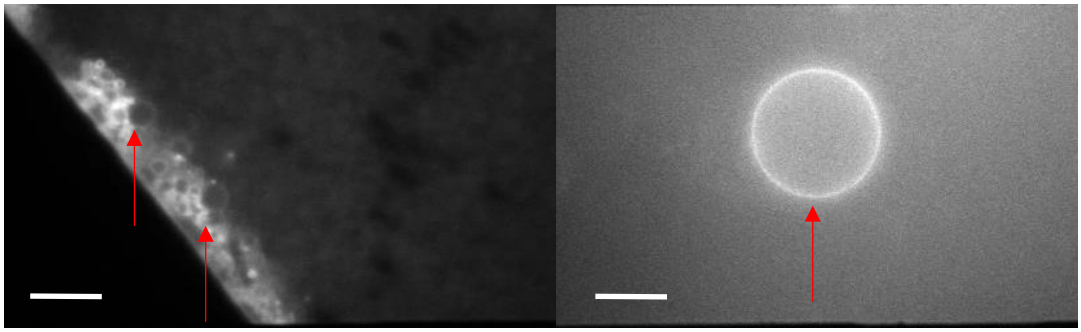

Figure 2.9- Micrographs demonstrating pure DPhPC vesicular membranes fluorescently labelled with CellMask Orange. *A sample of GUV suspension was applied on a glass slide allowing for epifluorescence visualization on an inverted microscopy setup. Smooth and approximately spherical vesicles can be seen. Scale bars: 10 μm.*

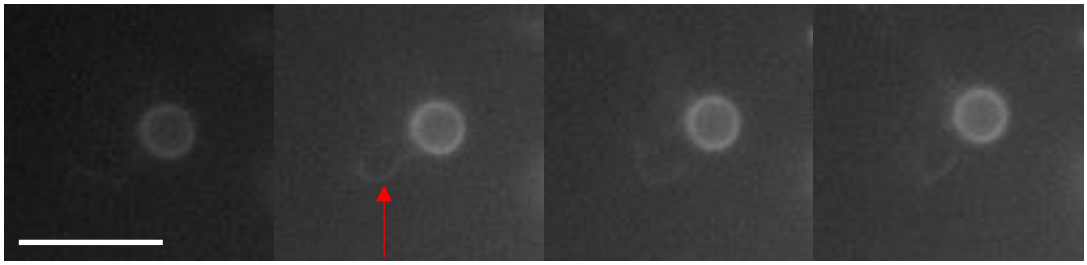

Figure 2.10- Selected frames showing the equatorial view of a vesicle with an attached moving tubular protrusion. *Scale bar: 10 μm.*

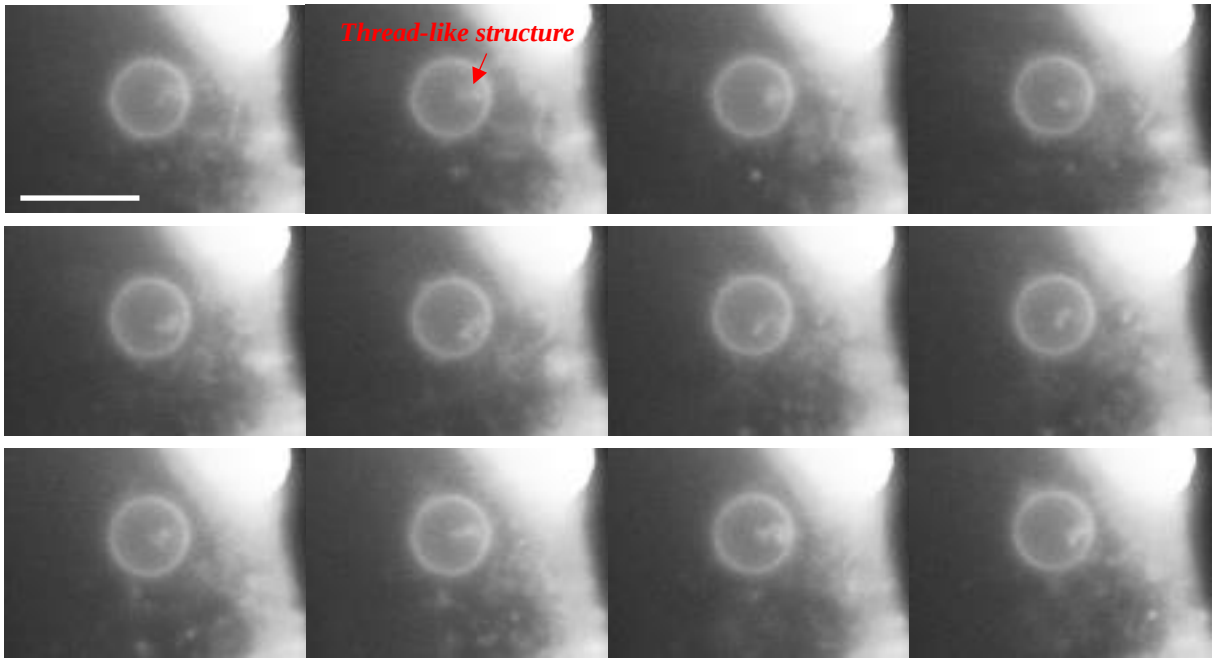

Figure 2.11- Arbitrarily selected micrographs of fluorescence images from a video of a GUV with a non-static thread-like structure restricted within the vesicular compartment. *Scale bar: 10 μm.*

Another morphological transformation is the intralumenal vesicle formation as depicted in Figure 2.12. According to Sanborn[57], this daughter vesicle involution can result from negative intravesicular pressure due to water efflux. Consequently, this membrane inclusion produces an inverse osmotic gradient across the mother and daughter vesicle membranes leading to tense boundaries and an accompanying suppression of the undulation amplitude of the membrane [57].

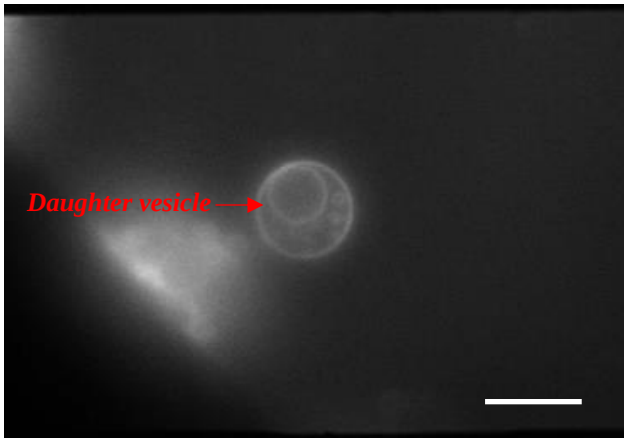

Figure 2.12- Depiction of daughter vesicle internalization. *Scale bar: 10 μm.*

Another notable feature is the emergence of optically microscopic domains on the surface of some vesicles as portrayed in Figure 2.13. In this GUV, a heterogeneous landscape with bright and dark patterns can be distinguished. Although the only lipid used in our experimental procedure was DPhPC, the silicone oil contained in the vacuum grease pre-coated rubber gasket, as a liquid polymerised siloxane, cannot be ignored. A study conducted by Bieligmeyer, et al. 2016 showed that lipopolymer vesicles comprised of more than 50 mol% DPhPC exhibit a heterogeneous distribution of the dye and a phase-separated profile between polymer and lipid [56]. Certainly, the scenario of ample marker concentration with a contributory role to domain formation due to its amphiphilic nature cannot be overlooked.

Taking this information into account, we cannot exclude the possibility that the bright areas are probe-enriched domains denoting Ld state and the dark regions indicate Lo phase. It has not gone unnoticed that the oscillatory behaviour of the microscopically phase-separated GUVs was supressed, a typical feature of tense vesicles [58]. Under this perspective the tense vesicle state justifies domain emergence. However, this observation needs further investigation before firm conclusions are drawn.

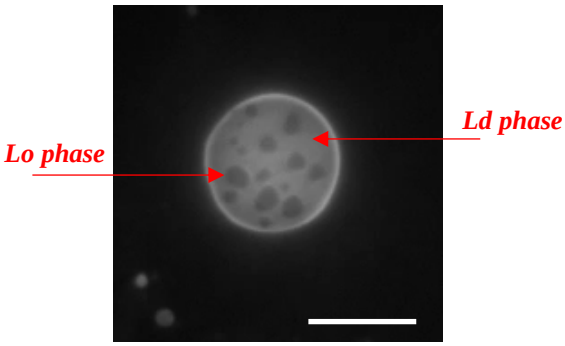

Figure 2.13- Fluorescence image illustrating a microscopically phase-separated topography with Lo (microscopically dark domains) and Ld phases (microscopically bright domains). *Scale bar: 10 μm.*

2.4 Discussion

Aiming to encapsulate and adhere a GUV to a DIB, electroformation was the first strategy utilized to materialize this preliminary objective. It was shown that GUV formation by means of the electoformation procedure was successfully realized under physiologically relevant conditions.

Some interesting findings from this experimental work are associated with heterogeneous size distribution, and structural effects in vesicle morphology, such as the presence of intralumenal vesicle formation (Fig. 2.12) and tubular arrangements (Fig. 2.10, 2.11), either restricted within the vesicular compartment (Fig. 2.11) or attached to the outer membrane leaflet (Fig. 2.10).

Moreover, the unintentional creation of phase transition states (Fig. 2.13), evident on the surface of some vesicles requires further investigation with regards to the inducing effect, although, it does not constitute a roadblock to the construction of our membrane model system.

2.5 Results: Phase Transfer Data: Impact of Aqueous-based Density Gradient and Interface Lipid Monolayer Formation on GUV Output and Size

Utilizing the inverted emulsion method, we manipulated various parameters to investigate how they affect GUV production with respect to vesicle size and concentration.

In the first section of the EPT experimental study, we focused on the influence of density gradients of the aqueous solutions, and interface lipid monolayer formation on GUV diameter and population. GUVs were entirely composed of DPhPC phospholipids and bright-field, phase contrast and fluorescence microscopy images were acquired at 25^{o}C.

In the second part, as aforementioned (in ***2.1.2 Chapter's Aims)***, a more thorough exploration of variables (such as droplet volume, lipid concentration of interfacial monolayer, interfacial monolayer formation incubation time, centrifugation duration and applied force) was followed, utilizing various lipid combinations (DOPC, DOPC+DOPG, DOPC+PE PEG) in symmetric and asymmetric GUV bilayer formations and monitored how they affect vesicle population and size. The pertinent analysis is presented in ***2.7 Results: Phase Transfer Data: Influence of Various Parameters on GUV Size and Yield.***

2.5.1 Density Gradient

An important element considered during GUV generation through inverted emulsion was the density difference between the water-in-oil droplet and the lipid oil intermediate phase. This is a critical component as density gradient inclusion between the lipid oil and the inner aqueous phase is a necessity for GUV production [59]. The inner solution needs to provide sufficient force for the water-in-oil emulsion to be transferred from the layered mineral oil to the aqueous phase. Most natural oils are of low density relative to pure water, and mineral oil that was exclusively used does not constitute an exception.

Another density difference that is worthy of heed, involves inner and outer aqueous solution density gradient, which impedes vesicle aggregation at the interface and is accountable for subsequent vesicle settlement at the bottom of the tube.

2.5.2 Sugar-based Density Gradients

Glucose and sucrose have been extensively used in GUV preparation with the inverted emulsion-based technique, due to the preservation of osmotic balance across membrane and their inertness towards the lipid bilayer[3].

2.5.3 Aqueous-based Density Gradient and Interface Lipid Monolayer Formation Impact on GUV Size and Yield

In the first set of these experiments, concentrations of 50 mM sucrose along with 50 mM NaCl and 0.5 mM Calcein versus 50 mM glucose along with 50 mM NaCl for the emulsions and the outer aqueous solution respectively, resulted in 0.0112 g/ml difference. Additionally, the sucrose droplets were 0.2474 g/ml higher density than the lipid-(mineral) oil monolayer on the surface of the aqueous glucose phase, sufficient to drive phase transfer. Although gravity is a means to propel droplets through lipid in oil intermediate phase, for this production method, a significant density gradient is necessary together with longer times to allow droplets to pass through the interfacial monolayer resulting in a good yield. An alternative strategy requires a centrifugal force which accelerates the vesicle formation process. This approach has been particularly exploited since inadequate incubation times can lead to droplet aggregation at the interface.

120 μl of the lipid-oil solution was poured on top of a medium (250 μl) containing 50 mM glucose and 50 mM NaCl, pH 7.6, and the entire setup was allowed to incubate for a period of 60 min to facilitate an interfacial lipid monolayer formation. Then, 100 μl of the

W/O emulsion (50 mM sucrose, 50 mM NaCl and 0.5 mM Calcein, pH 7.6) was gently poured on the oil-aqueous interface prior to centrifugation (9000 × g, 30 min).

Figure 2.14A displays a representative image obtained from vesicles deposited on plasma treated cover glass. The constructed histogram (Fig. 2.14B), obtained by analyzing a population of GUVs (N = 47), demonstrates that under the current experimental condition there is a large variability of vesicle diameters (from 1.7 to 100 µm), with a mean size of ~29 µm. This experimental condition was conducted twice with similar results.

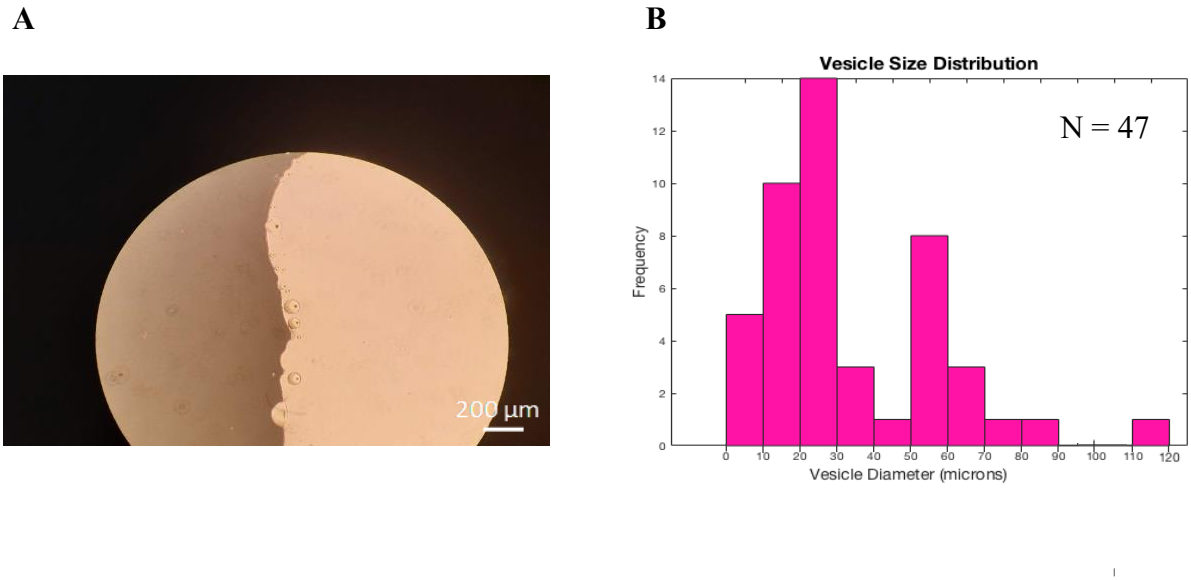

***Figure 2.14- (A) DPhPC vesicles prepared by the EPT method**. Bright-field image of GUVs with 10× magnification. Vesicles loaded with sucrose and Calcein were settled on the plasma-treated glass surface. The scale bar represents 200 µm. (B) Size distribution of 1,2-diphytanoyl-sn-glycero-3-phosphocholine (DPhPC) GUVs produced at 60 min intermediate phase incubation time. The average diameter for this data set (N = 47) was 28.9 µm with a polydispersity index of 0.83.*

The same conditions used in the aforedescribed sample were also preserved for the following group, except for intermediate phase incubation. The emulsion itself (100 µl), composed of lipid in oil with the aqueous phase (50 mM sucrose, 50 mM NaCl and 0.5 mM Calcein), was layered on top of 250 µl of 50 mM glucose and 50 mM NaCl in an

Eppendorf tube to form a water/oil column, bypassing prior formation of lipid monolayer at the oil-water interface. Following a 60 min incubation period for lipid assembly, a centrifugal force (9000 × g, 30 min) was applied.

The size distribution of this data set (N = 173) varied between 2.5 to 157 μm with the average size of the giant vesicles produced being around 22 μm (Fig. 2.15). This experiment was conducted in duplicate yielding similar results.

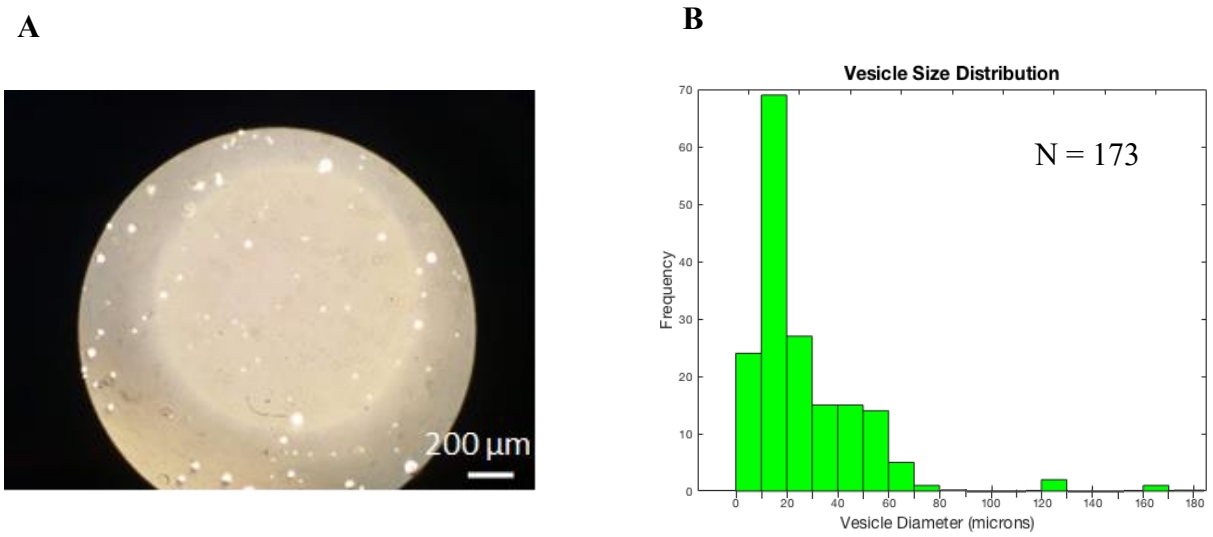

Figure 2.15- (A) Brightfield image of GUVs with 50 mM sucrose, 50 mM NaCl and 0.5 mM Calcein. *A good output of vesicles (in a single frame) was formed with high variation in size. (Scale = 200 μm). (B) Diameter distribution of GUVs generated without prior formation of the lipid monolayer at an oil-water interface. The average diameter for this data set (N = 173), was 21.98 μm with a polydispersity index of 1.*

In the third case, the phase transfer of the emulsion (100 μl) into the external aqueous solution (250 μl) was not driven by the sucrose/glucose concentration gradient of the mediums (as both contained 50 mM NaCl, pH 7.4), but by the internal aqueous encapsulant of 0.5 mM Calcein, adding an excess of only 0.00311 g/ml in the vesicle compartment relative to external aqueous environment and 0.17311 g/ml relative to the lipid monolayer interface. Moreover, a lipid in oil intermediate phase was not priorly

formed. The average diameter for this GUV population (N = 178) was 17.08 μm and the size distribution ranged from 1.3 to 112.6 μm (Fig. 2.16). The experiment was performed twice, yielding similar results.

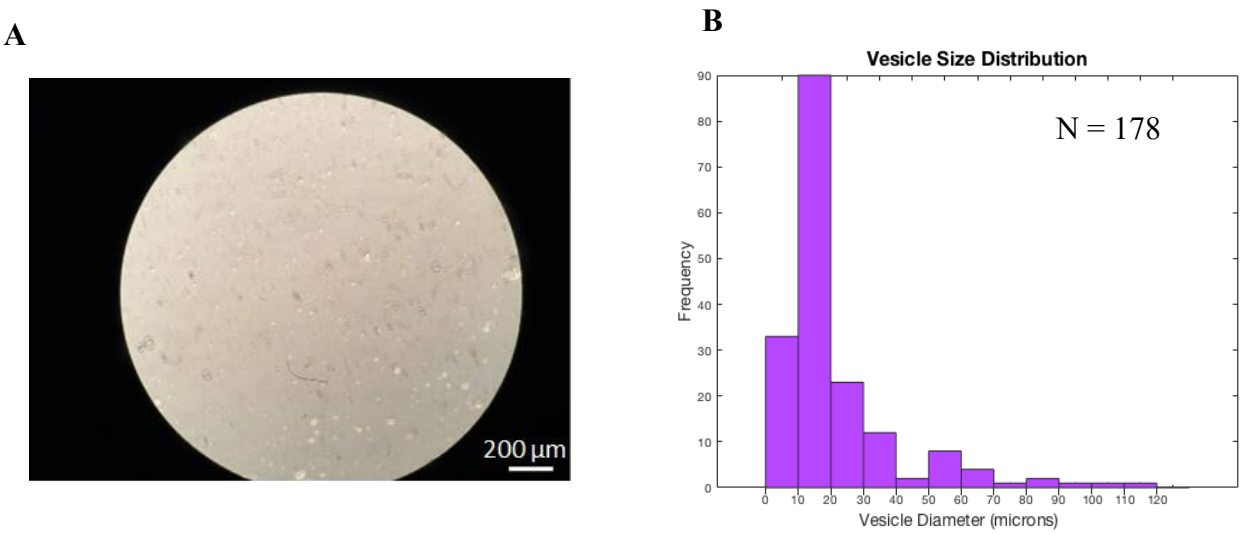

Figure 2.16- (A) Phase contrast image of GUVs composed of DPhPC, generated via phase transfer and loaded with 0.5 mM Calcein. *The bar corresponds to 200 μm. (B) Size distribution of a GUV population (N = 178). The mean vesicle size of this data set was 17.08 μm with a polydispersity index of 1.197.*

2.5.4 GUV Membrane Stability

GUVs prepared by the EPT method were successfully produced and their membrane stability was verified by fluorescence images of vesicles filled with 0.5 mM Calcein. The representative Calcein-filled GUV in Figure 2.17, engulfed in a DIB, preserved its cargo, as illustrated by its emission following a 12 h-incubation period following its formation.

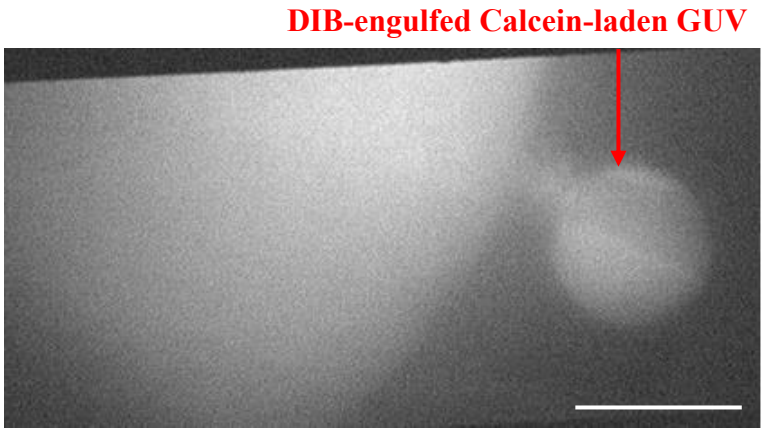

Figure 2.17- Illustration of DPhPC vesicle stability prepared by the EPT method. *DIB-encapsulated Calcein-loaded vesicle (0.5 mM) imaged by fluorescence microscopy following an overnight incubation. Scale bar: 30 µm.*

2.6 Discussion

Although all three GUV samples produced by EPT were characterized by a good yield, the first one, where interface monolayer was formed prior to the emulsion addition, resulted in the least GUV production (N = 47) (Fig. 2.14B) compared to the other two (N = 173 and N = 178) (Fig. 2.15B, 2.16B) in which emulsion was directly deposited on the aqueous medium.

A common characteristic among all groups was the high variation in size as shown by the high polydispersity indices in all 3 samples denoting lack of homogeneity. This non-uniform size distribution has been reported previously by Pautot et al (2003), in which case size discrepancy was determined via dynamic light scattering measurements[37].

Our data suggests that the average diameter of the giant vesicles produced, tend to slightly increase with growing density difference and formation of stabilized interfacial monolayer. The pink histogram (Fig. 2.14B), where vesicles were subjected to the highest concentration gradient (0.0112 g/ml difference between internal and external aqueous solutions and 0.2474 g/ml between lipid-oil monolayer and outer aqueous phase) and the emulsion was immersed in the already formed lipid monolayer interface, shows that the average vesicle size amounted to ~29 microns. In the green histogram (Fig. 2.15B), where the same density gradient was applied, but the intermediate phase was not formed prior to the addition of the emulsion, the average vesicle size was decreased to ~22 microns. In the purple histogram (Fig. 2.16B), a small concentration gradient (0.00311 g/ml in the vesicle compartment relative to external aqueous environment and 0.17311 g/ml relative to the lipid monolayer interface), with absence of intermediate phase seems to influence vesicle size the most, as it generated the smallest mean GUV diameter out of the 3 conditions, reaching ~17 microns.

Overall, it seems that a stabilized interfacial monolayer provides enough lipids to wrap the vesicles and replenish the interphase lipid monolayer after droplet crossing. Potentially, it does that at a faster rate compared to the other two groups (Fig. 2.15 and

Fig. 2.16), where the interface was formed solely by the lipids present in the w/o emulsion.

The last finding of this short study showed that vesicles produced by the inverted emulsion-based method, maintained their stability and cargo after a long period (12 h) (Fig.2.17); a piece of useful information for the upcoming fabrication of the artificial compartmentalized system.

2.7 Results: Phase Transfer Data: Influence of Various Parameters on GUV Size and Yield

For the second group of EPT experiments, we were interested in investigating the significance of the volume of the inner solution/droplet volume (5 µl or 20 µl), lipid concentration of the interfacial monolayer (2.5 mg/ml or 5 mg/ml), incubation time for the monolayer formation (15 min or 1 h), centrifugation duration (1 min or 5 min) and the applied force (50 g or 300 g) on GUV density and diameter, whose membrane leaflets were composed of the following lipid species: DOPC lipid alone, or lipid mixtures (99.5% w/w DOPC and 0.5% w/w DOPG), (90% w/w DOPC and 10% w/w PEG2000 PE), in symmetric and asymmetric bilayer configurations.

The variables manipulated are concisely summarized in the following Figure (2.18):

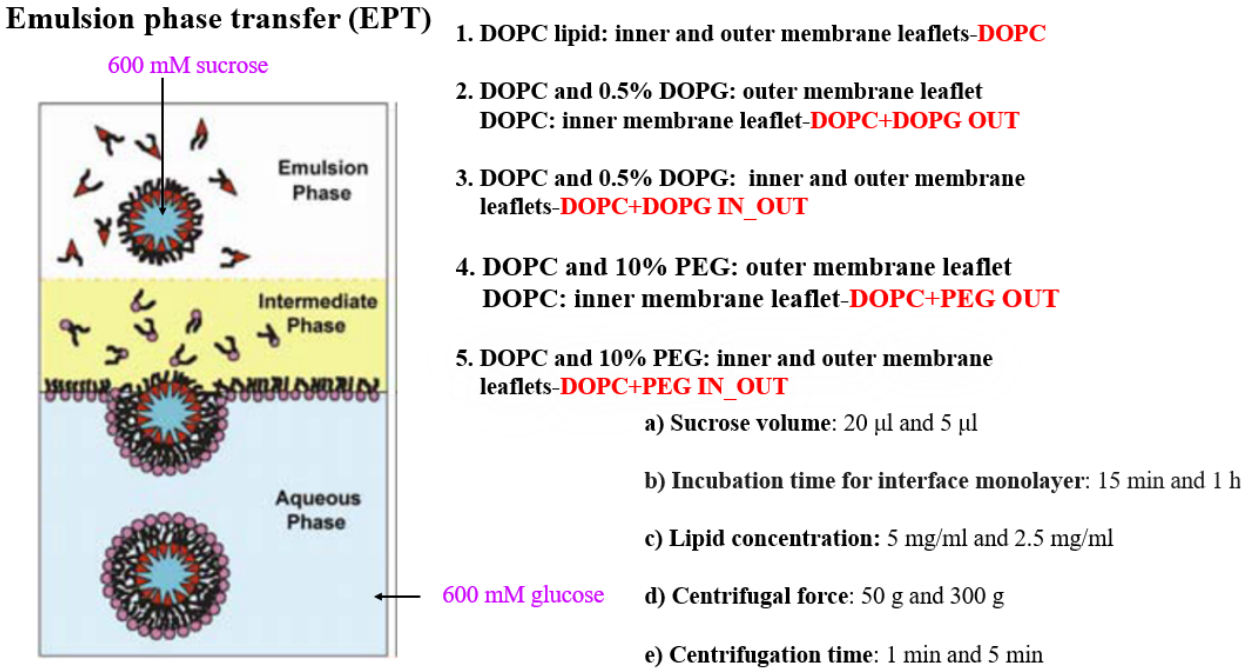

Figure 2.18- Details of variable manipulation for studying their effects on GUV output and size. *Red letters signify the sample names used in the analysis.*

In this set of experiments, the inner aqueous solution, used for the emulsion, and the outer aqueous solution, used for GUV deposition, composed of 600 mM sucrose and 600 mM glucose, respectively, which resulted in 0.0973 g/ml density difference. Additionally, the sucrose droplets were 0.36738 g/ml higher density than the lipid-(mineral) oil monolayer on the surface of the aqueous glucose phase, sufficient to drive phase transfer.

The typical phase transfer procedure started by pouring 100 µl of the chosen lipid or lipid mixture in oil on top of a 200 µl medium containing 600 mM glucose in an Eppendorf tube and the entire setup was allowed to incubate for a period of 15 min or 1 h to facilitate lipid monolayer stabilization. Then, 100 µl of the W/O emulsion (600 mM sucrose) was gently deposited on the oil-aqueous interface prior to centrifugation (50 g or 300 g for 1 min or 5 min).

2.7.1 Inner Solution Volume

2.7.1.1 GUV Yield

It is expected that GUV output depends on the number of water-in-oil droplets. To this end, two different volumes of the inner aqueous solution (5 µl or 20 µl) were used to produce the initial emulsion, while all other parameters were set as follows: 600 mM glucose and sucrose solutions, centrifugal duration of 5 min, centrifugation speed of 300 g, incubation time for the interface formation of 1 h, and with a lipid concentration of 5 mg/ml. For the two droplet volumes, (5 µl and 20 µl), the yield increased with the higher inner solution volume (20 µl) in all pairwise comparisons (Fig. 2.19A), containing either one lipid species or binary lipid combinations. The only exception was the DOPC-DOPG IN_OUT group (in which PC and PG lipids were incorporated in both vesicle leaflets), whose number of produced vesicles remained small and roughly the same under both conditions (5 µl and 20 µl).

This comparatively decreased output of the DOPC-DOPG IN_OUT sample was observed in all subsequent conditions it was subjected to; a phenomenon that could be ascribed to the higher load of PG's negative charge existing in both GUV leaflets, which enhances the repulsive forces between the negatively charged phosphate groups of PG lipids and potentially forestalls GUV formation and stabilization.

Of note, the highest production was observed in DOPC+PEG OUT containing GUVs (9-fold increase). Although the high molecular weight of the hydrophilic polymer, which generates a denser lipid construction, could be deemed as the main factor for this marked yield increase, the relatively lower GUV production (2.6-fold increase) observed in the DOPC+PEG IN_OUT group, suggests presence of other conducive factors. A potential assumption could be associated with PEGylated lipid's inverted-cone shape geometry (Fig. 2.20A), which favours positive curvature membrane structures (Fig. 2.20Ba) and can impose a built-in curvature stress in the confined frame of the vesicle bilayer arrangement, when existing in both leaflets (Fig. 2.20Bb), restricting in this manner bilayer formation in the process of GUV generation [60].

2.7.1.2 GUV Size Characterization

Regarding vesicle size, the bigger volume of inner solution, 20 μl, led to slightly higher average size of vesicles in each population (although non-significant), apart from the DOPC+PEG IN_OUT group that remained approximately the same and the DOPC+PEG OUT group, which was non-significantly reduced (Fig. 2.19B).

The ranges of the average diameters of the giant vesicles produced from the 20 μl droplet volume were between 9-15 μm for DOPC containing vesicles, 5.5-20 μm for PC+PG OUT group, 10-7 μm for PC+PG IN_OUT group, 5.5-9 μm for PC+PEG OUT vesicles and 7-11.5 μm for PC+PEG IN_OUT vesicles, representative samples of which are shown in Figure 2.19C.

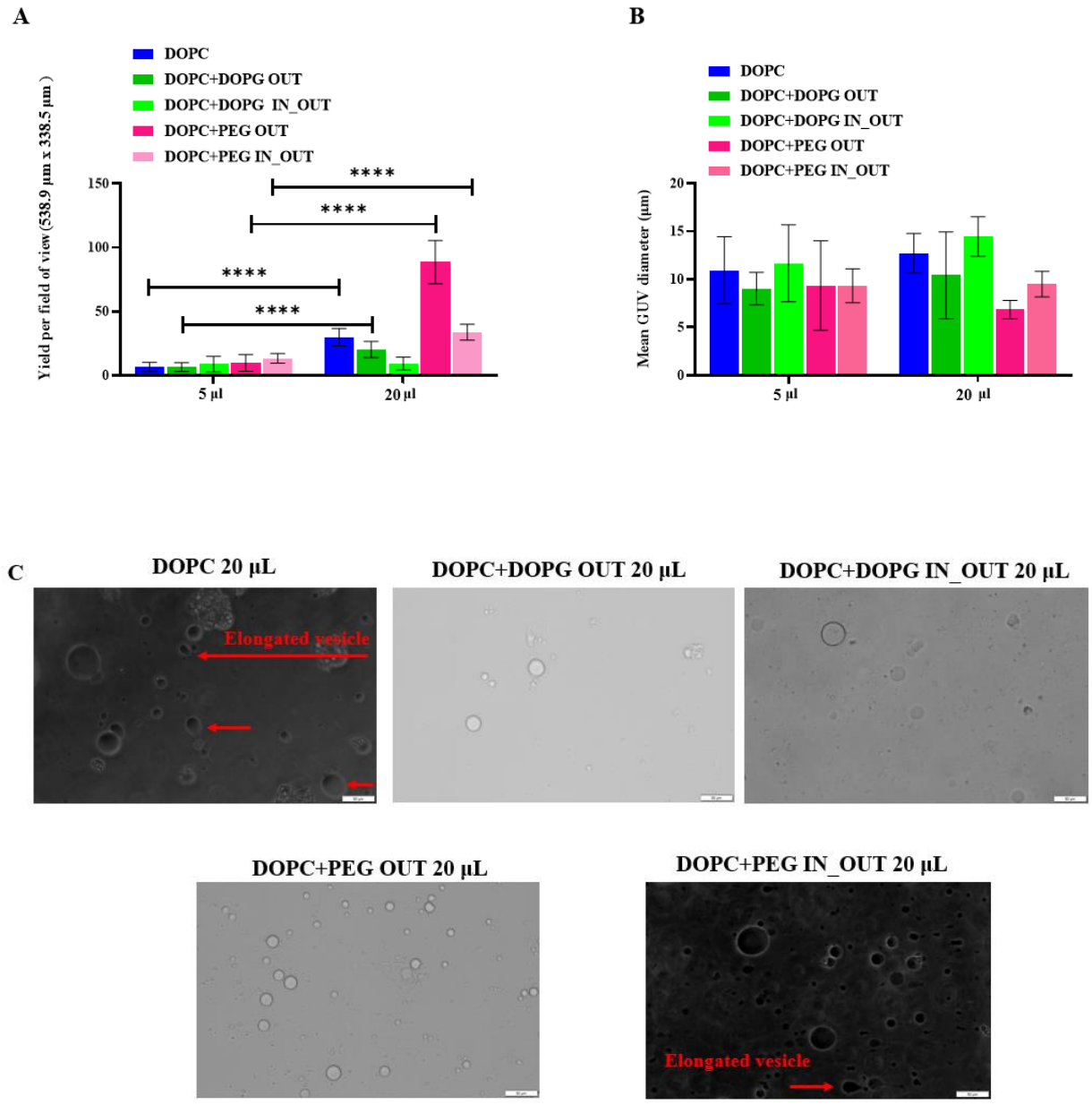

Figure 2.19- (A) Yield and (B) size distribution of DOPC, 99.5% (w/w) DOPC+0.5% (w/w) DOPG, and 90% (w/w) DOPC+10% (w/w) PEG-DOPE GUVs produced by varying the inner solution volume. *(C) Bright-field and phase contrast images of GUVs consisting of a single lipid or different lipid mixtures with inner volume solution of 20 µl. These results were obtained for fixed 600 mM sugar solutions, centrifugal time of 5 min, centrifugation speed of 300 g, incubation period for the interface formation of 1 h, and with a lipid concentration of 5 mg/ml. Statistical significance was determined via unpaired/independent t-test. Error bars were taken from the standard deviations throughout (n = 3). Asterisks represent adjusted p values: *, p < 0.05, **, p < 0.01, ***, p < 0.001, ****, p < 0.0001. Scale bars: 50 µm.*

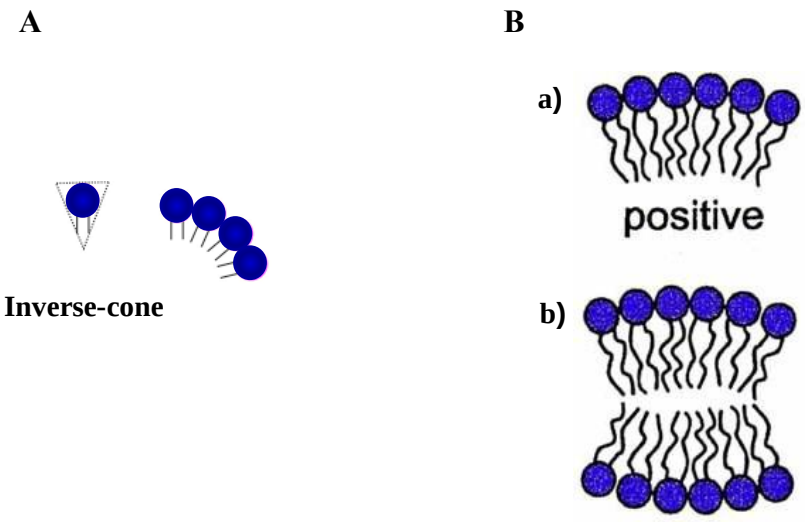

Figure 2.20- (A) Schematic representations of inverse-cone-shaped lipid. *(Ba) Inverted conicity of PEG−PE lipid molecule determines positive curvature of lipid monolayers. (Bb) Constrained monolayers in a bilayer suffer from integrated curvature stress potentially thwarting GUV formation. Image adapted from:[60].*

2.7.1.3 GUV Morphology Characterization

The lipid composition of PC alone formed vesicles with spherical, but also elongated shapes (Fig. 2.19C), a morphology, occasionally present among other liposomes made of mixes of PC+PE-PEG (Fig. 2.19C), but less frequently detected in vesicles of PC+PG lipid mixtures (Fig. 2.19C).

Vesicles that do not possess a charge, such as those containing PC alone (Fig. 2.19C), are less resistant to Brownian motion, since the repulsive forces between membranes are weak, and hence can be more easily elongated or deformed[61]. Conversely, the presence of the negatively charged DOPG lipid in the vesicle membrane may repel each other forcing them to maximize their distance and the electric repulsive forces can more readily defy the Brownian motions of surrounding molecules, e.g. water, mitigating chances of liposome deformation[61]. As a result, a stiffer spherical shape morphology

with less membrane fluctuations and potentially larger mean vesicle diameter are generated, especially when DOPG is introduced in both leaflets.

Considering that increased vesicle output and diameter is produced with the 20 µl droplet volume, we selected the same aqueous amount to prepare GUVs for the proceeding experiments, where interfacial lipid concentration and interfacial incubation time were manipulated, whilst all the other parameters remained the same as described in the ***2.7.1.1 GUV Yield*** section.

2.7.2 Lipid Concentration and Incubation Time

The monolayer formation at the oil–water interface can be affected by both the concentration of solubilized lipids and the incubation period, any of which can compromise GUV yield and size. For instance, an incomplete lipid monolayer at the interface can allow direct contact of the aqueous volume of the emulsion droplet with the aqueous outer solution, instead with the interfacial lipid monolayer, resulting in internal content escape and abrogation of vesicle formation.

2.7.2.1 GUV Yield Dependent on Interfacial Lipid Monolayer Concentration

We applied two lipid concentrations (2.5 mg/ml and 5 mg/ml) (Fig. 2.21), and two incubation periods (15 min and 1 h) (Fig. 2.22), for the assembly of the oil–water interface to explore their individual influence on population and size of produced GUVs.

For the two lipid concentrations tested (2.5 mg/ml and 5 mg/ml), following an 1 h-incubation for both conditions, pairwise comparisons in DOPC, DOPC+DOPG IN_OUT and DOPC+PEG OUT groups showed non-significant changes in vesicle numbers (Fig. 2.21A), suggesting that the lower interfacial lipid concentration (2.5 mg/ml) is adequate

for proper droplet covering and subsequent GUV formation for these lipid and lipid mixtures.

The improved vesicle output observed in the DOPC+PEG IN_OUT sample at 2.5 mg/ml, relative to 5 mg/ml, could be associated with the attenuated curvature stress and steric repulsion due to decreased DOPE-PEG lipid concentration (2.5 mg/ml) at the interface, which generates the outer GUV leaflet. Regarding the DOPC+DOPG OUT group, it seems that negative charge absence from the inner vesicle leaflet facilitates bilayer formation at higher lipid density (5 mg/ml) at the interface.

2.7.2.2 GUV Size Characterization Dependent on Interfacial Lipid Monolayer Concentration

Decreased concentration of lipid at the water-oil interface (2.5 mg/ml) produced bigger GUV sizes for both PEG-containing groups (Fig. 2.21B), indicating that the bulky PEG moiety dense occupancy has sub-optimal effects when used in higher amounts.

Another interesting feature in most DOPC+PEG DOPE groups examined was liposome aggregates (Fig. 2.21D) with fusion events, which inevitably resulted in larger vesicles. This phenomenon was previously documented by studies utilizing PE-PEG lipids and attributed to PEG's property to promote a relatively slow but significant aggregate growth[62, 63].

The significantly bigger mean GUV diameter in DOPC+DOPG IN_OUT sample at the 5 mg/ml intermediate lipid concentration confirms electrostatic repulsion dependence on higher surface charge density, with resulting maximized distance among charged lipid species.

The ranges of the average GUV sizes produced from the 2.5 mg/ml interfacial lipid concentration were between 1.8-44.8 μm for DOPC containing vesicles, 3.4-29.5 μm for

PC+PG OUT group, 1.1-21.6 µm for PC+PG IN_OUT group, 5.1-40.4 µm for PC+PEG OUT vesicles and 4-33 µm for PC+PEG IN_OUT vesicles. Representative samples are displayed in Figure 2.21C.

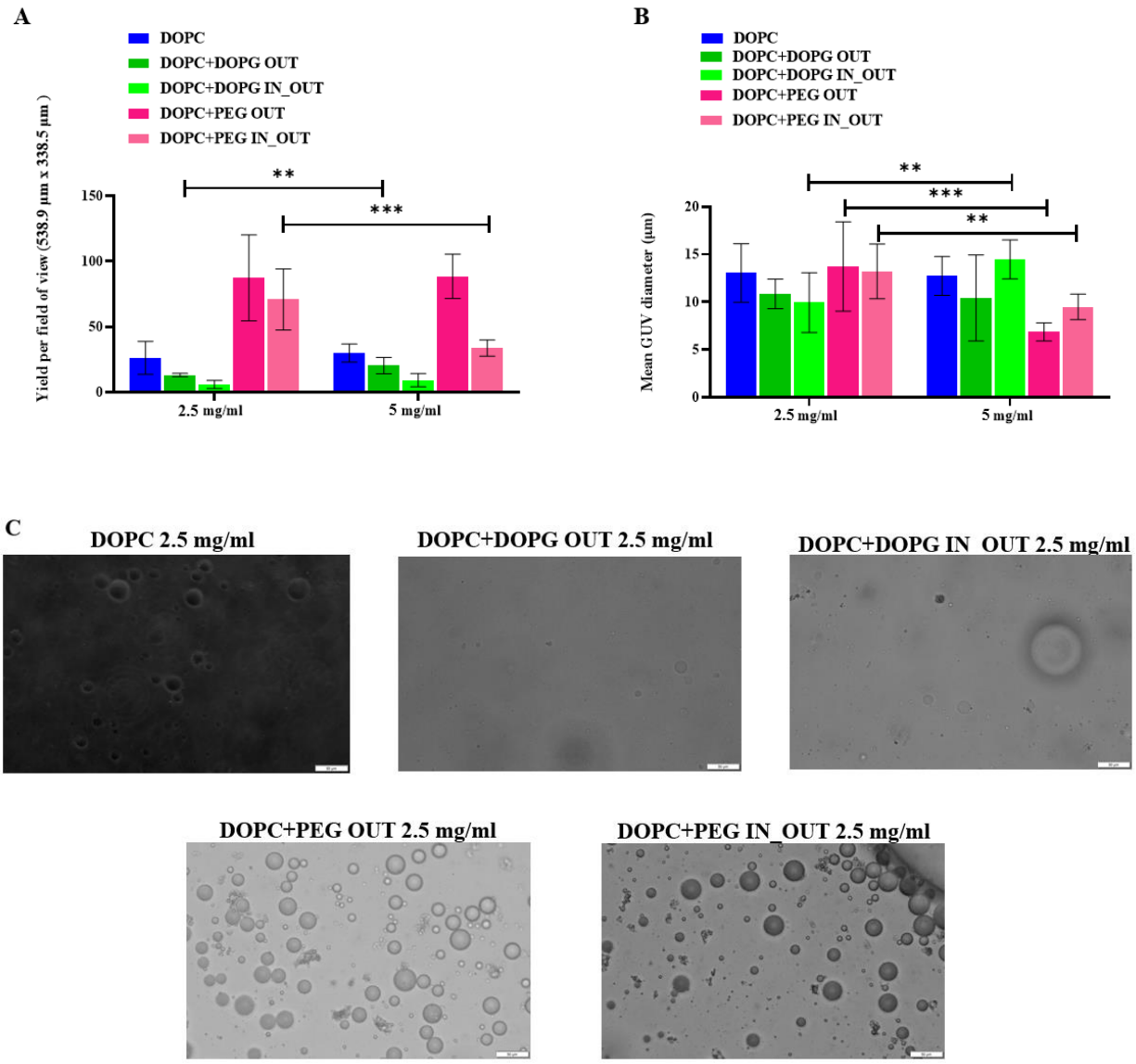

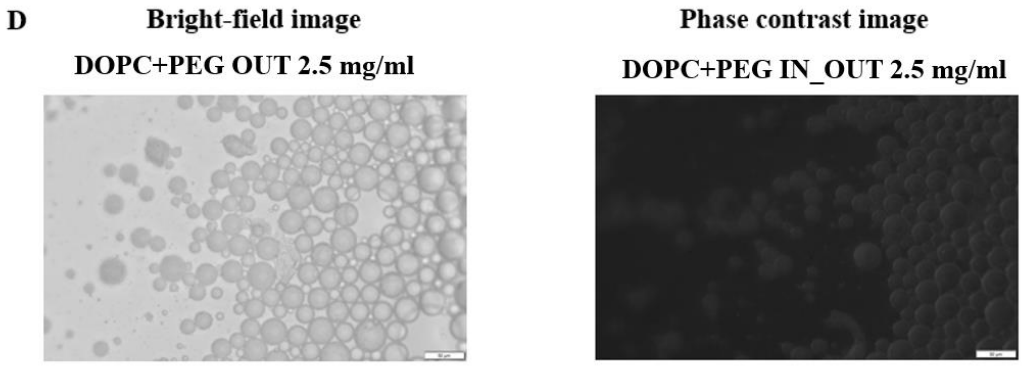

Figure 2.21- Plots showing the impact interfacial lipid concentration (2.5 mg/ml or 5 mg/ml), has on (A) the output and (B) the average size distribution of the GUVs. *(C) Bright-field and phase contrast images of GUVs produced by varying lipid monolayer concentration (2.5 mg/ml or 5 mg/ml), incubating for 1 h. (D) Bright-field and phase contrast images of vesicle aggregates under the condition of lipid monolayer concentration (2.5 mg/ml), incubating for 1 h. All micrographs were obtained from vesicles made from 20 µl droplet volume, containing 600 mM sucrose solution, tested at 300 g centrifugation speed and 5 min centrifugal time. Pairwise comparison tests, (independent t-tests), were conducted with error bars being taken from the standard deviations throughout (n = 3). Asterisks represent adjusted p values: *, p < 0.05, **, p < 0.01, ***, p < 0.001, ****, p < 0.0001. Scale bars: 50 µm.*

2.7.2.3 GUV Yield Dependent on Interfacial Lipid Monolayer Incubation Period

The lipid concentration of 5mg/ml for two different incubation periods (15 min and 1 h) (Fig. 2.22A) was employed, which did not seem to affect GUV output in any sample apart from the DOPC+PEG OUT group, where a ~7-fold vesicle number decrease was noticed at 15 min incubation period. Possibly, for this short time, there was incomplete lipid replenishment at the interface for adequate lipid coverage for all droplets passing through.

2.7.2.4 GUV Size Characterization Dependent on Interfacial Lipid Monolayer Incubation Period

Mean GUV diameter was relatively affected by the incubation time. Average vesicle size of the DOPC+DOPG IN_OUT group was significantly bigger at 1 h-incubation time than

at 15 min. The other groups, (with the exception of the PEG containing ones, which remained the same), displayed an increasing trend by eye inspection, yet not statistically significant (Fig. 2.22B).

It is not unlikely that the shorter incubation period of 15 min does not suffice for optimal lipid accumulation at the lipid-water interface for the swift process of droplet crossing, with resulting deficient outer lipid deposition for slightly bigger lipid-stabilized droplets.

The ranges of the giant vesicle average diameters produced for the 15 min-incubation were between 3.7-30.8 μm for DOPC containing vesicles, 1.7-34.9 μm for PC+PG OUT group, 4.5-30.1 μm for PC+PG IN_OUT group, 2.4-14.5 μm for PC+PEG OUT vesicles and 1.7-36.2 μm for PC+PEG IN_OUT vesicles. Representative samples are illustrated in 2.22C.

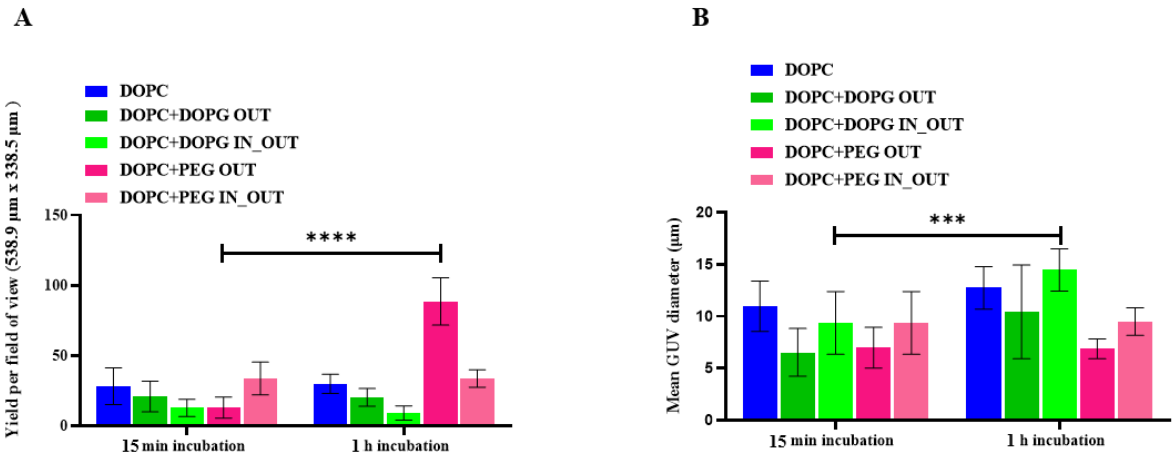

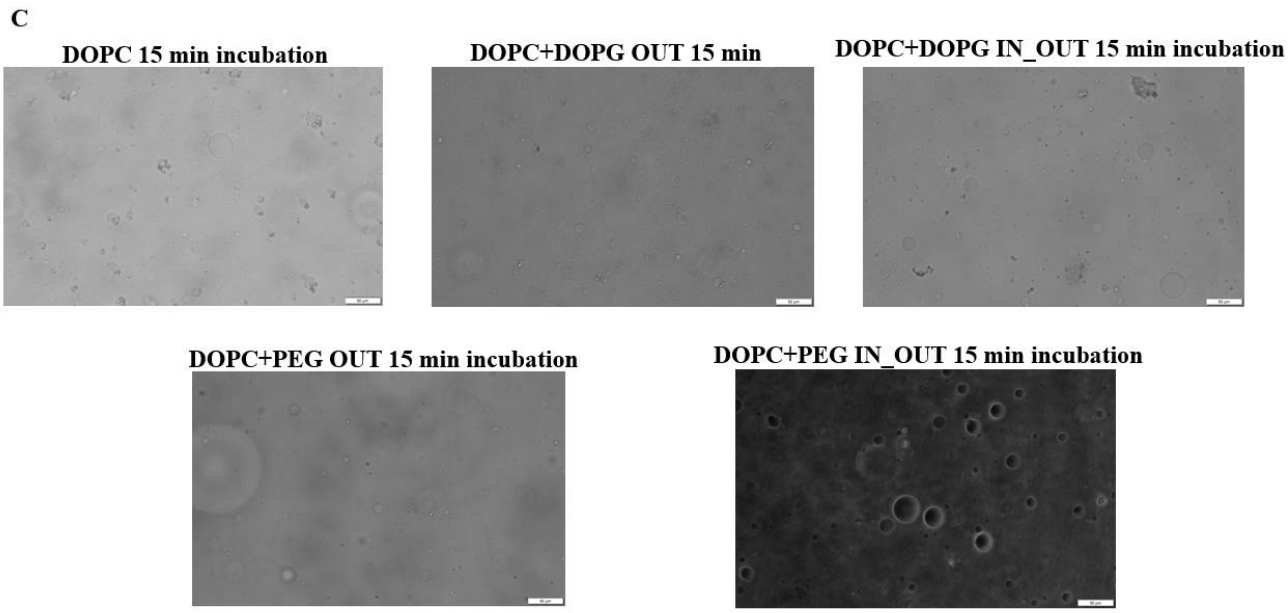

Figure 2.22- Plots of A) GUV yields and B) sizes produced at different incubation periods (15 min or 60 min) for interfacial monolayer formation. *C) Bright-field and phase contrast images of GUVs produced with 600 mM sugar solutions, 20 µl inner volume solution and 5 mg/ml interfacial monolayer concentration at 300 g centrifugation speed for 5 min. Statistical significance was determined via unpaired/independent t-test. Error bars were derived from the standard deviations throughout (n = 3). Asterisks represent adjusted p values: *, p < 0.05, **, p < 0.01, ***, p < 0.001, ****, p < 0.0001. Scale bars: 50 µm.*

Considering the aforedescribed results, for the following experiments, the lipid concentration at the water-oil interface was set at 5mg/ml and the interfacial lipid monolayer incubation time was fixed at 1 h.

2.7.3 Centrifugal Force and Duration

Several times, gravity has been used as the force to drive the droplets through the interface[3, 59], an approach that requires a significant density gradient, and prolonged periods for all the droplets to be transferred through the lipid monolayer. This process has been expedited by centrifugal force, which was applied in all our EPT experiments.

2.7.3.1 GUV Yield Dependent on Centrifugal Speed

Figure 2.23A presents GUV yield increment in all samples (non-significant, though) when the applied centrifugal force increased from 50 g to 300 g for a specified time (here it was fixed at 5 min).

2.7.3.2 GUV Size Characterization Dependent on Centrifugal Speed

The average GUV diameters of the PC, the PC+PG OUT and the PC+PEG IN_OUT groups remained approximately the same in both centrifugation speeds, while the PC+PG IN_OUT group displayed a small but significant increase at 300 g. On the other hand, the mean vesicle size of the PC+PEG OUT group soared 3-fold at 50 g (Fig. 2.23B), possibly due to mitigated bursting of bigger vesicles.

The ranges of the average sizes of the giant vesicles produced at the 50 g centrifugation speed were between 4.2-46.3 μm for DOPC containing vesicles, 2-18.5 μm for PC+PG OUT group, 3.3-30.1 μm for PC+PG IN_OUT group, 2.27-93.8 μm for PC+PEG OUT vesicles and 1.7-55.3 μm for PC+PEG IN_OUT vesicles (Fig. 2.24C).

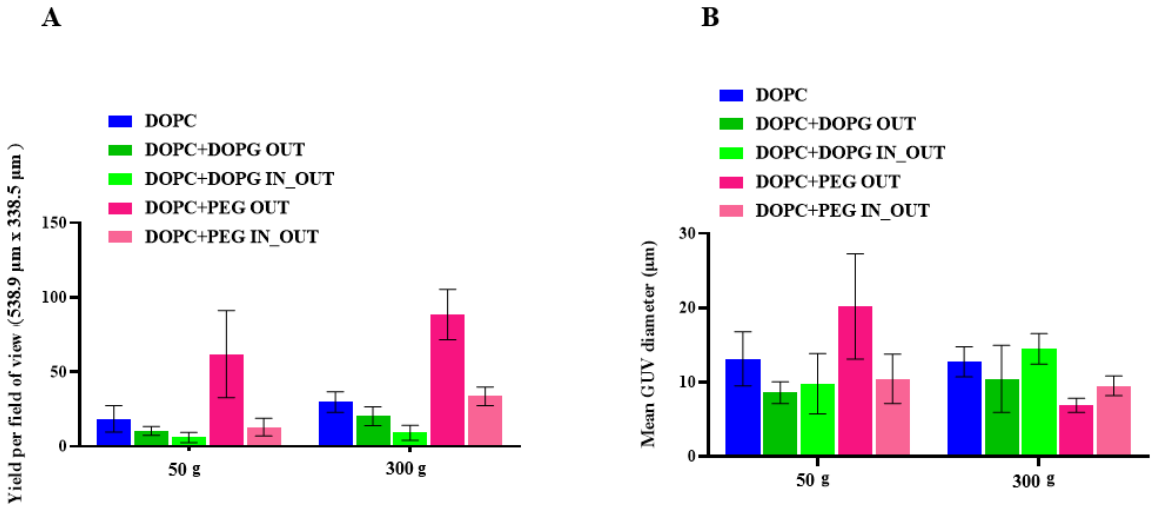

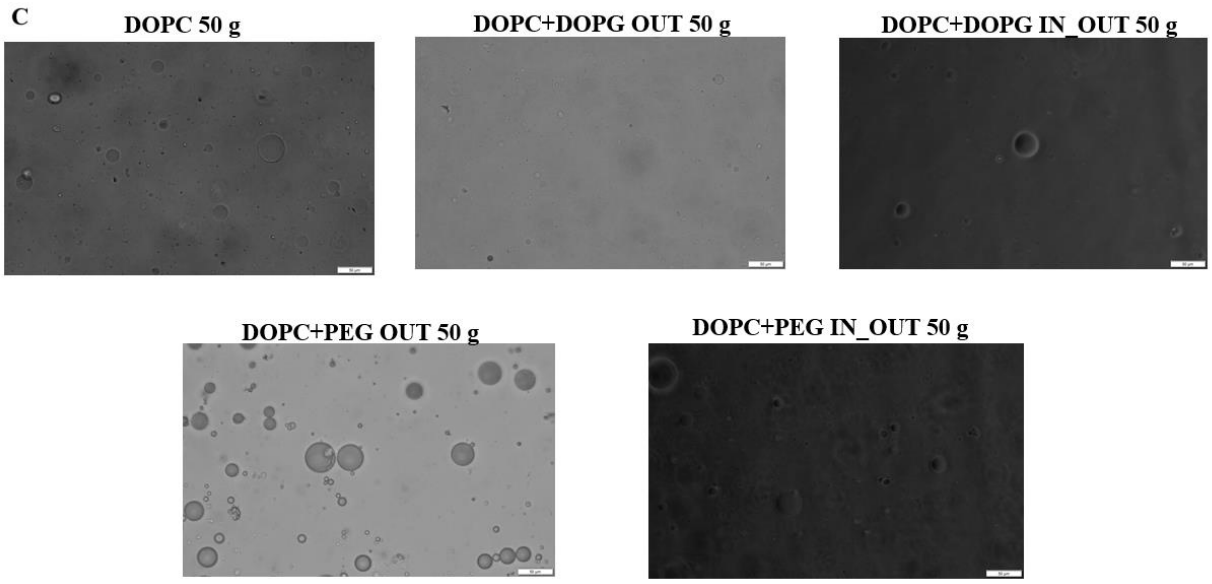

Figure 2.23- Plots of A) GUV yields and B) size distributions produced at two different centrifugation speeds (50 g or 300 g). *C) Bright-field and phase contrast images of GUVs were acquired for fixed 600 mM sugar solutions, 20 µl inner volume solution, centrifugal time of 5 min, 1 h incubation period for the interface monolayer formation, and interfacial lipid concentration of 5 mg/ml. Pairwise comparison tests (independent t-tests) were conducted. Error bars were derived from the standard deviations throughout (n = 3). Asterisks represent adjusted p values: *, p < 0.05, **, p < 0.01, ***, p < 0.001, ****, p < 0.0001. Scale bars: 50 µm.*

2.7.3.3 GUV Yield Dependent on Centrifugal Duration

Then, we investigated how the duration of centrifugal force, which was set either at 1 min or 5 min could influence vesicle size and density. Figure 2.24A illustrates that vesicle output was not affected in most groups by the two different centrifugation time periods, apart from the PEG containing ones; for the PC+PEG IN_OUT sample, GUV production was enhanced at shorter duration (1 min at 300 g centrifugal speed), whereas for the PC+PEG OUT group, at longer duration (5 min at 300 g centrifugal speed). It seems that the PC+PEG IN_OUT group could be more susceptible to bursting at longer time span (5 min) possibly due to the higher density of the PEG2000 polymer, (present in both leaflets), compared to the PC+PEG OUT group, with lower PEG2000 polymer density (as it was integrated only in the outer leaflet).

Although the unexpected yield increase (~2.4-fold) of PC+PEG IN_OUT group at 1 min suggests that shorter centrifugation time can contribute to greater number of vesicle formation for this lipid combination, this event occurrence is not easily interpretable and requires further exploration, possibly via computer simulations that could disclose PEG-PE effects on the biophysical and chemical properties of vesicle bilayers[64].

2.7.3.4 GUV Size Characterization Dependent on Centrifugal Duration

With respect to vesicle size, shorter centrifugation duration, (1 min), markedly increased (~3.7-fold) mean GUV diameter in the PC+PEG OUT group (Fig. 2.24B), denoting shorter centrifugation time can maximize PEGylated liposome size; this observation can be advantageous if high encapsulation efficiency is an issue of concern, at least with the current osmolarities and lipid compositions.

However, as aforementioned in the ***Experimental Section, (2.2.8 Optical Microscopy: Bright field and Phase Contrast Imaging of GUVs***), vesicle imaging was performed the following day after their preparation, and fusion was perceived solely in the DOPE-PEG doped GUVs; a phenomenon already documented in membranes containing lipids with inverted phases, such as PE-PEG2000[65].

Hence, membranes with DOPE-PEG lipid content should be analyzed and understood using shape and curvature considerations. Given that membrane properties can exhibit variations as a function of lipid composition and membrane components, the powerful tool of molecular dynamics (MD) computer simulation could be combined with EPT data to unveil many aspects of membrane behaviours at the nanoscale, conferring deeper comprehension and allowing rational interpretation of the current data [66].

The ranges of the average diameters of the giant vesicles produced with 1min centrifugation period were between 3-24.2 μm for DOPC containing vesicles, 2.8-30.4 μm for PC+PG OUT group, 2.3-46.9 μm for PC+PG IN_OUT group, 3.5-63.7 μm for PC+PEG

OUT vesicles and 3.1-30 µm for PC+PEG IN_OUT vesicles. Representative GUVs are presented in Fig. 2.24C.

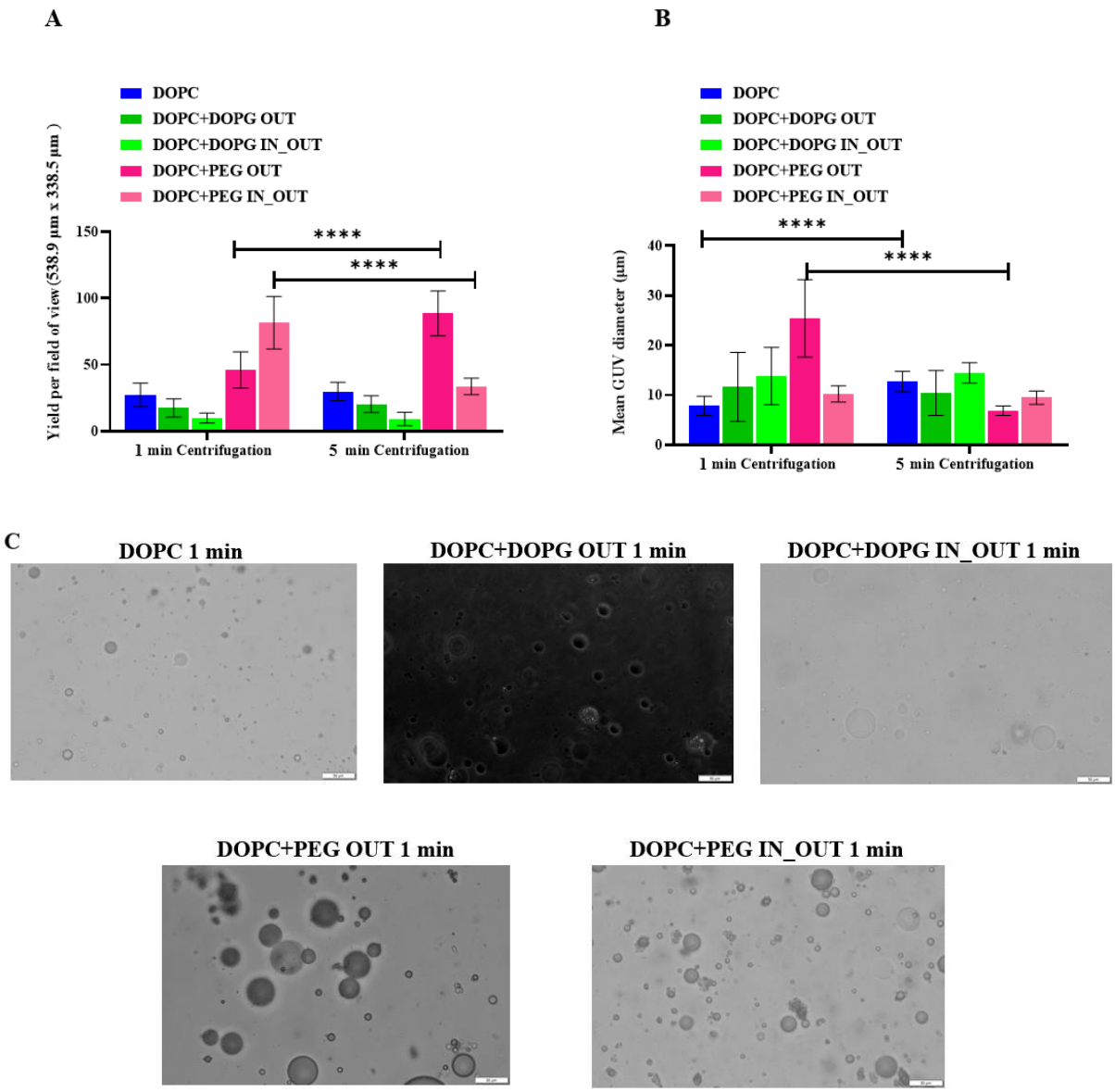

Figure 2.24- Plots presenting the effect the centrifugation duration has on A) the concentration and B) the average size distribution of the GUVs. *C) Images of GUVs with 600 Mm sucrose produced at 300 g speed, with 20 µl inner solution volume, 1 h incubation period for the interface monolayer formation, and 5 mg/ml lipid monolayer concentration. Pairwise comparison tests (independent t-tests) were conducted. Error bars were derived from the standard deviations throughout (n = 3). Asterisks represent adjusted p values: *, p < 0.05, **, p < 0.01, ***, p < 0.001, ****, p < 0.0001. Scale bars: 50 µm.*

2.8 Discussion

The inverted emulsion-based approach for generating GUVs has a series of advantages over older techniques, such as electroformation or gentle hydration. Its major advantage lies in its capacity to encapsulate large (bio)molecules inside vesicles under physiological conditions and holds the potential for optimization and high-throughput analyses.

The objective of the second part of the emulsion phase transfer work was to more systematically study vesicle size and yield, through manipulation of a range of parameters, including droplet volume (5 µl or 20 µl), lipid concentration of interfacial monolayer (2.5 mg/ml or 5 mg/ml), interfacial monolayer formation incubation time (15 min or 1 h), centrifugation duration (1 min or 5 min) and applied force (50 g or 300 g), using one lipid species (DOPC) and lipid combinations (99.5% w/w DOPC and 0.5% w/w DOPG), (90% w/w DOPC and 10% w/w PEG2000 PE) for symmetric and asymmetric vesicle production.

Our results demonstrated that increased droplet volume (20 µl), relative to (5 µl), attained higher liposome yields and relatively same or bigger sizes for all lipid (DOPC) and lipid mixtures (DOPC+DOPG and DOPC+PE-PEG) used (Fig. 2.19).

The two set interfacial lipid concentrations, at 2.5 mg/ml and 5 mg/ml, used for the interfacial lipid monolayer formation, had no detectable impact on vesicle size and yield for the DOPC sample (Fig. 2.21A). However, the higher oil-lipid intermediated phase concentration (5 mg/ml) rose vesicles' density for the DOPC+DOPG containing groups to a substantial degree (Fig. 2.21A) and significantly increased average vesicle diameter of the DOPC+DOPG IN_OUT sample, meeting the requirement of maximized distance among charged lipid species.

On the other side, the decreased lipid concentration (2.5 mg/ml) layered at the oil-glucose interface improved vesicle output and mean GUV diameters of the DOPC+PEG

containing groups, exposing the key role lipid shape (PEGylated lipid's inverted conicity) and polymer (PEG) density dependent configuration play in bilayer formation.

The incubation time, fixed at 15 min or 1 h, for the interfacial monolayer had negligible influence on the number of the GUVs produced for the DOPC and DOPC+DOPG containing groups (Fig. 2.22A), but favoured all these samples in terms of vesicle size at 1 h (Fig. 2.22B).

The shorter incubation period (15 min) adversely affected GUV output in the DOPC+PEG OUT group (Fig. 2.22A), as it dropped ~7-fold, relative to the population generated at the longer incubation period (1 h). It is not unlikely that more time is required for the lipids to re-assemble at the interface after droplet crossing, for this lipid combination, but this assumption could be confirmed by performing complementary simulations to investigate the minimum time needed for lipid monolayer re-formation.

Increased centrifugal force (300 g), over (50 g), had a positive impact on vesicle concentration for all samples (Fig. 2.23A) and the diameter of the DOPC+DOPG IN_OUT (Fig. 2.23B) containing vesicles. However, the lower applied speed (50 g), was significantly beneficial for the bigger-sized GUVs of the PC+PEG OUT group (3-fold increase) (Fig. 2.23B), as it could potentially protect them from bursting.

The smaller centrifugation period (1 min), over (5 min), enhanced GUV production for the DOPC+PEG IN_OUT group, but it decreased that of the PC+PEG OUT sample (Fig. 2.24A), while increasing its vesicle size (Fig. 2.24B). Apart from that, no other significant changes in any of the other samples were monitored.

Our work has shown that parameter variation did have differential impact on vesicle population and size, depending on lipid membrane composition. Some of the results provided were anticipated, whereas others, especially with the PC+PE-PEG containing groups, had been difficult to validly interpret just by relying on the presented data. Taking into consideration that membrane fusion in the PC+DOPE-PEG composed GUVs was

detected during the imaging process, we realize that an unexplored factor skews vesicle population and size distributions for the PC+PE-PEG containing groups. Hence, the increased mean GUV diameter in the PC+PEG OUT group in 1 min centrifugation time (Fig. 2.24A), for instance, could be the outcome of membrane fusion in PE systems.

Our findings and observations yielded interesting information on how variable manipulation can be used to optimize vesicle production and sizes for different lipids and lipid mixtures. At the same time, they raised inquiries that could be potentially addressed by a more in-depth investigation of each sample individually, under a broader range of parameter control and time-lapse imaging. The powerful tool of molecular dynamics (MD) computer simulation could serve as a complementary strategy in this type of research, disclosing many facets of membrane interactions that would allow better apprehension and elucidation of the current findings.

Nevertheless, the findings of this study offered us a better understanding of GUV making with desired characteristic manifestation based on parameter control. This knowledge directed modification procedures needed for the compartmentalized model synthesis (DIB-encapsulated GUV enriched with actin network), whose construction is gradually elaborated in ***Chapters 3, 4 and 5***.

2.9 References

1. Karamdad, K., Law, R.V., Seddon, J.M., Brooks, N.J. and Ces, O. *Preparation and mechanical characterisation of giant unilamellar vesicles by a microfluidic method. Royal Society of Chemistry*, 2015. **15**.
2. Litschel T., Ganzinger, K.A., Movinkel T., Heymann M., Robinson T., Mutschler H., Schwille P. *Freeze-thaw cycles induce content exchange between cell-sized lipid vesicles. New J. Phys*., 2018. **20**.
3. Moga A.Y.N., Dimova, R., Robinson, T. *Optimization of the Inverted Emulsion Method for High-Yield Production of Biomimetic Giant Unilamellar Vesicles. Chembiochem*., 2019. **20**(20).
4. Parigoris, E., Dunkelmann, D.L., Murphy, A., et al*. Facile generation of giant unilamellar vesicles using polyacrylamide gels. Sci Rep.,* 2020. **10**(4824).
5. Matsuoka, K., Orci, L., Amherdt, M., Bednarek, S.Y. Hamamoto, S., Schekman, R., and Yeung, T. *COPII-coated vesicle formation reconstituted with purified coat proteins and chemically defined liposomes. Cell*, 1998. **93**(2): p. 263–275.
6. Wollert, T., Wunder, C., Lippincott-Schwartz, J., and Hurley, J.H. *Membrane scission by the ESCRT-III complex. Nature*, 2009. **458**(7235): p. 172–177.
7. Melero, A., Chiaruttini, N., Karashima, T., Riezman, I., Funato, K., Barlowe, C., Riezman, H., and Roux, A. *Lysophospholipids Facilitate COPII Vesicle Formation. Current biology: CB*, 2018. **28**(12): p. 950–1958.
8. Allen, T.M., and Cullis, P.R. *Liposomal drug delivery systems: from concept to clinical applications. Advanced drug delivery reviews*, 2013. **65**(1): p. 36–48.
9. Rongen, H.A., Bult, A., and van Bennekom, W.P. *Liposomes and immunoassays. Journal of immunological methods*, 1997. **204**(2): p. 105–133.
10. Kubatta, E.A., and Rehage, H. *Characterization of giant vesicles formed by phase transfer processes. Colloid Polym Sci.,* 2009. **287**: p. 1117–1122.
11. Reeves, J.P., and Dowben, R.M. *Formation and properties of thin-walled phospholipid vesicles. J Cell Physiol*., 1969. **73**(1): p. 49-60.

12. Faucon, J.F., Mitov, M.D., Méléard, P., Bivas, I., and Bothorel, P. *Bending elasticity and thermal fluctuations of lipid membranes. Theoretical and experimental requirements. Journal de Physique*, 1989. **50**(17): p. 2389-2414.
13. Akashi, K., Miyata, H., Itoh, H., and Kinosita, K., Jr. *Preparation of giant liposomes in physiological conditions and their characterization under an optical microscope. Biophysical journal*, 1996. **71**(6): p. 3242–3250.
14. Angelova, M.I., Soléau, S., Méléard, P., Faucon, F., and Bothorel, P. *Preparation of giant vesicles by external AC electric fields. Kinetics and applications.* Trends in Colloid and Interface Science VI. *Progress in Colloid & Polymer Science*, 1992. **89**.
15. Angelova, M.I., and Dimitrov, D.S. *Liposome electroformation. Faraday Discuss. Chem. Soc.*, 1986, 81, 303-311, 1986. **81**: p. 303-311.
16. Bagatolli, L.A. *To see or not to see: lateral organization of biological membranes and fluorescence microscopy. Biochimica et biophysica acta*, 2006. **1758**(10): p. 1541–1556.
17. Dietrich, C., Bagatolli, L.A., Volovyk, Z.N., Thompson, N.L., Levi, M., Jacobson, K., and Gratton, E. *Lipid rafts reconstituted in model membranes. Biophysical journal*, 2001. **80**(3): p. 1417–1428.
18. Méléard, P., Gerbeaud, C., Pott, T., Fernandez-Puente, L., Bivas, I., Mitov, M.D., Dufourcq, J., and Bothorel, P. *Bending elasticities of model membranes: influences of temperature and sterol content. Biophysical journal*, 1997. **72**(6): p. 2616–2629.
19. Veatch, S.L., and Keller, S.L. *Miscibility phase diagrams of giant vesicles containing sphingomyelin. Physical review letters*, 2005. **94**(14): p. 148101.
20. Bagatolli, L.A., Parasassi, T., and Gratton, E. *Giant phospholipid vesicles: comparison among the whole lipid sample characteristics using different preparation methods: a two photon fluorescence microscopy study. Chemistry and physics of lipids*, 2000. **105**(2): p. 135–147.
21. Dimova R. Aranda, S. Bezlyepkina, N., Nikolov, V., Riske, K.A., Lipowsky, R. *A practical guide to giant vesicles. Probing the membrane nanoregime via optical microscopy. J Phys Condens Matter*., 2006. **18**(28): p. 1151-76.

22. Pott, T., Bouvrais, H., and Méléard, P. *Giant unilamellar vesicle formation under physiologically relevant conditions. Chemistry and physics of lipids*, 2008. **154**(2): p. 115–119.
23. Walde, P., Cosentino, K. Engel, H. and Stano, P. *Giant Vesicles: Preparations and Applications. ChemBioChem.*, 2010. **11**(7): p. 848-865.
24. Dimova, R. *Giant Vesicles and Their Use in Assays for Assessing Membrane Phase State, Curvature, Mechanics, and Electrical Properties. Annu Rev Biophys*., 2019. **48**: p. 93-119.
25. Stein, H., et al. *Production of Isolated Giant Unilamellar Vesicles under High Salt Concentrations. Front Physiol.*, 2017. **8**.
26. Hu, P.C., Li, S., and Malmstadt, N. *Microfluidic fabrication of asymmetric giant lipid vesicles. ACS applied materials & interfaces*, 2011. **3**(5): p. 1434–1440.
27. Akbarzadeh, A., Rezaei-Sadabady, R., Davaran, S., Joo, S. W., Zarghami, N., Hanifehpour, Y., Samiei, M., Kouhi, M., and Nejati-Koshki, K. *Liposome: classification, preparation, and applications. Nanoscale research letters*, 2013. **8**(1): p. 102.
28. van Swaay, D*.,* and deMello, A. *Microfluidic methods for forming liposomes. Lab Chip*, 2013. **13**: p. 752-767.
29. Patil, Y.P., and Jadhav, S. *Novel methods for liposome preparation. Chemistry and physics of lipids*, 2014. **177**: p. 8–18.
30. Deshpande, S., and Dekker, C. *On-chip microfluidic production of cell-sized liposomes. Nat Protoc.,* 2018. **13**: p. 856–874
31. Nishimura, K., Suzuki, H., Toyota, T., and Yomo, T. *Size control of giant unilamellar vesicles prepared from inverted emulsion droplets. Journal of colloid and interface science*, 2012. **376**(1): p. 119–125.
32. Deng, N.N., Yelleswarapu, M., and Huck, W.T. *Monodisperse Uni- and Multicompartment Liposomes. Journal of the American Chemical Society*, 2016. **138**(24): p. 7584–7591.
33. Kunz, P., Zinner, K., Mücke, N., Bartoschik, T., Muyldermans, S., and Hoheisel, J. D. *The structural basis of nanobody unfolding reversibility and thermoresistance. Scientific reports*, 2018. **8**(1).

34. Okano, T., Inoue, K., Koseki, K., and Suzuki, H. Deformation Modes of Giant Unilamellar Vesicles *Encapsulating Biopolymers. ACS synthetic biology*, 2018. **7**(2): p. 739–747.
35. Trantidou, T., Dekker, L., Polizzi, K., Ces, O., and Elani, Y. *Functionalizing cell-mimetic giant vesicles with encapsulated bacterial biosensors. Interface focus*, 2018. **8**(5).
36. Natsume, Y., Wen. H., Zhu, T., Itoh, K., Sheng L., and Kurihara K. *Functionalizing cell-mimetic giant vesicles with encapsulated bacterial biosensors. J. Vis. Exp*., 2017: p. 1-8.
37. Pautot, S., Frisken, B.J., and Weitz, D.A. *Production of Unilamellar Vesicles Using an Inverted Emulsion. Langmuir,* 2003. **19**: p. 2870-2879.
38. Guan, X.L., et al. *Functional interactions between sphingolipids and sterols in biological membranes regulating cell physiology. Mol Biol Cell*, 2009. **20**(7): p. 2083-95.
39. Fenz, S.F. and Sengupta, K. *Giant vesicles as cell models. Integr Biol. (Camb)*, 2012. **4**(9): p. 982-95.
40. Fadeel, B. and Xue, D. *The ins and outs of phospholipid asymmetry in the plasma membrane: roles in health and disease. Crit Rev Biochem Mol Biol.*, 2009. **44**(5): p. 264-77.
41. Osawa, M., and Erickson, H.P. *Liposome division by a simple bacterial division machinery. Proceedings of the National Academy of Sciences of the United States of America*, 2013. **110**(27).
42. Noireaux, V., and Libchaber, A. *A vesicle bioreactor as a step toward an artificial cell assembly. Proceedings of the National Academy of Sciences of the United States of America*, 2004. **101**(51): p. 17669–17674.
43. Whittenton, J., Harendra, S., Pitchumani, R., Mohanty, K., Vipulanandan, C., and Thevananther, S. *Evaluation of asymmetric liposomal nanoparticles for encapsulation of polynucleotides. Langmuir: the ACS journal of surfaces and colloids*, 2013. **24**(16): p. 8533–8540.

44. Natsume, Y., Wen, H. I., Zhu, T., Itoh, K., Sheng, L., and Kurihara, K. *Preparation of Giant Vesicles Encapsulating Microspheres by Centrifugation of a Water-in-oil Emulsion. Journal of visualized experiments: JoVE*, 2017. **119**: p. 2870-2879.
45. Lefrançois, P., Goudeau, B., and Arbault, S. *Electroformation of phospholipid giant unilamellar vesicles in physiological phosphate buffer. Integrative Biology*, 2018. **10**(7): p. 429-434.
46. Fujii, S., Matsuura, T., Sunami, T., Nishikawa, T., Kazuta, Y., and Yomo, T. *Liposome display for in vitro selection and evolution of membrane proteins. Nature protocols*, 2014. **9**(7): p. 1578–1591.
47. Karamdad, K., Hindley, J.W., Bolognesi, G., Friddin, M.S., Law, R.V., Brooks, N.J., Ces, O., and Elani, Y. *Engineering thermoresponsive phase separated vesicles formed via emulsion phase transfer as a content-release platform. Chemical science*, 2018. **9**(21): p. 4851–4858.
48. Pautot S., Frisken, B.J., and Weitz, D.A. *Production of unilamellar vesicles using an inverted emulsion. Langmuir*, 2003. **19**: p. 2870–2879.
49. Hillborg, H., Ankner, J.F., Gedde, U.W., Smith, G.D., Yasuda, H.K., and Wikström, K. *Crosslinked polydimethylsiloxane exposed to oxygen plasma studied by neutron reflectometry and other surface specific techniques. Polymer*, 2000. **41**: p. 6851.
50. Bhattacharya, S., Datta, A., Berg, J.M., and Gangopadhyay, S. *Studies on surface wettability of poly(dimethyl) siloxane (PDMS) and glass under oxygen-plasma treatment and correlation with bond strength. Journal of Microelectromechanical Systems*, 2005. **14**(3): p. 590-597.
51. Tan, S.H., Nguyen, N.T., Chua, Y.C., and Kang, T.G. *Oxygen plasma treatment for reducing hydrophobicity of a sealed polydimethylsiloxane microchannel. Biomicrofluidics*, 2010. **4**(3): p. 32204.
52. Karamdad, K. *Development of Microfluidic Platforms to Construct Giant Unilamellar Vesicles (GUVs) for the Biophysical Study of Lipid Membranes* in *Department of Chemistry*. 2017, Imperial College London.
53. Schindelin, J., Arganda-Carreras, I., and Frise, E., et al. *Fiji: an open-source platform for biological-image analysis. Nature methods*, 2012. **9**(7): p. 676-682.

54. Gudbergsson, J.M., Johnsen, K.B., Skov, M.N., and Duroux, M. *Systematic review of factors influencing extracellular vesicle yield from cell cultures. Cytotechnology*, 2016. **68**(4): p. 579–592.
55. Oglecka, K., et al. *Osmotic Gradients Induce Bio-Reminiscent Morphological Transformations in Giant Unilamellar Vesicles. Frontiers in Physiology*, 2012. **3**.
56. Bieligmeyer, M., et al. *Reconstitution of the membrane protein OmpF into biomimetic block copolymer–phospholipid hybrid membranes.* Beilstein *Journal of Nanotechnology*, 2016. **7**: p. 881-892.
57. Sanborn, J., et al. *Transient pearling and vesiculation of membrane tubes under osmotic gradients. Faraday Discussions*, 2013. **161**.
58. Oglęcka, K., et al. *Oscillatory phase separation in giant lipid vesicles induced by transmembrane osmotic differentials. eLife*, 2014. **3**.
59. Elani, Y., Law, R. and Ces, O. *Vesicle-based artificial cells as chemical microreactors with spatially segregated reaction pathways. Nat Commun.,* 2014. **5**(5305).
60. Mourigen, O.G. *Lipids, curvature, and nano-medicine. European journal of lipid science and technology: EJLST*, 2011. **113**(10): p. 1174–1187.
61. Kato, N., Ishijima, A., Inaba, T., Nomura, F., Takeda, S., and Takiguchi, K. *Effects of lipid composition and solution conditions on the mechanical properties of membrane vesicles. Membranes*, 2015. **5**(1): p. 22–47.
62. Johnsson, M., and Edwards, K. *Phase Behaviour and Aggregate Structure in Mixtures of Dioleoylphosphatidylethanolamine and Poly(Ethylene Glycol)-Lipids. Biophysical Journal,* 2001. **80**(1): p. 313-323.
63. Johnsson, M. *Sterically Stabilised Liposomes and Related Lipid Aggregates*, in *Faculty of Science and Technology*, 2001, Uppsala University.
64. Shi, L., Zhang, J., Zhao, M., Tang, S., Cheng, X., Zhang, W., Li, W., Liu, X., Peng, H., and Wang, Q. *Effects of polyethylene glycol on the surface of nanoparticles for targeted drug delivery. Nanoscale*, 2021. **13**: p. 10748-10764.
65. Holland, J.W., Hui, C., Cullis, P.R., and Madden, T.D. *Poly(ethylene glycol)-Lipid Conjugates Regulate the Calcium-Induced Fusion of Liposomes Composed of*

Phosphatidylethanolamine and Phosphatidylserine. Biochemistry, 1996. **35**(2618-2624).

66. Ding, W., Palaiokostas, M., Wang, W. and Orsi, M. *Effects of Lipid Composition on Bilayer Membranes Quantified by All-Atom Molecular Dynamics. J. Phys. Chem. B,* 2015. **119**(49): p. 15263–15274.

Chapter 3: Complementary Oligos Design and Hybridization Characterization through FRET Evaluation

3.1 Introduction

3.1.1 Fluorescence Excitation and Emission Fundamentals

Fluorescence is a member of the luminescence family of processes, in which molecules brought to electronically excited states, due to either a physical (for example, absorption of light), mechanical (friction), or chemical mechanisms, emit light[1].

3.1.1.1 Absorption Process

The electromagnetic spectrum utilized to bring a molecule to its excited state ranges from the ultraviolet to visible regions (250 to 700 nanometers). The process by which the molecule absorbs a photon raising one of its electrons to an electronic excited state and then radiates a photon as the electron returns to a lower energy state is known as photoluminescence and it involves two different types of reaction: phosphorescence and fluorescence[2].

In both categories, susceptible atoms and molecules absorb light at a particular wavelength[3], but the duration of their excited state lifetime differs, with the fluorescence

mode being extremely short, measured in only billionths of a second (10^{-8} s) [4], whereas the lifespan of the phosphorescence route is framed from 10^{-3} s up to a few seconds, minutes, or it can even persist for hours[5].

In the fluorescence mode, light absorption by a molecule, (which corresponds to fluorophore excitation from the ground to an excited state), is measured in discrete amounts, termed quanta. Likewise, photon emission either through fluorescence or phosphorescence also occurs in quanta. This energy in quantum is given by Planck's Law (1):

$$E = hn = hc/l \quad (1)$$

where *E* stands for energy, *h* is Planck's constant, *n* and *l* are the frequency and wavelength of the incoming photon, and c is the speed of light. Based on Planck's Law, it becomes evident that shorter incident wavelengths possess a greater quantum of energy since absorbed photon energy is directly proportional to light frequency, but inversely proportional to the wavelength[6].

Upon light absorption by a single atom or molecule, the quantum energy of the photon is communicated to atom/molecule, elevating it from a state of lowest energy (highest stability) to an energy-rich, excited state; this is the only kind of excited states possible in an atom. However, in a diatomic or polyatomic molecule, vibrational and rotational states are superimposed on each electronic state and in case of a complex molecule, there is a very close spacing among the various vibrational and rotational states. This phenomenon is manifested in both the absorption and emission spectra where the atom's sharp absorption (and emission) lines are replaced by broad, continuous bands[7].

In accordance with the quantum theory any molecule has discrete energy levels based on its structure that can be classified in rotational<vibrational<electronic written with increasing energy values. The lowest energies manifested in the microwave region are the rotational transitions (10^{-3} eV). The vibrational ones span the infra-red section,

requiring energies of > 10^{-1} eV and the electronic transitions that cover the ultraviolet and visible region of the electromagnetic spectrum, display higher energies of 1 eV[2].

Upon electromagnetic radiation therefore, the molecule apart from its transfer into an excited electronic state, it also acquires some vibrational energy[8]. The occurrence of this process is explained by so-called Franck-Condon principle. According to this principle, molecule excitation by a photon is practically an instantaneous process (that occurs in femtoseconds 10^{-15} s), since only electron rearrangement is involved. The atom nuclei in the molecule are enormously heavy compared to the electrons forcing the former to remain nearly stationary, meaning that there is no modification of the molecular geometry in the course of photon absorption. Yet, these much heavier atomic nuclei readjust themselves after photon absorption completion, entering in an unstable vibronic state[9].

The lifetimes of these vibrations are of the order of 10^{-13} or 10^{-12} seconds, way less than the lifespan of the excited electronic states (10^{-9} s), consequently providing sufficient time for many thousands of vibrations to occur during the excitation period[10].

Photon absorption by a fluorophore happens upon interaction of a molecule's electrons (charges) with the oscillating electric field vector of the light wave. This is an all or none phenomenon and can only be manifested at specific wavelengths of incident light known as absorption bands. If photon energy exceeds the energy requirements for a simple electronic transition, the surplus energy is usually transformed into vibrational and rotational energy. If, on the other hand, a molecule collides with a photon of insufficient energy, unable to promote a transition, absorption fails[11].

The surplus energy can excite fluorophores to higher vibrational levels of singlet energy states, as depicted in Jablonski diagram (Fig. 3.1A), where for instance the left-hand blue arrow (S0→S2) showcases an absorption transition from the lowest vibrational energy level of the ground state S(0) = 0 to a higher vibrational level in the second excited state S(2) = 2 (a transition denoted as S(0) = 0 to S(2) = 2)[12].

Fluorophore irradiation with a wide spectrum of wavelengths instigates a broad range of permitted excitation transitions on various vibrational energy levels, with some transitions having a higher degree of probability to occur[12]. The most favoured transitions involve maximal overlap of rotational and vibrational electron density probabilities between the ground and excited states. However, the incident photons of varying wavelength (and quanta), energetically sufficient to be absorbed, is this unstable factor that reinforces transitions from other internuclear separation distances and vibrational energy levels. Therefore, the emergence of broad band spectra (multiple peaks) [13] (Fig. 3.1B), instead of discrete lines, lies in the wide range of photon energies[14].

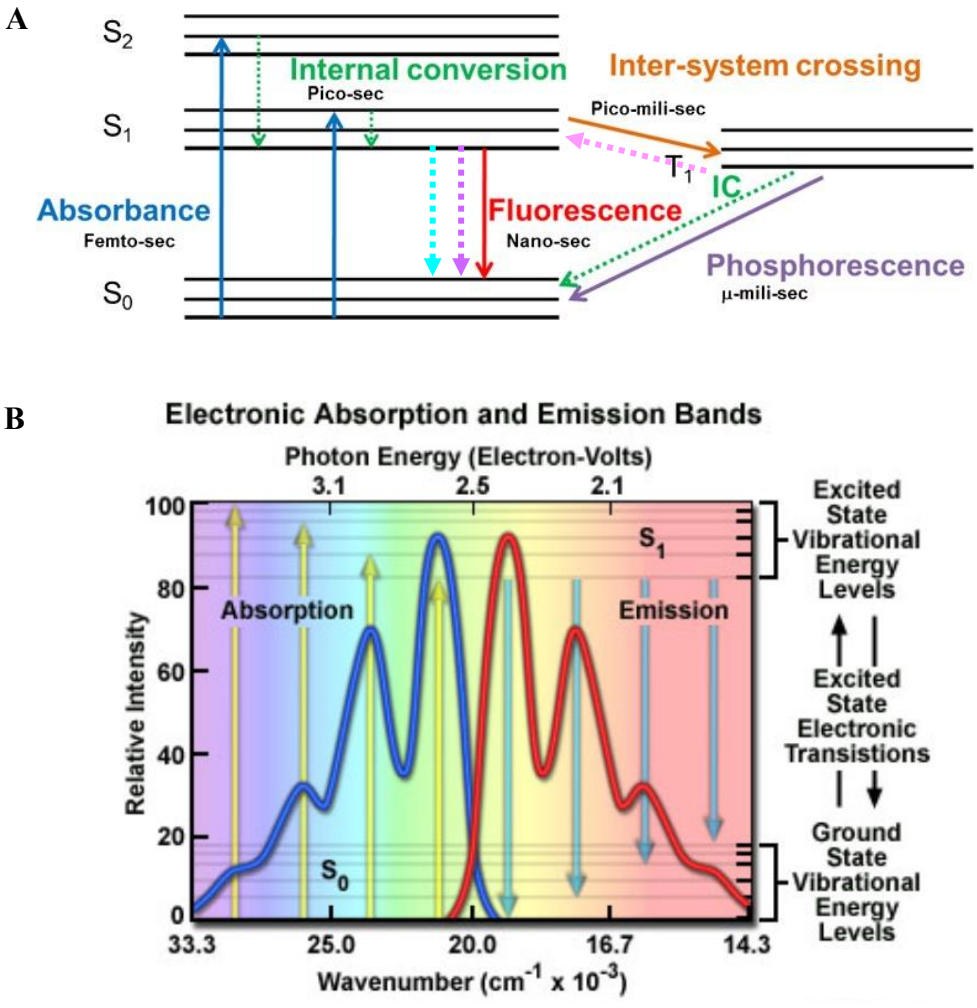

Figure 3.1- (A) Modified Jablonski energy diagram presents distinct energy levels and the excitation and emission cycle of a fluorophore. *Upon photon absorption, molecules transition to excited states S(2) or S(1) at the second and the third vibrational levels respectively, S(2) = 2*

and S(1) = 3. This is followed by internal energy conversion and relaxation to the lowest vibrational level of the first excited state S(1) = 0. Several de-excitation routes initiate from S1 including photon emission (red), spin conversion to triplet state (T1 orange), and other non-radiative mechanisms, such as, excited state energy dissipation as heat (vertical cyan dashed line), and quenching (vertical purple dashed line). Image (A) adapted from[14]. (B)Spectrally broad absorption and emission bands. Source of image (B):[15].

3.1.1.2 Emission Process

Following photon absorption, the second most likely step evinced is the internal conversion (loss of energy in the absence of light emission), where the molecule undergoes a very fast process of vibrational relaxation reaching the lowest vibrational energy level of the first excited state (S(1) = 0; Fig. 3.1A), lasting a picosecond or less[9].

During this time, much of the excess vibrational energy is converted into heat, a form of energy exchanged with the medium (temperature equalization), and eventually the molecule acquires ambient “vibrational temperature”[9]. Hence, fluorescence initiates from a thermally equilibrated excited state S1[16-18].

The ensuing electron landing on the closely spaced vibrational energy levels of the ground state, along with normal thermal motion, yields a range of photon energies upon emission explicating why fluorescence is not observed as a sharp line but rather as emission intensity over a band of wavelengths (Fig. 3.1B). This excitation and emission cycle can be usually iterated hundreds to thousands of times before the highly reactive excited state molecule is photobleached, during which the molecule ceases to respond to incident illumination[19].

As diagrammed in Figure 3.1A, there are several other relaxation routes that compete with the fluorescence pathway. These likely processes include non-radiative dissipation of the excited state energy in the form of heat (the cyan dashed arrow in Fig. 3.1A), energy transfer upon collision of the excited fluorophore with another molecule, which constitutes a second type of non-radiative process, for example, quenching, (defined as lifetime

shortening of the excited state), as indicated by the vertical purple dashed arrow in Figure 3.1A), or even the rare phenomenon of intersystem crossing (the orange arrow in Fig. 3.1), where a molecule is subjected to during the phosphorescence route[20].

The intersystem crossing phenomenon can occur when the electron in the S_1 state undergoes a conversion in its spin, (meaning that an electron's spin is not paired to the ground state, and consequently in its energy), relaxing into a triplet state T_1[21]. The electron descends to the lowest excited triplet state through vibrational relaxation[18], but overall, its residence in an excited triplet state persists longer than those in an excited singlet state[21]. This ultimately results in photon emission either via phosphorescence (diagonal purple arrow Fig. 3.1A) or delayed fluorescence (diagonal dashed pink arrow Fig. 3.1A), as a transition back to the excited singlet state is possible (Fig. 3.1A)[22].

Yet, phosphorescence is a long-lived process since unpaired electron (of the same spin) transition from the triplet excited state to the singlet ground state is a forbidden route. Hence, triplet/singlet transitions (phosphorescence) progress slowly, with much less probability than singlet/singlet transitions; a reason that justifies the prominent detection of fluorescence over phosphorescence[18].

3.1.1.3 Stokes Shift

As aforementioned, during photon absorption, the atomic nuclei, which are enormously heavy compared to electrons, can readjust themselves only after completion of the absorption act, bringing themselves into a vibration mode. This is best illustrated by the potential energy diagram presented in Fig. 3.2. The two curves show the molecule's energy levels (two electronic states, a ground and an excited one) as a function of distance between the nuclei, r_{xy}. According to the Franck-Condon principle, excitation is represented by the vertical ascending arrow (A) which hits the upper curve to a somewhere higher point than its lowest one (corresponding to a nonvibrating state). The molecule, therefore, finds itself in a nonequilibrium state which obliges it to initiate its own

vibration/oscillation. As the timeframe of these vibrations (10^{-13}, or 10^{-12} seconds) is a much shorter lifespan compared to excited electronic state lifetime (10^{-9} s), allowing adequate time for many thousands of vibrations to transpire during the excitation period, most, if not all the vibrational energy is lost through energy exchange (temperature equalization) with the medium, along this process[23].

Hence, the deactivation process of fluorescence emanates from the lowest level of the upper potential curve (due to vibrational relaxation) and follows the vertical descending arrow (F) striking the potential curve beneath (Fig. 3.2). The arrow doesn't hit the deepest point, but one of the elevated vibrational energy levels of the ground state S_0, as fluorescence emission is usually escorted by higher vibrational energy level transitions to the ground state. This excess vibrational energy is further dissipated through thermal equilibration[23].

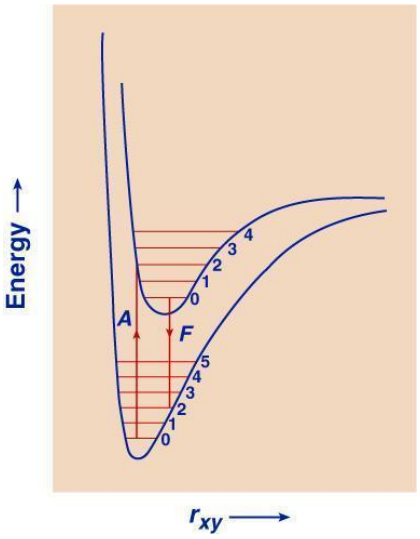

Figure 3.2- Frank-Condon Principle. *Ground and excited potential energy curves of a diatomic molecule. Numbers denote vibrational states; A, absorption; F, fluorescence and r, interatomic distance. Image taken from:[23].*

Thus, the absorption-emission cycle is comprised of two processes accountable for energy dispersal[9]: a) the internal conversion procedure, which involves the rapid decay of excited electrons to the lowest vibrational energy level of the S(1) excited state, prior to fluorescence commencement[24], and b) vibrational relaxation to the ground electronic state.

The diminution of excitation energy, as indicated by the shorter fluorescence arrow in Figure 3.2, manifests as a wavelength shift between absorption and emission, and is termed Stokes Shift[9, 25], given it was first reported by Sir G. G. Stokes in 1852[26]. A typical Stokes shift is represented in Figure 3.3 and demonstrates a characteristic emission band displacement towards the longer wavelength, (the red shift of the fluorescence spectrum), compared to the absorption bands[26], as a result of lower energy of emission spectra than that of the incident excitation.

The length of this shift can vary from just a few nanometres to over several hundred nanometres depending on the molecular structure. For instance, the Stokes shifts for fluorescein and for the porphyrins are approximately 20 nanometres and over 200 nanometres, respectively[2].

The difference between the excitation and emission wavelengths (energy) is highly desirable at it is considered a critical factor for optimal choice of light sources and optical filters (for a fluorescence microscope), which are employed to separate incident excitation photons from emitted fluorescence photons[2].

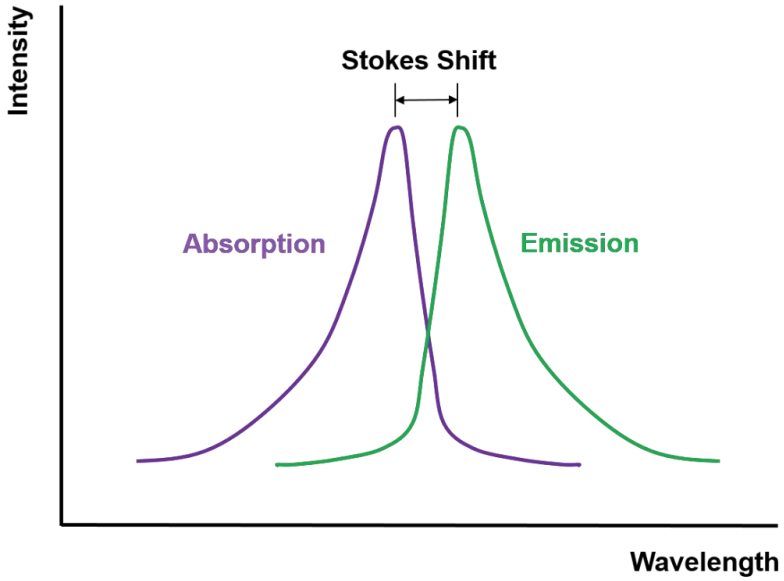

Figure 3.3- Pictorial representation of Stokes shift spectra with a typical displacement of fluorescence band relative to the absorption band of a molecule. *The differences in wavelength between absorption and emission peaks is the result of excitation energy loss due to electron relaxation and intramolecular vibration. Image taken from:[21].*

3.1.2 Förster Resonant/Resonance Energy Transfer (FRET)

A major interest in many areas of scientific research involves the investigation of the precise location and nature of the interactions between specific molecular species. However, these efforts are not often crowned with success due to resolution limitations imposed by standard objectives which restrict the amount of acquired information upon examination of these phenomena. Although the conventional widefield fluorescence microscopy enables fluorescently labelled molecule localization, this is limited within the optical spatial resolution demarcated by the Rayleigh criterion, which is approximately 200 nanometres (0.2 micrometre) [27].

The technique that permits determination of molecular proximity and interaction within nanometre scale distances is known as Förster resonance energy transfer, (more

commonly referred to by the acronym FRET)[27], a physical phenomenon first conceptualized by Förster[28] over 50 years ago (in 1948) [29, 30].

Its application to biomedical research has been materialised thanks to recent technical advances[31-33], turning it into a powerful tool in the investigation of molecular biological processes unfolding on this scale[34], by probing distance fluctuations through fluorescence measurements[2] and mapping spatio-temporal arrangement of protein interactions[35].

In the current project, in the hopes of detecting formation of inter-membrane bridges, generated by hybridization of two complementary single-stranded DNA sequences, each carrying an internally conjugated fluorophore (Cy3/Cy5) and being end-functionalized with a cholesterol moiety for GUV and droplet lipid bilayer integration (Fig. 3.4), Förster Resonance Energy Transfer (FRET) is employed[2].

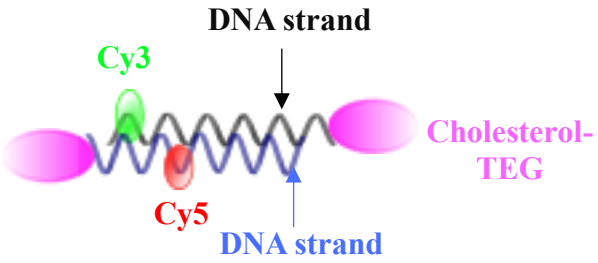

Figure 3.4- Schematic representation of annealed complementary DNA strands featuring internally positioned Cy3 and Cy5 molecules and cholesterol-TEG moieties*. Not to scale.*

3.1.2.1 FRET Principles

The first step in the molecular process underlying FRET involves energy absorption in the form of photons by the donor molecule[36], whose valence electron is promoted from the ground state to a higher electronic orbit, ascending to an excited state (Fig. 3.5)[30]. This energy is transmitted in a non-radiative fashion to a second chromophore in close vicinity, known as acceptor (Fig. 3.5)[2].

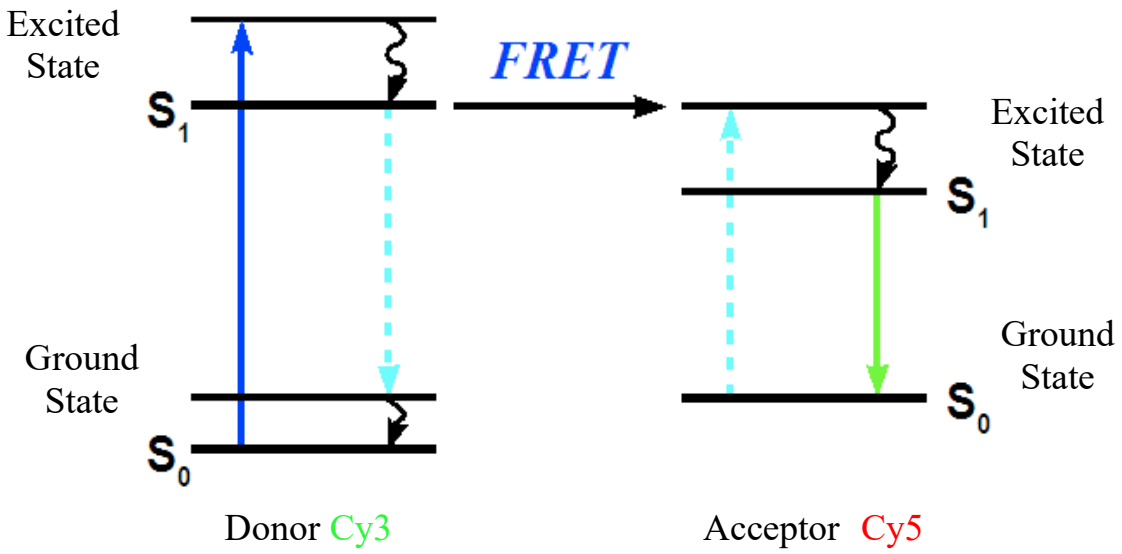

Figure 3.5- FRET schematic demonstration. *Energy level diagram describing donor's valence energy promotion from ground to an excited state (blue vertical ascending arrow), non-radiative energy transfer to a nearby ground state acceptor molecule (black horizontal arrow) and acceptor's photon emission (green vertical descending arrow).*

Thus, the fundamental mechanism of FRET is based on radiationless transmission of energy from a donor fluorophore in an excited state to a suitable nearby ground state acceptor fluorophore through long-range dipole-dipole interactions[37]. The energy transfer manifests itself through reduction of the donor's fluorescence intensity, (or through quenching of donor fluorescence), and shortening of its excited state lifetime, accompanied by an increase in the acceptor's intensity, with the characteristic fluorescence spectrum of the acceptor (Fig. 3.6B-right). As two molecules interact in such a manner enabling the FRET process, they are referred to as a donor/acceptor pair[2].

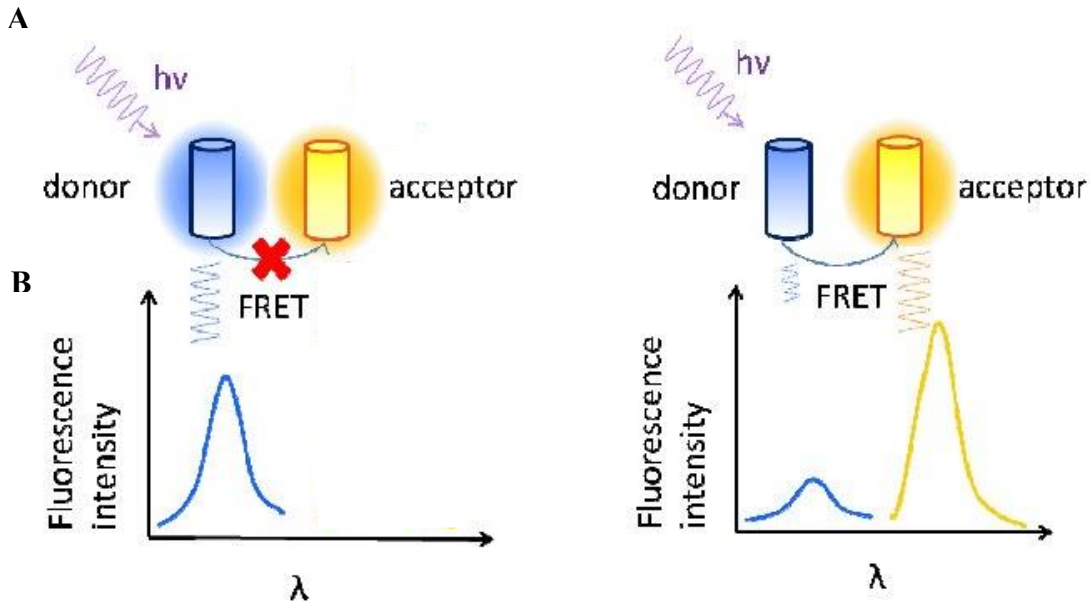

Figure 3.6- Principle of FRET. *In (A), on the left, as the distance between donor and acceptor molecules exceeds the FRET limit, only donor emission is detectable upon the system excitation without any energy transfer taking place. On the right-hand side of the picture, the intermolecular distance (of donor and acceptor) varies within the FRET limits enabling energy transmission from donor to acceptor and consequently, reducing donor emission as represented by the thinner blue arrow. The acceptor's intensity is increased or sensitized, as the yellow arrow indicates. Image adapted from:[38]. (B) depicts how donor and acceptor emission spectra are modified during non-FRET and FRET process, with the latter displaying a remarkable dissipation in the donor emission spectrum and the emergence of the acceptor emission spectrum. Image adapted from:[38].*

3.1.2.2 Criteria for FRET Occurrence

The non-radiative quantum mechanical process of resonance energy transfer does require the satisfaction of several criteria for its occurrence.

In principle, for an excited donor fluorophore to directly transfer its energy to an acceptor through long-range dipole-dipole intermolecular coupling, there should be some sufficient overlap between the fluorescence emission spectrum of the donor and the absorption spectrum of the acceptor (Fig. 3.7).

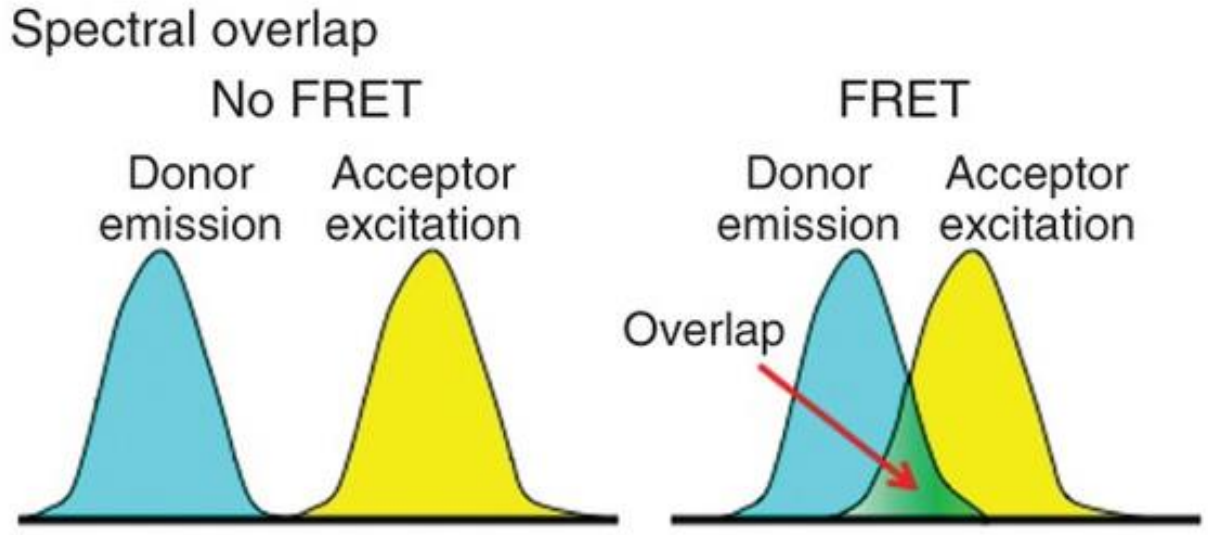

Figure 3.7- Spectral overlap between donor molecule emission spectrum with acceptor molecule excitation spectrum is a prerequisite for FRET*. Source:[39].*

In addition, the radial distance between two fluorophores, (Donor-Acceptor), should range within a minimal spatial radius of 1 to 10 nm[2].This distance dependence of the resonance energy transfer phenomenon is reflected in Förster equation (2) which demonstrates that this process varies with the inverse sixth power of the intermolecular separation.

$$E = \frac{R_o^6}{(R_o^6 + R^6)} \quad (2)$$

R is the inter-dye distance, and R_o is the Förster radius at which FRET efficiency (E) is 50 percent (Fig. 3.8), and typically ranges between 4 nm-6 nm[35, 40, 41]. For the well characterized Cy3-Cy5 FRET couple R_o has a distance of 5 nm[42]. R_o value can be determined for any pair of fluorescent molecules by the following equation (3):

$$R_0 = 2.11 \times 10^{-2} \cdot [\kappa^2 \cdot J(\lambda) \cdot \eta^{-4} \cdot Q_D]^{1/6} \qquad (3)$$

in which *κ*-squared/kappa squared represents the orientation factor between the transition dipoles of the donor and acceptor[43], *Q(D)* is the donor quantum yield, where quantum yield in fluorescence is defined as the number of photon emitted over the number of photons absorbed, *J*(λ) is the spectral overlap integral between donor emission and acceptor absorption and η represents the refractive index of the medium[43].

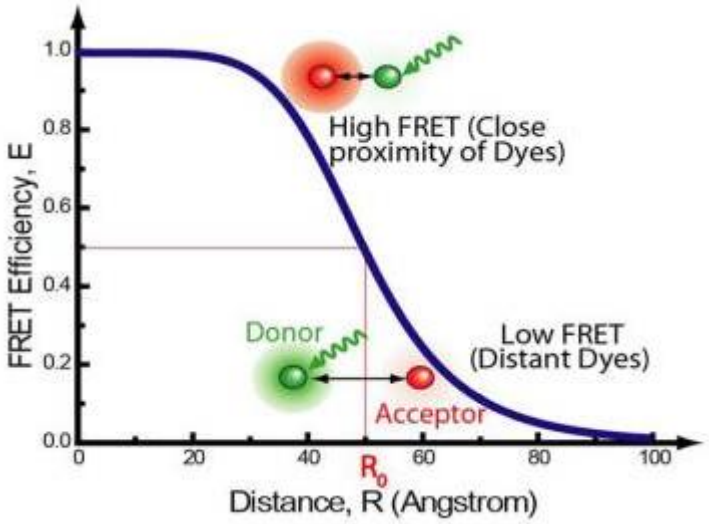

Figure 3.8- FRET principle. *Graphical representation of FRET efficiency as a function of intermolecular separation (R) for R_o = 50 Å. Direct donor probe excitation either leads to its fluorescence or to energy transfer to acceptor depending on its closeness. According to the function presented by the blue line, at R = R_o, E = 0.5, or 50% efficiency, whereas at smaller distances, E > 0.5 and at larger ones E < 0.5. Source:[41].*

In summary, energy transfer rate depends not only on the degree of the spectral overlap region between the donor emission and acceptor absorption spectra, and the donor-acceptor separating distance, but also on the transition dipole moment orientation of the two paired molecules, and the quantum yield of the donor.

3.1.2.3 FRET Efficiency

The efficiency of energy transfer, *E(T),* is a measure of the fraction of photons absorbed by the donor that are transferred to the acceptor non-radiatively, and it can be calculated from the lifetimes of donor in the presence of the acceptor *τ(DA)* and in the absence of the acceptor *τ(D)* according to the formula (4):

$$E_T = 1 - (\tau_{DA}/\tau_D) \qquad (4)$$

However, in many commonly applied techniques, the energy transfer efficiency is typically evaluated by steady state fluorescence intensity measurements of the donor in the presence (F_{DA}) and absence (F_D) of the acceptor[2] (5):

$$E_T = 1 - (F_{DA}/F_D) \qquad (5)$$

3.1.2.4 Methods for Measuring FRET Efficiencies

FRET efficiency is employed as a marker of interaction and colocalization permitting calculation of absolute distances and investigation of conformational modification magnitudes[44].The two most used quantification techniques for FRET efficiency are sensitized emission measurement, and acceptor photobleaching imaging or else, donor dequenching method[45].

3.1.2.4.1 Sensitized Emission

In the field of dynamic live cell FRET imaging, the most widely used measurement tool is sensitized emission[46-48]. This approach quantifies FRET efficiency by measuring acceptor emission increase upon energy transfer from the donor. This is accomplished through “FRET filter set” utilization which enables selective excitation of a donor molecule

by means of an excitation bandpass and selective acceptor emission collection via an emission window, referred to as an “acceptor channel”[45].

Although in theory, this FRET filter set directly assesses the amount of FRET in a sample, in reality, crosstalk signal contamination is integrated in the calculations (formula presented in ***3.2.6.1 Sensitized Emission, formula 10***). The two main roots of crosstalk are spectral bleed-through, which refers to the leakage of donor emission into the acceptor channel, and cross-excitation, which concerns direct acceptor fluorophore excitation by donor excitation[45].

For crosstalk to be corrected some additional reference measurements need to be performed. Bleed-through determination requires a control sample containing only donor fluorophore molecules excited at the donor’s wavelength. The other reference sample, which contains only acceptor fluorophores excited at the donor’s wavelength as well, determines direct acceptor excitation (cross-excitation)[45].

In actual FRET experiments, the contributory input of these effects needs to be known to recover the true FRET efficiency in the acceptor channel[45]. Some methods also take into account direct excitation of the donor by acceptor excitation and bleed-through of acceptor signal into the donor channel. However, careful selection of fluorophores, excitation filters and emission filters can result in more robust analysis, reducing the need for these corrections[45].

Finally, extraction of the true acceptor and donor intensities needed for FRET efficiency calculations further requires corrections relating to background (intensities)[45].

3.1.2.4.2 Acceptor Photobleaching or Donor Dequenching Method

An additional verification of the FRET efficiency comes from the acceptor photobleaching (also known as donor dequenching) method which basically refers to the photodestruction of the acceptor fluorophore through FRET excitation[45].

The underlying concept exploits the fact that during FRET, donor fluorescence is quenched because some of the donor fluorescence energy is channelled to the acceptor, which can lead to acceptor photobleaching. Acceptor photobleaching causes an irreversible elimination of the quenching effect, resulting in an increase in the level of donor fluorescence. This means that the acceptor fluorophore will cease absorbing or emitting fluorescence ensuing its transition to a dark state [45].

Overall, both these intensity-based imaging methods used for FRET measurements suffer from some drawbacks such as detector noise, light source instability, autofluorescence[2] and inadvertent bleaching of the photostable fluorophore or even unknown light induced phototoxicity[45].

3.1.3 Total Internal Reflection Fluorescence (TIRF) Microscopy

A special technique in fluorescence microscopy, developed by Daniel Axelrod at the University of Michigan in the early 1980s, is known as total internal reflection fluorescence (TIRF), and occupies a central place in the studies of membrane dynamics and membrane-associated processes[49]. This is achieved by the generation of an evanescent wave/field utilized for fluorophore excitation. Evanescent field is produced when (incident) excitation light (laser excitation as in Fig. 3.9) hits the interface boundary and propagates at an angle greater than the critical angle, undergoing in this way total internal reflection (TIR). The critical angle (θ_c) of incident light, at which total internal reflection transpires, is defined by Snell's Law [50] (6):

$$\theta_c = \sin^{-1}(n_2/n_1) \qquad (6)$$

where $n(1)$ is the higher refractive index (usually coverslip) and $n(2)$ is the lower refractive index (usually specimen)[50].

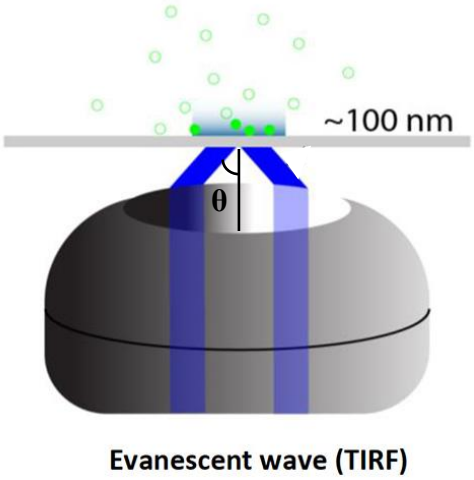

Figure 3.9- Evanescent waves, emerging due to TIRF, decay exponentially, attaining excitation within ~100 nm in depth, which affords extremely high axial resolution of this region. *Image adapted from:[51].*

The TIR phenomenon does not occur suddenly as there is a continuous transition from predominant refraction (bending of light in the lower index medium) with a small fraction of reflection, to total reflection upon exceeding the critical angle. On occurrence of total internal reflection, a fraction of the incident light energy will be converted to an electromagnetic field at the interface penetrating it and forming an evanescent field or wave (Fig. 3.9). The emerging evanescent wave, capable of exciting fluorophores, is the same wavelength as the light reflected during TIR (the incident light) and its intensity is maximal at the surface. The range over which fluorophore excitation is attained is limited by the exponential falloff of evanescent field intensity in the z direction and is given by the following equation (7) which defines this energy as a function of distance from the interface**:**

$$E(z) = E(0)\exp(-z/d) \qquad (7)$$

with *E(z)* being the energy in the *z* direction perpendicular to the interface and *E(0)* representing the energy at the interface. *(d)* stands for the depth to which evanescent wave penetrates[52].

The penetration depth of this field extends from 60 to 100 nm or it can even reach 200 nm, based on incidence of the light's angle, refractive indices of the two media and wavelength. By increasing the incident angle θ of the illuminating beam, the penetration depth is reduced. Moreover, increasing the refractive index of the medium with the higher refractive index *(n(1)),* while preserving a constant value for the medium of lesser refractive index *(n(2))* results in decreased evanescent wave's entrance into the z-dimension. Likewise, increasing the refractive index of medium two *(n(2)),* while the refractive index of medium one *(n(1))* is held constant, produces larger values for the penetration depth. In addition, longer wavelengths produce greater degrees of penetration. All the above can be demonstrated by the following formula (8):

$$d_p = \lambda_i/4\pi(n_1^2 \sin^2(\theta_{incident}) - n_2^2)^{1/2} \qquad (8)$$

which denotes that the length of the illumination intensity *(d)* attenuates exponentially with distance from the surface depended on the angle of incidence (θ_i), the illuminating wavelength λ_i and the refraction indices of the media $n_1 > n_2$. [52].

3.1.3.1 TIRF Geometries

There are two main optical schemes for attaining total internal reflection in optics: one is prism-based (p-TIRF) and the other objective-based (o-TIRF) or else, objective lens method.

3.1.3.1.1 Prism Type Setup

In p-TIRF geometry, a prism is placed on the coverslip's surface and the illumination light path is directed towards the coverslip/medium interface (Fig. 3.10)[53]. The prism configuration enables the mainstream of excitation to be directed away from the objective and by extension, away from the emission channel, minimizing stray light intensity and consequently, significantly increasing the signal-to-noise ratio[53].

Although its great advantage lies in its ability to scan a wider range of angles above the critical angle, which permits direct and smooth control of evanescent field penetration depth[53], its configuration confines access to and manipulation of the specimen (such as physiological measurements, add drugs etc.), as the objective lens plunges into the sample[53].

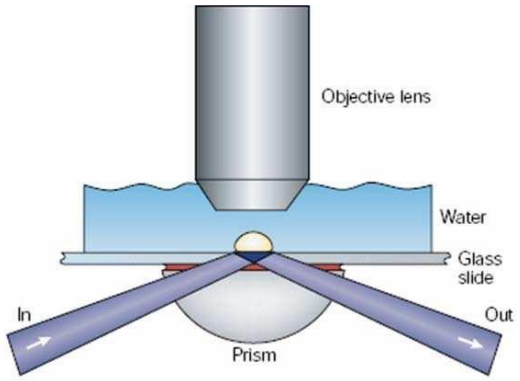

Figure 3.10- Illustration of prism-type optical scheme for TIRF microscopy. *Emergence of an evanescent field results by illuminating at an angle greater than the critical angle via a hemispherical prism optically paired with a coverslip by means of immersion oil. Appropriate illumination wavelength excites fluorescent molecules within the evanescent field section inducing fluorescent emission which is gathered by* (*high NA*) *water immersion lens. As the fluorescence needs to initially pass through the specimen, prior to being collected, there is potentiality of image distortion. Image taken from:[53].*

3.1.3.1.2 Objective Type Setup

In the objective-type TIRF geometry, which is most used in modern TIRF microscopy systems, the laser is introduced through the microscope, and it is mandatory that objectives are oil-immersion ones with an extremely high numerical aperture (NA) (ideally 1.45 NA or higher) (Fig. 3.11).

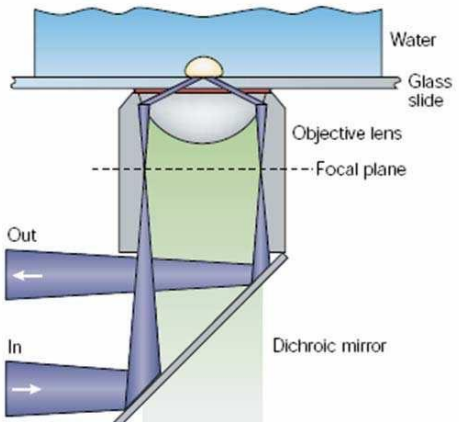

Figure 3.11- Objective lens method*. Evanescent field emergence is attained by focusing a laser beam at the peripheral area of the back focal plane (BFP) of the objective lens which results in a larger angle of incidence than the critical angle. The same high NA objective lens is used to collect the emitted fluorescence which passes through a dichroic mirror prior to being collected by a detector. Image taken from:[53].*

The immersion oil objective eliminates the problem of light diffraction/refraction (bending) and scattering that emerges when light rays pass from one medium to another, each carrying different refractive indexes (such as coverslips 1.5 and air 1.0)[54].

The numerical aperture (NA), which typically characterizes the light gathering capability of the lens, or conversely, determines the spectrum of angles at which light can escape

the objective, needs to be large, so that large angles of incidence, greater than the critical angle for glass/water interface, can be achieved (Fig. 3.12)[55].

The relationship between numerical aperture and angles of incident illumination are demonstrated by the following equation (9):

$$\textit{Numerical Aperture (NA)} = n \times \sin(\theta) \qquad (9)$$

where n represents refractive index of the medium between the objective front lens and the sample, and θ the one-half angular aperture of the objective [55].

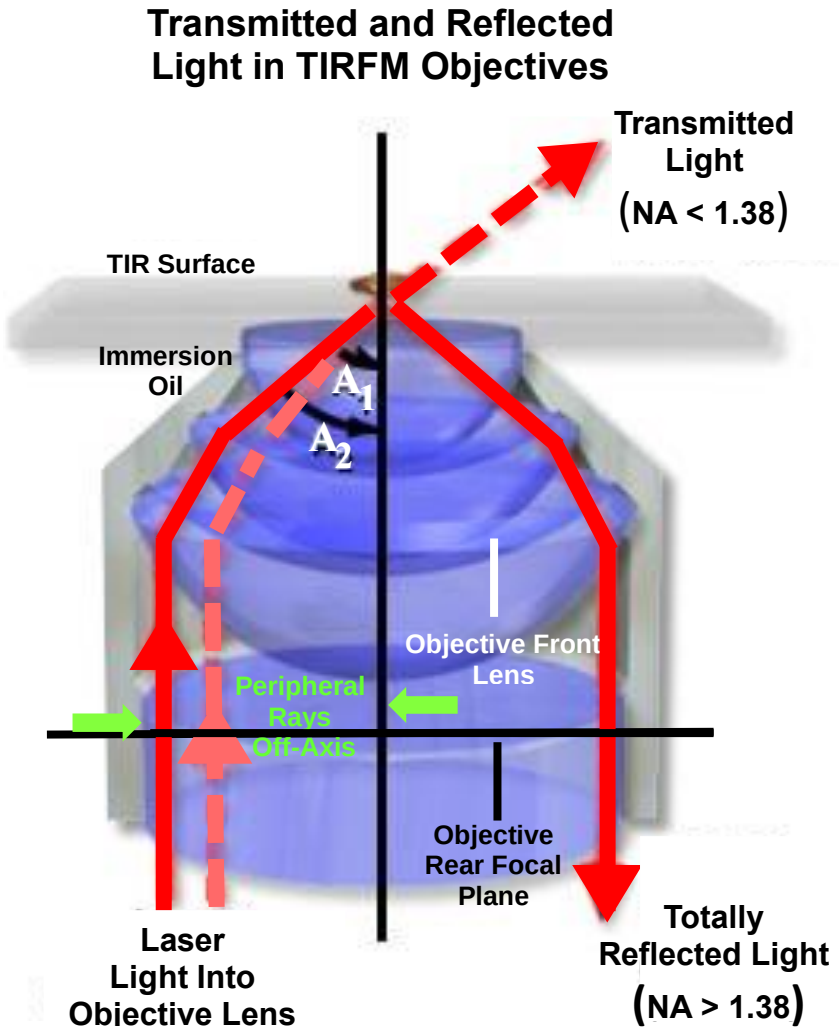

Figure 3.12- High Numerical Aperture Objective TIRFM. *Laser beam adjustment off-axis at the objective rear focal plane, at a suitable radial distance (red solid line), ensures total internal reflection. Image adapted from:[56].*

Objective lens technique carries the key advantage of sample accessibility and flexibility of measurement options[53]. The downside of the objective lens method lies in the common excitation and emission light path through a single objective, which can be a potential source of stray light, resulting in signal to background limitations.

The problem arises from the reflections originating from the excitation laser in combination with autofluorescence from immersion-oil objective which can be totally internally reflected through the same objective again, ultimately deteriorating the net effect of the signal to background ratio.

3.1.4 Fluorescence Spectrometer: Principle of Operation

Fluorometer or fluorimetry is a spectrometer designed to measure fluorescence emitted from a sample irradiated with light of one wavelength but giving off commonly a longer wavelength.

A fluorometer is equipped with a filter or monochromator which selects out a designated excitation wavelength group and directs it into the sample (Fig. 3.13)[57]. A proportion of the excitation light is absorbed by the sample resulting in molecules fluorescing. The fluorescent signal is scattered in all directions and some of this light is transmitted through a second filter or monochromator prior to reaching a detector (Fig. 3.13). The detector's position is at 90°C to the incident excitation beam mitigating the risk of interference of the transmitted excitation light accessing the detector[58].

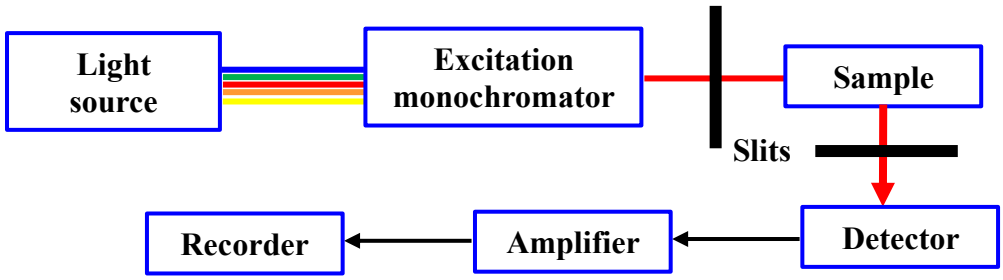

Figure 3.13- Depiction of the key components of a fluorometer. *The sample placed in a cuvette is excited by a light source orthogonally positioned in relation to the detector that collects fluorescence emission. The emitted signal from the sample is transmitted through another filter or monochromator separating the emission wavelength of interest from most of the excitation light prior to being measured by a detector.*

3.1.5 Chapter's Aims

Direct transient or stable cell-cell interactions drive numerous physiological processes critical to the maintenance and function of multicellular organisms[59]. Yet, studying cell-cell associations is challenging given the teeming activity of biological membranes[60]. Existing biomimetic models entail structural constraints[61] incapable of encapsulating the dynamic nature of intermembrane interactions. Inspired by direct transient intermembrane communication where information is relayed through ligand-receptor engagement, we aspire to construct a model system with intermembrane adhesion properties, analogous to the biological synapse.

This bio-inspired model is comprised of two artificial lipid membrane bilayers, a droplet interface bilayer (DIB), and a giant unilamellar vesicle (GUV), interlinked by annealed complementary DNA strands which serve as adhesion-promoting trans-tethers (Fig. 3.14).

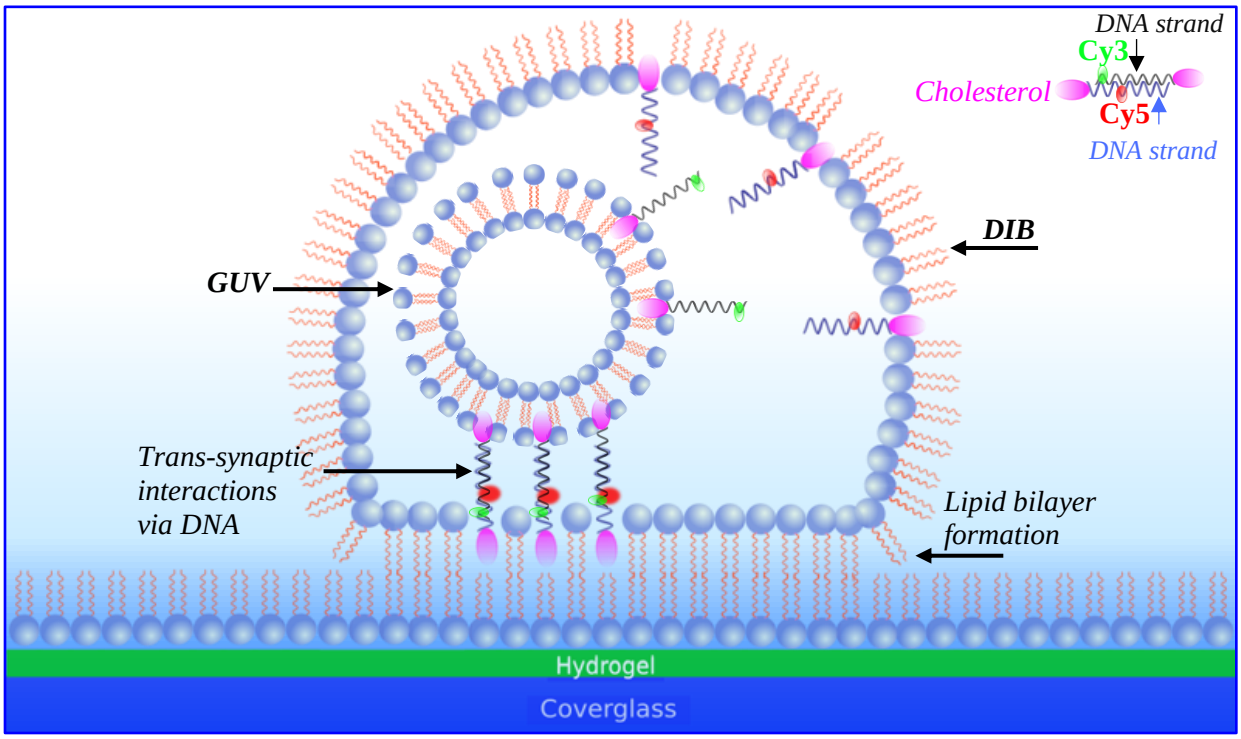

Figure 3.14- Schematics of a labelled DNA-functionalized GUV adhering to a labelled DNA-functionalized DIB via hybridized complementary oligonucleotide sequences. *Not to scale.*

In this chapter, internally labelled complementary single DNA strands, with end cholesterol modification, for membrane integration (Fig. 3.4), are custom designed to be used as trans-synaptic bridges between DIB and GUV bilayers. DNA hybridization is identified via Förster Resonance Energy Transfer (FRET), monitored through bulk fluorimetry measurements and single-molecule total internal reflection fluorescence microscopy (smTIRFm).

3.2 Methods

3.2.1 Microscopy

Imaging and fluorescence microscopy were conducted on a customized inverted widefield (WF) microscope (Nikon Eclipse Ti- inverted epifluorescence microscope) equipped with two lasers, a 635 nm diode laser (Shanghai queen laser technology, Ventus) and a 532 nm (laser quantum smd 600, Ventus). The two laser lines merged into a single-mode optical fibre (Thorlabs, Newton, NJ, USA) and collimated into a 2 mm diameter beam prior to coupling onto the backfocal plane of the objective.

The output of the fibre, after being focused at the rear focal plane of the objective, was displaced from its optical axis centre so that the angle of the incident excitation light formed at the coverslip/water interface was greater than the critical angle [62] giving rise to total internal reflection (TIR).

TIR was achieved with a 60× 1.49 NA Oil objective lens (Nikon PLAN APO), through which an evanescent field was generated resulting in an approximate penetration depth of 100-200 nm extending from the surface the sample was bound to (Fig. 3.15 inset). The coverslip position in relation to the objective lens was controlled by means of a motorized xy-scanning stage (Nikon, TI-SSR, Japan).

For sample loading, WF illumination was utilized and for single-molecule FRET measurements, the optical configuration consisted of manually alternated 532 nm and 635 nm lasers; the latter used for checking the presence of the acceptor. The laser powers utilized in all experiments ranged from 17 mW to 23 mW for both 532 nm and 635 nm wavelengths.

3.2.2 Emission Detection

Fluorescence signals from donor and acceptor molecules, assembled through the same oil-immersion objective, were first filtered to remove scattered light of the excitation laser through a dichroic mirror (DM1) (Di03-R405/488/532/635-t1-25×36, BrightLine, USA) in combination with a long-pass filter (HHQ542LP, Chroma, Taiwan) and a notch filter (NF03-633S-25, Semrock, USA) (Emission filter) (Fig. 3.15).

Then, the collimated image was introduced through a vertical slit placed at the imaging plane, close to the microscope side port. This aperture confines the image space of the final image to half the size of the CCD (charge-coupled-device) chip such that donor and acceptor's emission signals are projected onto one-half of the active area of a 512 × 512 pixel charge-coupled-device camera (CCD, iXon Ultra 897, Andor Technology, Belfast). Lastly, the emission fluorescence was spectrally separated by a second dichroic mirror (DM2) (FF640-FDi01, Semrock, USA) (in image splitter (W-view gemini Hamamatsu) into green and red emission channels. Band-pass filters 593/40 (FF01-593/40-25, BrightLine, USA) and 676/29 (FF01-676/29-25-STR, BrightLine, USA) (Emission filters) were selected for each channel respectively to minimize donor and acceptor emission bleed (Fig. 3.15).

Videos were recorded using Andor Solis software and saved as 16-bit Tagged Image File Format (TIFF) for subsequent analysis. Each image was acquired at 30-ms exposure time. Fluorophore exposure to the laser prior to image acquisition was prevented by a beam shutter TTL synchronized to the CCD.

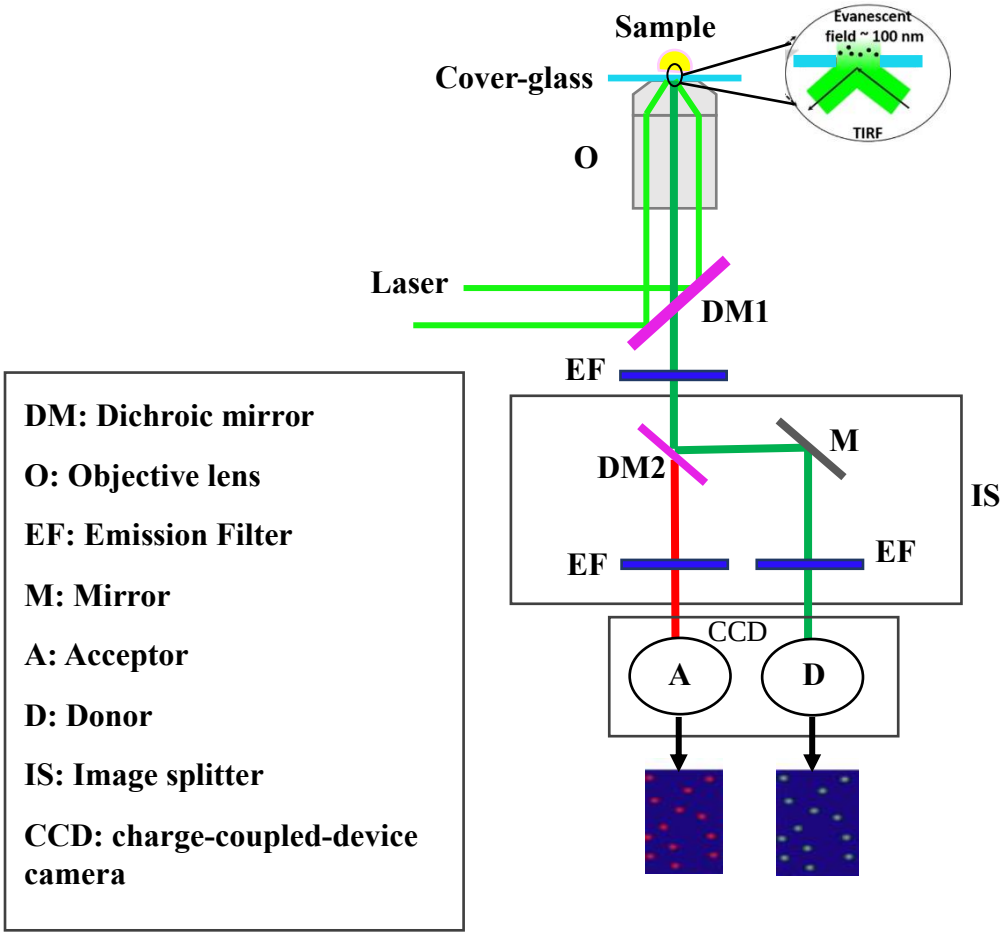

Figure 3.15- Schematic of TIRF microscope configuration for smFRET detection. *Evanescent field (inset) is produced when incident laser excitation at the donor wavelength (532 nm) impacts the interface boundary (cover-glass -sample) via the objective using a dichroic mirror and propagates at an angle greater than the critical angle undergoing in this way total reflection [63]. The electromagnetic field of the total internal reflected light extends into the sample in the z-direction selectively exciting a ~100-nm layer of the specimen beyond the surface leaving the bulk of the specimen illuminated free (inset) [64]. Fluorescence is collected through the objective and passes the dichroic mirror and emission filter. Then it is split by a second dichroic mirror into the donor and acceptor fluorescence emissions and imaged side by side on the CCD camera.*

3.2.3 DNA Preparation

Two sequences of internally Cy3/Cy5 labelled HPLC-purified oligonucleotides were purchased from Integrated DNA Technologies (100-nmol scale), in lyophilized form. The two complementary 52-nucleotide-long sequences were separately reconstituted in TE (10 mM Tris and 1 mM EDTA, pH 7.83) (Sigma) buffer, aliquoted and stored at -20^{o}C.

3.2.4 Ensemble FRET

Separate and mixed Cy3 and Cy5 species were diluted in a saline buffer (TE and 50 mM NaCl, pH 7.83) yielding a concentration of 0.5 μM and final volume of 200 μl.

For background fluorescence and scattering effect correction, 200 μl of the saline buffer solution was placed in a quartz cuvette and measured as a reference sample. Fluorescence emission spectra were acquired at room temperature on a fluorimeter (Agilent Cary Eclipse) with Xe pulse lamp single source and Optical Power 66 mW. The samples were excited with both 532 nm and 635 nm wavelengths and the fluorescence emission wavelengths were determined for the range between 450 nm to 750 nm.

Light intensity was measured as an analogue voltage signal via a photomultiplier. The analogue output was subsequently converted to digital format and stored in an attached computer. The settings were controlled on the computer and data were stored in a file for viewing and analysis.

3.2.5 Single-molecule FRET (smFRET) Image Analysis on Surface-Immobilized Molecules

smFRET time traces were acquired on surface-immobilized molecules with the aid of TIRF microscopy permitting high-throughput data sampling[45]. In our data processing

and analysis, smFRET measurements were performed on a custom-built TIRF microscope and all data were analyzed using ImageJ.

To pair pixels between donor and acceptor channels of the split-view image, each pair of Cy3 and Cy5 spots was translated in the x and y directions by an appropriate number of pixels (on a trial basis), included in the FIJI distribution of ImageJ[65], to account for image registration offset.

For spot detection, isolated single-molecule peaks from a composite image of donor and acceptor channels were identified. Donor and acceptor spot co-localization enabled Cy3-Cy5 pair selection for final analysis. The process continued by splitting donor and acceptor channel images (512 × 256 pixels) and pairs of immobilized Cy3 and Cy5 spots were manually picked.

Spot fitting was ensued by intensity extraction performed on the donor and acceptor channels of the split-view images, respectively. For single-molecule FRET efficiency extraction, a 2 × 2 pixel region was employed corresponding to ~0.25 μm^2 area, an estimated size area suitable to tightly enclose the fixed spot diameter, balancing the trade-off between more fluorescence intensity collection and more background noise inclusion.

Selected regions of donor and acceptor channels were merged to build two colour single spot image stacks of a single pair FRET, as illustrated in Figure 3.21B.

3.2.5.1 smFRET Calibration: Baseline Subtraction, Spectral Corrections

FRET efficiency estimation requires background subtraction and crosstalk (including bleed-through and cross-excitation) correction between the detection channels. Leakage of donor emission into the acceptor channel (bleed-through) and direct excitation of the acceptor (cross-excitation) was determined with donor-only and acceptor-only molecules

being excited at donor excitation wavelength (532 nm). This intensity fraction was subsequently subtracted from acceptor fluorescence traces, so that crosstalk was eliminated. Furthermore, the leakage of acceptor emission into the donor detection channel was determined by acceptor-only molecules being directly excited (635 nm); a correction factor applied to the donor dequenching method calculation (explained in ***3.2.6.2 Donor Dequenching Method, formula 14***).

To flatten baseline levels, easing molecule detection and accounting for non-uniform illumination, the baseline intensity levels, following donor photobleaching, were subtracted from fluorescence traces.

3.2.6 FRET Efficiency

The methods employed for FRET efficiency assessment are known as sensitized emission and donor dequenching.

3.2.6.1 Sensitized Emission

In the sensitized emission approach, FRET efficiency was calculated by formula (10):

$$E^* = \frac{IA_{pre}}{(IA_{pre} + ID_{pre})} \quad (10)$$

where IA_{pre} and ID_{pre} represent acceptor and donor intensities, respectively prior to acceptor photobleaching[41].

To obtain accurate FRET values, the *E** values (10) in the sensitized emission method need correction for crosstalk contribution of donor (Cy3) and acceptor (Cy5) dyes to the FRET signal. In particular, from the acceptor intensity IA_{pre}, leakage contribution to the acceptor signal, (bleed-through), and direct excitation contribution to the acceptor signal, (cross-excitation), were subtracted. Hence, crosstalk corrected FRET (E_{cc}) was acquired as demonstrated in formulas (11) and (12):

$$E_{cc} = \frac{(IA_{pre} - BLEED\text{-}THROUGH - CROSS\text{-}EXCITATION)}{(IA_{pre} - BLEED\text{-}THROUGH - CROSS\text{-}EXCITATION) + ID_{pre}} \quad (11)$$

$$\Rightarrow E_{CC} = \frac{FRET}{FRET + ID_{pre}} \quad (12)$$

3.2.6.2 Donor Dequenching Method

In the donor dequenching method, the formula used for FRET efficiency *(E)* estimation was (13):

$$E = \frac{(ID_{post} - ID_{pre})}{ID_{post}} \quad (13)$$

where ID_{pre} stands for donor (Cy3) intensity before acceptor (Cy5) photobleaching and ID_{post} represents donor (Cy3) intensity after acceptor (Cy5) photobleaching. This equation was corrected in relation to the leakage contribution of the acceptor into the donor channel as exemplified below (14):

$$E = \frac{ID_{post} - (ID_{pre} - \text{LEAKAGE TO DONOR CHANNEL})}{ID_{post}} \quad (14)$$

3.3 Results

3.3.1 Oligos Design

The specific nature of the DNA pairing offers the potentiality to program bottom-up fabrication of our composite membrane system. DNA “bricks” have been exploited in the design of internally labelled complementary DNA strands which demonstrate enhanced photostability in single molecule FRET experiments [66].

Cyanine fluorescent labelled DNA constructs are important substrates for single-molecule(sm) studies, and particularly the cyanine dyes Cy3 and Cy5 are the most broadly employed chromophores for smFRET applications [66].

Taking into consideration that fluorescent chromophores’ photo-physical properties are sensitive to the local environment dynamics [67-69], with internally labelled probes exhibiting a greater resistance to photo-damage and dramatic reduction in signal fluctuations in comparison to externally attached probes, we decided to design DNA hybrids whose cyanine dyes are rigidly incorporated into the sugar-phosphate backbone (Fig. 3.4) [70].

Building upon previous utilized dublex DNA constructs [71], Cy3 and Cy5 chromophores were firmly integrated into the sugar-phosphate backbone via phosphoramidite chemistry [66]. The sequences of internally Cy3/Cy5 labelled HPLC-purified oligonucleotides are shown below from 5’ to 3’.

Cy3: TCG **T** [CY3] AAA TCT AAA GTA ACA TAA GGT AAC ATA ACG TAA GCT CAT TCG CG*A AAA* [CHOL-TEG] (52mer)
Cy5: CGC GAA TGA GCT TAC GTT ATG TTA CCT TAT GTT ACT T**T** [CY5] AGA TTT ACG *AAA AA* [CHOL-TEG] (52mer)

The highlighted sections of the sequences were previously used in FRET measurements by Kapanidis (2016) [71] for both *in vitro* and *in vivo* studies. Research into these two

complementary single-stranded DNA (ssDNA), through the use of the OligoCalc: Oligonucleotide Properties Calculator tool [72], revealed lack of potential hairpin formation (Fig. 3.17), permitting some further intervention, which included slight oligo extension and fluorophore and termini modification accommodating the needs of our model engineering.

Specifically, the bold and underlined T bases denoting modification positions were labelled with Cy3 (as the donor molecule) at the top strand and Cy5 (as the acceptor dye) at the bottom strand. Moreover, 4 unpaired adenine bases (the italic letters) were designed between the cholesterol-TEG moiety and the ssDNA, endowing DNA tethers with rotating motion [73]. Cholesterol's hydrophobic nature allows it to be inserted into the lipid bilayer with the DNA linkers freely diffusing in the aqueous medium. The cholesteryl-TEG moiety, characterized by its hygroscopic quality, was covalently bound to the oligonucleotide, preventing lipid condensation and subsequent alteration of the lipid membrane structure [74]. Figure 3.4 illustrates a schematic of a hybridized complementary DNA pair, and the functionalization details are presented in Figure 3.16.

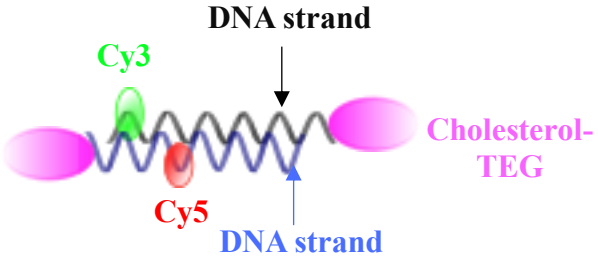

Figure 3.4- Schematic representation of annealed complementary DNA strands featuring internally positioned Cy3 and Cy5 molecules and cholesterol-TEG moieties. *Not to scale.*

5’-**TCG T[CY3] AAA TCT[] AAA GTA ACA TAA GGT AAC ATA ACG TAA GCT CAT TCG CG** *AAAA*- **Chol_TEG**-3’
3’-**Chol-TEG**-*AAAA* **AGCA[] TTT AGA[CY5] TTT CAT TGT ATT CCA TTG TAT TGC ATT CGA GTA AGC GC**-5’

Figure 3.16- DNA functionalization details. *Two sDNA strands were assembled to form hybrid DNA intended to be embedded into droplet and GUV lipid membranes. Each strand carries an internally positioned fluorophore, Cy3 and Cy5, respectively, and each 3’ terminus is functionalized with a cholesterol-TEG linker. The bold letters denote the two complementary overhangs forming the dsDNA construct (48mer), the italic letters, the inactive flexible spacer (4mer) and the magenta ones the Chol-TEG anchor.*

3.3.2 DNA Curvature Calculation

Based on two online analysis tools for DNA curvature calculation [75, 76], the two aforementioned oligonucleotide sequences were characterized by absence of curvature (Fig. 3.17); an important element for excluding the possibility of intra-membrane loop formation.

Potential hairpin formation :

None !

3' Complementarity:
None !

All potential self-annealing sites are marked in red (allowing 1 mis-match):

```
5' TCGTAAATCTAAAGTAACATAAGGTAACATAACGTAAGCTCATTCGCGAAAA                    3'
3'               AAAAGCGCTTACTCGAATGCAATACAATGGAATACAATGAAATCTAAATGCT      5'

5' TCGTAAATCTAAAGTAACATAAGGTAACATAACGTAAGCTCATTCGCGAAAA                    3'
3'                         AAAAGCGCTTACTCGAATGCAATACAATGGAATACAATGAAATCTAAATGCT 5'
```

Potential hairpin formation :

None !

3' Complementarity:
None !

All potential self-annealing sites are marked in red (allowing 1 mis-match):

```
5'                                  CGCGAATGAGCTTACGTTATGTTACCTTATGTTACTTTAGATTTACGAAAAA
3' AAAAAGCATTTAGATTTCATTGTATTCCATTGTATTGCATTCGAGTAAGCGC

5'                        CGCGAATGAGCTTACGTTATGTTACCTTATGTTACTTTAGATTTACGAAAAA
3' AAAAAGCATTTAGATTTCATTGTATTCCATTGTATTGCATTCGAGTAAGCGC

5' CGCGAATGAGCTTACGTTATGTTACCTTATGTTACTTTAGATTTACGAAAAA
3'          AAAAAGCATTTAGATTTCATTGTATTCCATTGTATTGCATTCGAGTAAGCGC

5' CGCGAATGAGCTTACGTTATGTTACCTTATGTTACTTTAGATTTACGAAAAA
3'                                        AAAAAGCATTTAGATTTCATTGTATTCCATTGTATTGCATTCGAGTAAGCGC
```

Figure 3.17- Exclusion of hairpin formation probability, for either of the two complementary DNA strands, based on the Oligonucleotide Properties Calculator.

3.3.3 DNA Hybridization Identification via Förster Resonance Energy Transfer (FRET)

For the creation of the inter-membrane tethering between the two opposed artificial lipid bilayers, DNA annealing is a requisite, a process identified via FRET.

Given that FRET occurrence requires the radial distance between the two fluorophores (donor-acceptor) to be within a 10 nm (100 Å) range, beyond which FRET efficiency becomes negligible [37], our hybridized DNA construct, with an inter-dye spacing of 2.72 nm, is anticipated to yield high FRET efficiency (> E = 0.77).

This energy transfer occurrence manifests itself as a decrease of the donor's fluorescence intensity and shortening of its excited state lifetime, accompanied by an increase in the acceptor's intensity[41, 78].

3.3.3.1 Förster Resonance Energy Transfer (FRET) Evaluation through Bulk Fluorimetry Measurements

DNA bond formation was identified via Förster Resonance Energy Transfer (FRET) which was initially monitored through ensemble fluorometric measurements. Controlled experiments were performed to measure Cy5 and Cy3 emission intensities separately when excited with 635 nm and 532 nm, respectively. As illustrated in Figure 3.18 A and B, samples containing only Cy5 and Cy3 fluorophores each were irradiated with the two aforementioned wavelengths giving off their representative emission spectra. Specifically, excitation of acceptor (Cy5)-only species at 635 nm induced a longer emission wavelength at 667 nm with peak intensity at 300.38 a.u (Fig. 3.18A). On the other hand, donor (Cy3)-only molecule emission spectrum pattern exhibited peak intensity (189.85 a.u) at 563 nm wavelength as presented in Figure 3.18B. The difference in wavelengths between absorption and emission peaks is the result of excitation energy loss due to electron relaxation and intramolecular vibration, known as Stokes shift phenomenon[21].

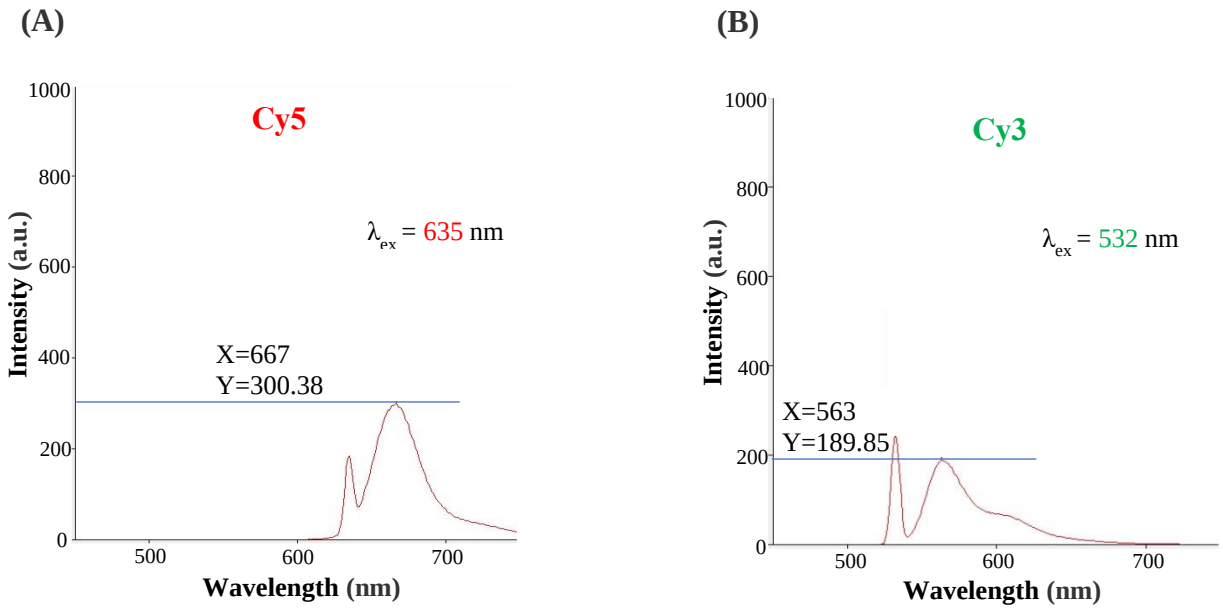

Figure 3.18- Peak wavelengths of emission for Cy5 (A) and Cy3 (B) fluorophores upon illumination with 635 nm and 532 nm laser lines, respectively.

Comparison of acquired emission spectra between Cy3-only species and mixed Cy3-Cy5 dublex DNA linkers of the same concentration (0.5 μM), both excited at 532 nm, revealed a 10.7-fold increase at 662 nm in the mixed sample (Fig. 3.19A, B).

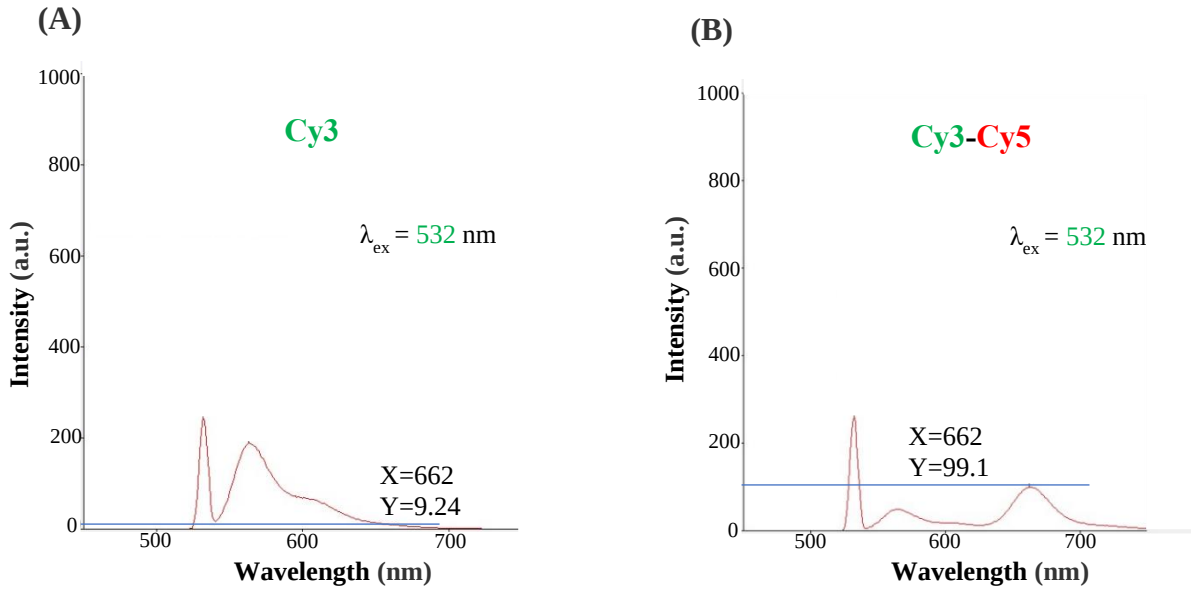

Figure 3.19- Comparison of fluorescence emission spectra between (A) Cy3-only (0.5 μM) and (B) Cy3-Cy5 (0.5 μM) molecules following 532 nm wavelength illumination.

A similar emission pattern was displayed with Cy3-Cy5 assembled constructs subjected to gradual thermal diminution (from 90ºC to 20ºC at a rate of 0.2ºC min^{-1}) in a PCR machine (Eppendorf Mastercycler), (*Appendix,* ***Fig. A1***). Such an appreciable emission intensity difference between Cy3-only dyes and Cy3-Cy5 pairs denotes FRET occurrence between bound DNA overhangs.

3.3.3.2 Förster Resonance Energy Transfer (FRET) Evaluation through Single-molecule Total Internal Reflection Fluorescence Microscopy (smTIRFm)

To confirm DNA hybridization at the single molecule level, single-molecule FRET experiments were conducted on surface-immobilized Cy3 and Cy5 conjugated-DNA on a plasma treated cover-glass. The inter-dye spacing (2.72 nm) in oligonucleotide sequences during DNA annealing was expected to promote energy transfer from donor to acceptor resulting in acceptor fluorophore emission in spite of the donor being initially excited [79]. Therefore, smFRET was used as a tool to assess DNA bond formation required for bridging DIB and GUV bilayers.

TIRF microscopy was employed to image donor (Cy3)-labelled and acceptor (Cy5)-labelled DNA strand fluorescence emission. Localization of single FRET particles was first performed using the acceptor channel, the signal of which was then mapped to the corresponding signal in the donor channel. Only spots displaying a single photobleaching step were selected for FRET analysis. Co-localization between two probes (donor-acceptor) was verified in superimposed donor and acceptor video (**Supplementary Movie S3.1**), where individual spots were observed to shift from acceptor (red) to donor (green) due to acceptor photobleaching and subsequent emergence of donor's fluorescence emission (Fig. 3.20).

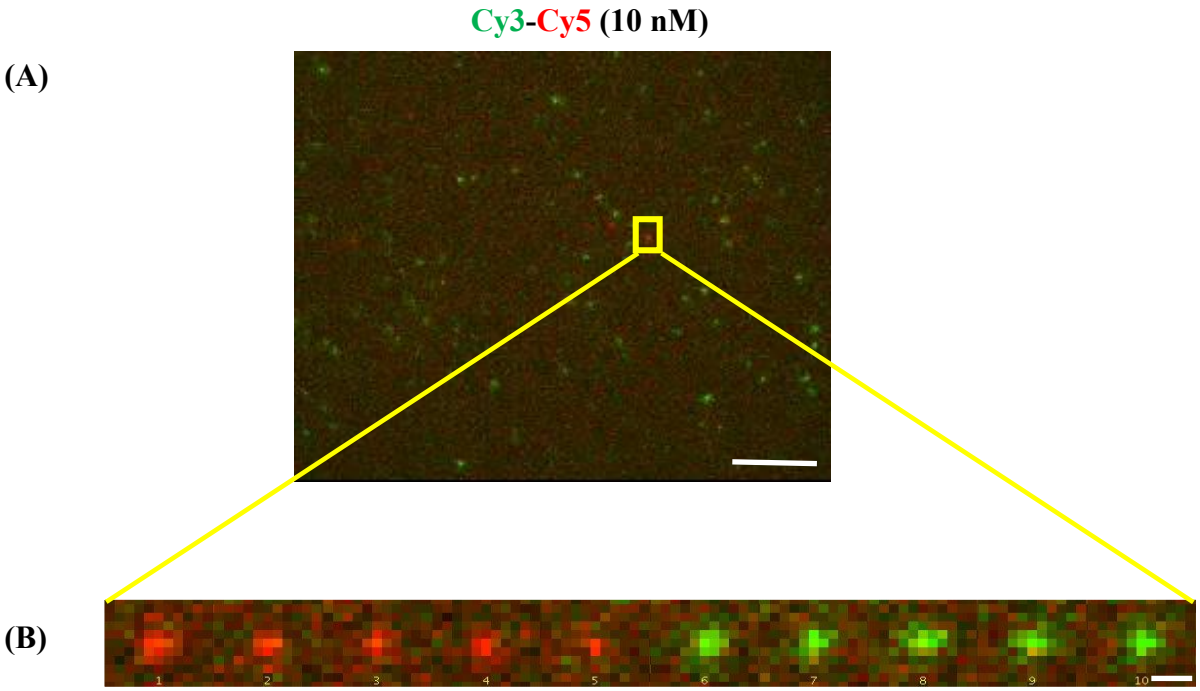

Figure 3.20- (A) Representative field-of-view of superimposed donor and acceptor channels showing immobilized equimolar Cy3 and Cy5 species (10 nM). *Scale bar: 50 μm. (B) Extraction of sequential frames (30 ms per frame) showing partial trajectory of a single FRET pair. A colour switch in the spot from red to green between frames 5 and 6 stems from FRET termination owing to acceptor photobleaching. Scale bar: 1 μm.*

Single FRET molecules were tracked for > 30 s to monitor their FRET signatures under green continuous-wave mode. The obtained long-lasting smFRET time-traces showed a rapid increase in donor intensity following acceptor photobleaching (Fig. 3.21). These anti-correlated donor and acceptor emission signals is a hallmark of single-molecule FRET (Fig. 3.21A, B). Figure 3.21B presents another single-particle FRET pair showing distinct donor and acceptor photobleaching events with a short-lived donor emission intensity ensuing acceptor photobleaching.

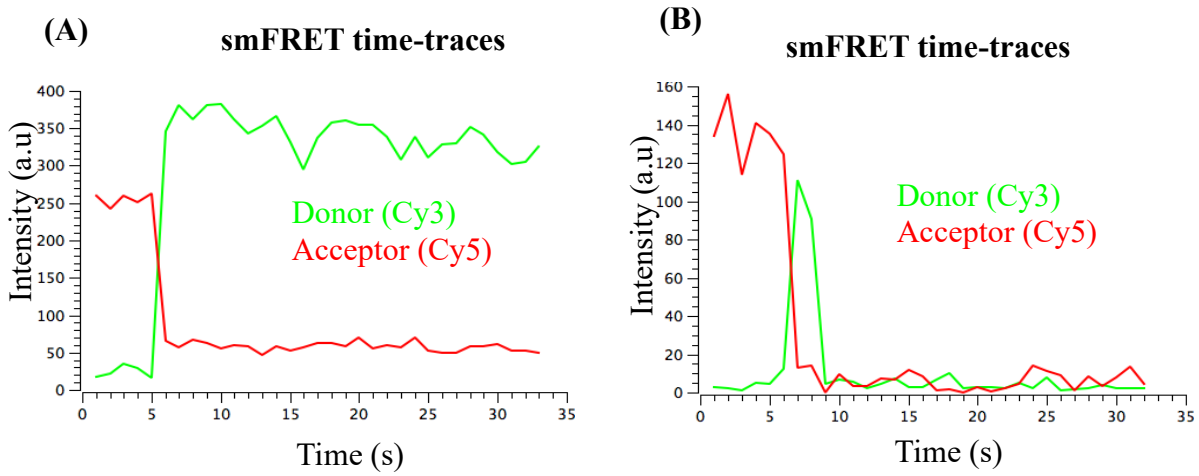

Figure 3.21- Long-lasting observation of smFRET time-traces. *(A) Representative anti-correlated donor and acceptor intensities from a single Cy3-Cy5 FRET coupling. (B) Another single FRET particle pair exhibiting a short donor fluorescence lifespan after FRET cessation.*

FRET efficiency (E) was calculated using both sensitized emission and donor dequenching methods (described in ***3.2 Methods: 3.2.6 FRET Efficiency***). E values were corrected for crosstalk contribution of donor and acceptor fluorophores to the FRET signal.

The obtained crosstalk corrected FRET values from the sensitized emission method were in close agreement with the FRET values calculated using the donor dequenching method. Specifically, in the efficiency histograms for the selected species (N = 104), the fitted Gaussian curve was centred at E = 0.88 ± 0.07 for the sensitized emission approach (Fig. 3.22A) and at E = 0.87 ± 0.08 for the donor dequenching method (Fig. 3.22B).

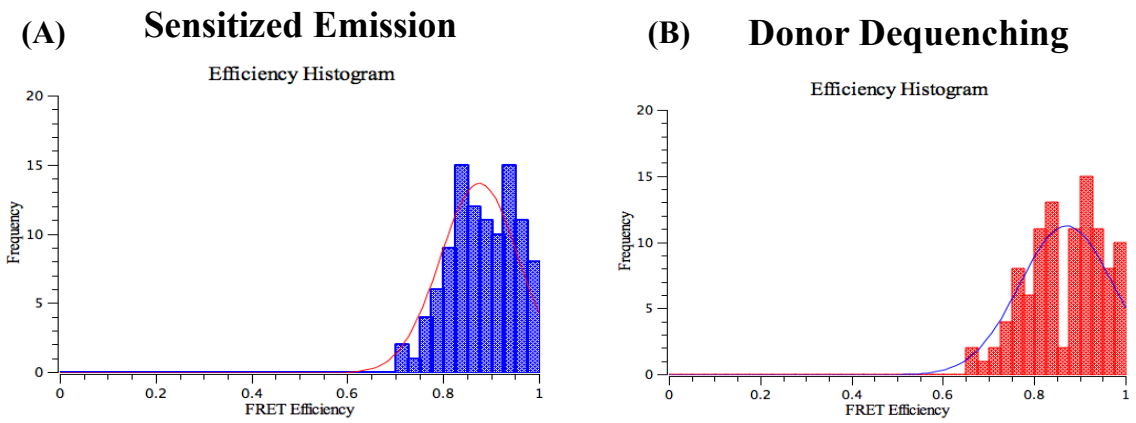

Figure 3.22- FRET efficiency histograms from 104 single FRET pairs. *(A) FRET efficiency distribution acquired with the sensitized emission technique, E = 0.88 ± 0.07, was in accord with (B) the FRET efficiency distribution obtained with the donor dequenching method, E = 0.87 ± 0.08.*

These smFRET measurements indicate that FRET efficiency was quite high leading to the assumption that DNA annealing efficiency was quite low, (approximately 25%), following estimation conducted on surface-immobilized single-molecules.

3.4 Discussion

In this chapter, we resumed our membrane model synthesis, DIB-anchored GUV via annealed DNA complements (Fig. 3.13), by custom-designing internally dye-conjugated complementary single DNA strands. Their integration into the DIB-GUV system requires traits of (a) self-insertion into the two adjoining artificial lipid membranes and (b) hybridization, enabling trans-synaptic adhesions between the two adjoining membranes.

To ensure their embedment in lipid membranes, both DNA hybrids were conjugated to a hydrophobic chol-TEG linker at each 3' terminus (Fig. 3.4, 3.15).

To monitor their annealing efficiency, each complement of the DNA pair was internally labelled with Cy3 and Cy5 fluorophores, respectively, the inter-dye spacing of which was set at 2.72 nm in their annealed configuration (Fig. 3.4, 3.15), permitting DNA coupling identification through single molecule Förster Resonant Energy Transfer (smFRET) measurements.

The possibility of DNA linkers to form intra-membrane loops has been minimized as the designed oligonucleotide sequences did not display any bending upon DNA curvature analysis (Fig. 3.16)[75,76].

High FRET efficiency was calculated using the sensitized emission and donor dequenching strategies, yielding $E = 0.88 \pm 0.07$ (Fig. 3.22A) and $E = 0.87 \pm 0.08$ (Fig. 3.22B) respectively, and thus, revealing successful DNA coupling, even in the absence of controlled temperature diminution (such as in a thermocycler). Nonetheless, the contribution of this high FRET efficiency observations corresponded to approximately ~25% DNA annealing efficiency following estimation conducted on surface-immobilized single-molecules.

In the current work, single molecule DNA hybridization between the two engineered

oligonucleotide complements was assessed on a hydrophilized coverslip under immobilization conditions by TIRF microscopy. Of comparable importance is to monitor DNA coupling efficiency in the dynamic environment of the DIB compartment and GUV surface, which impose DNA linker mobility rearrangements, after ensuring oligonucleotide sequence integration into the droplet and vesicle membranes, respectively. These issues are addressed in ***Chapter 4***, where synthesis of the double membrane model, utilizing the tailored-made complementary sDNA overhangs, is detailed.

3.5 References

1. Gregersen, S. *Fluorescent Peptide-Stabilized Silver-Nanoclusters: A Solid-Phase Approach for High-Throughput Ligand Discovery*, in *Department of Chemistry*. 2014, University of Copenhagen.
2. Bird, A. *Fluorescence Resonance Energy Transfer (FRET) Systems for Biomedical Sensor Applications*, in *School of Physical Sciences*. 2010, Dublin City University.
3. Siraj, N., El-Zahab, B., Hamdan, S., Karam, T.E., Haber, L.H., Li, M., Fakayode, S.O., Das, S., Valle, B., Strongin, R.M., Patonay, G., Sintim, H.O., Baker, G.A., Powe, A., Lowry, M., Karolin, J.O., Geddes, C.D., and Warner, I.M. *Fluorescence, Phosphorescence, and Chemiluminescence. Analytical chemistry*, 2016. **88**(1): p. 170–202.
4. Bu, S.D., Han, J.K., Hyeon, J.Y., and Kim, G.G. *Characteristics of and Control over Resonance in the Electromotive Force of Electromagnetic Induction. Journal of Electromagnetic Analysis and Applications*, 2013. **5**(8): p. 584-608.
5. Iqbal, A. *Towards Understanding the Photochemistry of Tyrosine*, in *Department of Chemistry*. 2010, University of Warwick.
6. Passon, O., and Grebe-Ellis, J. *Planck's radiation law, the light quantum, and the prehistory of indistinguishability in the teaching of quantum mechanics. European Journal of Physics,* 2017. **38**(3): p. 035404.
7. Hendrickson, L., Furbank, R.T. and Chow, W.S. *A Simple Alternative Approach to Assessing the Fate of Absorbed Light Energy Using Chlorophyll Fluorescence. Photosynthesis Research*, 2004. **82**: p. 73–81
8. Sponer, H. *Intra- and Intermolecular Radiationless Quantum Transitions in Complex Molecules. Radiation Research Supplement*, 1959. **1**: p. 558–576.
9. Sednev, M. *Fluorescent Dyes with Large Stokes Shifts of 80−200 nm for Optical Microscopy and Nanoscopy*, in *Department of Chemistry*. 2015, Georg-August University School of Science (GAUSS).

10. Lennard-Jones, J.E., and Strachan, C. *Interaction of Atoms and Molecules with Solid Surfaces. I. The Activation of Adsorbed Atoms to Higher Vibrational States. Proceedings of the Royal Society of London. Series A, Mathematical and Physical Sciences*, 1935. **150**(870): p. 442–455.
11. Müller, N., and Schäfer, S. Of electrons and photons., *Nat. Phys.*, 2023.
12. Lichtman, J.W., and Conchello, J.A. *Fluorescence Microscopy. Nature methods*, 2005. **2**(12): p. 910–919.
13. Bloino, J., Baiardi, A. and Biczysko, M. *Aiming at an accurate prediction of vibrational and electronic spectra for medium-to-large molecules: An overview. Quantum Chemistry*, 2016. **116**(21): p. 1543-1574.
14. Toceland, C.P. *Fluorescent labeling and modification of proteins. Journal of Chemical Biology*, 2013. **6**(3): p. 85–95.
15. *Fluorescence Excitation and Emission Fundamentals*. DOI: https://www.chem.uci.edu/~dmitryf/manuals/Fundamentals/Fluorescence Excitation and Emission Fundamentals.pdf.
16. Kennard, E.H. *On the interaction of radiation with matter and on fluorescent exciting power. Physical review*, 1926. **28**: p. 673-683.
17. Stepanov, B.I. *A universal relation between the absorption and luminescence spectra of complex molecules.* Lenin Byelorussian State University, 1956: p. 81-83.
18. Meyer, T.J.J. *Photon Transport in Fluorescent Solar Collectors*, in *School of Engineering Sciences*, 2009, University O Southampton.
19. Ramanujam, N. *Fluorescence spectroscopy of neoplastic and non-neoplastic tissues. Neoplasia (New York, N.Y.)*, 2000. **2**((1-2)): p. 89–117.
20. Usai, C., and Diaspro, A. *Fluorescence: General Aspects. Encyclopedia of Biophysics*, ed. G.C.K.e. Roberts. 2013, Berlin, Heidelberg: Springer.
21. Zhao, H. *Synthetic membranes in microfluidic interfaces.* 2017.
22. Salas Redondo C., Kleine, P., Roszeitis K., et al. *Interplay of Fluorescence and Phosphorescence in Organic Biluminescent Emitters. The Journal of Physical chemistry. C Nanomaterials and Interfaces.*, 2017. **121**(27): p. 14946-14953.

23. Rabinowitch, E., and Govindjee, D. *Light absorption and fate of excitation energy: Franck-Condon Principle*. 1969.
24. Atkins, P., and de Paula, J. *Atkin's Physical Chemistry 8th Edition*. 2006: W.H. Freeman And Company.
25. Piatkevich, K., Malashkevich, V., Morozova, K., et al. *Extended Stokes Shift in Fluorescent Proteins: Chromophore–Protein Interactions in a Near-Infrared TagRFP675 Variant. Sci Rep.,* 2003. **3**(1847).
26. Stokes, G.G. *On the Change of Refrangibility of Light. Abstracts of the Papers Communicated to the Royal Society of London*, 1850. **6**(195–200).
27. Sekar, R.B., and Periasamy, A. *Fluorescence resonance energy transfer (FRET) microscopy imaging of live cell protein localizations. The Journal of cell biology*, 2003. **160**(5): p. 629–633.
28. Tsien, R.Y., Bacskai, B.J., and Adams, S.R. *FRET for studying intracellular signalling. Trends in Cell Biology*, 1993. **3**(7): p. 242-245.
29. Cardullo, R.A. *Theoretical principles and practical considerations for fluorescence resonance energy transfer microscopy. Methods in cell biology*, 2013. **114**: p. 441–456.
30. Salatan, F. *Single-molecule FRET Analysis of the Dynamics of AMPA Receptor*. 2010, Rice University.
31. Gordon, G.W., Berry, G., Liang, X.H., Levine, B., and Herman, B. *Quantitative fluorescence resonance energy transfer measurements using fluorescence microscopy. Biophysical journal*, 1998. **74**(5): p. 2702–2713.
32. Berney, C., and Danuser, G. *FRET or no FRET: a quantitative comparison. Biophysical journal*, 2003. **84**(6): p. 3992–4010.
33. Clapp, A.R., Medintz, I.L., Uyeda, H.T., Fisher, B.R., Goldman, E.R., Bawendi, M.G., and Mattoussi, H. *Quantum dot-based multiplexed fluorescence resonance energy transfer. Journal of the American Chemical Society*, 2005. **127**(51): p. 18212–18221.
34. McCann, J.J., Choi, U.B., Zheng, L., Weninger, K., and Bowen M.E. *Optimizing methods to recover absolute FRET efficiency from immobilized single molecules. Biophysical Journal*, 2010. **99**(3): p. 961-970.

35. Bajar, B.T., Wang, E.S., Zhang, S., Lin, M.Z., and Chu, J. *A Guide to Fluorescent Protein FRET Pairs. Sensors (Basel, Switzerland)*, 2016. **16**(9): p. 1488.
36. Rogach, A.L., Klar, T.A., Lupton, J.M*.,* Meijerink*,* A*.,* and Feldmann*,* J*. Energy transfer with semiconductor nanocrystals. J. Mater. Chem.*, 2009. **19**: p. 1208-1221.
37. Chen, H., Puhl, H.L., Koushik, S.V., Vogel, S.S., and Ikeda, S.R. *Measurement of FRET Efficiency and Ratio of Donor to Acceptor Concentration in Living Cells. Biophysical Journal*, 2006. **91**(5): p. L39-L41.
38. Xu, F., Wei, L., Chen, Z., and Min, W. *Frustrated FRET for high-contrast high-resolution two-photon imaging. Optics express*, 2013. **21**(12): p. 14097–14108.
39. Broussard, J.A., Rappas B., Webb, D.J., and Brown, C.M. *Fluorescence resonance energy transfer microscopy as demonstrated by measuring the activation of the serine/threonine kinase Akt. Nat Protoc.*, 2013. **8**(2): p. 265-81.
40. *Method of the Year 2008. Nat Methods,* 2009. **6**(1).
41. Roy, R., Hohng, S., and Ha, T. *A practical guide to single-molecule FRET. Nature methods*, 2008. **5**(6): p. 507–516.
42. Snapp, E.L., Hedge, R.S. *Rational design and evaluation of FRET experiments to measure protein proximities in cells. Curr Protoc Cell Biol*., 2006. *Chapter 17:Unit 17.9.*
43. Woehler, A.T. *Quantitative analysis of Förster resonance energy transfer from spectrally resolved fluorescence measurements*, in *Faculty of Biology*. 2010, Georg August University Göttingen.
44. McCann, J.J., Choi, U.B., Zheng, L., Weninger, K., Bowen, M.E. *Optimizing Methods to Recover Absolute FRET Efficiency from Immobilized Single Molecules. Biophysical Journal*, 2010. **99**(3): p. 961-970.
45. Elder, A.D., Domin, A., Kaminski Schierle, G.S., Lindon, C., Pines, J., Esposito, A., and Kaminski, C.F. *A quantitative protocol for dynamic measurements of protein interactions by Förster resonance energy transfer-sensitized fluorescence emission. Journal of the Royal Society Interface*, 2009. **6**: p. S59–S81.
46. Selvin, P. *The renaissance of fluorescence resonance energy transfer. Nat Struct Mol Biol.,* 2000. **7**: p. 730–734.

47. Wouters, F.S., Verveer, P.J., and Bastiaens, P.I. *Imaging biochemistry inside cells. Trends in Cell Biology*, 2001. **11**(5): p. 203-211.
48. Zal, T., and Gascoigne, N.R.G. *Photobleaching-Corrected FRET Efficiency Imaging of Live Cells. Biophysical Journal*, 2004. **66**(6): p.3923-3939.
49. Brunstein, M., Teremetz, M., Hérault, K., Tourain, C., and Oheim, M. *Eliminating Unwanted Far-Field Excitation in Objective-Type TIRF. Part I. Identifying Sources of Nonevanescent Excitation Light. Biophysical Journal*, 2014. **106**(5): p.1020-1032.
50. Martin-Fernandez, M.L., Tynan, C.J., and Webb, S.E. *A 'pocket guide' to total internal reflection fluorescence. Journal of microscopy*, 2013. **252**(1): p.16–22.
51. *What is TIRF microscopy?* Teledyne Photometrics. DOI: https://www.photometrics.com/learn/single-molecule-microscopy/what-is-tirf-microscopy.
52. Blandin, P., Lévêque-Fort, S., Lécart, S., Zeller, P., Lenkei, Z., Druon, F. and Georges, P. *Development of a TIRF-FLIM microscope for biomedical applications. Confocal, Multiphoton, and Nonlinear Microscopic Imaging III*, 2007. p.6630.
53. Byrne, G. *Total internal reflection microscopy studies on colloidalparticle endocytosis by living cells*, in *Institute of Biophysics, Imaging and Optical Science (iBIOS)*. 2009, The University of Nottingham.
54. Liu, Y.Q., Sun, J., Che, Y., Qi, K., Li, L., and Yin, H. *High numerical aperture microwave metalens. Optics letters*, 2020. **45**(22): p. 6262–6265.
55. Tung, C.K., Sun, Y., Lo, W., Lin, S.J., Jee, S.H., and Dong, C.Y. *Effects of objective numerical apertures on achievable imaging depths in multiphoton microscopy. Microscopy research and technique*, 2004. **65**(6): p. 308–314.
56. Davidson, M.W. *Total Internal Reflection Fluorescence Microscopy Olympus Application Note*. Molecular Expressions, 1998-2022 DOI: https://www.photometrics.com/learn/single-molecule-microscopy/what-is-tirf-microscopy.
57. Royer, C.A. *Fluorescence spectroscopy. Methods in molecular biology (Clifton, N.J.)*, 1995. **40**: p. 65–89.

58. Lee, L.Y. *Study of the photodegradation and photostability of anti-cancer drugs in different media towards the development of both new actinometers and liquid formulations*, in *Leicester School of Pharmacy*. 2016, De Montfort University, Leicester.
59. Cooper, G.M. *The Cell: A Molecular Approach. 2nd edition*. 2000: Sinauer Associates.
60. Watson, H. *Biological membranes, Essays in Biochemistry*, 2015. **59**: p. 43–69.
61. Eeman, M. and Deleu, M. *From biological membranes to biomimetic model membranes (PDF Download Available). Biotechnol. Agron. Soc. Environ.*, 2010. **14**(4): p. 719-736.
62. Axelrod, D. *Total internal-reflection fluorescence microscopy. Methods Cell Biol.*, 1989. **30**: p. 245-270.
63. *Total Internal Reflectance Fluorescence (TIRF) Microscopy - Introduction and Product Solutions for TIRF Microscopy by Andor Technology.* [cited 2019 October 26].
64. Ambrose, W., Goodwin, P., and Nolan, J. *Single-molecule detection with TIRF: comparing signal-to background in different geometries. Cytometry*, 1999. **36**(3).
65. Schindelin, J., Arganda-Carreras, I. and Frise, E., et al. *Fiji: an open-source platform for biological-image analysis. Nature methods*, 2012. **9**(7): p. 676-682.
66. Lee, W., von Hippel, P.H. and Marcus, A.H. *Internally labeled Cy3/Cy5 DNA constructs show greatly enhanced photo-stability in single-molecule FRET experiments. Nucleic Acids Research*, 2014. **42**(9): p. 5967–5977
67. Luo, G., et al. *Single-molecule and ensemble fluorescence assays for a functionally important conformational change in T7 DNA polymerase. Proc. Natl. Acad. Sci. USA*, 2007. **104**(31): p. 12610-5.
68. Mujumdar, R.B., et al. *Cyanine dye labeling reagents: sulfoindocyanine succinimidyl esters. Bioconjug Chem.*, 1993. **4**(2): p. 105-11.
69. Gruber, H.J., et al. *Anomalous fluorescence enhancement of Cy3 and cy3.5 versus anomalous fluorescence loss of Cy5 and Cy7 upon covalent linking to IgG and noncovalent binding to avidin. Bioconjug Chem.*, 2000 **11**(5): p. 696-704.

70. Ranjit, S., Gurunathan, K., and Levitus, M. *Photophysics of backbone fluorescent DNA modifications: reducing uncertainties in FRET. J Phys Chem B*., 2009. **113**(22): p. 7861-6.
71. Plochowietz, A., et al. *Stable end-sealed DNA as robust nano-rulers for in vivo single-molecule fluorescence. Chem Sci.*, 2016. **7**(7): p. 4418–4422.
72. Kibbe, W.A. *Oligo Calc: Oligonucleotide Properties Calculator*, in *Nucleic Acids Res.* 2007.
73. Shimobayashi, S.F., et al. *Direct measurement of DNA-mediated adhesion between lipid bilayers. Physical Chemistry Chemical Physics*, 2015. **17**(24).
74. Bunge, A., et al. *Lipid Membranes Carrying Lipophilic Cholesterol-Based Oligonucleotides—Characterization and Application on Layer-by-Layer Coated Particles. J. Phys. Chem. B*, 2009. **113**(51): p. 16425-16434.
75. *Gohlke, C.*, *DNA curvature analysis*, in *Microbiology*. 2009, https://www.lfd.uci.edu/~gohlke/dnacurve/. p. 2127-2136.
76. *DNA curvature analysis*, in *Microbiology*. 2009, http://132.248.32.45/cgi-bin/mutacurv.cgi. p. 2127-2136.
77. Stryer, L. and Haugland, R.P. *Energy transfer: a spectroscopic ruler. PNAS*, 1967. **58**(2): p. 719-726.
78. Kremers G, Piston, D.W. and Davidson, M.W. *Basics of FRET Microscopy: Fundamental Principles of Förster Resonance Energy Transfer (FRET) Microscopy with Fluorescent Proteins.*
79. Bird, A. *Fluorescence Resonance Energy Transfer (FRET) Systems for Biomedical Sensor Applications*, in *School of Physical Sciences*. 2010, Dublin City University.

Chapter 4: GUV Anchorage to DIB Inner Leaflet via Membrane Integrated Labelled DNA Hybrids

4.1 Introduction

Intimate interaction between two opposing lipid bilayer membranes via “ligand-receptor” coupling is a state of vital importance for many biological processes [1]. Such direct interactions either between cells or between cells and the extracellular matrix are critical to cell function, maintenance and organization. Typical examples of such formations are the immune synapse, with a gap of 15 nm [2] and the neurosynaptic junction, with an intermembrane distance of 20-40 nm [3] that mediate cell–cell signalling.

Aspiring to recapitulate intermembrane interaction in the context of a synapse-like architecture that offers a dynamical, yet controlled microenvironment [4], we employ the engineered DNA linkers developed in ***Chapter 3*** to tether the GUV to the DIB bilayer.

Such a model development, where intermembrane contact can be mediated via trans-synaptic annealed DNA complements, serving as “ligand-receptor” pairs [5], within a

synapse-like framework will demonstrate a refined strategy able to overcome shortcomings already encountered in existing model systems, spanning short-term stability[6], spatial mobility restrictions[4], absence of dynamic molecule rearrangement[7] and incompatibility to be probed with current tools.

This model fabrication will enable integration of the spatiotemporal dynamic membrane rearrangements underpinning direct intercellular communication and hence, better mimic the natural world.

4.1.1 Chapter's Aims

The concept of adhesion-mediated synapse stabilization has been bolstered by expressions of synaptically localized and organized cell adhesion molecules (CAMs) bridging the synaptic cleft[8].

These synaptic cell adhesion molecules apart from connecting pre- and postsynaptic compartments, they also regulate signalling processes via trans-synaptic recognition (e.g., neurexins and neuroligins), needed for synaptic establishment and plasticity[9].

Our intention is to create a biologically inspired membrane model, a synapse analogue, amenable to single-molecule imaging methods, which will enable intermembrane interaction studies such as self-organization of mobile, paired intermembrane cleft components, and trans-synaptic adhesion dynamics (Fig. 4.1).

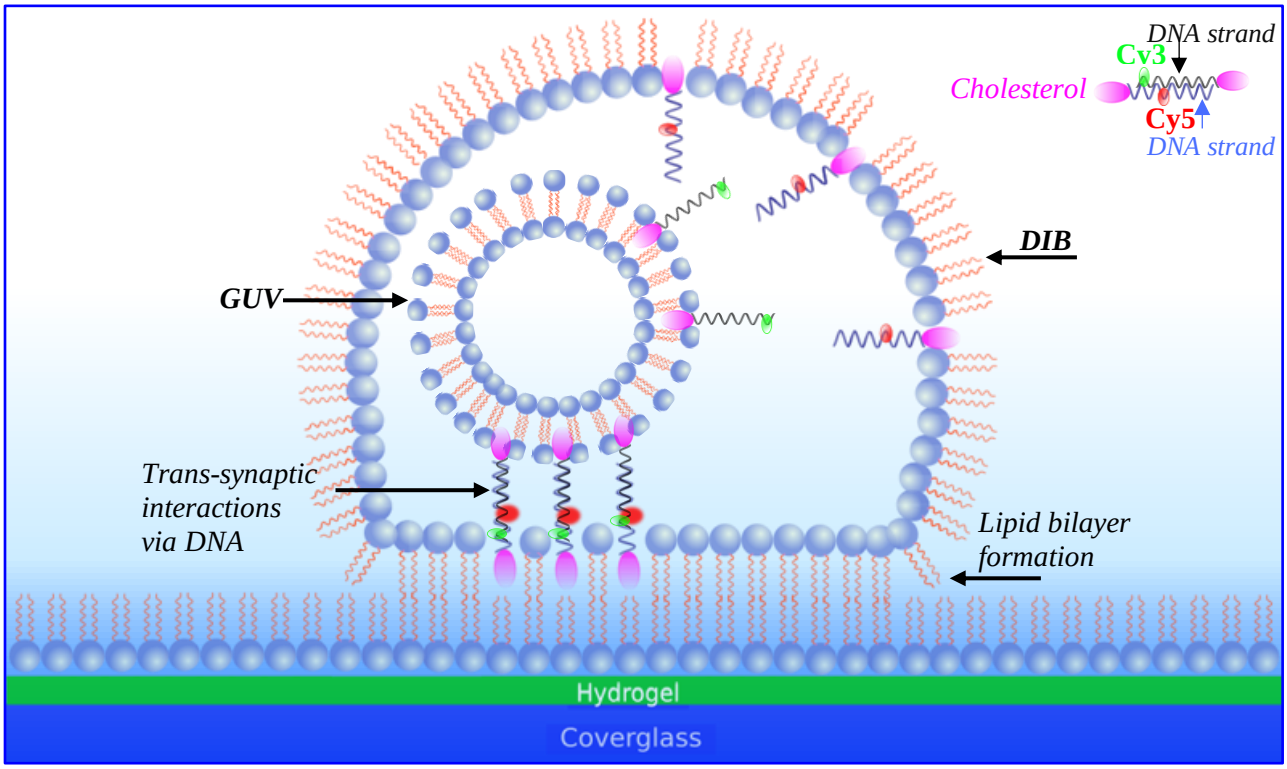

Figure 4.1- Schematics of GUV anchorage to a DIB via DNA-mediated trans-synaptic adhesions. *Not to scale.*

For the fabrication of this interlinked double membrane system, two very well characterized minimal membrane developments are utilized: (a) giant unilamellar vesicle (GUV) and (b) droplet interface bilayer (DIB). Due to size similarity with mammalian cells[10-14], GUVs, (with diameter between 1 μm and approximately 100 μm), are deemed the gold standard of cellular mimics[10]. DIB, on the other hand, constitutes a novel robust platform with a horizontal orientation allowing for visualization through total internal reflection fluorescence (TIRF)[15].

Formation of the synapse-like configuration entails DIB-GUV coupling through the custom-designed artificial trans-synaptic DNA linkers, (whose synthesis is described in ***Chapter 3***) (Fig**.** 4.1). DIB is formed by contacting a lipid monolayer-coated aqueous droplet with a lipid-monolayer coated hydrogel support submerged in an oil-lipid solution[16], and GUV, (a cell-sized aqueous containing single-bilayered liposome),

is generated via electroformation[17]. DNA-mediated intermembrane bridging is identified through single molecule Förster Resonant Energy Transfer (smFRET) measurements and diffusion coefficient (D) estimation.

4.2 Materials and Methods

4.2.1 DIB Device Assembly

A DIB poly(methyl methacrylate) (PMMA) reusable micro-device, comprised of 16 wells of 1-mm-diameter each with a microfluidic channel underneath framing each well, was employed (Fig. 4.2). This allows sealing of the device after liquified agarose addition to prevent lipid and oil outflow.

A glass coverslip was rendered hydrophilic by oxygen plasma treatment in the plasmochemical reactor (Femto, Diener electronic, Germany) for 3.5 minutes. Once the hydrophilic substrate was formed, 120 µl of 0.75% agarose (Fluka Analytical), prepared in distilled water (dH_2O) and warmed at 85^oC, was deposited on the hydrophilized coverslip, which underwent coating after spinning process (3000 rpm, 30 s), producing a thin agarose layer (< 100 nm). Subsequently, the agarose-facing side of the coverslip was positioned on top of the (PMMA) micro-device and sealed by addition of 170 µl of 3.5% liquified hydrating agarose (10 mM Tris-HCl, 1 mM EDTA, 50 mM NaCl, pH 7.83) through the microfluidic channel. The hydrating agarose surrounds each well affording hydration to the thin agarose layer suitable for evanescent field penetration in TIRF imaging. Inspection of proper well formation was made under a stereo microscope (Nikon SMZ 745T).

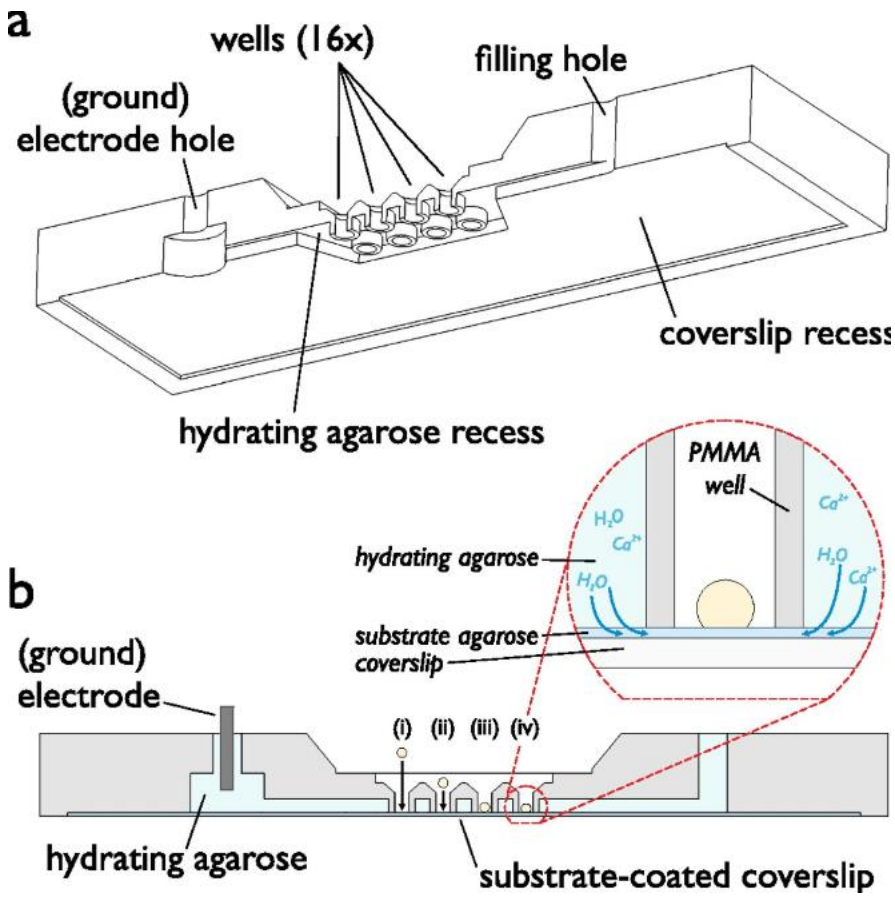

Figure 4.2- Schematic drawings of a 16 1-mm-diameter-well PMMA reusable device where droplet interface bilayers are formed. *(a) Cut-through view of the device. (b) Side view of (a). After agarose (dark blue in (b) inset) has been spun onto a coverslip, it is affixed onto the PMMA device. The hydrating agarose (light blue in (b) inset) is then flown through the device, which surrounds the wells. For electrophysiology experiments (presented in* ***Chapter 5****), an Ag/AgCl electrode is plugged into the hydrating agarose via one of the filling holes. Droplet deposition within a well is represented by Roman numerals, where (i) shows droplet placement in the well, (ii and iii) show droplet sinking toward the substrate due to gravity, and (iv) illustrates bilayer formation. (Inset) DIB in a well. The dotted arrows indicate water and electrolyte movement from the hydrating agarose into the substrate. Image taken from: [18].*

4.2.2 Droplet Preparation and DIB Formation

The lipid components, 1,2-diphytanoyl-sn-glycero-3-phosphocholine (DPhPC) (Avanti Polar Lipids) (Fig. 4.3A), 1,2-dipalmitoyl-sn-glycero-3-phosphoethanolamine-N-

[methoxy(polyethylene glycol)-2000] (ammonium salt) (16:0 PEG2000 PE) (Avanti Polar Lipids) (Fig. 4.3B) and 1,2-Dioleoyl-sn-glycero-3-phospho-rac-(1-glycerol) (DOPG) (Avanti Polar Lipids) (Fig. 4.3C) were dissolved in 200 µl chloroform in desired concentrations: (PEGylated lipid 10% w/w DPhPC), (DOPG 1% w/w DPhPC). The solvent was initially removed by applying a steady stream of nitrogen to form a dry lipid film on the walls of a vial. Subsequently, it was incubated in the plasmochemical reactor (Femto, Diener electronic, Germany) for 30 minutes to drain off the residual chloroform.

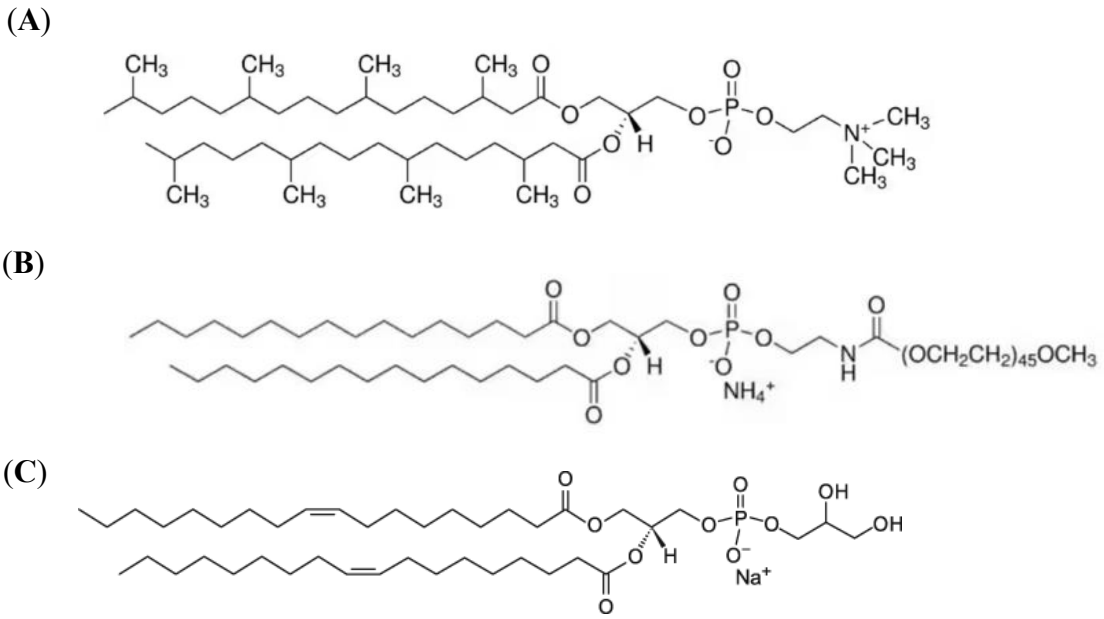

Figure 4.3- Lipid chemical structures*. (A) 1,2-diphytanoyl-sn-glycero-3-phosphocholine (DPhPC) chemical structure. Source:[19]. (B)1,2-dipalmitoyl-sn-glycero-3-phosphoethanolamine-N-[methoxy(polyethylene glycol)-2000] (16:0 PEG2000 PE) chemical structure. Source:[20]. (C) 1,2-Dioleoyl-sn-glycero-3-phospho-rac-(1-glycerol) (18:1 DOPG) chemical structure. Source:[21].*

The lipid film containing only DPhPC or DPhPC with (1% w/w) DOPG was then resolubilized in 9:1 (v/v) mixture of hexadecane (Sigma-Aldrich, H6703) and silicone oil (AR 20, Sigma-Aldrich, 10836) with a final lipid concentration of 3 mg/ml. For the DPhPC and (10% w/w) 16:0 PEG2000 PE composition, 6:4 (v/v) mixture of hexadecane and silicone was used, with a final lipid concentration of 3 mg/ml as well. Aqueous volumes of 20 nl composed of TE (10 mM Tris-HCl, 1 mM EDTA) and 50 mM NaCl (pH 7.83) were immersed in these lipid-oil solutions contained in a droplet incubation chamber

and spontaneous lipid self-assembly occurred on the aqueous surface. For GUV incorporation within the droplet, 20 nl of aqueous GUV suspension was submerged in the lipid-oil solution.

The assembled DIB device was subsequently filled with the lipid-oil solution (e.g. 3 mg/ml DPhPC in 90% hexadecane and 10% silicone oil) promoting lipid monolayer self-assembly on the hydrophilic agarose-coated substrate. A minimum stabilization period of 15 min was required before lipid monolayer-coated aqueous droplets were transferred by pipetting to each of the 16 wells of the DIB device, where spontaneous bilayer formation was observed upon contact with the hydrated support.

4.2.3 Vesicle Preparation

GUVs were prepared by the electroformation method. The experimental set up was adapted from[22]. Briefly, 15 µl of the DPhPC/chloroform or DPhPC and (1% w/w) DOPG/chloroform at a concentration of 2 mg/ml was spread evenly over the conductive side of an indium-tin oxide (ITO)-coated glass slide, which was subsequently submitted to a steady stream of nitrogen for 2 minutes to remove chloroform. A 2 mm thick rubber gasket was used to separate the conductive sides of 2 slides facing each other, assembled to form the growth chamber, and filled with 200 µl of 50 mM NaCl, TE, pH 7.83. An alternating electric field of 500 Hz and a sequence of rising electric sequence, (260 Vm^{-1} for 5 min, 670 Vm^{-1} for 5 min, 1000 Vm^{-1} for 15 min, 1330 Vm^{-1} for 30 min and 1670 Vm^{-1} overnight) [106] was applied across the ITO slides via a function generator (hewlett packard 33120A 15 MHz/arbitrary waveform generator). Following completion of the electroformation procedure, the resulting GUVs were harvested.

4.2.4 DNA Preparation and Membrane Functionalization/Staining

Functionalization of the DIB inner surface was carried out by submerging 20 nl buffer solution (TE and 50 mM NaCl, pH 7.83), consisting of 10 nM or 5 nM Cy5-DNA conjugated species, in the lipid-in-oil solution resulting in the self-assembly of lipid monolayer at water–oil interface. DIB was formed by contacting the 20 nanoliter lipid-covered aqueous droplet with a hydrogel support immersed in an oil solution in the presence of phospholipids (DPhPC)[16, 23].

GUV's outer membrane leaflet was decorated by mixing 20 μl of vesicle suspension with Cy3 cholesterol-tagged oligonucleotides (overnight incubation), diluted in TE and 50 mM NaCl (pH 7.83), attaining a 10 nM or 5 nM final concentration.

For a more detailed characterization of the GUV structure, the labelled membrane probe, CellMask™ Orange (C10045) (by life technologies), was diluted in the aqueous GUV suspension. Vesicles were incubated with CellMask Orange for 2 hours and the working solution for the stain's attachment to the GUV phospholipid membranes was determined at 1:10.000. Dye stock was prepared in DMSO at 1 mg/ml and stored in a plastic tube at -20^{o}C.

A mixture of equimolar Cy3 and Cy5 species in the saline buffer (TE and 50 mM NaCl, pH 7.83) with a final concentration of 5 nM was bathed in oil-lipid solution for FRET visualization in the inner bilayer surface of the DIB.

For droplet encapsulated GUVs, equal volumes of (2.5 nM) Cy3 functionalized vesicles and (5 nM) Cy5 containing solution (TE and 50 mM NaCl, pH 7.83) were mixed because the concentration ratio of 1:2 Cy3:Cy5 species ensures greater FRET incidence than equimolar labelling conditions.

4.2.5 Microscopy

Imaging and fluorescence microscopy was the same utilized in ***Chapter 3*** (in ***3.2 Methods, 3.2.1 Microscopy).***

4.2.6 smFRET Image Analysis on Mobile Fluorophores

For mobile fluorophores anchored to DIB and vesicle inner and outer lipid sheets respectively, spot detection and particle tracking was performed on each image stack of separate donor and acceptor channel images (512 × 256 pixels) using the ImageJ plugin trackmate[24], a distribution of the open source software ImageJ[25].

For spot detection, an estimated diameter of 3 pixels was employed with the detection algorithm being DoG (difference of Gaussians), which acts as a band-pass filter discarding high spatial frequency noise while retaining spatial information comparable to the gauged diffraction-limited spot of a single fluorophore[26].

The maximal linking distance for trajectory linking and the maximal distance for gap-closing was set at 5 pixels. The maximal frame interval between two spots to be bridged was adjusted at a 2-frame duration[27].

smFRET efficiency (E) was determined on separate donor and acceptor video pairs via frame-by-frame donor-acceptor intensity extraction. The excised two-colour single-spot trajectories (Fig. 4.24Bii, Fig.4.33Bii) were obtained from combined green-red channels selecting the region of interest with the aid of x/y/t spot trajectory data from the respective donor and acceptor stacks considering pixel offset.

Trajectory analysis, mean square displacement (MSD) and diffusion coefficient (D) calculation of Cy3 and Cy5 tracks were performed in Matlab (R2020a) (MathWorks) following preceding reported literature[28-32].

4.2.6.1 smFRET Calibration: Baseline Subtraction, Spectral Corrections

True FRET efficiency estimation requires background subtraction and crosstalk (including bleed-through and cross-excitation) correction between the detection channels. This analysis procedure is detailed in ***Chapter 3,*** (***3.2 Methods*** in ***3.2.5.1***) and was applied on ***smFRET Image Analysis on Mobile Fluorophores*** *in* ***Chapter 4*** as well.

.

4.2.7 FRET Efficiency

Sensitized emission and donor dequenching methods employed for FRET efficiency assessment are explicitly presented in ***Chapter 3,*** (***3.2 Methods*** in ***3.2.6 FRET Efficiency***).

4.2.8 Lateral Diffusion Coefficient Calculation

Mean squared displacement (MSD) is a measure of the deviation of a particle's position as regards a reference location over a given time series[28, 29] and it is calculated by the following equation (1):

$$msd(t) = \langle \Delta r_i(t)^2 \rangle = \langle (r_i(t) - r_i(0))^2 \rangle \qquad (1)$$

where $r_i(t)$-$r_i(0)$ is the distance (vector) a molecule, *i, t*ravels over some time interval, *t,* and the vector's squared amplitude is averaged over several time intervals as designated by the angle brackets.

The *x* and *y* coordinate data as a function of each determined time derived from the particle trajectories are used for the MSD assessment as denoted in formula (2):

$$\Delta r^2 = (x_{i+n} - x_i)^2 + (y_{i+n} - y_i)^2 \qquad (2)$$

For ensemble MSD calculations, a mean of the MSD quantity of all particle trajectories involved in the system is defined by summing from *i* to N (total number of all included molecules) and dividing by N[29].

4.3 Results

Herein, we report the development of an artificial double membrane system, a synthetic synapse analogue, comprised of DIB-encapsulated GUV interconnected via DNA-mediated interactions (Fig. 4.1).

4.3.1 Droplet Interface Bilayer (DIB) Formation

The stepwise construction of the bio-inspired model commenced by generating two artificial lipid membrane bilayers which were subsequently linked via hybridized DNA-mediated intermembrane bridges (Fig. 4.1). One of the synthetic membranes was derived from the droplet interface bilayer (DIB). For its formation, the principle of acquisition of a well-packed lipid monolayer around an aqueous solution was exploited before the droplet contacted a hydrogel-supported lipid monolayer immersed in a lipid in oil solution[16] (Fig. 4.4).

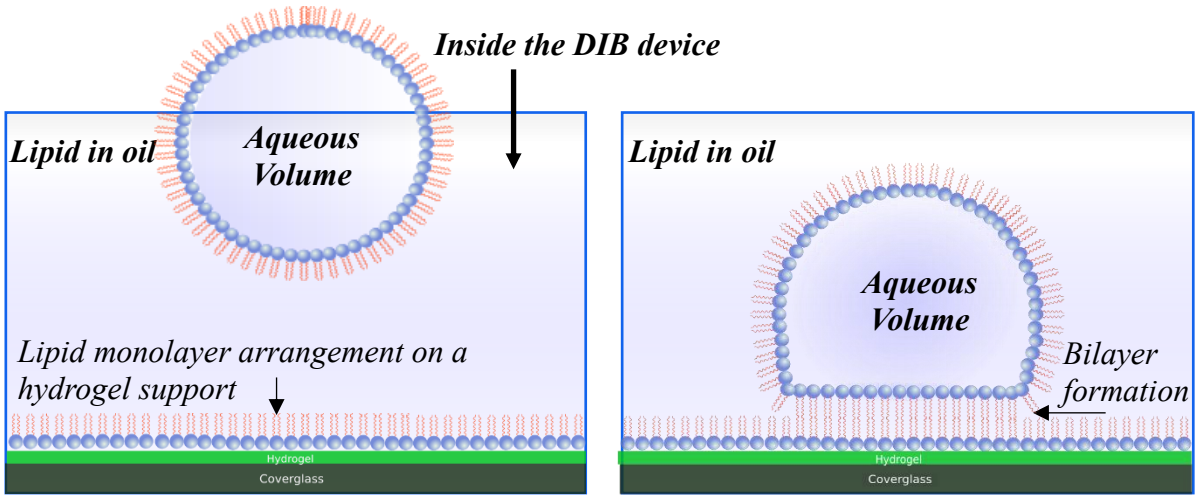

Figure 4.4- Schematic diagram of DIB formation.

Since the majority of studies have employed DPhPC lipid to form stable DIBs[33], we decided to use the same lipid for production of increased droplet robustness, whose

mechanical stability is further enhanced by the pivotal innovation of bilayer formation on a planar hydrogel surface[34]. In addition, this horizontal orientation can accommodate straightforward optical imaging of diffusing single fluorescent molecules by employing TIRF microscopy[35], due to the sufficiently thin agarose substrate[36].

The series of images in Figure 4.5 exhibit bilayer formation as the inner ring was progressively spreading out increasing in size. The outer dark circle corresponds to the droplet perimeter and the bilayer is indicated by the expanding inner ring.

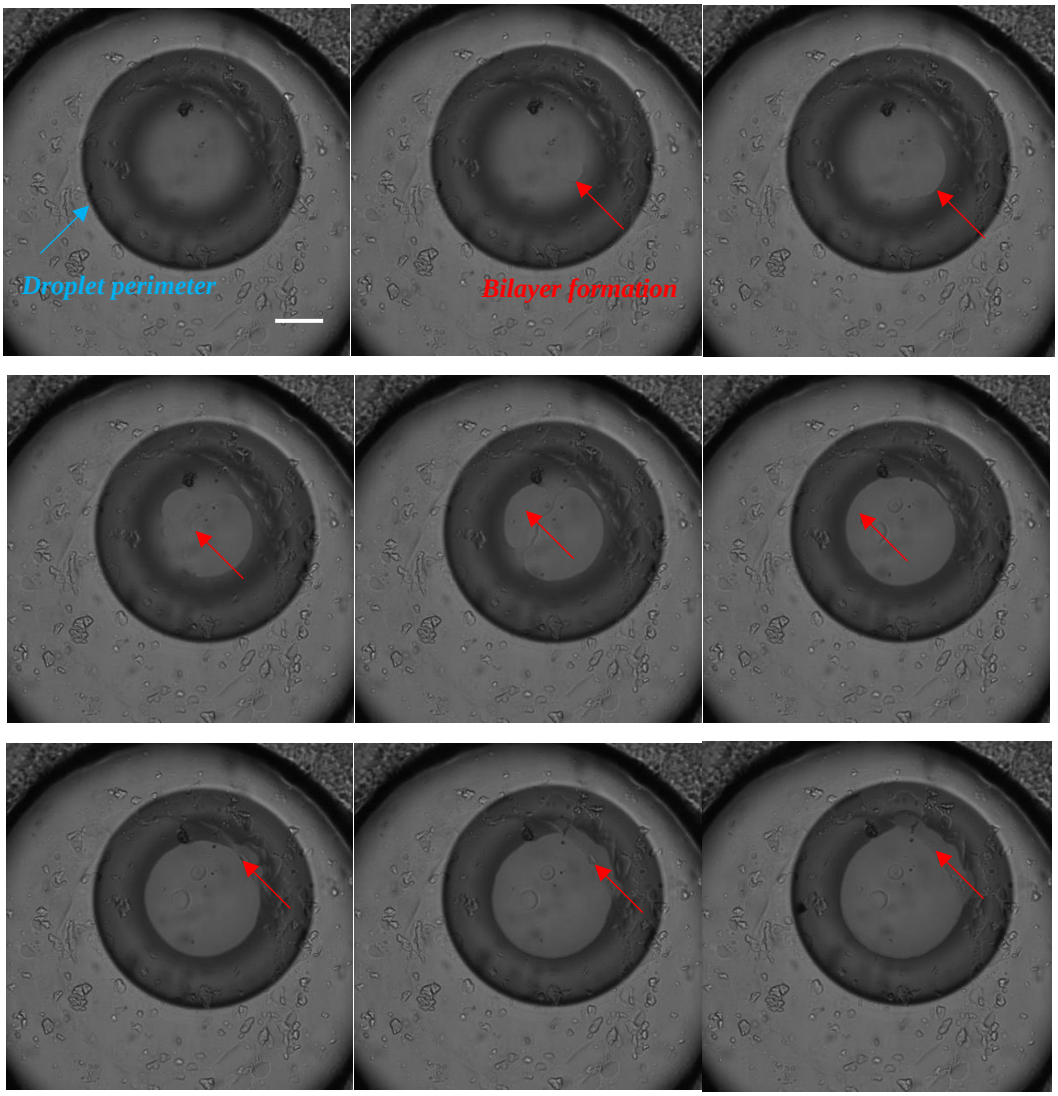

Figure 4.5- Successive bright-field figures demonstrating gradual bilayer formation with 10× magnification. *The droplet appears as a dark circle to the light background with the outer ring defining the droplet perimeter. The stepwise widening of the inner ring denotes bilayer formation. Scale bar: 100 µm.*

Following completion of DIB formation, droplet features were further visualized on light inverted and phase contrast microscopy as shown in Figure 4.6.

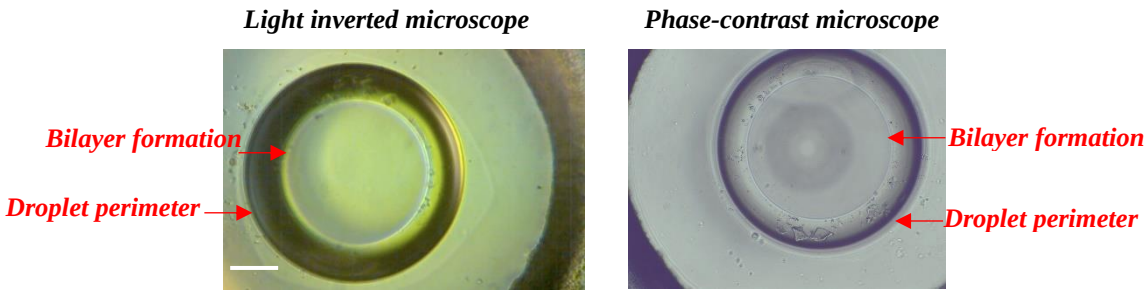

Figure 4.6- Droplet interface bilayer formation as shown on light inverted (left) and phase-contrast microscope (right). *10× magnification. Scale bar: 100 µm.*

4.3.2 Giant Unilamellar Vesicle (GUV) Generation

GUV populations were produced by the energy driven method of electroformation using the experimental setup described in ***Chapter 2*** (in ***2.2 Experimental Section, 2.2.3 Vesicle Preparation by Electroformation*** and ***1.2.3.1 Vesicle Electroformation Protocol***). Vesicle formation was observed within 2 hours after the initiation of the electroformation procedure and micrometer-sized vesicles were formed from DPhPC in saline solution (TE and 50 mM NaCl, pH 7.83). Figure 4.7 depicts some typical GUVs obtained with this protocol as visualized on a light inverted microscope (Fig. 4.7A) and by fluorescence imaging, following CellMask Orange staining (Fig. 4.7B). The fluorescent image exhibits a thread-like structure restricted within the vesicular compartment.

(A)

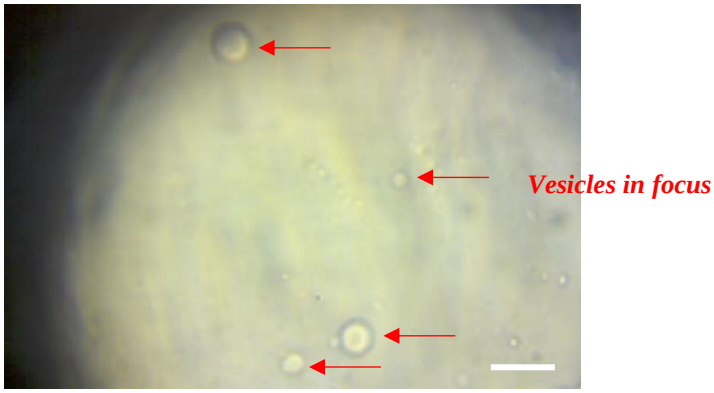

(B)

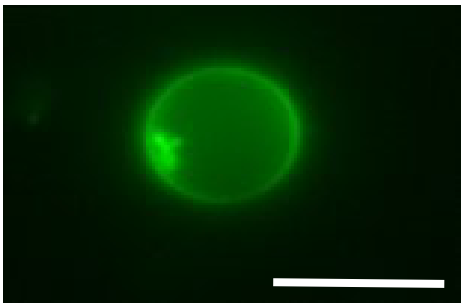

Figure 4.7- Typical GUVs obtained after electroformation in saline *medium as imaged (A) on an inverted microscope under bright-field with 10× magnification and (B) by fluorescence microscopy displaying an intralumenal morphological transformation. Scale bars: 100 μm and 10 μm, respectively.*

4.3.3 Doublex DNA Construct Use for Intermembrane Bridging

The custom-designed internally labelled complementary DNA strands, the synthesis of which is detailed in ***Chapter 3*** (in ***3.3 Results, 3.3.1 Oligos Design***), are exploited as trans-synaptic adhesion molecules for the interconnected double membrane system engineering.

4.3.4 Single-molecule FRET (smFRET) Data Analysis

Thus far, single molecule DNA hybridization between the two complement sequences was assessed on motionless Cy3- and Cy5-tagged oligonucleotides deposited on a hydrophilized coverslip by TIRF microscopy (***Chapter 3***). Yet, their coupling efficiency needed also to be determined in the fluid DIB inner membrane leaflet, which enables species mobility and dynamic rearrangement.

To this end, a DIB was formed with equimolar Cy3- and Cy5-conjugated oligos (5 nM total) in a saline solution (TE and 50 mM NaCl, pH 7.83) and irradiated with 532 nm laser line, giving rise to both donor (Cy3) and acceptor (Cy5) molecule emission, as displayed

in recorded videos (**Supplementary movie S4.1**), where Cy3- and Cy5-labelled DNA tethers freely diffused along the 2D plane of the inner DIB leaflet in donor (green) and acceptor (red) channels, respectively. The following micrographs (Fig. 4.8A,B), constituting snapshots of the video, unveil FRET manifestation on the DIB planar surface imaged by TIRF, confirming DNA annealing under dynamic reorganization conditions where cholesterol-TEG moieties drive DNA sequence integration in the lipid membrane.

In consonance with the smFRET measurements on the glass immobilized dyes, which displayed ~25% DNA annealing efficiency, a similar portion of DNA species in the fluid state of membrane lipids seemed to contribute to the DNA doublex formation manifesting FRET (Fig. 4.8).

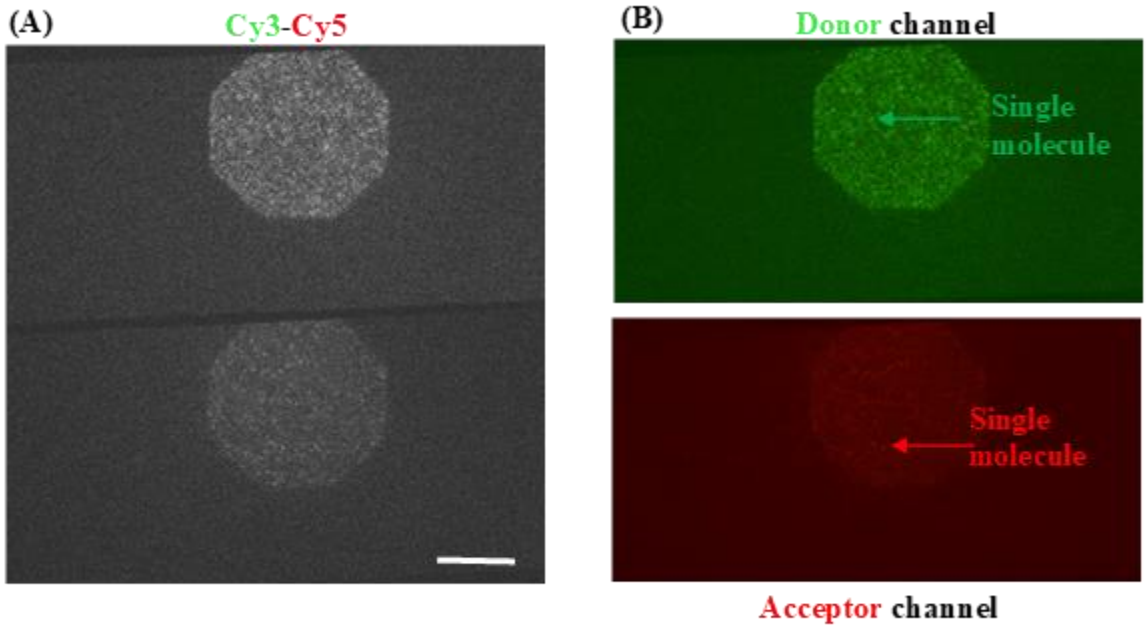

***Figure 4.8- Fraction of emitting Cy5-conjugated DNA species in the acceptor channel**, (bottom side of micrographs (A) and (B), where red pseudo-colour was applied), ensuing 532 nm wavelength illumination, evinces FRET occurrence. Scale bar: 50 μm.*

4.3.5 DIB and GUV Separate Membrane Functionalization

Having established that complementary ssDNA can assemble and yield FRET upon DNA pairing in both states of immobility and motion in the DIB membrane, these synthetic single DNA complements were used separately to functionalize DIB and GUV lipid sheets as shown in Figures 4.9 and 4.10, respectively.

DIB's inner surface was decorated with (10 nM) Cy5-labelled DNA tags, as demonstrated in the schematic diagram (Fig. 4.9A) and imaged by TIRF (Fig. 4.9B). Single molecule motion in a 2D plane (**Supplementary movie S4.2**) denotes DNA strand anchorage to the DIB bilayer through cholesterol-TEG segments.

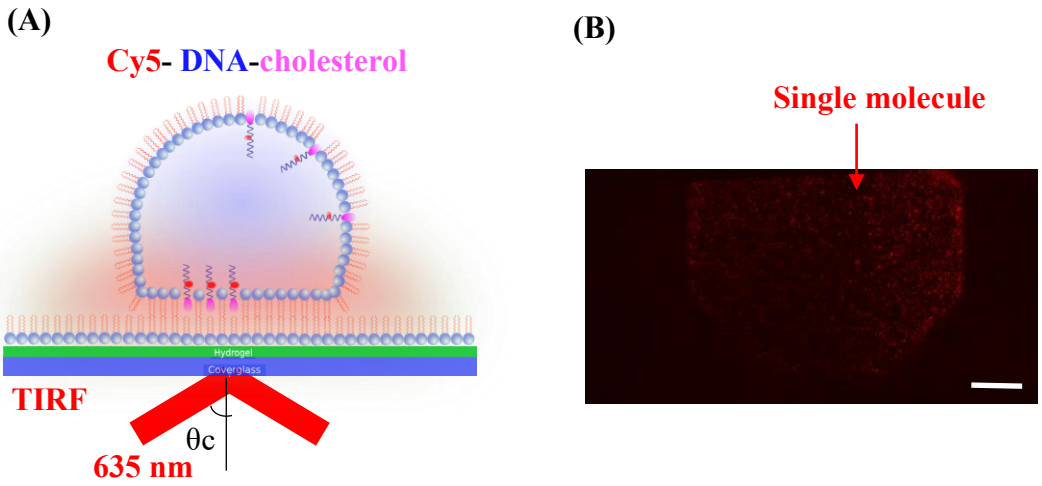

***Figure 4.9- (A) Not-to-scale schematic display of a DNA-functionalized DIB visualized by TIRF**. (B) Cholesteryl-anchored Cy5-conjugated single-stranded oligonucleotides inserted into the inner DIB lipid leaflet. Scale bar: 50 μm.*

GUV's outer lipid leaflet was also functionalized with equal molar fractions of (10 nM) Cy3 tracers, as illustrated in Figure 4.10A and imaged after vesicle deposition on an agarose-coated coverslip under a TIRF excitation field (Fig. 4.10B) and (**Supplementary movie S4.3**).

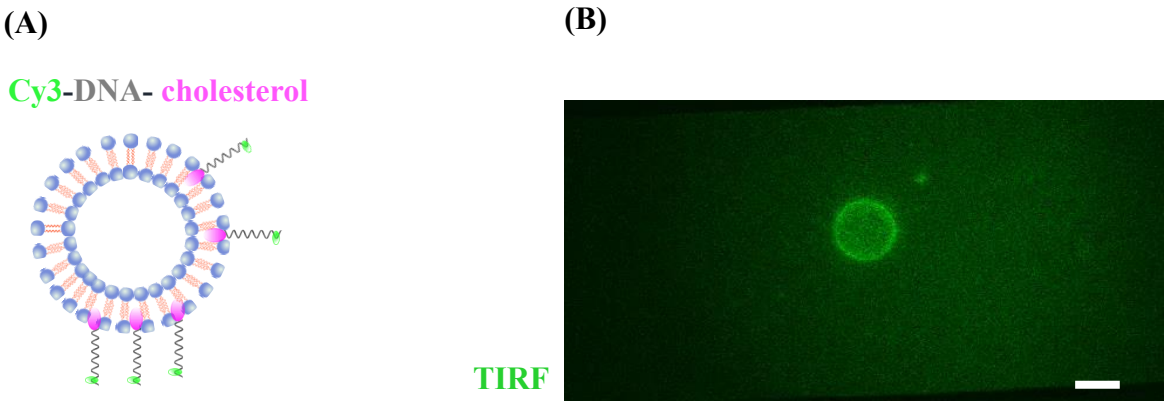

Figure 4.10- (A) Not-to-scale schematics of a DNA-functionalized GUV. *(B) Cholesteryl-anchored Cy3-tagged single-stranded oligonucleotides inserted into GUV outer lipid sheet and imaged by TIRF. Scale bar: 10 μm.*

4.3.6 DIB-encapsulated GUVs

GUVs' enclosure in the DIB lumen was first pursued prior to the tethering process. Thus, (10 nM) Cy3-functionalized GUVs (Fig. 4.11A) and CellMask Orange (1:10.000 dilution) stained GUVs (Fig. 4.11B), respectively, were engulfed into DIB compartments revealing that their coexistence in the same medium is feasible.

Ionic strength balance across the synthetic membranes was retained to eliminate osmotic differential[37], interdicting vesicle membrane shrinkage or rapture. NaCl presence that serves to screen membrane electrostatic repulsion[38], resulted in an adherent bilayer-bilayer patch formation, forcing lipid embedded DNA spacers to diffuse out and be excluded from the adhesive contacts of the apposed membrane leaflets (Fig. 4.12A).

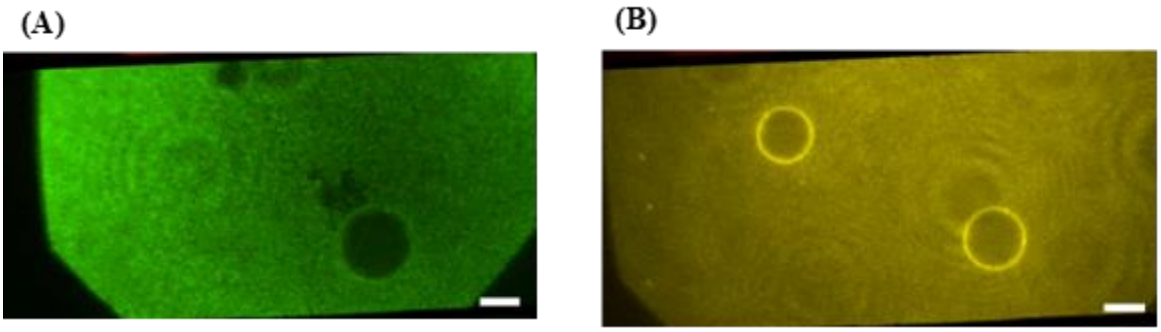

Figure 4.11- (A) DIB-encased Cy3-labelled GUVs (green pseudo-colour image) and (B) DIB-encompassed CellMask Orange stained GUVs (yellow pseudo-colour image) displayed bilayer-bilayer adhesion patches due to dominating electrostatic forces. *Visualized by TIRF and epifluorescence microscopy, respectively. Scale bars: 10 µm.*

The dominating attractive forces between the neighboring bilayers were even conspicuous in the DIB- enclosed GUV system following vesicle and droplet reciprocal but separate membrane functionalization with (5 nM) Cy3 and (5 nM) Cy5 species, respectively. This physical phenomenon led to adjoining membrane-membrane attachment upon contact, forcefully removing complementary strands out of the adhesion site and restraining diffusion of the trapped ones. (Fig. 4.12 and **Supplementary Movie S4.4**).

Cropped images extracted from overlaid donor (green—Cy3) and acceptor (red—Cy5) channels within the vesicle surface area demonstrate apparent confined Cy3 movement and perfect single molecule co-localization (Fig. 4.12 and **Supplementary Movie S4.4**), an indication of bleed-through stemming from Cy3-dye fluorescence leakage (an 8% intensity crossover in the acceptor channel) rather than FRET, which would have implied DNA-mediated intermembrane bridge formation.

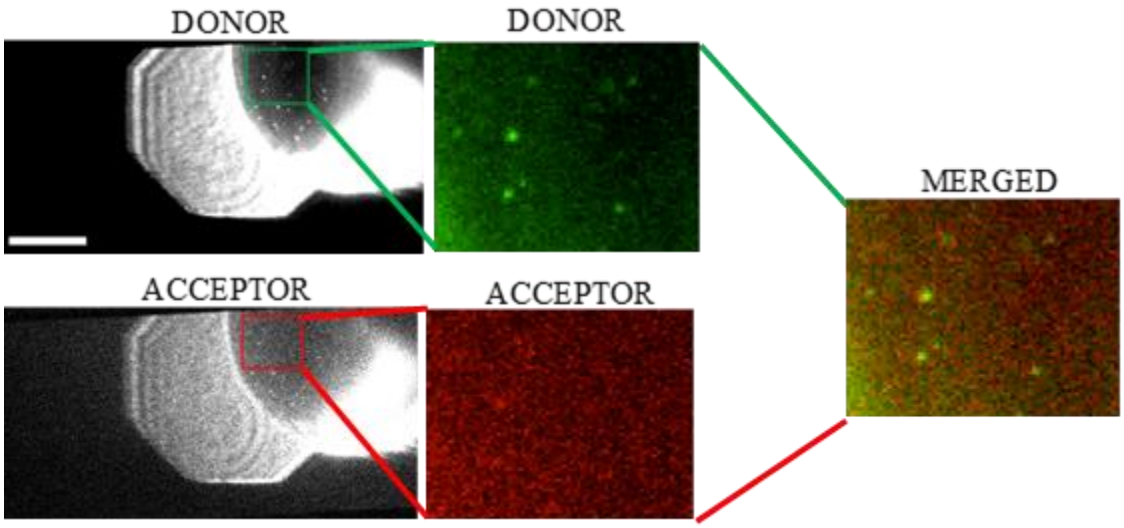

Figure 4.12- (5 nM) Cy3-functionalized GUV encapsulated in a (5 nM) Cy5 containing droplet. *Green (donor channel) and red (acceptor channel) cropped areas excised from the vesicle region exhibit single molecule hindered motion. The overlaid donor (green—Cy3) and acceptor (red—Cy5) channels divulge co-localization, a sign of spectral bleed-through. Scale bar: 50 μm.*

4.3.7 Mean-squared Displacements (MSDs) and Two-dimensional (2D) Diffusion Constants

The ostensibly hindered Cy3 probe mobility dynamics within the vesicle area (Fig. 4.12 and **Supplementary Movie S4.4**) and the wandering Cy5 species motion (Fig. 4.8 and **Supplementary Movie S4.4**) in the DIB bilayer were characterized via mean squared displacement (MSD) analysis, the mainstay of biophysics[39]. The essential purpose of MSD analysis is to extract physical information, such as the two-dimensional diffusion constant, D, which can help us better estimate particles' movement rate and through further analysis uncover the kind of diffusion regime particles are subjected to[28]. (Types of diffusion regimes are more closely presented in ***4.3.7.1*** (***Single-molecule Diffusive Mode in the Inner and Outer Vesicle Surface Area***).

Mean squared displacements of singular Cy3 and Cy5 trajectories (Fig. 4.13B, 4.14B) from a total of 41 and 47 representative tracks (Fig. 4.13A, 4.14A) within the vesicle

surface area (Fig. 4.12, 4.13A) and in the unrestricted DIB plane (Fig. 4.8, 4.14A), respectively, were assessed by performing time average on the millisecond time scale. The MSD-t plots (Fig. 4.13B, 4.14B) depict displacement versus time intervals (where frames × 0.03 s = t) of individual trajectories with the majority of curves exhibiting short delays. The ensemble-average over all trajectories was also estimated and designated with a thicker black curve (Fig. 4.13B, 4.14B).

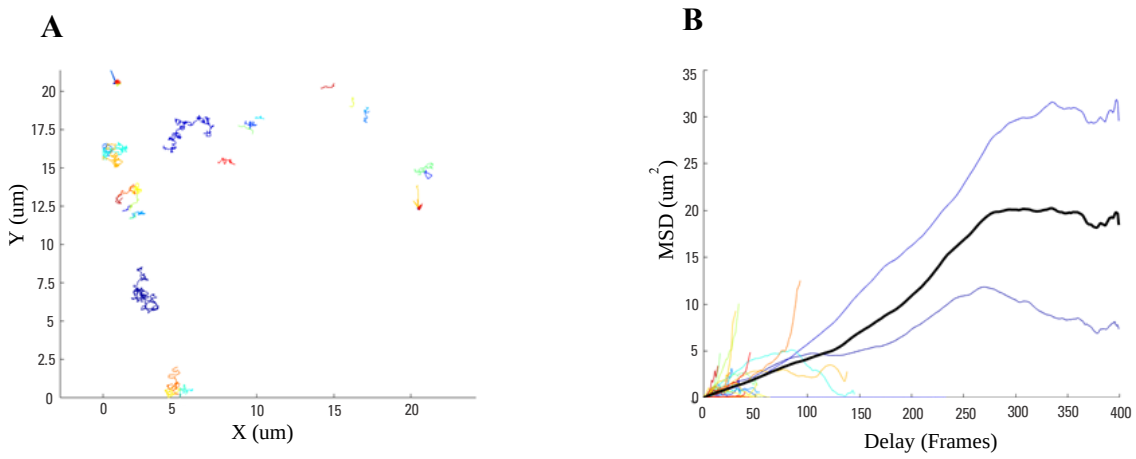

Figure 4.13- Experimental data for the mean-squared displacement (MSD) from (A) single particle tracking (SPT) within the vesicle surface area*. (B) Overall, 41 representative Cy3 trajectories with 400-time steps (12 s). Mean-squared displacement as a function of time values (400-time steps × 0.03 = 12 s). The color curves correspond to distinct molecule trajectories. Thicker black line corresponds to mean value.*

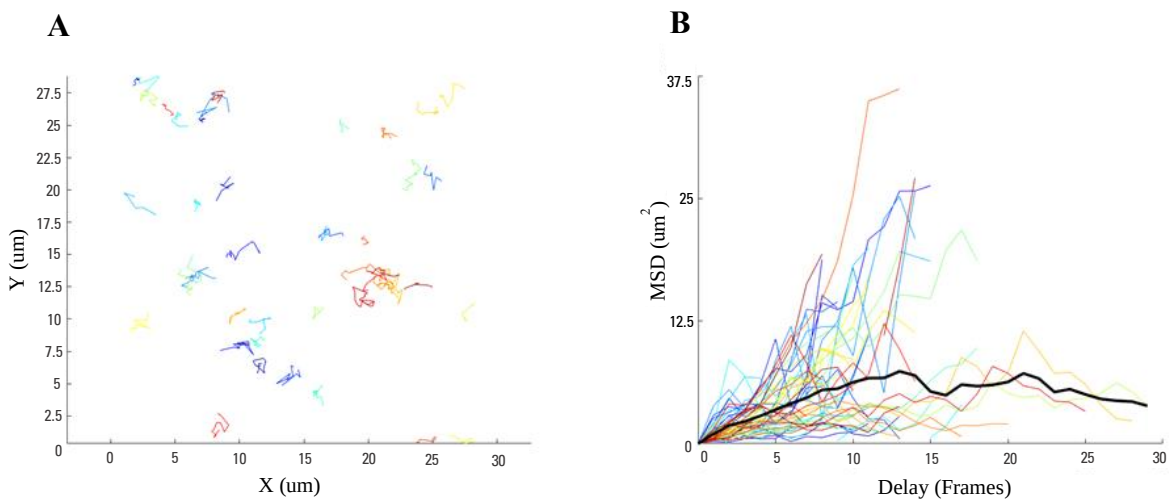

Figure 4.14- (A) Cy5 trajectories in the 2D DIB membrane. *(B) Mean-squared displacements as a function of time lag (30-time steps = 0.9 s) for 47 individual tracks with the black bold line representing the mean value.*

By performing a linear weighted fit to the MSD curve of all trajectories involved (the ensemble MSD), the diffusion coefficient (D) is derived [40]. Calculation of the lateral diffusion coefficients (D) revealed that vesicle trapped Cy3 molecules moved at a slower pace (D = 1.083e-04 with 95% confidence interval [1.070e-04 – 1.096e-04] $\mu m^2 s^{-1}$, n = 41 trajectories) (Fig. 4.15A), (by two orders of magnitude), than the unhindered Cy5 probes in the DIB plane (D = 2.277e-02 with 95% confidence interval [1.338e-02 – 2.700e-02] $\mu m^2 s^{-1}$, n = 47 trajectories) (Fig. 4.15B).

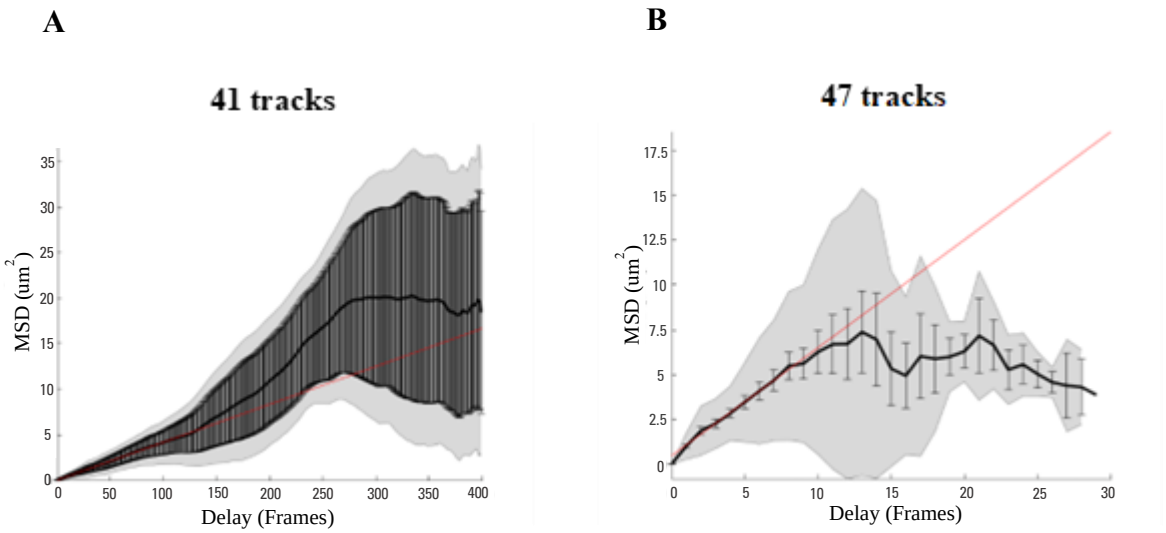

Figure 4.15- Average squared displacement of (A) 41 and (B) 47-particle trajectories. *Lateral diffusion constants obtained from linear weighted fits to long-time mean square displacements with (A) D = 1.083e-04 (with 95% confidence interval [1.070e-04 – 1.096e-04] μm^2 s^{-1}, n = 41 trajectories) for the trapped particles between GUV and DIB bilayers and (B)D = 2.277e-02 (with 95% confidence interval [1.338e-02 – 2.700e-02] μm^2 s^{-1}, n = 47 trajectories) for the freely diffusing species in the DIB planar surface. Error bars represent standard deviation of the mean of each of the data points. Grey shaded area represents the weighted standard deviation over all individual trajectory mean squared displacement (MSD) curves. The red straight line represents the fit which yields an acceptable estimate of D.*

Despite absence of statistical significance, as gauged by a two-sided unpaired t-test, the two groups displayed a constant diffusion difference of two orders of magnitude. The fact that statistical difference was not reached could be possibly ascribable to the small sample size.

4.3.7.1 Single-molecule Diffusive Modes in the Inner and Outer Vesicle Surface Areas

Apart from the mean-squared displacement (MSD) function, where molecules' two-dimensional diffusion coefficients can be derived from[41], another interesting approach to characterize molecules' movement modality in a system involves the quantification of the non-dimensional MSD exponent α[42], which is obtained by applying a linear fit to the logarithmic plot of MSD-t[43].

In normal diffusion, the mean-squared displacement (MSD) grows linearly with respect to time, (MSD ~t)[43]. Upon deviation from the normal diffusion mode, a particle's behaviour is classified as anomalous and is described by a power law (MSD = ~D t^{α})[44], where D is the diffusion coefficient, t is the elapsed time and α is the anomalous diffusion exponent. In a typical (Brownian) diffusion process, α = 1 and there is linear relation between the MSD and time lag. If α > 1, the phenomenon is called super-diffusion, where particles undergo directional motion due to drift or active transport and the trend is characterized by a parabolic MSD curve[45]. When α = 2, a ballistic growth is operating due to inertial effects (inertia is the resistance of any physical object to any change in its velocity)[46] and α below 1, suggests that sub-diffusion is at work with hindering origins involving obstruction barriers, trapping cages, crowding or stalling and the propensity is represented by a MSD that reaches a plateau for high time intervals[47, 48]. Hence, the slope produced by linearly fitting the MSD function in the double logarithmic scale, provides the α exponent value [41] and the distribution of all slopes in a given system can yield the motion type[49].

The histogram displayed in Figure 4.16A, (reflecting the diffusion mode of the intermembrane hindered Cy3 probes), shows an alpha mean value at 0.87, which is statistically significant below 1 (assessed by single sample t test), suggesting a sub-diffusive modality. However, we can't overlook the fact that there are several peaks below and above 1 revealing a mixed population which is better clarified through analysis of log-log fit. Out of 32 tracks (N = 32) analyzed, 18 of them (56.25%) yielded α exponent values below 1, indicative of constrained motility; 6 particles (18.75%) had a slope of 1(inside the

confidence interval), characteristic of Brownian movement and 8 of them (25%) exhibited slope values above 1 (super-diffusive motion type).

The fact that not the whole but only the preponderance of tracked species in the entrapped region of our lipid assembly exhibit obstructed diffusion could be attributed not only to the bilayer embedded cholesterol anchors, whose presence can drive liquid disordered domain formation instigating heterogeneous mobility states[46], but also, to variation in the surrounding space[50], in relation to the uneven width between the proximal membranes along the whole attachment zone generated due to electrostatic forces. Regardless of this variance, these diversified diffusion processes are typical of confined systems through which several regimes with nonlinear behaviour emerge[41].

With respect to the histogram acquired from unobstructed Cy5 moving molecules in the DIB bilayer, the alpha mean value of 0.95 estimated, is not significantly different from 1 (Fig. 4.16B). Moreover, the distribution of the alpha values in a sample of 36 species (N = 36) again presents a slight variation as that encountered in the Cy3 monitored species diffusing in between the two bilayers (Fig. 4.16A). Specifically, the majority, 17 particles over 36, (47.22%) exhibit an alpha exponent value of 1, Brownian process (inside the confidence interval) and the next smaller percentage (33.33%) (12 particles over 36) follows an impeded trend with a slope value below 1. The smallest fraction of the tracked molecules (7 particles over 36) (19.44%) shows a super-diffusive motility regime at the time scale of their appearance.

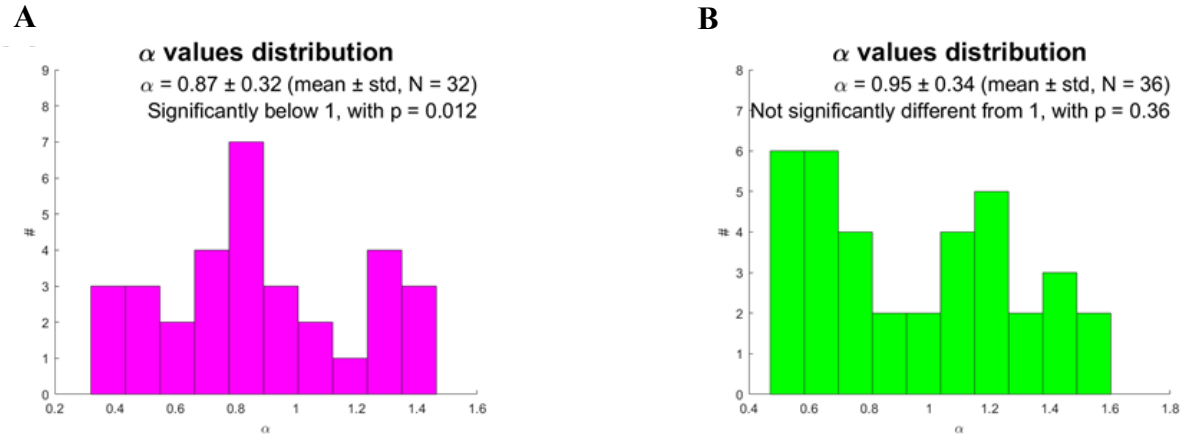

Figure 4.16- Distribution of mean-squared exponent values of α *for (A) 32 inter-membrane trapped and (B) 36 freely diffusing tracked molecules from one dataset each.*

In contrast to Figure 4.16A, the frequency distribution profile displayed by the freely walking Cy5 single molecules in DIB's surface (Fig. 4.16B) yields a slightly different motion character as most tracks undergo a Brownian motion, an anticipated deportment under the given unrestricted fluid state of membrane lipids.

This data analysis showcases a partial dissimilarity in the mobilities of single particles under the two conditions with the trapped Cy3 dyes primarily experiencing a corralled movement (due to presumably weak confinement), whereas Cy5 probes' unobstructed locomotion in the DIB surface mainly manifests a Brownian diffusion process. This motility type discrepancy reinforces the surmise of GUV residence on the DIB bilayer, owing to electrostatic interaction developing under physiological conditions[51], which ultimately moderately impedes lateral shifts of the caged particles.

4.3.8 Polyethylene Glycol-modified Lipid Incorporation in the Inner DIB Leaflet

In order to overcome the liability of nonspecific inter-bilayer interaction and facilitate apposed membrane detachment, droplet inner lipid sheet was enriched with (10% w/w) polyethylene glycol, alias, PEGylated lipid (PEG2000 PE (16:0)) (Fig. 4.17) which acts as hydrophilic cushion and introduces a steric hindrance[52].

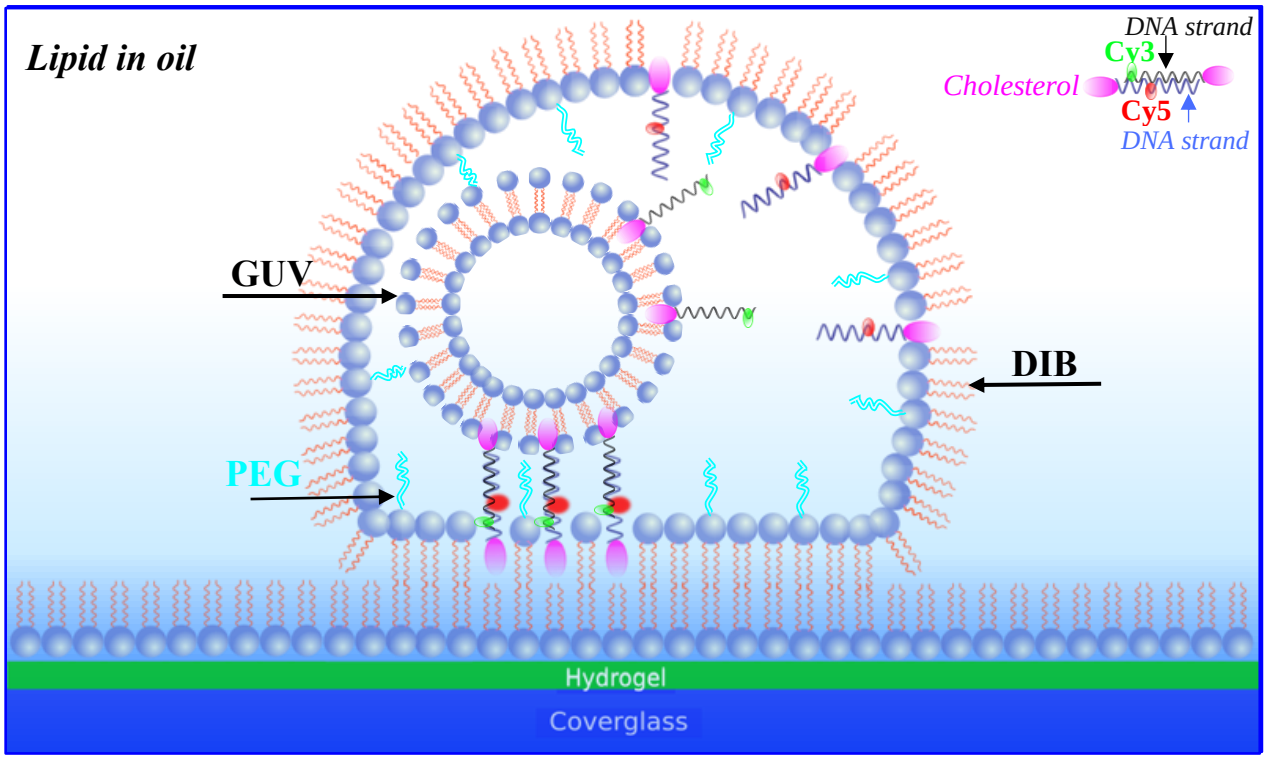

Figure 4.17- Schematic diagram of PEGylated lipid integration in the inner leaflet of the DIB. *Not to scale.*

Furthermore, taking into consideration that the surface area of a 20 nl droplet (3.6×10^{-7} m^2) is roughly 3 orders of magnitude larger than the surface area of a 10-micron sized GUV (3.14×10^{-10} m^2), which translates to 4.68×10^{10} DPhPC molecule recruitment for the droplet membrane composition as compared to 4.08×10^{7} DPhPC molecule assembly for the vesicle membrane architecture, the Cy3-Cy5 dye concentration for the two distinct synthetic membranes was modified accordingly.

4.3.8.1 MSDs and Two-dimensional (2D) Diffusion Constants in a (10% w/w) PEG Containing DIB

(2.5 nM) Cy3-labelled vesicles were incorporated in a (5 nM) Cy5-functionalized (10% w/w) PEG containing DIB (Fig. 4.17, 4.18 and **Supplementary Movie S4.5**).

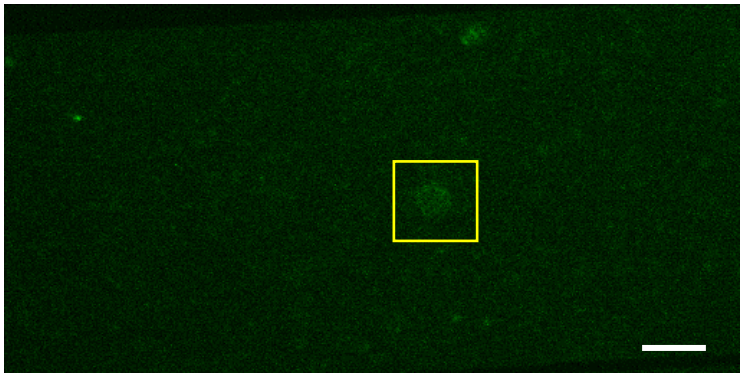

Figure 4.18- Encapsulated (2.5 nM) Cy3-functionalized GUVs in a PEG (10% w/w) composed DIB formed out of a (5 nM) Cy5 containing solution. *Particle trajectories were excised from the inner vesicle surface region (within the yellow frame) in the donor channel (green pseudo-color was applied). Scale bar: 10 µm.*

The MSDs of 27 excised trackable particle traces within the vesicle boundary (Fig. 4.18, 4.20A and **Supplementary Movie S4.5**) were calculated and plotted (Fig. 4.20B) and compared to the 74 tracks of randomly walking species extracted from the outer domain of the vesicle barriers (Fig. 4.19, 4.21A and **Supplementary Movie S4.6**).

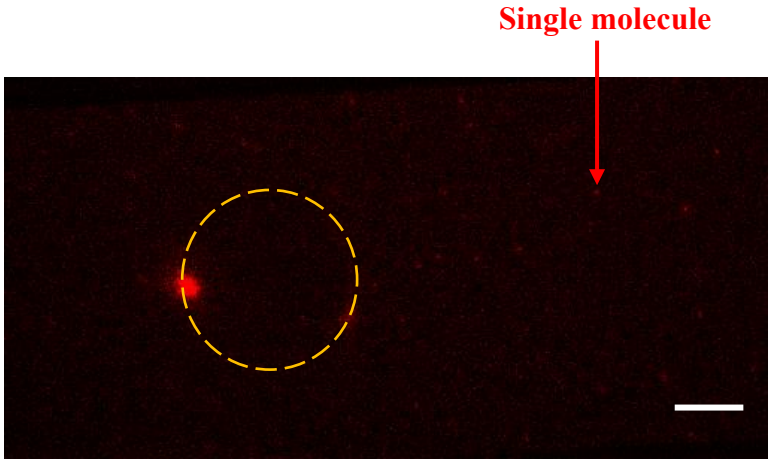

Figure 4.19- Enclosed (2.5 nM) Cy3-decorated GUV in a PEG (10% w/w) composed DIB formed out of a (5 nM) Cy5 containing solution. *In-focus single dye molecules and out-of-focus vesicle perimeter (GUV circumference denoted by the orange circular dashed line). Particle trajectories were excised from the outer vesicle bounds in the acceptor channel (where red pseudo-colour was applied and relative contrast adjustment was set). Scale bar: 10 μm.*

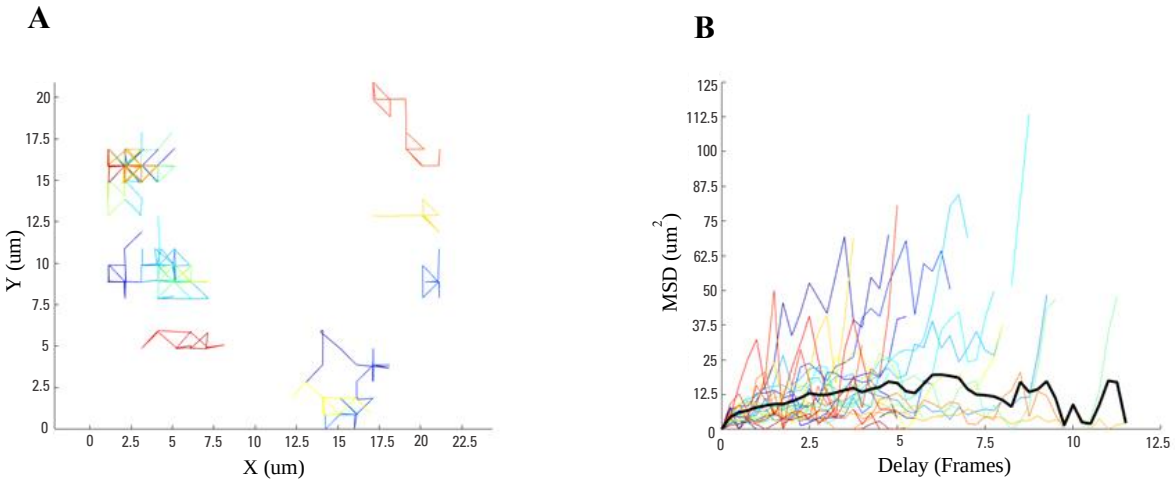

Figure 4.20- (A)Representative particle trajectories within the vesicle surface area*. (B) 27 individual MSD curves as a function of time delay (t), where t = frames × 0.03 s. Black bold line corresponds to ensemble MSD.*

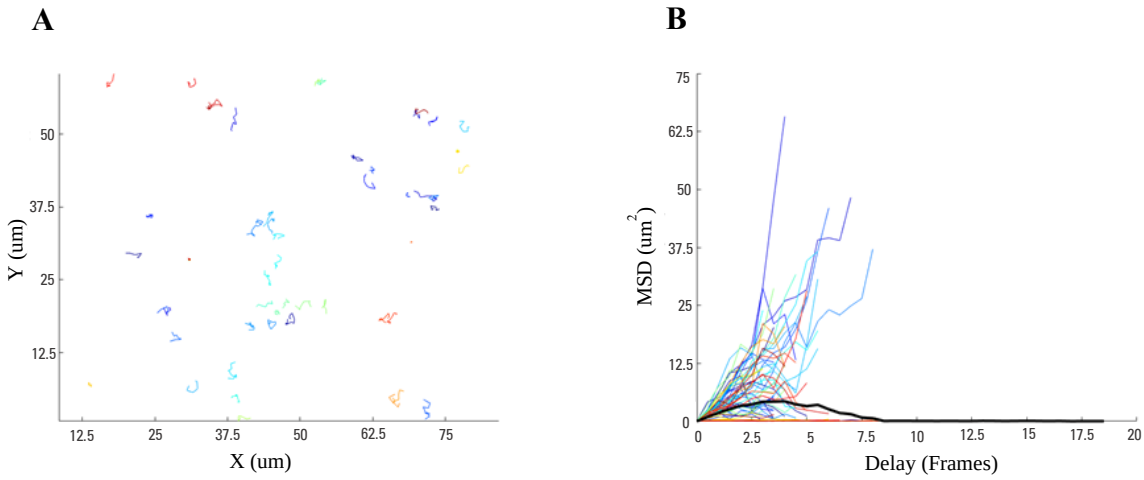

Figure 4.21- (A)Tracks extracted from the DIB surface area beyond the vesicle's edges*.* ***(B)****74 time-averaged mean square displacements versus time interval(t), where t = frames × 0.03 s. Black curve designates ensemble-averaged mean square displacements of all 74 trajectories.*

To investigate if bilayer-bilayer detachment occurs under the new experimental condition, which presumably enables unrestricted tracer mobility along the inner vesicle surface area, the 2D-diffusion coefficients were determined from the ensembled-averaged mean squared displacement of individual trajectories both within and beyond the vesicle circumference.

Gauged by an independent samples t-test, absence of statistical significance in the ensembled-averaged mean-squared displacements between the inner (D = 4.096 e-02 with 95% confidence interval [3.062e-02 – 5.279e-02], n = 27 trajectories) (Fig. 4.22A) and the outer vesicle region (D = 1.455e-02 with 95% confidence interval [5.979e-03 – 2.686e-02], n = 74 trajectories) (Fig. 4.22B) suggests comparable particle diffusion (the same magnitude order) in the two territories and hence, an inter-bilayer gap is speculated to be formed potentially sufficient to enable species unimpeded walk and possibly duly structured to be bridged by DNA coupling.

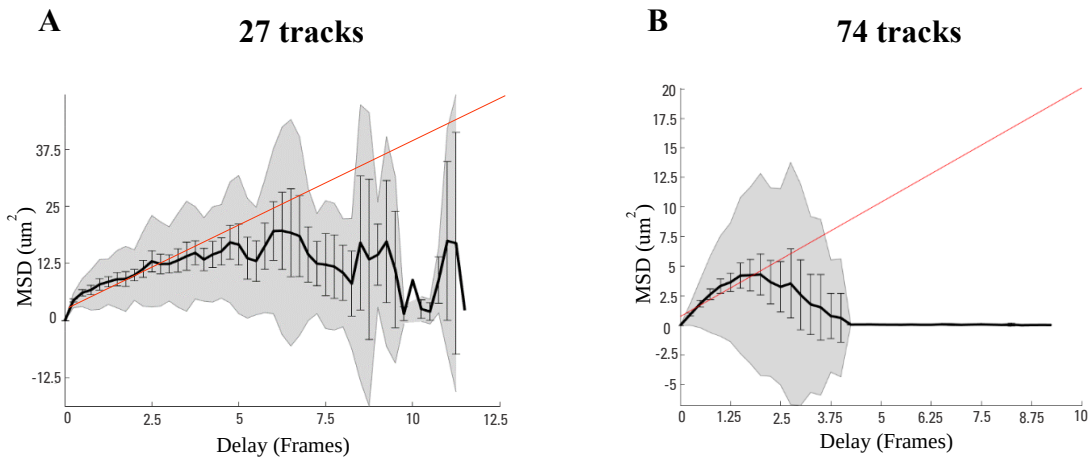

Figure 4.22- Lateral diffusion was assessed for the (A) donor (Cy3) and (B) acceptor (Cy5) imaged particles: *(A) D = 4.096 e-02 (with 95% confidence interval [3.062e-02 – 5.279e-02] $\mu m^2\ s^{-1}$, n = 27 trajectories). (B) D = 1.455e-02 (with 95% confidence interval [5.979e-03 – 2.686e-02] $\mu m^2\ s^{-1}$, n = 74 trajectories). Grey shaded area represents the weighted standard deviation over all individual trajectory mean-squared displacement (MSD) traces. Error bars represent standard error of the mean on each data point. The fit is represented with a red straight line producing a good D estimate.*

4.3.8.2 Single-molecule Diffusive Modes within and out of Vesicle Domain in a (10% w/w) PEG Containing DIB

Interestingly, the log-log fit of the mean-squared displacement and analysis at the single molecule level unveiled some particle movement disparities between the inner and outer vesicle regions. Specifically, the mean alpha value of the diffusing particles within the GUV perimeter was 0.63 +/- 0.12 (N = 7) (Fig. 4.23A), a collective constrained motility state, with the frequency distribution showing all molecules to have an α exponent value below 1, typical of a concerted corralled motion. However, this unanimous sub-diffusive behaviour could be due to the perceptibly very small sample size (N = 7).

Conversely, outside the vesicle borders, molecules presented Brownian diffusion with a mean α value of α = 1.01+/- 0.29 (N = 34) (Fig. 4.23B). Logarithmic fit analysis clearly demonstrated species preponderance towards a slope value of 1 (19 over 34) (55.9%). The percentage of 23.53% (8 particles over 34) displayed an α exponent value above 1 (super-diffusive mode), whilst 20.59% (7 particles over 34) had a slope value less than 1.

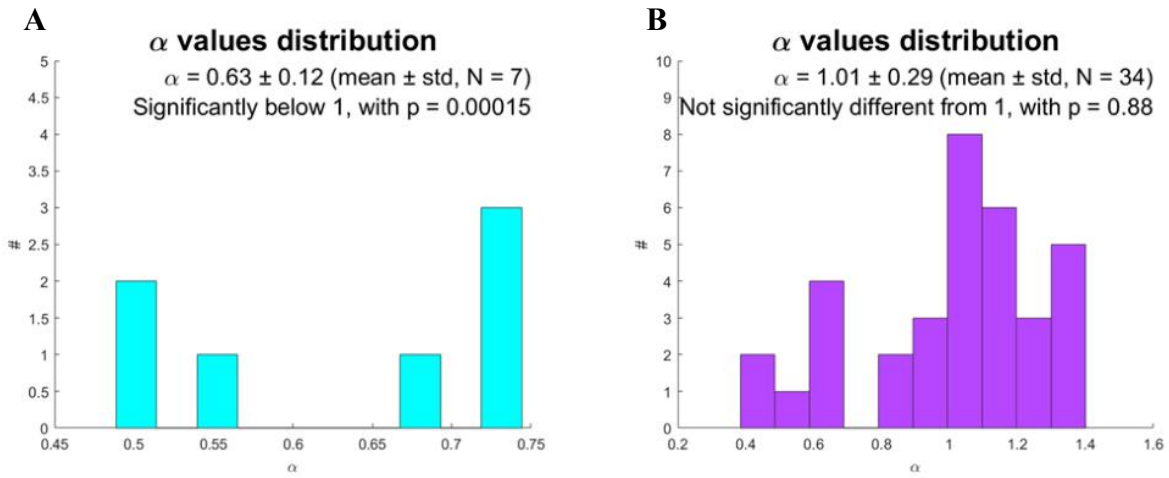

Figure 4.23- Histogram of α for (A) 7 and (B) 34 species, inside and outside the vesicle surface area respectively, *from 1 dataset each.*

The confined tracer movement within the vesicle's margins comes in sharp contrast to the primarily Brownian motion process unfolding in the unhampered DIB inner lipid leaflet. Of note, the element of super-diffusivity in the DIB planar region (Fig. 4.23B) has been previously reported in PEG treated membranes and explicated on the basis of the polymer's property to form discontinuous hydrophilic mesh domains on the (2-dimensional) lipid bilayer surface allowing the hydrophilic part of the probe (DNA/Cy3-DNA/Cy5 in our case) to diffuse at a swifter pace[48].

Nevertheless, the limited amount of the data derived from the vesicle domain does not allow us to draw firm conclusions on the current outcome although certain particles' ingress or exit across the vesicle perimeter (**Supplementary Movie S4.6**) could imply adequate intermembrane space for molecule transport.

4.3.8.3 FRET Efficiency in the GUV Territory Enclosed in a (10% w/w) PEG Composed DIB

FRET manifestation within the GUV territory is considered a sign of interlinked adjacent membranes mediated via formed DNA bonds. Indeed, FRET occurrence was observed within the vesicle circumference, as shown in recorded superimposed donor and acceptor videos (Fig. 4.24 and **Supplementary movie S4.5**). Characteristically, an individual captured spot (Fig. 4.24Bi) was shown to transition from acceptor (Cy5-red) to donor (Cy5-green) (Fig. 4.24Bii) consistent with FRET cessation during which donor's fluorescence recovers following acceptor's photodegradation.

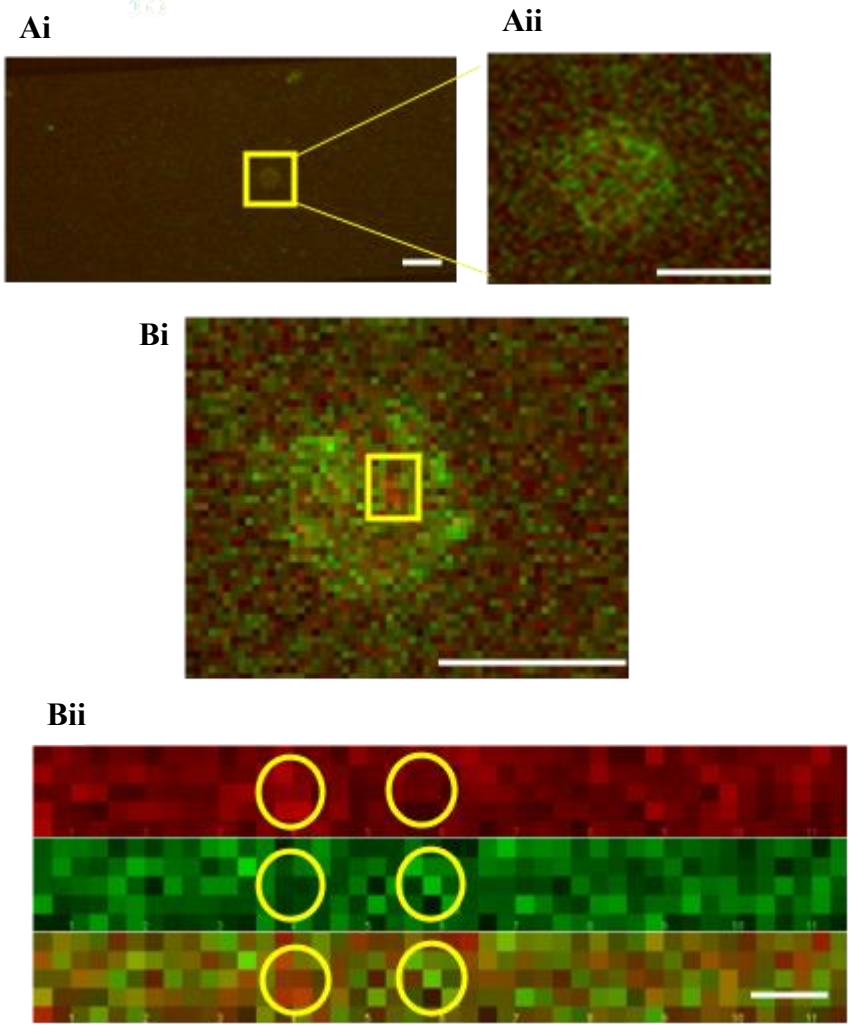

Figure 4.24- DIB-encased vesicle undergoes FRET. *(Ai) Vesicle lying on the (10% w/w) PEG containing DIB surface derived from superimposed donor (green) and acceptor (red) channels. (Aii) Magnified vesicle on the right. Scale bars: 10 µm and 4 µm, respectively. (Bi) A closeup snapshot of the vesicle region showing a single-molecule FRET (enclosed red spot). Scale bar: 4 µm. (Bii) Sequential frames (30 ms per frame) of the partial trajectory of the single-molecule FRET depicted in (Bi). Donor (green), acceptor (red) and overlaid channels show temporal fluctuations of the hybridized DNA species. Between frames 4 and 5, a single Cy3-Cy5 pair (encircled) switches from red to green with maximum donor (green) intensity in frame 6, indicative of FRET termination. Scale bar: 1 µm.*

The average FRET efficiency of 29 single FRET spots (N = 29) extracted from the vesicle surface area was E = 0.7 ± 0.19 for the sensitized emission approach (Fig. 4.25A) and

E = 0.69 ± 0.21 for the donor quenching method (Fig. 4.25B). The approximate 20% diminution in FRET efficiency relative to the value assessed from the surface sessile single molecules (N = 104) (***Fig. 3.23, Chapter 3***), could be attributed to PEG polymer hydrophobic contribution which has been reported to slightly increase stacked base pair inter-planar distance[53]. In this context, PEG introduction could possibly affect the fluorophore orientation factor[54] and dye intermolecular distance[55], ultimately impacting FRET intensity signal. Another possible reason for the attenuated FRET detection could be associated with the aforementioned idea of the membrane microdomain formation that drives the hydrophilic segment of the probe (DNA-Cy3/DNA-Cy5) to partition into and diffuse along such meshes, leading to a decreased fluorescence lifetime of both donor and acceptor species[48]. Such a presumption could justify the observation of short-lived low FRET states.

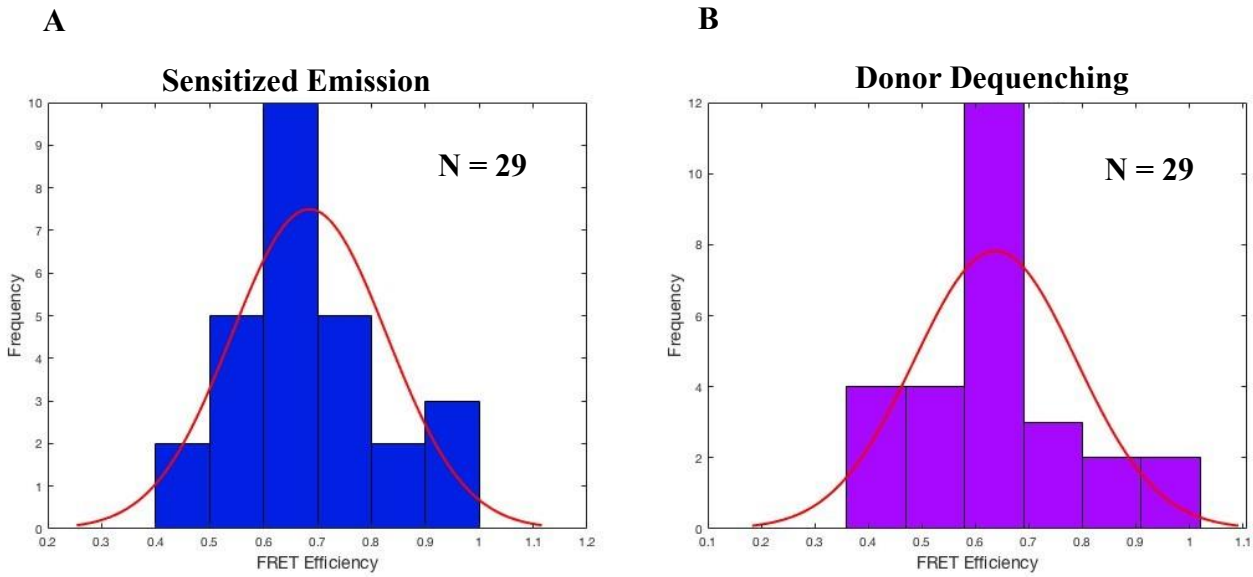

Figure 4.25- FRET efficiency histograms with Gaussian distributions *centered at (A) E = 0.7 ± 0.19 and (B) E = 0.69 ± 0.21 for the sensitized emission and the donor dequenching methods, respectively. N = 29 denotes the number of selected molecules.*

4.3.9 Ionic Lipid (DOPG-1% w/w) Incorporation in the Inner DIB Leaflet and GUV Bilayer for Inter-membrane Detachment

Another approach to overcome the liability of nonspecific inter-bilayer interaction and disassociate the adhered proximal membranes was based on the idea of giving rise to repelling forces by introducing 1% (w/w) of the anionic lipid 1,2-Dioleoyl-sn-glycero-3-phospho-rac-(1-glycerol) (DOPG) in both DIB and vesicle synthetic membranes as illustrated in Figure 4.26.

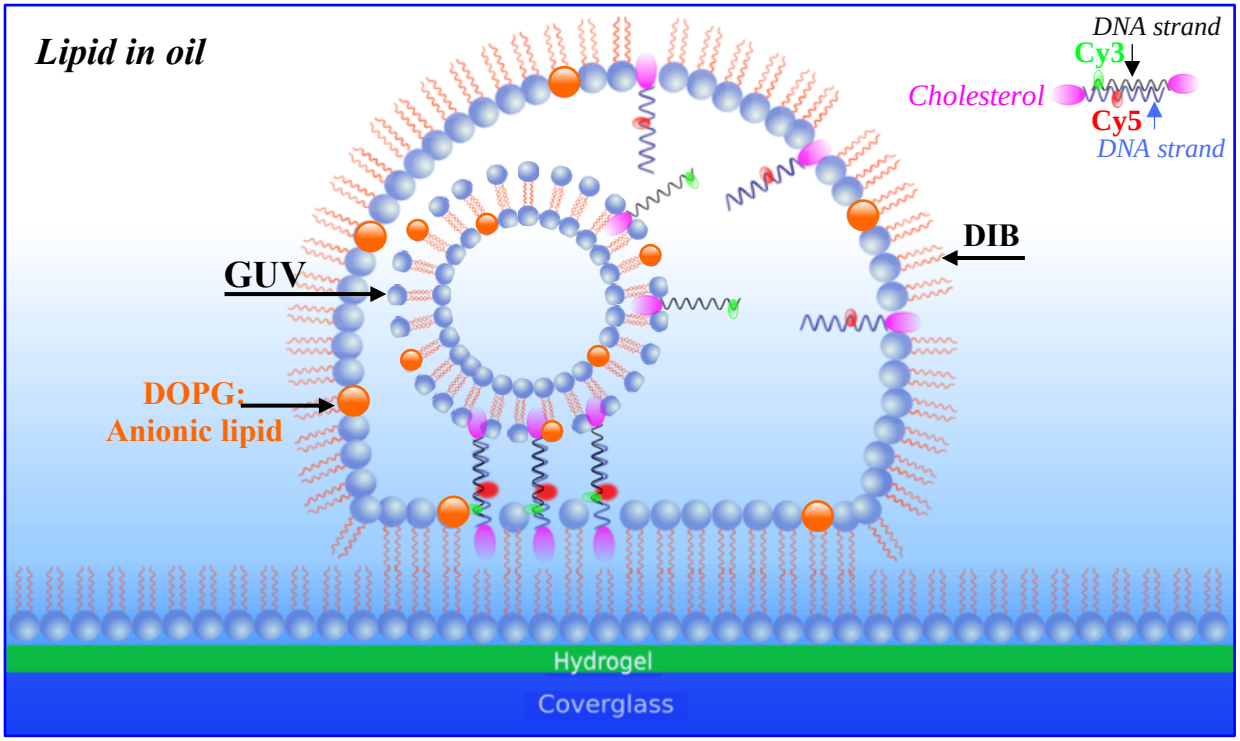

Figure 4.26- Schematic diagram of anionic lipid (DOPG) integration in the vesicle bilayer and inner DIB lipid sheet. *Not to scale.*

4.3.9.1 MSDs and Two-dimensional (2D) Diffusion Constants in a (1% w/w) DOPG Containing DIB and GUV

Moving on to estimate mean-squared displacements (MSDs), particle trajectories were obtained with ImageJ from the inner (Fig. 4.27, 4.29A and **Supplementary Movie S4.7**) and outer vesicle surface area (Fig. 4.28, 4.30A and **Supplementary Movie S4.8**) in (1% w/w) DOPG composed GUVs and DIBs. The two-dimensional vectors of MSDs over delay time (in frames, t = frames × 0.03 s) were computed for 65 tracks in the GUV bilayer (Fig. 4.29B) and for 50 tracks outside the vesicles' edges (Fig. 4.30B).

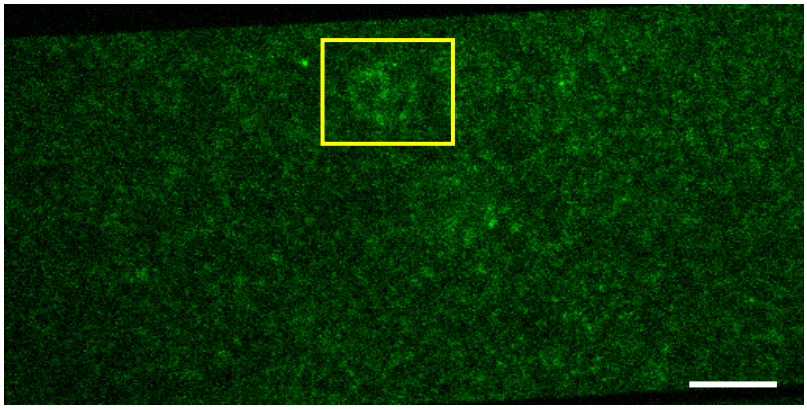

Figure 4.27- (1% w/w) DOPG composed vesicle encapsulation in a (1% w/w) DOPG containing DIB. *Enclosed (2.5 nM) Cy3-functionalized GUV in a (5 nM) Cy5-decorated DIB. Single tracer particle mobilities were acquired from the encased GUV within its boundaries. Green pseudo-colour was applied, and relative contrast was set to better illustrate single molecules. Scale bar: 10 µm.*

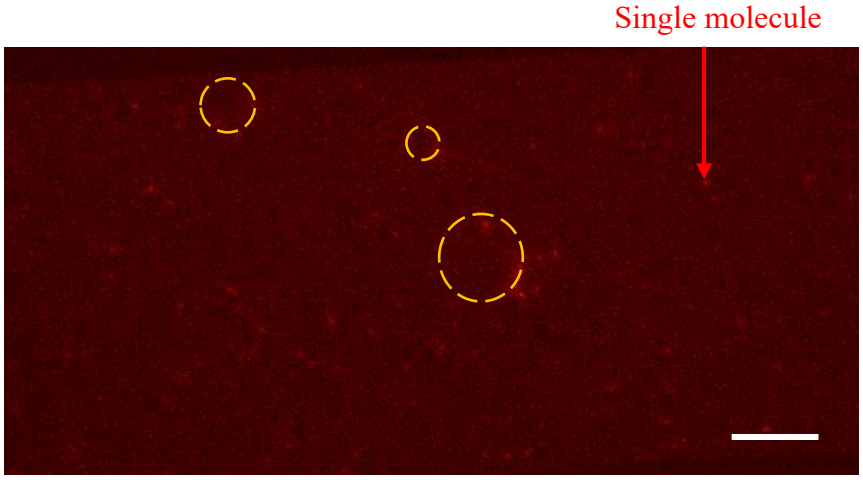

Figure 4.28- (1% w/w) DOPG composed GUV enclosure in a (1% w/w) DOPG containing DIB. *Encapsulated (2.5 nM) Cy3-functionalized GUV in a (5 nM) Cy5-labelled DIB. Particle trajectories were excised from the outer vesicle domains in the acceptor channel where red pseudo-colour was applied. GUV circumferences are designated with orange circular dashed lines. Scale bar: 10 µm.*

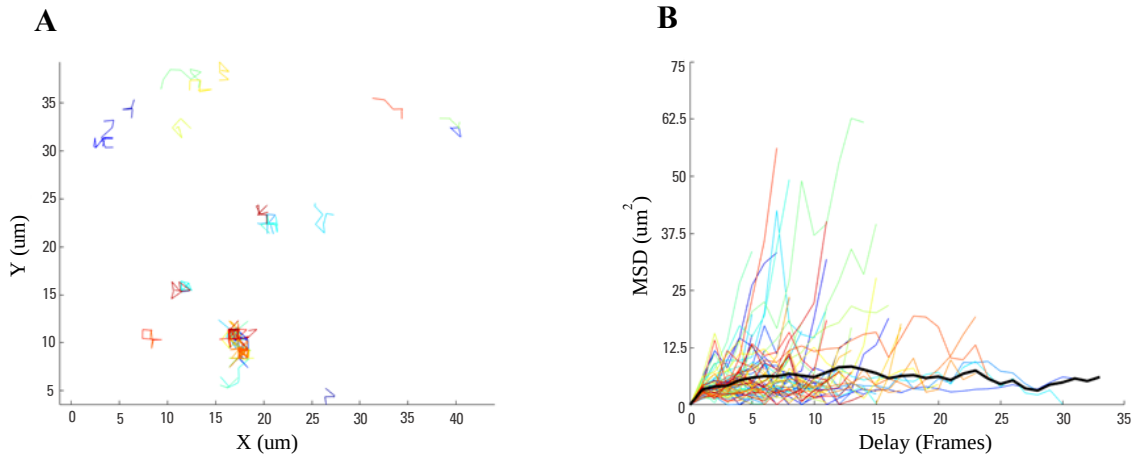

Figure 4.29- (A)Representative individual trajectories within the vesicle edge. *(B) Mean-squared displacements (MSDs) of labelled DNA molecules within the vesicle surface region with 33-time steps (1 s) for 65 tracks longer than 8 frames. Black bold line corresponds to ensemble-average over all 65 measured trajectories.*

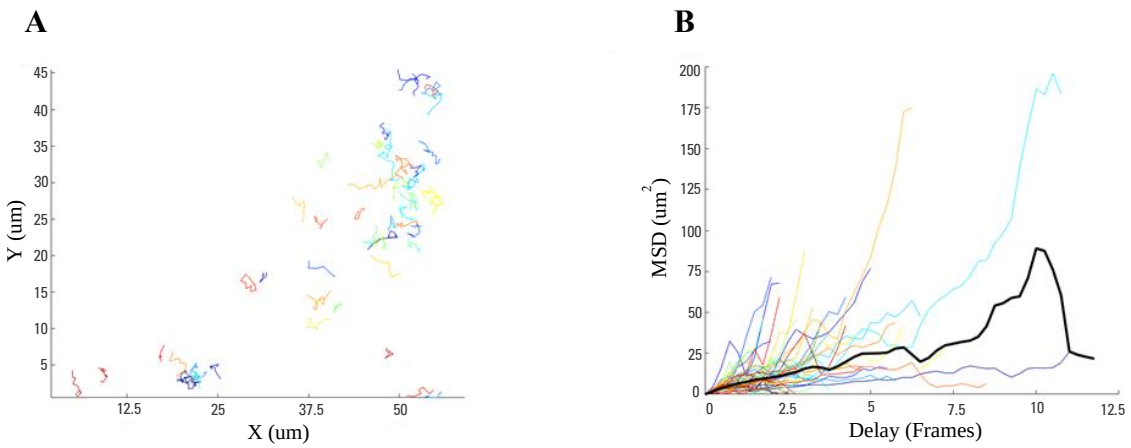

Figure 4.30- (A) Representative tracks with 48-time steps (1.44 s) outside GUV barriers. *(B) The MSDs of the fluorescent-labelled DNA particles were calculated as a function of time delay (t = frames × 0.03 s), for trajectories longer than 8 frames. Black curve, average of all 50 trajectories.*

Comparison of the particles' diffusion states between the inner and the outer vesicle surface area, implies an enhanced diffusion rate beyond the vesicles' barriers, D = 8.762e-02 (with 95% confidence interval [7.062e-02 – 1.062e-01] $\mu m^2 s^{-1}$, n = 50 trajectories) (Fig. 4.31 B), relative to the inner vesicle plane, D = 1.776e-02 (with 95% confidence interval [1.112e-02 – 2.595e-02] $\mu m^2 s^{-1}$, n = 65 trajectories) (Fig. 4.31A), despite the fact that the outcome does not reach statistical significance as estimated by a two sample t-test.

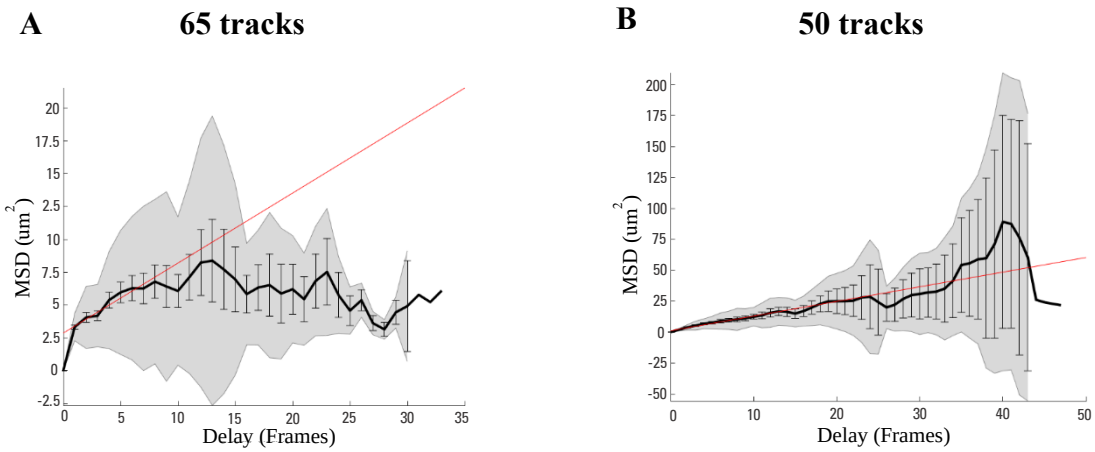

Figure 4.31- Average squared displacement of (A) sixty-five-particle and (B) fifty-particle trajectories with weighted linear fits (red lines). *((A) Mean fluorophore displacement is characterized by the lateral diffusion constant D = 1.776e-02 (with 95% confidence interval [1.112e-02 – 2.595e-02] $\mu m^2 s^{-1}$, n = 65 trajectories) for the species moving within the vesicle structure. (B)The 2D diffusion coefficient for the tracers outside the vesicle territory was estimated to be D = 8.762e-02 (with 95% confidence interval [7.062e-02 – 1.062e-01] $\mu m^2 s^{-1}$, n = 50 trajectories). D estimate is derived from the applied fit designated with the red straight line.*

The non-significant difference of the lateral diffusion constants between the two regions could denote an intermembrane gap allowing free species exploration. The inference of inter-bilayer distance can be further corroborated by the focal plane difference between the well-focused diffusing molecules and the ill-defined vesicle perimeter (**Supplementary Movie S4.8**) suggesting GUV suspension/hovering over the DIB membrane layer.

4.3.9.2 Single-molecule Diffusive Modes in and out of the Vesicle Territory in (1% w/w) DOPG composed DIB and GUV

Even if a small cleft was created between the two contiguous membranes due to the emerging repulsive forces, still DNA doublexes were bound to diffuse only along the mutually shared (droplet-vesicle) territorial area delimited by the vesicle's perimeter. Such a condition imposes dye mobility spatial obstruction within the vesicle's boundaries affecting particles' dynamics. Such a supposition is based on the fact that the MSD exponent α, within the physical constraints of the GUV was α = 0.72 +/- 0.26 (N = 15) (Fig. 4.32A) revealing a corralled propensity. Therefore, this anomalous sub-diffusion modality could potentially be due to caging formed by the structural margins of the vesicle's edge[46].

However, closer inspection of individual trajectories inside the GUV barriers unveils a bimodal character with 60% of the particles (9 out of 15) exhibiting an α slope below 1,

(subjected to anomalous sub-diffusion), while the rest 40% (6 out of 15) appearing to diffuse with Brownian movement (α exponent value of 1 inside the confidence interval).

Conversely, a Brownian diffusive process, with α = 0.98 +/- 0.28 (N = 40)) (Fig. 4.32B), was demonstrated in the outer vesicle domain, as it was theoretically devoid of space-based hindrances. In these hypothetically unobstructed DIB surroundings, beyond the vesicle perimeter, a more heterogeneous lateral motion profile was encountered. Specifically, the majority of the tracers, 65% (26 particles over 40) displayed a slope of 1 (inside the confidence interval), which seems to have played a dominant role in determining the α exponent value of the collective molecule behaviour. The motion of 22.5% (9 over 40) of the species was hindered with α < 1 and 12.5% (5 particles over 40) demonstrate a super-diffusive process.

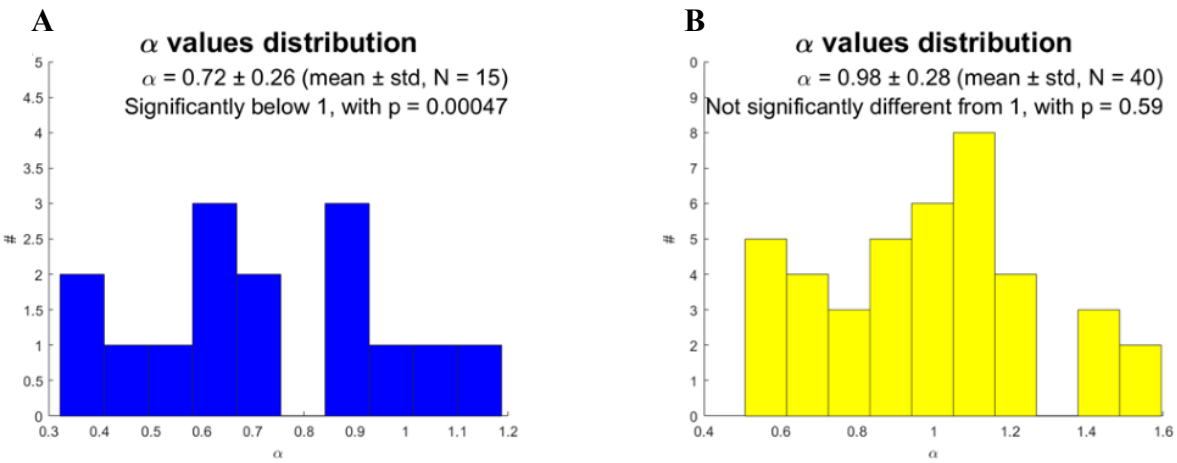

Figure 4.32- Histogram of α for (A) 15 and (B) 40 species, inside and outside the vesicle's margin, respectively*, from 1 dataset each.*

Emergence of super-diffusion in the DIB membrane could potentially be caused by bulk-mediated diffusion upon which membrane attached molecules dissociate from the bilayer and perform three-dimensional random walks until they return to the membrane again and readsorb at a new location. Negatively charged DNA linkers diffusing on similarly charged membrane leaflet can undergo alternate phases between two-dimensional and

three-dimensional diffusion with the latter exhibiting a much faster rate than diffusion on the lipid bilayer since these excursions into the bulk are seen as long jumps in the two-dimensional trajectories. Therefore, these hopping events can allow membrane anchored particles to explore large areas in a short time resulting in super-diffusive modes[56].

4.3.9.3 FRET Efficiency in the (1% w/w) DOPG Composed Vesicle Surface Area Encapsulated in (1% w/w) DOPG Containing DIB

Searching for FRET signals within the vesicle domain as an indication of interconnected juxtaposed membranes, fluorescence emission from the donor-labelled (Cy3-green) and acceptor-labelled (Cy5-red) DNA was imaged by total internal reflection fluorescence (TIRF) microscopy. In superimposed donor and acceptor videos (Fig. 4.33Ai, Aii) and (**Supplementary Movie S4.7B**), diffusive spots, from the GUV region, were observed to shift from acceptor (red) to donor (green) (Fig. 4.33Bi, Bii) consistent with FRET termination.

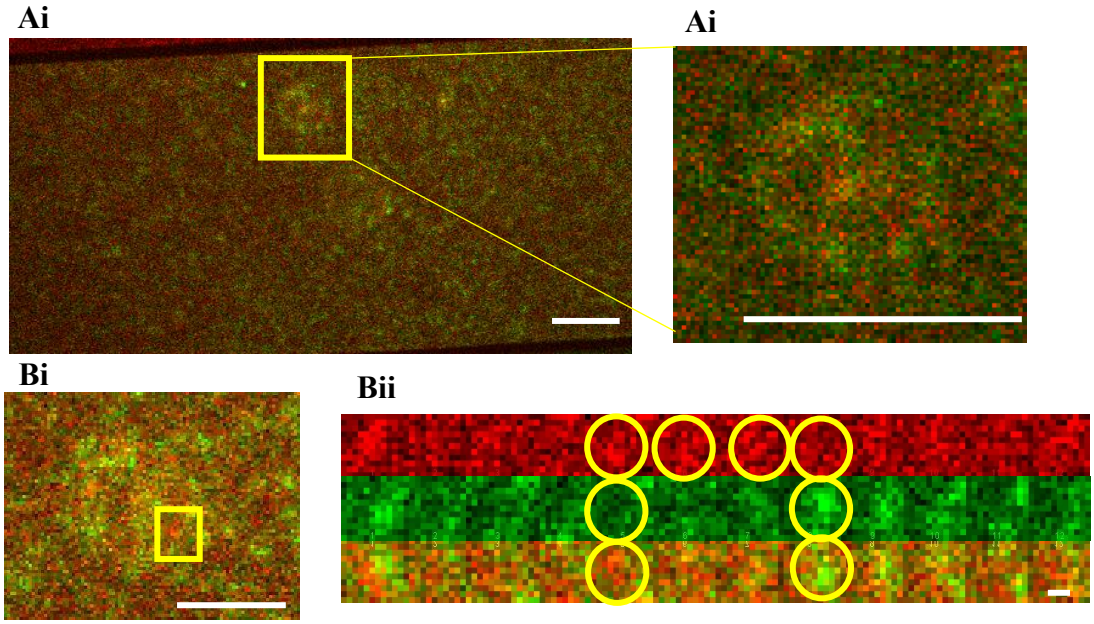

Figure 4.33- (Ai) Overlaid donor (green) and acceptor (red) channels of DIB-encapsulated GUV both mutually containing 1% (w/w) DOPG. *(Aii) Magnified scale of the vesicle domain on the right. Scale bars: 10 μm. (B) FRET manifestation within the vesicle perimeter possibly indicates annealed DNA complements in this intermembrane gap. (Bi) Single-molecule FRET depicted in the closeup snapshot (enclosed red spot). (Bii) Donor (Cy3-green), acceptor (Cy5-red) and superimposed channels show temporal fluctuations in the hybridized DNA species. FRET cessation is observed between frames 7 and 8, where the spot transitions from red to green. Scale bars: 5 μm and 1 μm, respectively.*

The mean FRET efficiency of 27 single FRET spots (N = 27) extracted from the vesicle surface area was E = 0.76 ± 0.17 for the sensitized emission approach (Fig. 4.34A) and E = 0.72 ± 0.17 for the donor dequenching method (Fig. 4.34B). A roughly 15% FRET efficiency attenuation in comparison to the surface immobilized single donor and acceptor FRET pairs (N = 104) (***Fig. 3.23, Chapter 3***), could be associated with the overstretched dsDNA evoked by electrostatic repulsion forces surfacing from anionic DNA polymer and a like-charged membrane[57].

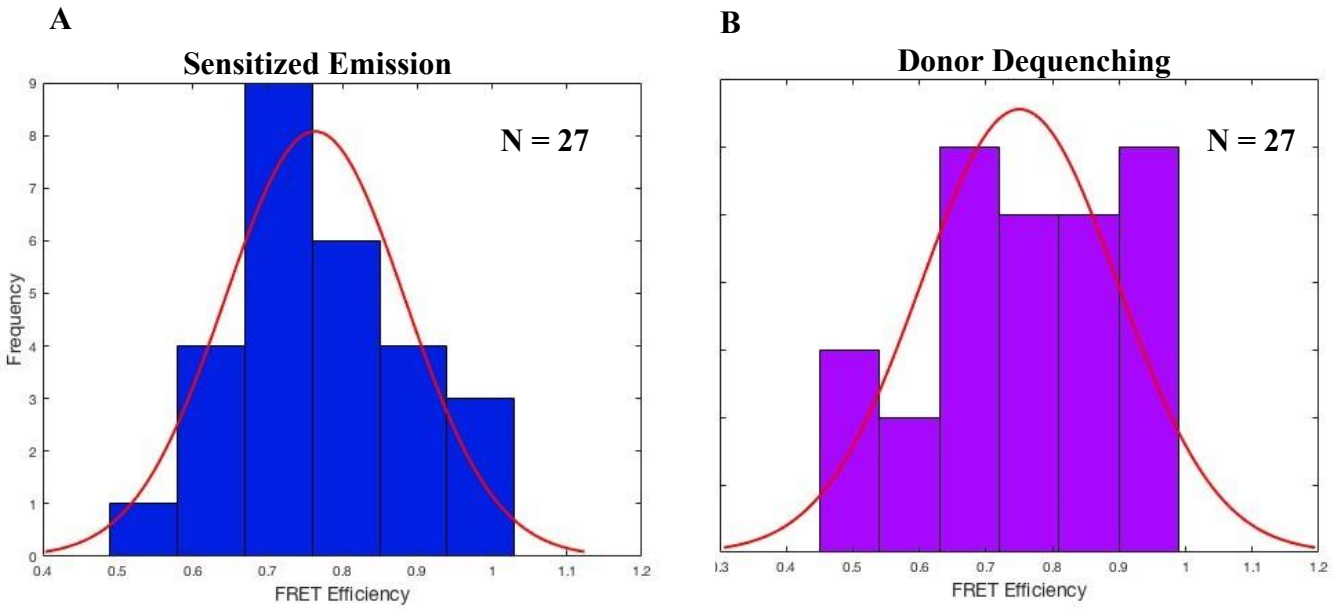

Figure 4.34- FRET efficiency histograms constructed from the trajectories of 27 DNA pairs within the vesicle domain. *The Gaussian curve is centred at (A) E = 0.76 ± 0.17 for the sensitized emission approach and at (B) E = 0.72 ± 0.17 for the donor dequenching method.*

4.4 Discussion

Our model development dramatically reduces the crowded cell membrane milieu by introducing easily controllable synthetic components including two well-characterized and versatile constructs, DIB and GUVs, interconnected via membrane-anchored nucleic acid moieties.

The experimental work presented herein shows that the essential building blocks for the biomimetic model fabrication were manufactured. Both DIB (Fig. 4.5, 4.6) and GUV artificial lipid membranes (Fig. 4.7) were generated, and the internally labelled complementary single DNA strands, required for their coupling, were successfully integrated in DIB's inner (Fig. 4.9) and GUV's outer membrane leaflets (Fig. 4.9) via cholesterol embedded anchors.

The initial endeavour to build the dual membrane model with mere zwitterionic headgroups (DPhPC), at neutral pH, in the presence of NaCl, exposed the electrostatic interfacial properties that engendered attractive inter-bilayer forces ostracizing DNA-mediated bridges from the intermembrane space (Fig. 4.11 and 4.12).

Two different experimental interventions targeting DIB-GUV bilayer detachment, involved either (10% w/w) PEG lipid incorporation in the droplet inner surface (Fig. 4.18), or (1% w/w) ionic lipid (DOPG) insertion in both adjoining membranes (outer GUV surface and inner DIB leaflet) (Fig. 4.26). In both cases, membrane dissociation was evident, as manifested through (a) single-molecule MSD analysis, where diffusion coefficients obtained from the trajectories of individual membrane integrated labelled DNA species of both DOPG (Fig. 4.31) and PEG containing model systems (Fig. 4.22) exhibited non-significant differences between inner and outer vesicle territories, but mainly through (b) intermembrane FRET occurrence. Specifically, FRET efficiency for the DOPG containing construct was assessed at $E = 0.76 \pm 0.17$ (based on the sensitized emission approach) and $E = 0.72 \pm 0.17$ (based on the donor dequenching method) (Fig. 4.33, 4.34 A,B). For

the PEG composed DIB bilayer, FRET efficiency was a little lower, giving values of E = 0.7 ± 0.19, (as derived from the sensitized emission method), and E = 0.69 ± 0.21 (as calculated with the donor dequenching method) (Fig. 4.24, 4.25AB).

More readily trackable and higher FRET signals obtained from the DOPG doped GUVs and DIBs relative to the PEG-grafted droplets gives an edge on the anionic lipid containing model, directing its use for the artificial model engineering. Given its ~15% attenuated FRET efficiency in comparison to the surface immobilized hybridized FRET pairs (N=104) (***Fig. 3.23, Chapter 3***), potentially due to the overwinding dsDNA conformation induced by repulsion forces in DOPG-carrying membranes, an optimization regime is followed in the stepwise synthesis and upgrade of the miniaturized two-membrane assembly. This regime entails inclusion of a smaller amount of DOPG in the total lipid concentration of the juxtaposed membranes of the system, within the range of 0.2%-0.5%, instead of 1%, which was used in this experimental setup. Anionic lipid concentration reduction is expected to mitigate repulsion forces in DOPG-doped membranes, while at the same time preserving intermembrane distance without intensifying DNA overstretching, potentially accountable for decreased FRET signals.

4.5 References

1. Bendix, P.M.P., and Stamou, D. *Quantification of nano-scale intermembrane contact areas by using fluorescence resonance energy transfer. PNAS*, 2009. **106**(30).
2. Alakoskela, J.M., Rudnicka, D., et al. *Mechanisms for size-dependent protein segregation at immune synapses assessed with molecular rulers. Biophysical Journal.*, 2011. **100**(12): p. 2865-2874.
3. Dharani, K. *The biology of thought: A neuronal mechanism in the generation of thought - A new molecular model.* 2014: Academic Press.
4. Baigl, D. *Systems Biomimetism: Artificial Cells in a Living World, Living Cells in an ArtificialWorld Proc. Natl. Acad. Sci. USA*, 2009. **106**(30).
5. Yu, C., Law, J.B.K., Suryana, M., and Sheet, M.P. *Early integrin binding to Arg-Gly-Asp peptide activates actin polymerization and contractile movement that stimulates outward translocation. PNAS*, 2011. **108**(51).
6. Sonnino, S. and Prinetti, A. *Lipids and membrane lateral organization. Front Physiol.*, 2010. **1**: p.153.
7. Chiantia, S. and London, E. *Lipid Bilayer Asymmetry*. 2013: Springer Berlin Heidelberg. 1250-1253.
8. Gorlewicz, A., and Kaczmarek, L. *Pathophysiology of Trans-Synaptic Adhesion Molecules: Implications for Epilepsy. Frontiers in cell and developmental biology*, 2018. **6**(119).
9. Missler, M., Südhof, T.C., and Biederer, T. *Synaptic cell adhesion. Cold Spring Harbor perspectives in biology*, 2012. **4**(4).
10. Moga A, Dimova, R., and Robinson T. *Optimization of the Inverted Emulsion Method for High-Yield Production of Biomimetic Giant Unilamellar Vesicles. Chembiochem*., 2019. **20**(20).

11. Dimova, R., Bezlyepkina N., Nikolov, V., Riske, K.A., and Lipowsky, R. *A practical guide to giant vesicles. Probing the membrane nanoregime via optical microscopy. J Phys Condens Matter.*, 2006. **18**(28): p. 1151-76.
12. Walde, P., Cosentino, K. Engel, H. and Stano, P. *Giant Vesicles: Preparations and Applications. ChemBioChem.*, 2010. **11**(7): p. 848-865.
13. Dimova., R. *Giant Vesicles and Their Use in Assays for Assessing Membrane Phase State, Curvature, Mechanics, and Electrical Properties. Annual review of biophysics*, 2019. **48**: p. 93–119.
14. Pereno, V., Carugo, D., Bau, L., Sezgin, E., Bernardino de la Serna, J., Eggeling, C. and Stride, E. *Electroformation of Giant Unilamellar Vesicles on Stainless Steel Electrodes. ACS Omega,* 2017. **2**(3): p.994-1002.
15. Rosholm, K.R., et al. *Activation of the mechanosensitive ion channel MscL by mechanical stimulation of supported Droplet-Hydrogel bilayers*, in *Sci Rep*., 2017.
16. Thompson, J.R., et al. *Enhanced stability and fluidity in droplet on hydrogel bilayers for measuring membrane protein diffusion. Nano Lett.*, 2007. **7**(12): p. 3875-8.
17. Bi, H., et al. *Electroformation of giant unilamellar vesicles using interdigitated ITO electrodes. Journal of Materials Chemistry A*, 2013. **1**(24): p. 7125-7130.
18. Sengel, J.T., and Wallace, M.I. *Imaging the dynamics of individual electropores. PNAS*, 2016. **3**(19): p. 5281 - 5286.
19. Andersson, M., et al. *Vesicle and bilayer formation of diphytanoylphosphatidylcholine (DPhPC) and diphytanoylphosphatidylethanolamine (DPhPE) mixtures and their bilayers' electrical stability - ScienceDirect. Colloids and Surfaces B: Biointerfaces*, 2011. **82**(2): p. 550-561.
20. Lipids, A.P. *1,2-dipalmitoyl-sn-glycero-3-phosphoethanolamine-N-[methoxy(polyethylene glycol)-2000] (ammonium salt)*. 2020.
21. Lipids, A.P. *1,2-dioleoyl-sn-glycero-3-phospho-(1'-rac-glycerol) (sodium salt)*. 2020.
22. Frolov, V.A., Shnyrova, A.V., and Zimmerberg, J. *Lipid polymorphisms and membrane shape. Cold Spring Harb Perspect Biol.*, 2011. **3**(11): p. a004747.

23. Leptihn, S., et al. *Constructing droplet interface bilayers from the contact of aqueous droplets in oil. Nature Protocols*, 2013. **8**: p. 1048-1057.
24. Jaqaman, K.L., Mettlen, D., Kuwata, M., Grinstein, H., Schmid, S., and Danuser, G., *Robust single particle tracking in live cell time-lapse sequences. Nature Methods,* 2008. **5**(8): p. 695-702.
25. Schindelin, J., et al. *Fiji - an Open Source platform for biological image analysis. Nat Methods*, 2012. **9**(7).
26. Dijkman, P.M., Castell, O.K., Goddard, A.D. et al. *Dynamic tuneable G protein-coupled receptor monomer-dimer populations. Nat Commun.*, 2018. **9**:1710.
27. Jean-Yves, T. *TrackMate documentation.* 2016.
28. Michalet, X. *Mean Square Displacement Analysis of Single-Particle Trajectories with Localization Error: Brownian Motion in Isotropic Medium. Phys Rev E Stat Nonlin Soft Matter Phys.*, 2010. **82**((4 Pt 1):041914).
29. Huang, F., Watson, E., Dempsey, C., and Suh, J. *Real-Time Particle Tracking for Studying Intracellular Trafficking of Pharmaceutical Nanocarriers. Methods Mol Biol.,* 2013. **991**: p. 211-223.
30. Silvaa, S.L.D., Judismar T., Juniora, G., Silvab, R.L.D., Emilson, V. R. and Leald, F.F. *An alternative for teaching and learning the simple diffusion process using Algodoo animations. arXiv*:1412.6666 [physics.ed-ph], 2015.
31. Ernst, D., and Köhler, J. *Measuring a diffusion coefficient by single-particle tracking: statistical analysis of experimental mean squared displacement curves. Phys Chem Chem Phys.*, 2013. **15**(3): p. 845-9.
32. Trigger, S.A., et al. *Mean-squared displacements for normal and anomalous diffusion of grains. J. Phys.*: Conf. Ser. 11 004, 2005.
33. Barriga, H.M.G., et al. *Droplet interface bilayer reconstitution and activity measurement of the mechanosensitive channel of large conductance from Escherichia coli. J R Soc Interface*, 2014. **11**(98).
34. Bayoumi, M., et al. *Multi-compartment encapsulation of communicating droplets and droplet networks in hydrogel as a model for artificial cells. Scientific Reports*, 2017. **7**: p. 1-11.

35. Hąc-Wydro, K., and Dynarowicz-Łątka, P. *Biomedical applications of the Langmuir monolayer technique. Annales UMCS, Chemistry*, 2008. **63**: p. 47-60.
36. Bayley, H., et al. *Droplet interface bilayers. Mol Biosyst*, 2008. **4**(12): p. 1191-208.
37. Karamdad, K., Bolognesi, G., Friddin, M.S., Law, R.V., Brooks, N.J., Ces, O., Elani, Y. *Engineering thermoresponsive phase separated vesicles formed via emulsion phase transfer as a content-release platform. ChemSci.*, 2018. **9**: p. 4851-4858.
38. Bolognesi, G., Friddin, M.S., Salehi-Reyhani, A. et al. *Sculpting and fusing biomimetic vesicle networks using optical tweezers. Nat Commun.*, 2018. **9**(1882).
39. Chen, H., Puhl, H.L., Koushik, S.V., Vogel, S.S., and Ikeda, S.R. *Measurement of FRET Efficiency and Ratio of Donor to Acceptor Concentration in Living Cells. Biophysical Journal*, 2006. **91**(5): p. 39-41.
40. Michalet, X. *Mean square displacement analysis of single-particle trajectories with localization error: Brownian motion in an isotropic medium. Phys Rev E Stat Nonlin Soft Matter Phys*., 2010. **82**(4 Pt 1):041914.
41. Riahi, M.K., Qatt*an*, I.A., Hassan, J. and Homouz, D. *Identifying short- and long-time modes of the mean-square displacement: An improved nonlinear fitting approach. AIP Advances*, 2019. **9**(055112).
42. Saxton, M.J. *Anomalous Subdiffusion in Fluorescence Photobleaching Recovery: A Monte Carlo Study. Biophysical Journal*, 2001. **81**(4): p. 2226-2240.
43. Douglas, S., Forstner, M.B., and Käs, J.A. *Apparent Subdiffusion Inherent to Single Particle Tracking. Biophysical Journal*, 2002. **83**(4): p. 2109-2117.
44. Jeon, J., Leijnse, N., Oddershede, L.B. and Metzler, R. *Anomalous diffusion and power-law relaxation of the time averaged mean squared displacement in worm-like micellar solutions. New Journal of Physics*, 2013. **15**.
45. Matysik, A., and Kraut, R.S. *TrackArt: the user friendly interface for single molecule tracking data analysis and simulation applied to complex diffusion in mica supported lipid bilayers. BMC Res Notes*., 2014. **7**(274).
46. Metzler, R., Jeon, J.H., and Cherstvy, A.G. *Non-Brownian diffusion in lipid membranes: Experiments and simulations. Biochimica et Biophysica Acta*, 2016. **1858**: p. 2451–2467.

47. Otten, M., Nandi, A., Arcizet, D., Gorelashvili, M., Lindner, B., and Heinrich, D. *Local Motion Analysis Reveals Impact of the Dynamic Cytoskeleton on Intracellular Subdiffusion. Biophys J.*, 2012. **102**(4): p. 758-767.
48. Tabarin, T., Martin, A., Forster, R. and Keyes, T.E. *Poly-ethylene glycol induced super-diffusivity in lipid bilayer membranes. Soft Matter*, 2012. **8**(33): p.8743-8751.
49. Tinevez, J.Y. *The NEMO Dots Assembly: Single-Particle Tracking and Analysis. In: Miura K., Sladoje N. (eds) Bioimage Data Analysis Workflows. Learning Materials in Biosciences.*, 2020.
50. Kepten, E., Weron, A., Sikora, G., Burnecki, K., and Garin,Y. *Guidelines for the fitting of anomalous diffusion mean square displacement graphs from single particle tracking experiments. PLoS One*, 2015. **10**(2).
51. Mikuchi, M., and Zhou, Y. *Electrostatic Forces on Charged Surfaces of Bilayer Lipid Membranes. SIAM Journal on Applied Mathematics*, 2014. **74**(1): p. 1-21.
52. Karpushkin, E. *Re: Why is poly ethylenglycol (PEG) so hydrophylic?* 2013: https://www.researchgate.net/post/Why_is_poly_ethylenglycol_PEG_so_hydrophylic/5232daa7cf57d70357c47d6f/citation/download.
53. Technology, C.U.O. *New insight into how DNA is held together by hydrophobic effects. ScienceDaily*, 23 September 2019.
54. Loura, L.M. *Simple estimation of Förster Resonance Energy Transfer (FRET) orientation factor distribution in membranes. Int J Mol Sci*., 2012. **13**(11): p. 15252-15270.
55. Shrestha, D., Jenei, A., Nagy, P., Vereb, G., and Szöllősi, J. *Understanding FRET as a research tool for cellular studies. Int J Mol Sci*., 2015. **16**(4): p. 6718-6756.
56. Campagnola, G., Nepal, K., Schroder, B.W., Peersen, O.B., and Krapf, D. *Superdiffusive motion of membrane-targeting C2 domains. Sci Rep*., 2015. **5**(17721).
57. Arnott, P.M., Joshi, H., Aksimentiev, A., and Howorka, S. *Dynamic Interactions between Lipid-Tethered DNA and Phospholipid Membranes. Langmuir*, 2018. **34**(49).

Chapter 5: Establishing Chemically Mediated Communication between DIB and GUV Chambers

5.1 Introduction

One of the main goals of bottom–up synthetic biology is to establish functional semi-permeable compartmentalization in and between synthetic cells that can mimic autonomous signalling between compartments[1].

Desiring to establish chemically mediated communication in the interconnected double membrane model with stimuli-triggered biochemical responses, we develop an actin-based system with chemically inducible control of actin polymerization inside DIB-encapsulated GUVs.

Initiation of vesicle actin polymerization is instigated by intercompartmental chemical gradient-dependent flux of salt and ATP content, via embedded alpha-hemolysin (aHL) nanopores in both DIB and GUV membranes. These processes are elaborated in ***5.1.10 Chapter's Aims***.

Intercompartmental communication in this artificial system is also validated by chemically and electrochemically driven Ca^{2+} ion relocation through DIB and GUV bilayer integrated aHL nanopores instigating fluorescence emission (detailed in ***5.1.10 Chapter's Aims***).

5.1.1 Actin Abundance in Eukaryotic Cells

Actin, with a molecular weight of ~42 kDa, is a highly abundant protein (10-100 micromolar on average), in all eukaryotic cells[2]. Its affluence becomes more comprehensive if we consider that a typical liver cell has approximately half a billion (0.5×10^9) actin molecules, whereas the insulin receptor molecules are 20.000. The actin predominance in muscle and nonmuscle cells, with 10% and 1-5% by weight of the total cell protein, respectively, is a common cell trait, since it forms structures that span extended cellular spaces[3].

5.1.2 Actin Filament Structure

The building block of actin is the globular actin monomer, G-actin. These globular monomers congregate via weak noncovalent interactions to form actin filaments (AFs), which is a two-stranded asymmetrical helical polymer with a diameter between 7 and 9 nm[3]. This asymmetrical quality enables distinct binding specificities at each tail end; one end displays a dent and is referred to as the barbed end or “plus end”, and the other one, which resembles an arrowhead, is dubbed pointed end or “minus end” [4](Fig. 5.1).

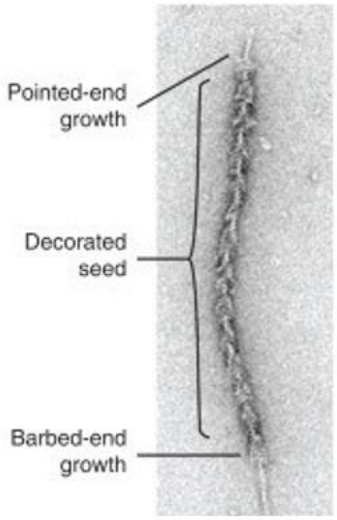

Figure 5.1- F-actin structure. *Electron micrograph of a negatively stained actin upon polymerization, where the pointed and barbed ends are demonstrated. Source:[5].*

In the course of actin filament turnover, the balance of G and F-actin is in a state of continuous flux, with the F-actin polymer rapidly constructing and deconstructing itself. During this process, globular subunits (G-actin) preferentially join the barbed end of the filamentous actin and older units are detached from the pointed end[5].

5.1.3 Actin Polymerization

For actin monomers to polymerize, they bind adenosine triphosphate (ATP) tightly, in the presence of Ca^{2+} or Mg^{2+}. Any of these divalent cations connects with the β- and γ-phosphates of ATP, securing a stable interaction with the protein[6].

Polymerization is a spontaneous process under physiological salt conditions requiring both monovalent and divalent cations in the buffer, which enhance subunit-subunit interaction in the filament formation[7]. This spontaneous mechanism begins with a lag period that is strongly associated with actin monomer concentration. Computer modeling has shown that initiation of polymerization, or preferably nucleation, is undermined by two

unfavorable steps: a) dimer and b) trimer formation. Although these association reactions are fast, dimers and trimers are very unstable, as dimers dissociate at ~10^6 sec^{-1}, and trimers dissociate (a subunit) at 100 sec^{-1} [8, 9]. Thus, dimer and trimer presence in a polymerization reaction is at exceedingly low concentrations, and only after the addition of the fourth subunit, the oligomer becomes stable enough, presumably because of the presence of the full complement of intermolecular contacts, to elongate at the same rate as long filaments[5].

Actin polymer is in a non-equilibrium state, which is attributed to its ATPase activity. This means that as an enzyme, it catalyzes the decomposition of ATP into ADP and a phosphate ion (P_i). This random ATP hydrolysis reaction transpires on the F-actin, rapidly after polymerization[5, 10]. Subsequently, the phosphate slowly dissociates, leaving ADP–actin[5], and finally, ADP disengages from ADP–actin monomers with a rapid replacement by ATP (Fig. 5.2)[5].

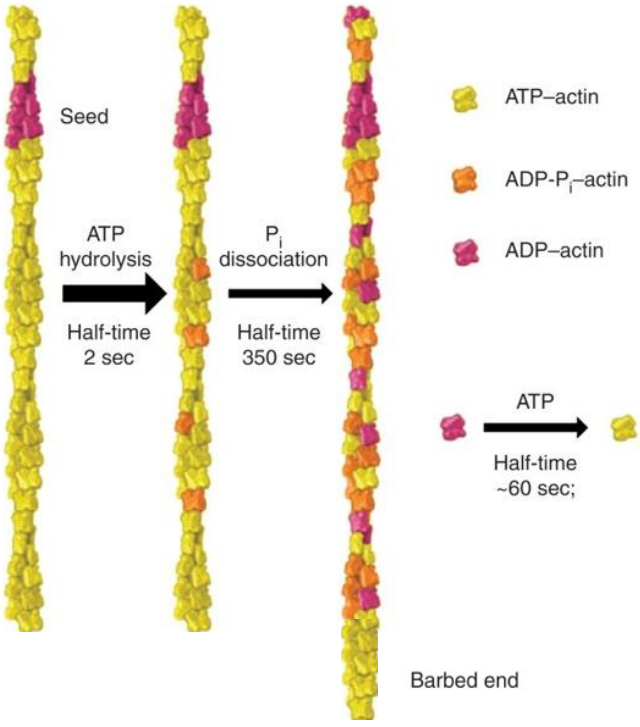

Figure 5.2- ATP-ADP reactions of actin. *The cartoon displays actin filament growth on both ends of an ADP–actin seed (left). Hydrolysis of the bound ATP to the polymerized subunits of ADP phosphate (P_i) occurs over time (middle-orange) with a gradual dissociation of the phosphate (P_i), leaving ADP–actin (right-pink). Finally, as the ADP disconnects from ADP–actin monomers, it is replaced by ATP (yellow). Source:[5].*

5.1.4 Role of Filamentous Actin in the Cell

In many cases actin filaments may bundle together with other actin filaments, or with other motor proteins (e.g., myosin superfamily), forming an elaborate network known as the actin cytoskeleton. This assembly primarily occurs at or near the plasma membrane generating a high actin filament density, known as the cell cortex, which determines movement, stiffness, and shape of the cell surface[11].

Furthermore, actin is involved in the transduction of mechanical signals, by transiently interacting with the plasma membrane, in the lateral movement of transmembrane proteins[11] and in the generation of intracellular forces implicated in various cellular operations such as cell motility, vesicle and organelle movement, cell division, cytokinesis, muscle contraction, and preservation of cell junctions[12].

5.1.5 Actin Cytoskeleton Reconstitution at or near Surfaces in Vitro

Studies of actin filament dynamics in pure protein solutions or in cell extracts have been underway for decades. A breakthrough in the field occurred at the turn of the century, when dynamic F-actin networks were successfully recreated on surfaces, with the intention to study and emulate cell shape changes and protrusions developing at the plasma membrane in a controlled manner[13].

Actin networks were directly immobilized to model membranes, such as synthetic supported lipid bilayers (SLBs), offering a more physiological imitation of the membrane-

bound cytoskeleton. This actin filament attachment was accomplished through magnesium ion (Mg^{2+}) use, which binds to both the negatively charged AF and phospholipids[14], or via biotin-streptavidin linkage, where both filamentous actin and lipids were biotinylated[15, 16].

At a later time point, in order to achieve a more naturally mediated interaction, experiments on actin-membrane interplay were extended to outer surfaces of giant unilamellar vesicles (GUVs)[17].

Around 20 years ago another great advance involved dynamic actin structure transferring to the inner compartment of a liposome via the inverted emulsion technique. This approach showed that the membrane-associated actin layer was the determinant factor for the liposome's mechanical properties[18, 19].

Although the encapsulation efficiency of multiple cytoskeletal components had been difficult, more recent studies, utilizing several methodological advances, showed successful actin network assembly on inner GUV membranes[20-23], despite low-throughput and reproducibility[24]. Overall, research on actin network-on-liposome are of great importance as they unveil information on actin-lipid bilayer interplay and actin-based deformations[13].

Unequivocally, cross-talk between different cytoskeleton substructures are always essential to be placed in a physiological context, yet, *in vitro* reconstitution studies are also needed to disentangle the inputs of signaling mechanisms and physical interactions[25].

This reductionistic approach that allows dissection of cellular phenomena is subject to the question of how "physiologically" relevant cell behaviour is. The fact that modern reconstitution experiments focus on studying a functional unit, instead of an individual molecule, and thus, present a more holistic view of a complex cellular process recreated *in vitro*, and render the phenomenon under investigation accessible to rigorous quantitative analysis, should be regarded as a means to refine questions and conceive new experiments to be executed in cells to test speculations[25].

5.1.6 α-Hemolysin (aHL)

α-Hemolysin or alpha-toxin (aHL), secreted by Staphylococcus aureus as a single-chain, 33kDa monomer [26], was the first bacterial exotoxin to be recognized as a pore former[27].

It is a β-barrel pore-forming, heptameric cytotoxin[28], involved in a broad range of biological activities. Specifically, it is a proven virulence factor in numerous animal infection models, as it has shown to disrupt epithelial barriers like the skin (dermonecrosis), the cornea (keratoconjunctivitis) and the lung (pneumonia)[29].

α-toxin is secreted as a water-soluble monomer, where at low concentrations (less than 100 nM), attaches to specific plasma membrane receptors of eukaryotic host cells [26, 30], including human platelets, rabbit erythrocytes, monocytes and endothelial cells[27]. At higher concentrations (>1 μmol/l), the toxin additionally binds, via non-specific absorption, to phospholipids containing choline headgroups (phosphatidylcholine and sphingomyelin)[31]. In this manner, it is membrane-damaging to both cells with deficient number of receptors and protein-free artificial lipid bilayers[27].

Upon binding, alpha-toxin individual monomers collide via lateral diffusion to form a heptameric pre-pore, which is still non-lytic [32]. However, in the presence of phosphocholine headgroups and cholesterol, the pre-pores usually form domains (lipid rafts) in the plasma membranes of eukaryotic cells[33], and rapidly assemble functional transmembrane pores[26].

During this process, α-hemolysin monomer, comprised of two beta-sheet structures, penetrates the plasma membrane, and undergoes oligomerization into a homo-oligomeric ring. Finally, all the monomers together form an aqueous transmembrane channel (beta-barrel)[34] that inserts into the lipid bilayer forming a discrete transmembrane pore of effective diameter 1 to 2 nm (Fig. 5.3)[26].

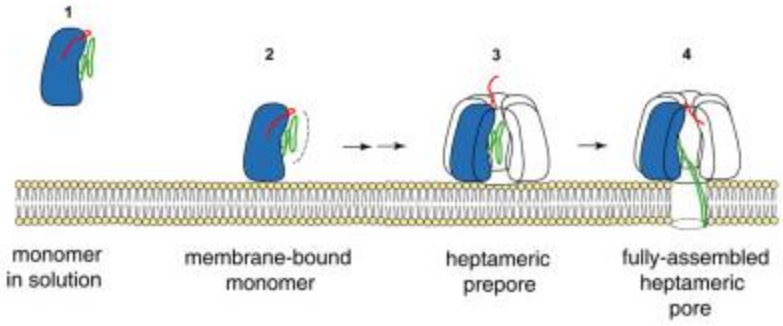

Figure 5.3- Proposed assembly pathway for α-hemolysin. *Image taken from:* [32].

5.1.6.1 Heptamer Structure

The pore is lined by amphiphilic beta-sheets, where one surface interfaces with lipids and the other one repulses apolar membrane components, creating an aqueous passage[27]. This pore formation facilitates water entry across the membrane and is a passageway permeable for a variety of cations like Ca^{2+}, Na^{+}, K^{+} [35, 36] and small organic molecules like ATP [37].

Thus, the detrimental effects of alpha-toxin originate not only from the annihilation of susceptible targets, but also, from the secondary cell responses instigated by Ca^{2+} influx through the pores[27].

The heptameric pore formed by aHL exhibits a mushroom-shaped structure consisting of three chief domains: the cap, the rim, and the stem (Fig. 5.4). The cap domain, which protrudes from the extracellular surface and is highly hydrophilic, is made up of β sandwiches and amino latches contributed by the seven subunits[38, 39].The rim domain, or better the 7 rim domains, located on the underside of the cap, are adjacent if not in direct contact with the outer leaflet of the cell membrane (Fig. 5.4)[40]. The stem domain, or else the transmembrane domain of the channel, has a β-barrel structure, with each monomer contributing to this configuration by the two antiparallel β-sheets it contains (Fig. 5.4)[32, 41].

The protein measures approximately 10 nm in height, and the ectopic domain is approximately 10 nm wide (Fig. 5.4). The central aqueous channel that spans the height of the protein has a diameter ranging from ~16 to ~46 ˚A[42].

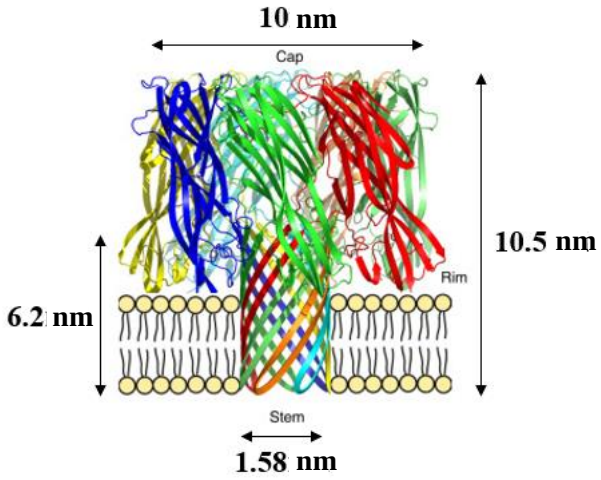

Figure 5.4- Heptameric structure of the aHL channel. *Channel subunits, in the cartoon representation, are shown with different colour each. The lengths/heights of the β-barrel domain and the entire channel are indicated by vertical lines. The horizontal lines display the mean value of the internal diameter of the stem domain and the external diameter of the extracellular cap. Image adapted from:[32].*

5.1.7 Single-Channel Recording Technique

Membrane pore formation and ionic transfer are stochastic processes which can be fully characterized with single-channel resolution[43].

Although patch-clamp recording has revolutionized studies on single-channel current measurements with exquisite resolution, subsequent optical techniques offered capabilities, which cannot be attained by electrophysiological techniques[43].

5.1.7.1 Optical Patch-Clamping Method

Optical patch-clamping technology holds potential as a complement to patch-clamp technique for single-channel recording [44, 45] as it enables visualization of individual ion channel activity [46, 47].

The advantages it displays over electrophysiological techniques lie in its provision of spatial information concerning channel location, applicability to inaccessible channels by a patch-clamp pipette and permission of concurrent recording from several channels[47]. This very promising method utilizes highly sensitive fluorescent Ca^{2+} indicator dyes to detect single channel Ca^{2+} fluorescent transients that emerge from local Ca^{2+} elevations in the vicinity of open membrane channels. Changes of Ca^{2+} concentration around the channel mouth can closely monitor a channel's opening and closing behaviour, whereas more distant signals from the channel present slow and attenuated amplitude due to Ca^{2+} diffusion away from the Ca^{2+}-bound indicator[44].

As thousands of Ca^{2+} ions can flow through an open channel per millisecond and considering that each dye molecule that binds Ca^{2+} can emit thousands of photons, due to its excitation, an enormous signal amplification is observed.

The first demonstrations of single-channel fluorescence signals were provided by Zou et al. [46] and Wang et al. [48], who managed to record simultaneously current flow and Ca^{2+} signals passing through PM channels, bringing into focus this powerful alternative to patch-clamping.

While optical calcium flux experiments are usually conducted in cells or oocytes, simultaneous optical and electrical measurements were also performed in DIBs with integrated α-hemolysin pores, displaying a direct correlation between fluorescence signal and current[49].

Among the different imaging modalities utilized in optical patch-clamping, TIRFM 100 nm optical "section", can afford independent readouts and highly localized signals from

hundreds of channels simultaneously, but its use is strictly restricted to plasma membrane [50].

5.1.8 Electrical Characteristics of DIBs

5.1.8.1 Specific Capacitance

A lipid bilayer membrane can be considered as a biological parallel plate capacitor, which consists of the polar head groups of the lipids, separated by the aligned hydrocarbon lipid tails; together with the attached or embedded proteins, they build an insulating layer/matrix[51].

This is an analogous configuration to a simple circuit device consisting of two parallel conductive sheets, which are separated by a distance d, have a charge density of +σ and −σ, respectively, and extend over an area A.

Upon applied voltage, positive charges are gathered on one side of the capacitor and are balanced out by the negative charge collection on the other side. A resulting static field is formed across the capacitor and the electric field of the two charged plates is given by the following formula (1):

$$E = \frac{\sigma}{\varepsilon} \qquad (1)$$

where ε stands for the dielectric permittivity of the insulating material[42]. The membrane capacitance, therefore, is the electrical capacitance, an inherent characteristic of a biological membrane, and it is expressed in units of Farads (F)[52].

In a DIB, electrical responses can be monitored by inserting a pair of electrodes into the droplets; the active electrode is placed in the DIB, while the ground one is fixed in the agarose as illustrated in Figure 5.5.

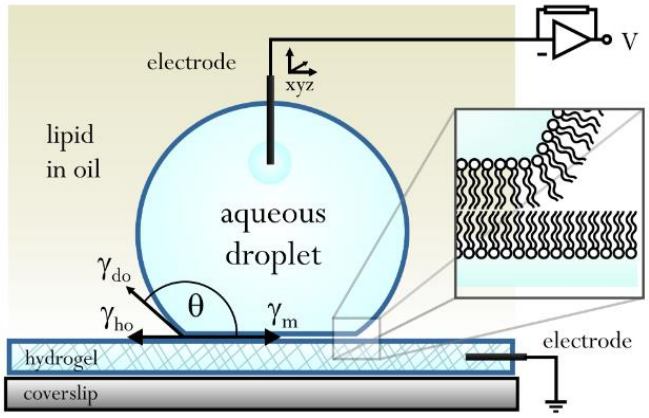

Figure 5.5- Schematic drawing of a Droplet Interface Bilayer (DIB) with a hydrogel substrate, accessible to concurrent optical and electrical measurements. *The droplet is pierced with a 100 μm diameter Ag/AgCl electrode, and the corresponding ground electrode is applied in the agarose, permitting output current measurements under applied voltages, which can be used for total capacitance calculations. Image taken from: [42].*

A voltage change across the capacitor induces a charging current, known as the capacitive current *(I_C)* and for small, applied voltages it is given by the following equation (2):

$$I_c = C\frac{dV}{dt} \qquad (2)$$

where *V* is the voltage and *C* is constant/specific capacitance[42].

Of particular interest as a way of characterizing lipid bilayers is the specific capacitance, C, one of the DIBs electrical features, the value of which is acquired by initially measuring the total capacitance, C_t, from the output current under an applied voltage[53]. Then, the background capacitance, C_0, is subtracted and normalized by the bilayer area, A_b, as presented in the formula (3):

$$C = \frac{(C_t - C_0)}{A_b} \qquad (3)$$

Overall, specific capacitance is a measure of DIBs ability to store charge. It is highly correlated with bilayer thickness[54], scales with the dielectric constants of the solvents and manifests a non-linear dependence on voltage when the voltages applied are large[55, 56].

5.1.8.2 Current–Time Characteristics

The current-time characteristic of DIB pertains to the association of the bilayer output current with the time evolution at a fixed voltage. This approach is used to confirm DIB formation, where an output current increase is monitored, and to probe DIB functionalization, with inserted membrane pores being translated into output current rise, whereas their deactivation, e.g., by pore blockers, is expressed as current decay[55].

5.1.8.3 Current–Voltage Characteristics

The relationship between current and applied voltage across the DIBs, under different conditions, is used to study current-voltage traces of DIBs with pore forming proteins,

such as aHL[55], which effect diminution in bilayer resistance and can rectify current at positive cis potentials.

Moreover, the current-voltage combination is used to probe and distinguish between channel formation via electroporation or protein assembly into the bilayers[57], as it enables comparisons of ion flux through pores. Studies have demonstrated higher current in electroporated DIBs, produced by both calcium and potassium flow, relative to those functionalized with aHL channels, denoting pore size difference, as aHL heptamers have a size of ~0.75 nm[58], whereas electroporated pores are around 1 to 2.5 nm[59].

5.1.9 Calcium as an Indicator of Activity

Calcium (Ca^{2+}) is a ubiquitous intracellular messenger, regulating a diverse range of cellular functions in both excitable and nonexcitable cell types[60-62]. Different approaches have been developed to probe Ca^{2+} changes over time, such as chemical and genetically encoded calcium indicators.

5.1.9.1 Chemical Calcium Indicators

Chemical calcium indicators are composed of a calcium chelator and a fluorophore, and upon calcium binding, the molecule undergoes a conformational change that causes it to emit a photon.

Chemical calcium indicators are grouped into two categories, single wavelength and ratiometric indicators. The ratiometric Ca^{2+} indicators, such as fura-2, mag-Fura-2 (furaptra), Fura-2FF, and BTC[63], when bound to calcium, the peak wavelength of either their excitation or emission curve is shifted. Although they can very accurately quantify Ca^{2+} concentrations in a cell, and be corrected for photobleaching, uneven dye loading and dye leakage happens at the expense of broader spectral bandwidth[64].

Conversely, single wavelength calcium indicators, such as Fluo-2, Fluo-4, Fluo-8, or Cal-520, upon Ca^{2+} binding, display significant Ca^{2+} dependent changes in fluorescence intensity without shifting their excitation or emission wavelengths[64].

The chemical calcium indicators exist in three different forms: salts, dextran-conjugates and acetoxymethyl (AM) esters, with the first two being membrane impermeable and thus, requiring invasive dye loading; an approach commonly used during patch-clamping for single-cell probing.

The AM ester calcium indicator, on the other hand, is membrane permeable, as the AM esters are hydrophobic enough to penetrate the plasma membrane. When fully encompassed in the cell membrane, intracellular esterases cleave the ester moiety and trap the dye within the cytosol.

5.1.9.2 Genetically Encoded Calcium Indicators (GECIs)

The other class, referred to as genetically encoded calcium indicators (GECIs), comes in two kinds, (a) the single wavelength GECIs and the (b) FRET-based ones.

Single wavelength GECIs comprise a Ca^{2+} sensing domain and a single fluorescent protein, whose emission intensity is modified based on Ca^{2+}-free and Ca^{2+}-bound states[65].

Those involving Föster resonance energy transfer (FRET) consist of two fluorescent proteins linked by the Ca^{2+} binding domain. When attached to Ca^{2+}, the fluorescent proteins, expressing donor and acceptor fluorophores, undergo a conformational change, which brings the donor and the acceptor spatially closer together, activating FRET, with light emission being elicited from the acceptor molecule[66].

5.1.10 Chapter's Aims

In a quest to develop more cell-like synthetic materials, with intercommunication capabilities and functional flexibility, the goal of the present work is to establish chemically mediated communication in the interconnected double membrane system with stimuli-triggered biochemical responses.

Cargo (G-actin or Fluo-8)-loaded GUVs, employed for the materialization of the dual membrane assembly, are generated by the EPT method. Incorporation of membrane protein channels, alpha-hemolysin, initially in the GUV bilayer (Fig. 5.6A) and subsequently, in both DIB-GUV membranes (Fig. 5.6C, Fig. 5.7), enables chemical message flow across compartments with measurable ion-dependent fluorescence responses (Fig. 5.7) and induced actin growth in the vesicle lumen (Fig. 5.6B, Fig. 5.6D). Membrane protein reconstitution is first conducted solely in the GUV bilayer (Fig. 5.6A), facilitating concentration gradient driven chemical signal (ion-ATP) translocation from the DIB chamber with emerging vesicular actin filament morphologies (Fig. 5.6B).

Aiming to expand the chemical signal communication across interconnected bilayers, heptamer pore reconstitution is then executed in both DIB and GUV membranes (Fig. 5.6C) through droplet formation of a GUV- and protein-containing aqueous phase facilitating stochastic alpha-hemolysin subunit distribution and protein channel formation in the interlinked double membrane assembly. Intercompartmental signalling results in initiation of vesicle actin polymerization triggered by concentration gradient-dependent flux of salt and ATP content, originating from the hydrogel substrate, via aHL nanopores in both DIB and GUV membranes (Fig. 5.6C,D).

Confirmation of DIB bilayer pore functionality is attained by the optical patch-clamping technique where channel ion currents correlate with Ca^{2+} signal flow in the planar surface of a Fluo-8-containing droplet (Fig. 5.7). Nanopore conductivity in Fluo-8-containing GUVs is also substantiated by Ca^{2+}-dependent change in vesicle fluorescence intensity (Fig. 5.7).

A

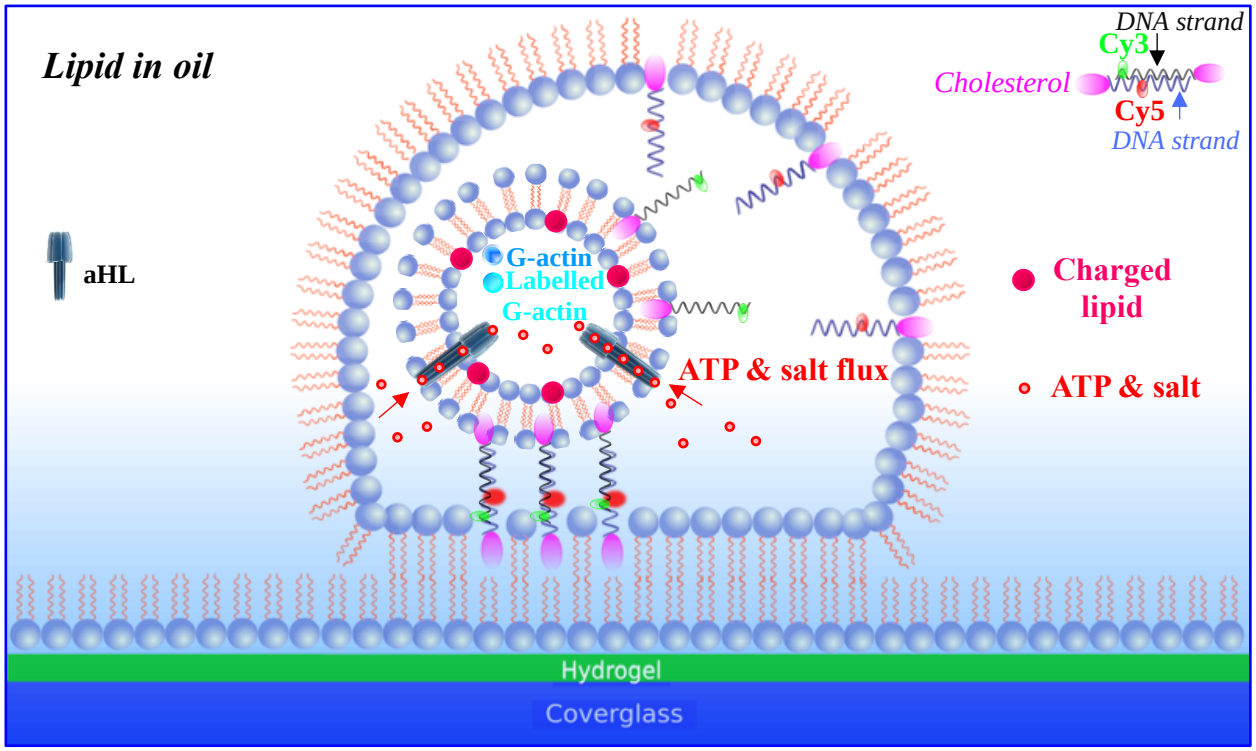
Lipid in oil
DNA strand
Cy3
Cholesterol
Cy5
DNA strand
aHL
G-actin
Labelled
G-actin
ATP & salt flux
Charged lipid
ATP & salt
Hydrogel
Coverglass

B

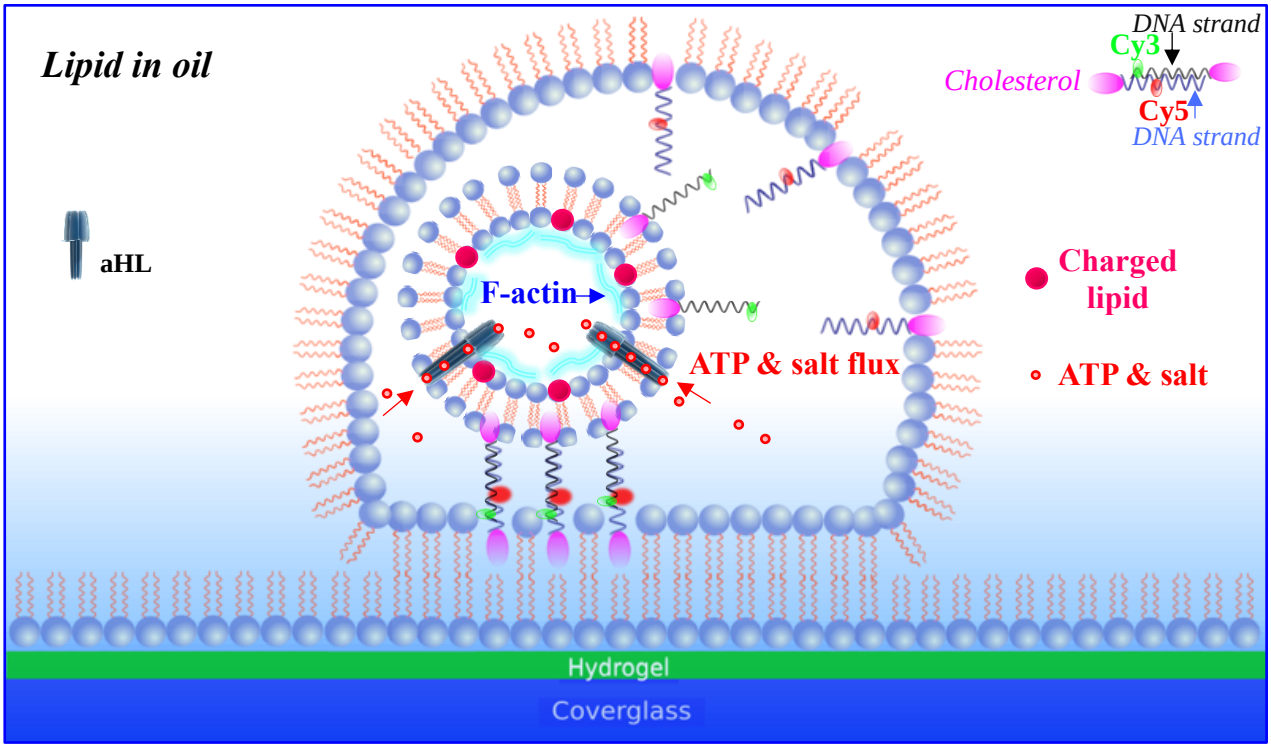
Lipid in oil
DNA strand
Cy3
Cholesterol
Cy5
DNA strand
aHL
F-actin
ATP & salt flux
Charged lipid
ATP & salt
Hydrogel
Coverglass

C

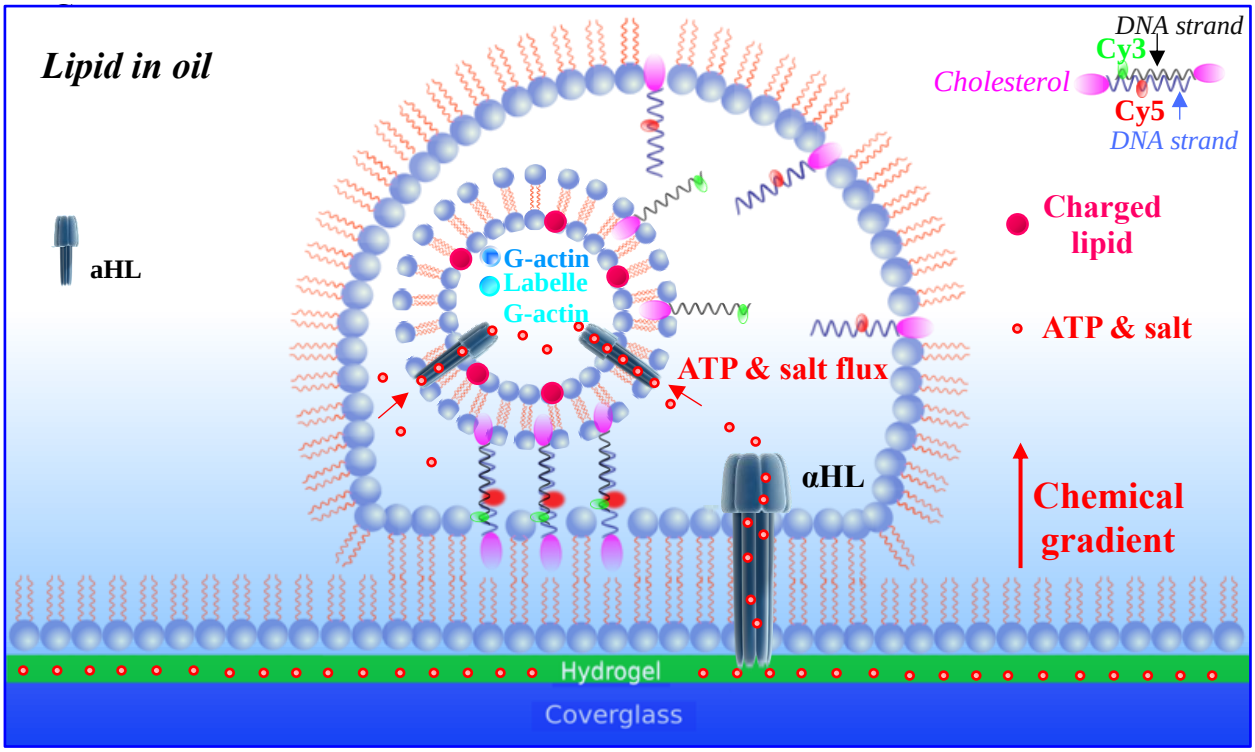
Lipid in oil
DNA strand
Cy3
Cholesterol
Cy5
DNA strand
aHL
G-actin
Labelle
G-actin
Charged lipid
ATP & salt
ATP & salt flux
αHL
Chemical gradient
Hydrogel
Coverglass

D

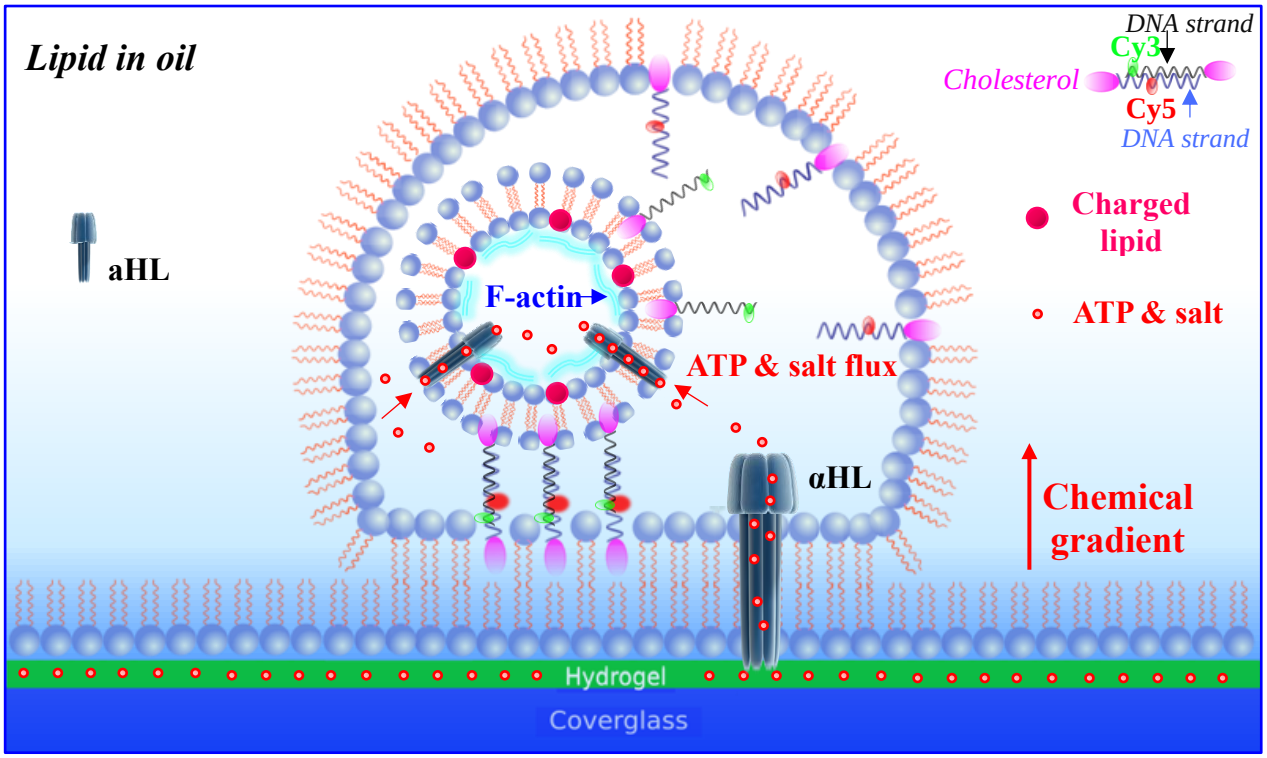
Lipid in oil
DNA strand
Cy3
Cholesterol
Cy5
DNA strand
aHL
F-actin
Charged lipid
ATP & salt
ATP & salt flux
αHL
Chemical gradient
Hydrogel
Coverglass

Figure 5.6- Not-to-scale schematic illustration of induced vesicular actin assembly via bilayer channel-mediated ion-ATP delivery from the DIB chamber and hydrogel matrix. *(A)Vesicle nanopore reconstitution in the DIB-tethered GUV bilayer. (B) Intercompartmental chemical gradient triggers vesicular F-actin elongated structures and bundle formations coupled to the inner lipid membrane via electrostatic interactions. (C) Protein channel reconstitution in the dual membrane architecture. (D) ATP and salt content in hydrogel substrate, driven by chemical gradient, translocate DIB and GUV bilayer integrated pores, and triggers vesicle actin polymerization.*

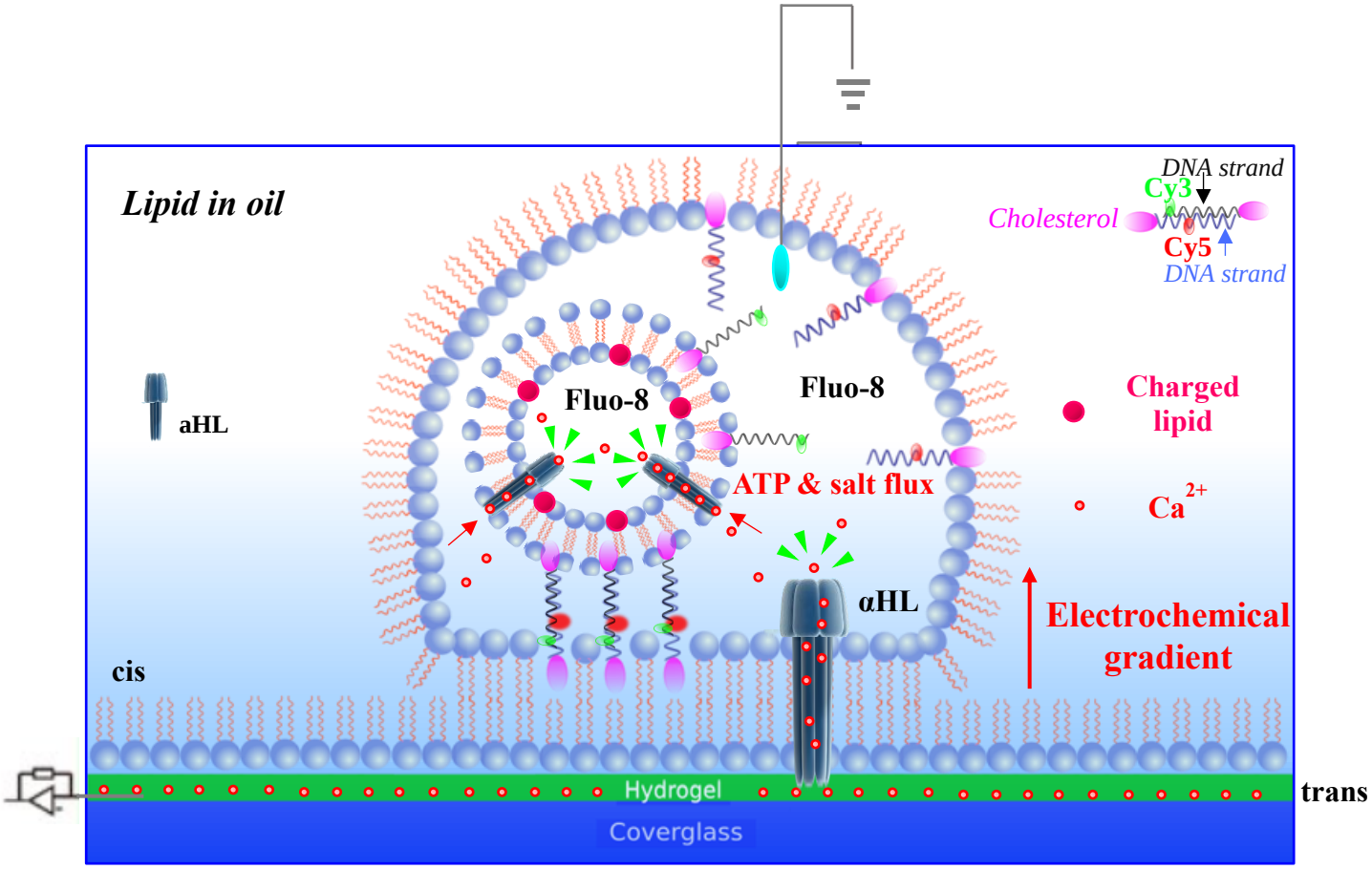

Figure 5.7- Not-to-scale schematic depiction of ion relocation through DIB and GUV bilayer integrated nanopores. *Cationic Ca^{2+} ion flow, chemically or electrochemically driven, from the agarose (trans) into the droplet (cis) and vesicle through individual nanopores. Upon binding with Fluo-8 in cis and GUV chambers, the Fluo-8/Ca^{2+} complex around pore vicinity elicits a strong fluorescence response.*

5.2 Materials and Methods

5.2.1 Materials

G-Actin (rabbit skeletal muscle alpha actin), Atto488-Actin for TIRFM (alpha-Actin, skeletal muscle rabbit) were purchased from Hypermol and used without further purification. Adenosine triphosphate (ATP), calcium chloride ($CaCl_2$), 4-(2-Hydroxyethyl)piperazine-1-ethanesulfonic acid (HEPES), mineral oil, hexadecane oil, silicone oil, agarose, dextrose, sucrose and α-hemolysin monomers were obtained from Sigma Aldrich. Fluo-8 was obtained from AAT Bioquest, Chelex resin (200–400 mesh) from Bio-Rad and CellMask DEEP RED and Actin tracking stain DEEP RED from Thermo Fisher Scientific. All lipids, 1,2-diphytanoyl-sn-glycero-3-phosphocholine (16:0 DPhPC), (1,2-dioleoyl-3-trimethylammonium-propane) DOTAP(18:1), 1,2-dioleoyl-sn-glycero-3-[phospho-rac-(1-glycerol)] (18:1 DOPG) and 1,2-dioleoyl-sn-glycero-3-phosphocholine (18:1 (Δ9-Cis) PC (DOPC)), were purchased from Avanti Polar Lipids.

5.2.2 Lipid and Aqueous Solutions

All lipids for experimentation were purchased as lyophilized powders and subsequently dissolved in chloroform at 25 mg/ml. Stocks of lipids were stored in chloroform at −20°C. For the preparation of the lipid-in-oil mixtures utilized for the inner membrane leaflets of the actin hosting vesicles, DPhPC (chemical structure in ***Chapter 4, Fig. 4.3A***), DOTAP (Fig. 5.8) and DOPG (chemical structure in ***Chapter 4, Fig. 4.3C***) lipids were used in the following combinations: DPhPC:DOTAP (70:30 w/w) or DPhPC:DOPG (99.5:0.5 w/w). Pure DPhPC lipid or DOPC:DOPG (99.5:0.5 w/w) mixture was used for the Fluo-8 carrying vesicles.

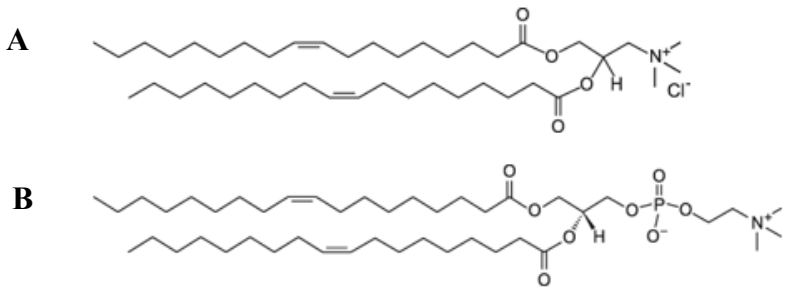

Figure 5.8- Structures of the (A) cationic lipid, DOTAP and (B) neutral lipid, DOPC. *Images taken from:[67, 68].*

For the outer membrane leaflet of the actin-containing GUVs, DPhPC:DOPG (99.5:0.5 w/w) mixture was used, whereas for inner and outer leaflets of the DIBs mere DPhPC lipid was employed.

The lipid mixtures were evaporated by streaming dry nitrogen into the vial for 2 minutes until a waxy film of lipid was visible in the bottom of the vial, which was then placed under vacuum for 30 min at RT. For GUV generation, mineral oil was added to make a final concentration of 10 mg/ml and for the DIB formation, 80:20 Hexadecane:Silicone oil was included to a final concentration of 8 mg/ml. The oil-lipid mixtures for GUV making were subsequently sonicated in a bath at 40^{o}C for 30 min at a power of 30 W, then cooled to room temperature and used within a week for GUV formation. The lipid film for DIB preparation was dissolved by vortexing for 3–5 minutes.

All aqueous solutions were prepared using doubly deionized 18.2 MΩ·cm MilliQ water. Low-melt agarose solutions were freshly prepared before each experiment and kept at 90°C to ensure homogeneity.

Calcium chloride solutions buffered with HEPES were treated with BioRad Chelex 100 resin at ~5% w/v ratio to reduce concentration of divalent cations that might affect the background fluorescence values upon Fluo-8 binding.

Calcium-sensitive Fluo-8 fluorescent dye was prepared as a 1 mg/ml stock solution in dH_2O water and stored at −20°C.

5.2.3 Actin Preparation

Actin monomers, G-Actin and Atto488-G-Actin, were pre-spun at 15.000 × g for 5 min at 7°C in a tabletop microcentrifuge before being rehydrated in 0.25 ml ultrapure water, yielding 1 mg/ml solution containing 2 mM Tris-Cl pH 8.2, 0.4 mM ATP, 0.5 mM DTT, 0.1 mM $CaCl_2$, 1 mM NaN_3 and 0.3% disaccharides (as calculated from the manufacturer's buffer description).

Actin solutions were kept on ice for the duration of the experiment and the remaining solubilized G-actin and atto488-G-actin were stored for up to 1 week on ice in the fridge.

5.2.4 Inside and Outside Buffer Solutions for Actin GUVs

The encapsulated protein solutions were mixed on ice directly before GUV preparation. Our experimental set up dictated different buffer solutions into the two distinct compartments of the artificial system. The inside buffer, (I-buffer), that is, the solution inside the vesicle lumen, hosted nonpolymerizing conditions (devoid of salts and ATP), (merely containing 600 mM HEPES, pH 7.6 together with 10 μM G-actin and 1 μM labelled actin), to thwart actin polymerization.

The 10% replacement of unlabeled G-actin by covalently labelled Atto488 actin, was used in all experiments to mark the network structures fluorescently.

The outside buffer solution, (O-buffer), surrounding the vesicle chamber in the DIB cavity or that being incorporated in the rehydrating substrate of the DIB device, contained the polymerization buffer with the following constituents: 90 mM KCl, 70 mM $MgCl_2$, 70 mM $CaCl_2$ and 10 mM ATP, (pH 7.5). In the instance of polymerization buffer exclusion from

the two-compartment system, both GUV and DIB were filled with 600 mM and 620 mM HEPES, (pH 7.6), respectively, while the polymerization solution was incorporated exclusively in the rehydrating agarose. For positive control, the O-buffer was also included in the GUV chamber along with actin monomers (10 μM G-actin and 1 μM labelled actin), to trigger F-actin assembly *in situ* for comparison purposes.

The osmotic pressure of the outside solution was adapted 10 to 20 mosmol higher compared to the encapsulated solution to enable vesicle fluctuations.

5.2.5 Protein Channel Reconstitution in the Double Membrane System

To attain ion K^+, Mg^{2+} or Ca^{2+} and ATP passage through the vesicle membrane from the exterior solution, activating actin polymerization within the liposome, 10 μl of GUV suspension was incubated with 0.5 μM α-hemolysin monomers for 1 h prior to GUV encapsulation into the DIB.

To allow cation and ATP ingress from the rehydrating agarose to DIB and GUV bilayers, α-hemolysin monomers (0.5 μM) were loaded in the droplet compartment, along with the GUV solution facilitating spontaneous monomer insertion and subsequent heptamer pore formation in both droplet and vesicle membranes. α-hemolysin was incorporated in large excess (0.5 μM) to facilitate instantaneous exchange, but it was completely excluded from the control sample. The incubation period of DIB-encapsulated actin-containing GUVs lasted for 1 hour at room temperature prior to imaging of actin filament (F-actin) formation via TIRF.

5.2.6 Preparation of Actin GUVs

For the vesicle generation process with encapsulated actin components, the emulsion phase transfer method (Fig. 5.9) was used, analytically described in ***Chapter 2*****,** (in ***2.1.1.2***

Emulsion Phase Transfer (EPT) and* 2.2.4 *Vesicle Preparation by Emulsion Phase Transfer (EPT)), and briefly presented below.

20 µl of I-solution was added to 200 µl phospholipid (DPhPC:DOTAP or DPhPC:DOPG) -containing oil and a gentle back-and-forth pumping with a syringe was applied for mixing, bypassing vortexing to preserve protein integrity. In a tube containing 200 µl O-buffer, 100 µl of the oil-lipid solution (DPhPC:DOPG) was layered on top, driving a monolayer lipid assembly at the interface (Fig. 5.9A). A volume of 100 µl of the emulsion was deposited on top of the oil-lipid mixture and subsequently, the whole tube was subjected to centrifugation (50 g for 1 min) (Fig. 5.9B) expediting emulsion droplet entrance into the O-buffer solution through the oil-lipid interface (Fig. 5.9C).

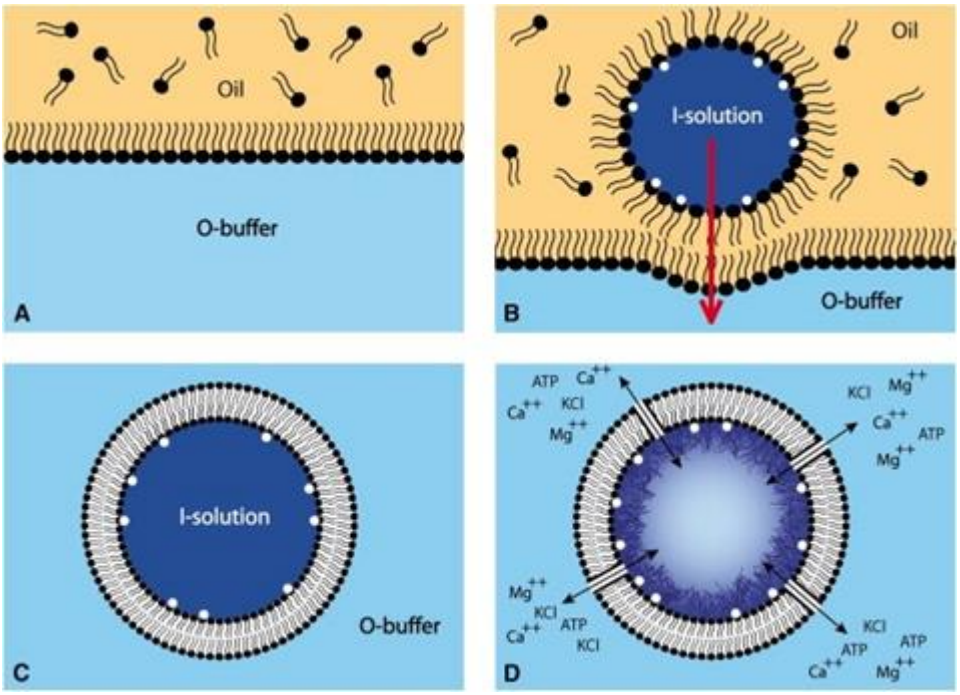

Figure 5.9- Schematic illustration of GUV generation via inverted emulsion. *(A) Oil-lipid interface formation for the assembly of the vesicle's outer layer. (B) Outer layer deposition around the inner membrane leaflet. (C) Liposome creation with different solutions between the inner and outer vesicle areas. (D) Salt and ATP flow, following membrane pore insertion, triggers actin polymerization. This figure is taken from:[23].*

5.2.7 Preparation of Fluo-8 GUVs: Inside and Outside Buffer Solutions

For the preparation of Fluo-8 liposomes via EPT, the inner vesicle lumen enclosed 600 mM sucrose, 1 M KCl, 1 mM EDTA, 10 mM HEPES, and 50 μM Fluo-8 (pH 7.2), whereas the GUV outer compartment contained 600 mM dextrose, 1 M KCl, 1 mM EDTA, 10 mM HEPES and 151 nM aHL (pH 7.2), which essentially constituted the aqueous solution of the droplet.

5.2.8 Vesicle Staining and DIB and GUV Functionalization

Prior to GUV encapsulation into the DIB chamber, actin hosting vesicles were stained with CellMask DEEP RED (1:5.000) for outer membrane labeling and functionalized with (2.5 nM) complementary Cy3-Cy5 internally labelled DNA linkers for anchoring to the DIB inner membrane leaflet.

Fluo-8-laden GUVs were also decorated with (5 nM) Cy3-Cy5 complementary DNA strands, serving as tethers between the droplet inner membrane and vesicle outer lipid sheets. The incubation period for the functionalization process lasted at least 15 min before vesicle encapsulation.

aHL monomers, to a final concentration of 0.5 μM (for actin carrying GUVs) and 151 nM (for Fluo-8 laden GUVs), respectively, were dissolved in the droplet to facilitate spontaneous insertion and channel formation in the DIB and GUV bilayers for ionic transport across membranes.

5.2.9 Device Preparation and DIB Formation

The procedure for creating DIB-encapsulated GUVs deposited into polymethylmethacrylate (PMMA) device was analytically described in ***Chapter 4*****,** (in ***4.2 Methods, 4.2.1 DIB Device Assembly and 4.2.2 Droplet Preparation and DIB Formation***)***.***

Briefly, plasma-treated coverslips were spin-coated with 0.75% (w/v) aqueous/molten agarose, and then affixed to a PMMA micro-channel device. The channels in the device were filled with higher concentration of molten agarose (3.5% w/v), made from the experimental buffer solutions, containing either (a) the polymerization buffer for actin-carrying GUVs, (detailed in ***5.2.4 Inside and Outside Buffer Solutions for Actin GUVs***) or (b) 1 M $CaCl_2$, and 10 mM HEPES at pH 7.0, for Fluo-8 loaded GUVs, in order to seal the PMMA device and rehydrate the thin agarose substrate. The small 1 mm diameter wells in the device were filled with 8 mg/ml DPhPC in 80:20 Hex:Sil lipid solution and left for 15 minutes to equilibrate.

Small lipid-coated aqueous droplets (~20-50 nl) containing GUVs were pipetted into the wells of the PMMA device, where under gravity they settled to its bottom and formed a bilayer upon contacting the lipid-covered agarose substrate. Thus, the aqueous solution required for the DIB formation was essentially composed of the GUV suspension, with the vesicles' cargo being either G-actin and Atto488-actin or Fluo-8 calcium dye.

5.2.10 Experimental Setup for Electrophysiology

5.2.10.1 Electrode Preparation

Ag/AgCl electrodes were prepared by immersing silver (Ag) wires (100 μm in diameter) in sodium hypochlorite (bleach) for around 30 min. The electrodes were washed with deionized (DI) water prior to dipping their tip into a molten solution of 7.5% agarose, which

was kept at 90ºC on a heating block. Upon cooling, the agarose solidifies creating a hydrophilic area at the tip of the electrode facilitating droplet adherence[69].

5.2.10.2 Electrical Recording

Prepared DIB devices were placed within a Faraday cage on an inverted microscope (Plan Apo TIRF: Nikon Instruments) and a pair of custom Ag/AgCl microelectrodes (~100 μm in diameter) was used to apply the potential.

A micromanipulator was deployed to insert the agarose-coated, 0.75% (w/v), electrode into the DIB and the other one was placed in the rehydrating agarose. Ag/AgCl electrodes were plugged into an Axopatch 200B patch-clamp equipment in voltage-clamp mode with the droplet being connected to the active electrode of the amplifier, while the hydrogel substrate electrode was connected to ground.

Fixed negative potentials of -50 mV were applied to drive Ca^{2+} ions from the hydrogel substrate into the droplet and subsequently, into the GUV, whereas positive potentials of +50 mV were applied to direct Ca^{2+} ions back into the hydrogel, when needed.

Electrical measurements were taken using the Axopatch 200B amplifier (Molecular Devices, USA) at a sampling frequency of 5 kHz and filtered post-acquisition with a 100 Hz low-pass Gaussian filter. Electrical traces were recorded with WinEDR software (University of Strathclyde, Glasgow, UK)[70].

5.2.11 Fluorescence Imaging

DIBs with encapsulated GUVs were imaged using a 60× TIRF oil objective (Plan Apo TIRF: Nikon Instruments). Fluo-8 and Atto488-Actin were excited by a 473-nm laser radiation (21 mW) (laser quantum mpc 6000, Ventus), and CellMask DEEP RED was excited by 635 nm wavelength (14 mW) (Shanghai queen laser technology, Ventus), both coupled to the inverted microscope by an optical fiber.

Atto488 and actin tracking stain DEEP RED fluorescence was collected by a combination of dichroic, notch, long pass and emission filters, (dichroic: Dio3-R405/488/532/635, BrightLine, USA, and FF640-FDio1 Semrock, USA; notch: NF03-633-25 Semrock, USA; long pass: BLPO1-473R; emission: et 525/50 Chroma, FF01-676/29 -25-STR, BrightLine, USA) and a charge-coupled device (iXon Ultra 897, Andor Technology, Belfast). Images were acquired by Andor Solis software at 33 Hz and analyzed with imageJ software.

5.2.12 Data Analysis

5.2.12.1 Quantification of F-actin Networks

Fluorescence intensity of F-actin was analyzed using ImageJ. TIRF images were cropped to a ROI, as centrally to the GUV of interest as possible and noisy background in the cropped images was subtracted by applying the (Process>Subtract Background) functions. *z*-stack projections of 100 frames were automatically thresholded using Otsu's method. A binary mask of the GUV fluorescent actin network (including membrane contour and enclosed filament actin formations/domains) was generated by the threshold, and the binary hole filling function was subsequently applied. Then, the created selection on the mask was applied to the original image, where measurements were conducted. Mean fluorescence intensity per actin GUV was calculated (using comparable inter-group vesicle sizes). The fluorescence intensities were normalized by the maximum fluorescence intensity. The values were compared using unpaired t test, one-way ANOVA, and significance was determined with post hoc Tukey's test. The results were plotted with MATLAB R2020a and GraphPad Prism 9.

5.2.12.2 Optical Measurements of DIB and GUV Ca^{2+} Fluxes

The raw imaging data obtained from fluorescence intensity arising from Ca^{2+} flux through aHL pores in DIBs and GUVs was saved in tiff format and optical data analysis was carried out in FIJI. Fluorescent emerging GUVs and aHL spots on droplet planar surface

were visually detected, manually checked, background-subtracted (20 framed averaged image of background fluorescence at a holding potential of 0 mV was subtracted from the "raw", unprocessed frames obtained during polarization to −50 mV) and filtered for quality. A 2D Gaussian was fitted to the brightest vesicle or spot (pore) within an image stack, and then the patch that contained the fit was subtracted from the original background-subtracted image. This region's mean pixel intensity versus time was then calculated (Fig. 5.21Bi and Fig. 5.23B). Normalized relative intensity from background-subtracted images was acquired by the change difference, ΔI, (subtraction of initial value[I-Io]), divided by the initial fluorescence [I-Io]/Io →ΔI/Io.

5.3 Results

5.3.1 Design of the Artificial Actin Cortex

For actin, the majority of de novo nucleation takes place at cell membranes inducing characteristic self-organization effects, with resulting filopodia or lamellipodia structures[71, 72]. Naturally, actin polymerization at the plasma membrane is mediated by nucleating proteins, such as the Arp2/3 complex[70], and the linkage between the cortex and the membrane is realized by linker proteins of the ERM (Ezrin, Radixin, and Moesin) family[73, 74].

Interestingly, *in vitro* studies have reported actin filament adsorption[75, 76] onto negatively and positively charged bilayers in the presence of divalent ions, (such as calcium or magnesium)[77], able to form stacked hierarchical structures[78]. In our system design, a small fraction of positively (DOTAP) or negatively (DOPG) charged lipids, together with the zwitterionic DPhPC lipid, was integrated into vesicle inner leaflets, to facilitate direct actin interaction with the slightly charged lipid sheets. In this manner, use of actin binding proteins or their artificial analogues, such as streptavidin-biotin complexes or His-tagged-Ni-NTA lipid affinity, was circumvented.

Specifically, actin reconstitution was performed in two lipid conditions for the vesicle inner leaflet, which consisted of a DPhPC and DOTAP (7:3 w/w) lipid mixture, or DPhPC and DOPG (9.5:0.5 w/w) composition.

Two basic building blocks were elected to produce actin cytoskeletal vesicles: (a) G-actin and (b) a fraction of Atto488- G-actin monomers, (the chemically modified G-actin with an Atto488 fluorescent group covalently bound to lysine residues), required for fluorescence visualization (Fig. 5.10A).

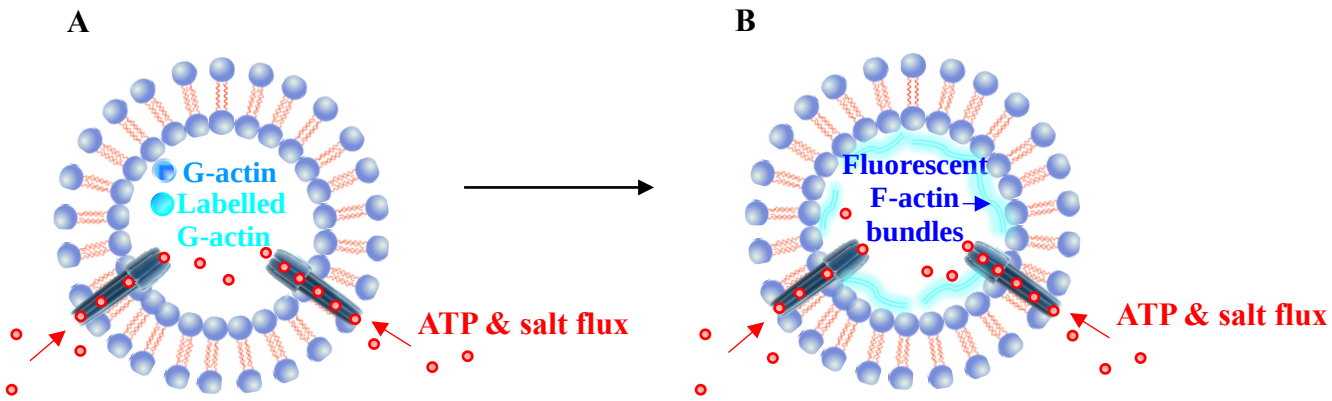

Figure 5.10- Not-to-scale localized actin polymerization model in the vesicle lumen. *(A)The schematic illustrates the elementary building blocks used to produce actin cytoskeletal vesicles: G-actin and a fraction of fluorescent G-actin monomers. Ion-ATP influx through GUV embedded aHL pores triggers (B) actin filament elongation in the vesicle lumen.*

As the intent of this work was to mimic chemical transmission across an artificial synapse-like configuration, membrane protein-mediated chemical communication between droplet and vesicle cavities was initially established. GUV channel (aHL) reconstitution enables intercompartment ion exchange, efficient to instigate vesicle actin cytoskeleton assembly through salt-ATP ingress (Fig. 5.10A,B). α-hemolysin pore formation, with characteristic ring structures, renders vesicles selectively permeable, allowing ion and ATP diffusion, but impeding any protein of the actin machinery enclosed to pass through, as it has a molecular mass cutoff of 3 kDa[23].

Aspiring to broaden the communication pathways of the compartmentalized model, aHL transmembrane pore integration was further targeted to both GUV and DIB bilayers permitting ion-ATP transfer from the hydrogel substrate to the vesicle chamber via DIB bilayer, more closely mimicking trans-synaptic signalling.

5.3.2 Actin Monomer Encapsulation in GUV via the Inverted Emulsion Technique

For actin GUV preparation, the inverted emulsion method was exploited, as it can accommodate proteins in the vesicle lumen and provides the benefits of asymmetric inner and outer membrane sheets and buffer composition.

The experimental principle of cargo-laden vesicle generation is schematized in Figure 5.9.

5.3.3 Actin Morphology in DIB-encapsulated Polymerization-free GUVs

GUVs were initially filled with the I-solution (10 μM G-actin and 1 μM labelled G-actin in 600 mM HEPES buffer, pH 7.6) and placed in an O-solution (90 mM KCl, 70 mM $MgCl_2$, 70 mM $CaCl_2$, 10 mM ATP, pH 7.5), constituting the polymerization buffer, which corresponds to the DIB inner volume and the GUV outer space. The I-solution and O-buffer compositions are detailed in ***5.2 Materials and Methods*** (***5.2.4 Inside and Outside Buffer Solutions for Actin GUVs***). All actin GUV experiments were performed in duplicates.

Images of control samples (polymerization-free conditions in DIB-encapsulated GUVs) are presented in Figure 5.11. GUVs under these polymerization-free conditions hosted solely monomeric actin components (G-actin and Atto488-G-actin), while the polymerization buffer was retained in the DIB compartment (Fig. 5.11A).

Several of the DIB-encapsulated vesicles collided with the DIB bilayer edge, leading to vesicle cargo release and subsequent actin assembly manifestations in the DIB space (Fig. 5.11A), where salt and ATP molecules were preserved.

Upon exclusion of O-buffer from the outer GUV space (replaced with 620 mM HEPES), actin fluorescence activity in the DIB chamber was reduced (Fig. 5.11B), yet, partially localized at the vesicle membrane. This event could be explicated by developing electrostatic interactions between the negatively actin subunits and positively charged lipid headgroups (DOTAP), attracting the former to the GUV bilayer (Fig. 5.11B); a common documented feature in previous pertinent studies[23, 70].

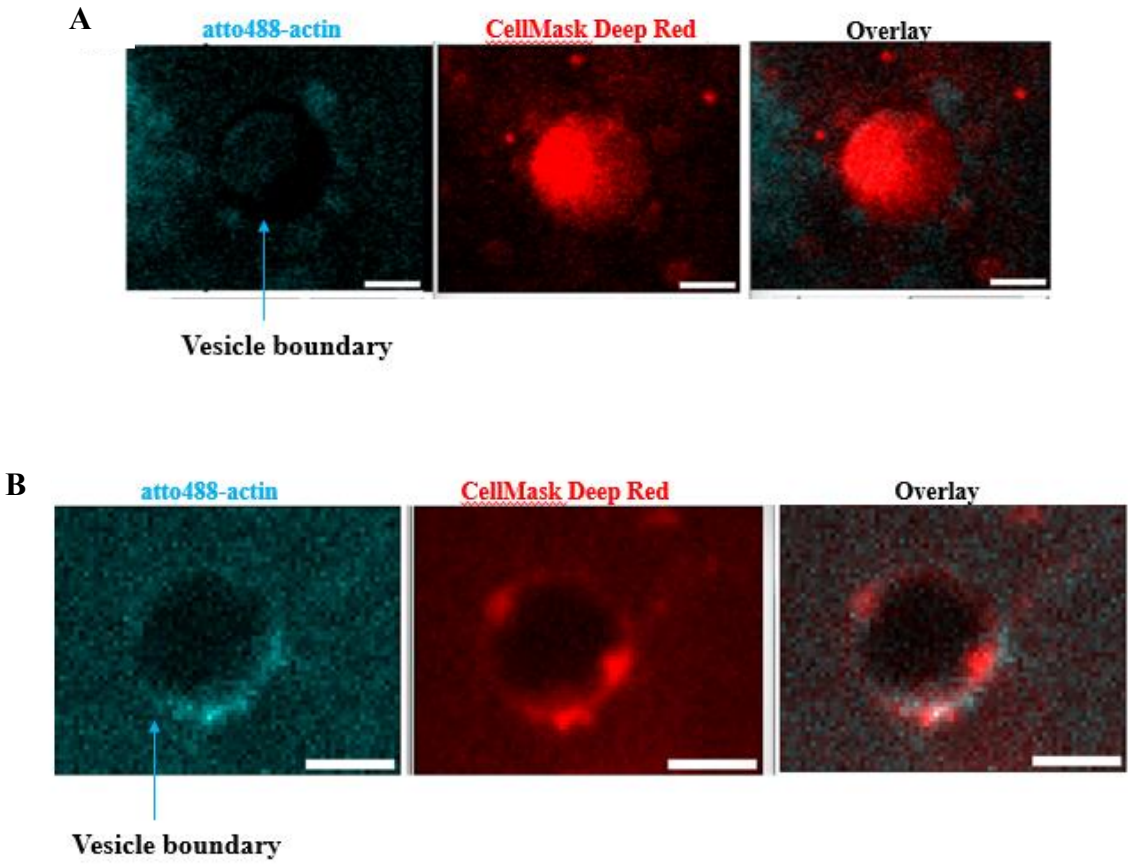

Figure 5.11- Background subtracted images (for vesicle boundary and actin feature highlight) of DIB-enclosed G-actin-laden vesicles under no polymerization conditions*. (A),(B) Actin components, (10 μM G-actin and 1 μM Atto488-G-actin), without the polymerization solution, (90 mM KCl, 70 mM $MgCl_2$, 70 mM $CaCl_2$,10 mM ATP), were encapsulated inside giant unilamellar vesicles (GUVs). The inner membrane vesicle composition consisted of a DPhPC-DOTAP (7:3 w/w) mixture, while the outer GUV leaflet contained DPhPC-DOPG (9.5:0.5 w/w). GUV outer leaflet was labelled with CellMask DEEP RED plasma membrane stain (1:5.000). Actin (cyan) was visualized by the inclusion of 10% of Atto488-G-actin. (A)Polymerization conditions*

(90 mM KCl, 70 mM $MgCl_2$, 70 mM $CaCl_2$,10 mM ATP, pH 7.5) were entertained in the droplet volume, but entirely excluded from DIB aqueous phase in (B). Scale bars: 5 μm.

5.3.4 Induced Vesicle Actin Structure Formation by GUV Membrane Nanopore-Mediated Salt-ATP Delivery

To induce actin assembly within the vesicle territory, α-hemolysin heptameric beta-barrel structures[79] were reconstituted in the vesicle bilayers by incubating 10 μl GUV suspension with (0.5 μM) monomeric aHL for a 30 min-period prior to vesicle encapsulation into the droplet. α-hemolysin concentration was used in a large excess, (0.5 μM), to facilitate instantaneous exchange.

Actin polymerized structures were recorded by TIRF imaging in 65% (13 out of 20) of the GUVs (from 2 independent experiments) with 92% of them (12 out of 13) displaying firm actin filament attachment to the positively charged (DOTAP doped) inner liposome membrane (Fig. 5.12A).

Given that more pronounced F-actin-membrane coupling was detected in DOTAP bearing vesicles, rather than in the DOPG ones, (where the membrane adsorbed F-actin area was noticeably smaller in 75% (3 out of 4) of the DOPG liposomes) (Fig. 5.12B), the rest of the experiments were performed with DOTAP composed vesicles.

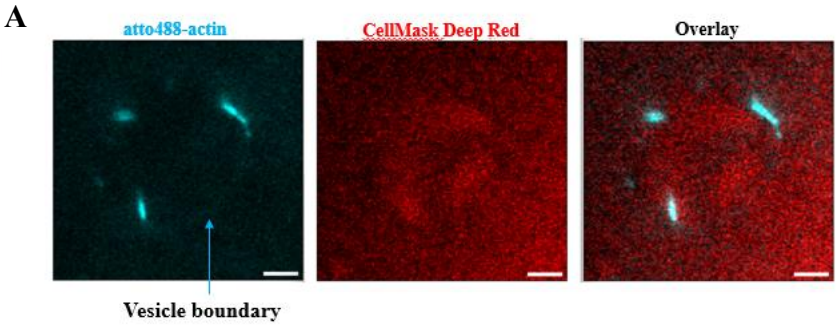

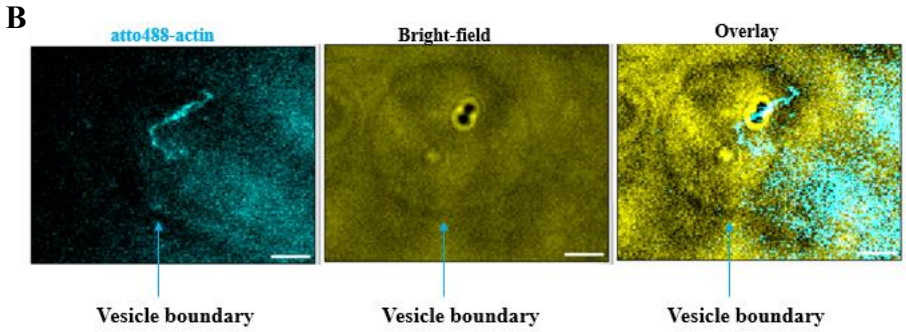

Figure 5.12- Triggered actin assembly in the GUV lumen by ion and ATP transport via vesicle membrane spanning pores. *(A) Distinct, membrane-bound small (1–4 μm) actin filament emergence in the positively charged (DOTAP) vesicle inner leaflet. (B) Elongated filamentous actin formation minimally interacting with the negatively (DOPG) composed inner vesicle membrane. Scale bars: 5 μm.*

5.3.4.1 Actin Cortex Characterization inside GUVs

Apart from distinct F-actin elongated structures (Fig. 5.12B) in 15% (2 out of 13) of the liposomes or short membrane-bound ones (Fig. 5.12A) in 23% (3 out of 13), another type of cortex morphology detected in the GUV lumen involves bulk polymerization covering a substantial segment of the vesicle's volume, with actin patch enrichment at the membrane (Fig. 5.13A); a formation identified in 23% (3 out of 13) of the vesicles. To a lesser extent, 15% (2 out of 13), polymerized actin resulted in a fine volume spanning network (Fig. 5.13B), especially in smaller-sized vesicles. Additionally, in 15% (2 out of 13) of the GUVs, actin polymerization predominantly shifted towards the membrane (Fig. 5.13C). The two later cases were also characterized by vesicle shape deformation into non-spherical shapes regulated by actin-based force generation.

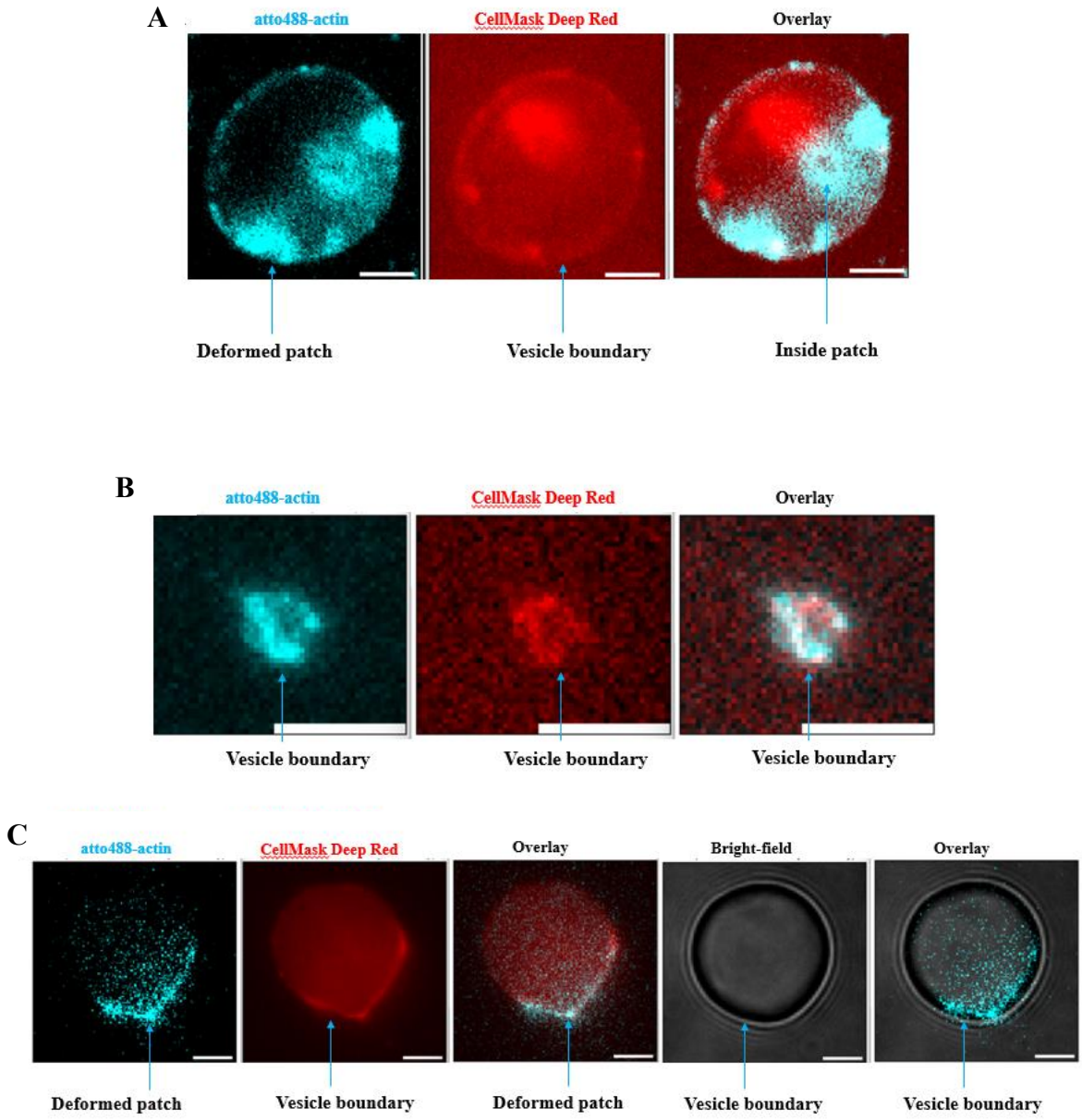

Figure 5.13- Induced GUV actin assembly by ion-ATP delivery through vesicle membrane pore forming proteins. *(A)Filamentous actin spans appreciable vesicle area with distinct domain formations attached to the membrane. (B)Volume spanning actin network with membrane-bound actin filaments and vesicle membrane bending. (C)Bulk polymerization suppression, but noticeable shape deformation as a result of membrane attached F-actin patch formation. Scale bars: 5 μm.*

5.3.4.2 Comparable F-actin Morphologies between Polymerization Buffer-containing GUVs and aHL-functionalized GUVs

Actin polymerization profiles sparked by salt and ATP flux through vesicle pore-forming proteins were analogous to the ones generated by existing polymerization conditions in vesicle chambers. Specifically, short and elongated filamentous actin structures (Fig. 5.12A,B and Fig. 5.14A), extended F-actin coverage (Fig. 5.13B, Fig. 5.14B), deformed actin membrane patches (Fig. 5.13C, Fig. 5.14B) and actin accumulation in vesicle membranes (Fig. 5.13C, Fig. 5.14B,C) were detected under both experimental conditions.

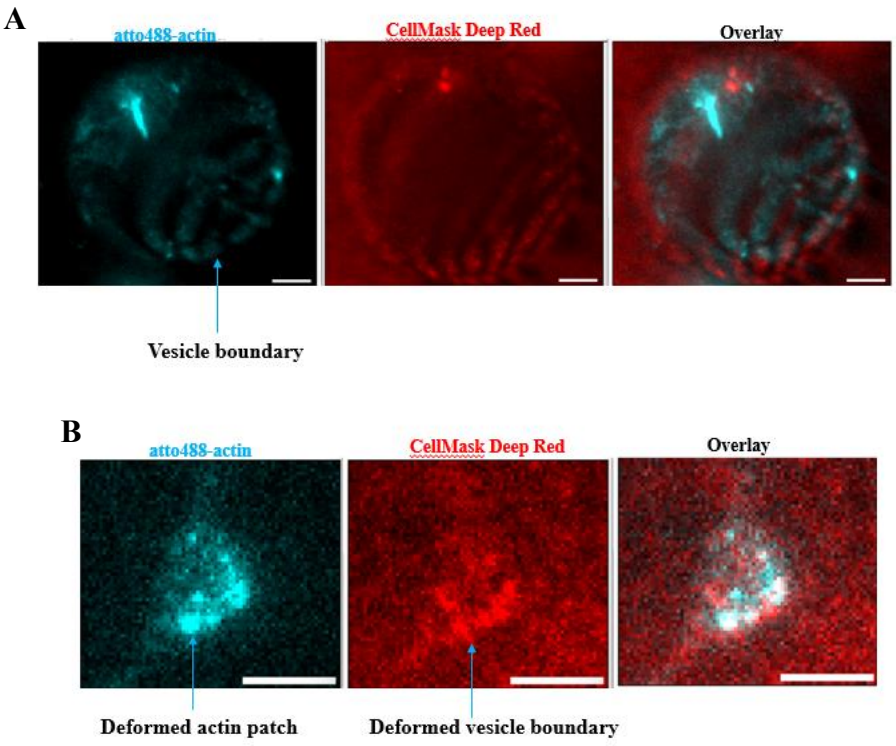

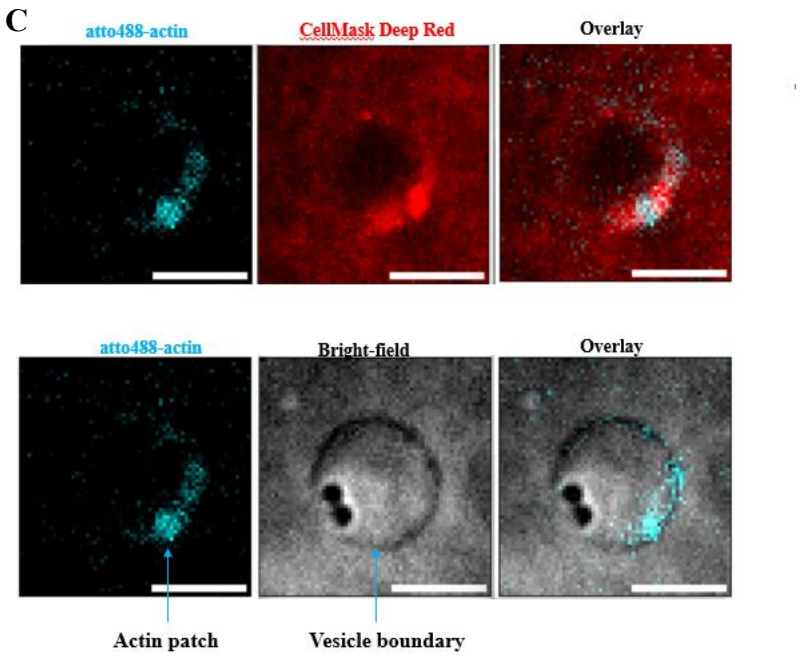

Figure 5.14- GUV-enclosed polymerization solution instigated comparable actin formations as those monitored in aHL-functionalized vesicles. *(A)Membrane bound stretched and small actin fibre assembly. (B)Diffused filamentous actin network with actin-induced membrane deformations. (C)Restricted bulk actin reconstitution with relocation to the membrane. Scale bars: 5 µm.*

Despite F-actin morphology similarities between polymerization buffer-containing GUVs and nanopore-integrated liposomes, the main difference lies in the mean actin intensity within and along the membrane contours, which was significantly higher (*** $p < 0.001$) in the former group (Fig. 5.15). This discrepancy is possibly attributable to the combined effect of ion-ATP diffusion rate dependency on chemical gradient, the membrane inserted heptameric channel number and vesicle volume, determining actin assembly rate within a specified timeframe.

The maximum 2-hour incubation period used in the current setup might not suffice for critical ion-ATP concentration entry and lengthier incubation periods (4-12 h) could be necessary for adequate salt-ATP amount translocation to trigger speedier actin elongation reactions within the α-hemolysin functionalized vesicles.

Although this approach is worth investigating, still the ostensible F-actin structure similarities between the two experimental conditions cannot be overlooked, as they signify successful GUV membrane pore formation (which, among others, suggests membrane unilamellarity and functionality) with consequent intercompartmental chemical communication.

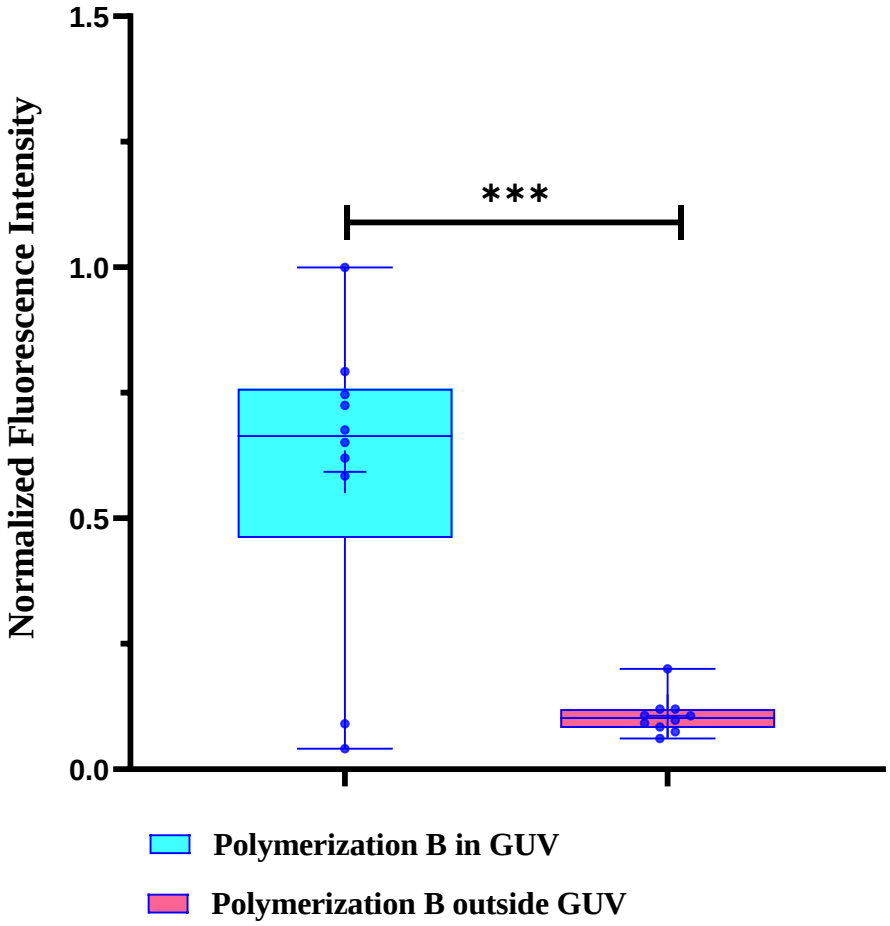

Figure 5.15- Box-and-whisker plot of the normalized fluorescence intensity values of F-actin in polymerization buffer-loaded GUVs (light blue) and in aHL-functionalized vesicles (pink). *The boxes represent interquartile range, with 75th percentile at the top and 25th percentile at the bottom. The middle line of the box represents the 50th percentile (median), the x marker shows the mean, and whiskers represent the rest of the distribution for each sample. The fluorescence intensities were normalized by the maximum fluorescence intensity. Unpaired two-samples t-test was applied in data analysis (n = 10 per sample). Error bars represent standard deviation. *** p < 0.001.*

5.3.5 Induced Vesicle F-Actin Assembly by DIB and GUV Membrane Nanopore-mediated Salt-ATP Transport

Evidence supporting signal crossing between the two interlinked membrane models (DIB and GUV) via transmembrane pores in the vesicle bilayer (Fig. 5.6A,B) encouraged us to expand the communication capabilities of the double membrane system, where chemical information (salt-ATP) could originate from the hydrogel substrate and travel across the droplet and vesicle bilayers inducing actin assembly in the liposome cavity (Fig. 5.6C,D). In this modified strategy, the polymerization conditions (90 mM KCl, 70 mM $MgCl_2$, 70 mM $CaCl_2$,10 mM ATP, pH 7.5) were entirely restricted in the rehydrating agarose, and the DIB and GUV compartments were filled with 600 mM HEPES solution, with the osmotic pressure of the outside solution being adapted 10 to 20 mosmol higher compared to the GUV enclosed buffer, allowing vesicle membrane undulations. Alpha-hemolysin monomers (0.5 μM) were incorporated in the DIB aqueous volume enabling their access to both DIB and GUV membranes. Imaging started at least 30 min following droplet deposition into the well of the DIB device so that gradient driven ion-ATP flux via membrane spanning pores in both DIB and GUV bilayers could be realized.

5.3.5.1 Actin Morphology Characterization inside and outside GUVs

In 50% of the vesicles (5 out of 10 from two independent experiments), a few actin patches/foci could be seen in the liposome membrane or within its confined space. (Fig. 5.16 A,B). Some of the samples, 20% (2 out of 10 from two independent experiments), displayed actin enrichment in the inner and outer liposome membrane leaflets with accompanied membrane misshaping (Fig. 5.16C), and others, 30% (3 out of 10 from two independent experiments), exhibited F-actin increment at the membrane which appeared as a continuous cortex within and around the vesicle boundary (Fig. 5.16D).

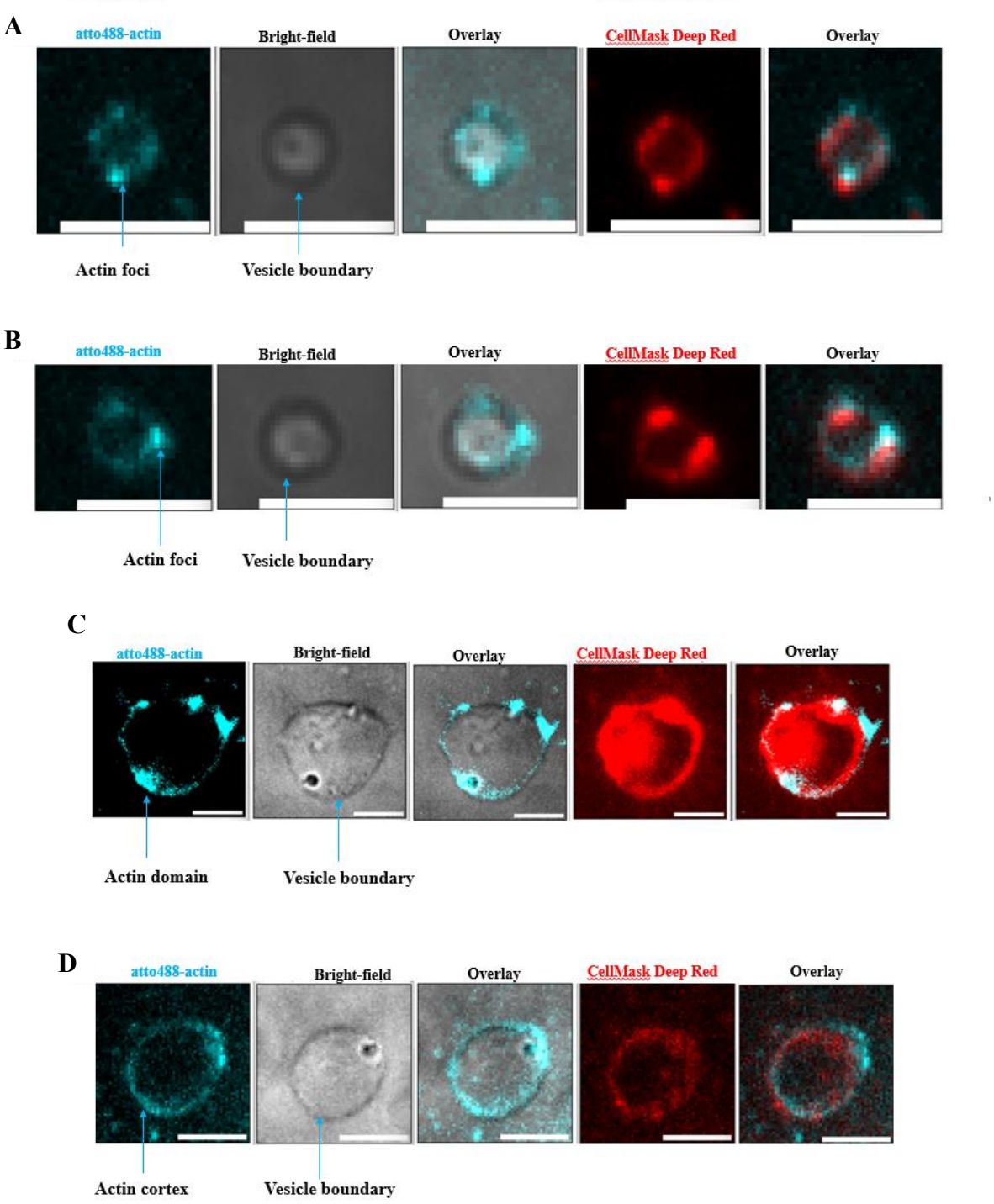

Figure 5.16- Induced GUV actin assembly by chemical delivery mediated through DIB and GUV membrane integrated nanopores. *(A),(B) Actin foci emergence on and around vesicle membrane. (C) Actin domain growth at GUV inner and outer membrane sheets. (D) Cortex-like actin network on both sides of vesicle bilayer. Scale bars: 5 μm.*

Undoubtedly, emerging filamentous actin morphologies were detected in all experimental conditions: (1) polymerization buffer-containing GUVs, (2) aHL-functionalized GUVs, granting access to ion flux from DIB compartment and (3) aHL-functionalized DIBs and GUVs, permitting ion flux from hydrogel matrix. Nevertheless, the box-whisker plot in Figure 5.17 displays significantly higher actin fluorescence intensity in polymerization buffer-containing GUVs (turquoise) compared to all other groups, which were either subjected to nanopore-mediated salt-ATP delivery (pink, green) or entirely refrained from it (control-yellow) (Fig. 5.17).

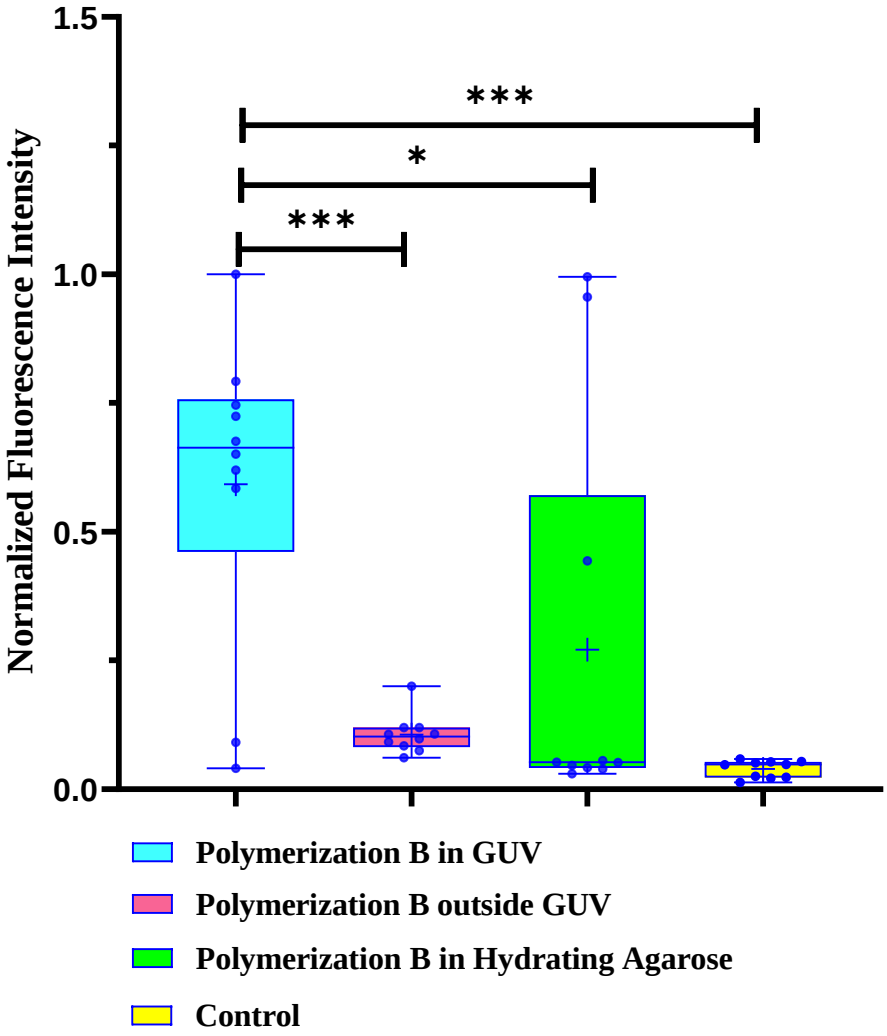

Figure 5.17- Box-whisker plot of normalized fluorescence intensity in DIB-encapsulated actin-containing GUVs*. Groups: (1) (turquoise) polymerization buffer-containing GUVs, (2) (pink) aHL-functionalized GUVs, ion-ATP permeable from DIB compartment, (3) (green) aHL-functionalized DIBs and GUVs, ion-ATP permeable from hydrogel matrix and (4) (yellow) polymerization buffer free GUVs. Normalized actin fluorescent intensity for each vesicle is represented as individual data point in the plot. The boxes represent interquartile range, IQR, (25th−75th percentiles), the centre line indicates the median and the whiskers extend to the maximum and minimum value. The median describes the centre of the distribution (central tendency) and is less affected by outliers compared to the mean. The larger interquartile range in the third group (green), relative to other groups, indicates a higher spread of the middle 50% of the data. n = 10 per group, values were compared through one-way ANOVA, with Tukey's post hoc test. * p < 0.05; *** p < 0.001.*

Ideally, longer incubation periods would be beneficial for sufficient ion and ATP influx and accumulation in the vesicle areas, especially when the polymerization buffer constituents are preserved in the hydrogel matrix and need to travel longer distances and fill in bigger volumes (DIB) till they reach their target destination (GUV) in critical concentrations. Furthermore, the number of functional pore reconstitution per GUV is unknown and stochastic, factors which play pivotal role in ion-ATP diffusion rate.

Based solely on the aforepresented visual data, optimization (longer incubation of aHL-functionalized DIB-encapsulated aHL-functionalized GUVs in DIB device) is a recommended strategy that would potentially facilitate adequate ion-ATP flow down the concentration gradient with resulting comparable actin fluorescent intensity measurements across polymerization content accessible groups.

Yet, this provisional data suggests open gateways for chemical signal crossing as demonstrated by the emerging vesicular F-actin structures observed in both nanopore reconstituted models: (1) DIB-enclosed aHL-functionalized GUVs and (2) aHL-functionalized DIB-engulfed aHL-functionalized GUV). This presumption is backed up by more tangible evidence coming from electrical recordings reported in ***5.3.8-5.3.11*** sections of this Chapter.

5.3.6 Characterization of DIB-anchored F-actin Expressing GUV via smFRET

In all experiments presented in this Chapter, DIB-encapsulated actin-laden GUVs were functionalized with 2.5 nM complementary Cy3-Cy5 overhangs, (detailed in ***Chapter 3***, ***3.3 Results, 3.3.1 Oligos Design***), serving as GUV-DIB intermembrane bridges. GUV's outer surface, composed of DPhPC:DOPG (99.5:0.5 w/w), was incubated with a mix of (2.5 nM) Cy3-Cy5-tagged ssDNA complements for 30 min prior to vesicle engulfment into the droplet.

To determine actin GUV anchorage to DIB bilayer, the smFRET approach was used. In Figure 5.18Ai, the cropped area, (composite of green–donor channel and red-acceptor channel), extracted from the DIB-engulfed vesicle region, displayed FRET occurrence within the GUV territory, sign of interconnected adjacent bilayers mediated via formed DNA bonds (**Supplementary Movie S5.1**). An indicative single captured spot in Figure 5.18Aii was shown to transition from acceptor (Cy5-red) to donor (Cy5-green) (Fig. 5.18Aiii), consistent with FRET cessation, yielding FRET efficiency of E = 0.85 (Fig. 5.18 Aiii). The average FRET efficiency of 37 individual FRET spots (N = 37), excised from the vesicle surface area, was calculated at $E = 0.75 \pm 0.14$ with the donor dequenching method (Fig. 5.18B), verifying interlinked juxtaposed DIB-GUV bilayers upon manifested vesicular self-organizing actin patterns.

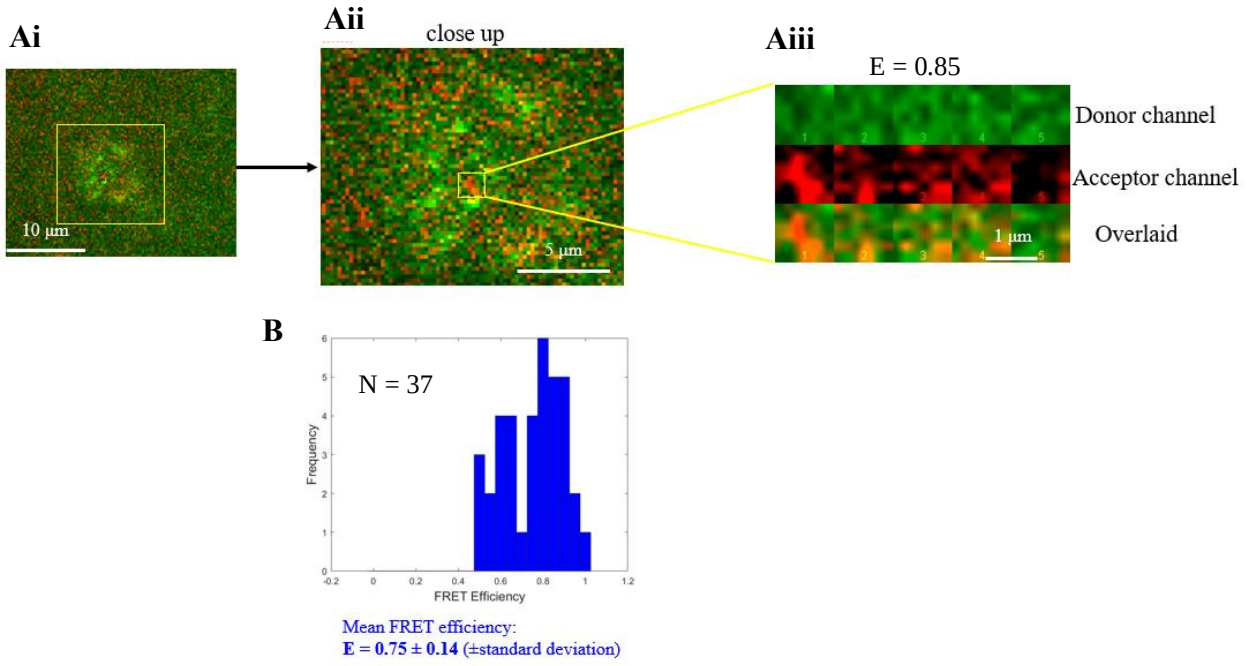

Figure 5.18- (Ai) smFRET occurrence in overlaid donor (green) and acceptor (red) channels of a DIB-enclosed F-actin expressing GUV*; (DIB's leaflets composed of DPhPC, GUV's outer leaflet contained 99.5% (w/w) DPhPC and 0.5% (w/w) DOPG. (Aii) Magnified scale of the vesicle domain. Single-molecule FRET depicted in the close-up snapshot (marked yellow spot) denotes DNA-mediated trans-synaptic adhesive interactions between DIB and GUV bilayers. (Aiii) Donor (Cy3-green), acceptor (Cy5-red) and superimposed channels show temporal fluctuations in the hybridized DNA species. Scale bars: 10 µm, 5 µm and 1 µm, respectively. (B) FRET efficiency histogram, constructed from the trajectories of 37 DNA pairs within the vesicle domain, yielded a mean FRET efficiency of E = 0.75 ± 0.14 applying the donor dequenching method.*

5.3.7 Design of Artificial System for Optical Patch-Clamping

In the series of experiments presented and analyzed so far, vesicular actin assembly in DIB-enclosed aHL-functionalized GUVs and aHL-functionalized DIB-encased aHL-functionalized GUVs was interpreted as functional pore reconstitution enabling salt and ATP translocation either from the DIB into the GUV compartments or from the hydrogel matrix into droplet and vesicle lumens, respectively.

Another strategy to probe channel formation and functionality, especially in the droplet planar surface that will allow us to confirm or disprove intercompartment chemically mediated communication, is through optical patch clamping use[80, 81], which is based on a combination of patch-clamp and optical technologies.

To implement this methodology in our system, the basic configuration entails asymmetric electrolyte buffers in the DIB, GUV compartments and hydrogel material as well. The DIB compartment (defined as the cis side) was filled with 600 mM dextrose, 1 M KCl, 10 mM HEPES and 1 mM EDTA, (pH 7.2); the droplet-enclosed GUV was loaded with 600 mM sucrose, 1 M KCl, 10 mM HEPES, 50 μM Fluo-8 and 1 mM EDTA, (pH 7.2); and the hydrating substrate (trans side) contained 1 M $CaCl_2$, and 10 mM HEPES, (pH 7.0).

Successful nanopore integration in droplet and vesicle bilayers can conduct a path between trans - cis sides and GUV lumen via thermodynamic diffusion, driven by the chemical gradient or electrochemical gradient under applied transmembrane potential. This phenomenon can be visualized by the FluoCa bound state, which elicits fluorescence in the vicinity of each nanopore in the DIB membrane (Fig. 5.19) and in the vesicle chamber, respectively[82].

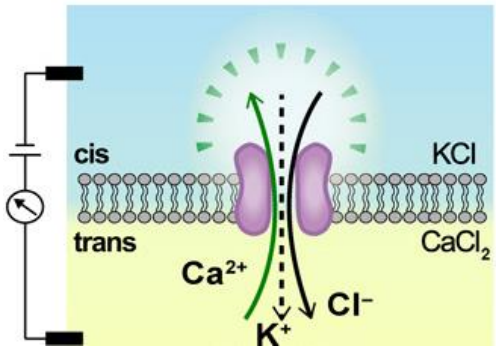

Figure 5.19- Schematics of ion translocation though alpha-hemolysin. *Source: [82].*

5.3.8 Electrophysiology of aHL Pore Reconstitution in the DIB

Before applying the optical patch-clamping technique, electrophysiology was employed to monitor protein channel reconstitution in the droplet bilayer. In this set of experiments, alpha-hemolysin subunits were incorporated in the aqueous droplet, together with the Fluo-8 loaded GUVs, allowing their randomized self-insertion into the DIB-GUV bilayer membranes, where conductive pores could be formed.

An Ag/AgCl electrode pair was placed in the DIB, as illustrated in Figure 5.20A, which serves to apply a transmembrane electrical potential, when needed, to sustain ion and charged analyte electromigration and record ionic current fluctuations[82].

Spontaneous aHL pore embedment into the DIB bilayer was monitored by electrophysiology measurements as a step-like increase in conductance (Fig. 5.20B) (under no applied potential), which is indicative of droplet planar surface transmembrane pore-formation. The measured current step was 210 pA and appeared to be a long-lived current state (< 6 s) with several fluctuations of much shorter duration (ms timescale) (Fig. 5.20B). The discrete and abrupt fluctuation of the long-lived (< 6 s) current state suggests stable channel integration[83].

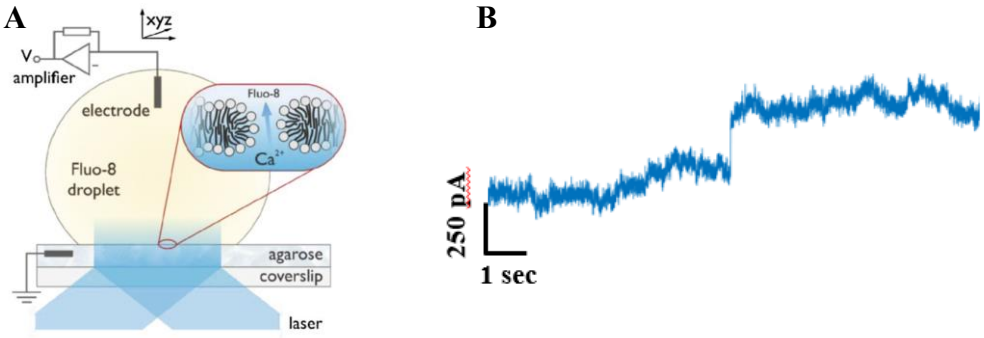

Figure 5.20- Electrophysiology of functional transmembrane aHL channel in DIB. *(A) Cartoon of the DIB experimental setup. Active Ag/AgCl electrode is fixed into the internal aqueous droplet. Source:[84]. (B) Bilayer aHL pore insertion was translated into a step change in the DPhPC DIB conductance level.*

5.3.9 α-Hemolysin Pore Detection in the DIB by Optical Patch-Clamping

Given that the optical patch-clamping technology development enables visualization of individual ion functioning through use of fluorescent indicator dyes, (able to sense Ca^{2+} presence translocating via channels), DIB-engulfed DNA-mediated anchored vesicles, loaded with the calcium-sensitive dye Fluo-8, (50 μM), were generated. EDTA, (1 mM), was also included in the vesicle volume to chelate residual divalents, and thus, reduce background fluorescence. Alpha-hemolysin monomers, (151 nM), were incorporated into the aqueous phase containing GUVs, for vesicle and droplet membrane channel reconstitution.

Some of these cargo-carrying GUVs ruptured upon contact with the droplet edge, releasing Fluo-8 dye in the DIB environment. When voltage was held at 0 mV, the reduced gradient driven Ca^{2+} fluxes through droplet bilayer embedded α-pores was hardly detectable by TIRF imaging (Fig. 5.21Ai).

Upon applied potential difference of -50 mV (Fig. 5.21Bii), individual conductive protein channels appeared on the surface bilayer (Fig. 5.21Aii) and (**Supplementary Movie S5.2**) as calcium was directed from the rehydrating agarose into the DIB where it was bound by the fluorogenic Ca^{2+} indicator dye Fluo-8. Thus, individual aHL channels were visualized as isolated bright spots in the bilayer (Fig. 5.21Aii) with the increase in fluorescence traces (Fig. 5.21Bi) correlating with the electrical signals (Fig. 5.21Bii).

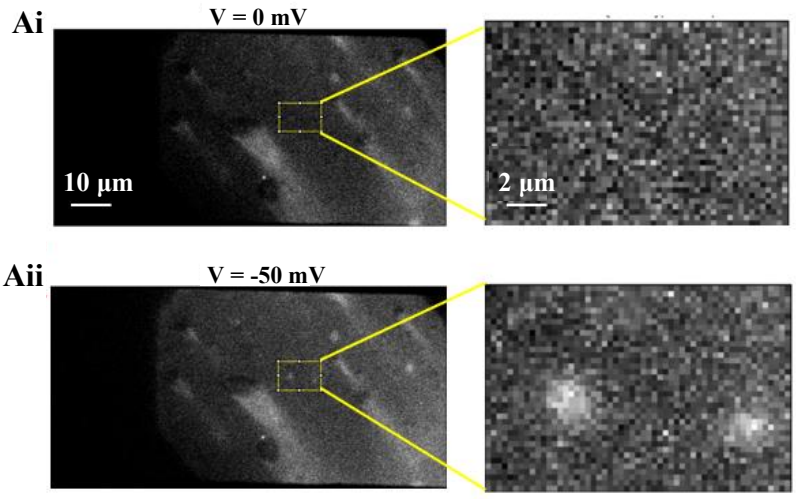

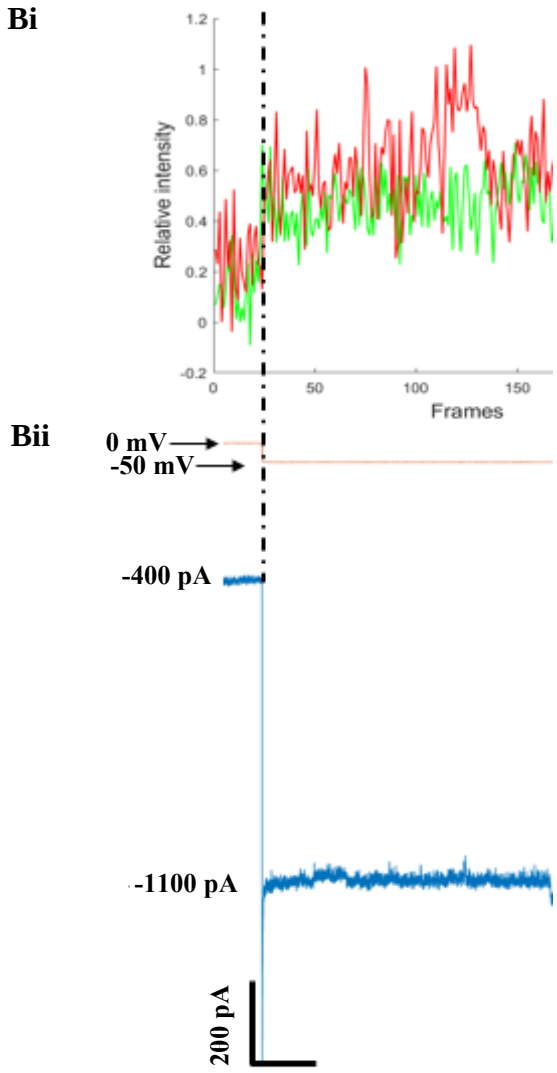

Figure 5.21- Single pore imaging in DIB membrane during polarization. *(Ai) Visually undetectable α-hemolysin heptameric protein pores at 0 mV. (Aii) Alpha-hemolysin channel detection as bright spots (within yellow marked box) in the agarose-supported DIB membrane under 473 nm TIRF-illumination during −50 mV polarization. (Ai) and (Aii) The close-up images on the right show the maximum pixel intensity of 100 frames, each recorded at 30 Hz, under a potential of 0 mV and -50 mV, respectively. In background-subtracted images, a 2D Gaussian filter was applied to remove noise and the patch containing the fit was subtracted from the original background-subtracted image. (Bi) The (red and green) Fluo-8 fluorescence traces (top) correspond to Ca^{2+} flowing through the two pores in the DIB (marked in the box (Aii)) as a function of time (t = 0.03 s × frames), when negative voltage (-50 mV) was applied. (Bi)The increased fluorescence signal dependence on transmembrane potential (-50 mV) correlated with (Bii) the ionic current across the bilayer (-1100 pA), which was cumulative from other DIB planar surface embedded pores, detectable in* ***(Supplementary Movie S5.2)****. Normalized relative intensity from*

background-subtracted images was acquired by the change difference, ΔI, (subtraction of initial value[I-Io]) divided by the initial fluorescence [I-Io]/Io → ΔI/Io.

5.3.10 Evidence of Channel Functionality in GUV Bilayer by Optical Approach

Having collected substantiating evidence in support of alpha-hemolysin channel functionality in the DIB planar surface, we also needed to probe vesicle membrane α-pore conductivity.

Given that upon DIB-encapsulated GUV construct fabrication, alpha-hemolysin monomers were encompassed in the aqueous droplet prior to DIB formation, randomized subunit distribution across membranes was anticipated.

A route to explore membrane-spanning pore functionality in GUV bilayer was to measure fluorescence intensity changes in DIB-enclosed Fluo-8-laden GUVs over time, after ensuring channel conductivity in DIB bilayer, as aforedescribed (Fig. 5.21Aii,B) that would permit chemical signalling across DIB and GUV membranes. Figure 5.22 shows steadily increased vesicle fluorescence intensity in channel reconstituted DIB bilayer. Time-lapse images, collected every 10 min for a total of 30 min, captured Fluo-8 fluorescence enhancement in the GUV lumen over the course of 30 min (Fig. 5.22A,B), suggesting calcium influx via vesicle membrane-spanning aHL pore(s).

As no potential was applied in this case, it is assumed that gradient directed Ca^{2+} flow traversed self-integrated DIB and GUV membrane channels, binding the Ca^{2+} indicator dye Fluo-8 in the vesicle compartment.

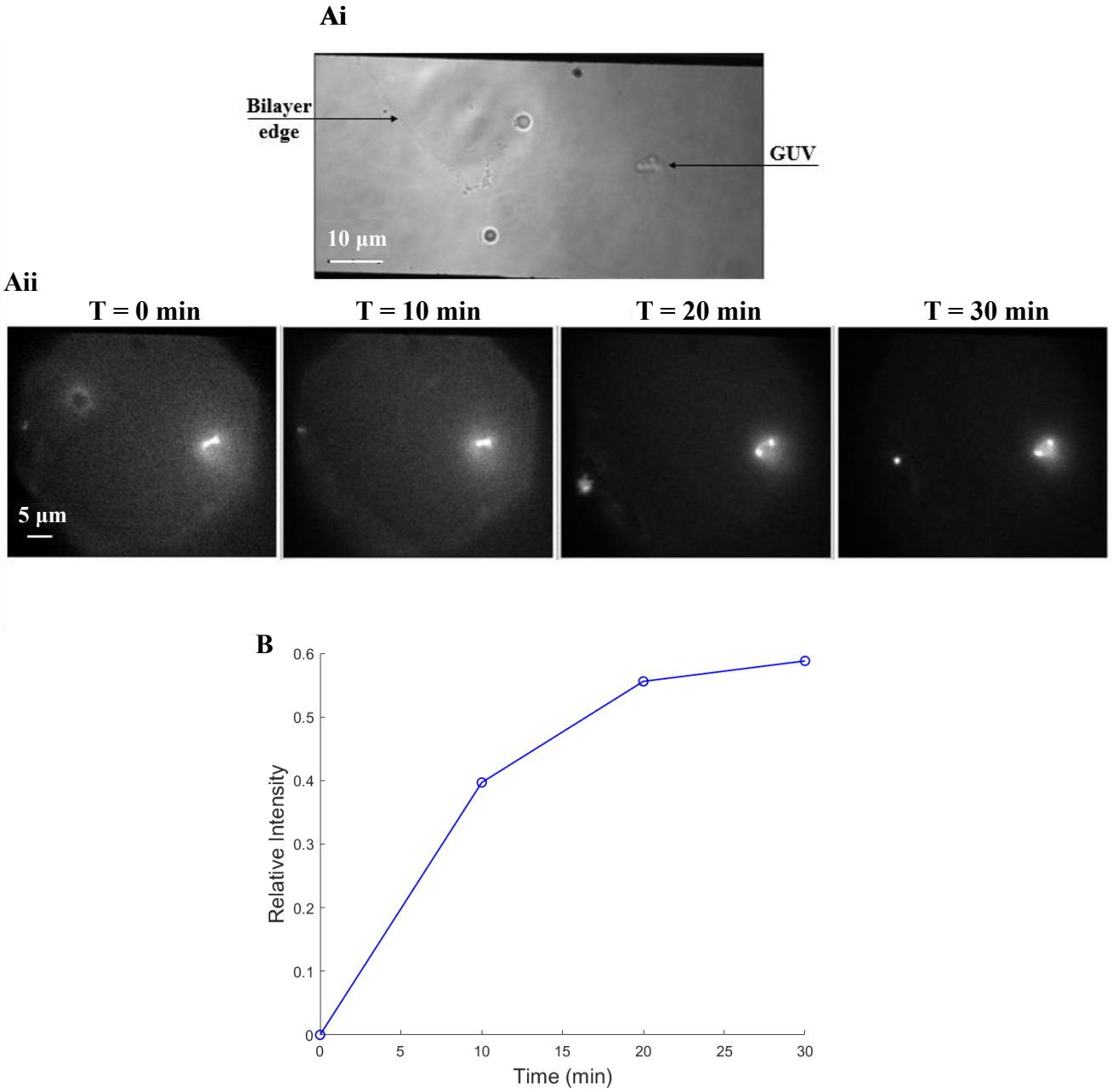

Figure 5.22- Time-course fluorescence of a DIB-encapsulated Fluo-8-loaded, ion permeable GUV. *(Ai)Bright-field image of a DIB-enclosed DPhPC GUV. (Aii)TIRF imaging of droplet-tethered GUV with calcium-sensitive fluorescent cargo and monomeric alpha-hemolysin (151 nM) incorporation into the droplet compartment. (B) The graph indicates time-course fluorescence (every 10 min for 30 min) of the DIB-enclosed GUV, with the increasing trend suggesting alpha-hemolysin pore reconstitution in the vesicle membrane enabling gradual Ca^{2+} entry. Fluorescence was calculated by applying the same tightly fitting perimeter around the vesicle in all time-lapse images in (Aii). Relative intensity from background-subtracted images*

was acquired by the change difference, ΔI, (subtraction of initial value[I-Io]) divided by the initial fluorescence [I-Io]/Io → ΔI/Io. Data obtained from a single experiment.

5.3.11 Evidence of Channel Conductivity in GUV Bilayer by Optical Patch-Clamping

Another strategy applied to verify calcium influx via channel proteins integrated in GUV membrane was by optical patch-clamping. aHL-functionalized DIB-engulfed Fluo-8-carrying GUVs were pulsed to a negative potential to direct calcium flow into the vesicle, where it could bind the Ca^{2+} indicator dye Fluo-8.

A small number (4 out of 93 → 4.3%) of detected individual DIB-anchored GUVs (data acquired from two droplet interface bilayers), pulsed to -50 mV, elicited gradual fluorescence intensity increase, as recorded by TIRF imaging. The enhanced background noise in the DIB lumen generated by the local Ca^{2+} fluorescence entry through nearby channels and their diffusive spread, rendering the emerging vesicle fluorescence FluoCa signal barely distinguishable, was corrected for signal optimization. Initially, an averaged image of background fluorescence, produced by averaging 20 frames before applying the hyperpolarizing step, was subtracted from the “raw”, unprocessed frames obtained during polarization to −50 mV[44]. Then, a smoothed copy of each frame, (constructed through Gaussian blur filter with width of 55 pixels; 9.36 μm), was subtracted from the original background-subtracted image to form a final corrected image (Fig. 5.23Aii)[44].

Figure 5.23Ai displays a distinct spot-like fluorescence emission (marked by yellow rectangle-on the right), not initially observable (same marked area -on the left) in the first 100 frames of the same image stack (movie) (**Supplementary movie, Fig. S5.3**). The spot-like fluorescence emission surfaced in the time course of 6 sec under DIB polarization (-50 mV).

Maximum pixel intensity of 100 frames before and after visual Fluo-8 emission detection showcases a 3.7-fold fluorescence increment in the same ROI (Fig. 5.23Aii), denoting vesicle membrane channel-mediated Ca^{2+} diffusion.

Fluorescent trace relative intensity derived from 100 frames before and 100 frames after optically detectable FluoCa emission, (extracted from the yellow marked circular area in Fig. 5.23 Aii), is graphically depicted in Figure 5.23B, displaying stark fluorescence enhancement over time.

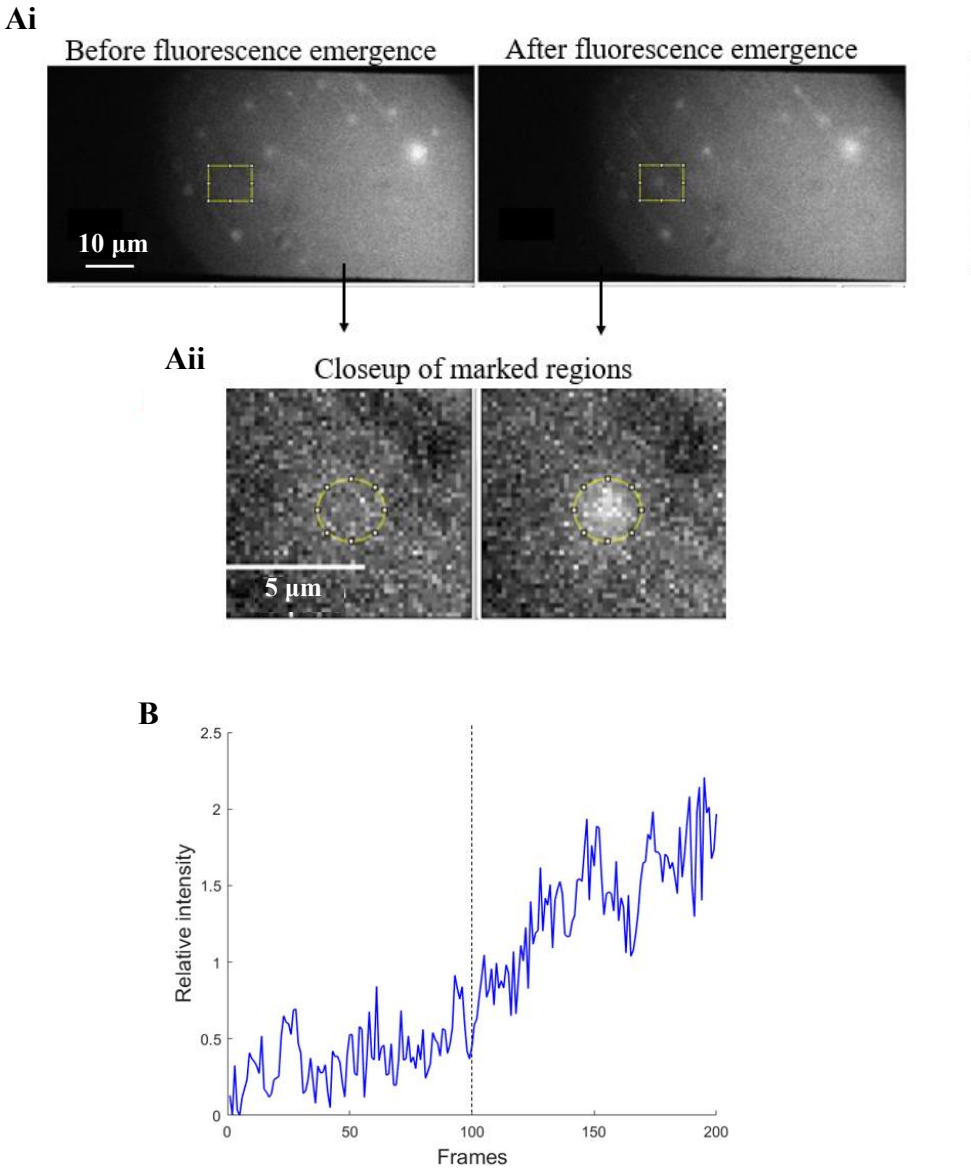

Figure 5.23- Time-course fluorescence of DIB-enclosed and -tethered DOPC:DOPG GUV (99.5:0.5 w/w) during DIB polarization; *total vesicle lipid concentration, 10 mg/ml, with (151 nM) monomeric alpha-hemolysin incorporation in the aqueous droplet. (Ai)Surfacing Fluo-8 emission (right), in the same ROI (as that in the left), at -50 mV droplet polarization for a total of 6 s (200 frames). (Aii) Closeups generated from the maximum pixel intensity of 100 frames each, recorded at 30 Hz, at an applied potential of -50 mV, after background and smoothed (55 × 55 pixel) image subtraction. (B) Relative intensity of fluorescence response over 6 s (200 frames) under -50 mV polarization, with vertical dashed black line denoting the point of visually detectable FluoCa emission. Relative change was obtained by the difference, ΔI, (subtraction of initial value[I-Io]) divided by the initial fluorescence [I-Io]/Io →ΔI/Io.*

Comparison of 93 frames before and after visual fluorescence detection in the total 4 identified gradually emitting vesicles (from two experimental replicates) (**Supplementary movie, Fig. S5.4**), within the observatory window of the applied voltage, demonstrated significant fluorescence increase (***p < 0.001) (Fig. 5.24), denoting facilitated Ca^{2+} diffusion through GUV membrane inserted α-hemolysin pores.

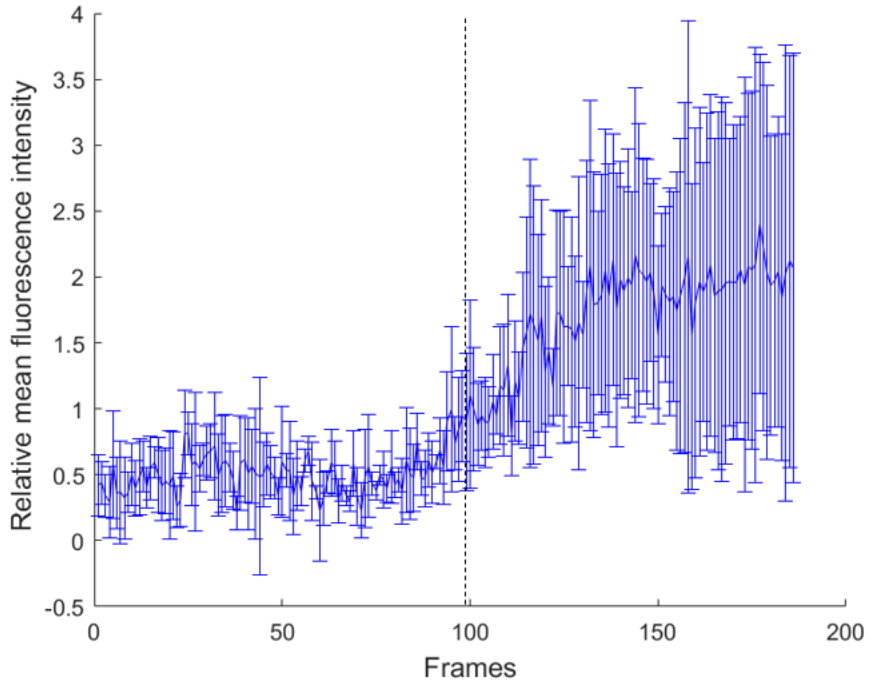

Figure 5.24- Relative mean fluorescence intensity of 4 pore-functionalized DIB-encapsulated Fluo-8-hosting vesicles under droplet polarization at -50 mV. *DIB contained (151 nM) alpha-hemolysin subunits. Comparison of 93 frames before and 93 after Fluo-8 emission*

*response detection yielded statistically significant GUV fluorescence increase, (paired t-test ***p < 0.001), suggesting vesicle bilayer pore-mediated Ca^{2+} influx. The vertical black dashed line at 2.8 s (t = 0.03 s × frames) signifies optically detectable FluoCa emission. Error bars show SD.*

5.4 Discussion

The concept of semi-permeable compartmentalization, which enables selective diffusion, retention, release, and protein expression constitutes a central tenet in synthetic cell modelling.

To upscale the functional capabilities of our synapse-like architecture, we thought of introducing intercompartmental communication pathways, mimicking intercellular communication mechanisms. This method facilitated stimuli-triggered biochemical responses, such as actin meshwork reproduction within the vesicle cytosolic chamber and ionic transfer measured by TIRFM.

Thus, the aim of the presented work was to realize a well-defined compartmentalized, chemically mediated communication system, whose trans-synaptic signalling properties would be trackable through elicited biochemical reactions, such as emission responses arising from Ca^{2+} relocation and self-organizing actin patterns, potentially competent to shape membrane framework.

For this biology-inspired build-up model, we made no use of actin binding proteins or their synthetic counterparts, such as biotin-streptavidin linkage. Given that direct interactions between actin strands and lipid membranes, which primarily depend on lipid composition and buffer ions, have been demonstrated *in vitro*[77], charge-dependent interactivity between monomeric and filamentous actin with lipid membrane was applied as a design principle.

Positively charged lipids were integrated in the GUV inner leaflet and alpha-hemolysin nanopores were reconstituted initially in the liposome bilayer, to open up communication pathways between the DIB and GUV chambers (Fig. 5.6A) and subsequently, in both vesicle and droplet membranes (Fig. 5.6C) to broaden signal crossing from the hydrogel substrate to the GUV cavity; an approach that more closely emulates intercellular “talk” in biological synapses.

Alpha-hemolysin reconstitution in liposome bilayer enabled gradient driven ion-ATP-mediated actin assembly in the GUV lumen, generating a variety of cortical actin distribution phenotypes (Fig. 5.13), similar in morphologies to those observed in vesicles with already enclosed actin polymerization conditions (Fig. 5.14), suggesting chemically meditated communication between the two interlinked compartments through functional heptameric pore formation.

Despite the statistically increased mean fluorescence intensity of the actin assembly in the polymerization buffer-containing vesicles, over the aHL-functionalized ones (polymerization buffer-free) (Fig. 5.15), still vesicular localized actin growth, filamentous actin elongated structures, and F-actin network formations (Fig. 5.12, Fig. 5.13) in the latter group indicate chemical signal flow between the two membrane demarcated chambers via vesicle reconstituted protein channels.

Pursuing to introduce another communication pathway, bridging the micro-compartmentalized assemblage with the hydrogel matrix, more closely replicating intercellular signalling, channel reconstitution was conducted in both membrane constructs through alpha-hemolysin subunit inclusion in the GUV-containing aqueous phase, facilitating transmembrane pore embedment in both interlinked membrane models alike (Fig. 5.6C). In this modified strategy, salt-ATP constituents were exclusively preserved in the rehydrating substrate (Fig. 5.6C,D).

Induced vesicular actin polymerization by salt-ATP influx via alpha-hemolysin nanopores in both DIB and GUV membranes was manifested as cortex-like actin morphologies within and outside vesicles' contours (Fig. 5.16).

Needing to validate DIB and GUV bilayer channel integration and conductivity, and not base our inferences merely on visual inspection of ion-ATP induced vesicular F-actin structures in aHL-functionalized GUVs (Fig. 5.13) and DIBs (Fig. 5.16), a combination of optical and electrical recordings was employed.

To probe DIB planar surface aHL nanopore functionality, we made use of electrophysiology and optical-patch clamping technologies. A 210 pA step-like increase

in droplet conductance (Fig. 5.20B) substantiated successful aHL heptamer insertion in the DIB bilayer. Voltage-dependent Ca^{2+} flux, generating spot-like patterns with incremental fluorescence FluoCa signals in the DIB planar surface (Fig. 5.7), with correlated DIB current changes (Fig. 5.21Aii, B), further attested to channel conductivity.

The applied voltage gradient (-50 mV) was critical to drive a sustained flow of Ca^{2+} ions through DIB bilayer integrated protein channels, facilitating fluorescent signal tracking around each nanopore (Fig. 5.21Aii), and thus, reporting their location and conductive modes. Ca^{2+} flux imaging, through TIRFM, provided us with simultaneous readout of both protein position and function, validating ion permeation through droplet bilayer embedded α-pores.

The next step was to ratify nanopore conductance in GUV bilayer, and the optical approach, which relies on fluorescence emission of a Ca^{2+}-sensitive dye (Fluo-8), was applied. Gradual fluorescence increases in an aHL-reconstituted DIB-encapsulated GUV (Fig. 5.7), over the course of 30 min (Fig. 5.22), indicated vesicle membrane nanopore-mediated Ca^{2+} diffusion.

Detection of analogous Fluo-8 fluorescence emission increases in aHL-reconstituted DIB-encapsulated GUVs under droplet polarization (Fig. 5.23), further supports vesicle membrane-spanning pore formation with resulting Ca^{2+} permeation.

Although the optical recording and the patch-clamping data for exploring aHL reconstitution in DIB-anchored GUVs was extracted from one dataset (Fig. 5.22) and a very small sample group (4.3%)(Fig. 5.24), respectively, (which ideally require experimental replication with a higher monomeric alpha-hemolysin concentration; possibly 5 μM instead of 151 nM that was used), still, appreciable vesicular fluorescence intensity amplification under non-polarization (0 mV) (Fig. 5.22) and hyperpolarization conditions (-50 mV) (3.7-fold enhancement) (Fig. 5.24) validates channel conductivity in the liposome bilayer.

Piecing together the data of (a) GUV luminal F-actin structure formations (Fig. 5.16) and (b) non-voltage- and voltage-dependent Ca^{2+}-evoked vesicular fluorescence FluoCa emission increases (Fig. 5.22, Fig. 5.23), following monomeric alpha-hemolysin inclusion in the GUV-containing aqueous phase, we can substantiate ion-ATP translocation via aHL nanopores in both DIB and GUV membranes.

Preferably, optimization procedures, like longer dwelling times of the nanopore reconstituted model system on the polymerization constituent-containing hydrating substrate, would be recommended to amplify vesicle actin assembly manifestations to a comparable degree to that expressed in the polymerization buffer-entertaining vesicles (Fig. 5.17). Nonetheless, solid evidence has been provided, showcasing intermembrane signaling across interconnected lipid bilayers through membrane protein channels.

Finally, DNA-mediated adhesion of F-actin-expressing GUV to the droplet bilayer (Fig. 5.18) was demonstrated by single-molecule FRET measurements, materializing in this way the fabrication of an artificial synapse-like configuration with intercommunication capacities.

As a future idea, further assay improvement and additional functional component inclusion, (e.g., actin binding proteins, like fascin, which promotes actin-rich migratory structures, such as filopodia [85-87] and lamellipodia[88], and myosin motor proteins that power force or movement on actin filaments[89]), can be introduced into the artificial communication system to enhance vesicle membrane dynamics and shed light on physical mechanisms behind cellular migratory events.

This group of experiments can be organized and conducted as a continuation step that will open up a portal for generating synthetic biological systems with ever-greater complexity and versatility.

5.5 References

1. Mukwaya, V., Mann, S., and Dou, H. *Chemical communication at the synthetic cell/living cell interface. Commun Chem.,* 2021. **4**(161).
2. Visa, N., and Percipalle, P. *Nuclear functions of actin. Cold Spring Harbor perspectives in biology*, 2010. **2**(4): p. a000620.
3. Shi, J., Sun, M., and Vogt, P.K. *Smooth muscle α-actin is a direct target of PLZF: effects on the cytoskeleton and on susceptibility to oncogenic transformation. Oncotarget*, 2010. **1**(1): p. 9-21.
4. Cooper, G.M. *The Cell: A Molecular Approach. 2nd edition*. 2000: Sinauer Associates.
5. Pollard, T.D. *Actin and Actin-Binding Proteins. Cold Spring Harbor perspectives in biology*, 2016. **8**(8): p. a018226.
6. Kabsch, W., Mannherz, H.G., Suck, D., Pai, E.F., and Holmes, K.C. *Atomic structure of the actin:DNase I complex. Nature*, 1990. **347**(6288): p. 37–44.
7. Kang, H., Bradley, M.J., Elam, W.A., and De La Cruz, E.M. *Regulation of actin by ion-linked equilibria. Biophysical journal*, 2013. **105**(12): p. 2621–2628.
8. Cooper, J.A., Buhle, Jr, E.L., Walker, S.B., Tsong, T.Y., and Pollard, T.D. *Kinetic evidence for a monomer activation step in actin polymerization. Biochemistry*, 1983. **22**(9): p. 2193–2202.
9. Frieden, C. *Polymerization of actin: mechanism of the Mg^{2+}-induced process at pH 8 and 20 degrees C. Proceedings of the National Academy of Sciences of the United States of America*, 1983. **80**(21): p. 6513–6517.
10. Korn, E.D., Carlier, M., and Pantaloni, D. *Actin Polymerization and ATP Hydrolysis.* Science, 1987. **238**(4827): p. 638-644.
11. Pernier, J., Kusters, R., Bousquet, H. et al*. Myosin 1b is an actin depolymerase. Nat Commun.*, 2019. **10**(5200).
12. Gibieža, P., and Petrikaitė, V. *The regulation of actin dynamics during cell division and malignancy. American journal of cancer research*, 2021. **11**(9): p. 4050–4069.

13. Cáceres, R., Abou-Ghali, M., and Plastino, J. *Reconstituting the actin cytoskeleton at or near surfaces in vitro. Biochimica et Biophysica Acta (BBA) - Molecular Cell Research*, 2015. **1853**(11): p. 3006-3014.
14. Hackl, W., Barmann, M., and Sackmann, E. *Shape Changes of Self-Assembled Actin Bilayer Composite Membranes. Phys. Rev. Lett.*, 1988. **80**(8): p. 1786-1789.
15. Heinemann, F., Vogel, S.K., and Schwille, P. *Lateral Membrane Diffusion Modulated by a Minimal Actin Cortex. Biophysical Journal*, 2013. **104**: p. 1465-1475.
16. Vogel, S.K., Petrasek, Z., Heinemann, F., and Schwille, P. *Myosin motors fragment and compact membrane-bound actin filaments. eLife,* 2013. **2**: e00116.
17. Litschel, T., Kelley, C.F., Holz, D. et al. *Reconstitution of contractile actomyosin rings in vesicles. Nat Commun.*, 2021. **12**(2254).
18. Luo, T., Srivastava, V., Ren, Y., and Robinson, D.N. *Mimicking the mechanical properties of the cell cortex by the self-assembly of an actin cortex in vesicles. Appl. Phys. Lett*., 2014: p. 153701.
19. Campillo, C., Sens, P., Köster, D., Pontani, L.-L., Lévy, D., Bassereau, P., Nassoy, P., Sykes, C. *Unexpected membrane dynamics unveiled by membrane nanotube extrusion. Biophys. J.*, 2013. **104**: p. 1248-1256.
20. Abkarian, M., Loiseau, E., and Massiera, G. *Continuous droplet interface crossing encapsulation (cDICE) for high throughput monodisperse vesicle design. Soft Matter*, 2011. **2011**(7): p. 4610-4614.
21. Li, T.H., Stachowiak, J.C., and Fletcher, D.A. *Chapter 4 - Mixing Solutions in Inkjet Formed Vesicles. Methods in Enzymology*, 2009. **465**: p. 75-94.
22. Pautot, S., Frisken, B.J., and Weitz, D.A. *Production of Unilamellar Vesicles Using an Inverted Emulsion. Langmuir,* 2003. **19**(7): p. 2870–2879.
23. Pontani, L.-L., van der Gucht, J., Salbreux, G., Heuvingh, J., Joanny, J.-F. and Sykes, C. *Reconstitution of an Actin Cortex Inside a Liposome. Biophysical Journal*, 2009. **96**(1): p. 192-198.
24. Tsai, F.-C., Stuhrmann, B., and Koenderink, G.H. *Encapsulation of Active Cytoskeletal Protein Networks in Cell-Sized Liposomes. Langmuir*, 2011. **27**(16): p. 10061–10071.

25. Ganzinger, K.A., and Schwille, P. *More from less – bottom-up reconstitution of cell biology. Journal of Cell Science*, 2019. **132**.
26. Möller, N., Ziesemer, S., Hildebrandt, P., Assenheimer, N., Völker, U., and Hildebrandt, J.P. *S. aureus alpha-toxin monomer binding and heptamer formation in host cell membranes - Do they determine sensitivity of airway epithelial cells toward the toxin? PloS one*, 2020. **15**(5): p. e0233854.
27. Bhakdi, S., and Tranum-Jensen, J. *Alpha-toxin of Staphylococcus aureus. Microbiological reviews*, 1991. **55**(4): p. 733–751.
28. Berube, B.J., and Wardenburg, J.B. *Staphylococcus aureus α-toxin: Nearly a century of intrigue. Toxins (Basel)*, 2013. **5**(1140-1166).
29. Inoshima, N., Wang, Y., and Wardenburg, J.B. *Genetic requirement for ADAM10 in severe Staphylococcus aureus skin infection. J Invest Dermatol.*, 2012. **132**: p. 1513-1516.
30. Hildebrand, A., Pohl, M., and Bhakdi, S. *Staphylococcus aureus alpha-toxin. Dual mechanism of binding to target cells. The Journal of biological chemistry*, 1991. **266**(26): p. 17195–17200.
31. Olson, R., Nariya, H., Yokota, K., Kamio, Y., and Gouaux, E. *Crystal structure of staphylococcal LukF delineates conformational changes accompanying formation of a transmembrane channel. Nature structural biology*, 1999. **6**(2): p. 134–140.
32. Jayasinghe, L., Miles, G., and Bayley, H. *Role of the amino latch of staphylococcal alpha-hemolysin in pore formation: a co-operative interaction between the N terminus and position 217. The Journal of biological chemistry*, 2006. **281**(4): p. 2195–2204.
33. Simons, K., and Ehehalt, R. *Cholesterol, lipid rafts, and disease. The Journal of clinical investigation*, 2002. **110**(5): p. 597–603.
34. Valeva, A., Palmer, M., and Bhakdi, S. *Staphylococcal alpha-toxin: formation of the heptameric pore is partially cooperative and proceeds through multiple intermediate stages. Biochemistry*, 1997. **36**(43): p. 13298–13304.
35. Walev, I., Martin, E., Jonas, D., Mohamadzadeh, M., Müller-Klieser, W., Kunz, L., and Bhakdi, S. *Staphylococcal alpha-toxin kills human keratinocytes by*

permeabilizing the plasma membrane for monovalent ions. Infection and immunity, 1993. **61**(12): p. 4972–4979.

36. Eichstaedt, S., Gäbler, K., Below, S., Müller, C., Kohler, C., Engelmann, S., Hildebrandt, P., Völker, U., Hecker, M., and Hildebrandt, J.P. *Effects of Staphylococcus aureus-hemolysin A on calcium signalling in immortalized human airway epithelial cells. Cell calcium.*, 2009. **45**(2): p. 165–176.
37. Baaske, R., Richter, M., Möller, N., Ziesemer, S., Eiffler, I., Müller, C., and Hildebrandt, J.P. *ATP Release from Human Airway Epithelial Cells Exposed to Staphylococcus aureus Alpha-Toxin. Toxins*, 2016. **8**(12): p. 365.
38. Song, L., Hobaugh, M.R., Shustak, C., Cheley, S., Bayley, H., Gouaux, J.E. *Structure of staphylococcal α-hemolysin, a heptameric transmembrane pore. Science*, 1996. **274**: p. 1859-1866.
39. Johnson, R.P., Fleming, A. M., Jin, Q., Burrows, C.J., and White, H.S. *Temperature and electrolyte optimization of the α-hemolysin latch sensing zone for detection of base modification in double-stranded DNA. Biophysical journal*, 2014. **107**(4): p. 924–931.
40. Gouaux, E. *α-Hemolysin fromStaphylococcus aureus:An Archetype of β-Barrel, Channel-Forming Toxins. Journal of Structural Biology*, 1998. **121**(2): p. 110-122.
41. Furini, S., Domene, C., Rossi, M., Tartagni, M., and Cavalcanti, S. *Model-based prediction of the alpha-hemolysin structure in the hexameric state. Biophysical journal*, 2008. **95**(5): p. 2265–2274.
42. Gross, L.C.M. *Applications of Droplet Interface Bilayers: Specific Capacitance Measurements and Membrane Protein Corralling*. 2011, University of Oxford. p. 238.
43. Demuro, A., and Parker, I. *Optical single-channel recording: imaging Ca^{2+} flux through individual ion channels with high temporal and spatial resolution. Journal of Biomedical Optics*, 2005. **10**(1).
44. Demuro, A., and Parker, I. *"Optical patch-clamping": single-channel recording by imaging Ca^{2+} flux through individual muscle acetylcholine receptor channels. The Journal of general physiology*, 2005. **126**(3): p. 179–192.

45. Neher, E., and Sakmann, B. *Single-channel currents recorded from membrane of denervated frog muscle fibres. Nature*, 1976. **260**(5554): p. 799–802.
46. Zou, H., Lifshitz, L.M., Tuft, R.A., Fogarty, K.E., and Singer, J.J. *Imaging Ca^{2+} entering the cytoplasm through a single opening of a plasma membrane cation channel. The Journal of general physiology*, 1999. **114**(4): p. 575–588.
47. Sonnleitner, A., and Isacoff, E. *Single ion channel imaging. Methods in enzymology*, 2003. **361**: p. 304–319.
48. Wang, S.Q., Song, L.S., Lakatta, E.G., and Cheng, H. *Ca^{2+} signalling between single L-type Ca2+ channels and ryanodine receptors in heart cells. Nature*, 2001. **410**(6828): p. 592–596.
49. Heron, A.J., Thompson, J.R., Cronin, B., Bayley, H., and Wallace, M.I. *Simultaneous measurement of ionic current and fluorescence from single protein pores. Journal of the American Chemical Society*, 2009. **131**(5): p. 1652–1653.
50. Demuro, A., and Parker, I. *Imaging the activity and localization of single voltage-gated Ca^{2+} channels by total internal reflection fluorescence microscopy. Biophysical journal*, 2004. **86**(5): p. 3250–3259.
51. Gross, L.C.M., Heron, A.J., Baca, S.C. and Wallace, M.I. *Determining Membrane Capacitance by Dynamic Control of Droplet Interface Bilayer Area. Langmuir,* 2011. **27**(23): p. 14335–14342.
52. Ahmadi, M., Rajamani, R., and Sezen, S. *Transparent Flexible Active Faraday Cage Enables In Vivo Capacitance Measurement in Assembled Microsensor. IEEE sensors letters*, 2017. **1**(5).
53. Schmitt, B.M., and Koepsell, H. *An improved method for real-time monitoring of membrane capacitance in Xenopus laevis oocytes. Biophys J.*, 2002. **82**(3).
54. Najem, J.S., Dunlap, M.D., Rowe, I.D., Freeman, E.C., Grant, J.W. Sukharev, S., et al. *Activation of bacterial channel MscL in mechanically stimulated droplet interface bilayers. Sci Rep.*, 2015. **5**(1): p. 1-11.
55. Huang, Y., Fuller, G.G., Suja, V.C. *Physicochemical characteristics of droplet interface bilayers. Advances in Colloid and Interface Science*, 2022. **304**(102666).

56. Rofeh, J.T. *Instantaneous tension measurements in droplet interface bilayers using an inexpensive, integrated pendant drop camera. Soft Matter*, 2020. **16**: p. *44*84-4493.
57. Szabo, M.I. *Imaging potassium-flux through individual electropores in droplet interface bilayers. Biochim Biophys Acta (BBA)-Biomembr.*, 2016. **1858**(3): p. 613-617.
58. Elfaramawy, M.A., Fujii, S., Uyeda, A., Osaki, T., Takeuchi, S., Kato, Y., et al. *Quantitative analysis of cell-free synthesized membrane proteins at the stabilized droplet interface bilayer. Chem Commun.*, 2018. **54**(86): p. 12226-12229.
59. Kotnik, T., Rems, L., Tarek, M., and Miklavčič, D. *Membrane electroporation and electropermeabilization: mechanisms and models. Annu Rev Biophys*., 2019. **48**: p. 63-91.
60. Koizumi, S., Bootman, M.D., Bobanović, L.K., Schell, M.J., Berridge, M.J., and Lipp, P. *Characterization of Elementary Ca^{2+} Release Signals in NGF-Differentiated PC12 Cells and Hippocampal Neurons. Neuron*, 1999. **22**(1): p. 125-137.
61. Berridge, M.J. *Inositol trisphosphate and calcium signaling. Nature*, 1993. **361**: p. 315-325.
62. Petersen, O.H., Petersen, C.C.H., and Kasai, H. *Calcium and hormone action. Annu. Rev. Physiol*., 1994. **56**: p. 297-319.
63. Hyrc, K.L., Bownik, J.M., and Goldberg, M.P. *Ionic selectivity of low-affinity ratiometric calcium indicators: mag-Fura-2, Fura-2FF and BTC. Cell calcium.*, 2000. **27**(2): p. 75–86.
64. Paredes, R.M., Etzler, J.C., Watts, L.T., Zheng, W., and Lechleiter, J.D. *Chemical calcium indicators. Methods (San Diego, Calif.)*, 2008. **46**(3): p. 143–151.
65. Lohr, C., Beiersdorfer, A., Fischer, T., Hirnet, D., Rotermund, N., Sauer, J., Schulz, K., and Gee, C.E. *Using Genetically Encoded Calcium Indicators to Study Astrocyte Physiology: A Field Guide. Front. Cell. Neurosci.*, 2021. **15**.
66. Miyawaki, A., Llopis, J., Heim, R. et al. *Fluorescent indicators for Ca^{2+} based on green fluorescent proteins and calmodulin. Nature,* 1997. **388**: p. 882–887.
67. Lipids, A.P. *1,2-dioleoyl-3-trimethylammonium-propane (chloride salt)*. 2023.

68. Lipids, A.P. *1,2-dioleoyl-sn-glycero-3-phosphocholine*. 2023.
69. Challita, E.J., Najem, J.S., Monroe, R. et al. *Encapsulating Networks of Droplet Interface Bilayers in a Thermoreversible Organogel. Sci Rep.*, 2018. **8**(6494).
70. Dürre, K., Keber, F.C., Bleicher, P., Brauns, F., Cyron, C.J., Faix, J., and Bausch, A.R. *Capping protein-controlled actin polymerization shapes lipid membranes. Nature communications*, 2018. **9**(1): p. 1630.
71. Gov, N.S., and Gopinathan, A. *Dynamics of membranes driven by actin polymerization. Biophysical journal*, 2006. **90**(2): p. 454–469.
72. Haviv, L., Brill-Karniely, Y., Mahaffy, R., Backouche, F., Ben-Shaul, A., Pollard, T.D., and Bernheim-Groswasser, A. *Reconstitution of the transition from lamellipodium to filopodium in a membrane-free system. Proceedings of the National Academy of Sciences of the United States of America*, 2006. **103**(13): p. 4906–4911.
73. Fehon, R.G., McClatchey, A. I., and Bretscher, A. *Organizing the cell cortex: the role of ERM proteins. Nature reviews*, 2010. **11**(4): p. 276–287.
74. Bretscher, A., Edwards, K., and Fehon, R. G. *ERM proteins and merlin: integrators at the cell cortex. Nature reviews. Molecular cell biology*, 2002. **3**(8): p. 586–599.
75. Taylor, K.A., and Taylor, D.W. *Formation of 2-D paracrystals of F-actin on phospholipid layers mixed with quaternary ammonium surfactants. Journal of structural biology*, 1992. **108**(2): p. 140–147.
76. Renault, A., Lenne, P.F., Zakri, C., Aradian, A., Vénien-Bryan, C., and Amblard, F. *Surface-induced polymerization of actin. Biophysical journal*, 1999. **76**(3): p. 1580–1590.
77. Schroer, C.F.E., Baldauf, L., van Buren, L., and Marrink, S.J. *Charge-dependent interactions of monomeric and filamentous actin with lipid bilayers. PNAS*, 2020. **117**(11): p. 5861 - 5872.
78. Wong, G.C., Tang, J.X., Lin, A., Li, Y., Janmey, P.A., and Safinya, C.R. *Hierarchical self-assembly of F-actin and cationic lipid complexes: stacked three-layer tubule networks. Science (New York, N.Y.)*, 2000. **288**(5473): p. 2035–2039.
79. Schlicht, B., and Zagnoni, M. *Droplet-interface-bilayer assays in microfluidic passive networks. Sci Rep.,* 2015. **5**(9*951*).

80. Demuro, A., Mina, E., Kayed, R., Milton, S.C., Parker, I., and Glabe, C.G. *Calcium dysregulation and membrane disruption as a ubiquitous neurotoxic mechanism of soluble amyloid oligomers. The Journal of biological chemistry*, 2005. **280**(17): p. 17294–17300.
81. Gross, L.C.M., Castell, O.K., and Wallace, M.I. *Dynamic and Reversible Control of 2D Membrane Protein Concentration in a Droplet Interface Bilayer. Nano Lett.*, 2011. **11**: p. 3324–3328.
82. Wang, Y. *Electrode-free nanopore sensing by DiffusiOptoPhysiology. Sci. Adv.*, 2019. **5**(9).
83. Baxani, D.K., Jamieson, W.D., Barrow, D.A., and Castell, O.K. *Encapsulated droplet interface bilayers as a platform for high-throughput membrane studies. Soft Matter*, 2022. **18**: p. 5089-5096.
84. Sengel, J.T., and Wallace, M.I. *Imaging the dynamics of individual electropores. PNAS*, 2016. **113**(19): p. 5281 - 5286.
85. Stricker, J., Falzone, T., and Gardel, M.L. *Mechanics of the F-actin cytoskeleton. Journal of biomechanics*, 2010. **43**(1): p. 9-14.
86. Salbreux, G., Charras, G., and Paluch, E. *Actin cortex mechanics and cellular morphogenesis. Trends in cell biology*, 2012. **22**(10): p. 536–545.
87. Borisy, G.G., and Svitkina, T.M. *Actin machinery: pushing the envelope. Current opinion in cell biology*, 2000. **12**(1): p. 104–112.
88. Lamb, M.C. *Fascin in Cell Migration: More Than an Actin Bundling Protein. Biology*, 2020. **9**(11).
89. Llinas, P., Isabet, T., Song, L., Ropars, V., Zong, B., Benisty, H., Sirigu, S., Morris, C., Kikuti, C., Safer, D., Sweeney, H.L., and Houdusse, A. *How actin initiates the motor activity of Myosin. Developmental cell*, 2015. **33**(4).

Chapter 6: Peptide Synthesis for Cell Anchorage to the DIB

6.1 Introduction

Cell-based research has been intensively applied in a variety of fields, such as medicine, pharmacology, basic neuroscience, and toxicology with diverse applications, due to its capacity to retrieve useful information from living cells. Cell-based techniques enable monitoring of drug, toxin and functional particle effects, processes not attainable through protein/DNA analysis or animal-based tests. Consequently, cell-artificial surface interactions have attracted considerable attention due to living cell immobilization on synthetic substrate and its physical interaction with it, while in vivo-like conditions are maintained[1].

Such hybrid models offer the advantage of preserving a native cellular framework on one side, where adhesion molecules/receptors can be expressed in their native cellular milieu, and a simplified environment on the other side, where control can be exerted[2].

Cells' adhesion efficiency has been reported on various types of materials, such as cover glass, ITO-coated glass, bare gold surfaces[3, 4] and supported lipid bilayers (SLB), functionalized with bioactive molecules[5], such as carbohydrates, extracellular matrix (ECM) proteins and/or their components, such as poly-L-lysine (PLL) and arginine-glycine-aspartic(RGD)[6, 7].

These biological molecules introduce reduced variation in cell attachment and increase cell-binding affinity[8, 9], rendering ligand-modified surfaces an effective method for cellular function studies, such as cell adhesion[1].

Materialization of this approach requires alteration of an artificial surface to a cell friendly environment by grafting synthetic peptide or ECM components establishing real in vivo-like conditions for cell attachment[1].

The Arg-Gly-Asp (RGD) tri-peptide motif, which is the minimal necessary binding domain of the peptide sequence found in several ECM proteins[10] [5, 11], has been broadly utilized in synthetic peptide-based biomaterial developments for investigating cell adhesion and proliferation processes on model bilayer surfaces[5, 10], based on its role in integrin engagement[12].

6.1.1 Integrin Structure

Integrins represent a major family of heterodimeric membrane spanning receptors, specific for integrating communication between the extracellular and intracellular microenvironments[13, 14].

The name "integrin" was first coined by Tamkun et al., in 1986, defining a protein complex that linked the extracellular matrix to the actin-based cytoskeleton[13, 14]. Integrins' presence from lower eukaryotes, such nematodes and sponges, to mammals signifies their role in essential biological functions in all (higher) organisms[15], mediating cell adhesion[12, 13], survival, proliferation, and migration[16, 17].

An integrin molecule consists of two noncovalently associated transmembrane glycoprotein subunits, α and β (Fig. 6.1)[18]. Each subunit contains an elongated N-terminal extracellular region, (1000 and 750 amino acids long for the α and β, respectively)[19], a single-span transmembrane domain (TMD), and a short C-terminal cytosolic tail (20 and 50 amino acids long for a and b subunits, respectively)[13, 19], connecting the intracellular cytoskeleton and the pericellular ECM and thus, acting as transmembrane linkers (or "integrators")[15, 18].

In mammals, combination of different types from 18a and 8b subunits assemble 24 integrin heterodimers[18], with specific pairings determining ligand binding specificity and signalling pathways[20]. For instance, $\alpha_5\beta_1$ binds to fibronectin, $\alpha_2\beta_1$ binds to selected collagen family members, and $\alpha_v\beta_3$ binds to several ligands encompassing vitronectin, fibronectin and fibrinogen[21].

All α subunits are composed of four extracellular domains, β-propeller, thigh, calf-1 and calf-2 (Fig. 6.1), with half of them enclosing a supplemental ~200 amino acid folding domain, termed the inserted domain (I domain), which constitutes the ligand binding domain in α I-containing integrins[22].

The β subunit ectodomain comprises of eight segments, β I domain, hybrid, PSI, β-tail and four integrin-EGF domains (Fig. 6.1), with the β I domain playing the role of the major ligand binding pocket in α I-less integrins[22].

Electron microscopy and X-ray crystal structure studies demonstrate that the overall shape of integrin ectodomain is that of a large "head" on two long "legs" with flexible "knees" [23, 24](Fig. 6.1), and the shape of a globular head projects more than 20 nm from the lipid bilayer[22].

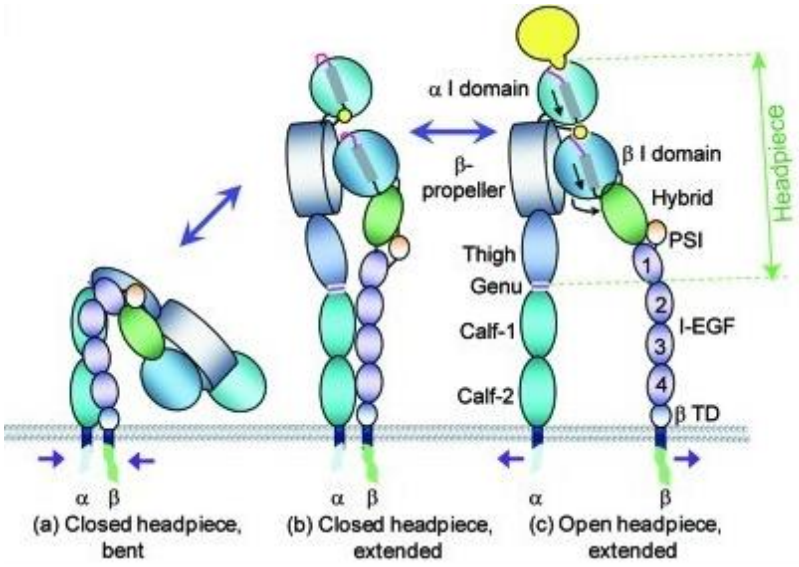

Figure 6.1- Schematic of integrin subunit structure and configuration rearrangement. *Each subunit comprises a short cytoplasmic tail, a transmembrane helix, and a large multi-domain extracellular segment. In a closed or "bent" conformation (a), integrins exhibit a low binding affinity for ligand, rendering them inactive. Upon activation, the extended and straighten shape(b), with open conformation (c) exposes the RGD-binding domain, leading to high affinity. Image taken from:[22].*

6.1.2 Integrin Conformational Changes Associated with Affinity Regulation

In the bent and folded arrangement (Fig. 6.1a), the RGD-binding site is hidden, forestalling ligand binding. Conversely, in the straight or unbent positioning, integrin can easily bind the RGD ligand (Fig. 6.1c)[20].

Activated integrins can induce global cell responses, but also localized cytoplasmic changes close to the cell-matrix contact. This fundamental feature of localized signaling has ramifications, for instance, in the developing nervous system, where the growing tip of an axon is guided primarily by the local adhesive or repellent cues in the milieu identified by the transmembrane cell adhesion proteins, rather than through cell-cell adhesion itself or signals delivered to the cell body[18].

In addition, the extracellular part of the α subunit carries four divalent-cation-binding sites (Fig. 6.2), whereas that of β constituent contains a single divalent-cation-binding site, as well as a repeating cysteine-rich motif (Fig. 6.2)[18]. The presence and the type of extracellular divalent cations (Ca^{2+} or Mg^{2+}, depending on the integrin), further influence integrin binding affinity and specificity to their ligands[18], as their role is fundamental in stabilizing integrin structure, mediating its interaction with the ligand and regulating integrin-ligand binding in either an enhancing or suppressing manner[19, 25, 26]. Therefore, their removal, (e.g., by EDTA), completely inhibits integrin-ligand interaction[22].

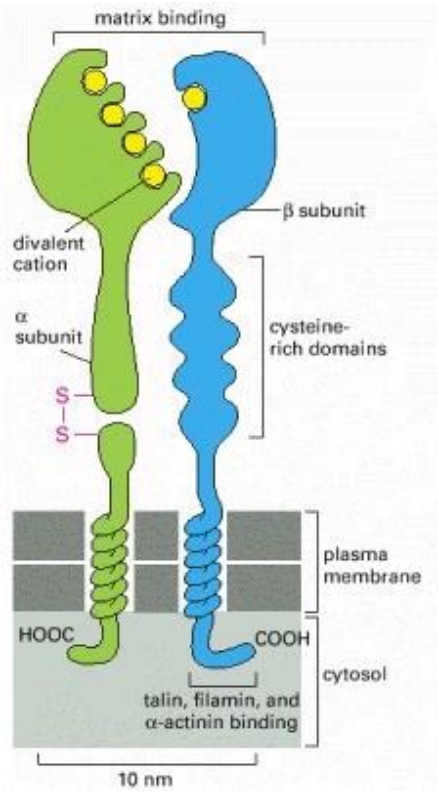

Figure 6.2- The αβ integrin subunits. *Source:[18].*

It is generally accepted that most integrins have “on” and “off” states which are determined by their extracellular domain configuration[20]. Interestingly, it has been demonstrated that integrins adopt at least three conformational positions: (a) the bent configuration with closed headpiece, (b) the extended conformation with closed headpiece and (c) the

extended arrangement with open headpiece, which correspond to the low-, intermediate- and high-affinity modes, respectively (Fig. 6.1)[22].

Typically, cell surface integrins are in equilibrium among these three conformational states and their activation is accompanied by extension of integrin's ligand-binding heterodimer headpiece away from the plasma membrane[27], commonly shifted by certain stimuli, such as extracellular metal ions[22].

6.1.3 Arg-Gly-Asp (RGD) Sequence Binding Specificity

It was in 1984 when Pierschbacher and Ruoslahti discovered the tripeptide Arg-Gly-Asp (RGD) sequence in fibronectin[15]. Later, this sequence was identified as a common recognition motif in various extracellular matrix proteins, not only in fibronectin, but also in vitronectin, fibrinogen, laminin, collagen, osteopontin, and bone sialoprotein[21], and was able to couple with multiple integrin species, including $\alpha_v\beta_3$ [21].

Although RGD is the principal integrin-binding domain present within ECM proteins, in some laminins and collagens, this motif is inaccessible due to its configuration changes that can modulate affinity accordingly. In these cases, other amino acid sequences operate as alternative binding modules for laminin and collagen-selective receptors[28, 29].

Proteins that enclose the RGD attachment site, along with the integrins that serve as receptors for them, represent a major recognition system for cell adhesion. The findings that the RGD sequence is the cell attachment site of manifold adhesive ECM, blood, and cell surface proteins[30] directed the development of multiple peptidic and non-peptidic RGD-based integrin ligands, with various degrees of specificity[31-33]. Up to now, 8 human integrin heterodimers, out of the known 24, were shown to bind the RGD-recognition sequence[29, 34], readily distinguishing among different RGD-containing ECM proteins (e.g. fibronectin, vitronectin, fibrinogen etc.) and yielding variable responses upon interaction[15].

RGD-containing integrin ligands also act as versatile cancer-targeting ligands and find applicability in many medical applications, extending from noninvasive integrin visualization *in vivo*, to functionalized biomaterial synthesis[35].

Crystal structures of integrin $\alpha_v\beta_3$- RGD ligand complexes have disclosed an atomic-based interaction[30, 36]. The integrin $\alpha_v\beta_3$, composed of a 125-kDa α_v subunit and a 105-kDa β_3 subunit, promotes RGD binding at an interface between the α and β subunits. The R peptide residue fits into a cleft in a β-propeller module in the α_v subunit, and the D amino acid coordinates a cation in the β_3 subunit[30].

6.1.4 Advantages of RGD Peptides for Directing Cell Association with Biomaterials

“RGD” is highly effective at promoting the attachment of numerous cell types to a plethora of diverse materials. Use of these small synthetic peptides, instead of the parent glycoprotein into the material surfaces[37] or scaffolds[38], minimizes immune reactivity or pathogen transfer, especially upon xenograft or cadaveric protein utilization[21].

Other benefits concern straightforward and minimal cost of peptide synthesis, (facilitating translation into the clinic), higher selectivity, and improved stability[38].

Moreover, the user can exert tight control over ligand presentation, orientation and densities, advantages not readily achievable when using full-length native matrix proteins to functionalize material surfaces[21].

6.1.5 Comparative Review of Linear (Flexible) and Cyclic (Fixed) Cell-targeting Peptides

Peptides are useful receptor-binding ligands and can be synthesized with relative ease employing well-established solid-state Fmoc and Boc synthetic methods. This type of production, as well as their unchallenging modification, make peptides comparably inexpensive for research and commercial purposes[39].

The process for the synthesis of cyclic peptides involves cyclization of linear peptides either in solution, (solution-phase approach), or on resin, (on-resin cyclization), with the latter regime being more efficient. The cyclization principle underlying this technique relies on peptide anchoring to the resin, through a side chain, and addition of orthogonal protecting groups for ring closure. This procedure's possessed advantages include cost-effectiveness, reduced side reactions and easy purification[40].

Cyclic peptide synthesis confers a constrained structure that enhances selective binding, uptake, stability, and potency compared to the linear precursors. Although peptide cyclization generally improves the selective binding and stability traits of a ligand, not all cyclization strategies can accomplish this goal to the same extent[39].

Usually, cyclic peptides, such as those with disulfide, thioether and rigid aromatic rings, exhibit enhanced biological activity over their linear equivalents due to the fixed geometry[40-42], which decreases the entropy of the Gibbs free energy, leading to improved integrin receptor binding affinity and selectivity[40].

The conformational rigidity of cyclic peptides is envisioned to bind more efficiently to their respective receptors because their constrained sequences are selective to particular receptor subtypes relative to their linear analogues.

The difference in peptide's selective binding capacity originates from the flexibility difference peptides possess between the two states, linear and cyclic. Linear peptides containing 2-10 amino acid residues, when in solution, can exist in fast equilibrium of interchanging conformations. Those carrying between 10-20 amino acid residues can

assume constrained secondary structures, such as a-helices, turns and b-strands, but their long sequences are not useful for receptor binding[39].

Conversely, the restrictions imposed by cyclization compel cyclic peptides to embrace a limited number of molecular configurations in solution, allowing the ligand to bind efficiently. These confined geometries can better mimic the biologically active segments of large endogenous proteins. The structural constraints induced by cyclization generally increase the propensity for b-turn formation in peptides, a secondary structure formation, frequently encountered in native proteins[43, 44].

Additional advantages of the cyclic structure are its hydrolysis resistance to exopeptidases, owing to the absence of both amino and carboxyl termini, where exoproteases preferentially cleave[39], and the diminished degradation by endopeptidases due to lessened flexibility relative to linear peptides[40, 45].

Certainly, there are cases, where linear peptide sequences evince similar or higher binding affinities, (or even) cell-penetrating abilities in comparison with their cyclic counterparts[39].

6.1.6 Click Chemistry Involving Peptides

Peptides have profoundly affected the development of the modern pharmaceutical industry and contributed considerably to the progress of chemical and biological science[46].

Peptides' intrinsic properties, such as biocompatibility and excellent recognition capabilities[47] [48], have led to their broad application in drug delivery and release, nano biomaterials and tissue engineering scaffold materials[49].Their utilization in these areas mandates biological or chemical peptide synthesis and sequence modification to heighten their target specificity and pharmacological properties[50].

Peptide modification has been achieved by click chemistry which has displayed a tremendous potential for diverse chemical alterations such as attachment of lipophilic or hydrophilic groups, ligands, or linkers etc. Click chemistry provides several avenues for peptide modifications, with the most prevalent involving cyclization, chemical ligation and bioconjugation, with the last one entailing the process by which synthetic molecules are coupled to biological targets, or by which biomolecules are linked together. Thus, this approach allows synthesis of multiple types of peptide functionality needed in functionalized system development[51].

6.1.6.1 Click Chemistry

Click chemistry is a category of simple reactions commonly used for linking two molecules or two modular units of choice. It basically describes the method of generating substances or products that follow examples in nature[35].

The term "Click Chemistry" was first coined by Sharpless in 2001 and the preparation process is performed rather easily due to the active building block availability and the possibility of conducting the reactions under mild conditions, for instance, at room temperature and in aqueous media, with almost complete conversions[52].

Other advantages of the click chemistry reactions involve high yields, easy purification, and use of water as the choice solvent. Most importantly, ligation occurs between functional groups not naturally present in macromolecules, avoiding side products[53].

Over the last few years, the process of conjugating relatively inert materials that minimize immune and fibrotic responses, such as polymers, to active biological molecules, forming defined structures which serve as biomaterial scaffolds to support cell attachment[21], has met an increasing success. A major role in their synthesis has played the growth of click chemistry which enriches and simplifies the strategies required for material and organic molecule combination[35].

From the early 2000s researchers have investigated the use of click chemistry to ligate targeting ligands to liposome surfaces[54-56], and nowadays several click chemistry approaches are employed for binding targeting ligands to bilayer surfaces[53].

The methods for coupling ligands are based on classical reactions such as crosslinking amines through homobifunctional linkers, amide bond formation, disulfide bridge, thioester bond formation by the maleimide-thiol addition reaction, and hydrazone bond formation, all of which are briefly summarized in Figure 6.3[53].

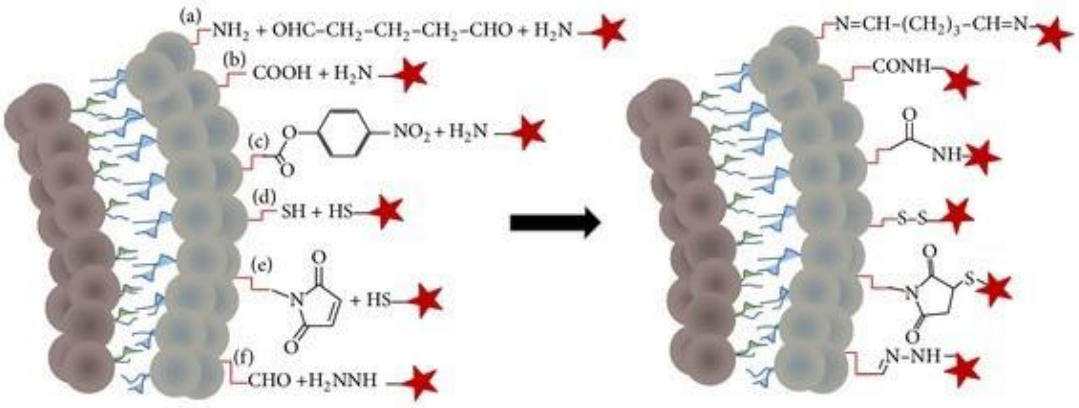

Figure 6.3- Click Chemistry reactions. *Schematic representation of liposome bilayer with functionalized functional groups demonstrating (a) conjugation of primary amines by glutaraldehyde, (b) carbonyl-amine crosslinking (c) formation of amide bond through para-nitrophenylcarbonyl and primary amine reaction, (d) disulfide bond generation, (e) maleimide-thiol reaction forming thioester bond, and (f) hydrazone bond formation. Red stars represent coupling ligands. Source:[53].*

6.1.7 Practical Approaches to Peptide Isolation

Peptides, peptide conjugates or synthetic peptides are increasingly attractive as potential therapeutics, diagnostics or tools to study the structure-activity relationships between cellular substrates[57].

Regardless of peptides' mode of synthesis, such as solution phase synthesis, solid-phase peptide synthesis or isolation from naturally occurring sources, crude peptide mixtures are complex and require purification. Synthesis reactions inevitably contain impurities stemming from truncations, deletions or chemically modified sequences including by-products formed during processing[57].

Peptide product isolation can be achieved through separation mechanisms such as native-PAGE and high-performance liquid chromatography (HPLC)[58]. HPLC has proved extremely versatile for peptide purification and has revolutionized the efficiency and speed of molecule and peptide separation over the past 25 years[59].

6.1.7.1 The High-Performance Liquid Chromatography (HPLC) System

Chromatography is a powerful separation method, and the working principle involves separation on the basis of adsorption[60].

High-performance liquid chromatography (HPLC) setups use a pumping device to generate a gradient of different solvents, a column to separate solutes, and a detector to measure the analytes' absorbance, including ions, organic molecules, polymers, and biomolecules[61].

6.1.7.1.1 Analytical HPLC

HPLC is classified into two main categories: analytical and preparative. The goal of the analytical or conventional HPLC is to identify as many constituents of a sample as possible and possibly determine the concentration of analyte(s) in a sample.

6.1.7.1.2 Preparative HPLC

The primary objective of preparative-scale high performance liquid chromatography (HPLC) is to isolate and purify a valuable compound in the most economical way, in a short period of time, depositing it into a fraction collector prior to its retrieval from the eluent[62].

6.1.7.1.3 Instrumentation of an HPLC System

The basic components of the preparative HPLC are shown in the Figure 6.4 and consist of a solvent reservoir, a pumping unit, which forces the mobile phase at a specific flow rate, a sample-injection unit, used to introduce a sample into the mobile phase, a preparative separation (column) unit, which separates the sample components using physical and chemical parameters, a detection unit, which monitors individual molecules eluting from the column, a data processing unit that controls the modules of the HPLC instrument and receives the detector signals to determine sample components, retention time and quantitative analysis, and finally, a fraction collector, where desired eluants are deposited[63].

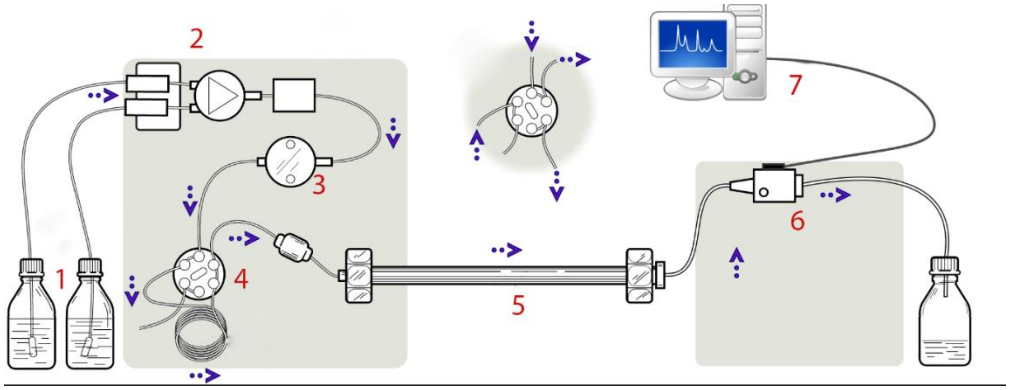

Figure 6.4- Schematics of *an HPLC instrumentation:* *1) solvent reservoir, 2) gradient valve, 3) pump, 4) sample injector, 5) column, 6) detector, 7) computer. Source:[63].*

6.1.7.1.4 Separation Mechanisms

For sample component separation, different properties of the stationary phase of the column are used, with the major types involving normal phase chromatography, reverse phase chromatography, size exclusion, ion exchange chromatography, and affinity chromatography. We will briefly refer only to normal-phase and reverse-phase chromatography, as the later mechanism is used in the current work.

6.1.7.1.4.1 Normal-phase Chromatography

In the normal-phase chromatography, the column contains polar, inorganic particles, while the mobile phase has a nonpolar character. This type of chromatography is primarily used for crude sample purification and very polar sample separation. The main downside is its incompatibility with water presence in the mobile phase, which can affect sample retention[63].

6.1.7.1.4.2 Reverse-phase Chromatography

Reversed phase (RP) is a commonly used column material, which consists of silica gel particles with long hydrocarbon chains (C8 or 18). Due to the presence of hydrocarbon chains, this stationary phase possesses non-polar/hydrophobic characteristics, facilitating its strong interaction with the highly non-polar sample components and permitting unrestricted polar constituent passage. Therefore, the more hydrophobic molecules of the analyte have longer retention times, while the inorganic ions, polar metal molecules and ionized organic compounds, show little retention time[62].

6.1.7.1.5 Preparative HPLC Operation

As illustrated in Figure 6.5, using a pump (A), the mobile phase, which usually contains a mixture of polar and non-polar components, is transported to a mixing chamber (B). Then, the mobile phase mixture travels to the sample injector (C), where the sample is introduced into the mobile phase, either manually or via an automated injector. The sample, already flowing with the mobile phase, encounters the HPLC column (D), which is the HPLC's stationary phase, responsible for separating the individual molecules before being characterized by the detector[62]. Subsequently, the continuous stream of solvent passes through the detector (E), which measures the absorbance of the sample constituents at a specified wavelength, through the use of ultraviolet, visible or fluorescence detectors. A chromatogram (F), which is a graphical representation of the data collected by the detector, is obtained, with the absorbance peaks of the individual samples, depicted in y-axis, and their retention times provided in x-axis. Finally, via a diverter valve, the flow of the sample can be directed either to waste (G) (Fig. 6.5) or into a fraction container through a fraction collection needle[62].

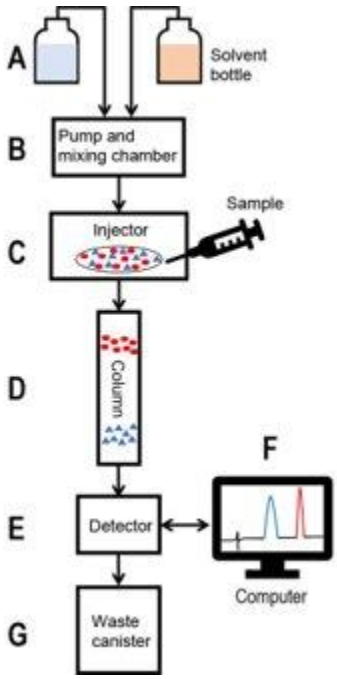

Figure 6.5- Diagram of an HPLC system. *Source:[64].*

6.1.8 Mass Spectrometry

Mass spectrometry (MS) is an analytical tool in which chemical substances are ionized into charged molecules and identified according to their mass-to-charge (m/z) ratios. Although its scope was initially limited to chemical sciences, electron spray ionization (ESI) and matrix assisted laser desorption ionization (MALDI) development, increased the MS applicability to large biological molecules. Both ESI and MALDI are based on “soft ionization”, meaning that compounds are converted into ions by loss or addition of one or more than one proton, an approach which minimizes significant loss of sample integrity. MALDI-TOF MS (Time of Flight Mass Spectrometry) outweighs ESI-MS in the fact that it (a) produces singly charged ions compared to ESI-MS, and hence provides easier data interpretation and (b) does not require prior separation by chromatography as ESI-MS analysis does[65, 66].

6.1.8.1 MALDI – Principle and Methodology

Matrix-assisted laser desorption ionization (MALDI) technology is a critical tool for the analysis, identification, and quantification of biomolecules like peptides, saccharides, lipids, or other organic macromolecules.

This technique is employed in mass spectrometry methods to generate ions by laser use, mainly in UV range, and is mostly combined with a time-of-flight (TOF) analyzer, primarily under high vacuum conditions, but even under atmospheric pressure[67, 68].

For analysis by MALDI, the sample needs to be mixed with solution of an energy-absorbent, organic compound, referred to as matrix. Upon drying, the matrix crystallizes, and the entrapped sample co-crystalizes as well. A laser beam, in an automated mode, is used for matrix ionization.

Laser radiation, (usually ultraviolet light (UV) and secondarily infrared (IR) wavelengths), strikes the crystallized mixture of the sample, and the irradiated spot (of the matrix) is rapidly heated and vaporized, together with the sample (Fig. 6.6).

The matrix mediates the transfer of energy to the test substance, and the molecules of the sample are desorbed and ionized by being singly protonated or deprotonated (Fig. 6.6). Thus, the matrix is employed to ionize the molecules, which cannot absorb laser radiation themselves[65, 67].

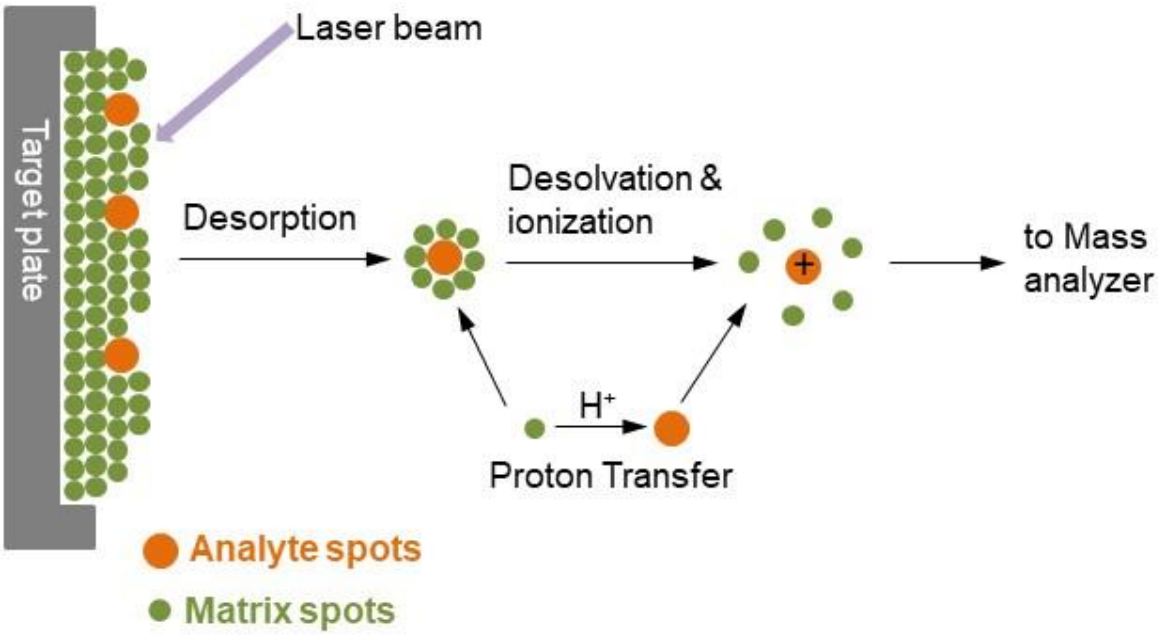

Figure 6.6- Analyte ionization by MALDI. *Image taken from:[69].*

6.1.9 Time of Flight (TOF) Analyzer

The charged analytes are then measured with different kinds of mass analyzers, the most common being time of flight (TOF) analyzers.

The basic principle of TOF is that the charged ions (protonated ions) of various sizes generated, under a potential difference (V_0), are accelerated and separated from each other on the basis of their mass-to-charge ratio (m/z).

The equation that defines the ions' kinetic energy, following acceleration, in the flight tube (in a field-free drift path) (Fig. 6.7), is the following (1):

$$E_{kin} = \frac{1}{2} mv^2 \quad (1)$$

where E_{kin} = Kinetic energy (J), m = Mass (kg), v = Velocity (ms^{-1})

and the velocity at which an ion moves determines its “time of flight”. Thus, the time of flight is calculated by combining equations (2) and (1):

$$t = d/v \quad (2)$$

where d = length of the flight tube.

Thus, for MALDI-TOF analysis, the time required for a charged molecule to travel the known length of the flight tube is used to determine the m/z ratio of an ion.

The MALDI separation principle simply states that the larger the m/z is, the slower an ion will fly, and therefore, the longer the measured flight time will be.

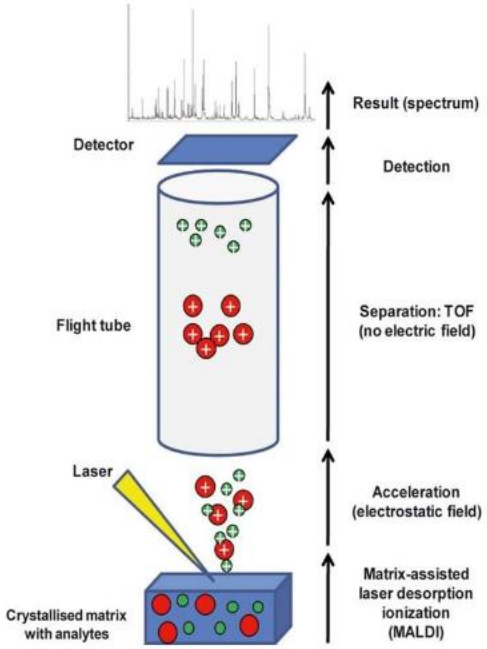

Figure 6.7- Schematic representation of a linear MALDI time-of-flight (TOF) mass spectrometer. *Source:[70].*

Although in theory, all ions are provided with the same initial kinetic energy, suggesting that ions of the same m/z reach the detector simultaneously, in practice, the pulse is not felt by all ions at the same intensity. This problem is usually rectified by a reflectron applied at the end of the field free region, which is composed of a series of ring electrodes with high voltage, repulsing the ions back, along the flight tube, at a slightly displaced angle (Fig. 6.8). In this manner, ions of disparate kinetic energies enter the reflectron in different depths prior to being expelled from it and sent back in the opposite direction. Ions with more kinetic energy (faster ions), will penetrate the reflectron deeper than ions carrying less energy (slower ions). With this remedy, the detector collects ions of the same mass at (about) the same time, thereby conferring increased resolution. Nevertheless, reflectron TOF analyzer is not a suitable approach for unstable analytes which cannot survive the electric field[70].

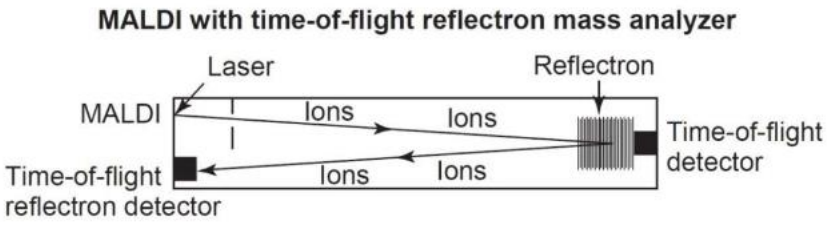

Figure 6.8- Schematic of Reflector TOF analyzer. *Source:[70].*

A characteristic spectral representation of these ions is generated based on the TOF information and analyzed by the MS software, producing an MS profile as shown in Figure 6.7 (Result Spectrum)[65].

6.1.10 Chapter's Aims

Moving towards our end goal to engineer a biohybrid interface system with intimate synthetic membrane-plasma membrane interconnecting sites, (cell anchorage to DIB inner surface via peptide linkers), we were in quest of bioconjugate compounds that can mediate cell adhesion.

Much of the research in this area has centered on utilizing adhesive peptides that engage and activate integrin cell-surface adhesion receptors[21].The highly recognized Arg-Gly-Asp (RGD) tripeptide motif, with tailored properties, has obtained remarkable interest, as it can bind selectively to transmembrane proteins on the cell surface inducing cellular adhesion.

Leveraging the RGD system and the beneficial effects of click chemistry, we synthesize a bioconjugate integrin targeting compound with fluorescent and membrane bound functionalities. A custom-made cyclic RGD peptide, cyclo(Arg-Gly-Asp-D-Phe-Lys)(Cys), is attached to a fluorophore (Atto488), for visualization by fluorescence microscopy, and coupled to a cholesterol functionalized PEG spacer arm, for membrane embedment (Fig. 6.9).

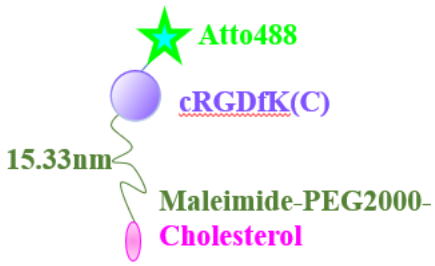

Figure 6.9- Schematic representation of intermembrane peptide conjugate, *composed of a cyclic peptide (purple), flanked by a cholesterol-carrying PEG polymer at one terminus (green-magenta) and a fluorophore, Atto488 (light green), at the other terminus.*

Specifically, both the chol-PEG polymer and the Atto488 dye are covalently bound to the thiol/sulfhydryl (HS) and primary amine ($-NH_2$) groups of the cysteine (Cys) residue of the cRGD-containing peptide via maleimide and NHS ester coupling, respectively.

The role of the PEG chain in this construct is not only to enhance the peptide's hydrophilic and binding properties, but through its modified cholesterol terminus to enable peptide's tethering to artificial membrane bilayer. Fluorophore dye conjugation is needed to facilitate direct imaging of single molecules within integrin-ligand complexes, revealing molecular, temporal, and spatial details of integrin-ligand mobilities.

The RP-HPLC technique is used for component separation, following constituent conjugation, and the collected HPLC fractions are subjected to MALDI-TOF mass spectrometer for end product characterization.

6.2 Materials and Methods

6.2.1 Conjugation of cRGDfK(C) with Atto488 NHS Ester

The cyclic Arg-Gly-Asp-D-Phe-Lys(Cys) (cRGDfK(C)) peptide, with molecular weight 706.83 g/mol, was custom-synthesized and reverse-phase HPLC (RP-HPLC) purified by Vivitide. Atto488 NHS ester, with molecular weight 981 g/mol, was purchased from Sigma Aldrich.

The reagent vials were equilibrated to room temperature before opening to avoid moisture condensation inside the containers. Both Atto488 NHS ester and cRGDfK(C) were dissolved in DMSO (anhydrous, 99.8%; sigma aldrich) and the peptide solution was subsequently diluted in PBS (pH 8.5) with 1mM EDTA, just before the conjugation reaction. EDTA was added to chelate divalent metals, thereby reducing disulfide formation in the sulfhydryl-containing peptide.

A 7 mM solution of Atto488-NHS ester reacted with a 1.4 mM solution of cRGDfK(C). The NHS ester dye was transferred dropwise under stirring to the peptide solution and the reaction was placed on a shaker (300 r.p.m.) and allowed to proceed overnight at room temperature.

6.2.2 Synthesis of CHOL-PEG-MAL-cRGDfKC-ATTO488

Cholesterol-PEG-Mal, with molecular weight 2000 g/mol, was purchased from CreativePEGworks. Cholesterol-PEG-Mal was resuspended in DMSO (anhydrous, 99.8%; sigma aldrich) and diluted with dH2O (pH 7.0), prior to bioconjugation. A 7 mM Cholesterol-PEG-Mal solution was mixed with the cRGDfK(C)-Atto488 conjugate solution and the reaction mixture was incubated on a shaker (300 r.p.m.) for 12 hours at room temperature.

6.2.3 Purification of CHOL-PEG-MAL-cRGDfKC-ATTO488 Conjugate by RP-HPLC

Dr Alexander Landen, from Chemistry Department at Cardiff University, instructed me and aided me in the operation of the HPLC equipment.

A reverse phase high performance liquid chromatography (RP-HPLC), equipped with a C18 column (250 × 4.6 mm, 5 µm), a binary pump system and photodiode array detector (Agilent Technologies 1260 Infinity II) with monitoring at 214 nm (absorbance of the peptide bond) and 500 nm (excitation peak of Atto488), was used to purify the final product (*Appendix,* ***Fig. A2***).

The flow rate of the reaction mixture, injected through the column, was optimized at 1 ml/min using a mobile phase consisting of 0.1% v/v trifluoroacetic acid in water (eluant A) and 0.1% v/v trifluoroacetic acid in acetonitrile (eluant B). The eluant gradient was set from 0% to 70% B over 30 min and followed by a second elution gradient of 70–99% B over 10 min to collect the more hydrophobic fractions. The injection volume was 100 µl.

6.2.4 Characterization of CHOL-PEG-MAL-cRGDfKC-ATTO488 Conjugate by MALDI-TOF

For the desired conjugated compound to be analysed and characterised, matrix-assisted laser desorption ionization time of flight (MALDI-TOF) mass spectrometer (Voyager-STR) was used.

This procedure was exclusively performed by the senior technician, Mr Peter Iafrate, at the School of Chemistry, Cardiff University.

Ensuing HPLC fraction collection, corresponding to chromatogram peaks, the eluted fractions were mixed with α-Cyano-4-hydroxycinnamic acid (CHCA) (saturated solution in acetonitrile) at a 1:1 ratio by volume (10 µl). Approximately 3-5 µl of this mixture was

applied to each sample well on the MALDI plate. Samples were allowed to dry fully at room temperature prior to MALDI analysis.

The plate was analyzed in an Bruker Autoflex Speed mass spectrometer in linear mode using a 340 nm nitrogen laser and positive polarity; compounds, were ionized as $[M+H]^+$ ions from the α-cyano-4-hydroxycinnamic acid (4-HCCA).

6.2.5 Lyophilization of CHOL-PEG-MAL-cRGDfKC-ATTO488 Peptide Construct

The fractions obtained from preparative separations were eluted in a large volume of volatile organic solvent: acetonitrile and water.

To determine peptide construct concentration, the samples were transferred into 2-ml vials, snap frozen by partial immersion in liquid nitrogen and then, underwent sublimation by being placed in a vacuum pump at a pressure of 0.300 mbar overnight.

The lyophilized samples were stored at –20°C until concentration quantification and further use.

6.2.6 Lyophilized Peptide Conjugate Reconstitution and Concentration Measurements

Each lyophilized peptide construct sample was resuspended in 30 µl of sterile PBS (pH ~7.4) and mechanically swirled till complete dissolution.

The peptide conjugates were quantified via the NanoDrop One spectrophotometer (NanoDrop® ND-1000) (Thermo scientific) by pipetting 2 µl sample solution onto the pedestal, following calibration with sterile PBS. A 500 nm wavelength (absorbance peak of the Atto488 fluorophore) was applied to measure fluorophore-peptide-mal-PEG-chol absorbance. The Beer-Lambert law (3):

$$A = \epsilon c l \quad \textbf{(3)}$$

where *A* stands for absorbance of sample (500 nm), ϵ represents molar extinction coefficient (90.000 M^{-1} cm^{-1}), *l* refers to length of the light path (1 cm), and c symbolizes concentration of solution, was used to calculate conjugate peptide concentration.

The reconstituted desired compound was aliquoted and stored at –20°C till further use.

6.3 Results

6.3.1 Design of Peptide Construct

Aiming to build a biohybrid interface system, where a living cell can directly interact with the DIB inner lipid sheet, through receptor-ligand engagement, we selected a cyclic RGD peptide to execute this task.

For bridging the living cell with the DIB bilayer, the cyclic RGD peptide needed to be endowed with (a) a membrane self-insertion capacity, for DIB and SLB anchorage purposes and (b) fluorescence properties, for direct imaging of single molecules.

To materialize this objective, a custom-designed cyclic RGD probe molecule, (cRGDfK(C)), was attached to the terminus of a cholesterol-functionalized polyethylene glycol polymer, (Cholesterol-PEG-Maleimide), conferring membrane integration capabilities via the hydrophobic cholesterol moiety, while being flanked by a fluorophore, (Atto488), for visualization by fluorescence microscopy (Fig. 6.9).

The cyclic RGD peptide, cyclo(Arg-Gly-Asp-D-Phe-Lys)(Cys), or in short (cRGDfK(C)), was elected to be used as an intermembrane linker for several reasons. Initially, the specific targeting group of (cRGDfK(C)) has been reported to strongly interact with the $\alpha_v\beta_3$ integrin receptor[71-73]. Furthermore, its fixed cyclic geometry, being resistant to hydrolysis by exopeptidases and endopeptidases, prolongs the peptide's integrity by thwarting degradation, and promotes its biological activity through targeted selectivity and stability[42, 45, 74, 75].The peptide's enzymatic stability against peptidases is also enhanced due to the aromatic amino acid, phenylalanine (Phe), at residue 4, which, among others, is essential for the $\alpha_v\beta_3$-binding affinity[15, 76].

The cysteine residue (C) inclusion in the peptide sequence has also a major role to play in the desired compound synthesis. The cysteine amino acid, bound to the ε-amine of

lysine of the peptide, contains a very reactive thiol/sulfhydryl side chain (HS), and a primary amine group (−NH_2) (Fig. 6.10), both of which, due to their nucleophilicity, (ability and tendency to donate electrons to an electrophile, an electron-deficient atom or molecule), can engage in intramolecular hydrogen transfer reactions with amino acid residues (in peptides and proteins), forming covalent bonds.

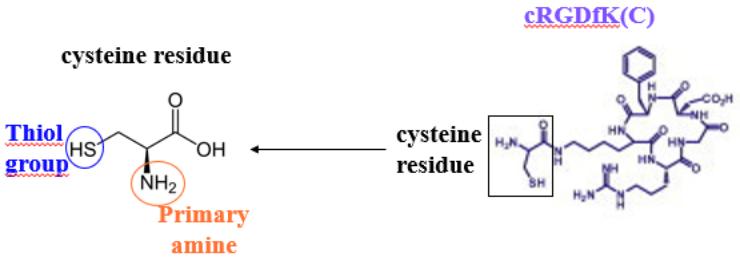

Figure 6.10- Cysteine chemical structure*: Cys being attached to the the ε-amine of lysine in the cyclic RGD peptide-(on the right), contains thiol/sulfhydryl (HS) and primary amine (−NH_2) groups, marked on the left.*

The surface grafted PEG chain (via cholesterol), which has been widely used in biomimetic systems, was included in the peptide construct design not only because it attenuates non-specific binding, due to developing steric repulsion forces and water dependent molecular conformations[77], but also because it facilitates specific interactions owing to its flexibility.

An additional advantage of the membrane inserted cholesterol functionalized-PEG linker regards the easiness to control cholesterol-surface distance by varying the spacer thickness. In our system, the PEG linker contour length is 12.7 nm, as it consists of 45 polyethylene oxide (PEO) units, which along with that of the maleimide compound, 2.63 nm, amounts to a total distance of 15.33 nm (Fig. 6.9); not much deviating from the width

of the neuron or immune synaptic cleft (20–30 nm wide for the former and 10–30 nm[78] for the latter) we aim to reproduce.

Lastly, cholesterol, instead of biotin-streptavidin linkage, was opted for as biomembrane anchor, because apart from providing synthetic membranes similar mechanical and biological functions to the native membranes, its single-module trait facilitates the translation process of peptide construct embedment from the SLB to the DIB inner surface for the biohybrid interface system fabrication.

6.3.2 Synthesis of Peptide Construct via Click Chemistry

Taking advantage of the click chemistry, the NHS ester reagent (crosslinker), contained in the fluorophore Atto488, (Atto488 NHS ester), was chemically attached to the primary amine ($-NH_2$) functional group of the cysteine residue of the peptide in slightly alkaline conditions (pH 8.5), yielding a stable amide bond and (NHS) N-hydroxysuccinimide release (Fig. 6.11A).

PEG linker conjugation to the peptide was achieved through maleimide incorporation in the PEG molecule, which promotes reaction with the sulfhydryl (thiol/SH) group in the cysteine residue of the peptide (at pH 6.5~7.5), leading to a stable thioether bond (Fig. 6.11B).

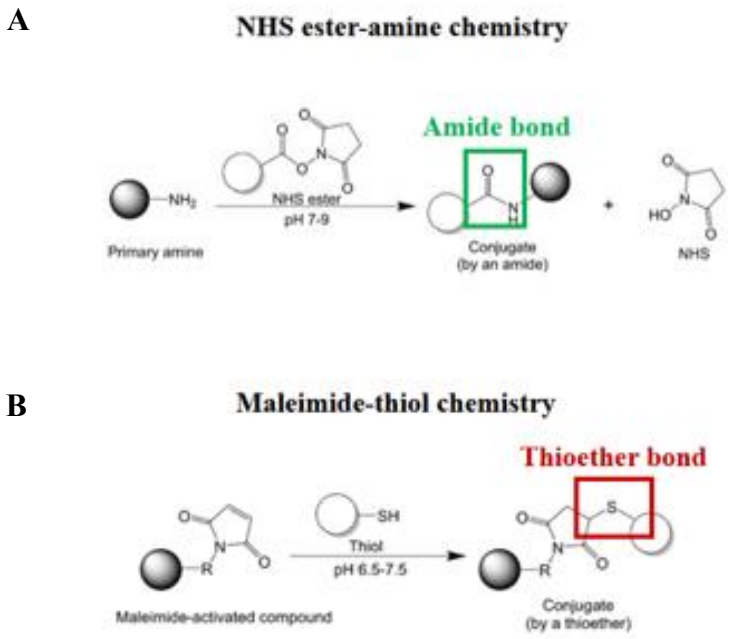

Figure 6.11- Schematics of NHS ester-amine and maleimide-thiol reactions with resulting stable amide and thioether bond formations. *Image adapted from:[79].*

Given that the maleimide group is more stable than the NHS-ester group, meaning that the NHS ester undergoes hydrolytic degradation at a faster rate than the maleimide group, conjugation between the NHS-ester and the targeted amine at pH 8.5 was performed first and the maleimide-sulfhydryl-targeted reaction followed.

6.3.3 Two-Step Synthesis of CHOL-PEG-MAL-cRGDfKC-ATTO488

For the synthesis of the Chol-PEG-Mal-cRGDfKC-Atto488 product, cRGDfK(C) peptides were initially labelled with Atto488 by adding a 5-fold molar excess of Atto488 NHS ester in the reaction (at pH 8.5) and applying gentle mixing. Under these conditions NHS esters reacted with amines forming amide bonds. Following an overnight incubation at R.T., a

5-fold molar excess of the solubilized chol-PEG-mal spacer arm (pH 7.0) was transferred to the reaction tube to complete the conjugation process, through which maleimide could react with the thiol containing peptide resulting in thioether bond formation. The second reaction was also allowed to proceed for another 12 h.

6.3.4 CHOL-PEG-MAL-cRGDfKC-ATTO488 Purification by RP-HPLC

The complete peptide product, Chol-PEG-Mal-cRGDfKC-Atto488, was purified using reversed phase-HPLC, as described in ***6.2 Materials and Methods*** (in ***6.2.3*** Purification of ***CHOL-PEG-MAL-cRGDfKC-ATTO488*** Conjugate by RP-HPLC).

The very first peak, at ~4.5 min, in the chromatography diagram (Fig. 6.12), potentially originated from DMSO absorbance, as its UV cut off is 268 nm, and 214 nm wavelength was applied for detection of peptide bonds. The next three eluted fractions were characterized by MALDI-TOF, (presented in ***6.3 Results,*** in ***6.3.5 CHOL-PEG-MAL-cRGDfKC-ATTO488 Identification by*** MALDI-TOF Mass Spectrometry), and the end product was identified in the middle out of the three peaks in the RP-HPLC chromatogram, as indicated in Figure 6.12 and (*Appendix,* ***Fig. A2***).

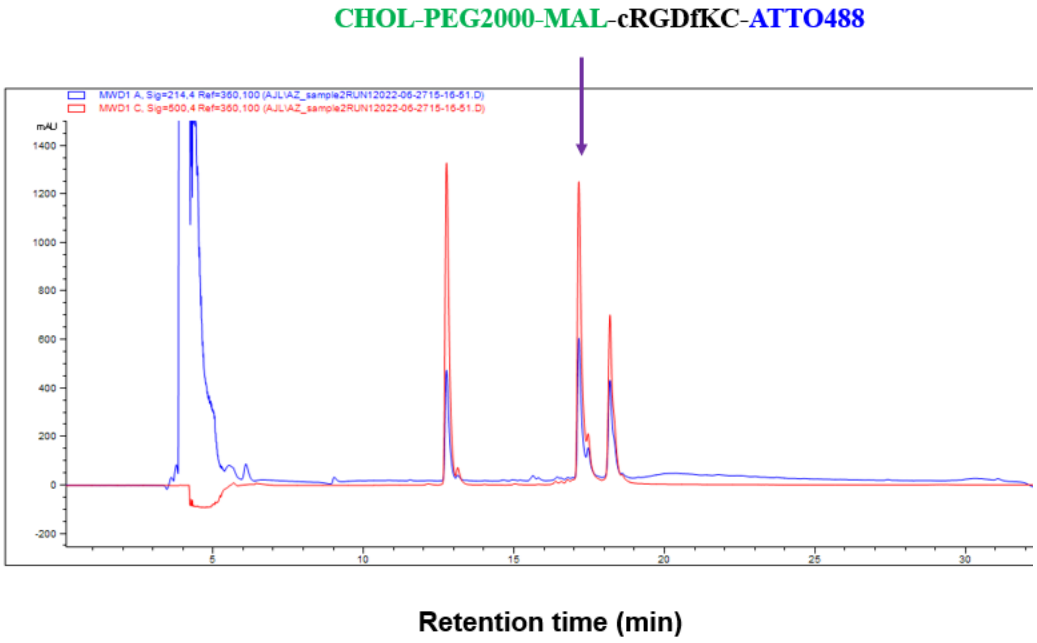

Figure 6.12- Purification of the Chol-PEG2000-Mal-cRGDfKC-Atto488 conjugate. *Reverse phase HPLC chromatogram of the Atto488 NHS, cRGDfKC, Chol-PEG2000-Mal reaction mixture. The absorbance was measured at 214 nm (absorbance of the peptide bond-blue) and 500 nm (absorbance of Atto488-red). 1 ml fractions were collected as they eluted off the column (flow rate = 1 ml/min). HPLC traces, gradient: 0-70% trifluoroacetic acid (TFA) in acetonitrile (ACN) over 30 min, retention time of the end product was t_R = 17.5 min.*

6.3.5 CHOL-PEG-MAL-cRGDfKC-ATTO488 Identification by MALDI-TOF Mass Spectrometry

Synthesis of the whole conjugated compound was determined by MALDI-TOF mass spectrometric analysis. Collected HPLC fractions, corresponding to the three RP-HPLC chromatogram peaks (Fig. 6.12), were subjected to matrix-assisted laser desorption ionization time-of-flight (MALDI-TOF) mass spectrometry to identify/characterize the synthesized final compound.

The expected molecular weight of the desired end product was 3.687.83 g/mol, based on summation of its components' individual masses, that is, cRGDfKC (molecular weight:

706.83 g/mol), Atto488 NHS ester (molecular weight: 981 g/mol) and Chol-PEG-Mal (molecular weight: 2000 g/mol).

The observed m/z in the MALDI-TOF mass spectrum was 3700.455 (Fig. 6.13), yielding very close estimates between the theoretical (3.687.83 g/mol) and the observed (3700.455) molecular weights, confirming final construct synthesis. The mass increment (3835.194), also detected in the MALDI-TOF mass analysis (Fig. 6.13), could correspond to the same synthesized product, but reflecting unexpected molecule modifications (e.g., end group modifications).

Interestingly, in this eluted HPLC fraction, the MALDI-TOF mass spectrometric analysis displayed two other peaks. The tiny peak, with observed molecular weight of 1693.850 (and possibly along with that of 1773.269) (Fig. 6.13), could correspond to peptide-Atto488 coupling, (uncompleted chemical reaction), with predicted m/z of 1687.83.

The highest “base” peak, around 1800, (and possibly that of 1773.269) (Fig. 6.13), representing the most abundant and stable formed fragment ion, could be the result of truncated polymeric chains (chol-PEG-mal), given the crosslinker’s initial MW of 2000 g/mol. This truncated molecule type is envisaged to be produced by in-source fragmentations during MALDI analysis or during sample work-up (e.g., storage or synthesis inappropriate conditions).

In addition, a peak at 1987.835 in the MALDI-TOF mass spectrum, is consistent with the unconjugated chol-PEG-mal spacer (molecular weight 2000 g/mol), which may have remained as unreacted starting material.

The side-product and unreacted compound presence in this specific HPLC fraction, which contained the final conjugated construct, could possibly justify the shoulder/split peak in the HPLC chromatogram (Fig. 6.12), denoting closely unresolved compounds.

Given that the whole synthesized compound was localized in this eluted fraction despite side product co-existence, (such as dye-peptide coupling, truncated and unreacted PEG crosslinkers) (*Appendix,* ***Fig. A2***), the sample was subsequently subjected to

lyophilization, resuspension and quantification prior to its integration in the biohybrid model fabrication.

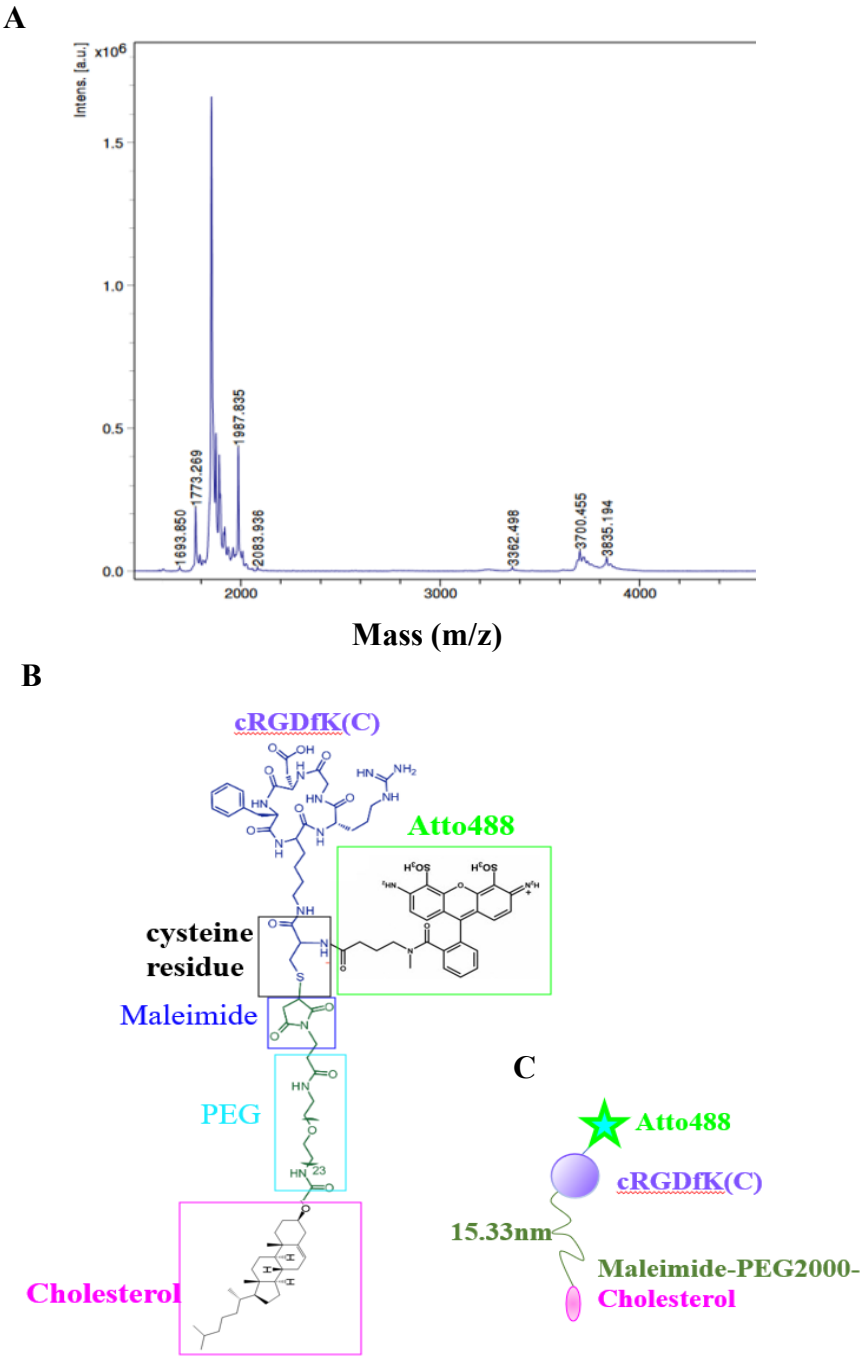

Figure 6.13- Identification of the Chol-PEG-Mal-cRGDfKC-Atto488 conjugate by MALDI-TOF MS. *(A) MALDI-TOF MS characterization of the 2nd HPLC peak (Fig. 6.12). The final integrin-targeting synthetic ligand product, Chol-PEG-Mal-cRGDfKC-Atto488, (with congruous MW obs = 3700.455 and MW expected = 3.687.83 g/mol values), was found to elute at 17.5 min. Detected small intensity peak at 1693.850 (and potentially 1773.269) could correspond to incomplete peptide-Atto488 coupling reaction. The highest peak at ~1800 (possibly together with the one at 1773.269), and at 1987.835, might reflect fragmented and unreacted chol-PEG-mal crosslinkers, respectively. (B) Structure of the final product. (C) Not-to-scale schematic representation of CHOL-PEG-MAL-cRGDfKC-ATTO488 peptide conjugate.*

Based on the MALDI-TOF mass spectra of the other two HPLC peaks, namely, 1 and 3, with retention times 12.8 min, 18.3 min, respectively, (Fig. 6.12) and (*Appendix,* ***Fig. A.3 and Fig. A.4***), we notice that their observed molecular weights are almost the same ~2557.457(Fig. 6.14). This mass seems to be relatively compatible with peptide coupling to two Atto488 molecules, yielding a theoretical MW of 2668.83 g/mol.

The 2-dye-peptide conjugate doesn't constitute an impossible scenario, given the exceptionally high nucleophilicity of cysteine's sulfhydryl/thiol (–SH) side chain, especially in its deprotonated thiolate form ($–S^-$), attainable at pH 8.5 (cysteine thiol pK_{a2} = 8.36), a condition that was implemented in the first step of the conjugation reaction.

Thiol reactivity, under alkaline conditions, renders this functional group accessible to modification by most amine-reactive reagents[80], such as Atto488 NHS ester molecule, permitting dye coupling to the sulfhydryl group.

However, the separate elution times of these two HPLC peaks (1^{st} and 3^{rd}) denote polarity differences, with the latter being comparatively more hydrophobic (longer retention time-18.3 min). The hydrophobicity element most likely stems from cholesterol participation, implying inclusion of single dye attachment and a truncated form of the cholesterol-PEG-mal crosslinker as full mass involvement of the polymer far exceeds the observed MW (MW obs = ~2557.457) in MALDI analysis. Thus, the 3^{rd} HPLC peak could represent peptide-Atto488 attachment to fragmented chol-PEG-mal chain. As these two eluted fractions did not contain the desired complete conjugated compound, we didn't proceed to any further investigation for resolving this issue.

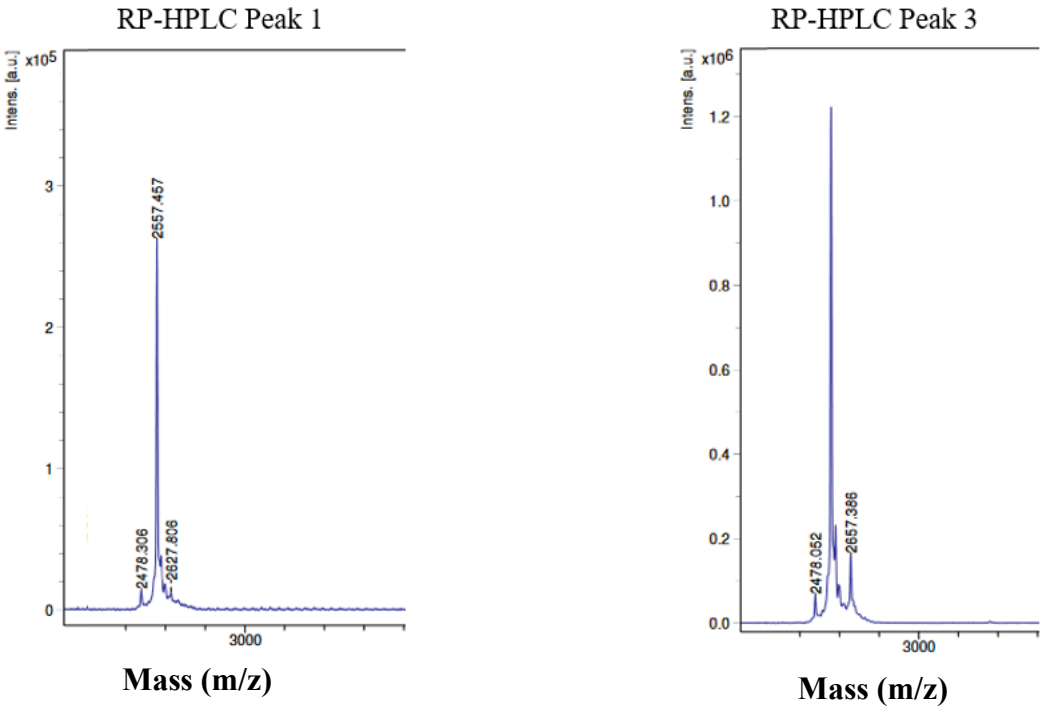

Figure 6.14- Characterization of HPLC peaks 1 and 3 by MALDI. *Both HPLC peak 1 and 3 with retention times 12.8 min and 18.3 min, respectively, displayed almost identical MW obs = ~2557.457. For the 1st peak, the MW obs possibly corresponds to two-Atto488 dye-peptide conjugate (with MW expected = 2668.83 g/mol). The hydrophobicity difference of the two HPLC peaks (shown in Fig. 6.12), though, could imply cholesterol-PEG involvement and single dye coupling for the 3rd peak.*

6.4 Discussion

The aim of the current work was to engineer and synthesize a type cholesterol-(PEG-[guiding ligand]), specific for selective binding to an integrin receptor type, $\alpha_v\beta_3$, expressed in a target cell.

The guiding ligand comprises a cyclic RGD peptide with the RGDfKC sequence, wherein the RGD, K and C residues are L-amino acids, and the f residue is a D-amino acid, generating a more robust peptide structure.

The RGD peptides are commonly known to interact with integrins, present in the PM of various cell lines, and draw interest for disclosing information on cell adhesion between cells and basement membrane or diverse tissues[81].

Studies have shown that peptide presentation does affect integrin engagement capacity, with extended large hydrophilic conformations, e.g. PEO (polyethylene oxide), promoting cell adhesion, whereas very short linker hydrophobic groups, effectively blocking it[38].

Considering that mere RGD amino acid sequence presence does not ensure cell adhesion, but ligand accessibility is an equally important parameter, a relatively long polymer chain, Chol-PEG45-Mal, bound to the cRGDfKC ligand was deemed indispensable to actuate receptor engagement.

The amphiphilic character of the Chol-PEG-Mal crosslinker was capitalized on its membrane embedment property and consequently, utilized for the development of the peptide-based cell membrane imaging probe needed for our bio-hybrid model engineering.

Bottom-up synthesis of the hybrid interface system, (peptide-integrin interaction mediated cell-DIB coupling), mandated chol-PEG-mal scaffold modification with the cRGDfKC sequence, which can serve as a targeting ligand for the cell surface integrin $\alpha_v\beta_3$ receptor.

In addition, peptide labeling with a fluorophore molecule (Atto488) was essential for probing ligand's localization on membrane surfaces.

The specific peptide sequence utilized, cyclo(Arg-Gly-Asp-D-Phe-Lys)(Cys), alias, (cRGDfK(C)), entertaining the C-terminal cysteine, enabled sequential fluorophore (Atto488 NHS ester) and polymer (Chol-functionalized PEG-mal) covalent binding to the cysteine primary amine and thiol side chain via the NHS group (Fig. 6.11A) and maleimide-thiol coupling reaction (Fig. 6.11B), respectively.

The conjugated Chol-PEG-Mal-cRGDfKC-Atto488 final compound was purified by RP-HPLC, displaying 17.5 min retention time (2^{nd} peak) (Fig. 6.12), and characterized/identified by MALDI-TOF (Fig. 6.13), the analysis of which corroborated to its synthesis; the observed (MW obs = 3700.455) and the predicted molecular weights (MW expected = 3.687.83 g/mol) of the engineered peptide construct yielded very close values, validating successful synthesis of the intended multiunit product.

MALDI-TOF MS analysis revealed end-compound co-existence with side-products, which probably involved incomplete peptide-dye coupling reaction (with MW obs = 1693.850 and possibly 1773.269, and MW pred = 1687.83 g/mol), fragmented chol-PEG-mal arm spacers (with MW obs = ~1800 and likely 1773.269, and MW pred = 2000 g/mol) and unreacted chol-PEG-mal chains (with MW obs =1987.835 and MW pred = 2000 g/mol) (Fig. 6.13), in the same collected HPLC fraction.

The other two eluted HPLC peaks, (1^{st} and 3^{rd}), with retention times 12.8 min and 18.3 min, respectively (Fig. 6.12), and their very close observed MW = ~2557.457, seemed to correspond to peptide double labelling by the Atto488 fluorophore (with MW expected = 2668.83 g/mol). However, the delayed elution time of the 3^{rd} peak, relative to the 1^{st} peak, reveals a slightly more hydrophobic character, suggesting truncated Chol-PEG-mal linker involvement, mitigating the possibility of double peptide labelling by Atto488, a supposition which agrees with the diminished absorbance intensity of the fluorophore in the HPLC chromatogram (Fig. 6.12).

As the focus of our interest was Chol-PEG-Mal-cRGDfKC-Atto488 compound development, detected at the eluted sample with t_R = 17.5 min (2^{nd} HPLC peak) (Fig. 6.12), side-product identity analysis in the other HPLC peaks wasn't of primary concern, although conjectures were expressed.

Regardless of impurity copresence with the end bio conjugated compound, the HPLC reaction mixture (corresponding to the 2^{nd} peak) was lyophilized (as described in 6.2 Materials and Methods, ***6.2.5 Lyophilization of CHOL-PEG-MAL-cRGDfKC-ATTO488 Peptide Construct***), redissolved in PBS, and quantified by nanodrop Spectrophometer, (where analyte concentration was determined from the Beer-Lambert law), before being grafted in the artificial DIB and SLB membranes, detailed in ***Chapter 7***.

6.5 References

1. Kafi, M.A., El-Said, W.A, Kim, T.-A., and Choi, J.W. *Cell adhesion, spreading, and proliferation on surface functionalized with RGD nanopillar arrays. Biomaterials*, 2012. **33**(3): p. 731-739.
2. Chamma, I., Sainlos, M., and Thoumine, O. *Biophysical mechanisms underlying the membrane trafficking of synaptic adhesion molecules. Neuropharmacology*, 2020. **169**.
3. Jin, L.H., Yang, B.Y., Zhang, L., Lin, P.L., Cui, C., and Tang, J. *Patterning of HeLa cells on a microfabricated au-coated ITO substrate. Langmuir*, 2009. **25**: p. 5380-5383.
4. Choi, C.K., Margraves, C.H., Jun, S.I., English, A.E., Rack, P.D., and Kihm, K.D. *Opto-electric cellular biosensor using optically transparent indium tin oxide (ITO) electrodes. Sensors*, 2008. **8**: p. 3257-3270.
5. Kilic, A., and Kok, F.N. *Peptide-functionalized supported lipid bilayers to construct cell membrane mimicking interfaces. Colloids and Surfaces B: Biointerfaces*, 2019. **176**: p. 18-26.
6. Kafi, M.A., Kim, T.-H., Yea, C.-H.,Kim, H. and Choi, J.-W. *Effects of nanopatterned RGD peptide layer on electrochemical detection of neural cell chip. Biosens Bioelectron*, 2010. **26**: p. 1359-1365.
7. Kafi, M.A., Kim, T.-H., An, J.H., and Choi, J.-W. *Electrochemical cell-based chip for the detection of toxic effects of bisphenol-A on neuroblastoma cells. Biosens Bioelectron*, 2011. **26**: p. 3371-3375.
8. May, K.M., Wang, Y., Bachas, L.G., and Anderson, K.W. *Development of a whole-cell-based biosensor for detecting histamine as a model toxin. Anal Chem.*, 2004. **76**: p. 4156-4161.
9. Yea, C.H., Min, J., and Choi, J.-W. *The fabrication of cell chips for use as bio-sensors. Biochip J.*, 2007. **1**: p. 219-227.

10. Ananthanarayanan, B., Little, L., Schaffer, D.V., Healy, K.E., and Tirrell, M. *Neural stem cell adhesion and proliferation on phospholipid bilayers functionalized with RGD peptides. Biomaterials*, 2010. **31**(33): p. 8706–8715.
11. Ruoslahti, E. *RGD and other recognition sequences for integrins. Annual review of cell and developmental biology*, 1996. **12**: p. 697–715.
12. Patel, P.R., Kiser, R.C., Lu, Y.Y., Fong, E., Ho, W.C., Tirrell, D.A., and Grubbs, R.H. *Synthesis and Cell Adhesive Properties of Linear and Cyclic RGD Functionalized Polynorbornene Thin Films.* B*iomacromolecules*, 2012. **13**(8): p. 2546–2553.
13. Springer, T.A., and Dustin, M.L. *Integrin inside-out signaling and the immunological synapse. Current opinion in cell biology*, 2012. **24**(1): p. 107–115.
14. Jurchenko, C., Chang, Y., Narui, Y., Zhang, Y., and Salaita, K.S. *Integrin-generated forces lead to streptavidin-biotin unbinding in cellular adhesions. Biophysical journal*, 2014. **106**(7): p. 1436–1446.
15. Kapp, T.G., Rechenmacher, F., Neubauer, S., Maltsev, O.V., Cavalcanti-Adam, E.A., Zarka, R., Reuning, U., Notni, J., Wester, H.J., Mas-Moruno, C., Spatz, J., Geiger, B., and Kessler, H. *A Comprehensive Evaluation of the Activity and Selectivity Profile of Ligands for RGD-binding Integrins. Scientific reports*, 2017. **7**.
16. Liu, Z., Liu, S., Niu, G., Wang, F., Liu, S., and Chen, X. *Optical imaging of integrin alphavbeta3 expression with near-infrared fluorescent RGD dimer with tetra(ethylene glycol) linkers. Molecular imaging*, 2010. **9**(1): p. 21–29.
17. Aplin, A.E., Howe, A., Alahari, S.K., and Juliano, R.L. *Signal transduction and signal modulation by cell adhesion receptors: the role of integrins, cadherins, immunoglobulin-cell adhesion molecules, and selectins. Pharmacological reviews*, 1998. **50**(2): p. 197–263.
18. Alberts, B., Johnson, A., Lewis, J., et al. *Integrins*, in *Molecular Biology of the Cell. 4th edition*. 2002: New York:Garland Science.
19. Xiong, J.-P., Stehle, T., Goodman, S.L., and Arnaout, M.A. *Integrins, cations and ligands: making the connection. J Thromb Haemost.*, 2003. **1**: p. 1642–54.

20. Danhier, F., Le Breton, A., and Préat, V. *RGD-Based Strategies To Target Alpha(v) Beta(3) Integrin in Cancer Therapy and Diagnosis. Mol. Pharmaceutics*, 2012. **9**(11): p. 2961–2973.
21. Bellis, S.L. *Advantages of RGD peptides for directing cell association with biomaterials. Biomaterials*, 2011. **32**(18): p. 4205–4210.
22. Zhang, K., and Chen, J. *The regulation of integrin function by divalent cations. Cell adhesion & migration*, 2012. **6**(1).
23. Xie, C., Zhu, J., Chen, X., Mi, L., Nishida, N., and Springer, T.A. *Structure of an integrin with an alphaI domain, complement receptor type 4. The EMBO journal*, 2010. **29**(3): p. 666–679.
24. Xiong, J.P., Stehle, T., Diefenbach, B., Zhang, R., Dunker, R., Scott, D.L., Joachimiak, A., Goodman, S.L., and Arnaout, M.A. *Crystal structure of the extracellular segment of integrin alphaV beta3. Science (New York, N.Y.)*, 2001. **294**(5541): p. 339–345.
25. Nieuwenhuizen, W., and Gravesen, M. *Anticoagulant and calcium-binding properties of high molecular weight derivatives of human fibrinogen, produced by plasmin (fragments X). Biochimica et biophysica acta*, 1981. **668**(1): p. 81–88.
26. Staatz, W.D., Rajpara, S.M., Wayner, E.A., Carter, W.G., and Santoro, S.A. *The membrane glycoprotein Ia-IIa (VLA-2) complex mediates the Mg++-dependent adhesion of platelets to collagen. The Journal of cell biology*, 1989. **108**(5): p. 1917–1924.
27. Qiu, M., Chen, J., Huang, X., Li, B., Zhang, S., Liu, P., Wang, Q., Qian, Z.R., Pan, Y., Chen, Y., and Zhao**,** J. *Engineering Chemotherapeutic-Augmented Calcium Phosphate Nanoparticles for Treatment of Intraperitoneal Disseminated Ovarian Cancer.* A*CS Appl. Mater. Interfaces,* 2022. **14**(19): p. 21954–21965.
28. von der Mark, K., Park, J., Bauer, S., and Schmuki, P. *Nanoscale engineering of biomimetic surfaces: cues from the extracellular matrix. Cell and tissue research* 2010. **339**(1).
29. Plow, E.F., Haas, T.A., Zhang, L., Loftus, J., and Smith, J.W. *Ligand binding to integrins. The Journal of biological chemistry*, 2000. **275**(29): p. 21785–21788.

30. Chen, K., and Chen, X. *Integrin Targeted Delivery of Chemotherapeutics. Theranostics*, 2011. **1**: p. 189-200.
31. Meyer, A., Auernheimer, J., Modlinger, A., and Kessler, H. *Targeting RGD recognizing integrins: drug development, biomaterial research, tumor imaging and targeting. Current pharmaceutical design*, 2006. **12**(22): p. 2723–2747.
32. Sheldrake, H.M., and Patterson, L.H. *Strategies to inhibit tumor associated integrin receptors: rationale for dual and multi-antagonists. Journal of medicinal chemistry*, 2014. **57**(15): p. 6301–6315.
33. Auzzas, L., Zanardi, F., Battistini, L., Burreddu, P., Carta, P., Rassu, G., Curti, C., and Casiraghi, G. *Targeting alphav beta3 integrin: design and applications of mono- and multifunctional RGD-based peptides and semipeptides. Current medicinal chemistry*, 2010. **17**(13): p. 1255–1299.
34. Takada, Y., Ye, X., and Simon, S. *The integrins. Genome biology*, 2007. **8**(5): p. 215.
35. Colombo, M., and Bianchi, A. *Click Chemistry for the Synthesis of RGD-Containing Integrin Ligands. Molecules,* 2010. **15**: p. 178-197.
36. Xiong, J.P., Stehle, T., Zhang, R., Joachimiak, A., Frech, M., Goodman, S.L., and Arnaout, M.A. *Crystal structure of the extracellular segment of integrin alpha Vbeta3 in complex with an Arg-Gly-Asp ligand. Science (New York, N.Y.)*, 2002. **296**(5565): p. 151–155.
37. Dillow, A.K., and Tirrell, M. *Targeted cellular adhesion at biomaterial interfaces. Curr. Opin. Solid State Mater. Sci.*, 1998. **3**: p. 252−259.
38. Stroumpoulis, D., Zhang, H., Rubalcava, L., Gliem, J., and Tirrell, M. *Cell Adhesion and Growth to Peptide-Patterned Supported Lipid Membranes. Langmuir*, 2007. **7**: p. 3849–3856.
39. Roxin, A., Zheng, G. *Flexible or fixed: a comparative review of linear and cyclic cancer-targeting peptides. Future Med. Chem*., 2012. **4**(12): p. 1601–1618.
40. Joo, S.H. *Cyclic peptides as therapeutic agents and biochemical tools. Biomolecules & therapeutics*, 2012. **20**(1): p. 19–26.

41. Horton, D.A., Bourne, G.T., and Smythe, M.L. *Exploring privileged structures: the combinatorial synthesis of cyclic peptides. Journal of computer-aided molecular design*, 2002. **16**(5-6): p. 415–430.
42. Zhu, J., and Marchant, R.E. *Solid-phase synthesis of tailed cyclic RGD peptides using glutamic acid: unexpected glutarimide formation. Journal of peptide science: an official publication of the European Peptide Society*, 2008. **14**(6): p. 690–696.
43. Lee, M., Gardner, B., Kahn, M., and Nakanishi, H. *The three-dimensional solution structure of a constrained peptidomimetic in water and in chloroform – observation of solution-induced hydrophobic cluster. FEBS Lett.*, 1995. **359**: p. 113–118.
44. Uma, K., Kishore, R., and Balaram, P. *Stereochemical constraints in peptide design: analysis of the influence of a disulfide bridge and an a-aminoisobutyryl residue on the conformation of a hexapeptide. Biopolymers,* 1993. **33**(6): p. 865–871.
45. Rezai, T., Yu, B., Millhauser, G.L., Jacobson, M.P., and Lokey, R.S. *Testing the conformational hypothesis of passive membrane permeability using synthetic cyclic peptide diastereomers. Journal of the American Chemical Society*, 2006. **128**(8): p. 2510–2511.
46. Henninot, A., Collins, J.C., and Nuss, J.M. *The Current State of Peptide Drug Discovery: Back to the Future? Journal of Medicinal Chemistry,* 2018. **61**(4): p. 1382-1414.
47. Weiland, T., and Bodanszky, M. *The World of Peptides:A Brief History of Peptide Chemistry*. 1991, Berlin-Heidelberg: Springer Verlag.
48. Doti, N., and Ruvo, M. *Synthetic Peptides and Peptidomimetics: From Basic Science to Biomedical Applications-Second Edition. International journal of molecular sciences*, 2024. **25**(2).
49. Nie, C., Zou, Y., Liao, S., Gao, Q. and Li, Q. *Peptides as carriers of active ingredients: A review. Current Research in Food Science*, 2023. **7**.
50. Wang, L., Wang, N., Zhang, W., et al. *Therapeutic peptides: current applications and future directions. Sig Transduct Target Ther.,* 2022. **7**(48).
51. Tang, W. Becker, M.L. *“Click” reactions: a versatile toolbox for the synthesis of peptide-conjugates. Chem. Soc. Rev.*, 2014. **43**: p. 7013-7039.

52. van Dijk, M., Rijkers, D.T., Liskamp, R.M., van Nostrum, C.F., and Hennink, W.E. *Synthesis and applications of biomedical and pharmaceutical polymers via click chemistry methodologies. Bioconjugate chemistry*, 2009. **20**(11): p. 2001–2016.
53. Marqués-Gallego, P., and de Kroon, A.I. *Ligation strategies for targeting liposomal nanocarriers. BioMed research international*, 2014.
54. Zhang, H., Ma, Y., and Sun, X.L. *Chemically-selective surface glyco-functionalization of liposomes through Staudinger ligation. Chemical communications (Cambridge, England)*, 2009. **21**: p. 3032–3034.
55. Koo, H., Lee, S., Na, J.H., Kim, S.H., Hahn, S.K., Choi, K., Kwon, I.C., Jeong, S.Y., and Kim, K. *Bioorthogonal copper-free click chemistry in vivo for tumor-targeted delivery of nanoparticles. Angewandte Chemie (International ed. in English)*, 2012. **51**(47): p. 11836–11840.
56. Said Hassane, F., Frisch, B., and Schuber, F. *Targeted liposomes: convenient coupling of ligands to preformed vesicles using "click chemistry". Bioconjugate chemistry*, 2006. **17**(3): p. 849–854.
57. Hellinger, R., Sigurdsson, A., Wu, W., et al. *Peptidomics. Nat Rev Methods Primers*, 2023. **3**(25).
58. Williams, B.A., and Chaput, J.C. *Synthesis of peptide-oligonucleotide conjugates using a heterobifunctional crosslinker. Current protocols in nucleic acid chemistry*, 2010.
59. Mant, C.T., Chen, Y., Yan, Z., Popa, T.V., Kovacs, J.M., Mills, J.B., Tripet, B.P., and Hodges, R.S. *HPLC analysis and purification of peptides. Methods in molecular biology (Clifton, N.J.)*, 2007. **386**: p. 3–55.
60. Jadhav, B.G., Jadhav, A.M., Shirode, A.R., and Kadam, V.J.*A. Comprehensive Review for the Learners and Users: Preparative High Performance Liquid Chromatography. International Journal of Chemical and Pharmaceutical Analysis*, 2014. **1**(3): p. 121-129.
61. Petrova, O.E., and Sauer, K. *High-Performance Liquid Chromatography (HPLC)-Based Detection and Quantitation of Cellular c-di-GMP. Methods in molecular biology (Clifton, N.J.)*, 2017. **1657**: p. 33–43.

62. Atlabachew, M., Chandravanshi, B.S. and Redi-Abshiro, M. *Preparative HPLC for large scale isolation, and salting-out assisted liquid–liquid extraction based method for HPLC–DAD determination of khat (Catha edulis Forsk) alkaloids. Chemistry Central Journal,* 2017. **11**(107).
63. Pavan, M.V., and Barron, R. DOI:https://chem.libretexts.org/Bookshelves/Analytical_Chemistry/Physical_Methods_in_Chemistry_and_Nano_Science_(Barron)/03%3A_Principles_of_Gas_Chromatography/3.02%3A_High_Performance_Liquid_chromatography.
64. Arnold, E. *The HPLC system: simply explained*. 2017.
65. Singhal, N., Kumar, M., Kanaujia, P.K., and Virdi, J.C. *MALDI-TOF mass spectrometry: an emerging technology for microbial identification and diagnosis. Front. Microbiol.*, 2015. **6**(791).
66. Everley, R.A., Mott, T.M., Wyatt, S.A., Toney, D.M., and Croley, T.R. *Liquid chromatography/mass spectrometry characterization of Escherichia coli and Shigella species. J. Am. Soc. Mass Spectrom.*, 2008. **19**: p. 1621–1628.
67. Pomastowski, P., and Buszewski, B. *Complementarity of Matrix- and Nanostructure-Assisted Laser Desorption/Ionization Approaches. Nanomaterials,* 2019. **9**(260).
68. Tanaka, K., Waki, H., Ido, Y., Akita, S., Yoshida, Y., Yoshida, T., and Matsuo, T. *Protein and polymer analyses up to m/z 100,000 by laser ionization time-of-flight mass spectrometry. Rapid Commun. Mass Spectrom.,* 1988. **2**: p. 151–153.
69. *MALDI-TOF Mass Spectrometry*. *Creative Proteomics.* DOI: https://www.creative-proteomics.com/technology/maldi-tof-mass-spectrometry.htm.
70. *MALDI-TOF/TOF mass spectrometer system: user information Mass Spectrometry Research Facility*. DOI: https://massspec.chem.ox.ac.uk/files/maldiuserinformationpdf.
71. Gambino, G., Gambino, T., Connah, L., La Cava, F., Evrard, H., and Angelovski, G. *RGD-Peptide Functionalization Affects the In Vivo Diffusion of a Responsive Trimeric MRI Contrast Agent through Interactions with Integrins. Journal of Medicinal Chemistry,* 2021. **64**(11): p. 7565-7574.

72. Chen, W., Jarzyna, P.A., van Tilborg, G.A., Nguyen, V.A., Cormode, D.P., Klink, A., Griffioen, A.W., Randolph, G.J., Fisher, E.A., Mulder, W.J., and Fayad, Z.A. *RGD peptide functionalized and reconstituted high-density lipoprotein nanoparticles as a versatile and multimodal tumor targeting molecular imaging probe. FASEB journal: official publication of the Federation of American Societies for Experimental Biology*, 2010. **24**(6): p. 1689–1699.
73. Park, J.A., Lee, J.J., Jung, J.C., Yu, D.Y., Oh, C., Ha, S., Kim, T.J., and Chang, Y. *Gd-DOTA conjugate of RGD as a potential tumor-targeting MRI contrast agent. Chembiochem: a European journal of chemical biology*, 2008. **9**(17): p. 2811–2813.
74. Rizo, J., and Gierasch, L.M. *Constrained peptides: models of bioactive peptides and protein substructures. Annual review of biochemistry*, 1992. **61**: p. 387–418.
75. Hruby, V.J., al-Obeidi, F., and Kazmierski, W. *Emerging approaches in the molecular design of receptor-selective peptide ligands: conformational, topographical and dynamic considerations. The Biochemical journal*, 1990. **268**(2): p. 249–262.
76. Melchionna, M., Styan, K.E., and Marchesan, S. *The Unexpected Advantages of Using D-Amino Acids for Peptide Self- Assembly into Nanostructured Hydrogels for Medicine. Current topics in medicinal chemistry*, 2016. **16**(18): p. 2009–2018.
77. Zimmermann, J., Nicolaus, T., Neuert, G., et al. *Thiol-based, site-specific and covalent immobilization of biomolecules for single-molecule experiments. Nat Protoc.,* 2010. **5**: p. 975–985.
78. Yang, X., and Annaert, W. *The Nanoscopic Organization of Synapse Structures: A Common Basis for Cell Communication. Membranes,* 2021. **11**(248).
79. Lu, L., Duong, V.T., Shalash, A.O., Skwarczynski, M., and Toth, I. *Chemical Conjugation Strategies for the Development of Protein-Based Subunit Nanovaccines. Vaccines*, 2021. **9**(563).
80. Koniev, O., and Wagner., A. *Developments and recent advancements in the field of endogenous amino acid selective bond forming reactions for bioconjugation. Chem. Soc. Rev.*, 2015. **44**: p. 5495-5551.

81. LaFoya, B., Munroe, J., Miyamoto, A., Detweiler, M., Crow, J., Gazdik, T., and Albig, A. *Beyond the Matrix:The Many Non-ECM Ligands for Integrins. International Journal of Molecular Sciences*, 2018. **19**(2).

Chapter 7: Fabrication of a Biohybrid Interface System: A549 Cell Anchorage to a DIB

7.1 Introduction

Shape modification and cell migration are at work both in embryonic stages, when cellular movements establish the body plan and shape tissues and organs, and in adult organs and systems, as they are crucial for body functionality and macroscopic movements. Typical examples are the subtle movements of tiny projections from neuronal processes in the formation and loss of synapse formation, and immune cells' role to surveil tissues, locate and destroy pathogens, which calls for fast immune cell motility[1].

Cell shape is defined by the plasma membrane interaction with the dynamic actin cytoskeleton[2]. Cell shape adjustments, as encountered in many cellular functions, (e.g. cell division, motility, differentiation, membrane trafficking and cancer cell invasion), are primarily directed by the controlled assembly of (globular) actin, (G-actin), into filamentous

networks, (F-actin), able to contract and push membranes especially with the aid of the molecular motor myosin[3].

7.1.1 The Actin Cytoskeleton

The actin cytoskeleton, with the filamentous actin (F-actin) being a key constituent[4], is larger than any cell organelle and plays a pivotal role in multiple aspects of cellular functions. It is the machinery that powers cell migration, determines cell shape and membrane remodeling and provides structure and mechanical support[5].

Actin monomer (G-actin) polymerization forms long helical filaments (F-actin), through monomer addition at the ends of the filaments. These actin filaments are in abundance beneath the plasma membrane and arranged into a meshwork that precludes most organelles from the cortical cytoplasm[6].

Yet, the distinctive shape of the cell does not only depend on the actin filament organization, but also on accessory proteins that link the filaments to the membrane. These proteins, known as membrane-microfilament binding proteins, such as spectrin, filamin and the members of the ERM (Ezrin, Radixin, and Moesin) family, tack the membrane sheet to the underlying cytoskeleton scaffolding. In this manner, the membrane can acquire a fingerlike shape, when attached to a bundle of filaments, or it can be held flat, when attached to a planar network of filaments[7].

7.1.2 Local Cell Shape Changes: Leading Edge Protrusions in Migrating Cells

Migration depends on several dynamic actin assemblies, and it has been associated with cell polarization, and morphologically and biochemically distinct formations at front and rear[8].

For a cell to generate a pushing force needed for protrusion of its leading edge during migration, it utilizes the energy of actin polymerization. The directionality of this force stems from the structural polarity of actin filaments [9], as the barbed end or 'plus end' polymerizes at a faster rate than the pointed end or "minus end" [10].The polymerizing actin filaments orient their barbed ends towards the plasma membrane promoting filament elongation, whereas depolymerization or disassembly occurs to the pointed ends, where monomers are released and subsequently used for recycling[11].

Individual actin filament elongation/protraction results in piconewton force production[11] with filaments either being organized into parallel bundles forming filopodia, or in branched networks creating lamellipodia (Fig. 7.1A,B).

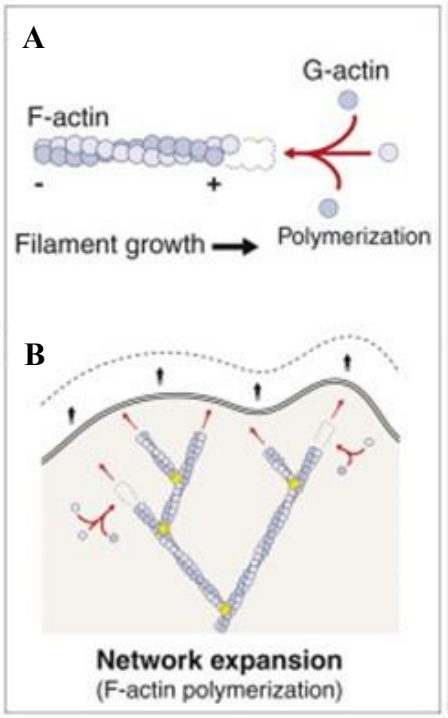

Figure 7.1- Pushing forces generated by F-actin network polymerization. *(A) Actin monomer addition to the plus or barbed end generates a small pushing force (~1.3 pN) during F-actin polymerization. (B) The force of actin polymerization in a branched actin network at the leading edge of the cell is adequate to deform the PM pushing forward. Image taken from:[12]*

7.1.2.1 Filopodia

Filopodia extend slender protrusions far beyond the cell edge touching remote targets. Filopodia's function as "fingers" to grab a target, leads to cell-to-cell or cell-to-extracellular molecule communication guiding cell motility during normal tissue morphogenesis, cell-cell junction formation in neurons and epithelia or cancer metastasis. Filopodia can also "arrest" various particles for subsequent internalization [13], an essential process for pathogen removal[1].

7.1.2.2 Lamellipodia

The branched networks of lamellipodia, on the other hand, can generate much greater protrusive forces than filopodia serving as an engine to impel the cell's leading edge forward. They also operate as navigation devices as they steer cells around obstacles, probing mechanical, soluble, and chemical cues of the substratum[1].

The required balance established between each cell's needs for swift locomotion and precise navigation is taken care of by these two (filopodia and lamellipodia) sets of actin architectures. However, cell culture studies, both on flat solid surfaces and three-dimensional matrix, have shown that cell migration depends on lamellipodia protrusion, but their overall morphology is affected by the geometry of the adhesive surface and the intracellular signaling pathways[14].

7.1.2.2.1 Lamellipodia Structure and Dynamics

Further scrutiny of specific structural parameters of the actin network architecture of lamellipodia, such as distribution of branches, density, orientation, length of actin filaments and frequency, reveals diversification among cell types. That leads to distinct lamellipodia responses with those containing a low density of long branched filaments

protruding swifter than the high-density ones, but also being more prone to buckling and consequently retraction[1, 15].

7.1.2.3 Stress Fibers

In addition to protrusive actin filament networks, where force is generated by actin polymerization, F-actin along with myosin II bundles form stress fibers that provide contractile forces for cell adhesion and migration[16, 17].

The actomyosin structure is the core mechanism for generating pulling forces. Myo-II, in its active, phosphorylated state, oligomerizes into a bipolar mini-filament and couples to two or multiple actin filaments with the myosin head domain driving their translocation towards their barbed ends in an ATP-dependent manner (Fig. 7.2A). This movement results in the extension or contraction of two bound actin filaments depending on myosin II position with respect to the middle of the actin filaments[17, 18] (Fig. 7.2A,B).

Thus, cell movement is a process governed by the coordinated action of actin-based protrusion of the cell front, cell adhesion to the substrate, and myosin-driven retraction of the cell rear [19, 20].

The whole mechanism is portrayed in a simplified form in Figure 7.2(C,D,E,F).

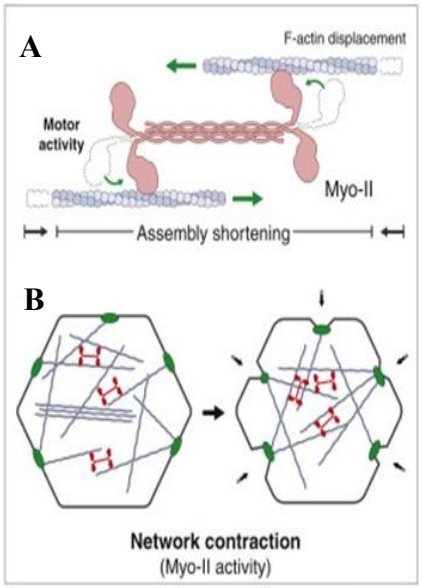

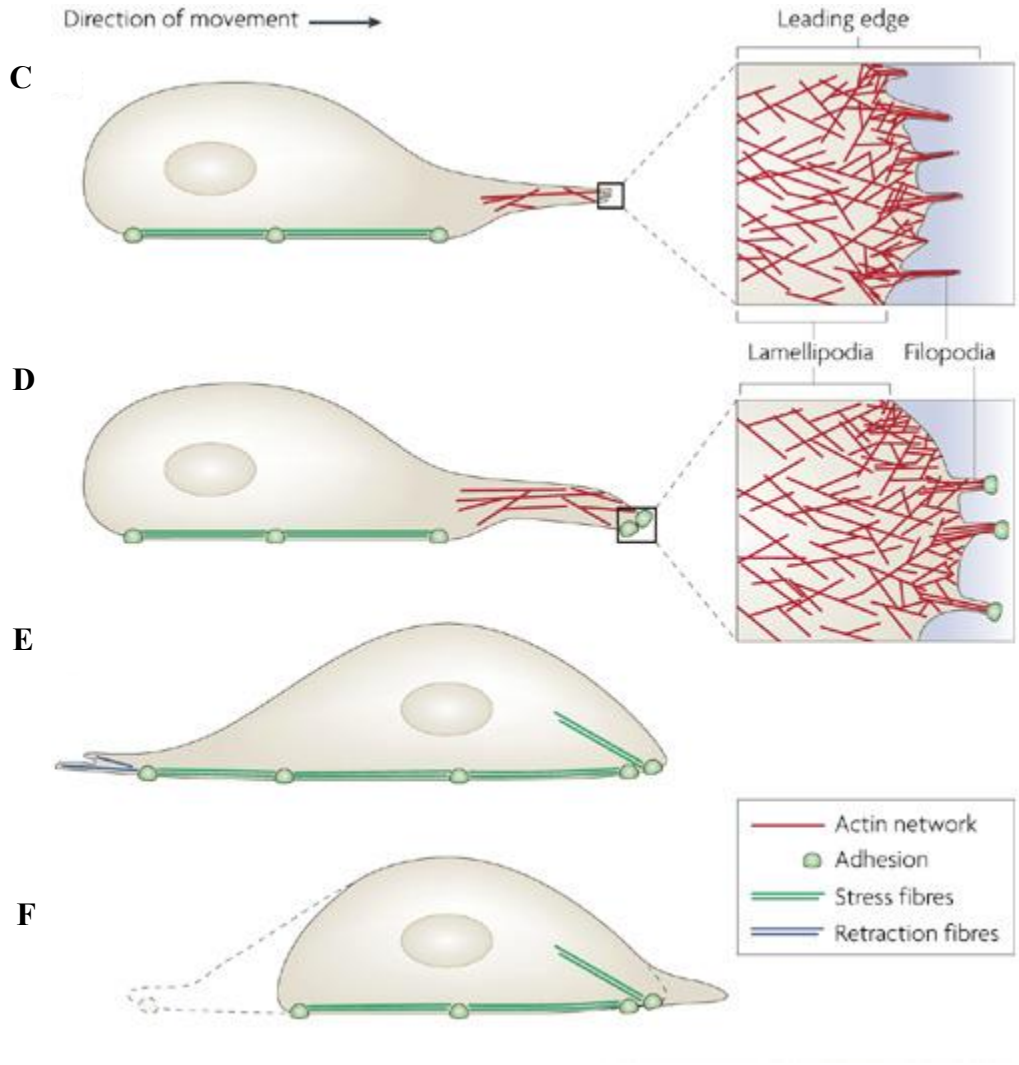

Figure 7.2- Cell migration is dependent on synergy of different actin filament structures. *(A) Myo-II mini-filaments (pink) produce actomyosin contractility by pulling against F-actin filaments of opposite polarity. It generates tension of ~4 pN. (B) Myo-II (red) contraction in an actomyosin meshwork can pull cell junctions (green), or other membrane points inwards contracting the cell surface. (C) In a cell, motility is initiated by an actin-dependent protrusion of the cell's leading edge, which is composed of armlike structures called lamellipodia and filopodia. These protrusive structures contain actin filaments, with elongating barbed ends orientated toward the plasma membrane. (D) During cellular arm extension, the plasma membrane sticks to the surface at the leading edge. (E) Next, the nucleus and the cell body are pushed forward through intracellular contraction forces mediated by stress fibres. (F) Finally, retraction fibres pull the rear of the cell forward. Images A,B taken from:[12] and images C,D,E,F taken from:[16].*

7.1.2.4 Plasma Membrane (PM) Blebs

Over the last 15 years, 3-dimensional (3D) imaging has revealed that cells migrating in 3D manifest a broader array of protrusions than what had been captured in 2D counterparts. Specifically, cell migration in 3D matrices can exhibit pressure-driven blebs at the leading edge. Contrary to lamellipodia and filopodia protrusions that grow as a result of actin polymerization, blebs are initially formed and inflated actin-free. They arise due to hydrostatic pressure in the cytoplasm and emerge at PM sites, where the membrane-to-cortex attachment is disrupted. However, following their expansion as spherical membrane bulges, actin cytoskeleton is reassembled over time[8, 21].

7.1.3 Cell Deformation Generates Propelling Force

Lamellipodia formation has been associated with the mesenchymal type of migration, characterized by cells' spread morphologies and strong adherence to substrate. Blebs, on the other hand, have been the signature of amoeboid cell motion, with the cell body being more rounded and cell-substrate attachment being less adhesive[22].

Although these classifications have been used for year as markers of migration modes, recent progress in 3D cell motility studies considers them as very restrictive since migrating rounded cells with lamellipodia have been also reported and different cell types can switch between protrusion types, based on internal and external cues. This cellular phenotypic plasticity seems to apply mostly in cancer cell dissemination and cells in the early development[8].

7.1.4 Integrins' Interaction with the Cytoskeleton Binds Cells to the Extracellular Matrix

Lamellipodia are considered as precursors of migrating cells and at the leading-edge form adhesive interactions with the substratum. Integrins at the tip of lamellipodium usually get activated by chemokines, such as interleukin-8 (IL-8), and monocyte chemoattractant protein-1 (MCP-1) and growth factor (GF), such as platelet-derived growth factor (PDGF) and transforming growth factor-β (TGF-β), which leads to integrin clustering and ligand binding in the ECM, ultimately resulting in adhesion strengthening[1].

Integrins function as transmembrane linkers, mediating cytoskeleton-extracellular matrix interaction, a requirement for cells' grip to the matrix. Following integrin's binding to its corresponding ligand in the matrix, the β subunit cytoplasmic tail of the integrin receptor associates with other intracellular adaptor proteins, such as talin, α-actinin, and filamin, which in turn directly bind to actin or to other anchor proteins such as vinculin, bringing in this way, in contact integrin with actin filaments in the cell cortex[23] (Fig. 7.3).

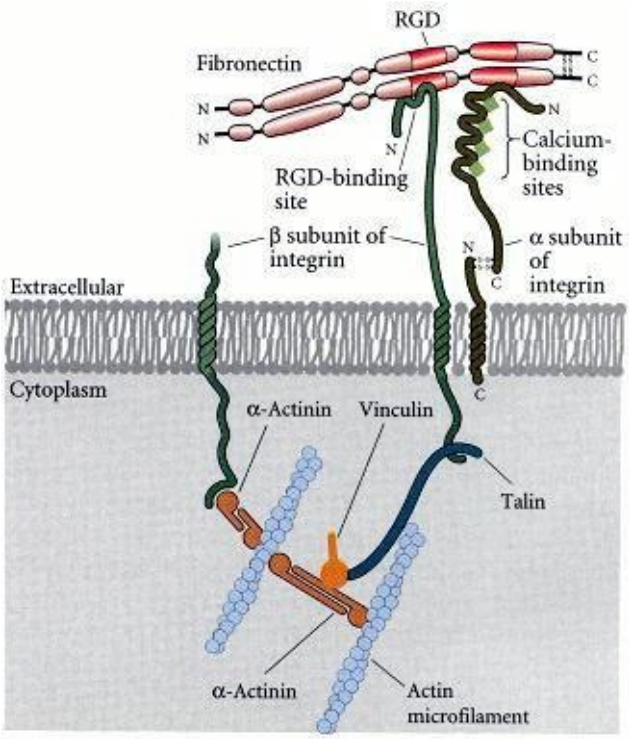

Figure 7.3- Diagram illustrating cytoskeleton binding to the extracellular matrix through the integrin molecule*. Source:[24].*

7.1.5 Chapter's Aims

The end goal of this project is a biohybrid model engineering comprised of an anchored living cell to DIB inner membrane leaflet, reminiscent of a biological synapse structure (Fig. 7.4). Conversion of the artificial communication system, tethered cell-sized GUV to the inner membrane of the DIB via cholesteryl functionalized DNA hybrids (its synthesis is detailed in ***Chapters 4 and 5***), into a biohybrid version, necessitates DIB microenvironment and intermembrane bridge adjustments for cell accommodation.

Cell-substrate adhesion between PM and DIB inner leaflet is realized via the Chol-PEG2000-maleimide-cRGDfKC-Atto488 conjugated product (***Chapter 6***), for preferential binding to $\alpha_v\beta_3$ integrin receptors, based on the tri-amino acid sequence, arginine-glycine-aspartate (RGD) motif being the basic module for $\alpha_v\beta_3$ integrin targeting.

Given $\alpha_v\beta_3$-integrin's overexpression on tumor cells of various types (e.g., glioblastoma, melanoma, breast and ovarian cancer), and its direct association with metastasis process[25], the A549 lung cancer cell line, a generous contribution by Pr Arwyn Jones, is employed, with documented expression of $\alpha_v\beta_3$ integrin receptors[26-29].

The cRGD-peptide construct with the functionalized cholesterol moiety on the one end, for membrane self-insertion, and the conjugated fluorophore on the other end, for single molecule detection, interconnected with a PEG linker, serves as an integrin-targeting ligand to bridge the two adjacent biological-synthetic membranes (Fig. 7.4).

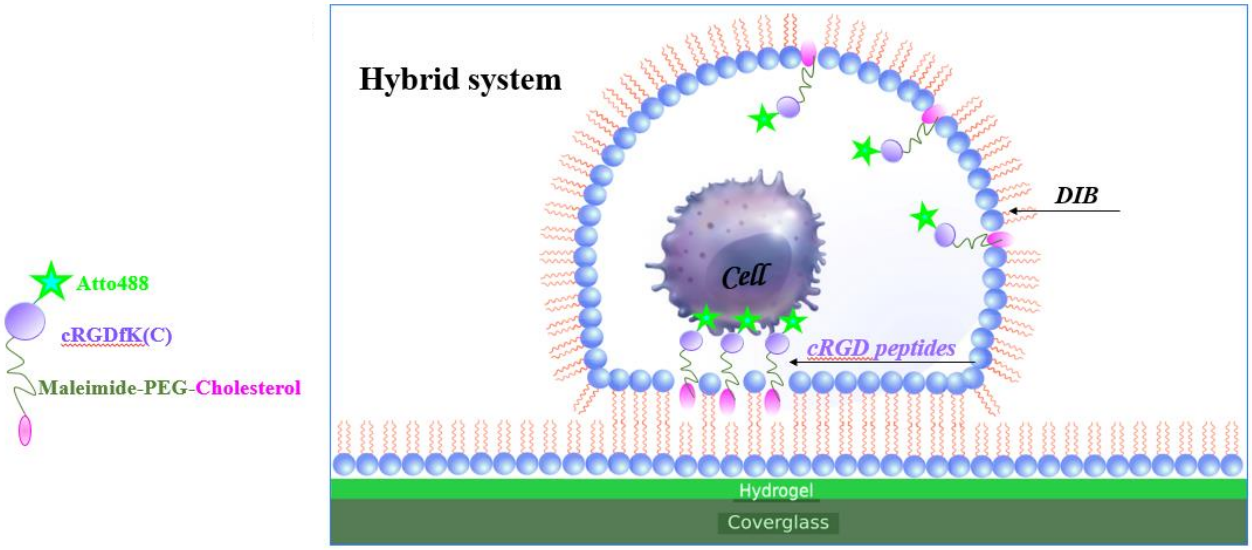

Figure 7.4- Schematics of a living cell anchored to a peptide-functionalized DIB. *Not-to-scale.*

The large PEG hydrophilic spacer in the peptide linker, with the assumed extended conformation in an aqueous environment, enhances RGD-integrin engagement capacity; a ligand-integrin accessibility trait not particularly manifested by the RGD amino acid sequence alone.

To demonstrate cell adherence to the synthetic membrane bilayer, a combination of morphodynamics (ADAPT and Kymography) and migration analysis strategies is deployed to investigate ligand-associated filamentous actin remodeling and cell mobility responses in ligand-grafted and ligand free DIBs.

Evaluation of this biosynthetic model validity as a tool of cell-surface attachment, mandates cell-adhesion efficiency assessment on simpler platforms that would enable comparisons to be made for inference verification and consolidation. To this end, a simpler substrate, a supported lipid bilayer (SLB) (Fig. 7.5), is also used to evaluate cell adhesion. The choice of this lipid-based platform lies in its compatibility with total internal fluorescence (TIRF) microscopy, which allows characterization of ligand−receptor interactions and actin dynamics occurring at the interface[30] and hence, can better capture cell surface and membrane-cytosolic boundary elicited biological responses in functionalized and non-functionalized SLBs, which can be compared to those of DIB-encapsulated cells.

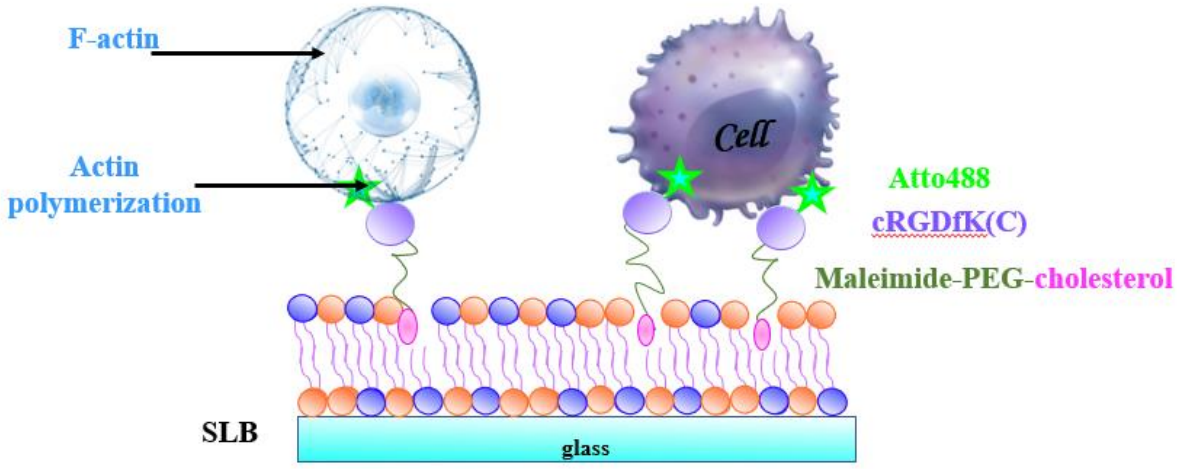

***Figure 7.5- Schematics of a living cell anchored to a peptide-functionalized SLB**. Not-to-scale.*

7.2 Materials and Methods

7.2.1 SUV Generation

Two types of SUVs were generated for the preparation of two kinds of supported lipid bilayers (SLBs). For the SLB used to monitor membrane fluidity, a lipid mixture consisting of 99.8% mol 1,2-diphytanoyl-sn-glycero-3-phosphocholine (DPhPC) and 0.2% mol labelled lipid, 1,2-dioleoyl-sn-glycero-3-phosphoethanolamine-N-(lissamine rhodamine B sulfonyl) (ammonium salt)(18:1 Liss Rhod PE) (Avanti polar) (Fig. 7.6), was used to generate SUVs, whereas for SLB formation required for cell seeding, only DPhPC was utilized for SUV production.

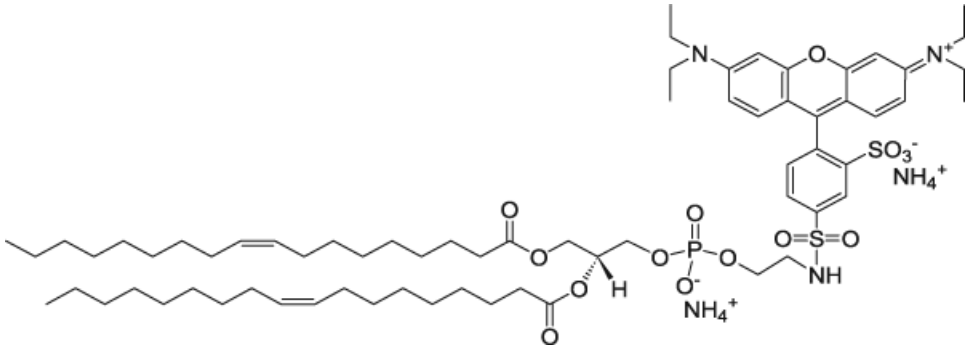

Figure 7.6- 1,2-dioleoyl-sn-glycero-3-phosphoethanolamine-N-(lissamine rhodamine B sulfonyl) (18:1 Liss Rhod PE) chemical structure.

The lipids were mixed in correct proportions and subsequently, the solution was dried by manually rotating the vial under nitrogen flow in a fume hood to ensure complete solvent evaporation. After rehydrating the dry lipid cakes with 1× PBS (sigma) to a final lipid concentration of 0.2 mg/ml, they were subjected to vigorous agitation (vortex) for 5-10 min.

The resuspended solution containing LMVs of various sizes was extruded through a 100 nm porous polycarbonate filtering membrane (Whatman) ten to fifteen times via a mini extruder (avanti). This procedure resulted in a solution containing SUVs of approximate 100 nm in diameter. The unilamellar liposomes were collected in a falcon tube, stored at +4°C and used within 3 days of preparation.

7.2.2 SLB Formation

Two kinds of supported lipid bilayers were prepared. For the one generated to monitor membrane fluidity, SUVs composed of 99.8% mol DPhPC and 0.2% mol labelled lipid, 18:1 Liss Rhod PE were used, whereas for the one employed for cell plating, merely DPhPC SUVs were utilized.

Glass bottom well plates (MatTek, Ashland, USA, 35 mm petri dish, 14 mm Microwell No. 1.0 coverglass, 0.13-0.16 mm) were treated with 1 M NaOH for 2 h to make the surface hydrophilic. After rinsing with MilliQ water, small unilamellar vesicles (0.2 mg/ml in 1× PBS; 100 µl/well) were placed onto the glass surface and incubated for 2 h in a moisture box to form SLB coatings. During the incubation period the vesicles adsorb to the glass, rupture, and fuse to form SLBs (Fig. 7.7). After SLB formation, excess vesicles were removed with 3 PBS rinses, (pipetting the solution up and down 3 times), and the formed bilayer was substituted with fresh 1× PBS after each wash. SLBs were preserved in 1× PBS to prevent structure destruction till their use.

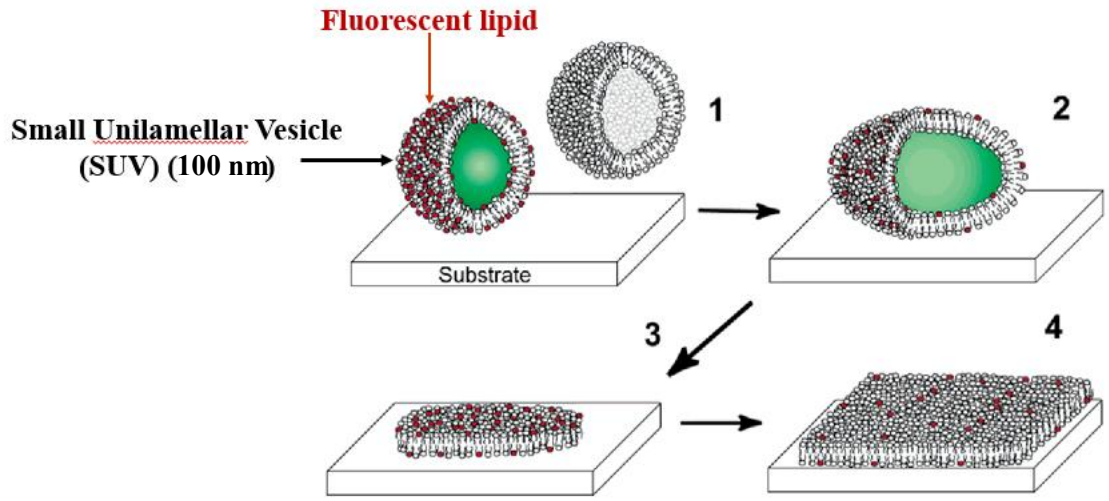

Figure 7.7- Schematics of supported bilayer formation via vesicle fusion. *(1) Adsorbed vesicles fuse among themselves at the surface (2) forming larger vesicles until a critical size is reached, (3) where they rupture forming bilayer disks (4) and finally extending on the surface through disk merging. Image adapted from:[31].*

7.2.3 Fluorescent Recovery After Photobleaching (FRAP)

7.2.3.1 Theory of the Technique

Membrane model systems need to maintain the lateral mobility (fluidity) of the lipid bilayer to mimic the natural membrane. Fluorescent recovery after photobleaching (FRAP) is a technique most used for this purpose, as it is based on determining the diffusion of fluorescently labelled lipids or proteins in supported bilayers. Intense light is applied on a spot area of the bilayer to bleach the labelled molecules and the bleached field can be subsequently replenished by new unquenched fluorescent molecules due to the Brownian motion caused by lateral diffusion[32].

7.2.3.2 SLB Fluidity

Homogeneous SLB formation and fluidity were verified by TIRF microscopy (Nikon Eclipse Ti) after introducing 0.2 mol% Liss Rhod PE lipid (Excitation/Emission wavelength 560 nm/583 nm) in small unilamellar vesicles.

SLB fluidity was monitored with fluorescence recovery after photobleaching (FRAP) measurements. To this end, an intense light was focused, through a 60-× objective (Plan Apo TIRF: Nikon Instruments), on the bilayer with a region of interest (ROI) around 30 μm in diameter, subjecting it to bleaching for 1 min. Then, the field was observed using the 60× objective and images were captured at 5 min intervals to track the recovery process. Fluorescent profiles were double normalized utilizing the following equation (1):

$$I_{norm}(t) = I_{ref\text{-}pre}/I_{ref} \times I_{frap(t)}/I_{frap\_pre} \quad (1)$$

with $I_{norm}(t)$ denoting normalized intensity, $I_{frap}(t)$ corresponding to the average intensity inside the bleached spot, $I_{ref}(t)$ indicating the measured average reference intensity. The "pre" subscript stands for the mean intensity in the corresponding ROI prior to bleaching time point. The double normalized FRAP data were scaled between 0–1.

7.2.4 SLB and DIB Functionalization

Stock lyophilized peptide conjugates (Chol-PEG2000-Mal-cRGDfKC-Atto488), reconstituted in PBS, were further diluted in HBSS+25 mM HEPES (pH 7.4) for SLB functionalization.

Peptide linkers were incorporated at a final concentration of 0.5 μM into supported lipid bilayer, after it had self-assembled to a single membrane thickness and incubated for 1 h in a humified dark chamber before cell seeding.

For DIB inner membrane leaflet functionalization, the reconstituted peptide constructs were first dried under a stream of N_2 and then diluted in the lipid oil solution (15 mg/ml DPhPC in 40:60 Hex:Sil), used for DIB preparation, to a final concentration of 0.5 µM. Thus, for DIB functionalization, the cholesterol carrying ligand was mixed with the lipid-oil solution prior to cell encapsulation in the DIB compartment. DIB preparation is detailed in ***Chapter 4*** in (***4.2 Materials and Methods, 4.2.1 DIB Device Assembly and 4.2.2 Droplet Preparation and DIB Formation***).

7.2.5 Cell Culture and Sample Preparation

Human lung carcinoma cell line A549 (#CCL-185), used for the biohybrid synapse fabrication, was a generous offer by Pr Arwyn Jones and cultured by Dr Jared Whitehead.

A549 is an adenocarcinomic human alveolar basal epithelial cell type, isolated from the lung tissue of a White, 58-year-old male with lung cancer[33]. A549 cells acquire a squamous shape and *in vitro* cultured conditions they grow as monolayer adherent to the culture flask (Fig. 7.8).

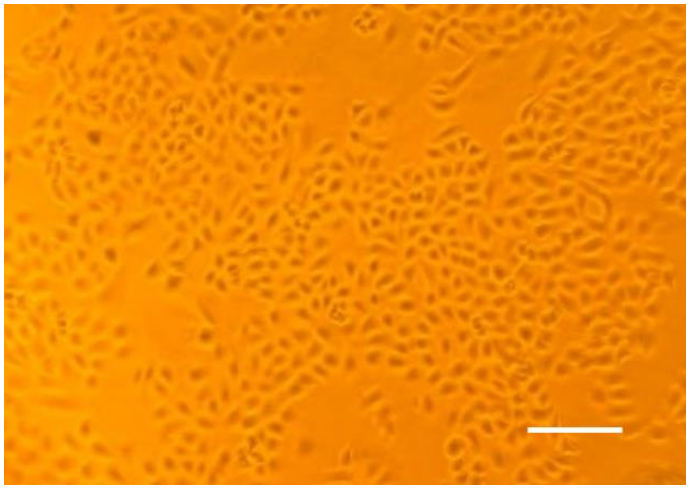

Figure 7.8- Phase contrast image of A549 cells, (*objective 20×). Scale bar: 200 µm.*

Cells were cultured as adherent monolayers in DMEM, enriched with 4.5 g L^{-1} glucose and sodium pyruvate (Thermo Fisher Scientific) and supplemented with 10% Fetal Bovine Serum (FBS), penicillin (100 μg/mL), and streptomycin (100 μg/mL). They were passaged every other day and for current experiments, cells of passage 6-10 were used.

All cells were maintained at 37°C under an atmosphere of 5% CO_2. At 80% confluency, and following washing with PBS, they were harvested using 0.05% trypsin and EDTA (Gibco) in PBS. After counting and centrifugation, they were resuspended in DMEM with 10% FBS and kept in falcon at 37°C and 5% CO_2 for 3 h. During this period, they were stirred up every hour and their morphology remained rounded for the whole period of incubation.

Subsequently, following centrifugation to remove DMEM with serum, cells were resuspended in Hank's balance salt solution (HBSS), deprived of phenol red (Sigma), and supplemented with 25 mM HEPES (pH 7.4) (Sigma), to a final density of 6×10^5 cells/ml.

Prior to being plated on or engulfed in cRGD-functionalized or non-functionalized SLBs and DIBs, respectively, they were stained with CellMask™ actin tracking stain DEEP RED (1:250) (Invitrogen) (Thermo Fisher Scientific) and incubated for 1 h at 37°C and 5% CO_2.

7.2.6 Live Cell Fluorescence Microscopy Imaging

For live-cell time-lapse imaging, DIB-enclosed and SLB-seeded A549 cells were imaged at 37°C in a heat stage (PECON tempcontrol-37) with an inverted motorized microscope (Nikon Eclipse Ti) equipped with a TIRF 60× oil, NA 1.49 objective (Nikon PLAN APO) and two laser lines: 473 nm (22 mW) (laser quantum mpc 6000, Ventus) and 635 nm (14.5 mW) (Shanghai queen laser technology, Ventus). Atto488 and actin tracking stain DEEP RED fluorescence was collected by a combination of dichroic, notch, long pass and emission filters, (dichroic: Dio3-R405/488/532/635, BrightLine, USA, and FF640-FDio1 Semrock, USA; notch: NF03-633-25 Semrock, USA; long pass: BLPO1-473R;

emission: et 525/50 Chroma, FF01-676/29 -25-STR, BrightLine, USA) and a charge-coupled device (iXon Ultra 897, Andor Technology, Belfast). The acquisition was steered by Andor Solis software. Bright-field and TIRF or hi-low TIRF fluorescence images were acquired every 30 min to 1 h, generating time-lapses of 3 h.

7.2.7 Single Particle Tracking (SPT) and Lateral Diffusion Coefficient Calculation

For mobile fluorophore (Atto488) conjugated peptides embedded in DIB inner leaflet, particle tracking and mean squared displacement (MSD) analysis was applied, explicitly described in ***Chapter 4*** in (***4.2 Materials and Methods, 4.2.6 smFRET Image Analysis on Mobile Fluorophores and 4.2.8 Lateral Diffusion Coefficient Calculation***). Briefly, for spot detection, an estimated diameter of 3 pixels was employed with the detection algorithm being DoG (difference of Gaussians). The maximal linking distance for trajectory linking and the maximal distance for gap-closing was set at 5 pixels. The maximal frame interval between two spots to be bridged was adjusted at a 2-frame duration. Trajectory analysis, mean square displacement (MSD) and diffusion coefficient (D) calculation of Atto488-peptide tracks were performed in Matlab (R2020a) (MathWorks).

7.2.8 Image Analyses

7.2.8.1 Morphodynamics Analysis

7.2.8.1.1 Kymography

7.2.8.1.1.1 Theory of Kymography

A kymograph is basically a graphical representation of spatial position of a molecule over time. It is generated by extracting the intensity profile for each frame of a time-lapse movie along a selected region (line of interest [LOI]) and then these profiles are laid side-by-side for all time points into rows producing a picture (kymograph). Thus, a kymograph displays

movement of objects within the selected region over time. Consequently, the x axis of the kymograph represents spatial position and y axis represents time[34-36]. The direction of the lines in the schematics (Fig. 7.9) helps us interpret the motion state of the molecule under investigation, with a straight vertical line suggesting a motionless molecule and diagonal paths denoting a molecule's lateral movement[37-39].

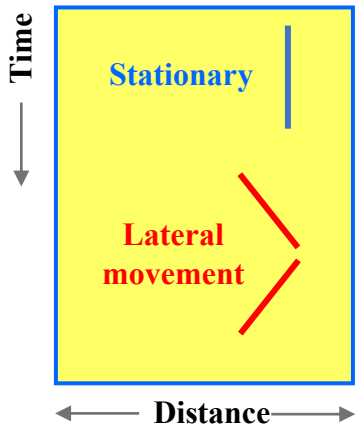

Figure 7.9- Schematic representation of a particle's movement or immobility via kymography. *Diagonal lines show inward and outward lateral movements, and vertical straight line indicates stationary condition.*

7.2.8.1.1.2 Kymograph Analysis

Image stacks from TIRF imaging were analyzed by generating kymographs using the KymoResliceWide plugin for FIJI (https://github.com/ekatrukha/KymoResliceWide), an open-source ImageJ.

As a ROI, a straight line with a thickness of 3 pixels was drawn across random cell areas and the kymographs were computed with the maximum intensity across the line (LOI-Line of interest). As FIJI cannot handle different scales in x and y axis, only the space scale was added while processing the kymograph, whereas a time scale was manually set based on the duration of the movie (100 frames→3 s). Brightness and contrast

adjustments were made on individual kymographs to enhance visual identification of actin trails.

The slope of actin trail provides the actin speed. Slopes/steepness of lateral shift events (actin movements) were determined by manually drawing lines in kymographs and actin velocities were quantified by measuring the angle of the slope (in pixels/frame) which was then converted to nm and sec, respectively, in Excel (Microsoft). All line properties were saved and loaded into GraphPad Prism 9 for plotting.

7.2.8.1.2 Automated Detection and Analysis of Protrusions (ADAPT)

7.2.8.1.2.1 ADAPT Theory

Cells expressing fluorescent actin in the cytosolic volume enable grey-level segmentation and boundary localization. Segmentation performed by ADAPT (automated detection and analysis of protrusions) is achieved through a region-growing approach, where the initial seed point is specified by the user. In the segmentation process, images are Gaussian filtered for noise suppression and a binary image is created by applying a grey-level threshold. Pixels bordering segmented regions of the cell demarcate the boundary. The resulting segmentation constitutes the seed for the region-growing algorithm in the following frame. Change in grey level between frames allows velocity calculation at each point on the emission margin; thus, an increase in grey level at a particular spatial coordinate over time translates to expansion, whereas a decrease to retraction[40].

7.2.8.1.2.2 ADAPT Analysis

Protrusion and retraction velocities, peptide and actin fluorescence boundaries and actin directionalities were calculated by the open-source ImageJ plugin “ADAPT”. The analyses were done on the maximum intensity projection of 100 frames of actin tracking stain

labelled A549 cells and plotted using Matlab R2020a (MathWorks) and GraphPad Prism 9.

7.2.8.2 Cell Migration Analysis

Time-lapse bright-field images of A549 cells were loaded onto FIJI. Cell perimeters were drawn to all cells in every image stack with the “oval selection tool” and the same spatially located circumferences were selected by the ROI Manager (Analyze→tools→ROI Manager) and then applied to the corresponding cells in subsequent time-lapse images to detect cell mobility changes. x,y coordinates of the centres of perimeters were obtained with the “measure” function as specified by the perimeter centroids. Upon cell migration, a new perimeter was drawn around the cell’s PM relocated position and the changed x,y coordinates were specified anew by the repositioned perimeter centroid. The changing x,y values along with the intercellular distance changes in each image allowed us to track and verify cellular migration behaviours, (after ensuring absence of sample displacement relative to the lens objective), which were plotted in GraphPad Prism 9.

7.2.9 Statistics and Reproducibility

All measurements were performed on 3-4 biological replicates from separate experiments with the number of independent experiments and n values being shown in the ***6.3 Result*** section. The data were analyzed by two-tailed unpaired t-tests and one-way analysis of variance (ANOVA) with Tuckey HSD post hoc tests. By convention, $p \geq 0.05$ is considered as statistically not significant and significance levels are provided as a range, *, $p < 0.05$; **, $p < 0.01$; ***, $p < 0.001$. Precise p values are shown in the figures or the text accordingly.

7.3 Results

7.3.1 TIRF Imaging Limitations for the DIB-Cell Hybrid System

The ultimate goal of this project has been to encapsulate and tether a A549 cell to the inner DIB membrane leaflet via peptide linkers aspiring to fabricate a hybrid synapse geometry, where a living cell can intercommunicate with a custom-made ECM- mimicking synthetic membrane suitable for directing *in vitro* cell-scaffold interaction[41].

Individual actin filaments in A549 cells were labelled with actin tracking stain (1:250), a probe that is cell compatible without genetic engineering, and is live cell permeable without microinjection or harsh electroporation.

After cell staining, A549 cells were seeded on SLB or enclosed in the DIB compartment with the inner membrane leaflet being grafted with Cholesterol-PEG45-Mal-cRGDfKC-Atto488 constructs at a concentration of 0.5 μM. The same ligand concentration was used for SLB functionalization. The DIB-encapsulated cells were deposited into the well of the DIB device resulting in the formation of a DIB bilayer at the lipid-covered spin-coated agarose cover-glass. Imaging was performed using TIRF microscopy, limiting the fluorescence excitation depth to the basal surface (< 200 nm) of the cell. To maintain living cells in a healthy state on the microscope stage, a temperature control platform (PECON tempcontrol-37) was used during cell monitoring.

TIRF imaging is well suited to capture both cell actin phenotype and fluid RGD ligands on artificial membrane-covered glass substrates (SLBs) and agarose spin-coated surfaces (DIBs) due to their planar geometry. Nevertheless, the spin-coated standards of the DIB device, (a platform component that is absent from SLB), which adds a ~100 nm depth to the axial coordinate of the evanescent field, limits observation on the z-axis.

The total basal thickness of the hybrid model engineering in the DIB device amounts to ~181 nm taking into account the layering of its individual components; specifically, the spin-coated agarose cover-glass thickness is ~100 nm, that of the DIB bilayer is ~5 nm,

Cholesterol-PEG45-Mal-cRGDfKC-Atto488 product span is ~16 nm, and the plasma membrane depth is ~10 nm. Considering that F-actin, in the actin regulatory layer, is localized > 50 nm above the PM[42], its visualization distance from the objective is elevated to a minimum of ~181 nm. To ensure actin architecture acquisition within the cytosolic volume, since only a subset of actin filaments is captured within the TIRF plane, both TIRF and high/low TIRF modes were employed for image recording. Comparative analysis of local organization and dynamics of the actin networks between the two imaging types was also conducted to track potential actin remodeling and velocity discrepancies given the imaging precision differences afforded by the two imaging modalities; a strategy permitting us to establish data consistency and credibility.

7.3.2 SLB Fluidity

Homogeneous coatings of SLBs, labelled with 0.2 mol% labelled lipid, (18:1 Liss Rhod PE), were formed on MatTek glass bottom culture dishes as shown by TIRF microscopy images (Fig. 7.10A).

SLB fluidity was monitored with fluorescence recovery after photobleaching (FRAP) by subjecting a region of interest (30 microns) to bleaching for 1 min (Fig. 7.10B, left) and the same field was recorded after a 5 min interval to detect the recovery process (Fig. 7.10B, right). Normalized average intensities of the highlighted rectangular regions in Figure 7.10B, Post 1 min Bleach (black curve) and Recovery after 5 min (red curve), displayed in graph C (Fig. 7.10C), present satisfactory recovery. During prebleach recording (30 s), attenuated fluorescence was detected (Fig. 7.10Dii- curve on the left), possibly due to acquisition bleaching. Following FRAP-bleaching point (Fig. 7.10Dii-red arrow on the left), recovery was monitored for the next 30 s (Fig. 7.10Dii). After 5 min, recovery of the curve reached a plateau, confirming SLB fluidity (Fig. 7.10Dii). FRAP experiment was conducted twice with similar results.

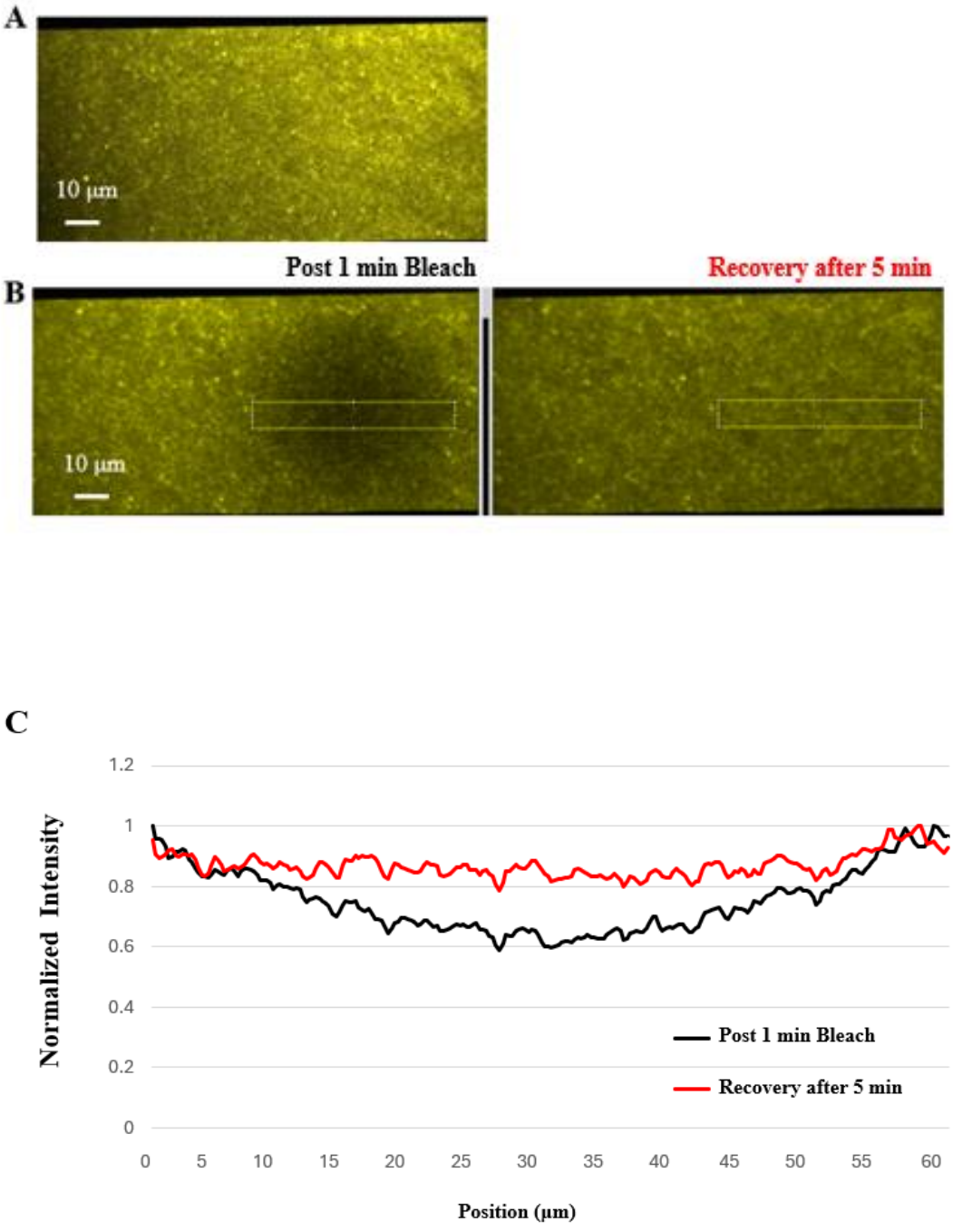
A
10 µm
Post 1 min Bleach
Recovery after 5 min
B
10 µm
C
Normalized Intensity
1.2
1
0.8
0.6
0.4
0.2
0
0
5
10
15
20
25
30
35
40
45
50
55
60
Position (µm)
Post 1 min Bleach
Recovery after 5 min

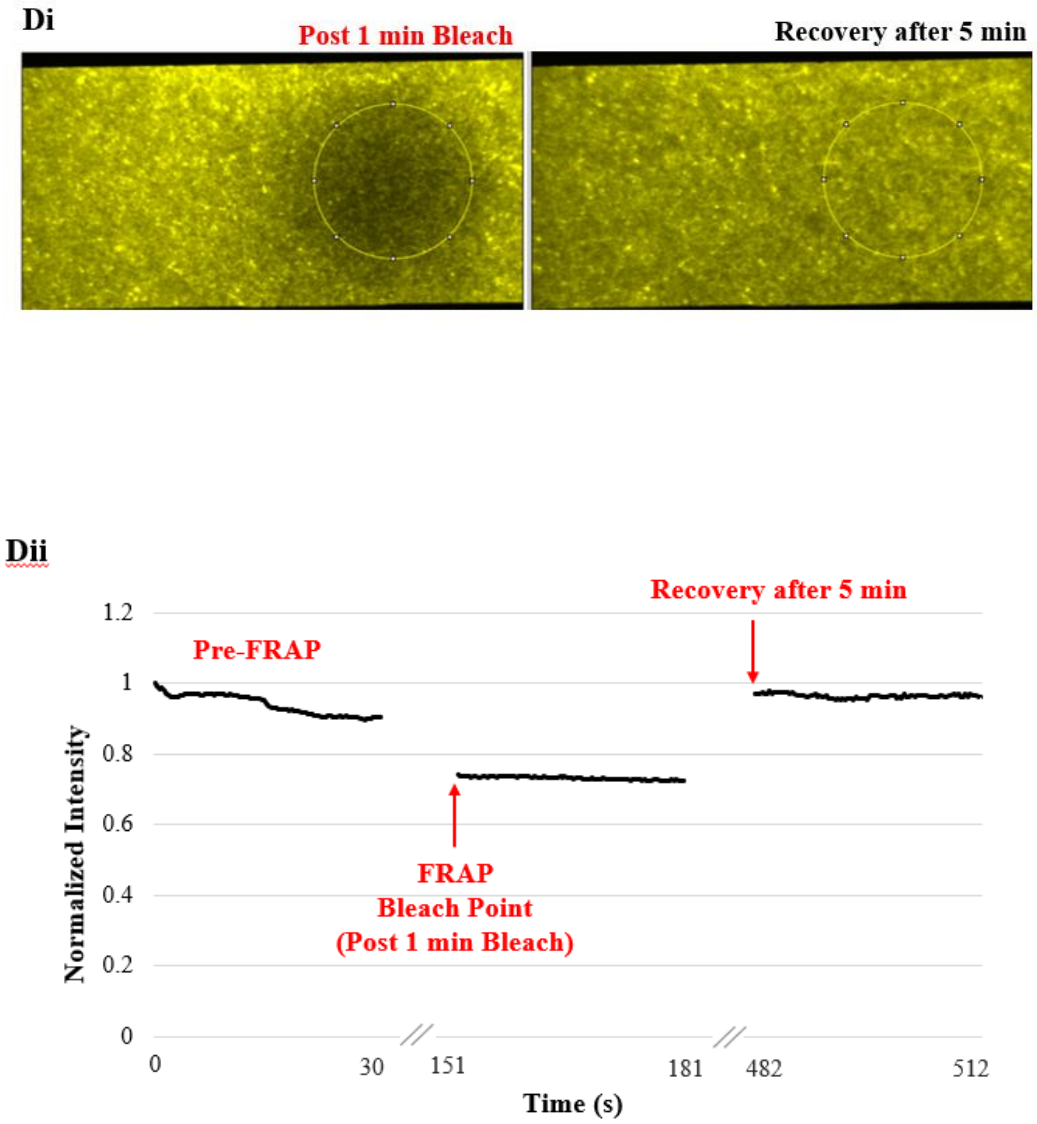

Figure 7.10- Supported lipid bilayer characterization. *(A) Typical example of SLB composed of (99.8 mol%) DPhPC and (0.2 mol%) Liss Rhod PE. (B) Fluorescent recovery after photobleaching revealed recovery of fluorescence over 5 min, demonstrating membrane fluidity. (C) Graph shows the normalized intensity of the bleached spot and its recovery after 5 min. (Dii) Pre-bleach and post-bleach time-course measurements of normalized average fluorescence intensities from the specified circular regions in (Di). Broken x-axis indicates elapsed time between measurements; pre-bleach and bleach point (post 1 min bleach) interval is 2 min. A 5-min recovery period elapses between the end of the 1st post-bleach acquisition and the beginning of the 2nd post-bleach acquisition.*

7.3.3 Investigation of Cell Adhesion Characteristics

Cells exhibit various morphological traits dependent on their physiological activities, and cell geometry changes are inherently linked to actin cytoskeleton restructuring[43].Cell integrin-ECM interactions play a pivotal role in regulating actin-associated adhesion complex formations that drive cell attachment, spreading, and migration[44].

To investigate cell attachment to DIB bilayer, time-lapse recordings of engulfed A549 cells in cRGD-functionalized and non-functionalized DIBs were analyzed in terms of cell morphologies and filamentous-actin dynamics. The same cellular responses were also assessed on seeded A549 cells on cRGD-grafted and ligand-free SLBs for comparison purposes.

7.3.3.1 Cellular Morphological Changes are Associated with Peptide Interaction

7.3.3.1.1 Lamellipodia Formations

Enclosed A549 cells in RGD-functionalized DIBs tended to display an intrinsic asymmetry with protrusion formations (Fig. 7.11A), a feature not readily detectable in cells contacting non-functionalized DIB substrates (Fig. 7.11B). A representative example is the cell in Figure 7.11A which displays a polarized morphology with advancing protrusions at one end. This morphological cell polarity was observed at a rate of 56% (in 23 out of 41 cells in 4 independent experiments). Time course of cell protrusion emergence and extension varied in the interval of the 3-hour visualization process in the DIB compartment.

Conversely, outgrowths in peptide-free DIB-enclosed cells were an infrequent occurrence with detection rate of 7.7% (2 cells out of 26 cells) as analyzed in bright-field images in 3 experimental replicates (Fig. 7.11B).

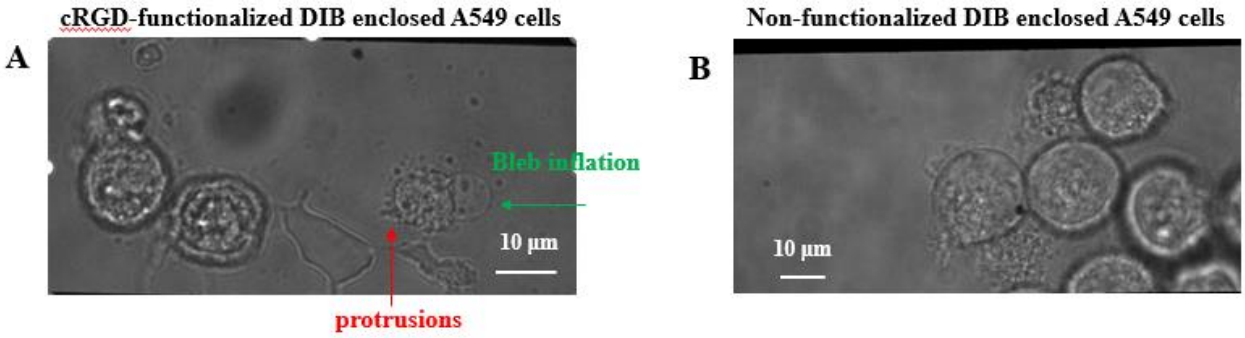

Figure 7.11- Bright-field images displaying morphological differences of encapsulated A549 cells in peptide-containing (left) and peptide-free DIBs (right) in the time course of 3 h. *(A) Protrusions and bleb formations at the cell edge of the polarized cell interacting with DIB membrane-embedded cRGD constructs. (B) Absence of apparent PM protrusions and blebs in peptide free DIBs. The number of cells forming protrusions was quantified using light inverted microscopy.*

Seeded cells on RGD-grafted SLBs expressed lamellipodia (Fig. 7.12A) at a high rate, ~65%, (40 out of 62 cells from 4 independent experiments), but this prevalence is not excessively higher than that numbered on peptide-free SLBs (Fig. 7.12B), where ~50% of cells, (11 out of 22 cells from 3 independent experiments) did manifest membrane outgrowths (Fig. 7.12B), suggesting that this cell type can interact with or attach to a synthetic membrane bilayer without peptide presence. Yet, the emanating cell protrusions on non-functionalized SLBs are overtly much smaller in size and length for the same incubation periods (3 h) on these platforms (Fig. 7.12 A,B).

Almost inconspicuousness of PM extensions in peptide-free DIB-encapsulated cells (Fig. 7.11B) could imply that other surface characteristics, like tensile strength, rigidity, surface tension, or environmental limiting factors, e.g., confined gas exchange across the interface, could thwart cell-substrate adhesion.

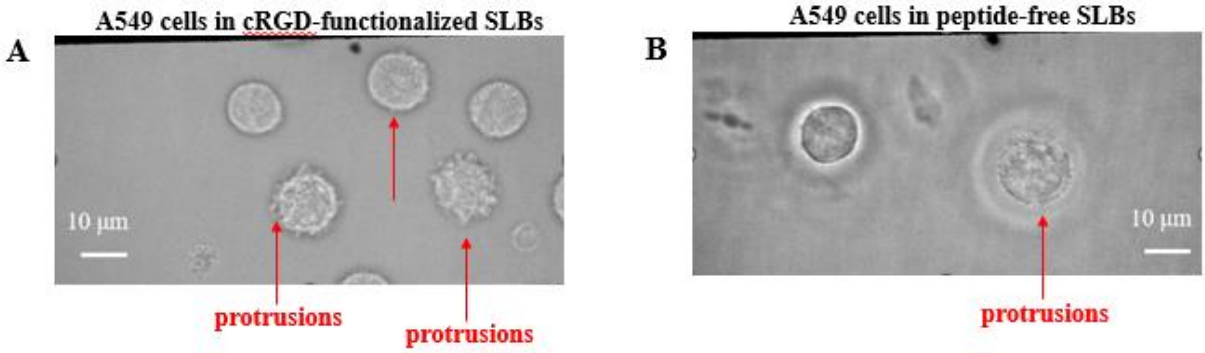

***Figure 7.12- Bright-field images of SLB-plated cells in the time course of 3h**. (A) Pronounced outgrowths of A549 cells contacting SLB-embedded peptides. (B) Small PM protrusion expression in peptide free SLB. The number of cells forming protrusions was quantified using light inverted microscopy.*

Percentages of cells with formed protrusions under the four experimental conditions are presented in the form of a bar graph in Figure 7.13.

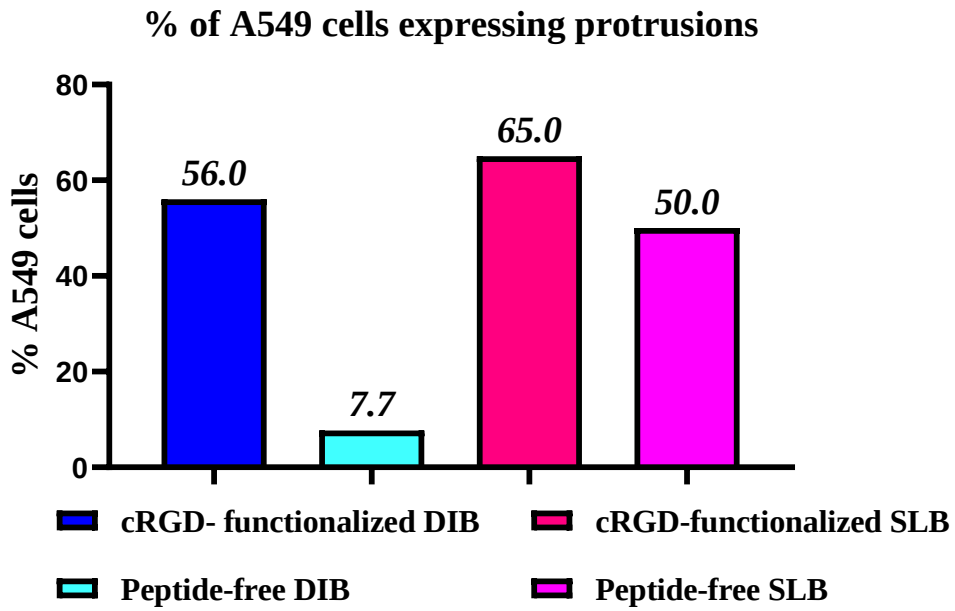

Figure 7.13- Percentage bar graph demonstrating PM protrusion detection in cRGD-functionalized and non-functionalized DIBs and SLBs*. Protrusion expression did not readily flourish in the DIB environment unless peptides were integrated in the inner membrane leaflet of the droplet.*

7.3.3.1.2 Bleb Formations

In addition to these classical membrane extensions, another morphological cellular phenotype, rather common in encapsulated cRGD-functionalized DIBs, is the PM blebs or bleb-like protrusions. Bleb is a distinct protrusion type generated by amoeboid-motile cells [21, 45, 46] portraying a bulgy, rounded morphology with an expansion up to 2 μm[47] (Fig. 7.11A).

The bleb-associated amoeboid translocation mode is preferentially used by some cancer cells, (including A549 human lung cancer cells)[48, 49], to switch modes of motility [50] enabling adaptability to environmental cues [51-55] and facilitating invasion and metastasis[45], as they can squeeze through narrow gaps in the extracellular matrix network, such as capillaries and perivascular spaces[48, 49, 56, 57], without causing extracellular matrix degradation[58].

The recurring bleb manifestation, 31.7% (in 13 out of 41 cells in 4 independent experiments) in peptide-containing DIB-encapsulated cells (Fig. 7.14) vs its scarcity, 3.8% (1 in 26 in 3 independent experiments) in peptide-free DIB-encapsulated cells seems to be a distinguishing component between the two conditions and possibly an indication of cell interaction with the membrane integrated peptide products, potentially able to instigate this cell reaction.

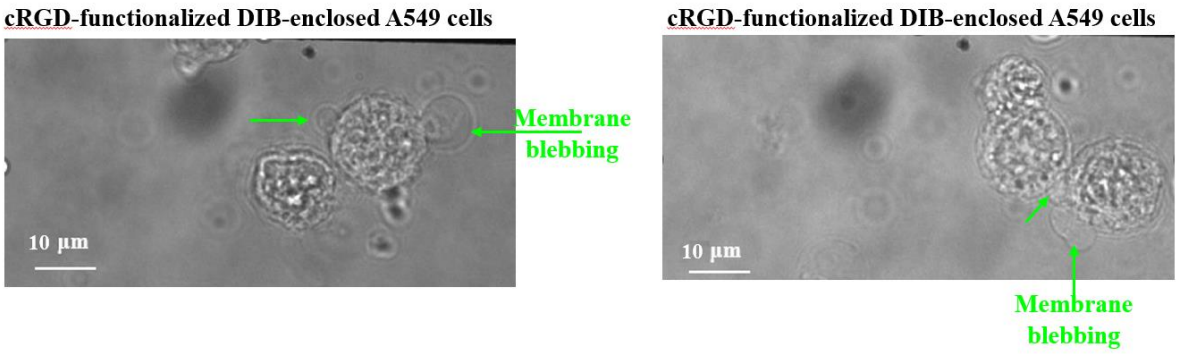

Figure 7.14- Bleb-protrusion type manifested in peptide-containing DIB-engulfed A549 cells within a 2 h-incubation period. *The number of cells forming blebs was quantified using light inverted microscopy.*

Bleb emergence was observed in 19.5% of the seeded cells on peptide grafted SLBs (12 out of 62 cells in 4 replicates) and in 9% (2 out of 22 cells in 3 replicates) on the non-functionalized SLBs.

Figure 7.15 presents percentages of cells with detectable membrane blebs in ligand containing and ligand-free DIBs and SLBs.

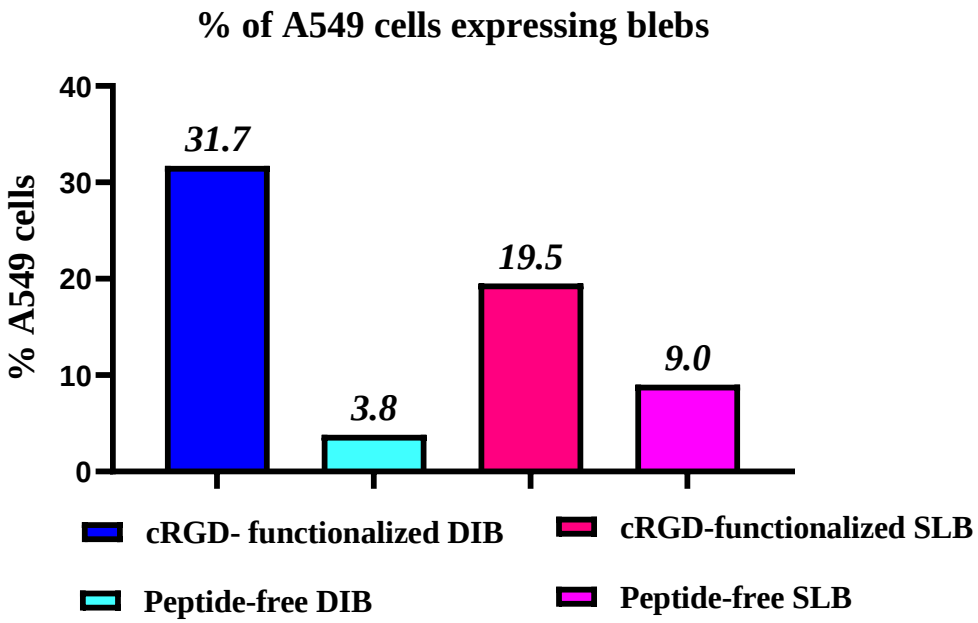

Figure 7.15- Bar graph illustrating cell percentages with membrane blebbings observed in BF images under the four experimental conditions.

The higher detection frequency of PM blebbing in peptide-functionalized DIBs (31.7%) over peptide-functionalized SLBs (19.5%) could be attributed to the constraint DIB chamber as confining platforms have been reported to scale with the number of blebs formed in various types of mammalian cells[45, 59, 60].

As the bleb-based cell migration is the primary locomotion means in response to physically confining environments, its manifestation in peptide-decorated DIB-enclosed A549 cells is an anticipated translocation mode as a metastatic mechanism.

7.3.3.2 Cellular Morphological Changes are Associated with Cell Migration

Cell motility depends on adhesive cell-substrate interactions as they are responsible for the required traction that propels cells[61]. With a few exceptions, cell migration relies on assembly and disassembly of actin filaments, organized into distinct subcellular domains, with crucial role in membrane protrusions including lamellipodia, filopodia as well as plasma membrane blebs[62].

Several peptide-containing DIB-encased cells analyzed (61.5%) (16 out of 26 cells) with expressed membrane protrusions and/or blebbings underwent migration during the 3-hour interval of imaging. Cell migration was determined with respect to a combination of reference points, such as cell centre x,y coordinates and intercellular distance changes (Fig. 7.17C). The circumference of each cell (with defined spatial coordinates) was selected (in ROI manager, analyze→tool→ROI Manager) and then applied in all time-lapse videos for the same cell group to monitor migration patterns. This approach apart from enabling cell movement measurements, it also allowed for DIB device displacement

detection in relation to the objective lens while imaging, instances that were excluded from cell motility or immobility estimations.

A representative example of cell migration associated with morphological modifications is provided in Figure 7.17A. On the top micrographs, cells were recorded at 30 min (left) and 2-hour incubation (right) in the DIB chamber. Protrusions emerged in all 3 cells at different time points and with variance in length. In the middle micrographs (Fig. 7.17B), cell perimeters were initially drawn around all observed cells incubating for 30 min in the DIB (left) and the same circular motifs (with the same spatial coordinates) were then applied to each cell at 2 h-incubation time (right). Cells 2 (middle) and 3 (bottom), developed different directionalities from one another with cell 2 moving to the left and cell 3 migrating south-west in the time course of two hours (Fig. 7.17B). The subtle locomotion in cell 1, is hardly detectable by eye. Cell motilities were also confirmed by intercellular distance changes among cells, as illustrated in Figure 7.17C, where new perimeters at the relocated cell spots were drawn at 2 h and their changed centroids were measured.

Figure 7.17D depicts migration distances of a sample of 16 DIB-encapsulated filopodia and/or bleb expressing A549 cells interacting with the peptide presenting membrane within a period of approximately 30 min-2 h.

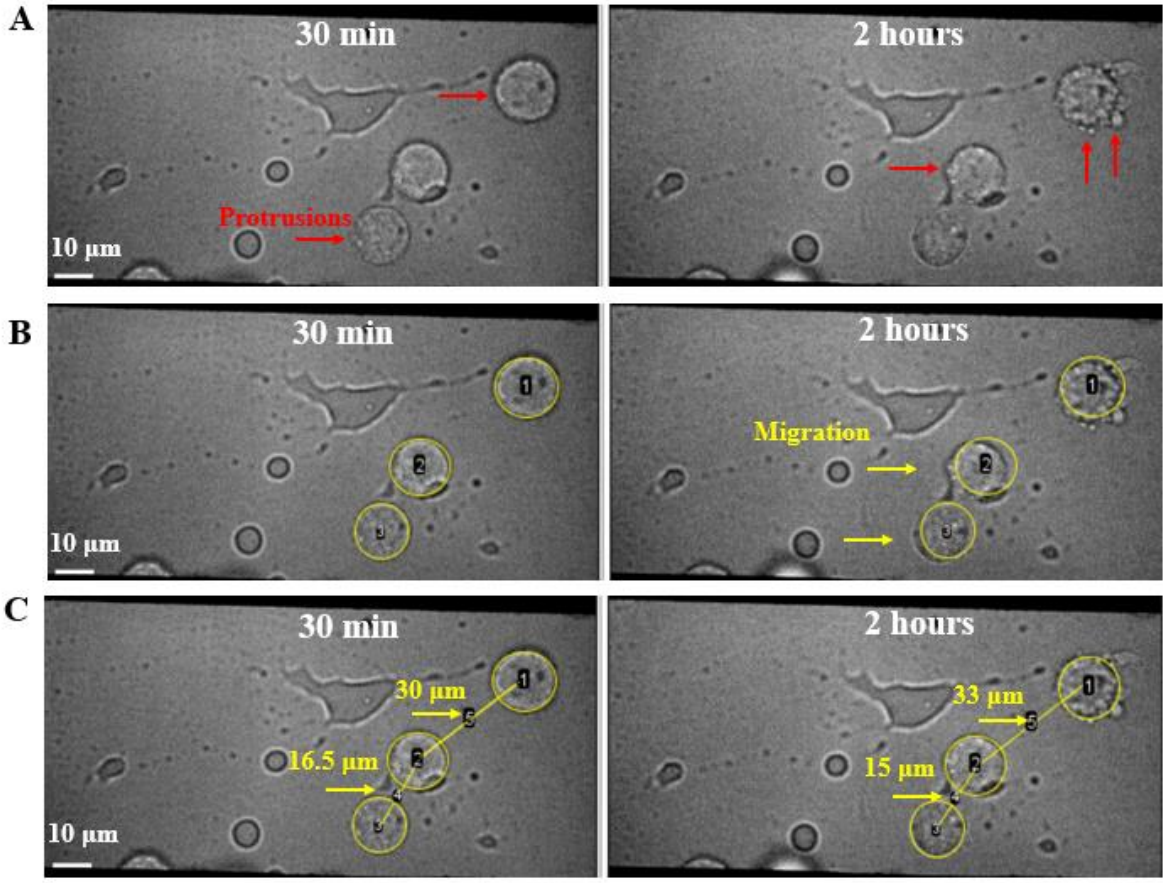
A
30 min
2 hours
Protrusions
10 µm
B
30 min
2 hours
Migration
10 µm
C
30 min
2 hours
30 µm
16.5 µm
33 µm
15 µm
10 µm

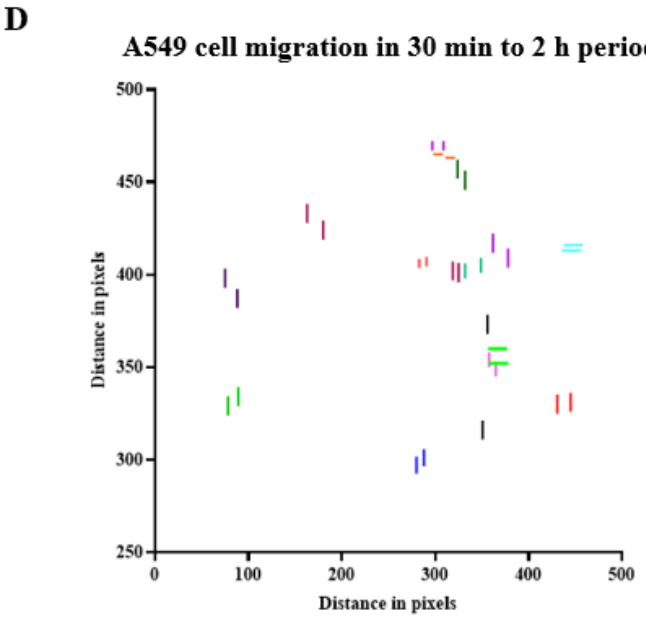
D
A549 cell migration in 30 min to 2 h period
Distance in pixels
Distance in pixels
500
450
400
350
300
250
0
100
200
300
400
500

Figure 7.17- Cell migration dependence on morphological changes. *(A) Protrusion formations are denoted with red arrows in 3 different cells in time-lapse bright-field images. (B) Time-lapse bright-field images showing left-directed movement for cell 2 and south-west direction for cell 3 in the course of 2 hours. Cell migration directionality was determined by cell centroid reposition, with the centre being established by circle perimeter (marked by the numbered label in each circle centre) and (C) intercellular distance changes among cells at two time-points (30 min and 2 h). (D) Plot illustrates distance travelled (in pixels) of protrusion and/or bleb expressing cells on peptide embedded DIB membranes. Same length and coloured lines correspond to the same cell during the time course of 30 min-2 h.*

7.3.3.3 Correlation between Cell Surface Peptide Recruitment and Actin Organization

Cell adhesion to its environment is mediated by transmembrane adhesion receptors, integrins, and the corresponding ligands, which present specific adhesive ECM epitopes. These adhesive ECM epitopes stabilize and mature integrin adhesions bridging the ECM with the actin cytoskeleton[63-66]. The ligand type used in our system, cRGD*,* is well-known to preferentially bind to the $\alpha_v\beta_3$ integrin[67], a receptor reported to be expressed in A549 cells[27, 68, 69].

Considering that (a) the cRGD lateral distribution in distinct plasma membrane areas facilitates integrin $\alpha_v\beta_3$ interrogation of the extracellular environment in quest of locations for cell anchoring and (b) the dynamic regulation of integrin-ligand coupling with associated actin cytoskeleton re-organization are crucial determinants of cell adherence and migration[70], we were interested in investigating the effect of cRGD cell surface distribution on actin reshaping.

As a first step, cRGD-functionalized-DIB-encapsulated A549 cells visualized by TIRF within ~10 to 15 min following their encasement, revealed two-dimensional (2D) single fluorescent peptide-molecule distribution throughout the droplet planar surface. Displacements derived from N = 80 particle trajectories (Fig. 7.18C) were inconsistent with Brownian diffusion, as the data deviated from a linear relationship (Fig. 6.18C, D) and the line of best fit (red line) in MSD-t plot (Fig. 7.18D), generated from the N = 80

tracks, yielded a diffusion constant of D = 8.897e-05 (with 95% confidence interval [7.793e-05 – 1.008e-04] $\mu m^2 s^{-1}$). This data analysis showcases peptide construct integration in the DIB bilayer, as the fluorescent ligand particles underwent 2D impeded lateral shifts, not congruous with Brownian diffusion (random walks).

At this stage it is presumed that cell adherence was not attained, not only due to the very short incubating time (~15 min), but also because the cells were not at the same focal depth as the diffusing peptides, despite the restricted motion of some DIB embedded ligands within specific cell territories (Fig. 7.18A,B) and (**Supplementary Movie S7.1**).

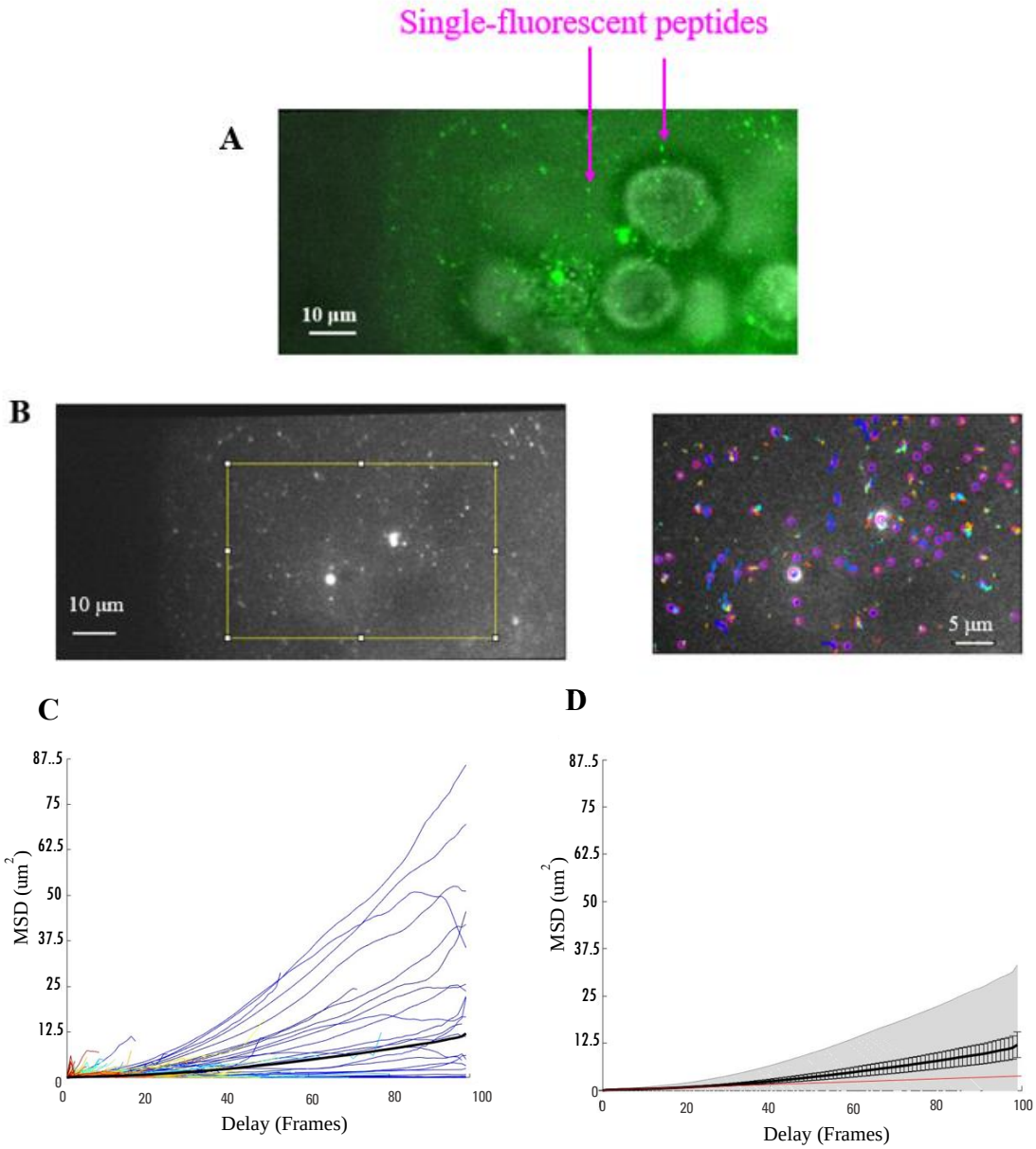

Figure 7.18- (A)Snapshot of single-molecule fluorescence imaging of Atto488-conjugated peptide diffusing to DIB bilayer. *(B) Lateral diffusion was calculated from N = 80 tracks (right) extracted from the inner space of the marked yellow rectangle (left) within the DIB surface. Single particle tracking (SPT) (right) performed in the yellow rectangle area (left) of the DIB planar surface. (C) 80 time-averaged mean square displacements versus time interval(t), where t = frames × 0.03 s. Black curve designates ensemble-averaged mean square displacements of all 80 trajectories. (D) D = 8.897e-05 (with 95% confidence interval [7.793e-05 – 1.008e-04] $\mu m^2 s^{-1}$, n = 80 trajectories). Grey shaded area represents the weighted standard deviation over all individual trajectory mean-squared displacement (MSD) traces. Error bars represent standard error of the mean on each data point. The fit is represented with a red straight line producing a good D estimate (R^2 = 0.978).*

Giving more time (minimum 30 min) for cells to settle and interact with the droplet membrane integrated peptides, ligand clusters within cell surface areas became the prevalent pattern (Fig. 7.19A) and (**Supplementary Movies S7.2A,B**). Tetrachoric correlation was initially used to measure the correlation between PM ligand assembly and actin fluorescence emission in a total number of 41 cells from 4 independent experiments. Data analyzed by eye inspection revealed a perfect positive correlation (r = 1) between peptide assembly on localized cell surface terrains and respective actin emission, usually, but not necessarily perfectly colocalized in all samples analyzed. A representative example is illustrated in Figure 7.19B.

7.3.3.3.1 Morphodynamics Analysis

This data was further explored and confirmed by whole-cell morphodynamics analysis that was generated using the open-source ImageJ plugin “ADAPT”, which stands for automated detection and analysis of protrusions[71].

ADAPT plugin-in, which can be applied to fluorescently labelled cells enabling grey-level segmentation, permits analysis of temporal changes of fluorescent molecules at the fluorescence border and velocity calculations at each point on the emission boundary[40]. Localization of fluorescent peptide (green) and fluorescent actin (red) was constructed

demonstrating regions of actin-peptide colocalization at their fluorescence edges (Fig. 7.19B). The boundary is taken as pixels bordering segmented regions of the cell. The red line denotes segmentation of the cell based on actin emission, whereas the green line represents segmentation of the cell based on the change in peptide emission (Fig. 7.19B).

7.3.3.3.1.1 Contour F-actin Restructuring Dependence on Ligand Assembly

Figure 7.19B depicts a typical case of peptide-actin co-existence within the region of an cRGD-functionalized DIB-engulfed A549 cell with colocalization segments presented in yellow. The green and red outlines mark the fluorescence boundaries of peptide (green-Atto488-5 µM) and actin (red- actin tracking stain-(1:250)) emissions, respectively (Fig. 7.19B-top), and the series of time lapse images illustrates concurrent temporal changes of actin-peptide remodelling following an incubation time of 1 h and 30 min (Fig. 7.19B-bottom).

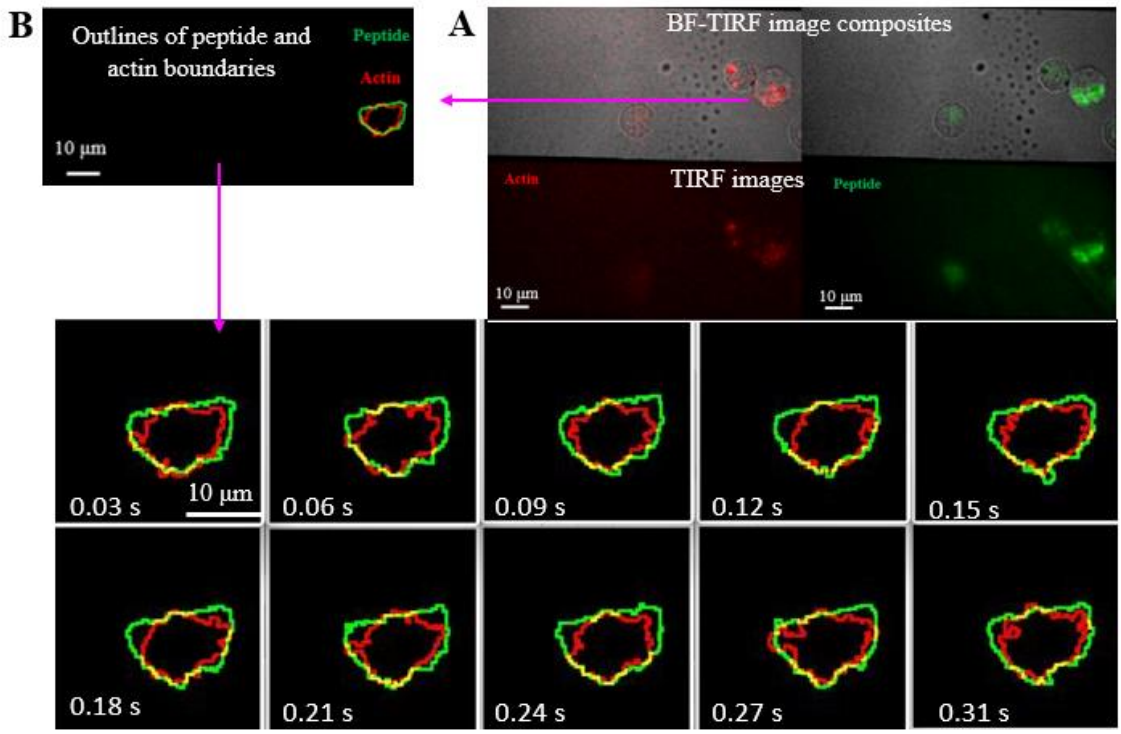

Figure 7.19- Representative outlines of actin (red) and ligand (green) emission edges extracted from time-lapse video of the cRGD-functionalized-DIB-enclosed A549 cell. *(A) BF-TIRF composite images of actin (left-red) and peptide assembly (right-green) within the cell area, respectively. (B) Peptide and actin fluorescence contour construction, generated from the TIRF images in (A), demonstrates regions of actin (red)-peptide (green) dynamics and F-actin-ligand colocalization (yellow) on their emission borders over time.*

Visualization of temporal changes in peptide and actin outlines exemplifies concurrent F-actin-ligand reshaping at the edges of their respective fluorescence emissions which is speculated to be the outcome of cRGD-integrin ligation complexes that effect conformational changes of external and cytoplasmic domains of integrin, instigating F-actin remodelling and further peptide recruitment[72] (this conjecture is explicitly explored in the ***7.3.3.3.1.2*** section below).

Conversely, contour of actin organization for the peptide-free-DIB enclosed A549 cell (Fig. 7.20A), exhibits comparatively less dynamic F-actin rearrangement at the fluorescence margin (Fig. 7.20B). This could be deemed as basal F-actin activity since it represents adherence-independent F-actin activity as the cell hadn't settled to DIB substrate by the time of imaging (1 h and 30 min); its unhindered mobility within the DIB compartment is revealed in the respective movie where Figure 7.20A was taken from **(Supplementary Movie S7.3)**.

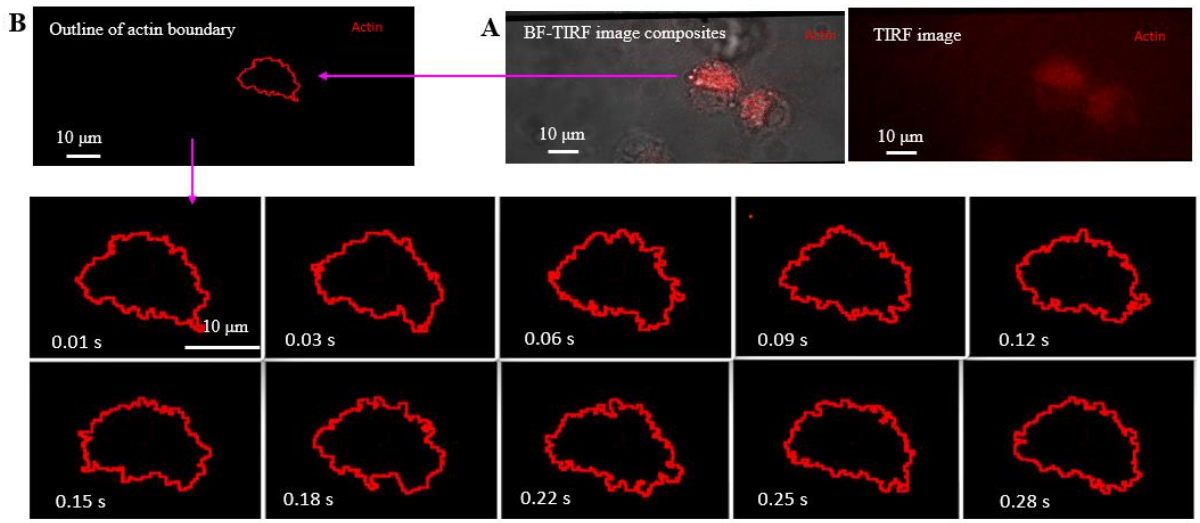

Figure 7.20- Representative silhouette of basal F-actin activity *of (A) a non-adherent cell enclosed in DIB in the absence of cRGD ligands. (B) Actin cytoskeleton self-organization displayed moderate reshaping at the actin fluorescence edge relative to the one interacting with membrane integrated ligand clustering shown in Figure 7.19B.*

7.3.3.3.1.2 Ventral F-actin Dynamics Modulation by Ligand Assembly

To investigate the impact of peptide-integrin interaction on F-actin dynamics at the cell's ventral area, and not merely at the fluorescence emission edges, kymographic analysis was employed.

7.3.3.3.1.2.1 Kymographic Analysis in DIBs

Most kymographs generated from peptide-free DIB-enclosed cells portrayed diffused/scattered profiles without any distinct patterns and/or readily detectable F-actin lateral motilities. A representative example is demonstrated in Fig. 7.21B, with the cell incubating for 1 h and 30 min in the DIB compartment prior to imaging. This diffused F-actin arrangement in the interior cell territory was a prevalent feature with detection rate of 77% (10 out 13 cells in 3 replicates). The remaining three cells manifested actin foci

(blue arrow in Fig. 7.21D), without major filamentous actin trace modifications and barely noticeable F-actin lateral shifts over the recording time (Fig. 7.21D).

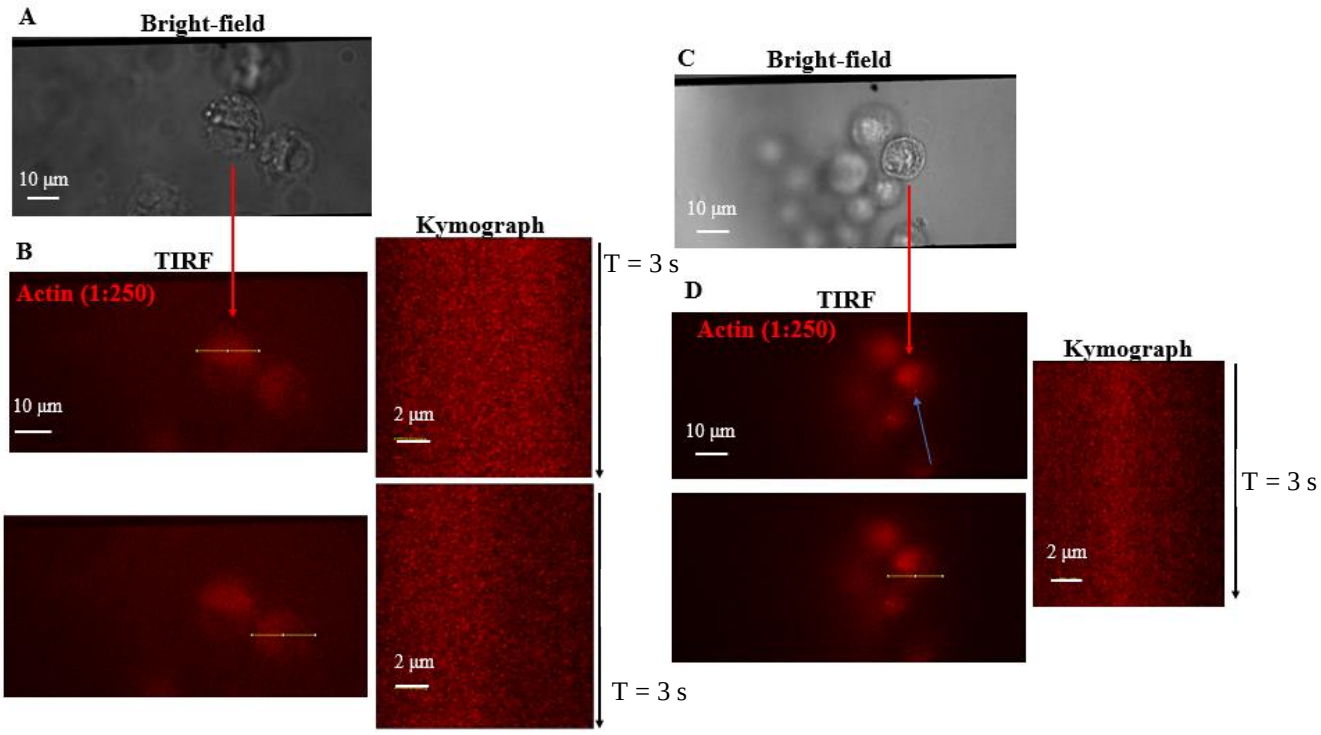

Figure 7.21- (A) and (C) Bright-field images of peptide-free DIB-enclosed A549 cells. *(B) and (D) Actin organization visualization in non-peptide containing-DIB-encapsulated A549 cells via kymography did not show filament restructuring or easily defined lateral motility patterns.*

On the other hand, the interior actin architecture of cells in cRGD-functionalized DIBs was markedly different (Fig. 7.22B) from that in non-functionalized DIBs (Fig. 7.21B,D) incubating for the same period (1 h and 30 min). Several kymographs are presented below to underscore dissimilarities in cell actin arrangement between the two experimental conditions in the DIB lumen. In the following samples, the green trail corresponds to peptides and the red one to F-actin.

In Figure 7.22B, where the cell incubated for 1 h and 30 min in the cRGD-functionalized DIB cavity, the yellow arrow (right) points to actin filament assembly, within the

observation window (3 s), as the intensity of the vertical red trail is enhanced from the highlighted point onwards. Furthermore, slight diagonal lines featured in both red trails, (pinpointed by magenta arrows), indicate actin lateral mobilities, the speed of which was determined based on the slope of these lines[38]. An indicative example of actin filament velocity, marked by the elongated magenta arrow, reached 3333.3 nm/sec (Fig. 7.22B). Following a 2.5-hour dwell time in the DIB, the same cell (Fig. 7.22C) exhibited an off/on event in the vertical red trail (right, yellow arrow), obtained from the line of interest (yellow line in left image), showcasing local actin depolymerization/polymerization.

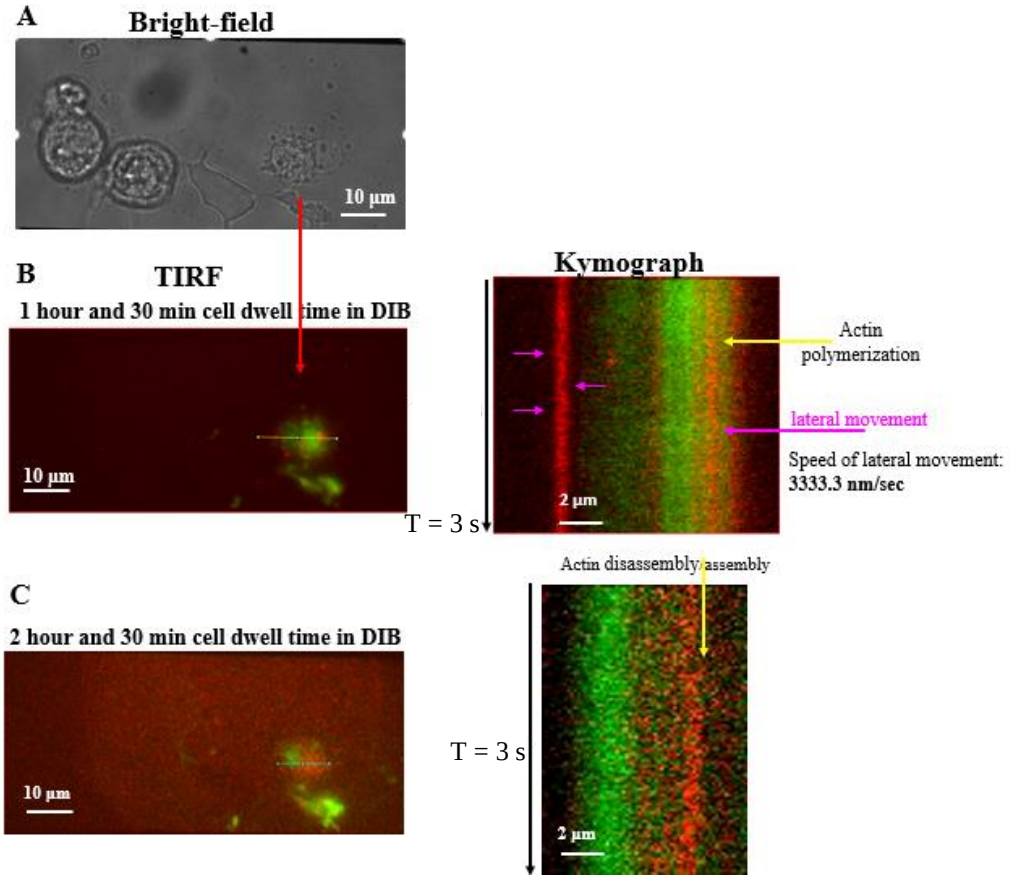

Figure 7.22- Representative actin filament dynamics of a (A) polarized cell engulfed in cRGD-grafted DIB. *(B) Following an 1 h and 30 min cell incubation in the DIB, diagonal lines in actin trails represent F-actin lateral translocations (right, indicated by magenta arrows), whereas the yellow arrow points to a filamentous actin polymerization event. (C) An off/on event in the vertical red trace (right, yellow arrow) showcases local actin depolymerization/polymerization after a 2 h and 30 min cell incubation in the DIB.*

The same pattern was also displayed in another lamellipodia-expressing cell after a 2-hour incubation in the DIB compartment (Fig. 7.23A). The two vertical interrupting red lines in Figure 7.23B suggest repeated F-actin assembly/disassembly (on/off) events in discrete microscopic zones. Two indicative velocities (4505.5 nm/sec and 5830.1 nm/sec) at positions specified by arrows are also presented (bottom kymograph, Fig. 7.23B).

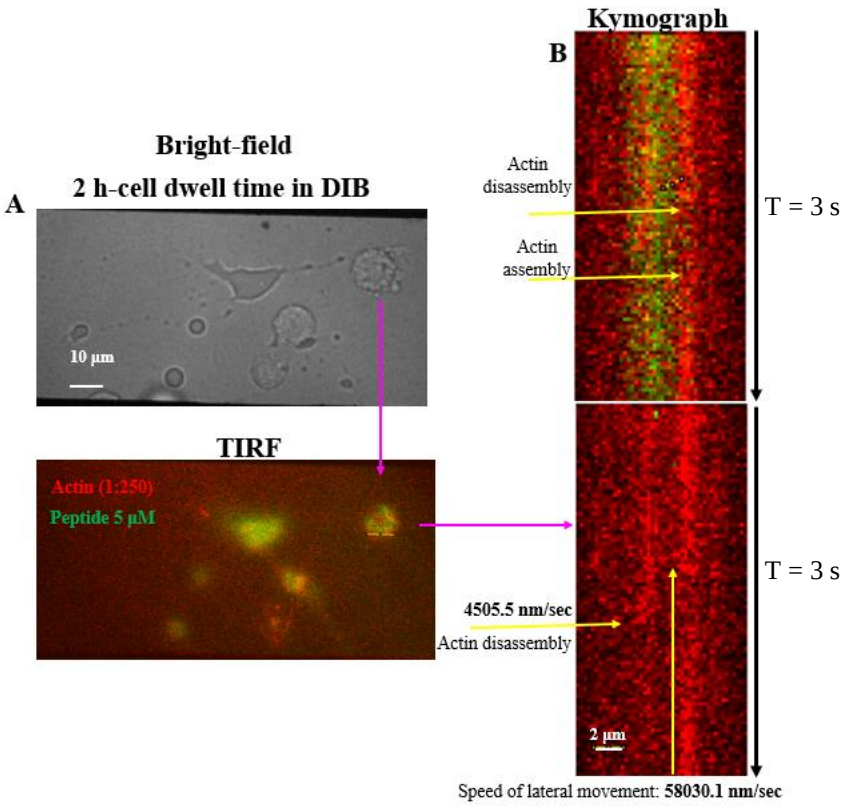

Figure 7.23- Events of actin assembly-disassembly and lateral shifts in the cytosol of a lamellipodia expressing cell. *(A) Bright-field (top) and superimposed high-low TIRF images (bottom) with green and red colours corresponding to peptide and filamentous actin, respectively. (B) Top kymograph displays actin (red) and peptide (green) trails (adjusted). In the bottom kymograph, green traces have been removed for better visualization of F-actin remodelling.*

These temporal changes in actin dynamics were evident quite frequently (68%) (in 28 out of 41 from 4 independent experiments) in cells lying on the peptide-decorated DIBs. Quantitative analysis of actin travel speed across n = 11 cells from 4 experimental replicates (with 3 lines of interest [LOI] drawn and analyzed per cell) yielded an average velocity speed of 3757.6 nm/sec, significantly (***$p < 0.001$) higher compared to that

calculated in the peptide-free DIB-enclosed A549 cells (1383.38 nm/sec) for the same number of cells n = 11, (3 LOI per cell), from 3 experimental replicates (Fig. 7.27).

7.3.3.3.1.2.2 Kymographic Analysis on SLBs

For comparison purposes, kymographic analysis was also utilized in non-encapsulated seeded cells on cRGD-functionalized and non-functionalized SLB platforms to probe actin remodelling.

Filamentous actin disassembly along with F-actin lateral mobilities were recurrent patterns in all examined cases (13 cells from 4 experimental replicates) on cRGD-grafted SLBs. It was strikingly obvious that in 92% of the cells, (12 out of 13), actin filaments were either smoothly or abruptly disrupted, losing mass from an end (Fig. 7.24B,C kymographs), an actin dynamic trait, not so much apparent in DIB-encapsulated cells interacting with cRGD-ligands for the same period of incubation time (established at 2.5 h in the following example).

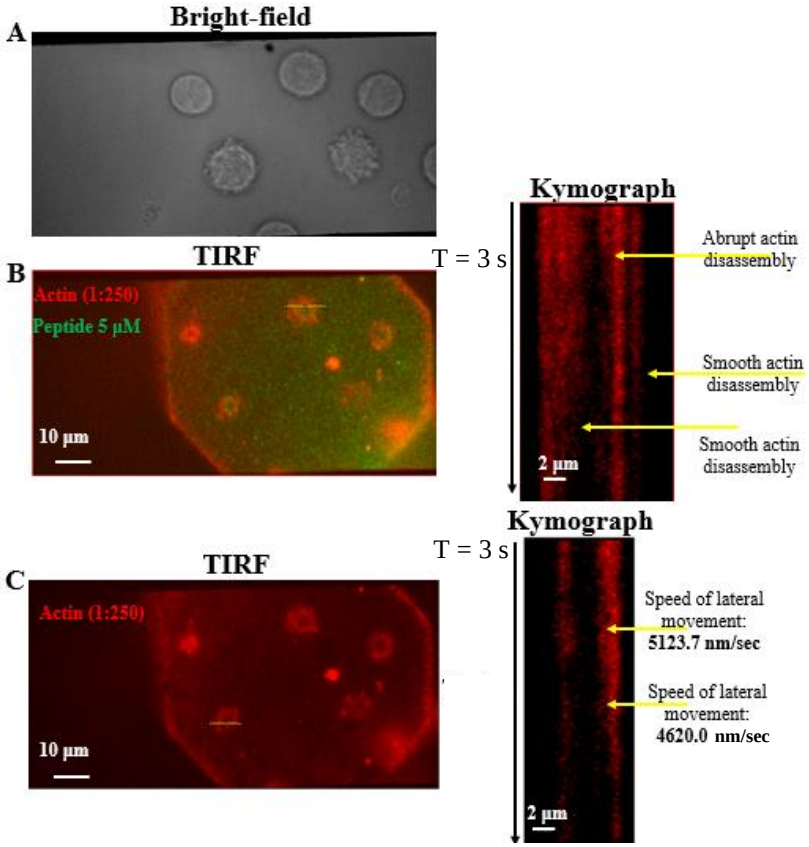

Figure 7.24- Actin reshaping/depolymerization of (A) seeded cells on cRGD-grafted SLBs. *(B) Superimposed TIRF images (left) with actin (red) and peptide (green) fluorescence emissions. The kymograph (right) extracted from TIRF composite images shows typical filamentous actin disappearance during the incubation period of 2.5 h. (C) TIRF image (left) with exclusive actin fluorescence emission. Green traces in TIRF (left) and kymograph (right) images were eliminated for better actin visualization. Indicative F-actin speeds are marked with yellow arrows in the bottom kymograph.*

The average speed of lateral movement measured in individual actin trails, from 11 cells in 4 experimental replicates, (3 LOI per cell) was 4427.7 nm/sec, higher, but non-statistically significant from the mean actin velocity in the ligand-functionalized DIB-encapsulating cells (3757.7 nm/sec) (Fig. 7.27).

Actin rearrangement in peptide-free SLB-plated cells was less pronounced (Fig. 7.25B), with mean actin speed reaching 2736.9 nm/sec (11 cells in 3 experimental replicates, [3 LOI per cell]); significantly lower (*$p < 0.05$) than that calculated on cRGD-grafted SLB-seeded cells (4427.7 nm/sec) (Fig. 7.27).

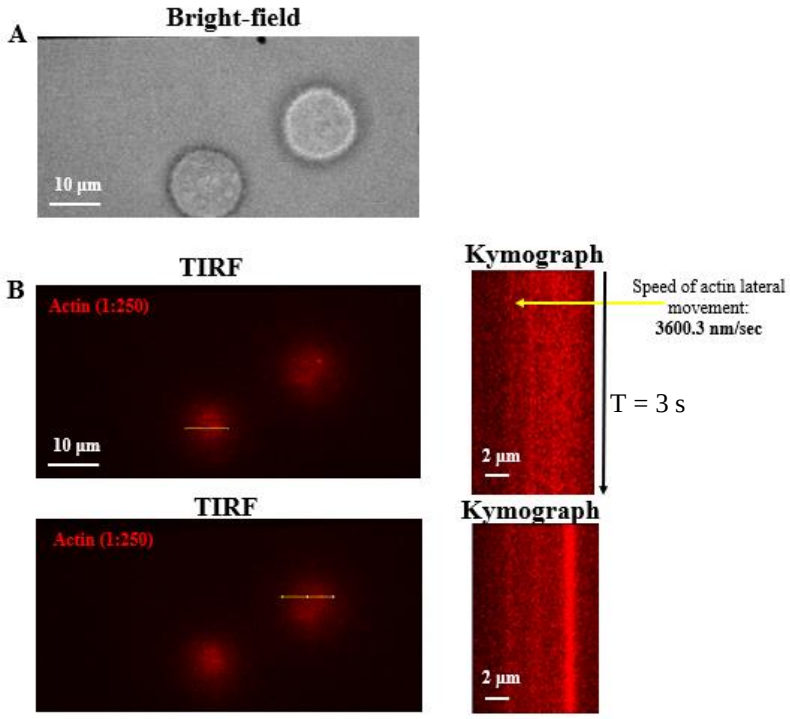

Figure 7.25- (B) Kymograph analysis on peptide-free SLB-plated cells did not show prominent actin dynamics.

However, in seeded cells manifesting protrusions while contacting the non-functionalized SLB substrate, occasional F-actin polymerization/depolymerization events occurred in 90% of the cells (10 out of 11) (Fig. 7.26B). The average actin velocity calculated (n = 11 cells with 3 LOI per cell from 3 independent experiments) reached 3052.68 nm/sec (Fig. 7.27); non-statistically significant increase from non-protrusion expressing cells plated on peptide-free-SLB (2736.9 nm/sec) (Fig. 7.27).

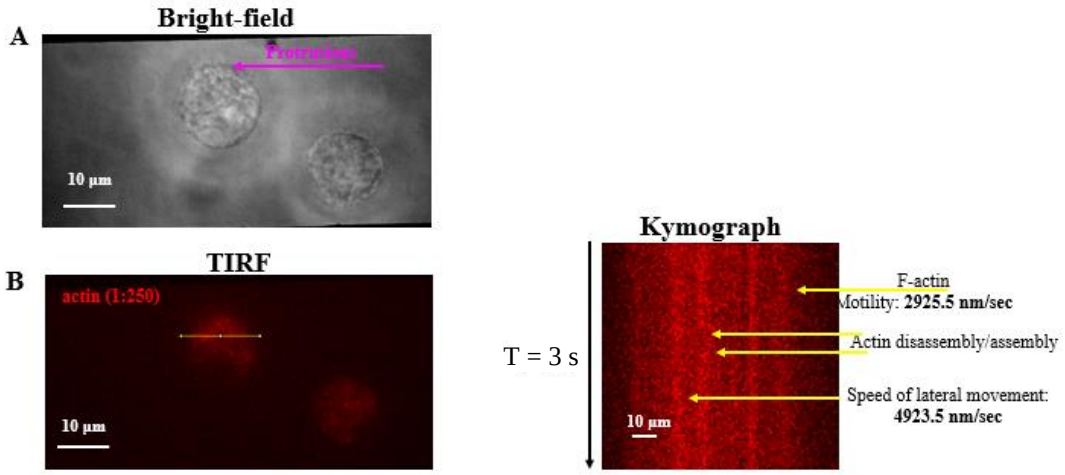

Figure 7.26- (B) Kymograph analysis on (A) peptide-free SLB-seeded A549 cells with growing protrusions *illustrates actin polymerization-depolymerization events and F-actin lateral motilities.*

Kymograph-based analysis of average F-actin velocities in A549 cells demonstrates that peptide-PM assembly can significantly speed up actin velocities in both DIB and SLB substrates relative to their homogeneous counterparts ***($p < 0.001$), *($p < 0.05$), respectively (Fig. 7.27).

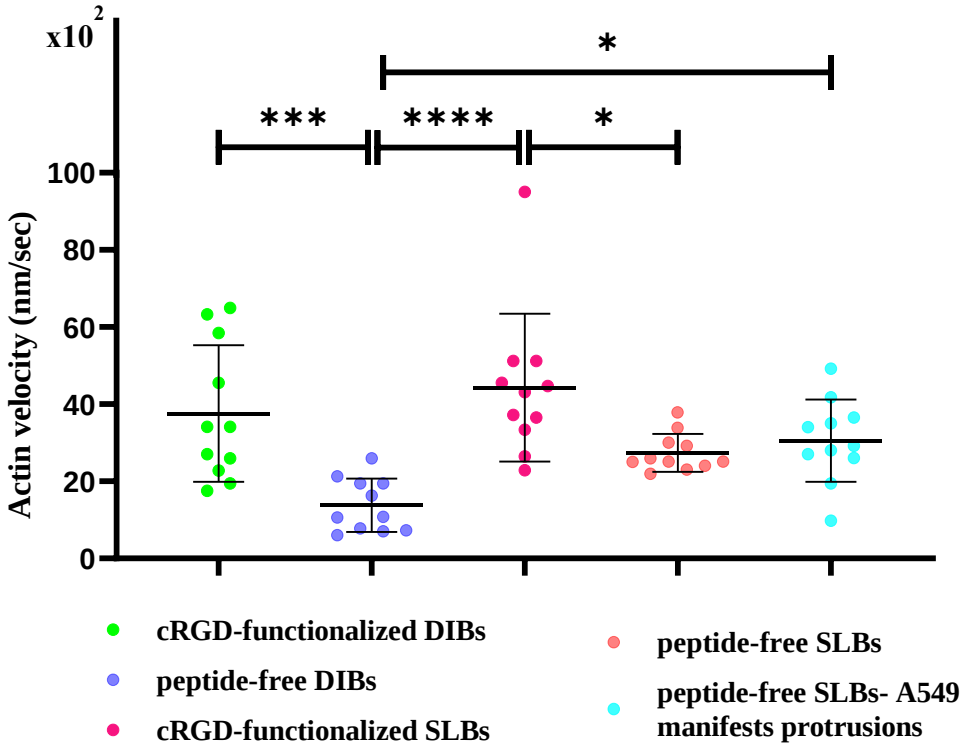

Figure 7.27- Scatter plot of the average actin speeds of A549 cells plotted versus different experimental conditions. *Each point corresponds to an average of 3 LOIs drawn and measured per cell (from 3 to 4 independent experiments). One-way ANOVA with Tuckey HSD post hoc test was performed. Error bars show SD and significant differences are shown by ****($p < 0.0001$), ***($p < 0.001$), *($p < 0.05$).*

Distinct actin cytoskeleton arrangements and significant actin velocity disparities between cells on ligand-functionalized and non-functionalized bilayers do provide firm evidence of actin velocity dependence on cRGD-integrin interaction. Potentially different stages of cell-ECM adhesions, which range from nascent adhesion, focal complexes, focal adhesions or even fibrillar adhesions[73], could be operating under the different conditions, but a more-in-depth investigation is required for such conclusions to be drawn.

7.3.3.4 Peptide Assembly Regulation of the Actin Cytoskeleton Correlates with Cell Motility

Cell adhesive interaction with its extracellular environment is an essential function for cell motility[61, 74], which entails actin cytoskeleton reorganization as its driving mechanism[75].

7.3.3.4.1 Kymograph Analysis

Actin lateral movement of cRGD decorated DIB-encapsulated cells, detected via kymography, is highly correlated (r = 0.83) with cell migration, as 23 out of 28 cells monitored to interact with membrane-inserted peptide constructs with associated F-actin temporal changes, were slightly repositioned in the time course of three hours.

Figure 7.28A represents an example of an encapsulated cell's right-directed translocation, within a period of 1 h and 30 min, accompanied by peptide-regulated dynamic actin detection (Fig. 7.28B). Kymograph (Fig. 7.28B-right), extracted from respective TIRF composite images (Fig. 7.28B-left), illustrates actin lateral mobility of the migrating cell, reaching the speed of 5853.3 nm/sec.

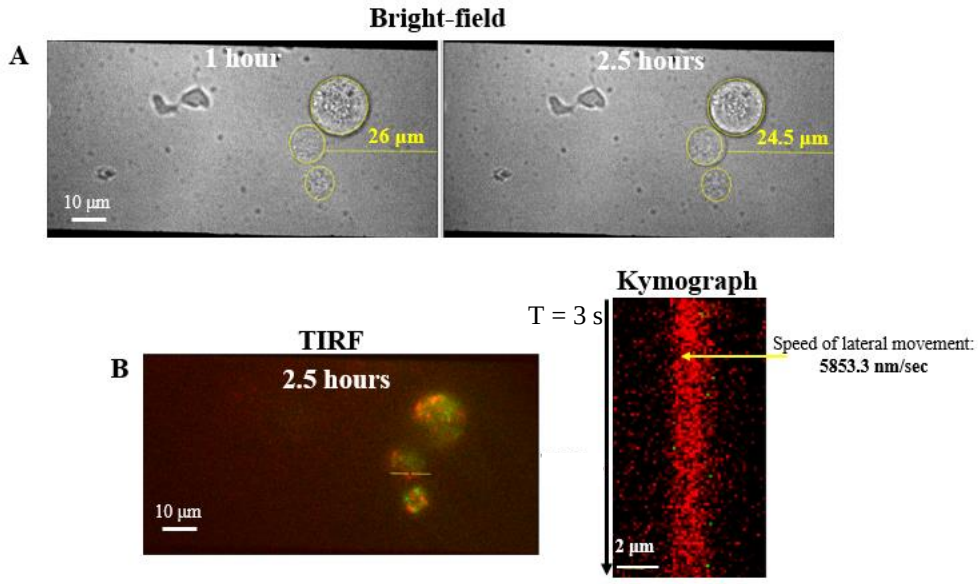

Figure 7.28- Actin dynamics of functionalized DIB-enclosed cells correlate with cell migration. *(A) Bright-field images depicting right-directed cell motility in the time-interval of 1 h and 30 min. (B) Representative kymograph (right), derived from the line of interest from the cell on the superimposed TIRF images (left), displays actin lateral movement with velocity of 5853.3 nm/sec; peptide trail (green) has been removed.*

7.3.3.4.2 ADAPT Analysis

Almost universally, cell motility involves a four-step cycle: protrusion of the leading edge, substratum adhesion, retraction of the rear, and de-adhesion[76]. Quantitative analysis of protrusion and retraction velocities along the actin emission edges of the cells, obtained from ADAPT analysis, shows that fluid cRGD-integrin ligation caused significantly higher protrusion and retraction speeds over time in relation to respective velocities expressed in cells on non-functionalized analogues for the same time period (1.5 h), (***$p < 0.001$, *$p < 0.05$), (Fig. 7.29).

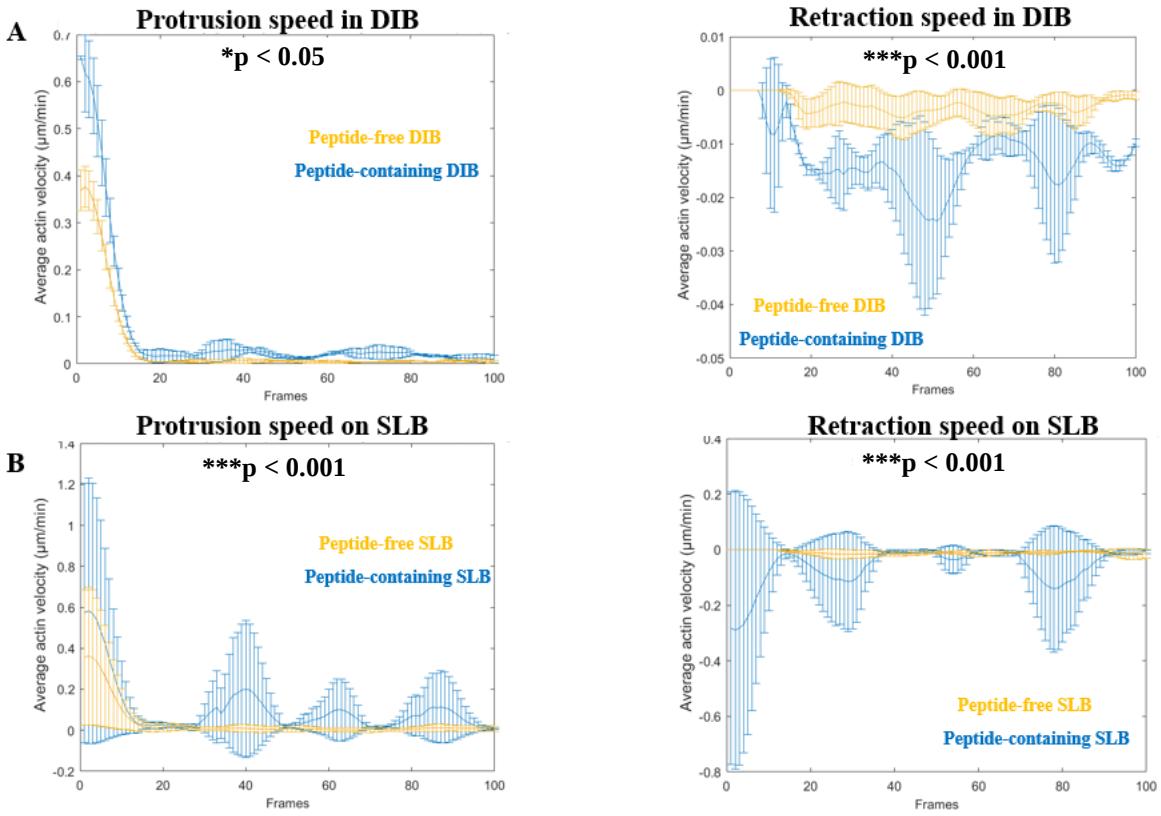

Figure 7.29- Mean protrusion (left) and retraction (right) speeds of A549 cells on cRGD-functionalized and non-functionalized (A) DIBs and (B) SLBs. *Both protrusion and retraction velocities (μm/min) of cells interacting with ligands were significantly higher than those of the non-interacting ones. X-axis depicts time, where t = frames × 0.03 s. Averages of 3 cells per experimental condition from 3 replicates. Unpaired two-samples t-tests were applied in data analysis. Error bars represent standard deviation, and significant differences are shown by ***(p < 0.001), *(p < 0.05).*

In addition, pairwise comparisons of protrusion velocities between cRGD-functionalized DIBs and cRGD-functionalized SLBs and between non-functionalized DIBs and non-functionalized SLBs (from averages of 3 cells per experimental condition from 3 replicates) yielded non-significant differences.

These findings are in consonance with actin velocity differences among groups, derived from kymography analysis (Fig. 7.27), and altogether substantiate the inference of cytoskeleton-substrate adhesion mediated via integrin-ligand coupling.

7.3.3.5 ADAPT Analysis: Actin Directionality Changes in cRGD-functionalized DIB-enclosed A549 Cells

ADAPT analysis provides numerical data on a variety of cell morphodynamics, among which are average actin velocity, directionality, and MSD that we also investigated to better understand actin behavioural profiles under all presented conditions. One interesting finding relates to actin directionality changes in cells interacting with the cRGD-functionalized DIB substrates along the time course of imaging (3 h). A representative example is the polarized cell in Figure 7.30. In the *xy*-Cartesian coordinate system (Fig. 7.30D), F-actin direction of movement was calculated as angle θ = -90° at 1 h and 30 min (Fig. 7.30B 1b), θ = 71.56° at 2 h and 30 min (Fig. 7.30B 2b), and θ = 123.69° at 3 h (Fig. 7.30B 3b). Actin directionality shifts have been tracked in all cells examined, (4 cells from 3 independent experiments), throughout the time course of the 3 h-imaging.

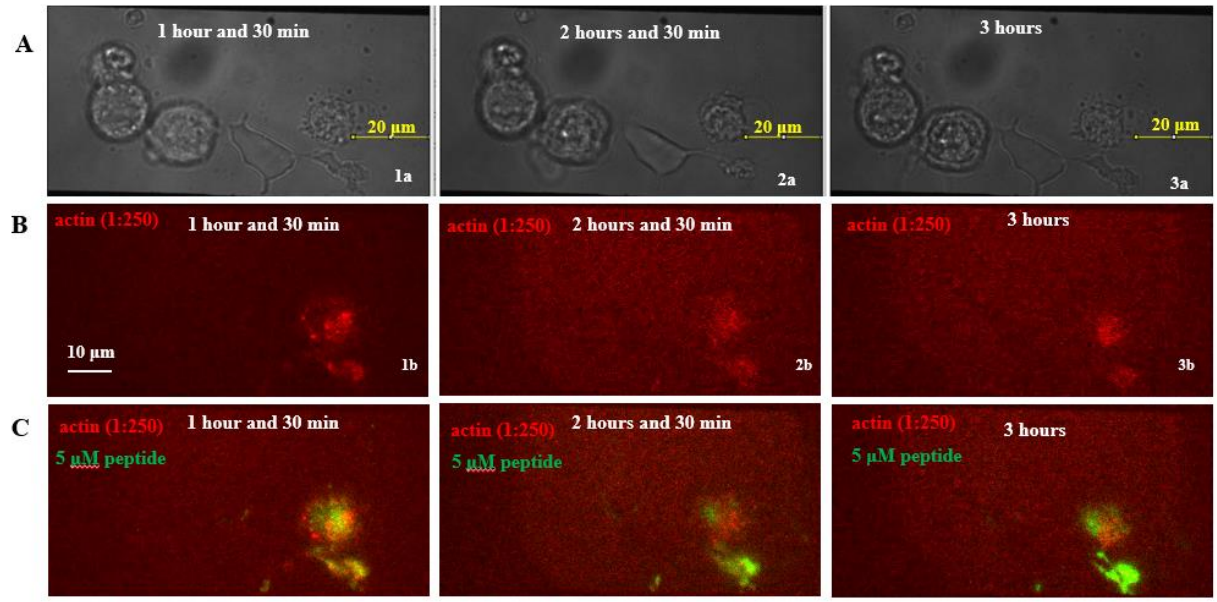

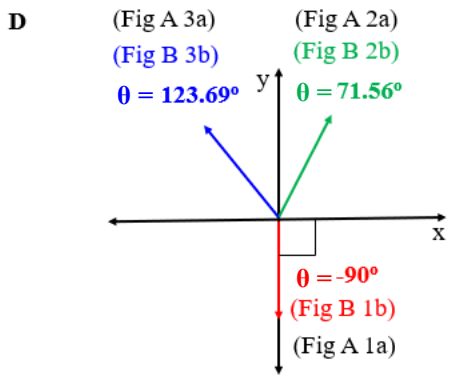

Figure 7.30- Changing actin directionality of a cRGD-functionalized DIB-anchored A549 cell, measured in a time-series method of 3 h. *(A) Bright-field time lapse images of a polarized cell (B),(D) undergoing shifting actin directional motion during a 3 h-course, (C) upon integrin-ligand interaction (superimposition of green-peptide and red-actin pseudo-coloured images).*

A possible scenario for cell changing direction pertains to RGD density, with cells more easily and strongly adhering to homogeneously peptide modified surfaces than the non-homogeneous ones (grafted with lower peptide densities), reflecting instability of cell contacts formed on less dense space patterns[63].

This assumption was affirmed by another relevant study showcasing the association between directionally persistent cell migration with increasing local RGD density and substrate adhesion[77].

Given that imaging in all other groups was not performed at intervals, as it was done for the ligand-grafted DIB-enclosed cells, inter-sample comparisons of actin directionality modifications over time could not be realized. Nonetheless, this finding still constitutes an interesting observation that is worth exploring in a comparative manner, as it could unveil potential inter-group differences, yielding insights into cell adhesion strength variations, especially between peptide containing DIB and SLB surfaces. Such data could direct, if necessary, DIB inner surface optimization strategies aiming to instigate stronger cell-matrix “gripping” forces.

Although other ADAPT measurements, such as average actin velocity and MSD measurements, were also explored, comparative data analysis didn't reveal significant or major disparities among groups that could further endorse/validate DIB-encapsulated cell adhesion.

7.3.3.6 Comparable Cytoskeletal F-actin Dynamics in Peptide-Grafted DIB Substrates between TIRF and High/Low TIRF Imaging Modalities.

To address the possibility/probability of differential measurement acquisition dependent on the imaging precision afforded by the two imaging modalities (TIRF vs High/Low) applied to secure focal peptide-actin visualization within the cell terrain, comparisons in cellular actin organization and velocity profiles were drawn between TIRF and non-TIRF conditions.

Cells residing in ligand-functionalized DIBs for the same period (1.5 h) were captured by TIRF and high/low TIRF modes (7.31A,B). Peptide recruitment and protrusive lamella were associated with cell motile behaviour within the 1.5 h-period for both cells. Irrespective of which imaging mode was applied (TIRF (7.31A) and high/low TIRF(7.31B)) to monitor cytoskeletal architecture, representative kymographs, constructed from the basal cell membranes, demonstrated similar speeds of actin motility and comparable actin filament patterns.

To better illustrate actin cytoskeleton reshaping similarities under TIRF and high-low microscopy use, while preserving the rest of experimental conditions the same, two more kymographs are illustrated in Figure 7.31C,D, showcasing analogous F-actin arrangements with prolonged lateral shifts of cells incubating for 3 h in ligand-functionalized DIBs.

Apart from this single cell data presentation, actin velocity measurements extracted from peptide-presenting DIB-encapsulated protrusion expressing cells (3 cells per imaging mode from 2 replicates), with equal DIB dwelling times, using either imaging type, displayed non-significant differences in actin speed ($p > 0.05$) and similar actin patterns, substantiating data comparability between the two imaging techniques.

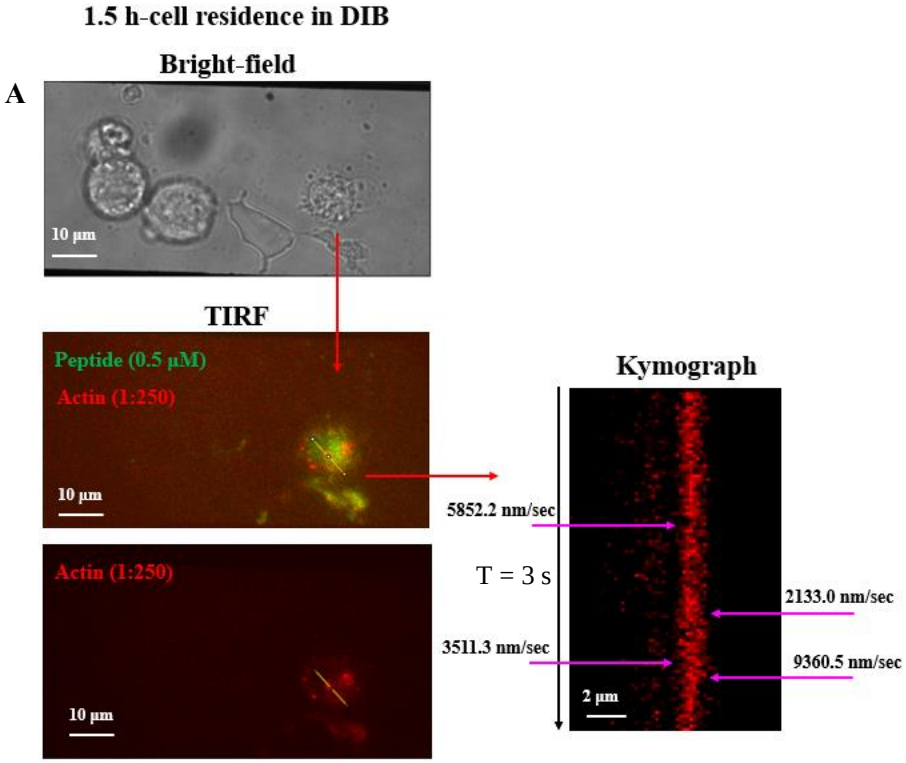

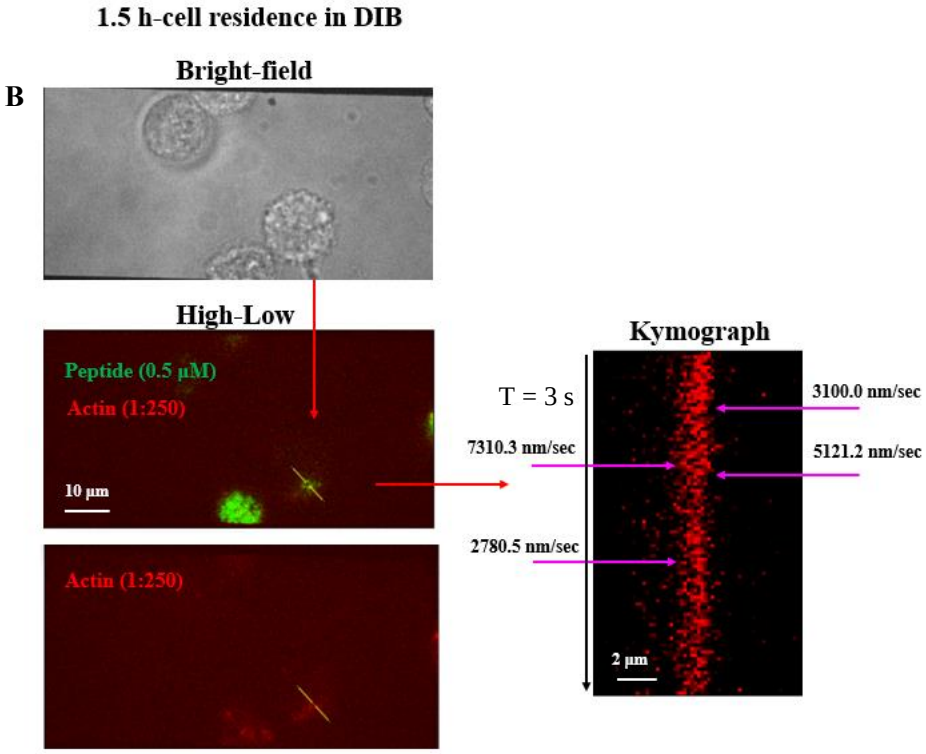
1.5 h-cell residence in DIB
B
Bright-field
High-Low
Peptide (0.5 µM)
Actin (1:250)
10 µm
Actin (1:250)
Kymograph
T = 3 s
3100.0 nm/sec
7310.3 nm/sec
5121.2 nm/sec
2780.5 nm/sec
2 µm

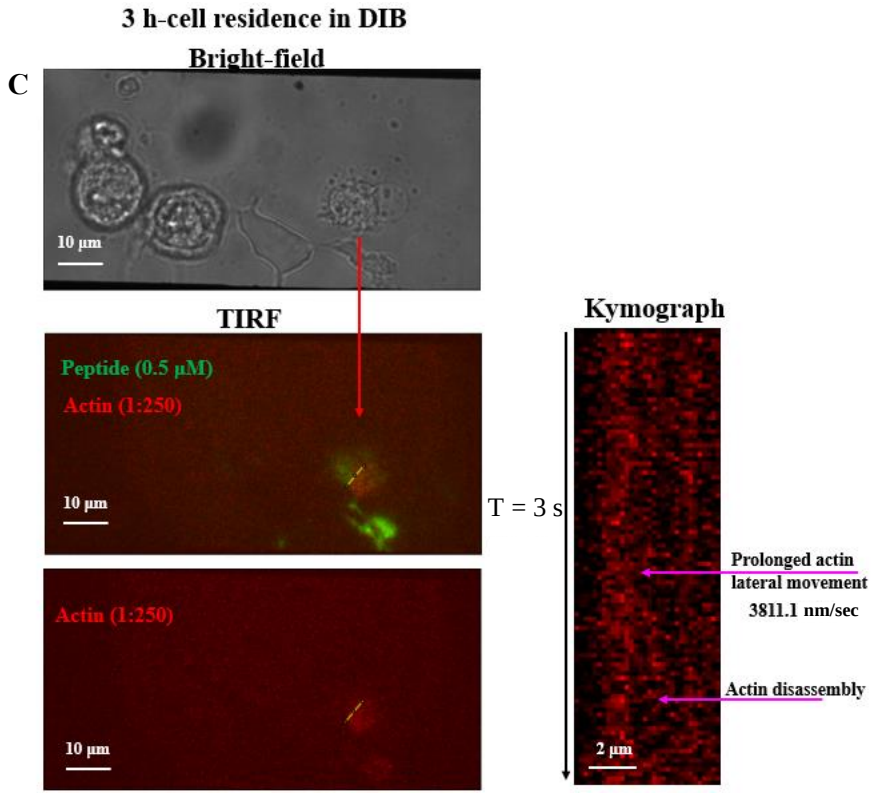
3 h-cell residence in DIB
C
Bright-field
10 µm
TIRF
Peptide (0.5 µM)
Actin (1:250)
10 µm
Actin (1:250)
10 µm
Kymograph
T = 3 s
Prolonged actin
lateral movement
3811.1 nm/sec
Actin disassembly
2 µm

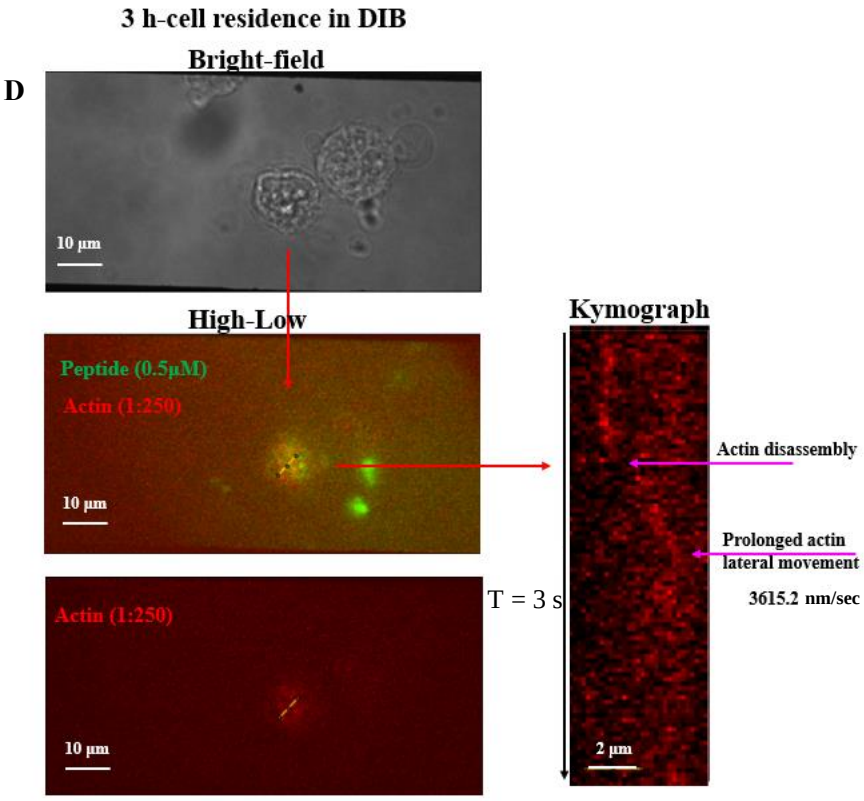

Figure 7.31- Analogous F-actin dynamics illustrated by TIRF and High-Low imaging modes in ligand-grafted DIB-engulfed A549 cells for the same incubation periods. *Evanescent-wave and longer penetration depths, acquired by (A) TIRF and (B) high-low microscopy, respectively, present similar actin remodelling and motility speeds at 1 h and 30 min. Comparability of F-actin lateral reorganization patterns was also detected by (C) TIRF and (D) high-low modalities at 3 h-cell residence in the DIB. Peptide traces were removed from kymographs for better actin trail visualization.*

7.4. Discussion

Aiming to engineer a hybrid interface system, comprised of a tethered cell to a DIB inner leaflet via membrane integrated cRGD ligands, we needed to analyze elicited cellular responses that could disclose cell adhesion behaviours.

Firstly, it was shown that following cell encasement in a cRGD-functionalized DIB, the conjugated peptide products, (Chol-PEG2000-Mal-cRGDfK-Atto488), were successfully inserted into the DIB inner leaflet (Fig. 7.18) as estimated by the ensemble-averaged mean square displacement of single fluorescent peptide molecules depicting a 2D confined tracer movement in the DIB planar surface (Fig. 7.18C,D), suggesting entrapped molecule distribution in the lipid-oil substrate.

As cell-attachment to RGD-grafted surfaces instigates a deluge of mechanisms, the analysis was focused on cellular morphological modifications with associated actin cytoskeletal reorganization and cell migration responses linked to integrin-peptide ligation.

Experimental data demonstrated that lamellipodia and bleb formations were key features of A549 cells interacting with cRGD-presenting platforms, (both DIB and SLB) (Fig. 7.13, Fig. 7.15). PM bleb, as a signature of amoeboid cell motion, especially in constraint spaces, primarily emerged in the functionalized droplet-enclosed cells (Fig. 7.15). These cellular morphological changes were associated with cell migration (Fig. 7.17), a process that calls for adhesion to the substrate, and retraction of focal adhesion at the rear[78]. Moreover, morphodynamics analysis (via ADAPT) presented a strong correlation between peptide cell surface recruitment and dynamic contour actin restructuring (Fig. 7.19), an attenuated characteristic in peptide free DIB-encapsulated cells (Fig. 7.20).

In corroboration with this data, kymography, another morphodynamic analysis tool employed for studying actin emission in the ventral region of the cell, presented dynamic

filamentous actin rearrangements, characterized by distinct polymerization-depolymerization events, in both peptide-decorated DIB-engulfed cells and peptide containing SLB-seeded cells (Fig. 7.22, Fig. 7.23, Fig. 7.24)**,** manifestations not readily detectable in A549 cells contacting non-grafted substrates (Fig. 7.21, Fig. 7.25)**.** In addition, F-actin lateral shifts, indicative of actin velocities, were significantly more pronounced in peptide interacting cells (Fig. 7.22, Fig. 7.23, Fig. 7.24) relative to those deposited on non-functionalized surfaces (DIBs and SLBs) (Fig. 7.21, Fig. 7.25, Fig. 7.26, Fig. 7.27), denoting primarily filamentous actin modulation by ligand assembly. Finally, actin cytoskeleton regulation by fluid ligand clustering correlated with cell migration (Fig. 7.28) and increased membrane protrusion and retraction velocities (Fig. 7.29).

Taken together, the results of this study provide solid evidence in support of ligand-integrin-mediated adhesion of DIB-engulfed A549 cells, where the cell demonstrates morphological and morphodynamic features, such as outgrowth formations and actin cytoskeleton restructuring/re-organization with associated locomotion capabilities that can arise mainly under cell-substrate adhesive conditions.

The frequent occurrence of these cellular responses in the cRGD-functionalized DIB lumen is adequate to attest to DIB-cell anchorage materialization. The DIB environment itself does not prove to be the ideal milieu to promote focal adhesions; on the contrary, it seems to hamper cell-surface binding (Fig. 7.13, Fig. 7.15, Fig. 7.27). Yet, when decorated with cRGD-peptide conjugates, receptor-ligand complexes develop and stabilize, actuating physical integrin-actin linkage, which provides traction for migration, through actin assembly force generation transmitted via integrins to their ligands[79].

Leveraging the ECM composition, local changes and mechanics can be driven by a feed forward interplay between the cell and the matrix itself. Cues arising from the extracellular environment can be perceived by the cell and transferred by the mechanosensing activity of focal adhesions into the intracellular layer inducing specific cellular behaviours[80, 81]. In that context, it seems plausible to reckon that the cRGD engineered inner DIB layer

can function as an attachment promoting substrate with tunable capabilities, allowing one to mimic cell-cell synapse structures.

In our model, only one type of ligand for integrins was used and only one cell type was engulfed, either of which or their combination might not be the optimal choice for strong adhesions to be established. Such assumption stems from the observation that despite the commonalities of actin dynamics and velocities exhibited between cRGD-functionalized DIBs and SLBs, there are still differences in actin architectures (with more prevalent depolymerization incidents in ligand-embedded SLBs), potentially denoting strength magnitude variabilities.

There are plenty of ways for DIB surface and chamber surrounding condition optimization, including variation in types of ligands and densities, combination of mobile and immobile ligand presentation, and membrane lipid composition permitting diverse fluidities, which collectively could create a more promising and thriving environment for cell-matrix adhesions.

Arguably, 2D cell migration is typically characterized by lamellipodial protrusion at the front, spread morphologies, mature focal adhesions, and high myosin contractility at the trailing edge[82]; traits that equally testify to cell-matrix adhesion. Nevertheless, cell motility is a non-uniform event, which entails distinct migration modes that depend on cell type and context and are accompanied by variation in cell shape, adhesion strength and migration speed[83].

The most well-known cell migration type is the mesenchymal migration, associated with an elongated cellular morphology and strong cell-matrix adhesions[84], while the simplest one is the amoeboid movement[85], driven by a roundish to ellipsoid cell shape, diffusely organized adhesion sites to the substrate and actin cytoskeleton involvement that lacks stress fibres[83].

However, recent studies in 3D migration have underscored the restrictive nature of these classifications, (mesenchymal and amoeboid), as migration strategies exist over a broad spectrum that cannot be readily reduced to cell morphology differences[86, 87]. For instance, arm-like projections, morphologically reminiscent of lamellipodia, have been observed in an assortment of rather rounded cells moving in 3D matrices and *in vivo*[88], a cell structural profile regularly noticed in migrating cancer cells[86].

In addition, while some cell lines solely exhibit one protrusion type, several others, depending on external cues, can shift between protrusions (blebs, lamellipodia, pseudopodia)[89] or can even express them simultaneously[90]. This phenotypic plasticity in cell shape and protrusion formation is deemed as an adaptation process to the microenvironment condition, where cells try to explore the substrate to select an optimal environment and structure the position of adhesion sites[91].

Our findings demonstrate heterogeneity in cellular morphology and protrusive activity in cells interacting with ligand-presenting matrices, DIB and SLB, where both cell shape asymmetry (Fig. 7.22A, Fig. 7.31D), (with 40% detection rate-determined by cell aspect ratio), and more rounded cell bodies with expressed lamellipodia/pseudopodia and/or bleb protrusions (Fig. 7.23A, Fig. 7.24A, Fig. 7.31B) (with 60% detection rate), were escorted by dynamic remodelling of the actin cytoskeleton (Fig. 7.22B, Fig. 7.31D, Fig. 7.23B, Fig. 7.24B, Fig. 7.31B). Comparison of cell aspect ratios between peptide-functionalized DIB-enclosed cells and peptide-functionalized SLB-plated cells revealed same percentages of cells manifesting slightly elongated structures (40%) and preserved rounded morphologies (60%) ($n = 10$ per sample from 3 replicates each, unpaired t-test, $p > 0.05$), suggesting microenvironment factor similarities contributing to analogous morphological cell responses.

These apparently different cellular morphological characteristics suggest that cells displayed both ameboid-like migrating behaviour and polarized cell migration mirroring cell-attachment strength variations, potentially ranging from weak nascent adhesions to strong/mature focal ones within the same experimental context. This might relate to

peptide cell surface distribution dependent on number of cells interacting with the peptide containing substrate.

This parameter could be explored in a future study by fine-tuning cRGD densities, where more homogeneously peptide modified substrates could better promote robust griping strength in cell-matrix contact, enhancing polarized structure manifestation in a larger cell percentage.

In addition, cell aspect ratio comparisons among all groups showed non-significant differences ($n = 10$ per sample from 3 replicates each, One-Way Anova, $p > 0.05$), substantiating reported cases of migrating rounded cells with lamellipodia or rapidly protruding and retracting blebs; cellular responses mostly observable in cancer cell dissemination [8, 92, 93].

Another point of consideration pertinent to cell shape diversity, (polarity and non-polarity), in peptide-presenting platforms, is the migration mode plasticity of disseminating tumour cells that need to navigate various extracellular matrix geometries to break free from their point of origin and spread to remote destinations. During this metastasis process, studies have shown that cancer cells display both mesenchymal and amoeboid migration modes, or can switch between the two, a phenomenon termed the mesenchymal-amoeboid transition (MAT)[94].

This suggests that A549 cancer cells could go through sequential transitions, exhibiting both migration states dependent on ligand distribution, cell-cell interaction (sensing mechanical forces exerted by adjacent cells), and degree of pulmonary surfactant component release in the confined DIB compartment[95], (which is known to reduce membrane surface tension)[95], either or all of which can lead to softer substrates, where cells get more weakly adherent to[96].

The generic scenario for spontaneous onset of shape polarization and directed cell migration requires a single protrusion development when a strong front–back asymmetry

has been achieved, to direct a persistent motion[97]. Instead, the relatively high frequency detection of lamellipodia formation running around the cell's periphery in functionalized DIBs (Fig. 7.23A) and SLBs (Fig. 7.24A,) has been reported upon membrane tension decrease that apparently hinders this global asymmetry establishment[97].

Hence, DIB-cell anchorage realization has brought to surface other determinants that possibly affect cellular morphology and response homogeneity, which despite being beyond the scope of this work, they could be addressed by future optimization interventions.

Undoubtedly, the foundation for constructing a hybrid communication system, able to recapitulate elementary processes of a synaptic junction has been laid. Further advancement can be accomplished through incorporation and consolidation of biologically relevant modules, especially fitted in the artificial segment of the system, enabling a closer emulation of a biological/immunological synapse. Yet, even at this infant stage, this materialized biohybrid fabrication constitutes a promising tool for initiating studies at the molecular level of a cell and for exploiting it for synthetic biology applications; a subject elaborated in ***Chapter 8***.

7.5 References

1. Svitkina, T. *The Actin Cytoskeleton and Actin-Based Motility. Cold Spring Harb Perspect Biol.*, 2018. **10**(1):a018267.
2. Ganzinger, K.A., and Schwille, P. *More from less – bottom-up reconstitution of cell biology. Journal of Cell Science*, 2019. **132**.
3. Cáceres, R., Abou-Ghali, M., and Plastino, J. *Reconstituting the actin cytoskeleton at or near surfaces in vitro. Biochimica et Biophysica Acta (BBA) - Molecular Cell Research*, 2015. **1853**(11 PartB): p. 3006.
4. Chen, M., Zhu, W., Liang, Z., Yao, S., Zhang, X., and Zheng, W. *Effect of F-Actin Organization in Lamellipodium on Viscoelasticity and Migration of Huh-7 Cells Under pH Microenvironments Using AM-FM Atomic Force Microscopy. Frontiers in Physics*, 2021. **9**.
5. Mierke, C.T. *Role of the actin cytoskeleton during matrix invasion*, in *Physics of Cancer*. 2018, IOP Publishing Ltd. p. 7-1 to 7-87.
6. Gimenez-Molina, Y., Villanueva, J., del Mar Francés, M., Viniegra, S., and Gutiérrez, L.M. *Multiple Mechanisms Driving F-actin-Dependent Transport of Organelles to and From Secretory Sites in Bovine Chromaffin Cells. Front. Cell. Neurosci.*, 2018. **12**.
7. Pore, D., and Gupta, N. *The ezrin-radixin-moesin family of proteins in the regulation of B-cell immune response. Critical reviews in immunology*, 2015. **35**(1): p. 15–31.
8. Bodor, D.L., Ponisch, W., Endres, R.G., and Paluch, E.K. *Of Cell Shapes and Motion: The Physical Basis of Animal Cell Migration. Developmental Cell*, 2020.
9. Huxley, H.E. *Electron microscope studies on the structure of natural and synthetic protein filaments from striated muscle. J Mol Biol.*, 1963. **7**: p. 281–308.
10. Woodrum, D.T., Rich, S.A., and Pollard, T.D. *Evidence for biased bidirectional polymerization of actin filaments using heavy meromyosin prepared by an improved method. J Cell Biol.*, 1975. **67**: p. 231–237.

11. Kovar, D.R., and Pollard, T.D. *Insertional assembly of actin filament barbed ends in association with formins produces piconewton forces. Proc Natl Acad Sci.*, 2004. **101**: p. 14725–14730.
12. Clarke, D.N., and Martin, A.C. *Actin-based force generation and cell adhesion in tissue morphogenesis,* 2021. **31**(10): p. R667-R680.
13. Romero, S., Grompone, G,. Carayol, N., Mounier, J., Guadagnini, S., Prevost, M.C., Sansonetti, P.J., and Tran Van Nhieu G. *ATP-mediated Erk1/2 activation stimulates bacterial capture by filopodia, which precedes Shigella invasion of epithelial cells. Cell Host Microbe*, 2011. **9**: p. 508–519.
14. Petrie, R.J., and Yamada, K.M. *At the leading edge of three-dimensional cell migration. J Cell Sci*., 2012. **125**: p. 917–5926.
15. Bear, J.E., Svitkina, T.M., Krause, M., Schafer, D.A., Loureiro, J.J., Strasser, G.A., Maly, I.V., Chaga, O.Y., Cooper, J.A., Borisy, G.G., et al. *Antagonism between Ena/VASP proteins and actin filament capping regulates fibroblast motility. Cell,* 2002. **109**: p. 509–521.
16. Mattila, P., and Lappalainen, P. *Filopodia: molecular architecture and cellular functions. Rev Mol Cell Biol*., 2008. **9**: p. 446–454.
17. Tojkander, S., Gateva, G. and P. and Lappalainen, P. *Actin stress fibers – assembly, dynamics and biological roles. J Cell Sci.*, 2012. **125**(8): p. 1855–1864.
18. Murrell, M., Oakes, P.W., Lenz, M., and Gardel, M.L. *Forcing cells into shape: the mechanics of actomyosin contractility. Nat Rev Mol Cell Biol*., 2015. **16**(8): p. 86-98.
19. Parsons, J.T., Horwitz, A.R., and Schwartz, M.A. *Cell adhesion: integrating cytoskeletal dynamics and cellular tension. Nature Reviews. Molecular Cell Biology*, 2010. **11**: p. 633–643.
20. Ryan, G.L., Holz, D., Yamashiro, S., Taniguchi, D., Watanabe, N., and Vavylonis, D. *Cell protrusion and retraction driven by fluctuations in actin polymerization: A two-dimensional model. Cytoskeleton*, 2017. **74**(12).
21. Charras, G., and Paluch, E. *Blebs lead the way: how to migrate without lamellipodia. Nat Rev Mol Cell Biol.,* 2008. **9**: p. 730–736.

22. García Arcos, J.M. *Stabilization and motility mechanism of blebs in cancer cells*, in *Biochemistry, Molecular Biology*, 2020, Université Paris.
23. Alberts, B., Johnson, A., Lewis, J., et al. *Integrins*, in *Molecular Biology of the Cell. 4th edition*. 2002: New York: Garland Science.
24. Gilbert, S.F. *Juxtacrine Signalling*, in *Developmental Biology. 6th edition*. 2000: Sunderland (MA): Sinauer Associates.
25. Colombo, M. and A. and Bianchi, C. *Click Chemistry for the Synthesis of RGD-Containing Integrin Ligands. Molecules,* 2010. **15**(1): p. 178-197.
26. Guo, L., Zhang, F., Cai, Y., and Liu, T. *Expression profiling of integrins in lung cancer cells. Pathol Res Pract.*, 2009. **205**(12): p. 847-53.
27. Nestić, D., Uil, T.G., Ma, J., Roy, S., Vellinga, J., Baker, A.H., Custers, J., and Majhen, D. *$\alpha_v\beta_3$ Integrin Is Required for Efficient Infection of Epithelial Cells with Human Adenovirus Type 26. J Virol.*, 2018. **93**(1): p. e01474-18.
28. Sun, S.J., Wu, C.C., Sheu, G.T., et al. *Integrin β_3 and CD44 levels determine the effects of the OPN-a splicing variant on lung cancer cell growth. Oncotarget*, 2016. **7**(34): p. 55572-55584.
29. Ma, Y., Ai, G., Zhang, C., Zhao, M., Dong, X., Han, Z., Wang, Z., Zhang, M., Liu, Y., Gao, W., Li, S., and Gu, Y. *Novel Linear Peptides with High Affinity to $\alpha_v\beta_3$ Integrin for Precise Tumor Identification. Theranostics*, 2017. **7**(6): p. 1511-1523.
30. Vafaei, S., Tabaei, S. R., Guneta, V., Choong, C., and Cho, N. *Hybrid Biomimetic Interfaces Integrating Supported Lipid Bilayers with Decellularized Extracellular Matrix Components. Langmuir*, 2018. **34**(11): p. 3507–3516.
31. Schönherr, H., Johnson, J.M., Lenz, P., Frank, C.W., and Boxer, S.G. *Vesicle adsorption and lipid bilayer formation on glass studied by atomic force microscopy. Langmuir: the ACS journal of surfaces and colloids*, 2004. **20**(26): p. 11600-6.
32. Kilic, A., and Kok, F.N. *Peptide-functionalized supported lipid bilayers to construct cell membrane mimicking interfaces. Colloids and Surfaces B: Biointerfaces*, 2019. **176**.
33. Lin, Y., Zhang, M., and Barnes, P.F. *Chemokine production by a human alveolar epithelial cell line in response to Mycobacterium tuberculosis. Infection and Immunity*, 1998. **66**(3): p. 1121–6.

34. Vig, A.T., Földi, I., Szikora, S., Migh, E., Gombos, R., Tóth, M. Á., Huber, T., Pintér, R., Talián, G.C., Mihály, J., and Bugyi, B. *The activities of the C-terminal regions of the formin protein disheveled-associated activator of morphogenesis (DAAM) in actin dynamics. The Journal of biological chemistry*, 2017. **292**(33): p. 13566–13583.
35. Alexandrova, A.Y., Arnold, K., Schaub, S., Vasiliev, J.M., Meister, J.J., Bershadsky, A.D., and Verkhovsky, A.B. *Comparative dynamics of retrograde actin flow and focal adhesions: formation of nascent adhesions triggers transition from fast to slow flow. PloS one*, 2008. **3**(9): p. e3234.
36. Miller, C.M., Korkmazhan, E., and Dunn, A.R. *Extraction of accurate cytoskeletal actin velocity distributions from noisy measurements. Nat Commun.,* 2022. **13**.
37. Vendel, K.J.A. *On the role of microtubules in cell polarity: A reconstituted minimal system.*, in *Physics*, 2020. Universiteit Leiden.
38. Jankowska, K.I., and Burkhardt, J.K., *Analyzing Actin Dynamics at the Immunological Synapse. Methods in molecular biology,* 2017. ***1584***: p. 7–29.
39. Babich, A., Li, S., O'Connor, R.S., Milone, M.C., Freedman, B.D., and Burkhardt, J.K. *F-actin polymerization and retrograde flow drive sustained PLCγ1 signalling during T cell activation. The Journal of cell biology*, 2012. **197**(6): p. 775–787.
40. Barry, D.J., et al. *Open source software for quantification of cell migration, protrusions, and fluorescence intensities. Journal of Cell Biology*, 2015. **209**(1): p. 163–180.
41. Luo, W., et al. *Analysis of the local organization and dynamics of cellular actin networks. Cell Biol.*, 2013. **202**(7): p. 1057–1073.
42. Case, L.B., and Waterman, C.M. *Integration of actin dynamics and cell adhesion by a three-dimensional, mechanosensitive molecular clutch. Nat Cell Biol.*, 2015. **17**(8): p. 955-63.
43. Li, H., Liu, S., Deguchi, S., and Matsunaga, D. *Knowledge "installed" diffusion model predicts the geometry of actin cytoskeleton from cell morphology. bioRxiv*, 2023.

44. Guan, X.L., et al. *Functional interactions between sphingolipids and sterols in biological membranes regulating cell physiology. Mol Biol Cell.,* 2009. **20**(7): p. 2083-95.
45. Schick, J., and Raz, E. *Blebs—Formation, Regulation, Positioning, and Role in Amoeboid Cell Migration. Front. Cell Dev. Biol.*, 2022. **10**.
46. Paluch, E.K., and Raz, E. *The Role and Regulation of Blebs in Cell Migration. Curr. Opin. Cell Biol.*, 2013. **25**: p. 582–590.
47. Fackler, O.T., and Grosse, R. *Cell motility through plasma membrane blebbing. J Cell Biol.*, 2008. **181**(6): p. 879–884.
48. Bergert, M., Erzberger, A., Desai, R.A., Aspalter, I.M., Oates, A.C., Charras, G., et al. *Force Transmission during Adhesion-independent Migration. Nat. Cell Biol.*, 2015. **17**: p. 524–529.
49. Logue, J.S., Cartagena-Rivera, A.X., Baird, M.A., Davidson, M.W., Chadwick, R.S., and Waterman, C.M. *Erk Regulation of Actin Capping and Bundling by Eps8 Promotes Cortex Tension and Leader Bleb-Based Migration. Elife*, 2015. **4**: p. e08314.
50. Sahai, E., and Marshall, C.J. *Differing modes of tumour cell invasion have distinct requirements for Rho/ROCK signalling and extracellular proteolysis. Nat. Cell Biol.*, 2003. **5**: p. 711–719.
51. Friedl, P. *Prespecification and plasticity: shifting mechanisms of cell migration. Curr. Opin. Cell Biol.*, 2004. **16**: p. 14–23.
52. Friedl, P., and Wolf, K. *Tumour-cell Invasion and Migration: Diversity and Escape Mechanisms. Nat. Rev. Cancer,* 2003. **3**: p. 14-23.
53. Paňková, K., Rösel, D., Novotný, M., and Brábek, J. *The Molecular Mechanisms of Transition between Mesenchymal and Amoeboid Invasiveness in Tumor Cells. Cell. Mol. Life Sci.*, 2010. **67**: p. 63–71.
54. Sanz-Moreno, V., and Marshall, C.J. *The Plasticity of Cytoskeletal Dynamics Underlying Neoplastic Cell Migration. Curr. Opin. Cell Biol.*, 2010. **22**: p. 690–696.
55. Taddei, M.L., Giannoni, E., Comito, G., and Chiarugi, P. *Microenvironment and Tumor Cell Plasticity: An Easy Way Out,* 2013. **341**.

56. Lavenus, S.B., Tudor, S.M., Ullo, M.F., Vosatka, K.W., and Logue, J.S. *A flexible network of vimentin intermediate filaments promotes migration of amoeboid cancer cells through confined environments. Journal of Biological Chemistry*, 2020. **295**(19): p. 6700-6709.
57. Paul, C.D., Mistriotis, P., and Konstantopoulos, K. *Cancer cell motility: lessons from migration in confined spaces. Nat. Rev. Cancer*, 2017. **17**: p. 131-140.
58. Ikenouchi, J., and Aoki, K.*A. Clockwork Bleb: cytoskeleton, calcium, and cytoplasmic fluidity. FEBS Journal*, 2022. **289**(24): p. 907-7917.
59. Zatulovskiy, E., Tyson, R., Bretschneider, T., and Kay, R.R. *Bleb-driven Chemotaxis of Dictyostelium Cells. J. Cell Biol.*, 2014. **204**: p. 1027–1044.
60. Liu, Y.-J., Le Berre, M., Lautenschlaeger, F., Maiuri, P., Callan-Jones, A., Heuzé, M., et al. *Confinement and Low Adhesion Induce Fast Amoeboid Migration of Slow Mesenchymal Cells. Cell*, 2015. **160**: p. 659–672.
61. Cao, Y., Karmakar, R., Ghabache, E.*,* Gutierrez, E.*,* Zhao, Y.*,* Groisman, A.*,* Levine, H.*,* Camley*,* B.A.*,* and Rappel, W. *Cell motility dependence on adhesive wetting. Soft Matter*, 2019. **9**(15): p. 2043-2050.
62. Schaks, M., Giannone, G., and Rottner, K. *Actin dynamics in cell migration. Essays in biochemistry*, 2019. **63**(5): p. 483–495.
63. Cavalcanti-Adam, E.A., Volberg, T., Micoulet, A., Kessler, H., Geiger, B., and Spatz, J.P. *Cell Spreading and Focal Adhesion Dynamics Are Regulated by Spacing of Integrin Ligands. Biophysical Journal*, 2007. **92**(8): p. 2964-2974.
64. Hynes, R.O., *Integrins: a family of cell surface receptors. Cell*, 1987. **48**: p. 549-554.
65. Pavalko, F.M., and Otey, C.A. *Role of adhesion molecule cytoplasmic domains in mediating interactions with the cytoskeleton. Proc. Soc. Exp. Biol. Med.*, 1994. **205**: p. 282-293.
66. Geiger, B., and Bershadsky, A.D. *Transmembrane crosstalk between the extracellular matrix-cytoskeleton crosstalk. Nat. Rev. Mol. Cell Biol.*, 2001. **2**: p. 793-805.

67. Danhier, F., Le Breton, A., and Préat, V. *RGD-Based Strategies to Target Alpha(v) Beta(3) Integrin in Cancer Therapy and Diagnosis. Mol. Pharmaceutics*, 2012. **9**(11): p. 2961–2973.

68. Shah, P., Fong, M., and Kakar, S. *PTTG induces EMT through integrin $\alpha_v\beta_3$ -focal adhesion kinase signaling in lung cancer cells. Oncogene,* 2012. **31**: p. 3124–3135

69. Zhou, W., Ma, J., Meng, L. et al*. Deletion of TRIB3 disrupts the tumor progression induced by integrin $\alpha_v\beta_3$ in lung cancer. BMC Cancer*, 2022. **22**: p. 459.

70. Carragher, N.O., and Frame, M.C. *Focal adhesion and actin dynamics: a place where kinases and proteases meet to promote invasion. Trends in cell biology*, 2004. **14**(5): p. 241–249.

71. Hu, X., Roy, S.R., Jin, C. et al*. Control cell migration by engineering integrin ligand assembly. Nat Commun*., 2022. **13**(5002).

72. Yu, C., Law, J.B.K., Suryana, M., and Sheet, M.P. *Early integrin binding to Arg-Gly-Asp peptide activates actin polymerization and contractile movement that stimulates outward translocation. PNAS*, 2011. **108**(51).

73. Bachir, A.I., Horwitz, A.R., Nelson, W.J., and Bianchini, J.M. *Actin-Based Adhesion Modules Mediate Cell Interactions with the Extracellular Matrix and Neighboring Cells. Cold Spring Harbor perspectives in biology*, 2017. **9**(7): p. a023234.

74. Mierke, C.T. *The Pertinent Role of Cell and Matrix Mechanics in Cell Adhesion and Migration. Front. Cell Dev. Biol.*, 2021. **9**.

75. Yamazaki, D., Kurisu, S., and Takenawa, T. *Regulation of cancer cell motility through actin reorganization. Cancer science*, 2005. **96**(7): p. 379–386.

76. Pollard, T.D., and Borisy, G.G. *Cellular Motility Driven by Assembly and Disassembly of Actin Filaments. Cell*, 2003. **112**(4): p. 453-465.

77. Casanellas, I., Jiang, H., David, C.M., Vida, Y., Pérez-Inestrosa, E., Samitier, J., Lagunas, A. *Substrate adhesion determines migration during mesenchymal cell condensation in chondrogenesis. bioRxiv preprint*, 2022.

78. Heck, T., Vargas, D.A, Smeets, B., Ramon, H., Van Liedekerke, P., and Van Oosterwyck, H. *The role of actin protrusion dynamics in cell migration through a*

degradable viscoelastic extracellular matrix: Insights from a computational model. BioRxiv, 2019.

79. Nordenfelt, P., Elliott, H. and Springer, T. *Coordinated integrin activation by actin-dependent force during T-cell migration. Nat Commun.*, 2016. **7**(13119).
80. Seetharaman, S. *Integrin diversity brings specificity in mechanotransduction. Biol. Cell,* 2018. **110**: p. 49–64.
81. Martino, F., Perestrelo, A. R., Vinarský, V., Pagliari, S., and Forte, G. *Cellular Mechanotransduction: From Tension to Function. Frontiers in physiology*, 2018. **9**(824).
82. Trepat, X., Chen, Z., and Jacobson, K. *Cell migration. Comprehensive Physiology*, 2012. **2**(4): p. 2369–2392.
83. Schmidt, S., and Friedl, P. *Interstitial cell migration: integrin-dependent and alternative adhesion mechanisms. Cell Tissue Res.,* 2010. **339**: p. 83–92.
84. Khoo, A.S., Valentin, T.M., Leggett, S. E., Bhaskar, D., Bye, E.M., Benmelech, S., and Wong, I.Y. *Breast Cancer Cells Transition from Mesenchymal to Amoeboid Migration in Tunable Three-Dimensional Silk-Collagen Hydrogels. ACS biomaterials science & engineering*, 2019. **5**(9): p. 4341–4354.
85. Friedl, P., Borgmann, S., and Bröcker, E.B. *Amoeboid leukocyte crawling through extracellular matrix: lessons from the Dictyostelium paradigm of cell movement. Journal of leukocyte biology*, 2001. **70**(4): p. 491–509.
86. Bodor, D.L., Ponisch, W., Endres, R.G., and Paluch, E.K. *Of Cell Shapes and Motion: The Physical Basis of Animal Cell Migration. Developmental Cell*, 2020. **52**.
87. Te Boekhorst, V., Preziosi, L and Friedl, P. *Plasticity of Cell Migration In Vivo and In Silico Plasticity of Cell Migration In Vivo and In Silico. Annual Review of Cell and Developmental Biology*, 2016. **32**(1): p. 491-526.
88. Fritz-Laylin, L.K., Riel-Mehan, M., Chen, B.C., Lord, S.J., Goddard, T.D., Ferrin, T.E., Nicholson-Dykstra, S.M., Higgs, H., Johnson, G.T., Betzig, E., and Mullins, R.D. *Actin-based protrusions of migrating neutrophils are intrinsically lamellar and facilitate direction changes. eLife*, 2017. **6**.

89. Bergert, M., Chandradoss, S.D., Desai, R.A., and Paluch, E. *Cell mechanics control rapid transitions between blebs and lamellipodia during migration. Proceedings of the National Academy of Sciences of the United States of America*, 2012. **109**(36): p. 14434–14439.

90. Tyson, R.A., Zatulovskiy, E., Kay, R.R., and Bretschneider, T. *How blebs and pseudopods cooperate during chemotaxis. Proceedings of the National Academy of Sciences of the United States of America*, 2014. **111**(32): p. 11703–11708.

91. Reeves, C., Winkler, B., Ziebert, F. et al*. Rotating lamellipodium waves in polarizing cells. Commun Phys.,* 2018. **1**(73).

92. Lorentzen, A., Bamber, J., Sadok, A., Elson-Schwab, I., and Marshall, C.J. *An ezrin-rich, rigid uropod-like structure directs movement of amoeboid blebbing cells. Journal of cell science*, 2011. **124**((Pt 8)): p. 1256–1267.

93. Poincloux, R., Collin, O., Lizárraga, F., Romao, M., Debray, M., Piel, M., and Chavrier, P. *Contractility of the cell rear drives invasion of breast tumor cells in 3D Matrigel. Proceedings of the National Academy of Sciences of the United States of America*, 2011. **108**(5): p. 1943–1948.

94. Liu, Y.-J., Le Berre, M., Lautenschlaeger, F., Maiuri, P., Callan-Jones, A., Heuze, M., Takaki, T., Voituriez, R., and Piel, M. *Confinement and Low Adhesion Induce Fast Amoeboid Migration of Slow Mesenchymal Cells. Cell*, 2015. **160**: p. 659–672.

95. Han, S., and Mallampalli, R.K. *The Role of Surfactant in Lung Disease and Host Defense against Pulmonary Infections. Annals of the American Thoracic Society*, 2015. **12**(5): p. 765–774.

96. Reinhart-King, C.A., Dembo, M., and Hammerz, D.A. *Cell-Cell Mechanical Communication through Compliant Substrates. Biophysical Journal*, 2008. **95**: p. 6044–6051.

97. Reeves, C., Winkler, B., Ziebert, F., et al*. Rotating lamellipodium waves in polarizing cells. Commun Phys.*, 2018. **1**(73).

Chapter 8: Artificial and Biohybrid System Applicabilities/Capacities

8.1 Outlook

8.1.1 Contribution of Novel Intermembrane Model to Synthetic Biology

Although recent decades have seen rapid advances in establishing methods to model and dissect tissue development and regeneration [1, 2] current available technologies still cannot provide full understanding of a good number of basic cellular mechanisms.

Biological system complexity along with technology insufficiency, which entails model system engineering deprived of unrestrained movable cues and spatiotemporal regulation of biophysical and biochemical signals[2], necessitates further technological developments, (more refined tools), with configuration and functional characteristics analogous to the biological system under investigation to enable cell-based studies and decipher key pathways in multifactorial issues[3].

Our work has produced a novel dual membrane platform with a synapse-like architecture, intercommunication pathways through reconstituted protein channels and tunable nanofabricated microenvironment suitable to accommodate synthetic and living cells. This engineered communication model system, which can interact with both artificial and plasma membranes via diffusible “ligand-receptor” pairs, marks a significant advancement in intercellular communication studies affording unprecedented access to single-cell’s natural chemistry and its subsequent visualization. It enables interrogation of a cell’s molecular machinery unravelling physiological mechanisms which underly intercellular communication along spatial and temporal axes.

This innovative tool can profile a broad range of membrane mechanics with single molecule sensitivity and cellular mechanisms advancing our knowledge of fundamental cell biology and driving the development of revolutionary therapeutic strategies which can address a broad range of diseases[4, 5].

The avenues through which this newly designed platform can be exploited are diverse; here, I detail applicable ideas and potential research directions in which this development can be capitalized on aiming to foster innovation in biotechnology and synthetic biology research and healthcare outcomes.

8.1.2 Biohybrid Interface System Applications

The prime advantage of the biohybrid system lies in the simplification of the cell-to-cell communication complexity, where multitudes of subcellular components and networks meddle, by establishing an artificial to biological cell interfacing system, reducing behavioural sophistication.

With this hybridization model, (tethered living cell to the synthetic bilayer through DIB embedded RGD-recognizing integrins), our objective was to recapitulate contact-dependent membrane-membrane interplay in a semi native three-dimensional (3D)

structure, while offering the benefits of planar orientation, which enables easy and direct imaging.

The encapsulated and anchored cell in the droplet-on-a-hydrogel bilayer, via the synthetic membrane integrated cell-adhesive materials, (cRGDfKC), recreates a flexible and tunable cell-based composition that facilitates elucidation of the spatial organization and variation generated due to single-type extrinsic signals.

This single-cell – matrix pairing occurring on the platform allows monitoring of static parameters and dynamic processes from both participants concomitantly, thus enabling pairwise-correlated multiparametric profiling of cell-RGD peptide interactions[6].

Although our experimental work, so far, has produced a single component peptide surface pattern interfaced with a single cell type, adjustments can be easily made to entertain multiple component ligands generating multivariable biological signaling environments, with tunable control over each ligand concentration. These adjustable engineering strategies can add much more complexity to the system, permitting single-cell behaviour interrogation at several levels, through multiparametric phenotypic data acquisition[7]; information that will enhance understanding of how heterogeneous signaling networks spatially coordinate to modulate cell behaviour and instigate activation cascades that potentially direct cell and tissue function[7-9].

This platform can be used not only to address fundamental biological questions through presentation of membrane-anchored single-type ligands, exploring the effect of how one specific biological cue can modulate cellular process(es) of interest, (e.g., actin-based cell locomotion), but also, through integration of multiplexed ligand patterns, it can coordinate and orchestrate mechanisms evoking more organized and intricate cellular responses[7]. Thus, tapping into the adaptability of gradual multicomponent ligand incorporation, we can study a range of biological processes extending from basic mechanisms to perplexing cellular reactions[7].

In addition, apart from actin staining use, plenty of other live cell-markers can be introduced to visualize the dynamics of other proteins or protein subsets, e.g., microtubule

cytoskeleton labelling with StableMARK (Stable Microtubule-Associated Rigor-Kinesin staining)[10] or myosin staining, applying HaloTag technology and electroporation [11], and explore their operation modes in physiological and pathophysiological cellular states.

Moreover, comparisons of elicited cellular activities triggered by differently micro engineered surroundings can reveal the type of constituents and the chemical composition needed to support tissue growth[12].

Even accommodation of various cell types, (e.g., cancer and normal cell), each per DIB, can allow inter-sample comparisons between physiological and pathogenic cellular processes, empowering identification of specific molecule involvement and degree of component participation in cases of health and disease[12, 13].

With this simplified model, we can entrap and controllably pair any cell type of our choice and wrap specific microenvironments around the dynamic crosstalk between a living cell and cell constituents, thereby inducing cellular activation in a precise setting with real-time imaging.

Incorporation of more than one cell type per DIB, facilitating intercellular interplay together with the artificial substrate, can bridge scales of complexity into the system, where individual cells start acting collectively and in cooperation with the ECM ligands. In this context, outstanding challenges encountered during signal orchestration of interacting cells, where multifactorial signalling networks operate, can be explored.

A typical example of intricate cellular crosstalk is found in cancer microenvironment where cancerous and surrounding cells encompass a two-way process and engagement of a broad range of mechanisms. The biggest barrier towards understanding cancer pathogenesis is cell communication in this tumor microenvironment (TME) where cancer cells do not associate only with themselves, but also with other non-cancerous host cells such as immune cells, (B cells, T cells, macrophages, NK cells, dendritic cells), fibroblasts and endothelial cells. As interactions within the TME are diverse, differentially promoting cancer progression[14], our model can stand as a platform, upon which single component or multiple component ligands and single or heterogeneous cell types can be hosted,

producing a gradually more complex interaction network, where current fundamental questions of the cell–TME teamwork can be tackled; information that will yield insight into cancer biology in the hope of identifying new therapeutics.

Therefore, this bottom-up reconstitution approach can expand our understanding of biology at higher level, as it allows continual increase in the number of elements, (adhesion material and cell types), it can accommodate that eventually might lead to analogous complexity of intercommunicating living cells, but still with a reduced level of entanglement relative to the *in vivo* cellular connectivity[15].

This permissible increased pattern multiplicity can explicate tissue engineering requirements, serving as an ideal first step for modeling heterogeneous signalling environments with controlled spatial presentation[7].

An additional perk regards the possibility to execute fine control over indirect cell-cell communication via adjustment of soluble factor gradients. For instance, by incorporating different soluble factors, (e.g., cytokines, growth factors, hormones, neurotransmitters, salt ions), in the hydrogel layer, deposited on the coverslip of the PDMS device, trans-synaptic chemically mediated communication can be attained via reconstituted DIB channels, enabling systematic assessment of the combinatorial effects of secretory determinants.

Overall, the unsurpassed strength of this model lies in its potential for single or multiple biochemical and biophysical signal presentation within a synapse-like configuration that offers unimpeded cell component diffusion and affords high spatiotemporal resolution.

8.1.2.1 Upcoming Demonstrations of the Biohybrid Interface System

The prime objective of the present model engineering was to fabricate a platform with capabilities of mimicking a realistic cell–cell interaction which is based on well-founded biophysical principles.

Already conceived ideas of current model use awaiting materialization involve chemical signal manipulation in DIB-enclosed A549 cells and recreation of a neuronal synapse structure exhibiting neurogenic characteristics with measurable excitatory behaviour.

Chemical signal manipulation can be exploited to instigate diverse cellular responses replicating intricate biological mechanisms in a simplified manner. For example, use of the same cancer cell line (A549) in an acidic DIB microenvironment (pH 5.9), reported to facilitate cancer cell migration[16], in the presence and absence of cRGD ligand can allow single cell reaction monitoring in these two diversified tumour conducive conditions, delineating the distinct input of each component involved and their synergistic interaction responsible for cancer dissemination.

In addition, cumulative ion flux can be achieved through aHL pore insertion into the DIB bilayer, permitting Ca^{2+} translocation from the rehydrating substrate. Given that acidic extracellular pH increases cell Ca^{2+} influx through voltage dependent Ca^{2+} channel (VDCC)[17] and promotes opening of the $\alpha_v\beta_3$ headpiece, facilitating integrin activation[18], studies on how extracellular Ca^{2+} store availability can impact actin-regulated cancer cell motility could be organized by fine-tuning ambient adjustments.

Another demonstration of the bio-hybrid model application is the recreation of a neuronal synapse, where nerve cell type properties can be probed. DIB-engulfment of PC12 cells in a differentiated state, which can display neurogenic characteristics, like ion and neurotransmitter receptor expression, neurotransmitter (e.g., dopamine, norepinephrine, epinephrine) secretion and axon-dendrite elongation, can be subjected not only to Ca^{2+} influx, (through Ca^{2+} permeable channel opening in the DIB bilayer), but also to plasma membrane depolarization under external K^+ stimulation, (through K^+ permeable channel opening in the DIB bilayer), allowing investigation of neurotransmitter release by calcium-regulated exocytosis.

Reproduction of such a biological process, within the droplet confined space, shares several similarities with the native biological synapse, where Ca^{2+} triggers synaptic

vesicle exocytosis, releasing vesicle contained neurotransmitters, and thus actuating synaptic transmission[19, 20].

This endeavour can go beyond a mere illustration of neuronal synapse geometry as it can be used to shed light on which of the two competing models, (namely, clathrin-mediated endocytosis or the kiss-and-run model), proposed for the compensatory endocytosis process, needed for plasma membrane size and composition preservation following exocytosis[21], has an edge.

For a neuron to replenish the synaptic vesicle pools and recycle the membrane added to the plasma membrane during synaptic vesicle exocytosis[22], it is believed that either (a) the full fusion model, in which synaptic vesicle components, (such as proteins and lipids), travel laterally into the PM and are retrieved by clathrin-mediated endocytosis at remote sites from the exocytic portals[23], or (b) the kiss-and-run fusion, where synaptic vesicle transiently fuses with the presynaptic membrane, releasing neurotransmitter cargo, after which the vesicle is uptaken to the cytoplasm[24], operates.

FM dyes, e.g., FM4-64, (with both a hydrophobic and hydrophilic moiety), which afford intense fluorescence upon interaction with the lipid membrane but remain completely nonfluorescent in extracellular environment, (synaptic cleft), could allow synaptic vesicle behaviour tracking (a. complete/flattened or b. transient membrane fusion), after external K^+ stimulation, when the cell uptakes the dispersed FM dye via endocytosis following neurotransmitter release via exocytosis. Spatiotemporal localization and analysis of fluorescence fluctuations, indicative of distinct vesicle exocytosis modes, could lead to insightful interpretations of fusion dynamic patterns.

Exemplifying two tangible concepts with considered element incorporation for their actualization, we showcase the applicability of this innovative tool in scientific research for real biological issues.

8.1.3 Artificial Communication System Applications

Taking into consideration that crucial cellular processes such as division, endocytosis, motility, and cell polarization are preserved by the plasma membrane, our highly dynamic artificial membrane system has been designed with the prospect of rebuilding these mechanisms enabling their spatial and temporal separation.

The manufactured double membrane assembly, apart from its morphological resemblance to a cell-to-cell communication network, contains biomolecular components, such as transmembrane channels (aHL), cytoskeletal elements (actin), and biologically-relevant molecules (complementary DNA strands), combined to replicate intercellular responses, including DNA-mediated trans-synaptic adhesion forces, self-organization of mobile, paired intermembrane cleft components and stimuli-triggered intermembrane signal communication with elicited biochemical reactions, (vesicular actin filament growth and Ca^{2+}-dependent change in fluorescence intensity), and biophysical responses, (induced vesicle membrane deformation by actin-based force generation), shedding light on fundamental biological mechanisms under a simplified and highly controlled environment.

The simplified synapse-like structure development apart from enabling DNA- and potentially actin-based intermembrane tension measurements by *in situ* FRET microscopy, additional biomolecular component integration in the artificial system, including cytoskeletal elements, (e.g., myosin motor proteins, actin-bundling proteins, such as fascin, with promoting membrane protrusion properties)[25, 26], enzymes[27], transcription/translation machinery[28] and integrin-ligand pairs[29], can recapitulate modular organization of cellular networks that control specific biological mechanisms, such as motility, energy generation, and signalling cascades.

Furthermore, this model can serve as a tool to satisfy scientific curiosity. Typically, liposomes or vesicles have been so far successfully implemented for transporting and delivering drugs or probes[30, 31]. Yet, the chemical and physical principles for their performance leading to their engulfment by the cell membrane have not hitherto been

completely unravelled. Identification of essential tenets underpinning their mechanism of action as delivery systems would allow more targeted therapeutic intervention.

In the reconstituted model system we have developed, the encapsulated actin-containing vesicle demonstrates features of cytoskeletal organization, though in a far simpler version than its cellular counterparts, empowering potential biophysical studies on cellular uptake mechanisms that rely on actin engagement.

Considering that synthetic “ligand-receptor” interactions have been established via complementary DNA strands, their involvement in the cellular uptake processes could be also explored and compared to those in the biohybrid system, where natural cell surface receptors and their cognate ligands are in operation.

A DIB-encapsulated actin GUV constitutes a more robust reconstructed *in vitro* cell model and provides a unique opportunity to study membrane-cytoskeleton interactions, and cytomechanics in association with intermembrane adhesion forces.

Vesicle misshaping induced by combined effects of actin-based force generation and osmotic pressure difference across the liposomal membrane could also play an active role in the endocytic process, permitting studies of this nature as well.

Moreover, the mechanical forces in T cell signaling, present within the nano-scale gap of the immunological synapse, (between T cell and antigen presenting cell), could be replicated in this membrane platform, based on the adhesive cross-bridges formed by DNA complements between DIB and GUV. Intermembrane force generation could be triggered and promoted by vesicle actin assembly-based force production following incorporation of mechanosensitive MS ion channel proteins, such as Piezo 1, into the vesicle membrane. This MS protein can be activated through direct physical deformations of the lipid bilayer[32] mediated through osmotic pressure difference across the bilayers. Subsequently, ion/Ca^{2+} influx through the mechanically gated channels could drive vesicle actin filament growth, further enhancing trans-synaptic adhesion forces; processes naturally regulating TCR signalling[33].

Quantification of these minute forces generated, acting at the “single-receptor” level, could be possible by leveraging donor–acceptor fluorophore pairs integrated into the complementary DNA-constructs, both embedded into the two adjoining bilayer surfaces (DIB-GUV). Stretches and relaxations across “receptor-ligand” can be captured by FRET measurements and translated to mechanical force modifications[33].

This methodology could be applied at different GUV actin polymerization stages yielding quantitative data that reflect force magnitude variations as a function of actin assembly and network formations.

Monitoring membrane-membrane interplay phenomena, (e.g., endocytosis, fusion), between GUV- DIB bilayers at the single-particle level grants access to the intermediate states of these mechanisms, commonly not accessible in bulk fusion assays, where individual events are hidden[34].

With this micro engineered platform, we can detect individual fusion/endocytosis events using TIRF microscopy[35, 36] and track “ligand” distribution patterns during these processes. Additionally, visualization could be approachable from both sides, (DIB and vesicle lipid bilayers), disclosing information about the degree of each construct’s engagement.

Currently, several cellular entry routes of vesicles have been identified ranging through receptor-mediated endocytosis, clathrin interactions, lipid raft interactions, macropinocytosis, phagocytosis, and possibly direct fusion[37]. Thus, vesicle uptake, as an undeciphered biological mechanism, calls for more in-depth assessment and subcellular analyses, achievable through proper tool use and high-resolution microscopy.

Acknowledging that several endocytic pathways are mostly defined in their dependency on distinct key proteins and lipids, using this platform we could elucidate the complex interplay of biomolecules in the lipid-driven endocytosis process. This approach can be easily materialized since highly interconnected players, (interplay of lipids, incorporated

membrane proteins and the underlying cytoskeleton), can be gradually integrated and thus, their contribution can be gauged accordingly.

Adding to the list of the advantages, the artificial context of this model can be enriched with life-like characteristics. Stepwise incorporation of biological elements in the synthetic substrates can expand its degree of response. Mingling of synthetic entities with biological components can allow us to untangle and hijack cell capabilities and sophistication. For instance, in a future practice, incorporation of coding sequence for functional proteins within the GUV, could be accompanied by enclosure of extracted chromatophores from Rhodobacter sphaeroides, which under illumination, can convert ADP to ATP, instigating and sustaining DNA transcription to mRNA and its subsequent translation into proteins[29].

In addition, this artificial system gives us the opportunity to compare ligand spatial distribution between artificial and biohybrid interfaces, where the liposome has been substituted with a living cell, unravelling the concealed physics driving membrane constituents. Pinpointing distinct component's role in specific membrane responses is not only essential for uncovering the underlying physical principles, but it also empowers cell-like artificial cell synthesis.

Using the biohybrid model as a proxy for how "life-like" the synthetic platform can be and potentially as a yardstick to determine which complementary cell modules are essential to be introduced in the artificial system, we could more precisely reproduce basic physiological functions.

Overall, whilst key insights have been acquired through *in vitro* culture exposure to extrinsic cues, still, underlying aspects of dynamic, *in vivo* signaling surroundings, (such as spatial cue variation impacting cell behaviour), remain unaddressed. Thus, our novel platform, with the aforedescribed capacities and its flexibility to be translated into a biohybrid version, can be readily employed to elucidate simple and complex signalling logic encountered across a broad range of cells.

8.1.4 Concluding Statements

The thesis outlined the steps towards artificial and biohybrid model fabrication which configures the neuronal or immunological synapse geometry stabilized by dynamic “ligand-receptor” coupling.

Such a novel technology is expected to advance substantial improvements in our understanding of how diverse layers of biological information interact with each other. It will allow researchers to map single cell type behaviours and diverse cell states emerging due to the molecular and cellular components in their adjacent microenvironment. Even multiplex molecular component detection is attainable enhancing deeper understanding on biological synergies that shape cell fate.

Ultimately, this engineered communication platform, which makes a novel contribution to the field of synthetic biology, is expected to open new routes for cell-based research with profound implications for basic and applied biomedicine and therapeutics.

8.2 References

1. Nishikawa, S., Jakt, L.M., and Era, T. *Embryonic stem-cell culture as a tool for developmental cell biology. Nat. Rev. Mol. Cell Biol*., 2007. **8**: p. 502–507.
2. Spiteri, C., Caprettini, V., and Chiappini, C. *Biomaterials-based approaches to model embryogenesis. Biomater. Sci.*, 2020. **8**: p. 6992-7013.
3. Bi, D., Almpanis, A., Noel, A., Deng, Y., and Schober, R. *A Survey of Molecular Communication in Cell Biology: Establishing a New Hierarchy for Interdisciplinary Applications. IEEE Communications Surveys & Tutorials*, 2020. **23**: p. 1494-1545.
4. Yang, B.A., Westerhof, T.M., Sabin, K., Merajver, S.D., and Aguilar, C.A. *Engineered Tools to Study Intercellular Communication. Advanced science (Weinheim, Baden-Wurttemberg, Germany)*, 2020. **8**(3).
5. Mant, C.T., Chen, Y., Yan, Z., Popa, T.V., Kovacs, J.M., Mills, J.B., Tripet, B.P., and Hodges, R.S. *HPLC analysis and purification of peptides. Methods in molecular biology (Clifton, N.J.)*, 2007. **386**: p. 3–55.
6. Dura, B., Dougan, S., Barisa, M. et al. *Profiling lymphocyte interactions at the single-cell level by microfluidic cell pairing. Nat Commun.*, 2015. **6**(5940).
7. Scheideler, O.J., Yang, C., Kozminsky, M., Mosher, K.I., Falcón-Banchs, R., Ciminelli, E.C., Bremer, A.W., Chern, S.A., Schaffer, D.V., and Sohn, L.L. *Recapitulating complex biological signaling environments using a multiplexed, DNA-patterning approach. Science advances*, 2020. **6**(12).
8. Choi, C.K., Breckenridge, M.T., and Chen, C.S. *Engineered materials and the cellular microenvironment: a strengthening interface between cell biology and bioengineering. Trends in cell biology*, 2010. **20**(12): p. 705–714.
9. Rompolas, P., Mesa, K.R., and Greco, V. *Spatial organization within a niche as a determinant of stem-cell fate. Nature*, 2013. **502**(7472): p. 513–518.
10. Jansen, K.I., Iwanski, M.K., Burute, M., and Kapitein, L.C. *A live-cell marker to visualize the dynamics of stable microtubules throughout the cell cycle. The Journal of cell biology*, 2023. **222**(5).

11. Hatakeyama, H., Nakahata, Y., Yarimizu, H., and Kanzaki, M. *Live-cell single-molecule labeling and analysis of myosin motors with quantum dots. Molecular biology of the cell*, 2017. **28**(1): p. 173–181.
12. Zhang, Y., Du, Y., Zhuo, Y., and Qiu, L. *Functional Nucleic Acid-Based Live-Cell Fluorescence Imaging. Frontiers in chemistry*, 2020. **8**.
13. Ebrahimi, S.B., Samanta, D., and Mirkin, C.A. *DNA-Based Nanostructures for Live-Cell Analysis. Journal of the American Chemical Society*, 2020. **142**(26): p. 11343–11356.
14. Nishida-Aoki, N., and Gujral, T.S. *Emerging approaches to study cell-cell interactions in tumor microenvironment. Oncotarget*, 2019. **10**(7): p. 785–797.
15. Good, M., and Trepat, X. *Cell parts to complex processes, from the bottom up. Nature*, 2018.
16. Boedtkjer, E., and Pedersen, S.F. *The Acidic Tumor Microenvironment as a Driver of Cancer. Annual Review of Physiology*, 2020. **82**(1): p. 103-126.
17. Kato, Y., Ozawa, S., Tsukuda, M., Kubota, E., Miyazaki, K., St-Pierre, Y., and Hata, R. *Acidic extracellular pH increases calcium influx-triggered phospholipase D activity along with acidic sphingomyelinase activation to induce matrix metalloproteinase-9 expression in mouse metastatic melanoma. The FEBS journal*, 2007. **274**(12): p. 3171–3183.
18. Paradise, R.K., Lauffenburger, D.A., and Van Vliet, K.J. *Acidic Extracellular pH Promotes Activation of Integrin $\alpha_v\beta_3$. PLoS ONE*, 2011. **6**(1).
19. Südhof, T.C. *Calcium control of neurotransmitter release. Cold Spring Harbor perspectives in biology*, 2012. **4**(1).
20. Bader, M.-F., Doussau, F., Chasserot-Golaz, S., Vitale, N., and Gasman, S. *Coupling actin and membrane dynamics during calcium-regulated exocytosis: a role for Rho and ARF GTPases. Biochimica et Biophysica Acta (BBA) - Molecular Cell Research*, 2004. **1742**(1-3): p. 37-49.
21. Sochacki, K., Larson, B., Sengupta, D. et al. *Imaging the post-fusion release and capture of a vesicle membrane protein. Nat Commun.,* 2012. **3**(1154).

22. Ogunmowo, T.H., Jing, H., Raychaudhuri, S., et al. *Membrane compression by synaptic vesicle exocytosis triggers ultrafast endocytosis. Nat Commun.,* 2023. **14**(2888).
23. Mettlen, M., Chen, P.H., Srinivasan, S., Danuser, G., and Schmid, S.L. *Regulation of Clathrin-Mediated Endocytosis. Annual review of biochemistry*, 2018. **87**: p. 871–896.
24. Wen, X., Saltzgaber, G.W., and Thoreson, W.B. *Kiss-and-Run Is a Significant Contributor to Synaptic Exocytosis and Endocytosis in Photoreceptors. Frontiers in cellular neuroscience*, 2017. **11**(286).
25. Chen, Z., De Queiros Silveira, G., Ma, X., Xie, Y., Wu, Y.A., Barry, E., Rajh, T., Fry, H. C., Laible, P.D., and Rozhkova, E.A. *Light-Gated Synthetic Protocells for Plasmon-Enhanced Chemiosmotic Gradient Generation and ATP Synthesis. Angewandte Chemie (International ed. in English)*, 2019. **58**(15): p. 4896–4900.
26. Bashirzadeh, Y., and Liu, A.P. *Encapsulation of the cytoskeleton: towards mimicking the mechanics of a cell. Soft matter.*, 2019. **15**(42): p. 8425–8436.
27. Elani, Y., Law, R.V., and Ces, O. *Vesicle-based artificial cells as chemical microreactors with spatially segregated reaction pathways. Nature communications*, 2014. **5**.
28. Shin, J., and Noireaux, V. *An E. coli cell-free expression toolbox: application to synthetic gene circuits and artificial cells. ACS synthetic biology*, 2012. **1**(1): p. 29–41.
29. Elani, Y. *Interfacing Living and Synthetic Cells as an Emerging Frontier in Synthetic Biology. Angewandte Chemie*, 2021. **60**(11).
30. Vitiello, G., Luchini, A., D'errico, G., Santamaria, R., Capuozzo, A., Irace, C., et al. *Cationic liposomes as efficient nanocarriers for the drug delivery of an anticancer cholesterol-based ruthenium complex. J. Mater. Chem.*, 2015. **B3**: p. 3011–3023.
31. Irace, C., Misso, G., Capuozzo, A., Piccolo, M., Riccardi, C., Luchini, A., et al. *Antiproliferative effects of ruthenium-based nucleolipidic nanoaggregates in human models of breast cancer in vitro: insights into their mode of action. Sci. Rep.*, 2017. **7**(45236).

32. Botello-Smith, W.M., Jiang, W., Zhang, H. et al. *A mechanism for the activation of the mechanosensitive Piezo1 channel by the small molecule Yoda1. Nat Commun.,* 2019. **10**.
33. Pageon, et al. *Mechanoimmunology: molecular-scale forces govern immune cell functions. Molecular Biology of the Cell*, 2018. **29**(16).
34. Schwenen, L., Hubrich, R., Milovanovic, D. et al. *Resolving single membrane fusion events on planar pore-spanning membranes. Sci Rep.,* 2015. **5**(12006).
35. Weber, T., Zemelman, B.V., McNew, J.A., Westermann, B., Gmachl, M., Parlati, F., Söllner, T.H., and Rothman, J.E. *SNAREpins: minimal machinery for membrane fusion. Cell*, 1998. **92**(6): p. 759–772.
36. Fix, M., Melia, T.J., Jaiswal, J.K., Rappoport, J.Z., You, D., Söllner, T. H. Rothman, J.E., and Simon, S.M. *Imaging single membrane fusion events mediated by SNARE proteins. Proceedings of the National Academy of Sciences of the United States of America*, 2004. **101**(19): p. 7311–7316.
37. Herrmann, I.K., Wood, M.J.A. and Fuhrmann, G. *Extracellular vesicles as a next-generation drug delivery platform. Nat. Nanotechnol.*, 2021. **16**: p. 748–759.

Appendix

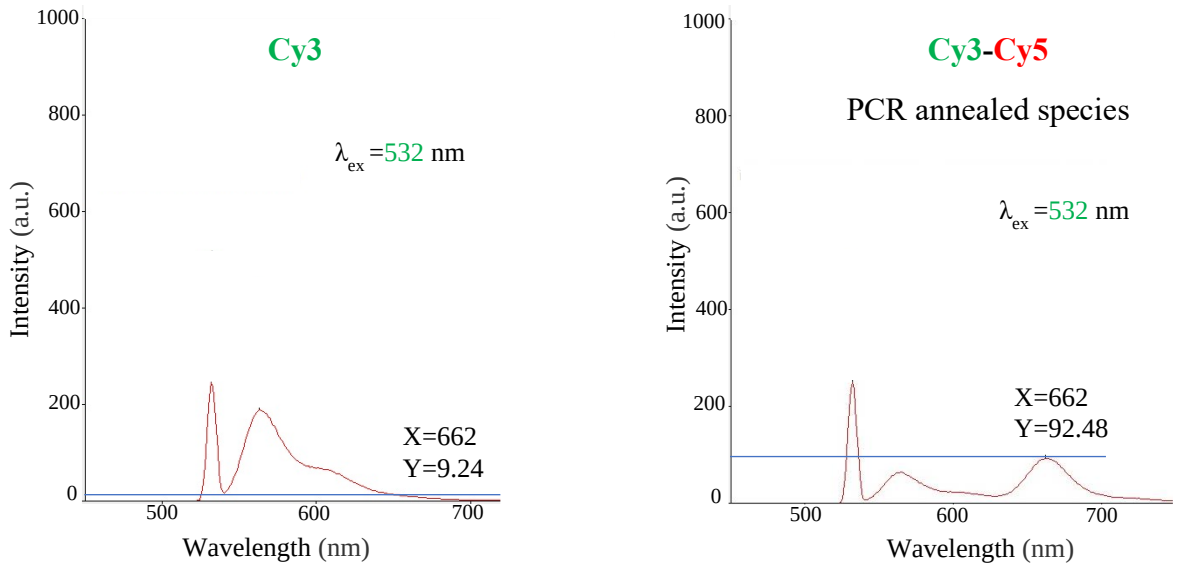

Figure A1- *Comparison of fluorescence emission spectra between Cy3-only (0.5 μM) and Cy3-Cy5 (0.5 μM) species, (subjected to DNA hybridization through controlled temperature decrease), following laser irradiation at 532 nm wavelength.*

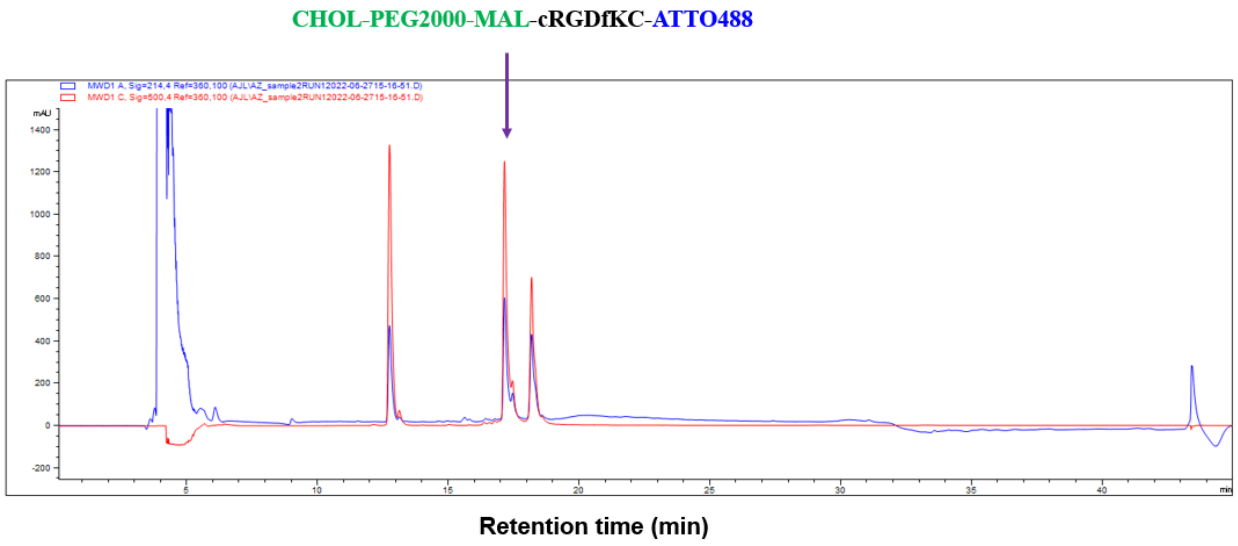

Figure A2- Reverse phase HPLC chromatogram of the Atto488 NHS, cRGDfKC, Chol-PEG2000-Mal reaction mixture. *Monitoring at 214 nm (absorbance of the peptide bond) and 500 nm wavelength (excitation peak of Atto488) was used to purify the final product.*

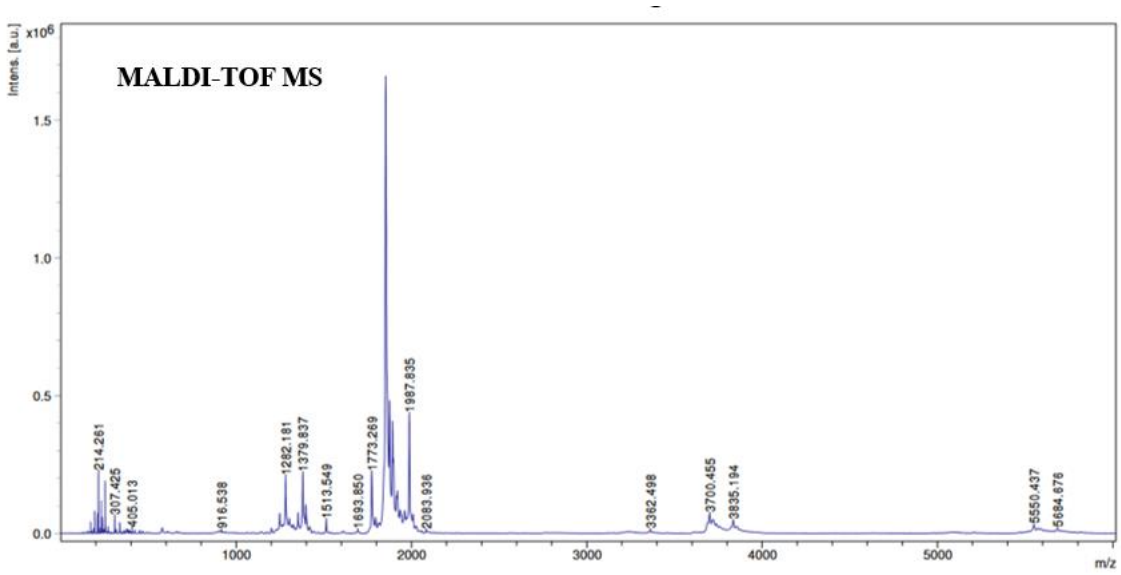

Figure A3- MALDI-TOF MS characterization of the 2nd HPLC peak *shows end compound synthesis (CHOL-PEG2000-MAL-cRGDfKC-ATTO488) with (MW exp = 3687.83 g/mol, MW obs = 3700.455, and possibly 3835.194) and side-product presence in the same eluted HPLC fraction.*

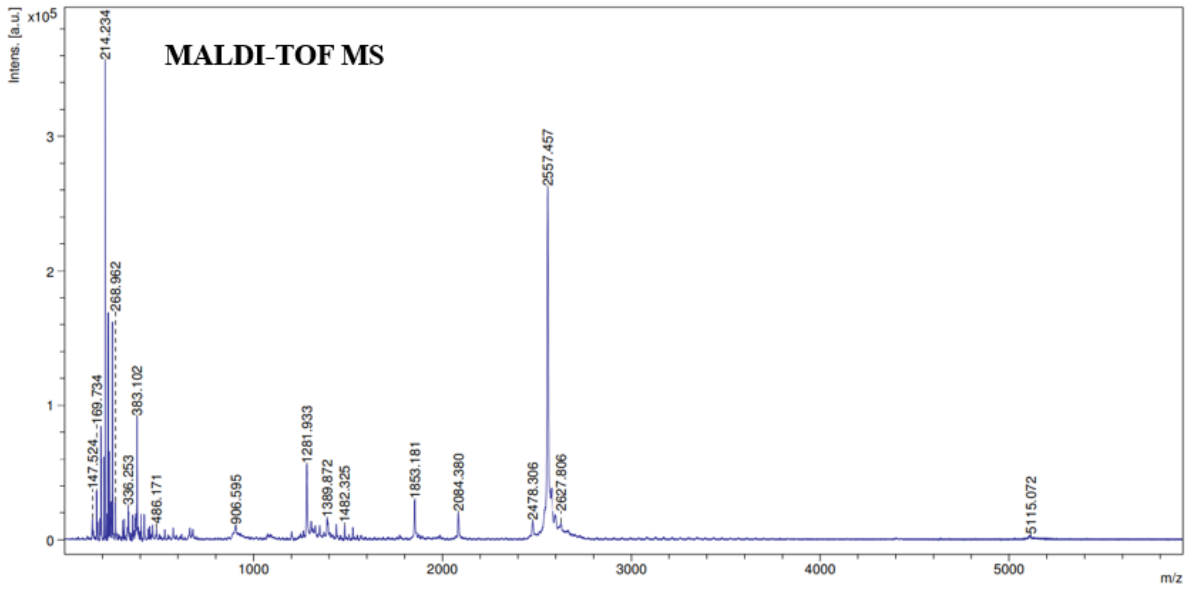

Figure A4- MALDI-TOF MS characterization of the 1st HPLC peak.

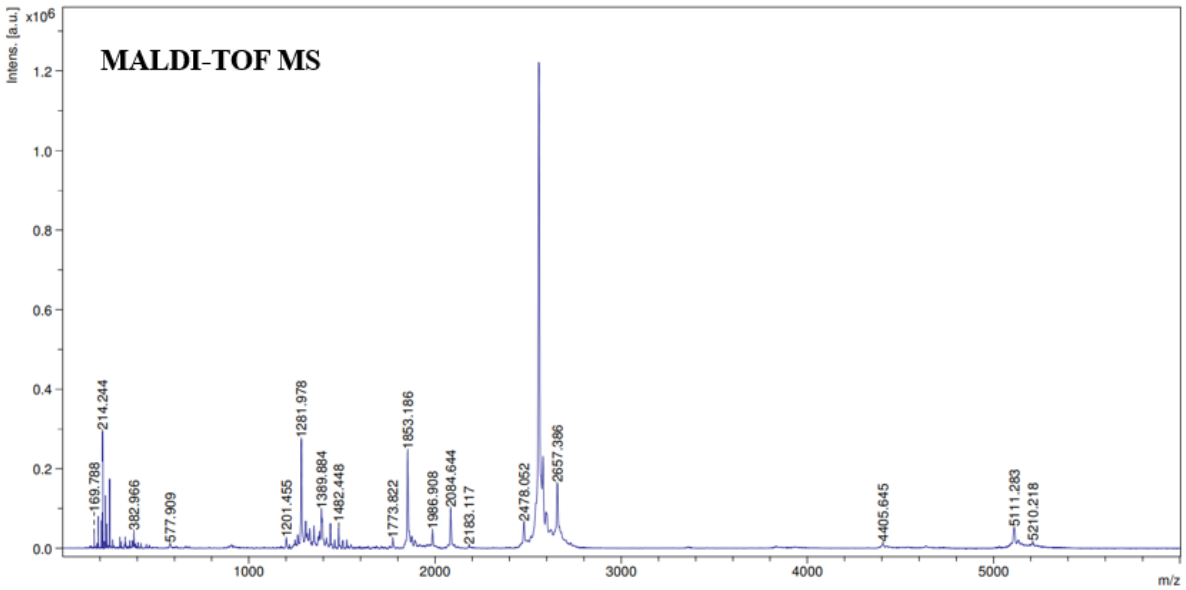

Figure A5- MALDI-TOF MS characterization of the 3rd HPLC peak.

Biophysical Society Conference Abstract

Bio-inspired artificial synapse with chemically mediated intercompartment communication for single molecule cell-synthetic cell interaction studies

Aspasia Zoupa, William D. Jamieson, Jared Whitehead, Arwyn T. Jones and Oliver K. Castell

Cardiff School of Pharmacy and Pharmaceutical Sciences, Redwood Building, Cardiff University, U.K. CF10 3NB

Living systems do not operate in solitude, rather, intimate intercellular communication regulates and coordinates their behaviour. Yet, studying cell-cell interactions is challenging due to the demands of recreating the biological membrane complexity and interfacing with biophysical measurement tools. The study of current models is usually unable to capture the dynamic intermembrane communication encountered in living cells.

We present the development of an artificial double membrane system, a synapse-like architecture, comprised of an encapsulated giant unilamellar vesicle (GUV) and a droplet interface bilayer (DIB), interlinked by cholesterol-tethered DNA interactions.

A DIB is formed by contacting a lipid monolayer-coated aqueous droplet with a lipid-monolayer coated hydrogel support within an oil environment. GUVs generated via electroformation or emulsion phase transfer (EPT) are included within the DIB droplet, affording compositional control of each membrane.

The intermembrane DNA-mediated coupling was characterised by single molecule FRET and diffusion coefficient estimation. Chemical communication across interconnected bilayers was instigated by content exchange via alpha-hemolysin (aHL) nanopores in both DIB and GUV membranes. Vesicular biochemical responses, including initiation of actin polymerisation and ionic transfer, were measured by TIRF microscopy.

The method was expanded to tether individual living cells to the DIB membrane. Here, DIB-anchored integrin-targeting ligands enabled adhesion-mediated artificial membrane/live-cell interaction, creating a biohybrid system. This dual membrane system with synaptic-like intermembrane space constitutes a novel platform for studying self-organisation of mobile, paired intermembrane cleft components, inter-membrane signalling, and trans-synaptic adhesion dynamics with single molecule sensitivity.

Both artificial and biohybrid systems are amenable to precise compositional control and single molecule study, demonstrating the potential to interrogate fundamental membrane mediated biochemistry and multifaceted cellular responses. This will increase fundamental understanding and expand the repertoire of molecularly engineered tools for synthetic biology and biotechnology applications.

Biophysical Society Conference Poster

Bio-inspired Artificial Synapse with Chemically Mediated Intercompartment Communication for Single Molecule Cell-synthetic Cell Interaction Studies

Aspasia Zoupa, William D. Jamieson, Jared Whitehead, Arwyn T. Jones , Oliver K. Castell
Cardiff School of Pharmacy and Pharmaceutical Sciences,
Redwood Building, Cardiff University, U.K. CF10 3NB

Contact details:
ZoupaA@Cardiff.ac.uk
CastellO@Cardiff.ac.uk

Background:

- Cell-cell interactions drive numerous physiological processes associated with health and disease.[1]
- Studying cell-cell interactions is challenging due to the dual demands of recreating the biological membrane complexity and interfacing with biophysical measurement tools.
- The study of current models is usually unable to capture the dynamic intermembrane communication encountered in living cells as they suffer from several constraints,[2] including short-term lifespan, mobility restrictions, absence of dynamic molecule rearrangement, and incompatibility to be probed with current tools.

Objectives:

Develop an artificial double membrane system, a synapse-like architecture, comprised of an encapsulated giant unilamellar vesicle (GUV) and a droplet interface bilayer (DIB), interlinked by cholesterol-tethered DNA interactions, with chemically mediated communication. Expand the artificial system to a biohybrid version by tethering living cells to DIB bilayer via DIB-anchored integrin-targeting ligands.

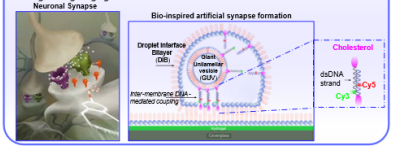

Methods:

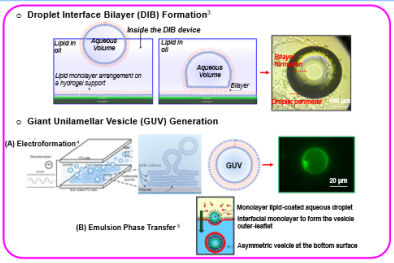

Results:

Artificial Communication System Development

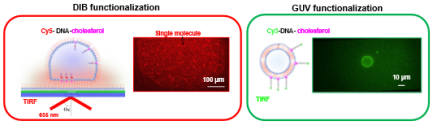

GUV anchorage to DIB via hybridized DNA complements identified by smFRET

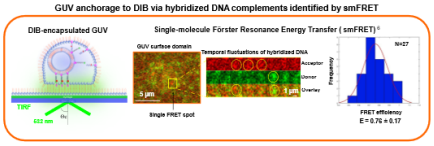

Chemically mediated intercompartment communication viaalpha hemolysin (aHL) nanopores in both DIB and GUV membranes

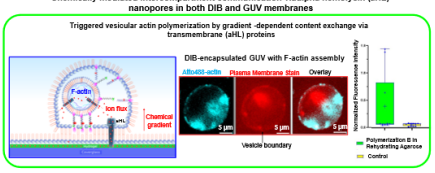

Validation of protein channel functionality in DIB and GUV membranes by optical patch-clamping

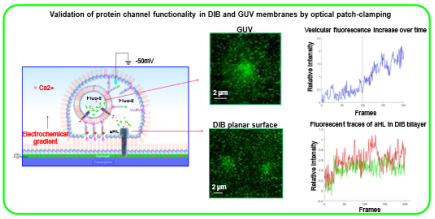

Results:

Biohybrid Interface System Development

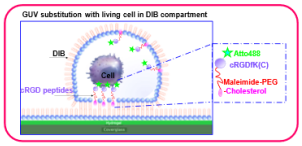

Cell adhesion to peptide-functionalized DIB membrane

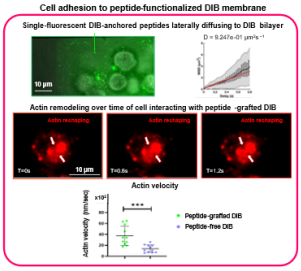

Outlook:

- Construction of artificial and biohybrid double membrane models with synapse-like configurations.
- Incorporation of more cytoskeletal components in the GUV, e.g., myosin motor proteins, to create a force-generating system, more closely mimicking cytoskeletal-dependent membrane processes, such as endocytosis, lamellipodium extension and receptor assortment.
- The hybrid model version could host the T-cell-virus interaction for studies towards effective T-cell activation against different viral variants.
- Recreation of the neuronal synapse to probe vesicle exocytosis modes following plasma membrane depolarization.

Citations:

1. Cooper GM. The Cell: A Molecular Approach. 2nd edition. Sinauer Associates 2000.
2. Castell OK, Allan DW. From biological membranes to biomimetic model membranes. Biotechnol Agron Soc Environ. 2010; vol.14(4):715-725.
3. Thompson PI, Heron AJ, Santoso Y, Wallace MI. Enhanced stability and fluidity in droplet on hydrogel bilayers for measuring membrane protein diffusion. Nano Lett 2007; vol.7(12):3870-3876.
4. Bi R, Yang B, Wang L, Cao W, Han X. Electroformation of giant unilamellar vesicles using interdigitated ITO electrodes. Journal of Electroanal Chemistry. 2013; vol.1(24):7129-7136.
5. Kamiranzad K, Hindley JW, Bolognesi G, Friddin MS, Law RV, Brooks NJ, Ces O, Elani Y. Engineering thermoresponsive phase separated vesicles formed via emulsion phase transfer as a content release platform. Chem Sci. 2018; vol.9(21):4881-4888.
6. Hwy R, Heiring S, Ha T. A practical guide to single molecule FRET. Nature Methods. 2008; vol.5:507-516.